Jets and Energy Flow in Photoproduction using the ZEUS Detector at HERA

Claire Gwenlan

Department of Physics and Astronomy
University College London

Submitted for the degree of
Doctor of Philosophy
March 2003

ProQuest LLC
789 East Eisenhower Parkway
P.O. Box 1346
Ann Arbor, MI 48106-1346

Jets and Energy Flow in Photoproduction using the ZEUS Detector at HERA

Claire Gwenlan

Abstract

The hard photoproduction of jets has been studied using the ZEUS detector at HERA. The data were collected during the 1996-1997 e^+p running period and correspond to an integrated luminosity of 38.6 pb^{-1}. Events were selected with a photon-proton centre-of-mass energy in the range $134 < W_{\gamma p} < 277$ GeV with photon virtualities of $Q^2 < 1$ GeV^2. Jets were defined using the longitudinally invariant $k_\perp$ algorithm in the inclusive mode.

Cross sections for the photoproduction of four high transverse energy jets have been measured. This is the highest order process in QCD to have been studied at HERA to date. Two kinematic regions have been defined: the inclusive and the high mass samples. The high mass sample contains only events with a four jet invariant mass satisfying $m_{4\mathrm{J}} > 50$ GeV. The data are compared to parton shower models which resum leading logarithms to produce multi-parton final states. The inclusive distributions are found to be very sensitive to the underlying event model. Models with no simulation of the underlying event are unable to describe the shape of the distributions. Inclusion of only a soft underlying event is also disfavoured. However, the description of the data is significantly improved by inclusion of multi-parton interactions, which introduces a hard, partonic scattering component to the underlying event. The high mass cross sections are well described by the parton shower models and are relatively insensitive to the underlying event model and, consequently, are considered suitable for comparison with fixed order perturbative QCD calculations when they become available. The rate of four jet photoproduction, relative to that of three jet, shows an excess over the predictions of models which use only initial- and final-state QCD radiation to produce multi-parton final states. The data can be described by models including multi-parton interactions, which provides an additional mechanism for the production of four jets. The data from this analysis have also been used to provide constraints on the parton shower model parameters.

Cross sections for the photoproduction of two jets separated by a large region in rapidity have been measured. Rapidity gap events are defined in terms of the energy flow in the region between the two highest transverse energy jets. Gap fractions, defined as the ratio of the two jet gap cross sections to the two jet inclusive cross sections, have also been measured. An excess of events with a rapidity gap, over that expected from standard QCD, is observed. This can be interpreted as evidence for the exchange of a strongly interacting colour singlet object. The data are well described by the leading logarithmic approximation BFKL pomeron with a choice of $\alpha_s^{pre.} = \alpha_s^{den.} = 0.18$ and $\omega_0 = 0.48$. Taking into account the constraints imposed on the underlying event model from the multi-jets analysis, an estimate of $\mathcal{S} = 65 - 70\%$ has been estimated for the gap survival probability.

In memory of my grandparents

Contents

List of Figures

List of Figures

List of Tables

Chapter 1

Introduction

Present-day elementary particle physics represents mankind's most organised and ambitious effort to answer the apparently simple question: "From what is the Universe made?".

Since Greek times, philosophers and scientists have believed that matter consists ultimately of fundamental particles with no internal structure. Anaximenes of Miletus (570-500 BC) proposed that all matter consists of combinations of the four basic "elements"; air, earth, fire and water. Later, Democritus of Abdera (460-370 BC) developed a theory in which an infinite number of small, indestructible particles combine in different ways to produce all living and non-living matter. These elementary particles were dubbed **atoms**, originating from the Greek word $\alpha\tau\omega\mu\omega\xi$, meaning indivisible.

In 1808, John Dalton proposed that a given element consists of identical atoms and used this model to explain how elements combine to form compounds. Since then, the word atom has been used specifically to describe the smallest unit of an element where *all* atoms of the *same* element have identical chemical properties. In 1869, Dmitri Mendeleev arranged all the known elements into a **Periodic Table** based on atomic mass. The proliferation of elements and the apparent organisation of the table were suggestive of an underlying substructure. Indeed, using this table, Mendeleev was able to correctly predict the existence and properties of further elements.

In 1911, almost half a century later, Rutherford tested the structure of the atom by scattering α-particles off a target of gold atoms [1]. The results of this experiment showed that an atom consists mainly of vacuum, with a small, compact nucleus surrounded by a cloud of electrons. The mass of the atom is concentrated in the central nucleus and the chemical properties arise largely from the orbits of the outer electrons, which vary between different atoms.

Since the Rutherford experiment, the technique of using particles to probe the structure of matter in order to search for further, underlying substructure has been used

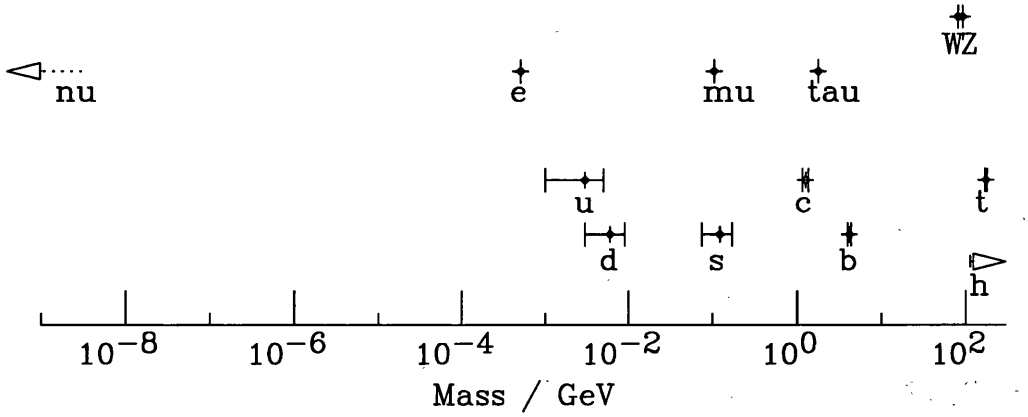

Figure 1.1: The mass values of the Standard Model particles. The error bars indicate the uncertainties on the measured values. Lower limits are shown for the Standard Model Higgs particle. Approximate upper limits on the neutrino masses are shown, based on the direct limit on the mass of the electron neutrino. The photon is assumed to be massless. Diagram taken from [3].

extensively. For example, in 1913, Franck and Hertz [2] showed that atoms have discrete energy levels by scattering electrons on a variety of gases. By 1932, scattering experiments had shown that the nucleus itself consists of sub-atomic particles called protons and neutrons. Later experiments, most notably at the Stanford Linear Accelerator Center (SLAC) during the 1960's, showed that protons and neutrons are also composed of more fundamental particles. These constituents are often referred to as **partons**.

There are four fundamental forces of nature: gravity, electromagnetism and the weak and strong nuclear forces. The latter three have been successfully combined to form the so-called **Standard Model** of particle physics, which embodies all current understanding of the fundamental particles and the interactions between them. The weak interaction is responsible for the radioactive β-decay of nuclei whilst the strong interaction holds together the protons and neutrons in a nucleus. These nuclei then bind together with electrons via the electromagnetic interaction to produce the observed chemical elements.

Within the Standard Model, **elementary** particles are classified according to three basic types: **leptons** (from the Greek meaning "light"), **quarks** and **gauge-bosons**. The mass spectrum of these particles is shown in Fig. 1.1. The leptons and quarks are all fermions (spin-$\frac{1}{2}$ particles), obeying Fermi-Dirac statistics. They are divided into three generations, the properties of which differ only in the mass. The basic properties of these particles, indicating the generations, are listed in Tab. 1.1. The charged leptons (e, μ, τ) can interact via the electromagnetic and weak forces whilst the electrically

		Baryon No. B	Lepton No. L	Charge Q	Mass (GeV)
Leptons	e^-	0	1	-1	0.511×10^{-3}
	ν_e			0	$< 3 \times 10^{-9}$
	μ^-			-1	105.658×10^{-3}
	ν_μ			0	$< 0.19 \times 10^{-3}$
	τ			-1	1.777
	ν_τ			0	$< 18.2 \times 10^{-3}$
Quarks	d	1/3	0	-1/3	$3 - 9 \times 10^{-3}$
	u			+2/3	$1 - 5 \times 10^{-3}$
	s			-1/3	$75 - 170 \times 10^{-3}$
	c			+2/3	1.15-1.35
	b			-1/3	4.0 – 4.4
	t			+2/3	174.3 ± 5.1

Table 1.1: Some basic properties of leptons and quarks. The particles are grouped into the three generations, the properties of which differ only in their mass. The charge units are defined such that the electron charge is -1. Not listed in the table are the anti-particles of the leptons and quarks. For the present illustration, these are identical to the corresponding particles except for the reversal of the sign on their B, L and Q quantum numbers. The mass values have been taken from [4].

neutral neutrinos (ν_e, ν_μ, ν_τ) interact only via the weak force. In contrast, the quarks (*u, d, s, c, b, t*) are able to interact via the electromagnetic, weak and strong forces. All corresponding anti-particles in both the lepton and quark sectors also belong to the fundamental particles in the Standard Model. The leptons and quarks are currently thought to be point-like, or elementary particles, with no internal structure. Composite particles containing three quarks (e.g. proton, neutron), are called **baryons** (from the Greek meaning "heavy"), while those containing a quark and an anti-quark (e.g. π, ρ, K) are called **mesons**. These particles, which have in common that they all interact via the strong force, are collectively known as **hadrons**. The fundamental interactions of the Standard Model are mediated via the exchange of the intermediate vector gauge-bosons. These are spin-1 particles obeying Bose-Einstein statistics. The basic properties of these particles are listed in Tab. 1.2.

The structure of matter was first translated into a theoretical framework in the 1930's by the development of Quantum ElectroDynamics (QED). This is a **gauge theory**, which describes the interactions of electrons and photons in a way that is both quantised and relativistically invariant. In current particle physics, both the weak and strong interactions of leptons and quarks are also described by gauge theories.

	Charge Q	Mass (GeV)	Interaction	Range	Relative Coupling
γ	0	$< 2 \times 10^{-25}$	electromagnetic	∞	10^{-2}
Z^0	0	91.188 ± 0.002	weak	$\frac{1}{M_W}$	10^{-6}
$W^{\pm}$	± 1	80.419 ± 0.056			
g	0	$\sim$ MeV	strong	1 fm or $\sim \frac{1}{m_\pi}$	1

Table 1.2: Some basic properties of the gauge bosons. The charge units are defined with respect to the electron charge as in Tab. 1.1. The mass values are taken from [4]. Note that the masses of the particles refer to the experimental values and limits. The theoretical mass values of the photon and the gluon are 0. The relative couplings are defined such that the strong coupling has a value of 1.

The electromagnetic and weak interactions are not independent and are recognised in the Standard Model as being manifestations of a single **electroweak** force. While the electromagnetic and weak forces forces have different coupling strengths at "everyday" energy scales, they are similar in strength at high energies. In 1979, A. Salam, S. L. Glashow and S. Weinberg received the Nobel Prize for the unification of these two forces into a single electroweak theory.

The strong interaction is described by the theory of Quantum ChromoDynamics (QCD). This emerged as a mathematically consistent theory in the 1970's. Within the Standard Model, the strong force is independent of the electroweak interaction. However, one of the aims of particle physics is to unify all the forces (including gravity) so that they can all be described in terms of one, fundamental interaction.

The parameters of the electroweak theory have been measured at SLAC and by the LEP experiments at CERN with great precision [5]. Experiments at LEP, HERA and the Tevatron have also verified the validity of QCD theory to a reasonable degree of precision [6]. However, the nature of the strong interaction continues to pose many questions and the final state in hadronic collisions remains, in general, poorly understood. This is largely due to the fact that the theory of QCD is not completely analytically calculable. For example, processes such as the **fragmentation** of partons into hadrons and interactions between beam remnants (the so-called **underlying event**), which occur at low energy scales, are not well understood. Additional complications include the calculation of (for example) multi-jet final states at higher orders. Although, in principle, such calculations are possible, they soon become impractical.

In this thesis, two studies are presented which aim at both establishing the current level of understanding and highlighting areas that require further theoretical input.

The first analysis is a study of multi-jets in photoproduction. Measurements of inclusive, two jet and three jet production [7–19] have already been carried out at HERA. In this thesis, the first HERA measurement of four jet photoproduction is presented (see Chapter 7). This is the highest order QCD process to have been measured at HERA to date. The aim of the analysis is to study the underlying QCD dynamics of such higher order processes. The data presented here have also been included in the JETWEB [20] database, together with a variety of other measurements from LEP, HERA and the Tevatron, to tune the parameters of QCD models. The aim of the tuning is to provide a global set of recommended parameters that produce results consistent with all current measurements. This is a large endeavor and a summary of the initial results is presented here.

The second analysis is a study of rapidity gaps between jets in photoproduction (see Chapter 8). The results of previous gaps-between-jets measurements carried out at both the Tevatron [21, 22] and at HERA [23–25] have been interpreted as evidence for the exchange of a strongly interacting colour singlet object. This thesis presents the latest and highest-statistics HERA measurement of this type. The ultimate aim is to fully understand the gap producing mechanism within the context of QCD. However, the model predictions are extremely sensitive to the effects of fragmentation and the underlying event. These processes must be better understood before a detailed interpretation of the measurement is possible. In this thesis, the constraints imposed on the models from the JETWEB tuning are considered when interpreting the results.

Chapter 2

Lepton-Hadron Physics and Quantum Chromodynamics

The HERA collider provides the opportunity to test current understanding of the theory of QCD through measurements of lepton-proton scattering. In this chapter, QCD theory is introduced, concentrating particularly on those aspects of relevance to the physics taking place at HERA. Following a brief historical review, the fundamental properties of QCD are discussed. The physics of lepton-proton scattering is then described, with emphasis on the specific physics processes relevant to this thesis. A brief description of the phenomenology behind a general QCD model is also given.

2.1 Historical Preface

The development of QCD was prompted in the 1960's by the accumulation of data on hadronic resonances. The results suggested that the observed mesons and baryons were not fundamental particles, instead consisting of some other, more elementary particles. In 1961, Gell-Mann and Ne'eman [26] independently proposed a classification scheme which used SU(3) symmetry to arrange particles according to their charge and strangeness. This scheme, dubbed the **Eightfold Way**, was used to predict the existence of the Ω^-. This particle, which carries charge -1, strangeness -3 and spin 3/2, was discovered in 1964 at the Brookhaven National Laboratory [27].

The success of the Eightfold Way led Gell-Mann [28] and Zweig [29] to independently suggest that hadrons were composed of a family of spin-1/2 particles, which they called quarks. Each quark was required to carry a fractional charge and transform under an SU(3) symmetry called **flavour**. This so-called Quark Model was able to explain the properties of all hadrons known at the time. In this model, baryons consist of three **valence** quarks, and mesons consist of quark-anti-quark pairs.

However, despite the apparent success of the Quark Model, the existence of particles such as the Δ^{++} and Ω^{-}, which carry three quarks of the same flavour and in the same spin-state, was an apparent violation of the **Pauli Exclusion Principle**. In 1965, Greenberg [30] postulated the existence of an additional quantum number, called **colour**. Quarks would be allowed to carry one of three possible colour quantum numbers (red, green, blue) and naturally occurring particles must be colourless*. However, the lack of any observable evidence for the existence of quarks led many to believe that they were useful only as mathematical tools. Indeed, Gell-Mann himself said in 1964: "...such particles [quarks] presumably are not real, but we may use them in our field theory anyway".

In 1968, **Deep Inelastic Scattering** (DIS) experiments (in which incident electrons are scattered with large momentum transfer off a hadronic target) taking place at SLAC provided evidence to support the Quark Model. The results showed that the electron behaved as if it were scattering off free point-like constituents (partons) within the proton. In 1969, Bjorken and Paschos [31] identified these constituents with the spin-$\frac{1}{2}$ quarks of Gell-Mann and Zweig. The eight neutral gluons (which are the field quanta responsible for the strong interaction) were added to the model in 1971 [32]. The identification of partons as quarks and gluons led to the emergence of QCD as a mathematically consistent theory during the 1970's.

2.2 Quantum Chromodynamics

Just as the theory of QED describes the interactions of leptons and quarks via the electromagnetic interaction, QCD describes the interactions of quarks via their colour quantum numbers. QCD is an unbroken Yang-Mills† gauge theory with the gauge-bosons being the massless, chargeless gluons. Both quarks and gluons carry colour, which is an exact internal SU(3) symmetry of the QCD Lagrangian. Although the structure of QCD is very similar to that of QED, there is one fundamental difference. The gauge group of QCD is **non-abelian**. This means that gluons, unlike the photons in QED, carry the charge of their gauge field and so are able to couple to each other.

The consequences of this gluon self-coupling may be deduced by comparing the **charge-screening** effects in QED and QCD. For example, in QED an electron may emit a photon which can then fluctuate into an electron-positron pair. In this way, the original electron is surrounded by electron-positron pairs which become polarised so that the positive charges are preferentially closer to the original, negatively charged, electron. The charge of the initial electron is said to be *screened*. At large distances, less of

*Allowed combinations are: qqq ($\bar{q}\bar{q}\bar{q}$) each carrying a different colour rgb (anti-colour $\bar{r}\bar{g}\bar{b}$) or $q\bar{q}$ pairs carrying the colour and corresponding anti-colour ($r\bar{r}$,$g\bar{g}$,$b\bar{b}$).

†That is, a locally gauge invariant theory.

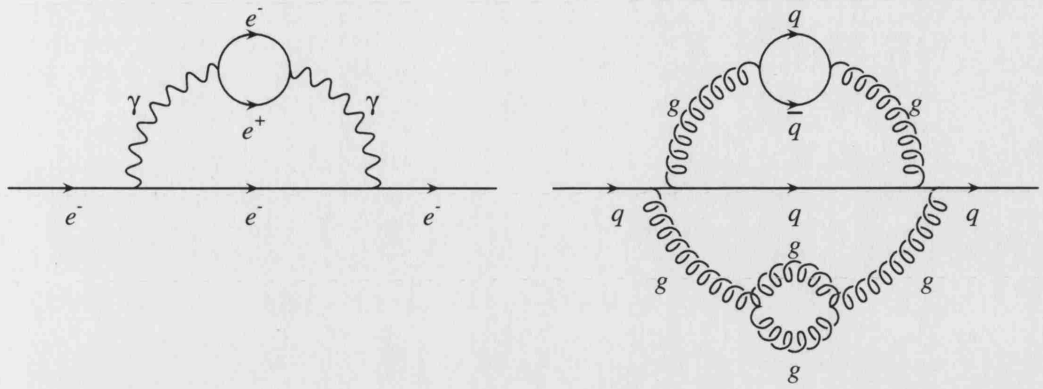

Figure 2.1: Charge-screening in (left) QED and (right) QCD. In QED, the initiating electron emits a photon which can fluctuate into electron-positron pairs which screens the charge of the original electron. In QCD, an emitted gluon may fluctuate into a quark-anti-quark or a gluon-gluon pair.

the charge can be "seen" and the coupling strength of the electromagnetic interaction, described by the coupling constant α, decreases. Analogously, a quark in QCD will constantly emit gluons, some of which fluctuate into quark-anti-quark pairs. However, the additional gluon coupling means that fluctuations into gluon-gluon pairs are also possible. In QCD, the latter effect dominates. Consequently, the value of the strong coupling α_s increases at large distances (or small energies); a phenomenon known as **running**. The charge screening effects in QED and QCD are illustrated in Fig. 2.1.

2.2.1 The Running Coupling

The so-called running of the coupling constant with energy (distance) has been confirmed experimentally, as illustrated in Fig. 2.2. At Leading Order (LO), the running coupling of QCD obeys an equation of the form,

$$\frac{\mathrm{d}\alpha_s(\mu^2)}{\mathrm{d}\log\mu^2} = -b_0\alpha_s^2(\mu^2) \tag{2.1}$$

where μ^2 is some external energy scale, usually taken to be the negative square of the four-momentum transfer in the interaction, Q^2. The constant term, b_0, is given by $b_0 = (33 - 2n_f)/12\pi$ where n_f is the number of active flavours at the scale μ^2. Equation 2.1 integrates to give,

$$\alpha_s(\mu^2) = \frac{1}{b_0 \log\left(\mu^2/\Lambda^2_{\mathrm{QCD}}\right)} \tag{2.2}$$

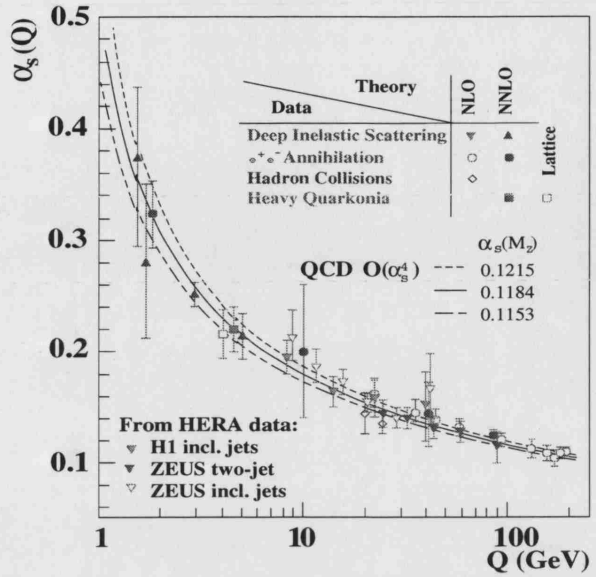

Figure 2.2: A compilation of data showing the running of $\alpha_s(Q)$. The downwards pointing triangles show measurements made from HERA data and the lines show the QCD predictions for three different values of $\alpha_s(M_Z)$. Diagram from [34].

where Λ_{QCD} is a parameter of QCD which depends on the renormalisation scheme and scale μ_r, and also on the number of active flavours at the scale μ^2. The running of the coupling constant is discussed in more detail in Appendix A.

The parameter Λ_{QCD} must be determined experimentally and is typically $\mathcal{O}(100\text{ MeV})$. The value of α_s must also be extracted from experiment, since it determines the strength of the QCD interaction and is not predicted by the theory. The most precise values have been obtained from studies of Z^0 and τ decays at LEP, scaling violations in structure functions at HERA, quarkonium decay branching fractions and lattice calculations of quarkonium mass splittings. These results, together with those from other, less precise, measurements, yield a current world average of $\alpha_s(M_Z) = 0.1172 \pm 0.0020$ [33] at the scale of the Z^0 boson mass ($M_Z = 91.1876$ GeV).

Equation 2.2 shows that $\alpha_s(\mu^2)$ varies as the inverse of the logarithm of the scale μ^2. For $n_f \leq 16$, b_0 is positive. This means that α_s decreases as μ increases (corresponding to decreasing distance) so that when $\mu^2 \gg \Lambda^2_{QCD}$ then $\alpha_s \ll 1$. This is known as **asymptotic freedom** ($\alpha_s \to 0$ as $\mu \to \infty$). In this case, perturbative methods may be applied in QCD calculations. Processes where perturbative QCD (pQCD) is applicable are often called **hard interactions** and require the presence of a **hard scale**. In contrast, as $\mu^2 \to \Lambda^2_{QCD}$, $\alpha_s \sim \mathcal{O}(1)$. In this case, each successive order in a perturbative expansion is not necessarily smaller than the previous order. This means that the expansion does not converge and pQCD is not applicable. Interactions at these scales

are often called **soft processes**. The description of soft interactions generally requires non-perturbative techniques such as phenomenological models, empirical calculations or experimental results. The HERA collider provides an ideal testing ground for QCD since both hard and soft processes occur within the same experiment.

A consequence of the increase in α_s with increasing distance is the property of **confinement** ($\alpha_s \rightarrow \infty$ as $\mu \rightarrow \Lambda_{\mathrm{QCD}}$). As two colour charges are separated, the potential energy between them increases until it is energetically favourable for further particles to be created from the vacuum to shield the colour charge. As a result, free quarks and gluons are not observed directly. Instead, they are *confined* inside hadrons. In a hard QCD interaction, hadrons are produced which travel in a direction approximately along that of the incoming particle. These streams of particles are commonly called **jets**, the properties of which can be measured in a detector. According to **Local Parton Hadron Duality** (LPHD) [35], the distribution of hadrons reflects that of the partons involved in the initiating subprocess. Therefore, the measurement of (for example) jets provides information on the underlying dynamics of the interaction.

2.3 Lepton-Proton Scattering at HERA

In a general lepton-proton (ep) collision, the incoming, high-energy lepton scatters from the hadronic system via the exchange of a virtual gauge-boson, as illustrated in Fig. 2.3. The scattering process is mediated by either the electromagnetic or the weak force. In the first case, the exchanged boson is a virtual photon (γ^*) while, in the second, the interactions may proceed via the exchange of either a Z^0 or $\mathrm{W}^{\pm}$. The exchange of the virtual boson results in some hadronic final state and the interacting parton from the proton is scattered through an angle γ_h. In a Neutral Current (NC) event, the exchanged boson can be a γ^* or a Z^0. In this case, the incoming lepton is simply scattered through some angle, θ_e. A correct treatment of the NC cross section should include contributions from both the γ^* and the Z^0 separately, together with the $\gamma^* - \mathrm{Z}^0$ interference term. In the case of a Charged Current (CC) event, the interaction is mediated by a $\mathrm{W}^{\pm}$ boson. In this case, the final-state lepton is a neutrino, which can only be detected via missing energy and momentum.

A generic lepton-proton scattering event is illustrated in Fig. 2.3. Here, the four-momenta of the incoming and scattered lepton are labelled k and k', the four-momentum of the proton is p and the four-momentum transferred between the lepton and proton system is denoted by,

$$q = k - k'.$$

The exchanged boson is **space-like** with $q^2 < 0$ GeV^2. Therefore lepton-proton scattering at HERA provides a complementary kinematic regime to that of other

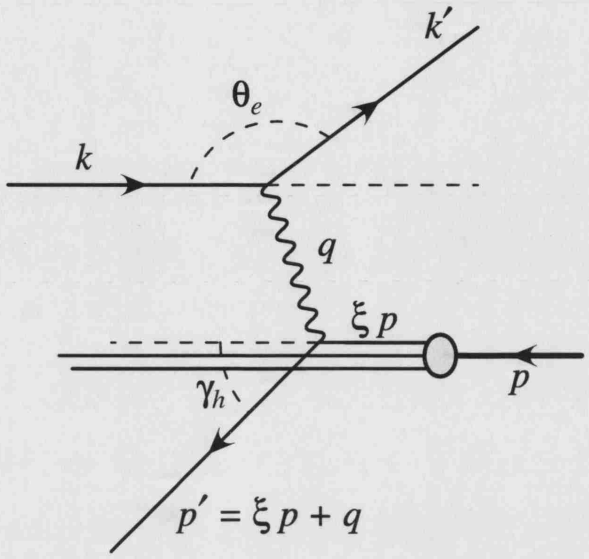

Figure 2.3: The kinematics of lepton-proton scattering at HERA.

collider experiments such as LEP and Tevatron, in which the exchanged boson can be **time-like**. For convenience, the positive quantity, Q^2 , is introduced such that,

$$Q^2 = -q^2 = -(k - k')^2 \approx 2k.k', \tag{2.3}$$

where all lepton masses have been neglected. This quantity is often referred to as the **virtuality** of the exchanged gauge-boson and ranges from $0 < Q^2 < s$ where s is the centre-of-mass energy squared. In high energy processes, the mass of the proton may also, to a good approximation, be neglected. In addition, the invariant mass of the final hadronic system, which is also the centre-of-mass energy squared of the virtual boson-proton system, is given by,

$$W^2 = (p + q)^2 \approx 2p.q + q^2 \equiv 2p.q - Q^2. \tag{2.4}$$

Introducing the Lorentz invariant, dimensionless quantities, x and y,

$$x = \frac{-q^2}{2p.q} = \frac{Q^2}{2p.q}, \tag{2.5}$$

$$y = \frac{p.q}{p.k}, \tag{2.6}$$

such that $0 \leq x, y \leq 1$, leads to an alternative expression for W^2,

$$W^2 = Q^2 \left[\frac{1}{x} - 1\right]. \tag{2.7}$$

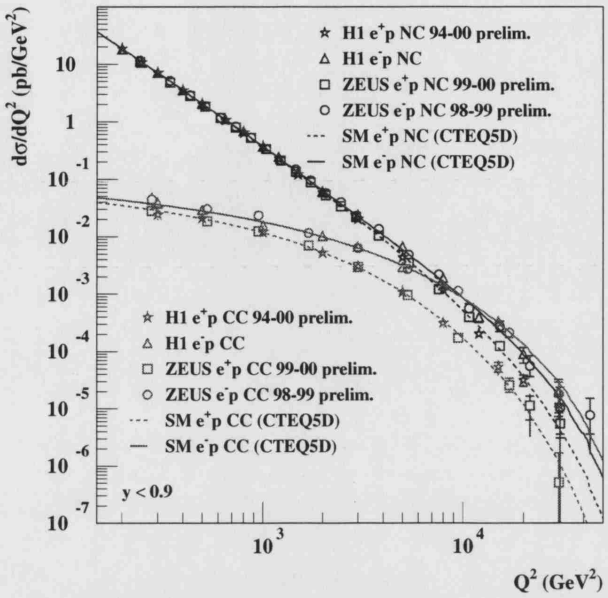

Figure 2.4: The neutral and charged current DIS cross sections as a function of Q^2.

The quantity, x, is called the **Bjorken Scaling variable** [36]. In a frame where the proton has infinite momentum, x corresponds to the fraction of the proton momentum taking part in the interaction. In the proton rest frame, the variable y, also referred to as the **inelasticity**, is the fraction of the lepton-beam energy transferred to the photon such that,

$$y = \frac{E - E'}{E} = \frac{E_\gamma}{E}. \tag{2.8}$$

The total invariant mass of the colliding system, s, is given by

$$s = (p + k)^2 \approx 2p.k = \frac{Q^2}{xy}. \tag{2.9}$$

Hence, for a fixed centre-of-mass energy, $\sqrt{s}$, any two of the three Lorentz invariant quantities given in Eqs. 2.3, 2.5 and 2.6 are required to completely describe the kinematics of lepton-proton scattering. Note also, that in the **collinear approximation** (see Section 2.7.1), $Q^2 \to 0$ GeV^2 and $q = yk$ such that the photon and scattered lepton are collinear. In this case, Eq. 2.4 becomes,

$$W^2 \approx 2p.q = ys. \tag{2.10}$$

The variable Q^2 may be visualised as a measure of the resolving power of the virtual boson. The wavelength of the bosonic probe, λ, is related to the magnitude of its

three-momentum, $|\mathbf{q}|$, via $\lambda = \frac{1}{|\mathbf{q}|}$. With $\mathbf{q} = \mathbf{k} - \mathbf{k}'$ and $q_0 = E - E' = \nu$ then,

$$|\mathbf{q}| = \left[q_0^2 + Q^2\right]^{1/2} = \left[\nu^2 + Q^2\right]^{1/2}. \tag{2.11}$$

In the proton rest frame, $p.q = M(E - E') = M\nu$, where M is the mass of the proton. The variable ν is then simply interpreted as the energy transferred by the lepton to the proton in the proton rest-frame. Substitution into Eq. 2.5 leads to the expression,

$$\nu = \left(\frac{Q^2}{2Mx}\right). \tag{2.12}$$

Substitution of 2.12 into 2.11 then gives,

$$|\mathbf{q}| = \left[\left(\frac{Q^2}{2Mx}\right)^2 + Q^2\right]^{1/2} = \left(\frac{Q^2}{2Mx}\right)\left[1 + \frac{(2Mx)^2}{Q^2}\right]^{1/2} \approx \left(\frac{Q^2}{2Mx}\right) \tag{2.13}$$

for $\frac{Q^2}{2Mx} \gg 1$. Therefore, the wavelength of the resolving virtual boson is,

$$\lambda = \frac{2Mx}{Q^2}. \tag{2.14}$$

Clearly, an increase in Q^2 causes a decrease in the wavelength, allowing the boson to resolve smaller objects.

In the case of γ^* exchange, the form of the propagator is $\frac{-ig_{\mu\nu}}{q^2}$. Therefore, the cross section falls as $\sim \frac{1}{Q^4}$, causing the low Q^2 processes to dominate. At low Q^2, the total lepton-proton cross section is dominated by γ^* exchange, with contributions from the massive Z^0 and $W^{\pm}$ being heavily suppressed for $Q^2 \ll M^2_{Z,W} \sim 10^4$ GeV^2. The limit $\sim 10^4$ GeV^2 is known as the **electroweak unification scale**. For $Q^2 \gtrsim 10^4$ GeV^2, the NC and CC cross sections are found to be of comparable size. This behaviour is illustrated graphically in Fig. 2.4 and supports electroweak unification.

In the theory of QCD, perturbative calculations can be applied down to a scale of $Q^2 \approx \Lambda^2_{\mathrm{QCD}}$. **Deep Inelastic Scattering** (DIS) events are classified as those for which the boson virtuality is much larger than the QCD scale parameter, $Q^2 \gg \Lambda^2_{\mathrm{QCD}}$. In this case it is the quantity Q^2 itself that provides the hard scale for the interaction. However, as indicated by the expression for the γ^* propagator, events are dominated by the exchange of quasi-real photons with virtuality $Q^2 \sim 0$ GeV^2. This type of process is known as **photoproduction** and is the class of event that is studied in this thesis. In photoproduction events, Q^2 is too small to be viewed as the hard scale of the interaction. In order to allow the possibility of comparing experimental results with pQCD calculations, an alternative hard scale is required. Such alternatives include the transverse energy of the observed jets, the large quark masses in heavy flavour production etc.

2.4 The ep Cross Section and Structure Functions

The expression for the total NC lepton-proton (ep) scattering cross section can be written in terms of a leptonic tensor, $L^{\mu\nu}$, and a hadronic tensor, $W^{\mu\nu}$, such that,

$$d\sigma^{ep} \sim L_{\mu\nu}W^{\mu\nu}. \tag{2.15}$$

The leptonic vertex is independent of the hadronic vertex and is completely calculable within electroweak theory. In LO QED, the leptonic tensor $L_{\mu\nu}$ is given by,

$$L_{\mu\nu} = 2\left[k'_\mu k_\nu + k'_\nu k_\mu + \frac{q^2}{2}g_{\mu\nu}\right] \tag{2.16}$$

where $g_{\mu\nu}$ is the metric tensor and the mass of the electron has been ignored ($Q^2 \gg m_e^2$). The hadronic tensor, $W_{\mu\nu}$, parameterises everything that occurs at the hadronic vertex. This includes a completely unknown non-perturbative component. In its most general form, $W_{\mu\nu}$ is constructed from $g_{\mu\nu}$ and the four-momenta of the proton, p, and the photon, q, as

$$W^{\mu\nu} = -W_1 g^{\mu\nu} + \frac{W_2}{M^2}p^\mu p^\nu + \frac{W_4}{M^2}q^\mu q^\nu + \frac{W_5}{M^2}(p^\mu q^\nu + q^\mu p^\nu) \tag{2.17}$$

where M is the mass of the proton and the W_i's are the inelastic **structure functions**. Note that the anti-symmetric contribution (W_3) to $W^{\mu\nu}$ has been ignored in this expression. $L_{\mu\nu}$ is symmetric since weak interactions are being ignored in this discussion. Therefore, after insertion into Eq. 2.15, all anti-symmetric terms vanish.

Assuming conservation of current at the proton vertex, $q_\mu W^{\mu\nu} = q_\nu W^{\mu\nu} = 0$,

$$W_5 = -\frac{p.q}{q^2}W_2; \quad W_4 = \left(\frac{p.q}{q^2}\right)^2 W_2 + \frac{M^2}{q^2}W_1. \tag{2.18}$$

Therefore, only two of the four inelastic structure functions are independent. It is then possible to rewrite Eq. 2.17 as,

$$W^{\mu\nu} = W_1\left(-g^{\mu\nu} + \frac{q^\mu q^\nu}{q^2}\right) + W_2\frac{1}{M^2}\left(p^\mu - \frac{p.q}{q^2}q^\mu\right)\left(p^\nu - \frac{p.q}{q^2}q^\nu\right) \tag{2.19}$$

where W_1 and W_2 are dimensionless functions of the Lorentz scalar variables that can be constructed from the four-momenta at the hadronic vertex. For example, the Lorentz invariants ν and Q^2 may be used, such that $W_1 \equiv W_1(\nu, Q^2)$ and $W_2 \equiv W_2(\nu, Q^2)$ where,

$$\nu = \frac{p.q}{M} = \frac{Q^2}{2Mx} = y\left(\frac{p.k}{M}\right). \tag{2.20}$$

In the proton rest frame, $\nu = E - E'$, as stated in Section 2.3.

Using the form of the lepton tensor, $L_{\mu\nu}$, it can be shown (see for example [37]) that in the proton rest frame, the cross section can be written as,

$$d\sigma^{ep} \sim 4E_e E'_e \left[2W_1(\nu, Q^2) \sin^2 \frac{\theta}{2} + W_2(\nu, Q^2) \cos^2 \frac{\theta}{2} \right]. \tag{2.21}$$

where the angle θ is that between the initial and scattered lepton directions.

It is conventional to rewrite the structure functions, W_i, in terms of x and Q^2,

$$F_1(x, Q^2) = MW_1(\nu, Q^2) \tag{2.22}$$

$$F_2(x, Q^2) = \nu W_2(\nu, Q^2) = \frac{p.q}{M} W_2(x, Q^2). \tag{2.23}$$

The $F_i(x, Q^2)$ are now the structure functions which parameterise the structure of the proton, as seen by the virtual boson.

Introducing a term which takes account of parity violation (which is equivalent to the addition of the anti-symmetric term $i\epsilon^{\mu\nu\rho\sigma} p_\rho q_\sigma W_3$ in Eq. 2.17), the double differential cross section for NC scattering is then given by,

$$\frac{\mathrm{d}^2\sigma^{e^\pm p}}{\mathrm{d}x\mathrm{d}Q^2} = \frac{4\pi\alpha^2}{xQ^4} \left[xy^2 F_1(x, Q^2) + (1-y) F_2(x, Q^2) \mp (y - \frac{y^2}{2}) x F_3(x, Q^2) \right] \tag{2.24}$$

where α is the fine structure constant. The quantity F_2 is the generalised structure function of γ and Z^0 exchange and F_3 is the parity violating term arising only through the $\gamma - \mathrm{Z}^0$ interference and Z^0 terms. At large Q^2 ($\sim M_{\mathrm{Z}}^2$), Z^0 exchange is important and gives contributions to all structure functions from both Z^0 exchange alone (suppressed by a factor $\frac{Q^4}{(Q^2+M_{\mathrm{Z}}^2)^2}$) and $\gamma - \mathrm{Z}^0$ interference (suppressed by $\frac{Q^2}{(Q^2+M_{\mathrm{Z}}^2)}$).

The **longitudinal structure function**, F_{L} is given by,

$$F_{\mathrm{L}} \equiv F_2 - 2xF_1. \tag{2.25}$$

Substitution of Eq. 2.25 into Eq. 2.24 then gives,

$$\frac{\mathrm{d}^2\sigma^{e^\pm p}}{\mathrm{d}x\mathrm{d}Q^2} = \frac{4\pi\alpha^2}{xQ^4} \left[Y_+ F_2 - y^2 F_{\mathrm{L}} \mp Y_- x F_3 \right], \tag{2.26}$$

where the helicity dependence of the electroweak interaction is contained within,

$$Y_\pm = 1 \pm (1-y)^2 \tag{2.27}$$

and mass terms have been neglected. The cross section is given at the **Born level**, including no corrections for higher order QED contributions. For $Q^2 \ll M_{\mathrm{Z}}^2$, xF_3 is negligible and so is neglected in all further discussion. A more detailed description of each term is given, for example, in [6].

2.4.1 Factorisation

It is not possible to treat the *ep* scattering process using *only* perturbative methods. Small scale, long-distance interactions which contribute to the scattering cross section, and which occur long before the hard scatter, are absorbed into the **Parton Distribution Functions** (PDFs). These long-distance contributions can be factored out and the remaining cross section depends only on high Q^2 (small α_s) contributions. As a result of asymptotic freedom, this is calculable in pQCD. This **factorisation** property is valid to all orders in pQCD [38]. However, factorisation introduces an additional scale, μ, into QCD theory. Physics at a scale smaller than μ cannot be calculated using perturbative methods. In mathematical terms, μ reduces the range of integration over the relevant diagram. To first order, the structure functions may be written as,

$$F_1(x,Q^2) = \sum_i \int_x^1 \frac{\mathrm{d}z}{z} C_1^i \left(\frac{x}{z}, \frac{Q^2}{\mu^2}, \alpha_s(Q^2)\right) f_i(z,Q^2) \tag{2.28}$$

$$\frac{F_2(x,Q^2)}{x} = \sum_i \int_x^1 \frac{\mathrm{d}z}{z} C_2^i \left(\frac{x}{z}, \frac{Q^2}{\mu^2}, \alpha_s(Q^2)\right) f_i(z,Q^2) \tag{2.29}$$

where i denotes a gluon, quark or anti-quark and e^i is the charge of i. The C_j^i are coefficient functions which are calculable in pQCD and depend on the physics process being considered. The $f_i(z,Q^2)$ are the PDFs which now contain all non-perturbative contributions. At LO,

$$C_j^i = c_j^i e_i^2 \delta\left(1-\frac{x}{z}\right); \qquad j = 1,2$$

with $c_1 = 1/2$ and $c_2 = 1$.

Integrating Eq. 2.28 gives,

$$\begin{aligned} F_1(x,Q^2) &= \frac{1}{2}\sum_i \int \frac{\mathrm{d}z}{z} e_i^2 \delta\left(1-\frac{x}{z}\right) f_i(z,Q^2) \\ &= \frac{1}{2}\sum_i \int \frac{\mathrm{d}z}{z} z e_i^2 \delta(z-x) f_i(z,Q^2) \\ &= \frac{1}{2}\sum_i e_i^2 f_i(x,Q^2). \end{aligned} \tag{2.30}$$

Similarly, Eq. 2.29 integrates to give,

$$F_2(x,Q^2) = \sum_i e_i^2 x f_i(x,Q^2). \tag{2.31}$$

At Next-to-Leading Order (NLO), the parton densities depend on the **renormalisation scheme**. Different schemes arise from different methods to handle the divergences in the renormalisation. In the Modified Minimal Subtraction ($\overline{\text{MS}}$) scheme [39], all higher-order loop corrections to the $q\bar{q}g$ vertex are defined such that they are at zero momentum transfer. In the DIS scheme [40], the contributions from the gluon are absorbed into the parton distribution functions such that Eqs. 2.30 and 2.31 are also valid at NLO.

2.4.2 The Naïve Quark Parton Model

The form of the cross section given in Section 2.4 is completely general, with all the physics detail being contained within the structure functions. *A priori*, these may be expected to be complicated functions of x and Q^2 , reflecting the complexity of the inelastic scattering process. However, in 1968, Bjorken predicted that at very high energies, their dependence on Q^2 would decrease and that they would become functions of x only, such that,

$$\begin{aligned} F_1(x,Q^2) &\rightarrow F_1(x) \\ F_2(x,Q^2) &\rightarrow F_2(x). \end{aligned} \tag{2.32}$$

In his **Parton Model**, Feynman gave an intuitive explanation of Bjorken's argument [41]. In this model, the proton is assumed to be composed of point-like objects called partons. At the hadronic vertex, the *inelastic* scattering of the lepton off the proton is, instead, viewed as the *elastic* scattering of the lepton off a parton within the proton. Since the constituent partons are considered to be point-like, an increase in Q^2, which is equivalent to an increase in resolution (see Eq. 2.14), would not change the result. In the Parton Model, the lepton-proton cross section is given by the incoherent sum of contributions from individual free quarks to the lepton-proton scattering cross section.

In order to establish the form of the structure function within the parton model, it is necessary to work in the infinite momentum frame of the proton. This is the frame in which the four-momentum of the proton is entirely light-like. In such a frame, the proton momentum is so large that all constituents can be assumed to move along the direction of the proton (since transverse momentum components are negligible) and all masses can be neglected. In the infinite momentum frame, the longitudinal size of the proton is Lorentz contracted by a factor M/p with respect to its size in the rest frame. Partons with finite values of x and fixed transverse size are distributed on the proton "disc", and the number of partons per unit longitudinal phase-space is small. Furthermore, the time dilation of the proton means that any parton-parton

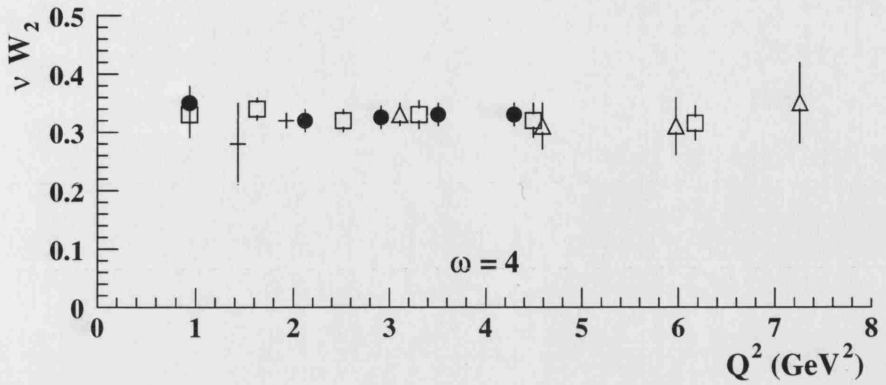

Figure 2.5: A compilation of data from SLAC showing the scaling behaviour of the structure function $F_2 = \nu W_2$ for different Q^2 values at $\frac{1}{\omega} = x = 0.25$. Diagram modified from [37].

interactions within the proton occur on a large time-scale compared to the parton-photon interaction of the hard scatter. Therefore, they can be considered as non-interacting, free particles. This is the so-called **impulse approximation**.

In the impulse approximation, the transverse momentum of a parton, i, within the proton may be neglected so that the parton carries a fraction ξ_i of the proton's longitudinal momentum. In this case, $p_i = \xi_i p$ and conservation of four-momentum gives,

$$0 \approx m_i^2 = (\xi_i p + q)^2 = \xi_i^2 p^2 - Q^2 + 2\xi_i p \cdot q$$

where m_i is the mass of parton i. Neglecting this mass leads to the expression,

$$\xi_i \approx \frac{Q^2}{2p.q} \equiv x.$$

Therefore, in this model, the Bjorken Scaling variable, x, can be identified with the fraction of the longitudinal proton momentum carried by the parton in the hard scatter (in a frame where the proton has infinite momentum).

In the Parton Model, the structure functions are given by,

$$F_1(x) = \frac{1}{2}\sum_i e_i^2 f_i(x) \tag{2.33}$$

$$F_2(x) = \sum_i e_i^2 x f_i(x) \tag{2.34}$$

where the e_i are the electric charges carried by the partons. The $f_i(x)$ are the PDFs, which now depend only on x and may be interpreted as the probability of finding a

parton, i, with momentum fraction, x, inside the proton. The partons included in the sum over i are all the flavours of quarks and anti-quarks allowed to participate in the interaction within the bounds of conservation laws.

In Eqs. 2.33 and 2.34, the $F_i(x)$ depend *only* on the scaling variable, x, and not on the value of Q^2. Consequently, the differential cross section in terms of the structure functions also scales,

$$\frac{\mathrm{d}^2\sigma^{ep}}{\mathrm{d}x\mathrm{d}Q^2} = \frac{4\pi\alpha^2}{xQ^4}[xy^2F_1(x) + (1-y)F_2(x)], \tag{2.35}$$

where the Q^2 dependence arises only from the hard interaction itself. This so-called **Bjorken Scaling** was confirmed in 1969 by DIS experiments taking place at SLAC [42]. Some of the early results from SLAC are shown in Fig. 2.5.

From Eqs. 2.33 and 2.34, it follows that,

$$2xF_1(x) = F_2(x). \tag{2.36}$$

This is known as the **Callan-Gross** relation [43] and is valid if the proton consists *only* of massless, charged, spin-1/2 particles[‡]. The form of Eq. 2.36 means that the longitudinal structure function, F_L, is equal to zero. From this it also follows that the cross section for the longitudinally polarised photon is also zero, since,

$$F_\mathrm{L} = \frac{Q^2}{2\pi^2\alpha}\sigma_\mathrm{L} = 0. \tag{2.37}$$

The experimental confirmation of scaling and of the Callan-Gross relation provided the first compelling evidence to suggest that the objects in the Parton Model were, in fact, the quarks of Gell-Mann and Zweig. Consequently, the model became known as the **Quark Parton Model** (QPM).

2.4.3 The QCD Improved Quark Parton Model

At higher four-momentum transfer, Q^2, the measured cross section deviates from predictions that assume scaling. In order to understand how these **scaling violations** arise, it is necessary to modify the QPM to include predictions from QCD. The assumption that the proton consists solely of charged quarks implies that the sum of the momentum of the charged partons should be equal to the total momentum of the proton. From Eq. 2.34, the structure function $F_2(x)$ sums the momentum fraction of

[‡]If quarks were spin-0 particles, the relation would be $\frac{2xF_1}{F_2} = 0$.

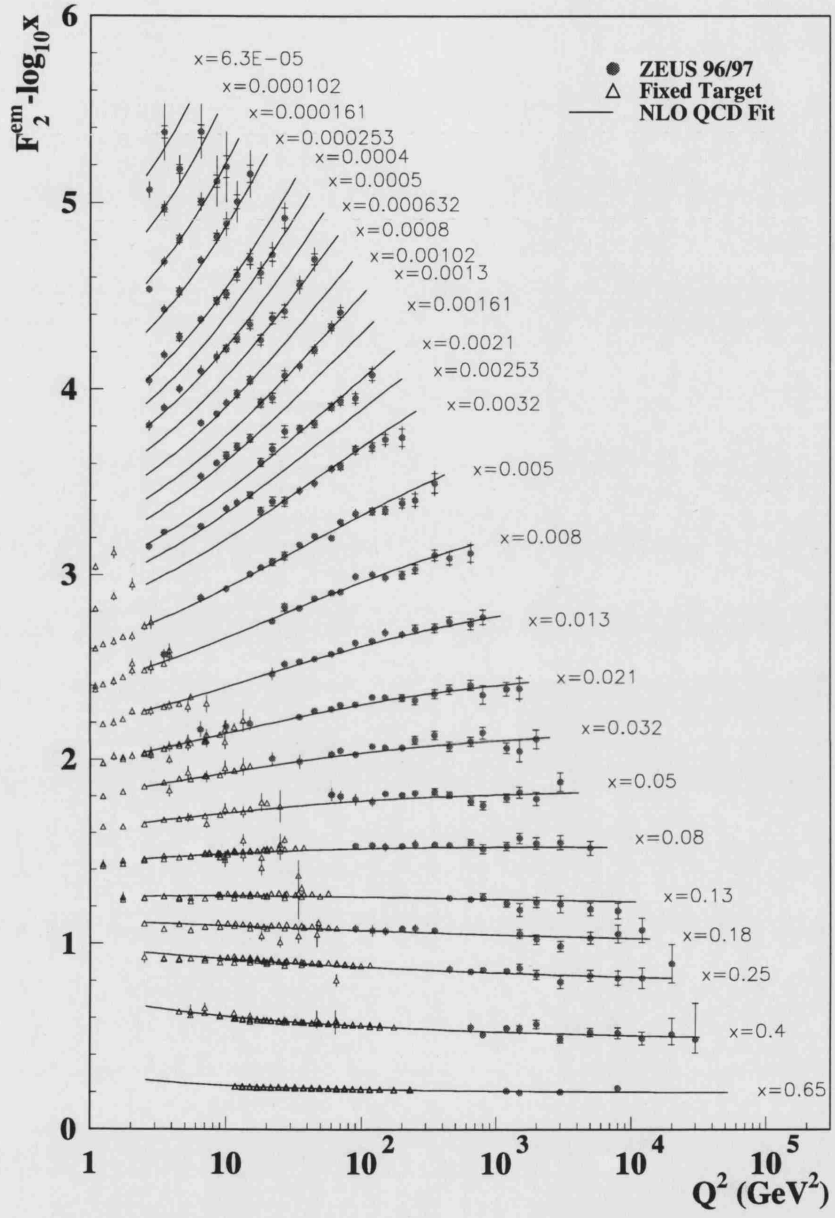

Figure 2.6: The structure function F_2^{em} as a function of Q^2 for different values of fixed x. The results are plotted as $F_2^{em} - \log_{10} x$ to accentuate the details of the measurement. The ZEUS data is shown by the solid points. The results from the fixed target experiments NMC, BCDM5 and E665 are also shown. The line is the ZEUS NLO QCD fit.

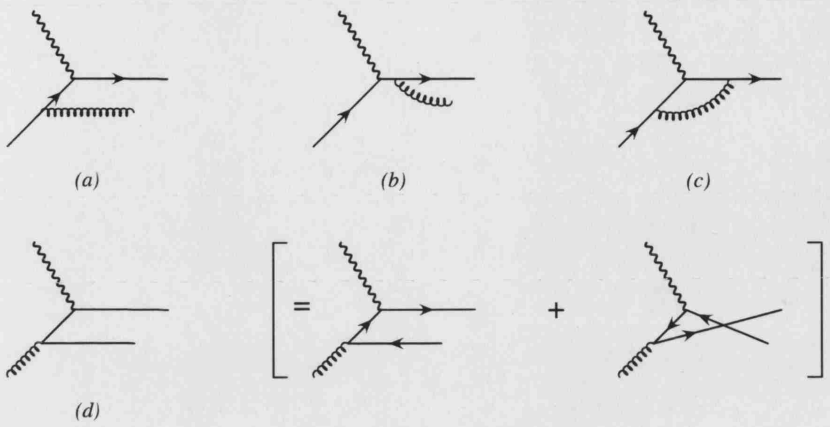

Figure 2.7: Examples of $\mathcal{O}(\alpha_s)$ corrections to DIS. $\gamma^* q \rightarrow qg$ contributions are shown in a), b) and c) and $\gamma^* q \rightarrow q\bar{q}$ contributions are shown in d).

all charged partons. Consequently, in the simple QPM, where the parton is considered to consist only of charged quarks, the following relation must hold,

$$\sum_i \int_0^1 \mathrm{d}x f_i(x) x = 1. \tag{2.38}$$

The parton densities, f_i, are integrated over the momenta of the partons inside the proton and summed over each type of parton, i. Equation 2.38 is known as the **momentum sum rule** [44]. However, experimentally, this quantity is found to sum to just over half of the proton's total momentum. This is interpreted as evidence for the existence of neutral partons within the proton, which carry $\sim 50\%$ of the proton momentum. These partons are identified with the eight gluons which are the gauge bosons of QCD. Evidence for the existence of gluons was first provided in 1979 at DESY, via the observation of three-jet events in e^+e^- annihilation [45].

The addition of gluons to the model leads immediately to the possibility that a quark can radiate gluons either before or after the hard interaction. Furthermore, a gluon could produce a quark-anti-quark pair ($g \rightarrow q\bar{q}$), either of which could interact with a virtual boson. The inclusion of both gluons and **sea** quarks in the model, as well as the original valence quarks of the QPM, led to the QCD improved QPM. Several examples of $\mathcal{O}(\alpha_s)$ QCD corrections to DIS are shown in Fig. 2.7.

The inclusion of QCD interactions leads immediately to the prediction that scaling is violated. This follows from the fact that, when a quark emits a gluon, it may acquire a large transverse momentum, k_T, with probability proportional to $\alpha_s \mathrm{d}k_\mathrm{T}^2/k_\mathrm{T}^2$ at large k_T. This is in contrast to the simple QPM where the parton's transverse momentum is restricted to be small. The integral extends up to the kinematic limit, $k_\mathrm{T}^2 \sim Q^2$, and

gives rise to contributions proportional to $\alpha_s \log Q^2$ which break scaling. Violation of scaling was confirmed experimentally by the observation of a logarithmic dependence on Q^2 of $F_2(x, Q^2)$ and was one of the first major successes of pQCD. Figure 2.6 shows the ZEUS measurements of the x and Q^2 dependence of F_2 . The phenomenon of scaling violation can be clearly observed. At large values of x, the valence quarks dominate and F_2 (and hence the quark density) is relatively flat with increasing Q^2. As x decreases, the number of sea quarks and gluons increases, and F_2 rises as Q^2 becomes larger. The observation of a strong rise in the cross section with decreasing x at large Q^2, and the discovery that this behaviour persists to relatively low $Q^2 \approx 2$ GeV^2, is one of the most important discoveries of HERA to date.

A second consequence of the improved model is the fact that the longitudinal structure function F_{L} no longer has a value of zero but can vary between $0 < F_{\mathrm{L}} < F_2$. Since the non-zero value of F_{L} is caused by the gluons, a measurement of F_{L} can provide information about the gluon density in the proton, where

$$F_{\mathrm{L}}(x, Q^2) = \frac{\alpha_s}{\pi}\left[\frac{4}{3}\int_x^1 \frac{\mathrm{d}z}{z}\left(\frac{x}{z}\right)^2 F_2(z, Q^2) + 2c\int_x^1 \frac{\mathrm{d}z}{z}\left(\frac{x}{z}\right)^2\left(1-\frac{x}{z}\right) z g(z, Q^2)\right] \quad (2.39)$$

with $c = \sum e_i^2$. For $x < 10^{-3}$ the dominant contribution is from the gluons. However, the measurement of F_{L} is particularly challenging. The separation of F_2 and F_{L} in the cross section requires the energy dependence (and hence y) to be measured at fixed x and Q^2. This either requires a measurement at different beam energies (hence varying the centre-of-mass energy $\sqrt{s}$), or using events with **Initial State Radiation** (ISR) to achieve a wide-band beam in s. In ISR events, the interacting electron has lost part of its energy as a result of the emission of a real photon, thus causing a reduction in s.

2.5 QCD Evolution Equations

The factorisation theorem states that in a general hard collision between hadrons, all non-perturbative effects can be factorised into universal (process-independent) parton densities. This leads to a perturbatively calculable dependence on the hard scattering scale, Q^2, called **parton evolution**. The essential idea is that the parton being probed may not be the original constituent of the proton i.e. the original quark or gluon may radiate another parton before interacting with the photon. More explicitly, the Q^2 dependence arises because a quark probed at a scale Q_0^2 with a fraction of the proton momentum, x_0, can be resolved into more quarks and gluons, having $x < x_0$, when the scale Q^2 is increased.

The concept of parton evolution is needed to describe the variation in F_2 with Q^2, which was introduced in Section 2.4.3. In the context of pQCD, the evolution of $F_2(x, Q^2)$

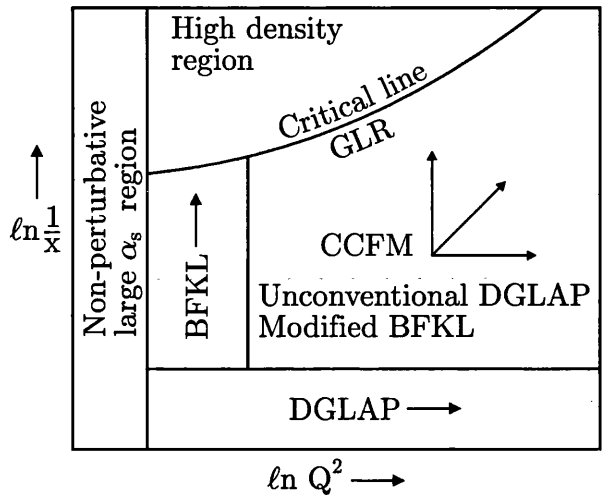

Figure 2.8: Diagrammatic representation of the applicability in the (x, Q^2) plane of the different evolution schemes. The DGLAP and BFKL schemes are relevant to this thesis. The critical line indicates the transition between the dominance of gluon radiation and splitting, described by the linear evolution equations, and the saturation due to gluon recombination and shadowing.

contains terms of order $\alpha_s^n \log^m Q^2$ and $\alpha_s^n \log^m \frac{1}{x}$ with $m \leq n$, where n is the order of the perturbative expansion. In different kinematic regions of the (x, Q^2) plane, different terms dominate the expansion, as illustrated in Fig. 2.8. In the following subsections, the DGLAP and BFKL evolution schemes are discussed.

2.5.1 The DGLAP Equations

The Dokshitzer-Gribov-Lipatov-Alterelli-Parisi (DGLAP) Evolution Equations [46] describe the way in which the quark and gluon momentum distributions in a hadron evolve with the scale of the interaction Q^2. The DGLAP equations are given by,

$$\frac{\mathrm{d}q_i(x,Q^2)}{\mathrm{d}\log Q^2} = \frac{\alpha_s(Q^2)}{2\pi}\int_x^1 \frac{\mathrm{d}y}{y}\left[\sum_i q_i(y,Q^2)P_{qq}\left(\frac{x}{y}\right) + g(y,Q^2)P_{qg}\left(\frac{x}{y}\right)\right] \quad (2.40)$$

$$\frac{\mathrm{d}g(x,Q^2)}{\mathrm{d}\log Q^2} = \frac{\alpha_s(Q^2)}{2\pi}\int_x^1 \frac{\mathrm{d}y}{y}\left[\sum_i q_i(y,Q^2)P_{gq}\left(\frac{x}{y}\right) + g(y,Q^2)P_{gg}\left(\frac{x}{y}\right)\right] \quad (2.41)$$

where $q_i(x, Q^2)$ is the quark density function for each quark flavour, i, and $g(x, Q^2)$ is the gluon density function. The Alterelli-Parisi **splitting functions** $P_{jk}\left(\frac{x}{y}\right)$ represent

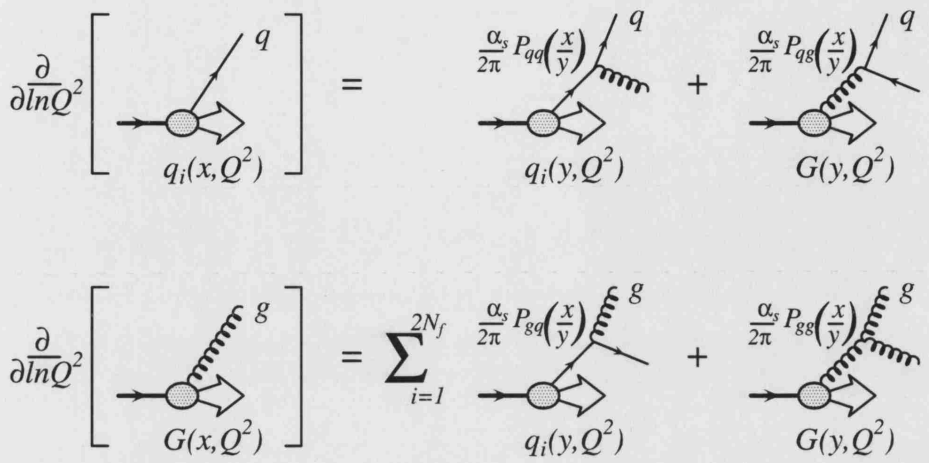

Figure 2.9: The singlet DGLAP Evolution Equations or the proton PDFs.

the probability of a parton k of momentum fraction y emitting a parton j of momentum fraction x in the interval $Q^2 \to Q^2 + \mathrm{d}\log Q^2$. These splitting functions have been calculated to LO and NLO in QCD [47]. The LO splitting functions are illustrated diagrammatically in Fig. 2.9. Given a specific factorisation and renormalisation scheme, the splitting functions $P_{jk}\left(\frac{x}{y}\right)$ are obtained in QCD by perturbative expansion in α_s,

$$P_{jk}\left(\frac{x}{y}\right) = \sum_i \left(\frac{\alpha_s}{2\pi}\right)^i P_{jk}^{(i)}\left(\frac{x}{y}\right) = P_{jk}^{(0)}\left(\frac{x}{y}\right) + \frac{\alpha_s}{2\pi} P_{jk}^{(1)}\left(\frac{x}{y}\right) + \ldots \tag{2.42}$$

Note that, at LO, they are given by,

$$\begin{aligned} P_{qq}^{(0)}(z) &= \frac{4}{3}\left[\frac{1+z^2}{1-z}\right] \\ P_{qg}^{(0)}(z) &= \frac{1}{2}\left[z^2 + (1-z^2)^2\right] \\ P_{gq}^{(0)}(z) &= \frac{4}{3}\left[\frac{1+(1-z)^2}{z}\right] \\ P_{gg}^{(0)}(z) &= 6\left[\frac{z}{1-z} + \frac{1-z}{z} + z(1-z)\right]. \end{aligned} \tag{2.43}$$

where $z = x/y$.

The derivation of the DGLAP evolution equations uses the Leading Logarithm Approximation (LLA), where terms in $(\alpha_s \log Q^2)^n$ are re-summed[§]. This re-summation ensures the convergence of the perturbative expansion. In the LLA DGLAP evolution scheme, terms of the form $\log\left(\frac{1}{x}\right)$ are neglected. This approach assumes that the

[§]A more detailed discussion of this derivation can be found, for example, in [6, 37].

dominant contribution to the evolution comes from successive parton emissions which are strongly ordered in transverse momenta, k_{T}^{i}, the largest of which corresponds to the parton interacting with the probe ($k_{\mathrm{T},1}^2 \ll k_{\mathrm{T},2}^2 \ll ... \ll k_{\mathrm{T,n}}^2 \ll Q^2$). This is illustrated in Fig. 2.10.

The truncation of Eq. 2.42 after the first two terms in the expansion defines the NLO DGLAP evolution. In this case, NLO log terms must also be included. The largest contribution from these terms arises if $\log\frac{1}{x}$ is large. This region is described by the Double Leading Log Approximation (DLLA) where leading terms in $\log\frac{1}{x}$ are summed provided they are coupled with leading $\log Q^2$ terms. In addition to the k_{T} ordering, the DLLA additionally demands an ordering in the longitudinal momentum x ($x_1 > x_2 > ... > x_{\mathrm{n}}$). This means that the DGLAP formalism is applicable in the region where pQCD is valid and where $\log\left(\frac{1}{x}\right) \ll \log\left(\frac{Q^2}{Q_0^2}\right)$.

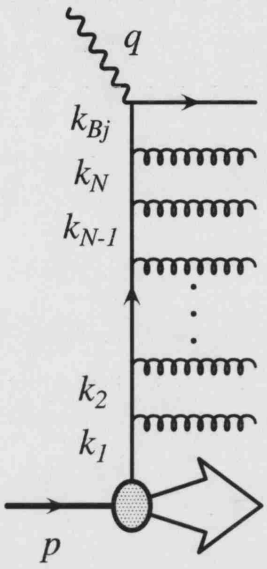

Figure 2.10: DGLAP parton evolution showing the k_{T} ordered gluon emissions.

The solutions of the DGLAP equations give the PDFs as a function of x at any scale Q^2, provided the x dependence at an input scale Q_0^2 is known. The parton densities at the scale Q_0^2 are determined from experiment since they are not predicted by the theory.

In the DGLAP framework, the growth of the parton densities is interpreted as being a result of their Q^2 evolution. Parameterisations of $F_2(x, Q^2)$ based only on their DGLAP evolution, such as those of Martin, Roberts and Stirling (MRS) [48], have been successful in describing all HERA data above $Q^2 \sim 4$ GeV^2.

2.5.2 BFKL Evolution

At sufficiently small x, terms of the form $\log\frac{1}{x}$ that are not coupled to leading $\log Q^2$ terms may become large. The conventional DGLAP evolution may then become inadequate. The Balitsky-Fadin-Kiraev-Lipatov (BFKL) [49] evolution equation allows the re-summation of terms with a leading $(\alpha_s \log\frac{1}{x})^n$, independent of $\log Q^2$ Consequently, the BFKL evolution scheme is valid in the region where pQCD is applicable and where $\log\left(\frac{Q^2}{Q_0^2}\right) \ll \log\left(\frac{1}{x}\right)$.

The derivation of the BFKL equation involves considering the evolution of a given distribution which is not integrated over k_{T}, since destroying the association to leading $\log Q^2$ implies that the gluon ladder need not be ordered in k_{T}. This evolution

corresponds roughly to cascades with emissions strongly ordered in x with no restriction on k_{T}. The gluon density can be written as,

$$xg(x,Q^2) = \int_0^{Q^2} \frac{\mathrm{d}k_{\mathrm{T}}^2}{k_{\mathrm{T}}^2} \mathcal{G}(x,k_{\mathrm{T}}^2) \tag{2.44}$$

where $\mathcal{G}(x,k_{\mathrm{T}}^2)$ is the unintegrated gluon density. The evolution of $\mathcal{G}(x,k_{\mathrm{T}}^2)$ with $\log\frac{1}{x}$ is then described by the BFKL equation,

$$\frac{\mathrm{d}\mathcal{G}(x,k_{\mathrm{T}}^2)}{\mathrm{d}\log(1/x)} = \int \mathrm{d}k'^2_{\mathrm{T}} K(k_{\mathrm{T}}^2, k'^2_{\mathrm{T}}) \mathcal{G}(x,k'^2_{\mathrm{T}}) = \lambda\mathcal{G}, \tag{2.45}$$

where K is the **kernel**. The solution is dominated by the largest eigenvalue λ. For fixed α_s and leading order in $\log\frac{1}{x}$, the BFKL gluon distribution at small x gives,

$$xg(x,Q^2) \sim \mathcal{G}(Q^2) x^{-\lambda}$$

with $\lambda = \frac{3\alpha_s}{\pi} 4\log 2 \sim 0.5$ for $\alpha_s \approx 0.25$ (which is appropriate at $Q^2 \approx 4$ GeV^2). In order for the BFKL equation to make predictions (of F_2 for example), the gluon ladder must be convoluted with the quark box according to the k_{T} factorisation theorem,

$$F_2(x,Q^2) = \int_x^1 \frac{\mathrm{d}y}{y} \int \frac{\mathrm{d}k_{\mathrm{T}}^2}{k_{\mathrm{T}}^2} \mathcal{G}(y,k_{\mathrm{T}}^2) \sigma^{box}\left(\frac{x}{y}, k_{\mathrm{T}}^2, Q^2\right). \tag{2.46}$$

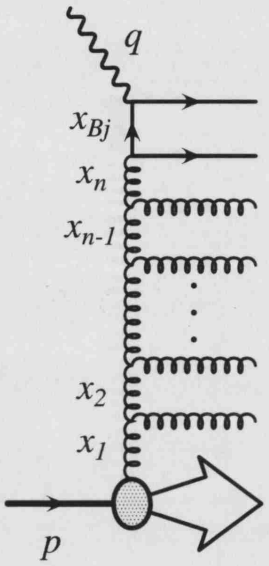

Figure 2.11: The BFKL gluon ladder and quark box showing the ordering in x.

This is illustrated in Fig. 2.11. In general, for the low x region, the BFKL equation predicts a faster increase of F_2 with Q^2 than the DGLAP equations.

2.6 Proton Parton Density Functions

As previously mentioned, the proton PDFs at any value of x and Q^2 are determined by measuring their values at a particular scale Q_0^2 and then evolving the parton densities to higher values of Q^2 using the DGLAP equations. The x dependence of the PDFs is parameterised at the starting scale Q_0^2. In practice, parton densities are not theoretically calculable. Therefore, they are derived at the scale Q_0^2 by fits to structure function data from a variety of experiments [50]. The factorisation theorem means that

the PDFs extracted experimentally at HERA are also applicable to processes occurring at other colliders such as the Tevatron and the LHC.

It is necessary to choose a renormalisation scheme in which higher order corrections are progressively smaller than the lower order results i.e. a scheme in which calculations rapidly converge. In addition, the scheme should preserve this property in other perturbatively calculable processes, such as e^+e^- scattering. Usually, the $\overline{\text{MS}}$ scheme is used, although the DIS scheme is also used extensively in LO Monte Carlo programs. In the following subsections, the two parameterisations used in this thesis are described in more detail.

2.6.1 Glück, Reya & Vogt (GRV)

In the GRV [51] parameterisations of the proton parton densities, the evolution begins at a scale of $Q_0^2 = 0.34$ GeV^2. The motivation for this low scale is that the nucleon consists only of the constituent valence quarks since they are fully constrained by the charge and momentum sum rules. This is introduced to remove the dependence of the PDFs on the input scale. The sea quarks are then generated dynamically from the NLO DGLAP equations and the long evolution length from the low scale is then able to generate dynamically the rise at low x from the flat distribution. In this thesis, the GRV94 [52] set is used.

2.6.2 CTEQ

In the Coordinated Theoretical-Experimental Project on QCD (CTEQ) [53] parameterisations, the evolution begins at a scale of $Q_0^2 = 2.56$ GeV^2. These parameterisations are constrained by global fits to data from a large number of experiments, including both lepton-hadron (e.g. HERA, NMC, E665) and hadron-hadron (e.g. Tevatron) experiments. The PDFs are evolved from the starting scale using the NLO DGLAP equations. In this thesis, the CTEQ5L [54] parameterisation is used.

2.7 The Photoproduction Regime

In DIS, the high virtuality ($Q^2 \gg 1$ GeV^2) photon is able to resolve the structure of the proton. However, the lepton-proton scattering cross section exhibits a simple $\frac{1}{Q^4}$ suppression from the photon propagator. This means that the total cross section is dominated by the exchange of very low virtuality photons. At these virtualities, the physics processes have different characteristics. When $Q^2 \sim 0$ GeV^2 events are classified as photoproduction and the low virtualities of such events means that Q^2

can no longer be viewed as the hard scale in the interaction. In order for perturbative methods to remain applicable, an alternative hard scale is required. This is usually achieved by requiring the observation of jets carrying a significant transverse energy. The transverse energy of the jets is then taken to be the hard scale of the interaction.

The lifetime of an exchanged photon varies approximately as $t_\gamma \sim \frac{E_\gamma}{Q^2}$. Consequently, for very low virtualities, the lifetimes are considered to be long compared to the characteristic time-scale of the hard subprocess. The lepton beam can then be considered as a source of approximately massless, very low virtuality ("quasi-real") photons, emitted collinear to the beam-line.

The lepton vertex is a purely electroweak process and can be calculated with no further assumptions, as discussed in Section 2.4. Therefore, the total cross section $\sigma^{ep}_{\rm tot}$ can be factorised into contributions from the photon-proton (γp) cross section $\sigma^{\gamma p}_{\rm tot}$ and some flux factor $f^{e\to\gamma}(y, Q^2)$ which is the probability that a lepton radiates a photon of energy $E_\gamma = yE_e$ and a given virtuality, Q^2.

For $Q^2 > 0$ GeV^2, photons may have both transverse and longitudinal polarisation so that the total photon-proton cross section may be written as the sum of two terms,

$$\sigma^{\gamma p}_{\rm tot} = \sigma^{\gamma p}_{\rm T} + \sigma^{\gamma p}_{\rm L}. \tag{2.47}$$

The lepton-proton scattering cross section can then be written as,

$$\mathrm{d}\sigma^{ep\to eX} = \int \mathrm{d}y[f^{e\to\gamma_{\rm T}}(y, Q^2)\mathrm{d}\sigma^{\gamma_{\rm T}p\to X}_{\rm T} + f^{e\to\gamma_{\rm L}}(y, Q^2)\mathrm{d}\sigma^{\gamma_{\rm L}p\to X}_{\rm L}]. \tag{2.48}$$

In the DIS limit of large Q^2, the structure functions are related to $\sigma^{\gamma p}_{\rm T}$ and $\sigma^{\gamma p}_{\rm L}$ by,

$$F_1 = \frac{Q^2}{8x\pi^2\alpha}\sigma^{\gamma p}_{\rm T} \tag{2.49}$$

$$F_2 = \frac{Q^2}{4\pi^2\alpha}(\sigma^{\gamma p}_{\rm T} + \sigma^{\gamma p}_{\rm L}). \tag{2.50}$$

The double differential cross section is then given by,

$$\frac{\mathrm{d}^2\sigma^{ep}(y, Q^2)}{\mathrm{d}y\mathrm{d}Q^2} = \frac{\alpha}{2\pi}\frac{1}{Q^2}\left[\left(\frac{1+(1-y)^2}{y} - 2\frac{(1-y)}{y}\frac{Q^2_{\rm min}}{Q^2}\right)\sigma^{\gamma p}_{\rm T} + 2\frac{(1-y)}{y}\sigma^{\gamma p}_{\rm L}\right]. \tag{2.51}$$

The quantity $Q^2_{\rm min} = m_e^2\left(\frac{y^2}{1-y}\right)$ is the kinematic lower bound [55]. In the limit that $Q^2 \to 0$ GeV^2, the longitudinal component vanishes, and the total γp cross section consists only of the transverse component $\sigma^{\gamma p}_{\rm tot} = \sigma^{\gamma p}_{\rm T}$. Then, $\sigma^{\gamma p}$ can be calculated from the measured cross section σ^{ep} according to,

$$\frac{\mathrm{d}^2\sigma^{ep}(y, Q^2)}{\mathrm{d}y\mathrm{d}Q^2} \sim f^{e\to\gamma_{\rm T}}(y, Q^2)\sigma^{\gamma p}_{\rm T}(y, Q^2). \tag{2.52}$$

The photon flux, $f^{e\to\gamma_T}(y,Q^2)$, is given by the **Equivalent Photon Approximation** (EPA),

$$f^{e\to\gamma}_{\rm EPA}(y,Q^2) = \frac{\alpha}{2\pi}\frac{1}{Q^2}\left[\frac{1+(1-y)^2}{y} - \frac{2(1-y)}{y}\frac{Q^2_{\rm min}}{Q^2}\right]. \tag{2.53}$$

An alternative expression for the photon flux is given by the **Weizsäcker-Williams Approximation** (WWA) [56],

$$f^{e\to\gamma}_{\rm WWA}(y) = \frac{\alpha}{2\pi}\left[\frac{1+(1-y)^2}{y}\log\frac{Q^2_{\rm max}}{Q^2_{\rm min}} - 2m_e^2\left(\frac{1}{Q^2_{\rm min}} - \frac{1}{Q^2_{\rm max}}\right)\right]. \tag{2.54}$$

Here, the Q^2 dependence of the γp cross section has been neglected and integration has been carried out over photon virtualities. The range of integration is from the lower kinematic limit up to some, experimentally fixed, maximum.

2.7.1 The Collinear Approximation

In the limit $Q^2 \to 0$ GeV^2, then $q = \xi k$. In this case, the definition, $y \equiv \frac{p\cdot q}{p\cdot k}$ reduces to, $y = \frac{E_\gamma}{E_e}$ where E_γ and E_e are the photon and lepton energies, respectively. Therefore, $y = \xi$ so that $q \to yk$ and $W^2 \to ys$. In this so-called **collinear approximation**, y is simply the fraction of the lepton momentum carried by the photon in the proton rest frame.

2.7.2 The Photon-Proton Interaction

As the gauge-boson of QED, the photon is a point-like particle. However, in quantum field theory, the photon is able to fluctuate into a pair of charged particles. Fluctuations to lepton-anti-lepton states are well understood within the framework of the electroweak interaction. However, fluctuations to quark-anti-quark states are more complicated due to the possibility of further QCD interactions. In photoproduction, the lifetime of the photon is long enough for fluctuations to low virtuality quark-anti-quark states to develop a complex hadronic structure, which cannot be described using *only* perturbative methods [57, 58]. This property of the photon allows two possible types of high transverse energy photoproduction process. In addition to the **direct** interaction of the photon in the hard subprocess, it is also possible for the photon to act as a source of partons. The ability of the photon to interact hadronically in so-called **resolved** photoproduction events means that much of the formalism from hadron-hadron interactions may be applied. Interactions where the photon behaves hadronically are useful for the study of both perturbative and non-perturbative aspects of the strong interaction. In particular, photon-proton interactions allow the study of the hadronic structure of the photon.

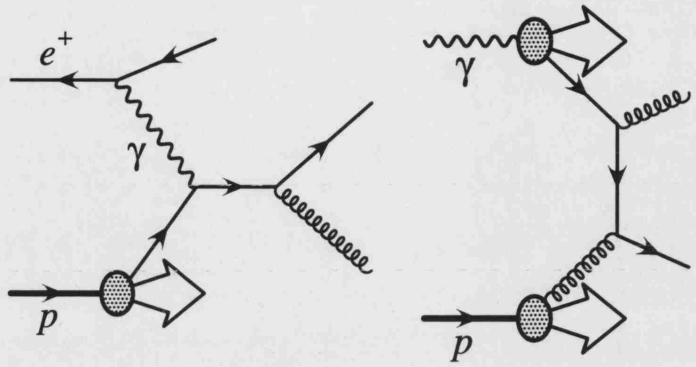

Figure 2.12: Examples of LO direct (left) and resolved (right) photoproduction processes occurring at HERA. In the resolved process, the photon contributes a fraction x_γ of the total photon momentum to the hard scattering.

2.7.3 Hard Photoproduction at HERA

In direct photoproduction the photon acts as a point-like object and enters directly into the hard subprocess, thereby contributing all of its energy to the interaction. The LO direct photoproduction processes give rise to two jets in the final hadronic state. There are two main types of LO direct photoproduction process occurring at HERA. The relevant diagrams are similar to the $\mathcal{O}(\alpha_s)$ diagrams for DIS. However, in that case, the hard scale is provided by the photon virtuality while in photoproduction Q^2 is low, and the hard scale is provided by the transverse energy of the outgoing jets in the final state. In the **boson-gluon** fusion process, the photon couples to a quark arising from a gluon in the proton that has first split into a quark-anti-quark pair. In this case, the internal propagator can be considered to have an analogous role to that of the photon in DIS, with one of the outgoing quarks corresponding to the scattered lepton and the other giving rise to the so-called **current jet**. However, the boson-gluon fusion diagram means that, in contrast to DIS, high transverse energy LO direct photoproduction is sensitive to the gluon density in the proton. In the **QCD Compton** process (shown in Fig. 2.12 (left)), the photon couples directly to a quark within the proton which then radiates a gluon prior to hadronisation.

In a resolved photon process, the photon splits into a quark-anti-quark pair prior to the hard interaction. Following this (QED governed) process, QCD evolution can occur so that the photon acts as an extended source of partons. A parton from the photon, carrying a fraction x_γ (< 1) of the total photon momentum, participates in the hard subprocess. In this way, the scatter can be viewed as having resolved the structure of the photon. As a result of the smaller momentum fraction taking part in the interaction, resolved photoproduction events are expected to be softer than the corresponding direct processes for the same value of y in the event. Similarly, there will be a tendency for

resolved events to be boosted further forward with respect to direct processes for events with the same x_p. In Fig. 2.12 (right), an example of a LO resolved process is shown. Resolved events are characteristically different from direct events since they have a photon remnant in the final state. In addition, they are dominated by gluon exchange processes while in direct photoproduction, the propagator must always be a quark.

The processes shown in Fig. 2.12 are formally $\mathcal{O}(\alpha\alpha_s)$. However, higher order (in α_s) processes containing three or more jets also occur at HERA. At LO, three and four jet photoproduction are $\mathcal{O}(\alpha\alpha_s^2)$ and $\mathcal{O}(\alpha\alpha_s^3)$ respectively. The study of these intrinsically higher order processes can provide direct tests of pQCD, as well as providing information on the dominant jet production mechanisms.

2.8 The Resolved Photon

The partonic structure of the resolved photon can be further separated into two components depending on the virtuality at the $\gamma \rightarrow q\bar{q}$ vertex. This virtuality governs the lifetime of the fluctuation and means that the photon may couple to either bound or unbound quark-anti-quark pairs.

- If the virtuality is low, the lifetime of the hadronic state is long enough for the photon to fluctuate into a bound state which must have the same quantum numbers as the photon. These correspond to light vector mesons $V = \rho^0, \omega, \phi, J/\psi, ...$ This feature of the photon is described by the **Vector meson Dominance Model** (VDM) [59] in which the hadronic state of the photon is taken to be a superposition of the vector mesons, V. In the VDM model, the γp cross section is given by,

$$\sigma^{\gamma^* p}_{\mathrm{VDM}}(W) = \sum_V \frac{4\pi\alpha}{f_V^2}\sigma^{Vp}(W) \tag{2.55}$$

  where f_V is the probability that the photon will fluctuate into a particular vector meson V. The lifetime of this fluctuation is $t_V \sim \frac{2E_\gamma}{m_V^2+Q^2}$ where E_γ is the energy of the photon and m_V is the mass of the vector meson. Since t_V has an inverse dependence on Q^2, the fluctuations of the photon into a vector meson state is highly suppressed in DIS compared to photoproduction. However, in the proton centre-of-mass frame, $E_\gamma = \frac{p\cdot q}{M}$ and $x = \frac{Q^2}{2ME_\gamma}$ which means that $t_V \sim (Mx)^{-1}$. Therefore, the VDM behaviour of the photon can still be observed at large Q^2 provided x is sufficiently small. VDM processes in hard photoproduction involve large transverse momenta (by definition). In such cases pQCD can be applied. When the transverse momentum of the hard scatter is high, the parton structure of the vector meson is probed (rather than observing the interaction of the vector meson as a whole).

- In the case where the $\gamma \to q\bar{q}$ splitting produces an unbound quark-anti-quark pair of higher virtuality, the photon is described as being **anomalous**. In this case, the high transverse momentum at the $\gamma \to q\bar{q}$ vertex means that the anomalous photon can, in principle, be calculated in pQCD [60].

The total γp cross section can be written as $\sigma_{\text{tot}}^{\gamma p} = \sigma_{\text{VDM}}^{\gamma p} + \sigma_{\text{anomalous}}^{\gamma p} + \sigma_{\text{dir}}^{\gamma p}$. In general, the transverse momenta of the outgoing partons produced from anomalous photon interactions is higher than those from VDM photons. Therefore, it is the anomalous component that dominates the resolved contribution to hard photoproduction at HERA. However, the separation between the VDM and anomalous photon is not well defined and it is found that for very small momentum fractions, singularities are observed for both components of the resolved photon if they are treated in isolation. In fact, it is only the *sum* that gives a finite result. This means that the VDM component cannot be neglected even at very high transverse momentum. The VDM and anomalous components are usually combined into a single *resolved* photon so that $f_{\text{res}} = f_{\text{VDM}} + f_{\text{anomalous}}$ and the total cross section is written as $\sigma_{\text{tot}}^{\gamma p} = \sigma_{\text{res}}^{\gamma p} + \sigma_{\text{dir}}^{\gamma p}$.

2.9 The Generalised Photoproduction Model

A general model exists for LO photoproduction processes. The cross section for $\gamma p \to cd + X$, where c and d are the outgoing partons from the hard interaction, can be factorised into a perturbatively calculable partonic interaction for partons a and b, and non-perturbative parton densities, which describe the probability of finding partons a and b within the photon and proton.

The scales μ_p and μ_γ are the factorisation scales for the proton and photon respectively. These scales delineate the separation between the perturbative and non-perturbative parts of the process. In principle, the factorisation scales are arbitrary. However, a common choice is $\mu_p^2 = \mu_\gamma^2 = \mu^2 \sim p_{\text{T}}^2$, where p_{T} is the transverse momentum of the jet. This choice allows the incoming parton a large region of phase space in which to evolve. The hard subprocess is independent of the factorisation scale and so only the parton densities are affected by a variation in scale. The scale μ^2 enters into the photoproduction cross section in the same way that Q^2 does for DIS and therefore gives the resolution with which the structure of the photon and proton can be probed.

The differential cross section for the generalised photoproduction model can be separated into direct and resolved components so that,

$$\mathrm{d}\sigma^{\gamma p \to cd} = \mathrm{d}\sigma_{\text{res}}^{\gamma p \to cd} + \mathrm{d}\sigma_{\text{dir}}^{\gamma p \to cd}. \tag{2.56}$$

The two separate components can be written,

$$\mathrm{d}\sigma_{\mathrm{res}}^{\gamma p\to cd} = \sum_{ab}\int_{x_p}\int_{x_\gamma} \mathrm{d}x_p f^{p\to b}(x_p,\mu_p^2)\mathrm{d}x_\gamma f^{\gamma\to a}(x_\gamma,\mu_\gamma^2)\mathrm{d}\hat{\sigma}^{ab\to cd}, \tag{2.57}$$

$$\mathrm{d}\sigma_{\mathrm{dir}}^{\gamma p\to cd} = \sum_{b}\int_{x_p} \mathrm{d}x_p f^{p\to b}(x_p,\mu_p^2)\mathrm{d}\hat{\sigma}^{\gamma b\to cd}. \tag{2.58}$$

The $\mathrm{d}\hat{\sigma}$ represents the perturbatively calculable $2\to 2$ scattering matrix element, and two-body phase-space, such that,

$$\mathrm{d}\hat{\sigma} = \frac{1}{2s}|\overline{\mathcal{M}}|^2\mathrm{dPS}. \tag{2.59}$$

The $f^{p\to b}(x_p^2,\mu_p^2)$ and $f^{\gamma\to a}(x_\gamma^2,\mu_\gamma^2)$ are the PDFs of the proton and photon respectively. At LO, there is a clear distinction between the direct case, where $x_\gamma = 1$, and the resolved case, where $x_\gamma < 1$. Equation 2.58 can then be viewed as a specific case of Eq. 2.57, where the photon distribution is a delta function at $x_\gamma = 1$.

The factorisation scales, μ_p and μ_γ are not physical observables and are artificially introduced. Therefore, the results of a full QCD calculation must not depend on the choice of these parameters. However, any theoretical calculation will exhibit a strong sensitivity to variations in the factorisation scales due to the dependence of the parton densities on the particular choice of scale.

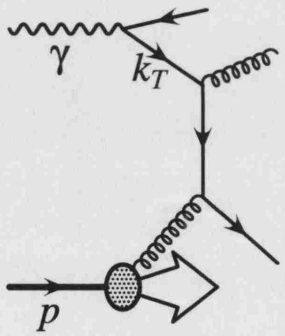

Figure 2.13: A next-to-leading order direct photoproduction event.

At NLO, there are also contributions from $2\to 3$ parton scattering. These are dependent on the factorisation scale. By varying the scale, μ_γ, the contributions to the cross section from $2\to 3$ parton scattering processes at NLO, and the amount which are simply LO, varies. In other words, an ambiguity arises between NLO direct and LO resolved processes, which is dependent on μ_γ. This is illustrated by Fig. 2.13 which has been classified as direct photoproduction at NLO. Although the diagram contributes nominally at $\mathcal{O}(\alpha\alpha_s^2)$, if the virtuality k_{T}^2 of the propagator is less than the factorisation scale squared, μ_γ^2, then this diagram should have already been included in the LO resolved contribution. Consequently, the terms *direct* and *resolved* are only unambiguously defined at LO and only their *sum* is physically meaningful. One of the advantages of the inclusion of NLO diagrams in the calculation is that the dependence on the factorisation scale is reduced. It is then the choice of parton distribution that introduces the largest uncertainty in the cross section.

2.10 Photon Structure Functions

The structure of the photon is measured directly in deep inelastic $e\gamma$ scattering [61, 62], which is formally analogous to the ep DIS taking place at HERA. The cross section for a probing photon of virtuality $Q^2 \equiv -q^2$, scattering off a real target photon with virtuality $P^2 \approx 0$ GeV^2 and producing a final state eX is given by,

$$\frac{\mathrm{d}^2\sigma^{e\gamma}}{\mathrm{d}x\mathrm{d}Q^2} = \frac{2\pi\alpha^2}{xQ^4}\left[\left(1+(1-y)^2\right)F_2^\gamma(x,Q^2) - y^2F_\mathrm{L}^\gamma(x,Q^2)\right]. \tag{2.60}$$

Analogously to ep scattering the structure function F_2^γ can be written in terms of the PDFs of the photon such that (at LO),

$$F_2^\gamma(x,Q^2) = 2\sum_i e_i^2 x f_i^\gamma(x,Q^2), \tag{2.61}$$

where the sum runs over all quark flavours, i, of charge e_i and the factor of two accounts for quarks and anti-quarks. The photon PDFs obey a set of inhomogeneous evolution equations [63],

$$\frac{\mathrm{d}q_i^\gamma(x,Q^2)}{\mathrm{d}\log Q^2} = a(x) + \frac{\alpha_s(Q^2)}{2\pi}\int_x^1 \frac{\mathrm{d}y}{y}\left[q_i(y,Q^2)P_{qq}\left(\frac{x}{y}\right) + g(y,Q^2)P_{qg}\left(\frac{x}{y}\right)\right] \tag{2.62}$$

$$\frac{\mathrm{d}g^\gamma(x,Q^2)}{\mathrm{d}\log Q^2} = \frac{\alpha_s(Q^2)}{2\pi}\int_x^1 \frac{\mathrm{d}y}{y}\left[2\sum_i^f q_i(y,Q^2)P_{gq}\left(\frac{x}{y}\right) + g(y,Q^2)P_{gg}\left(\frac{x}{y}\right)\right] \tag{2.63}$$

where

$$a(x) = 3e_i^2\frac{\alpha}{2\pi}\left[x^2+(1-x)^2\right]. \tag{2.64}$$

Except for the additional $a(x)$ term, Eqs. 2.62 and 2.63 are the standard DGLAP evolution equations (described in Section 2.5.1). The **anomalous** term, $a(x)$, arises from $\gamma \to q\bar{q}$ branchings of the anomalous photon and is therefore unique to the photon evolution equations. The solution of the photon DGLAP equations can be written as the sum of two terms [64],

$$f_i^\gamma(x,Q^2) = f_i^{\gamma,\mathrm{NP}}(x,Q^2;Q_0^2) + f_i^{\gamma,\mathrm{P}}(x,Q^2;Q_0^2). \tag{2.65}$$

The first term is a solution to the homogeneous equation with a non-perturbative input at $Q = Q_0$, and the second is a solution to the full inhomogeneous equation with the boundary condition $f_i^{\gamma,\mathrm{P}}(x,Q^2;Q_0^2) \equiv 0$. The $f_i^{\gamma,\mathrm{NP}}(x,Q^2;Q_0^2)$ is usually attributed to

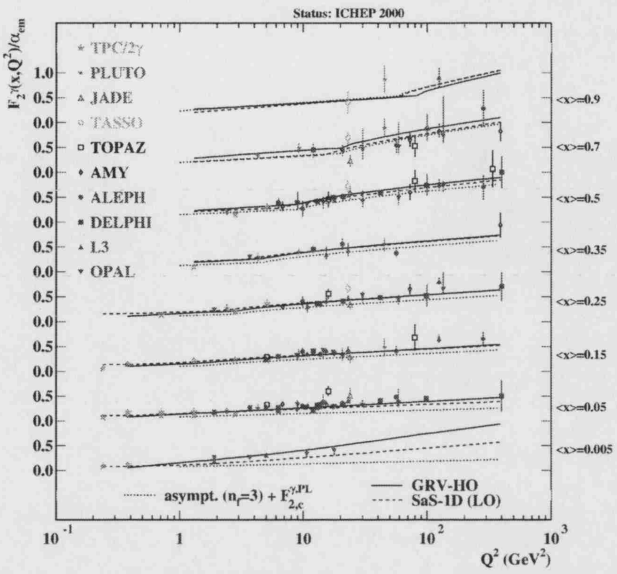

Figure 2.14: A compilation of current results on the measurement of F_2^γ.

the VDM photon while the $f_i^{\gamma,\mathrm{P}}(x,Q^2;Q_0^2)$ arises from the anomalous photon. The PDFs of the photon can be written in the form,

$$f_i^\gamma(x,Q^2) = \sum_V \frac{4\pi\alpha_{em}}{f_V^2} f_i^{\gamma,V}(x,Q^2;Q_0^2) + \frac{\alpha_{em}}{2\pi}\sum_q 2e_q^2 \int_{Q_0^2}^{Q^2} \frac{\mathrm{d}k^2}{k^2} f_i^{\gamma,q\bar{q}}(x,Q^2;k^2) \quad (2.66)$$

where each component, $f_i^{\gamma,V}$ and $f_i^{\gamma,q\bar{q}}$ obeys a unit momentum sum rule.

In 1977 it was argued by Witten [60] that in the framework of pQCD, the behaviour of F_2^γ was very different from that of F_2 for the proton. *A priori*, the hadronic structure functions are unknown and must be determined from experiment. Only the evolution of the structure functions can be calculated. However, the structure functions of the photon are completely determined provided that the energy scales are large enough that the VDM component plays a negligible rôle. In contrast to F_2, the value of F_2^γ peaks at $x_\gamma \sim 1$. In addition, the scaling behaviour is different to that of hadrons. Specifically, the PDFs in the photon rise slowly as a function of Q^2 for all x [65]. This results from the fact that as x increases, it becomes more likely that quarks are produced from $\gamma \to q\bar{q}$ splitting rather than gluon splitting. A summary of the current measurements of F_2^γ is shown in Fig. 2.14. The data covers the range $0.24 < Q^2 < 390$ GeV and $0.005 < x_\gamma < 0.9$. At values of $x_\gamma \gtrsim 0.5$ experimental uncertainties are large and F_2^γ is not strongly constrained.

2.11 Photon Parton Density Functions

There are several different parameterisations of the parton distributions in the photon. However, each of the current parameterisations follow the same general approach. Each parameterisation uses some (usually VDM motivated) non-perturbative input, to fix the perturbatively incalculable quark and gluon distributions at some low scale, Q_0^2. The distributions are then evolved up to the scale of the current data.

For reasonably high reference scales ($\sim$ 2 GeV^2) a purely VDM motivated input is not sufficient [66] and must be supplemented by a hard quark component. There are two methods which are commonly invoked to achieve this. The first approach is to assume some reasonably high input scale of $\sim$ 1 GeV^2 and to fit the parton densities within the photon to data [64, 67, 68]. The second is to assume a pure VDM input with assumptions for unknown meson parameters and begin the evolution at a very low scale of typically $\sim 0.5 - 0.7$ GeV^2 [69–71]. In this way, the parton densities can be generated dynamically. Different parameterisations therefore differ mainly in the form of their input distributions and in their input scales, as well as in the factorisation scheme chosen. The free parameters are normally constrained by experiment. In the following subsections, the parameterisations for several photon PDFs are discussed in more detail.

2.11.1 Glück, Reya and Vogt (GRV)

The GRV parameterisations [72] for the photon are available at both LO and NLO. These authors have previously produced parameterisations for the proton (see Section 2.6.1) and the pion [73].

For the photon parameterisation, the evolution is started from a low scale of $Q_0^2 = 0.25$ GeV^2 and $Q_0^2 = 0.30$ GeV^2 for the LO and NLO fits respectively. Since it is assumed that the anomalous couplings of the photon vanish at these low input scales, the parameterisation is based on a purely valence-like, non-perturbative, VDM input model of the form $f_{q,g}^{\gamma}(x, Q_0^2) = \kappa \frac{4\pi\alpha}{f_\rho^2} f_{q,g}^{\pi}(x, Q_0^2)$. The $f_{q,g}^{i}$ are the quark and gluon densities within particle i. In practice, the ρ structure function is not known. Hence, the pion form factors are used, with the quantity f_ρ determining the $\gamma \rightarrow \rho$ transition probability. The κ parameter is introduced to describe contributions from heavier vector mesons and is the only free parameter in this formulation. In the threshold region, $W \gtrsim 2m_q$ GeV charm and bottom quarks are included via the lowest order Bethe-Heitler cross section, with $m_c = 1.5$ GeV and $m_b = 4.5$ GeV while at high W, they are treated as massless in the evolution. The factorisation scheme used in the GRV parameterisation is the DIS$_\gamma$ scheme.

A priori, it is not clear whether the densities within the pion quantitatively resemble those of a vector meson. Neither is it clear whether QCD is applicable at such low scales without further assumption [74, 75]. However, the resulting fits to the data are good at all currently accessible scales.

2.11.2 Schuler and Sjöstrand (SaS)

The SaS parameterisations are available only at LO. However, they are available in four forms [64] using both the DIS_γ and $\overline{\mathrm{MS}}$ factorisation schemes for the cases of both a very low starting scale, $Q_0^2 = 0.36$ GeV^2 (the SaS1D and SaS1M sets) and a higher scale $Q_0^2 = 4$ GeV^2 (the SaS2D and SaS2M sets). In principle, the distinction between factorisation schemes should not need to be considered at LO but since the difference is non-negligible, fits within both schemes are included.

In these parameterisations a VDM input is assumed. For the SaS2 sets, the shape and normalisation of the hadron-like input distribution is determined from fits to F_2^γ data. For the SaS1 sets, only the shape is obtained from fits to F_2^γ, while the normalisation is taken from an analysis of γp data. Bethe-Heitler contributions of charm and bottom are included, with $m_c = 1.3$ GeV and $m_b = 4.6$ GeV.

2.11.3 Hagiwara et al. (WHIT)

The WHIT parameterisations [76] are available only at LO and can be found in six different forms, each with systematically different gluon contents. Each of the WHIT sets begins begins the evolution at a high scale of $Q_0^2 = 4$ GeV^2.

The initial quark input distribution has the form $xf_q(x, Q_0^2)/\alpha = \frac{1}{B(B_q+1, C_q+1)} A_q x^{B_q}(1-x)^{C_q}$, where A_q, B_q and C_q are parameters which are obtained by global fits to structure function data in the range $4 < Q^2 < 100$ GeV^2. The quantity $B(\alpha, \beta)$ is the beta function that ensures the proper normalisation. The strange quark distribution is approximated by the Bethe-Heitler formula using $m_s = 0.5$ GeV. Charm is included via Bethe-Heitler for $Q^2 < 100$ GeV^2, with the charm mass taken to be $m_c = 1.5$ GeV, and at higher Q^2 through the use of massive evolution equations.

The input gluon distribution is parameterised by $xf_g(x, Q_0^2)/\alpha = A_g(C_g + 1)(1-x)^{C_g}$, where A_g and C_g are the free parameters which determine the normalisation and shape of the gluon distribution, respectively. These coefficients are systematically varied within limits which maintain consistency with the data.

2.11.4 The Photon Gluon Density

As previously mentioned, the F_2^γ data is relatively insensitive to the gluon content of the photon [68]. The photon gluon density is, therefore, effectively unconstrained. Since different assumptions motivate the choice of gluon input for each parton density parameterisation, it is informative to compare gluon distributions from the various parameterisations. The gluon distribution of GRV is derived from the gluon distribution obtained for the pion [69, 73] in πp collisions, while the SaS gluon component is fixed by purely theoretical, rather than experimental, constraints. Finally, the WHIT parameterisation has six different sets with systematically different gluon contents. Constraints on the range of possible values for A_g and C_g (see previous subsection) are obtained from QCD dynamics and then the values of these parameters are systematically varied within the specified ranges.

2.12 The Underlying Event

In a typical hadronic collision, the final state consists of the high-transverse-energy jets resulting from the hard interaction, as well as contributions from ISR, FSR and additional particles originating from the beam remnants. These different types of hadronic activity can be broadly classified into two separate groups,

- the **hard scattering component** which consists only of the high-transverse-energy jets arising from the hard interaction itself and containing the information about the underlying subprocess;
- the **underlying event** which incorporates all remaining hadronic activity.

Comparisons of HERA data with QCD predictions [14, 77–79] have shown that the observed jets are not well described, even if they include phenomenological models for QCD radiation and fragmentation effects. In particular, the underlying event energy (or jet pedestal) has been found to exceed QCD expectations. An excess of the measured underlying event energy has also been observed in hadron-hadron collisions [80]. It was found that the data could be described by adding interactions of the beam remnants into the calculations [57].

If the underlying event energy is integrated into the measured jet energy, the jet production rate is altered. Since the underlying event is largely non-perturbative, it is not well understood in QCD. However, if comparisons of measured jet cross sections are to yield useful conclusions, then the effects of the underlying event on the final state must be understood.

2.12.1 Multi-Parton Interactions

Due to the proliferation of low x partons, which can be inferred from the strong growth of the proton structure function (discussed in Section 2.4.3), it is possible for secondary scatters to take place between the partons in the beam remnants in hadronic collisions. This phenomenon is known as **Multi-Parton Interactions** (MPI) or multiple parton scattering [81]. Such interactions are expected at reasonably high centre-of-mass energies and signal the onset of unitarisation corrections to the simple pQCD picture of $2 \rightarrow 2$ parton scattering. In photoproduction, the probability of multi-parton interactions is larger at low x_γ since there is then significant momentum remaining in the photon remnant to undergo additional scatters.

The existence of multi-parton interactions has a direct impact on the hadronic final state. For example, the increased energy flow as a result of multi-parton interactions forms a hard partonic scattering component to the underlying event. In addition, the jet energies themselves will be increased. In extreme cases, the secondary scatters may also have sufficient energy to produce additional pairs of jets with the same topology as the primary pair of jets.

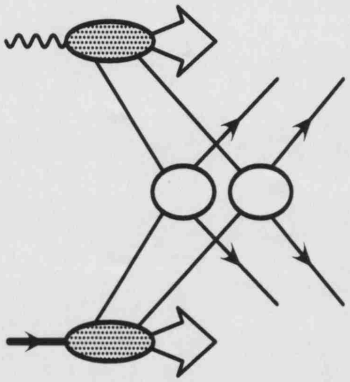

Figure 2.15: Illustration of multi-parton interactions in resolved photoproduction.

The AFS and UA2 Collaborations have searched for evidence for multi-parton interactions [83]. However, the first direct evidence for their existence has been reported more recently by the CDF Collaboration [84]. Since the dynamics of hadronic final state products in photoproduction is expected to be similar to that in hadron-hadron collisions, HERA is an ideal environment in which to study models of the underlying event. In particular, since multi-parton interactions can occur only in resolved photoproduction, HERA offers the opportunity to study events both with and without the possibility of multiple parton scattering in exactly the same physical environment.

Figure 2.16 shows the transverse energy profiles of jets in two jet photoproduction events from ZEUS 1994 data. At low transverse energy a discrepancy becomes apparent in the forward direction between the data and the predictions of the QCD models. The model including a simulation of multi-parton interactions gives an improved description of the data. Figure 2.17 shows the transverse energy density in the region outside the two jets of highest transverse energy in two jet photoproduction, as measured by H1. The data is compared to a variety of QCD models. The models including a simulation of the underlying event compare favourably with the data.

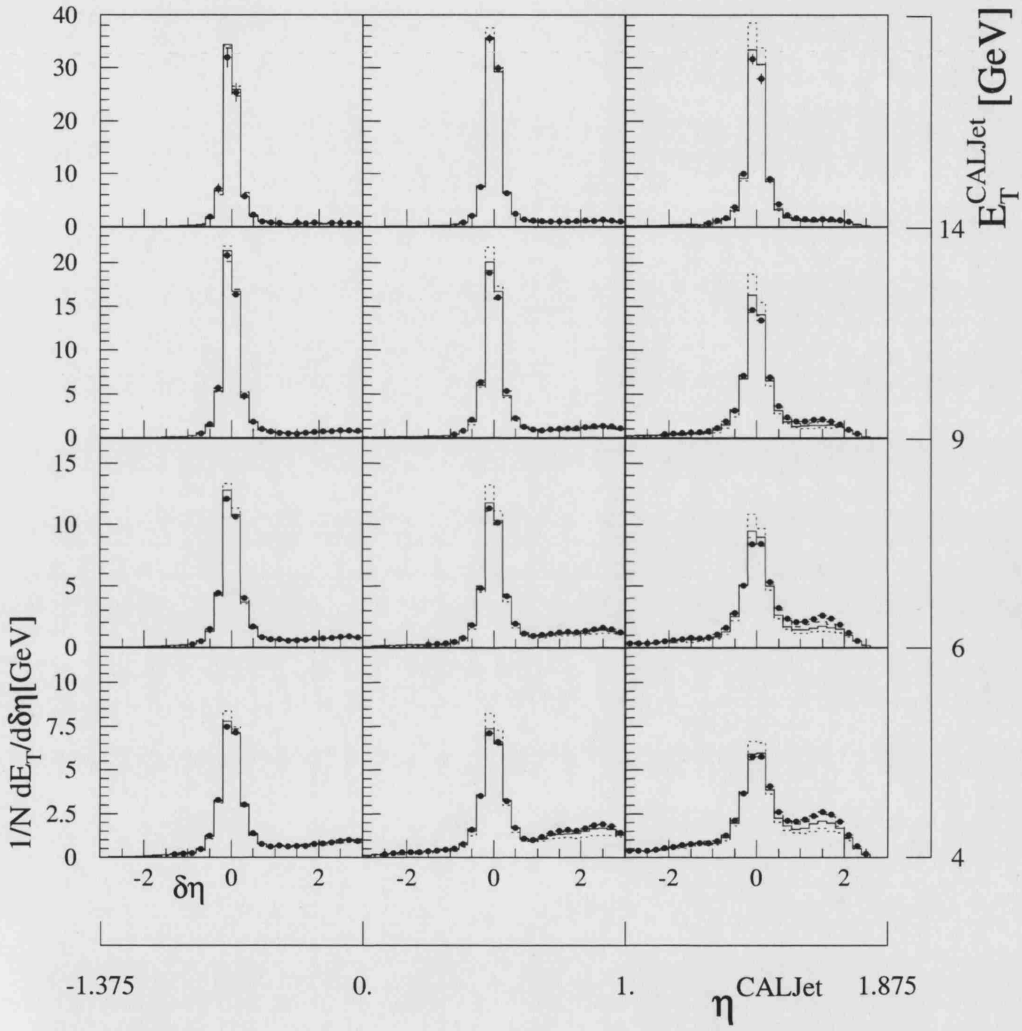

Figure 2.16: Jet profiles from the ZEUS 1994 two jet photoproduction analysis [82]. The uncorrected data are shown by the solid points and the predictions of HERWIG with and without a simulation of multi-parton interactions are shown by the solid and dashed lines, respectively.

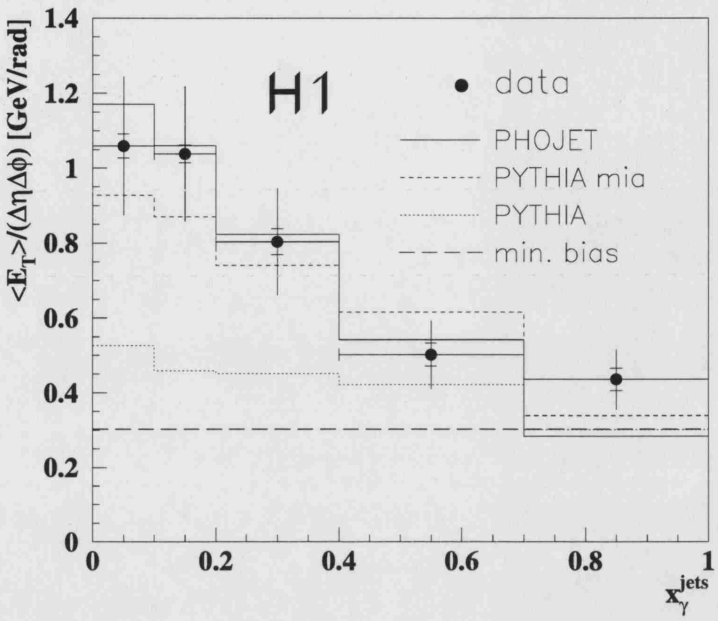

Figure 2.17: The H1 measurement of the transverse energy density per event and per unit area in $\eta - \phi$ space, outside the two jets of highest transverse energy in two jet photoproduction. The variable x_γ^{jets} is a measure of the momentum fraction of the parton from the photon. The solid points are the corrected data. The inner error bars show the statistical uncertainty and the outer error bars show the statistical and systematic uncertainties combined in quadrature. The histograms show the calculations of different QCD generators with (full=PHOJET [85], dashed=PYTHIA) and without (dotted=PYTHIA) interactions of the beam remnants.

2.13 Colour Coherence

QCD colour coherence describes the phenomenon arising from the interference of soft gluon radiation emitted between colour connected partons. The main consequences of coherence may be separated into two types:

- **intrajet coherence**
  This refers to the way in which a jet evolves from an initial parton. The multi-parton system that develops can be viewed as a sequence of parton branchings. The description of the evolution of a jet in terms of successive partons splittings in general requires an angular ordering condition $\theta_1 > \theta_2 > \theta_3 ...$ in order that each quark or gluon can resolve the parton from which is was emitted.

- **interjet coherence**
  This refers to the manner in which the angular distribution of gluon radiation is affected by the colour flow in an event. In addition to the gluon radiation involved in the evolution of the final state jets, there is a background of soft partons. The behaviour of such partons depends on the colour topology of the event. In photoproduction events, the colour flow can be complicated and different processes, with very different colour flows, make up the total cross section.

2.14 Diffractive Scattering

This section concentrates on the description of diffractive events which is relevant to the **Rapidity Gaps in Photoproduction** analysis presented in this thesis. The term **diffraction** was introduced to high energy physics to describe the observation that the scattering of a beam of hadrons off a target has aspects in common with the diffractive scattering of light from an opaque object.

Diffractive processes occur in the limit that the centre-of-mass energy is larger than any other invariant scale ($s \gg -t$). Such events can be selected experimentally by searching for large regions in rapidity[¶] which are void of activity. Such **rapidity gaps** are correlated with diffractive processes since the requirement of a large separation in rapidity is equivalent to the requirement of a large parton-parton centre-of-mass energy.

In present-day high energy physics, the presence of a large rapidity gap provides a working experimental definition of a diffractive process. Indeed, according to Bjorken [86] "A process is diffractive *if and only if* there is a large rapidity gap in the produced particle phase space which is not exponentially suppressed".

In "ordinary" QCD events, the production of rapidity gap events is exponentially suppressed as a function of increasing gap width. This can be understood with reference to the colour flow in an event. For example, in a standard photoproduction event, the propagator is a quark or gluon and a colour field exists between the outgoing particles. This can be envisaged as a colour string which connects the partons. As the partons move away from each other and undergo hadronisation, the string stretches and develops so that the final state is colourless. This process causes soft gluon emission and the creation of quark-anti-quark pairs. This gives rise to particle production and energy flow in the region between the outgoing jets. An analogous situation occurs in hadron-hadron scattering and in DIS. In such cases, a gap will only be produced through multiplicity fluctuations which follow a Poisson distribution and are exponentially

[¶]The rapidity of a particle y is defined in Section 4.8. Experimentally, the pseudo-rapidity η is used. This is equivalent to y in the limit $m \to 0$.

suppressed as the rapidity interval increases. In contrast, the diffractive scattering process is assumed to proceed via the exchange of a colour singlet object which carries vacuum quantum numbers[‖]. In this case, the outgoing partons are not colour connected and particle production in the region between the jets is suppressed.

One of the most interesting results to arise from the early HERA data was the large number of events ($\sim$ 10%) containing a large rapidity gap [87]. Similar large rapidity gap events have also been observed in hadron-hadron scattering [21, 22]. These results have been interpreted as evidence for the exchange of a strongly interacting colour singlet object. The object responsible for the diffractive exchange is generically referred to as the pomeron ($\mathbb{P}$). The idea of the pomeron was first introduced in the context of Regge theory [88]. In QCD models, the colourless object consists of a minimum of two gluons.

2.14.1 Regge Theory

Prior to the development of QCD, significant progress had already been made in developing a framework to understand the scattering of strongly interacting particles. The phenomenological model of **Regge theory** was developed in the 1960's and has been shown to give a good description of the behaviour of the total hadronic cross section. Regge theory is founded on some very general assumptions about the scattering process. The aim of the model is to determine the asymptotic behaviour of the scattering amplitude in the limit that the centre-of-mass energy is larger than any other invariant. A comprehensive description of the theory is given, for example, in [89]. Only the basics of the Regge approach are described here.

Regge theory makes use of crossing symmetry. For the general two-to-two body (s-channel) process $ab \rightarrow cd$, s is the centre-of-mass energy squared and t is the four-momentum transfer squared relative to the scattering angle θ. For the crossed (t-channel) process $a\bar{c} \rightarrow \bar{b}d$, the centre-of-mass energy squared and four-momentum transfer squared can be denoted by $\bar{s}$ and $\bar{t}$ respectively. These processes are related by crossing symmetry so that $\bar{s} = t$ and $\bar{t} = s$. This means that the physically different s- and t-channel processes have the same scattering amplitudes, so that,

$$\mathcal{A}_{a\bar{c}\rightarrow\bar{b}d}(s,t) = \mathcal{A}_{ab\rightarrow cd}(t,s). \tag{2.67}$$

The scattering amplitudes can be written as a **partial wave expansion**. For the t-channel scattering process,

$$\mathcal{A}_{a\bar{c}\rightarrow\bar{b}d}(s,t) = \sum_{l=0}^{\infty}(2l+1)a_l(s)P_l(\cos\theta), \tag{2.68}$$

[‖]Isospin I = 0 and even under the charge conjugation operator.

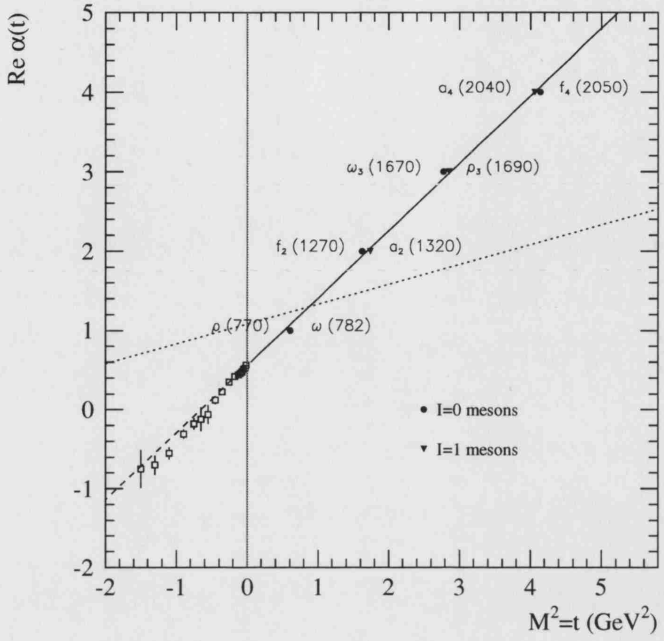

Figure 2.18: The Chew-Frautschi plot for the ρ, ω, f and a mesons. The solid line shows a fit to the mesons of the form of Eq. 2.71, while the dashed line is the extension of the fit to $t < 0$. The points at $t < 0$ were derived from $\pi^- p \to \pi^0 n$ scattering data [90]. The dotted line represents the trajectory corresponding to pomeron exchange.

where $\cos\theta = 1 + \frac{2t}{s}$ in the centre-of-mass frame, $P_l(\cos\theta)$ are the Legendre polynomials for a particular angular momentum, l, and $a_l(s)$ are the partial wave amplitudes. Similarly, the amplitude for the s-channel process may be obtained (using crossing symmetry) by interchanging s and t everywhere in Eq. 2.68.

Using the **Sommerfeld-Watson transform** [91], the partial wave expansion of Eq. 2.68 can be rewritten in terms of a contour integral in the complex angular momentum plane. The poles in the l^{th} partial wave take the form,

$$a_l(t) \approx \frac{\beta(t)}{l - \alpha(t)}, \tag{2.69}$$

where $l = \alpha(t)$ is called the **Regge pole** and $\beta(t)$ is the residue function which specifies the coupling of the pole to external particles. The poles (or singularities) are usually identified with resonances. The asymptotic behaviour of the scattering amplitude as $s \to \infty$ is given by,

$$\mathcal{A}(s,t) \to \beta(t) s^{\alpha(t)}. \tag{2.70}$$

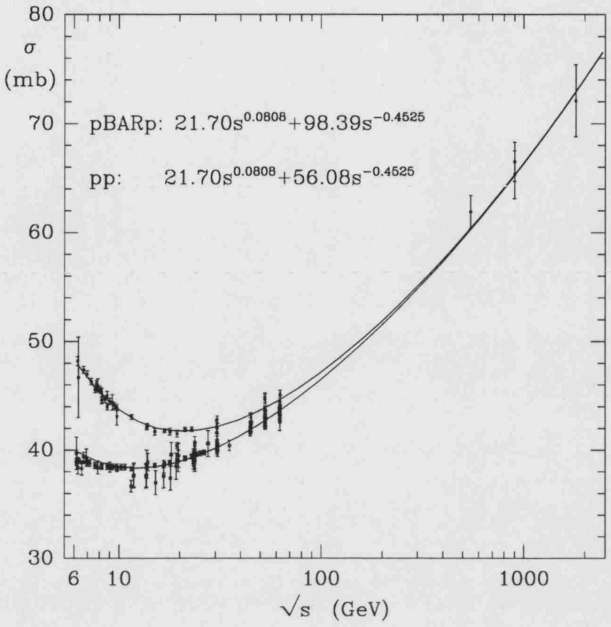

Figure 2.19: A compilation of data showing the total proton-proton and proton-anti-proton cross sections as a function of centre-of-mass energy, $\sqrt{s}$. The curves show the fits by Donnachie and Landshoff, the coefficients of which are shown as text in the plot.

This is the characteristic Regge-pole asymptotic power behaviour of the scattering amplitude from the exchange of a Regge trajectory. This can be viewed as the exchange of a **reggeon** ($\mathbb{R}$) with angular momentum $\alpha(t)$. The angular momentum $\alpha(t)$ is a continuous complex variable and so the reggeon is not a physical particle. Rather, the amplitude effectively sums the contributions from all possible exchange particles with appropriate quantum numbers.

For the t-channel process with positive t, the amplitude will have resonances corresponding to the exchange of physical particles of spin $J_i = \alpha(t)$ and mass $m_i = \sqrt{t}$. Chew and Frautschi [92] studied the relationship between the spin of mesons and their mass squared and found a linear correspondence of the form $J_i(m_i^2) = J_i(0) + J_i' m_i^2$. In terms of α and t this is written,

$$\alpha(t) = \alpha(0) + \alpha' t. \tag{2.71}$$

This defines the **Regge trajectory**. An example of the Chew-Frautschi plot for the ρ, ω, f and a mesons is shown in Fig. 2.18. The Regge trajectory has parameters,

$$\alpha(0) = 0.55; \quad \alpha' = 0.86 \text{ GeV}^{-2}. \tag{2.72}$$

From Eq. 2.70, the amplitude is now given by,

$$\mathcal{A}(s,t) \sim s^{\alpha(0)+\alpha' t}. \tag{2.73}$$

and the differential cross section is,

$$\frac{\mathrm{d}\sigma}{\mathrm{d}t} \propto \frac{1}{s^2}|\mathcal{A}(s,t)|^2 \sim s^{2(\alpha(0)+\alpha' t-1)}. \tag{2.74}$$

This functional form has been shown to correctly describe the differential cross section for a number of processes [93]. It is also possible to extrapolate the trajectory to give predictions for negative t. The extrapolated fit has been found to give good agreement with a measurement of $\pi^- p \rightarrow \pi^0 n$ processes [90] over a wide range of pion energies. This is illustrated by the dashed line in Fig. 2.18.

2.14.1.1 The Soft Pomeron

From the **optical theorem** [89], which relates the total cross section σ_{tot} to the imaginary part of the forward elastic scattering amplitude, the following relation can be obtained,

$$\sigma_{tot} = \frac{1}{s}\Im m\left(\mathcal{A}(s,0)\right). \tag{2.75}$$

Substitution of Eq. 2.73 gives,

$$\sigma_{tot} \sim s^{\alpha(0)-1} \tag{2.76}$$

where $\alpha(0)$ is the intercept of the appropriate trajectory. The Regge trajectory has $\alpha(0) < 1$. Therefore, the total cross section should decrease with increasing s. Experimentally, this is found to be true only for $s \lesssim 10$ GeV^2. At higher energies, the measured cross sections are either constant or slowly rising as a function of increasing energy [94]. This observation motivated the postulation that a trajectory with $\alpha(0) > 1$ could describe the behaviour of the total cross section.

Pomeranchuk and Okun [95] showed that in any scattering process in which charge is exchanged, the cross section vanishes asymptotically as $s \rightarrow \infty$. Foldy and Peierls [96] showed that if the cross section does *not* fall as s increases, then that process must be dominated by the exchange of vacuum quantum numbers. If the slow rise in the total hadronic cross section is to be attributed to Regge exchange then it must therefore correspond to a reggeon with vacuum quantum numbers and an intercept of $\alpha(0) > 1$. The trajectory which would fulfill these requirements was suggested by Gribov [97] and was named the pomeron**.

**In honour of Pomeronchuk who carried out much of the early work on diffraction.

Fits to inclusive hadron-hadron cross sections give the following coefficients for the pomeron trajectory,

$$\alpha(0) = 1.08; \quad \alpha' = 0.25 \text{ GeV}^{-2}. \tag{2.77}$$

This trajectory is known as the **soft pomeron**. In contrast to the mesons which lie on the trajectory represented by the solid line in Fig. 2.18, there is no conclusive evidence for the observation of a physical particle lying on the pomeron trajectory (dotted line on the same figure). However, in QCD, particles with vacuum quantum numbers can exists in a bound state of gluons called **glueballs**. The WA91 Collaboration have reported a glueball candidate [98], with a mass 1926 ± 12 MeV, making it possibly the first observation of a particle lying on the pomeron trajectory. However, there is no evidence so far that this object is responsible for diffractive exchange.

Figure 2.19 shows the measured proton-proton (pp) and proton-anti-proton ($p\bar{p}$) total cross section, together with fits performed by Donnachie and Landshoff [99]. The functional form of the fits is given by,

$$\sigma_{tot} = As^{\alpha_{\mathbb{P}}-1} + Bs^{\alpha_{\mathbb{R}}-1} \tag{2.78}$$

where $\alpha_{\mathbb{P}} = 1.08$ is the pomeron intercept and $\alpha_{\mathbb{R}} = 0.55$ is the reggeon intercept.

Since the pomeron carries vacuum quantum numbers it couples to particles and anti-particles with equal strength. Therefore the value of A in the fits is the same for both the pp and $p\bar{p}$ cross sections. In contrast, reggeons have different couplings to particles and anti-particles and so the value of B is different in the fits. Therefore, it is the second term in Eq. 2.78 that distinguishes between the cross sections. This is visible in the difference between the cross sections at low $\sqrt{s}$. If this is the correct model, the total cross section for other processes should also be described by a superposition of two Regge trajectories. Fits to $\pi^{\pm}p$ and γp total cross sections [100] have also been performed and it is found that they can also be described by a function of the form of Eq. 2.78. This suggests that the pomeron is a universal object.

2.14.2 Diffractive Processes at High-t

With the advent of QCD, much of the attention was diverted away from the Regge theory approach. However, high energy colliders (e.g. HERA, Tevatron) have shown that hadron-hadron cross sections at high energies are dominated by long range, soft physics. The low momentum transfer means that pQCD is not applicable. In contrast, Regge theory successfully parameterises the soft physics and explains the observed behaviour of the total hadronic cross section at high centre-of-mass energies by the exchange of a pomeron.

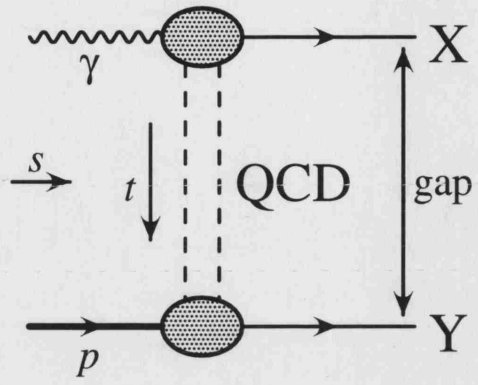

Figure 2.20: A generic rapidity gap process.

As a consequence of the large distances involved, diffractive scattering is not currently well understood within the framework of QCD. However, if QCD is to be regarded as the complete theory of the strong interaction, it must be able to reproduce Regge behaviour. The predictions of Regge theory then act as a constraint on the high energy properties of QCD [101].

In general, rapidity gaps are produced with little or no momentum transfer t, making an attempt to use pQCD rather difficult. However, it is possible to search for a class of hard diffractive events in which a large momentum is transferred across the gap [102, 103]. In the limit that $-t \gg \Lambda^2_{\rm QCD}$, perturbative methods can be applied [104].

A generic rapidity gap event in photoproduction[††] is shown in Fig. 2.20 where X and Y represent the hadronic products of the photon and proton respectively. There are several examples of high-t diffractive processes that can be studied:

- **quasi-elastic vector meson production** at high transverse momentum ($\gamma p \rightarrow Vp$). In this case, the system X is a single vector meson $V = \rho, \omega, \phi ...$. This process has been studied at HERA and is believed to contribute about 10% to the total photoproduction cross section [100]. In Regge theory, the s dependence of the quasi-elastic cross section should be the same as that of the total photon-proton cross section. Figure 2.21 shows the W dependence of the vector meson production cross section. The energy dependence of the ρ production cross section is very similar to that of the total cross section, while the J/ψ cross section has a steeper dependence due to its larger mass which introduces a hard scale. This suggests that the soft pomeron is not sufficient to explain the behaviour of the cross section in the presence of a hard scale. Attempts have been made [108, 109] to describe the dependence in the framework of the Regge model by introducing a **hard pomeron** trajectory ($\alpha_{I\!P}^{\rm hard}(0) \gg \alpha_{I\!P}^{\rm soft}(0) = 1.08$).

[††]Note that this also applies to hadron-hadron collisions where the γ is replaced by a p in Fig. 2.20.

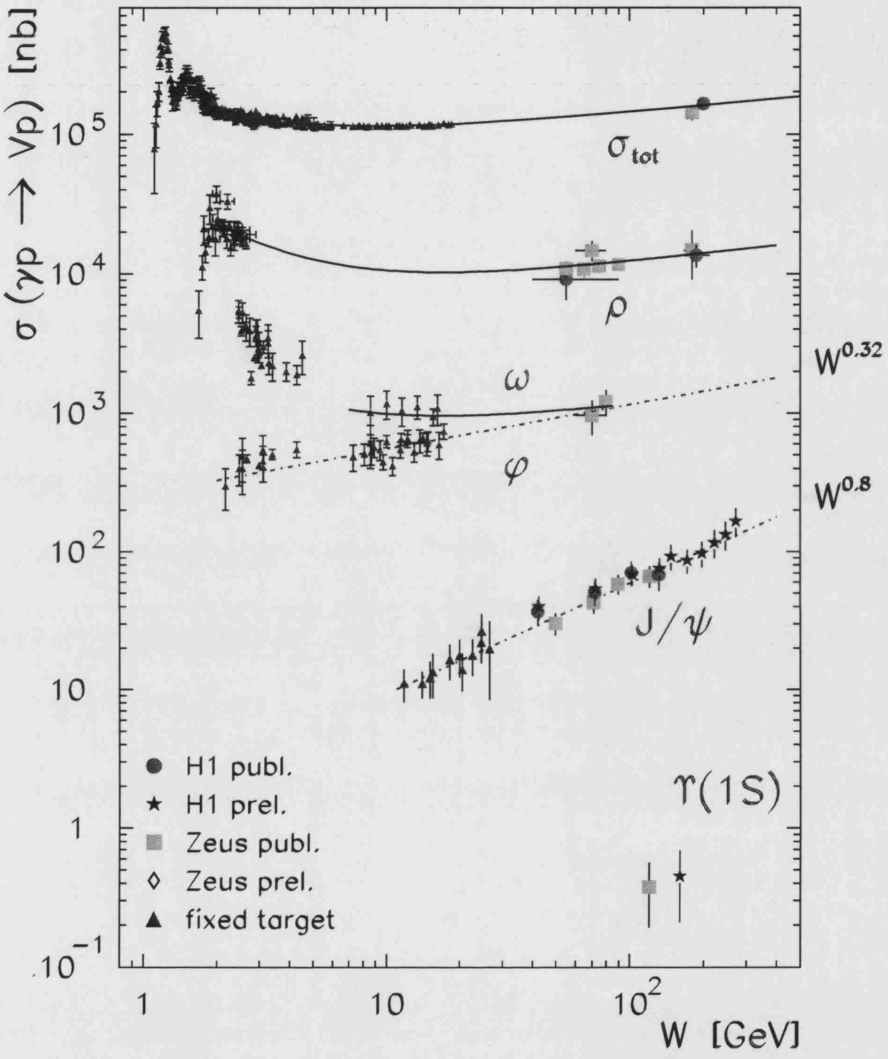

Figure 2.21: The centre-of-mass energy dependence of the total $\gamma^* p$ cross section and the total cross sections for vector meson production measured at HERA and fixed target experiments. Diagram taken from [105] with data from [106, 107].

- **single diffractive dissociation** ($\gamma p \to XV$ or $\gamma p \to VY$). In this case, one of the systems X or Y is a vector meson while the remaining system breaks up (or **dissociates**).
- **double diffractive dissociation** ($\gamma p \to XY$). In this case, both the photon and the proton dissociate. Events in which both the systems X and Y are required to contain at least one jet have been studied in hadron-hadron collisions at the Tevatron [21, 22] and in photoproduction at HERA [23–25]. This is called the **gaps-between-jets** approach.

The diffractive contribution to the total γp cross section at $\sqrt{s} \sim 300$ GeV is approximately 40% [100]. Proton and/or photon dissociation corresponds to non-zero momentum transfer across the gap. The requirement of large momentum transfer means that the gap producing mechanism is dominated by short-distance physics [104]. This means that pQCD can, in principle, be applied and the pomeron can be pictured as coupling in a point-like way. The process can then be treated as a convolution of the PDFs with elastic parton-parton scattering. The requirement that $s \gg -t \gg \Lambda^2_{\rm QCD}$ means that events are in the perturbatively calculable Regge limit of QCD.

The study of high-t diffractive scattering can be viewed as an attempt to understand the underlying process responsible for the rapidity gap in the context of QCD. In addition, it is important to other areas of high energy physics. For example, it has been suggested that the characteristic radiation patterns of colour-singlet exchange could be used to search for Higgs production in W^+W^- scattering at the Large Hadron Collider (LHC) [110] but that diffractive exchange via a strongly interacting colour singlet object could produce a significant background to the process [103].

2.14.3 The Perturbative Pomeron

The cross section for the soft pomeron falls as $\frac{d\sigma}{dt} \sim s^{2(1.08+0.25t-1)}$ leading to a vanishingly small cross section at high values of $|t|$. However, the hard scale makes it possible to use pQCD and leads to the concept of a perturbative (or hard) QCD pomeron.

The simplest model for a QCD-driven gap-producing mechanism is a bound state of two (t-channel) gluons existing as an overall colour singlet. This was first suggested by Low and Nussinov [111]. A calculation based on this model yields a rate of (two gluon) colour-singlet exchange of $\sim$ 10% [103]. Gluon exchange in the t-channel increases with $1/t^2$. However, gluon exchange between this t-channel gluon pair can further enhance the cross section so that it rises faster than $1/t^2$ at small t. These gluons can be summed using the BFKL Equation [112, 113]. The resulting object is often referred to as the **BFKL pomeron**.

The LLA BFKL colour-singlet exchange cross section for the elastic scattering of two partons, as calculated by Mueller and Tang [102], is given by,

$$\frac{\mathrm{d}\sigma(qq \to qq)}{\mathrm{d}\hat{t}} = (\alpha_s^{pre.} C_F)^4 \frac{2\pi^3}{\hat{t}^2} \frac{\exp(2\omega_0 y)}{[7\alpha_s^{den.} C_A \zeta(3) y]^3} \tag{2.79}$$

for $y = \Delta\eta = \log(\frac{x_\gamma x_p s}{-t}) \gg 1$ where $C_F = 4/3$, $C_A = N_C = 3$ and $\zeta(3) \approx 1.202$ is the Reimann zeta function. The ω_0 parameter is given by $\omega_0 = \frac{C_A \alpha_s^{den.}}{\pi} 4 \log 2$, where $(1 + \omega_0)$ is the pomeron intercept. The values of α_s in the pre-factor ($\alpha_s^{pre.}$) and in the denominator ($\alpha_s^{den.}$) are free parameters in the model and can be chosen independently.

2.14.4 Gap Survival and the Underlying Event

The gap producing mechanism is complicated by the concept of **gap survival**. If a rapidity gap is produced in the hard interaction, it may subsequently be destroyed by soft gluon emission during hadronisation which can "spill" into the central rapidity region. A gap may also be destroyed by additional activity in the underlying event. In particular, the re-scattering of spectator partons in the beam remnants (MPI) may destroy the gap signature since any additional scatter is likely to be colourful. An example of the destruction of a gap by this means is illustrated in Fig. 2.22.

Since these effects are largely non-perturbative, the calculation of a gap survival probability is complicated. In one model, the effect can be considered as an overall multiplicative **gap survival probability**, $\mathcal{S}$, which is independent of the nature of the hard interaction [86]. The value of $\mathcal{S}$ is the probability that a gap produced at the level of the interacting partons retains its gap signature at the hadron level. The value of $\mathcal{S}$ is expected to depend on the centre-of-mass energy. In particular, as s increases, so too does the number of low-x partons making the probability of secondary scatters more likely.

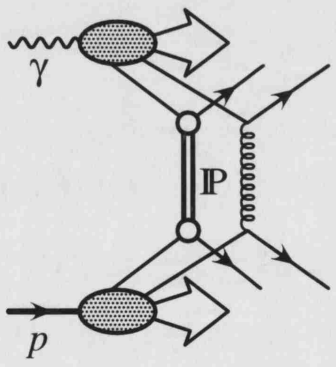

Figure 2.22: Illustration of the destruction of a gap by multi-parton interactions.

Since QCD colour singlet exchange proceeds at LO via the exchange of a composite object, it is also reasonable to consider whether the constituents of the exchanged object might destroy the gap signature. An NLO calculation of the radiation patterns of soft gluons in colour-singlet exchange has been performed [114]. The results show that the radiation pattern of soft gluons is suppressed in the central rapidity region for two gluon exchange in the same way as it is for photon exchange.

2.15 Theoretical QCD Models

QCD processes involving a hard scale are directly calculable in pQCD. However, in practice, the short-distance, perturbatively calculable processes are always accompanied by non-perturbative interactions which can only be described by phenomenological models. A hadronic event may be broadly classified into three main parts, each of which can be independently modelled:

1. **structure of the interacting hadrons**
   This is described by the PDFs. The PDFs are evolved from the starting scale μ_0 to the factorisation scale μ_F using the DGLAP parton evolution equations. The scale μ_F separates the structure of the hadron from the hard scatter and is usually taken to be the momentum transfer in the hard interaction. The processes occurring above and below this scale are assumed to be completely independent.

2. **hard interaction**
   This involves a hard scale and can be calculated in a fixed order perturbative expansion. The dependence of the calculation on the renormalisation scale, μ_r, is reduced by including NLO contributions to the process under consideration.

3. **fragmentation**
   Outgoing partons are subject to colour confinement, causing them to fragment and form colour neutral hadrons. This process consists of both perturbative and non-perturbative parts. Firstly, the parton produced in the hard scatter will emit further partons via **parton showering**. Provided the transverse momentum of these emissions is sufficiently large, they can be described by the re-summation of dominant logarithmic terms to infinite order in α_s (similar to the parton evolution in the initial state). The partons produced in the showering then undergo **hadronisation**. Only phenomenological models can be used to describe the hadronisation process.

Two types of QCD model are currently available. The first type is a **Fixed order pQCD Calculation**. Such calculations currently model only steps 1 and 2 (above). The hard interaction is calculated using the exact matrix element for the process under consideration. To date, pQCD calculations are available in photoproduction up to and including $\mathcal{O}(\alpha\alpha_s^2)$. The second type of model is a **Monte Carlo** generator. The Monte Carlos currently available contain only LO matrix elements. Higher order processes are modelled through the simulation of initial- and final-state parton showers. Phenomenological models, such as the **cluster** [115] or **string** [116] models, are then used to simulate the non-perturbative hadronisation process.

Measurements at HERA (for example, in [117]) have shown that NLO corrections to two jet photoproduction cross sections are large. Therefore, measured cross sections should ideally be compared to pQCD calculations that are at least NLO for the process under consideration. However, for the analyses presented in this thesis, no fixed order calculations are currently available. Instead, the measured distributions are compared to the predictions of Monte Carlo models, thereby providing sensitive tests of parton-shower extensions to fixed order calculations. In this thesis, the HERWIG [118] and PYTHIA [119] Monte Carlos are used for the generation of events. A more detailed description of these programs is given in Appendix C.

Monte Carlo programs make several approximations that can affect the prediction of the cross section. Most importantly, since the models only include the LO matrix elements, the results are dependent on the factorisation scale (see Section 2.9). Other factors may also influence the cross section prediction. For example, HERWIG uses the two-loop calculation of α_s while PYTHIA uses the one-loop calculation. This has been shown to give a factor of 1.3 difference in the predicted cross section [82]. However, measurements have shown that the uncertainties present in the cross section prediction usually lead only to differences in normalisation, while the shape of the distributions are well described. For this reason, the absolute normalisation of the Monte Carlo (and of the predicted cross section) may be varied.

Chapter 3

HERA and the ZEUS Detector

The lepton-proton collider, HERA, provides an ideal laboratory to test current understanding of the theory of QCD. In this chapter, the HERA accelerator and the ZEUS detector are introduced. Following a description of HERA and its injection system, a brief overview of the ZEUS detector is given. The components important to this analysis are then reviewed in more detail. Finally, the ZEUS trigger and data acquisition systems are described.

3.1 The HERA Collider

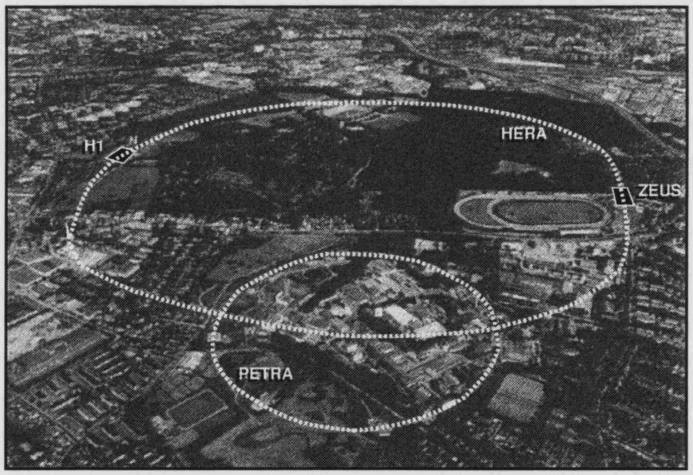

Figure 3.1: The Hamburg Volkspark showing the DESY site. The location of the HERA and PETRA rings are shown. Also illustrated are the locations of the two colliding-beam experiments, ZEUS and H1.

Luminosity (pb^{-1})

Year	e^-p	e^+p
1992	0.03	-
1993	1.1	-
1994	1.1	5.1
1995	-	12.3
1996	-	17.2
1997	-	36.4
1998	8.1	-
1999	17.1	28.5
2000	-	66.4

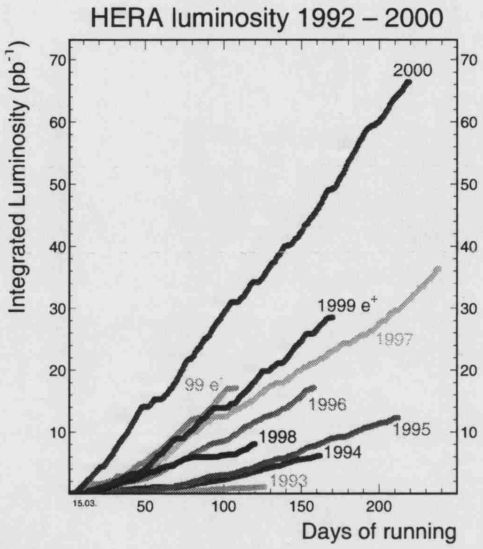

Figure 3.2: The HERA integrated luminosity as a function of time.

The Hadron Elektron Ring Anlage (HERA) accelerator [120] is the world's first and, to date, only lepton-proton collider. It is situated at the Deutsch Elektronen SYnchrotron (DESY) laboratory in Hamburg, Germany. An aerial view of the location of the HERA collider and of the DESY site is shown in Fig. 3.1. The construction of HERA began in April 1984 and in October 1991, following a period of machine tests with separated beams, the first electron-proton collisions were observed. In May 1992, the two colliding-beam experiments, ZEUS [121] and H1 [122] began regular data-taking.

The HERA ring is located at a depth which ranges from between 10 m and 30 m beneath ground level. The leptons and protons are accelerated in two separate machines of 6.34 km circumference. The crossing interval of the lepton and proton bunches is 96 ns. The HERA ring is not a circle, instead consisting of four straight sections joined together by four arcs, each having a radius of 797 m. Located within the straight portions of the ring are the four experiments associated with HERA. The ZEUS detector is located in the south experimental hall, whilst the H1 experiment occupies the north hall. Both the ZEUS and H1 experiments study the physics of lepton-proton collisions. The east hall is occupied by the HERMES [123] experiment. Here, the lepton beam is caused to collide with fixed targets of either H, ^{2}D or ^{3}He, in order that the polarised structure function of the nucleon may be studied. Lastly, the HERA-B [124] experiment, which is located in the west hall, uses a wire target placed in the proton beam halo in order to study CP violation in the decay of B-mesons.

HERA was originally designed to collide beams of 820 GeV protons with 30 GeV electrons. However, between 1994 and 1997, HERA switched from electrons to

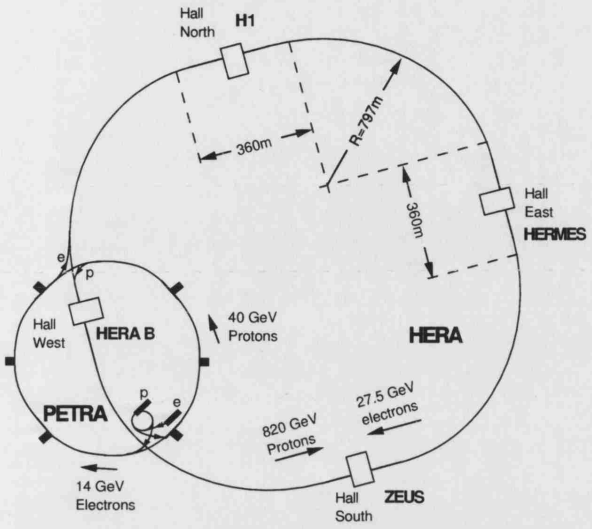

Figure 3.3: The HERA ring and injection system. The PETRA pre-accelerator ring and the locations of the four experimental halls are labelled.

positrons since electron beams have a shorter lifetime than those of its anti-particle. This is partly due to the fact that, when running with electrons, positive ions remaining in the beam-pipe are attracted to the centre of the beam-line. This increases the interaction rate of the electrons with the beam-gas and, hence, decreases the lifetime of the beam. In contrast, positrons repel the positive ions and the beam lifetime is enhanced. Since 1998, HERA has used both electrons and positrons during different data-taking periods.

Since full operation began in 1992, until the long shut-down at the end of 2000, the luminosity delivered by HERA has shown a steady increase. This is illustrated in

Parameter	Design	1996	1997
Centre-of-Mass Energy (GeV)	314	300	300
Proton Beam Energy E_p (GeV)	820.0	820.0	820.0
Lepton Beam Energy E_e (GeV)	30	27.5	27.5
Proton Beam Current $< I_p >$ (mA)	163	65	77-105
Lepton Beam Current $< I_e >$ (mA)	58	33	36-43
Number of Colliding Bunches	210	174	174
Number of Pilot Bunches ($e(p)$)		6 (15)	6 (15)
Bunch Crossing Interval (ns)	96	96	96
Instantaneous Luminosity $\mathcal{L}$ (10^{30} cm^{-2}s^{-1})	15	$6.1 - 10.3$	$8.44 - 14.0$
Integrated Luminosity $\mathcal{L}^{\text{int}}$ (pb^{-1} per year)	100	17.2	36.4

Table 3.1: Performance of HERA during the 1996-1997 running period.

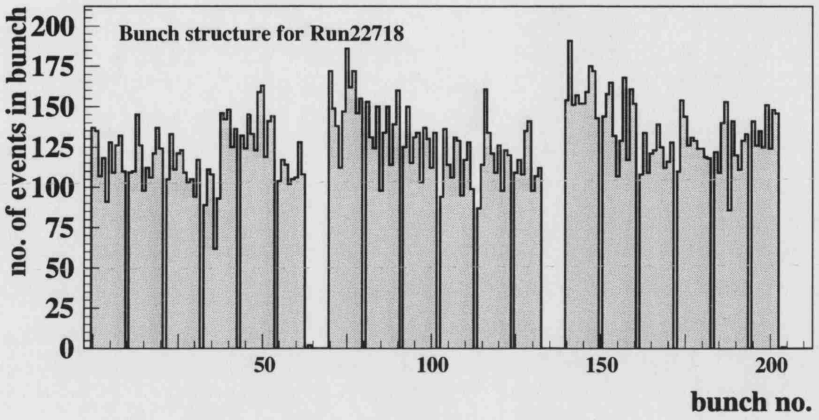

Figure 3.4: The bunch structure of a typical run in 1997 for paired ep bunches. The small spaces are reserved for the unpaired e and p pilot bunches and the larger gaps indicate the empty bunches for the beam dump.

Fig. 3.2 which shows the integrated luminosity as a function of time.

Neglecting the mass of the protons and leptons, the HERA centre-of-mass energy squared is given by $s \approx 4E_pE_e$, where E_p and E_e are the energies of the proton and lepton beams, respectively. During the 1996-1997 running period, HERA collided 820 GeV protons with 27.5 GeV positrons, giving a centre-of-mass energy of $\sqrt{s} \simeq 300$ GeV*. The HERA centre-of-mass energy represents an order of magnitude increase over the centre-of-mass energies of previous fixed-target experiments. This has significantly extended the accessible kinematic region in x and Q^2. Table 3.1 lists the values of several HERA parameters during the 1996-1997 running period compared to the design values.

3.1.1 The HERA Injection System

Leptons and protons are accelerated in two separate machines which use conventional and superconducting magnets, respectively. The injection of leptons and protons into the HERA accelerator occurs in several different stages, as illustrated in Fig. 3.3.

In the proton injection system, a LINear ACcelerator (LINAC) is used to accelerate H^- ions to an energy of 50 MeV. These H^- ions are then passed to the DESY III proton synchrotron. Here, they are stripped of their electrons (by passage through a thin foil) to yield protons and accelerated to 7.5 GeV in 11 bunches with the same 96 ns bunch spacing as in the main HERA ring. The protons are then passed to the PETRA storage ring where they are further accelerated to an energy of 40 GeV

*From 1998-2000, the proton energy was increased to 920 GeV giving $\sqrt{s} \approx 318$ GeV.

before finally being injected into HERA. A maximum of 70 bunches can be stored in PETRA. This process continues until HERA is filled with 210 bunches[†]. Once in the ring, conventional radio frequency cavities are used to accelerate the protons to their operating energy. The proton beam is focussed and guided by superconducting quadrapole and dipole magnets, respectively. The superconducting magnets are cooled using liquid helium.

In the lepton injection system, lepton beams[‡] are accelerated to 220 MeV and 450 MeV using LINACs I and II, respectively. From here, the leptons are passed to the DESY II synchrotron and are further accelerated to 7.5 GeV before being injected into the PETRA II storage ring in bunches with 96 ns spacing. Here, their energy is increased to 14 GeV before they are finally injected into the HERA lepton machine. After filling with 210 bunches, conventional and superconducting cavities are used to accelerate the beam to its operating energy of 27.5 GeV.

3.2 The ZEUS Coordinate System

The ZEUS coordinate system is a right-handed, Cartesian system with the origin defined as the nominal Interaction Point (IP). The positive z-axis points in the direction of the proton beam and is often referred to as the **forward** direction. The x-axis points from the IP towards the centre of the HERA ring and the y axis lies at 90° to the other two axes and points approximately vertically upwards. Since the proton-beam axis has a slight tilt, the y-axis is not precisely coincident with the vertical. The actual IP varies from event to event, and the run average and proton tilt varies on a fill-by-fill basis. However, the nominal IP is close to the geometric centre of the experiment.

For event analysis, a cylindrical polar coordinate system is often used. In this system of coordinates, the polar angle, θ, is defined as the angle with respect to the proton-beam direction. According to this definition, $\theta = 0°$ points in the forward direction and $\theta = 180°$ points in the extreme rear direction of the detector. The azimuthal angle, ϕ, is defined to be the angle with respect to the x-axis. The ZEUS coordinate system is illustrated in Fig. 3.5.

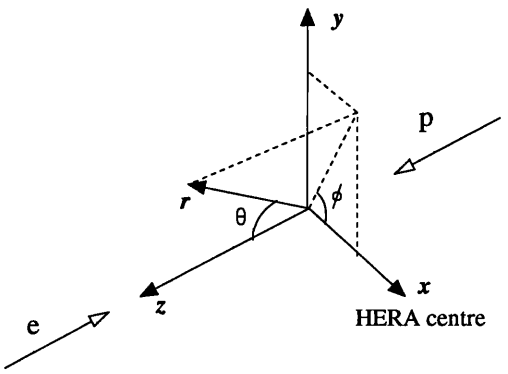

Figure 3.5: The ZEUS coordinate system.

Due to the asymmetric nature of lepton-proton interactions, physically interesting frames are often boosted along the z-axis. Therefore, in the laboratory frame, polar

[†]Although HERA can hold up to 210 bunches, it usually operates with an average of 174 colliding bunches (paired), 15 lepton pilot (unpaired) and 6 proton pilot (unpaired) bunches as well as 15 empty bunches. This is for background calibration purposes. The empty bunches are also used as a safety precaution in case of the need for an emergency beam dump.

[‡]Electrons are produced directly via an electron gun. Positrons are obtained from e^+e^- pair production via electron bremsstrahlung interacting in a tungsten target.

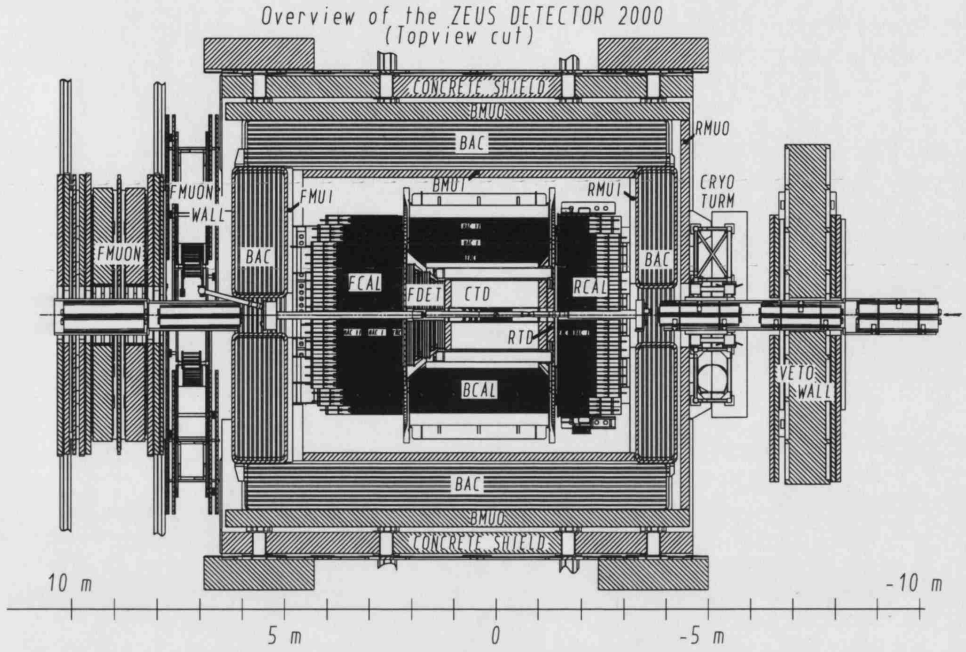

Figure 3.6: View of the ZEUS detector in the zy-plane, showing the configuration of the main detector components. In this diagram, the proton enters the detector from the right and the lepton from the left.

angles are often expressed in terms of the pseudo-rapidity, η, where,

$$\eta = -\log\left(\tan\frac{\theta}{2}\right). \tag{3.1}$$

With this definition, $\eta \to \infty$ in the proton direction and $\eta \to -\infty$ in the lepton direction. The pseudo-rapidity is an exceptionally useful quantity since any boost along the z-axis modifies its value only by the addition of a constant[§].

3.3 The ZEUS Detector

Figure 3.6 shows a cross sectional view of the ZEUS detector, indicating schematically the layout of its components in the zy-plane. In this section, a brief overview of the main components of the ZEUS detector is given. This is followed by a slightly more detailed description of the components relevant to the present analysis. A complete description of ZEUS and its detector components can be found in [121].

[§]Strictly, it is differences in the rapidity y that is boost invariant. However, in the limit of massless particles $m \to 0$, $y \to \eta$. This is shown in Appendix B.

ZEUS is a general purpose, magnetic detector. It measures $12 \times 10 \times 19$ m^3 and weighs 3600 tonnes. The ZEUS detector is (almost) hermetic, with only the forward and rear beam-pipes preventing it from having 4π coverage in solid angle.

As a result of the asymmetric beam energies, the forward direction generally contains more particles of higher average energy than the rear direction. Consequently, the detector itself has an asymmetric design with extra instrumentation in the forward and barrel regions compared to the rear direction.

At the centre of ZEUS, surrounding the beam-pipe, lie the inner charged particle tracking detectors. During 1996 and 1997, the Central Tracking Detector (CTD) was the innermost component of the ZEUS detector[¶]. It is situated in a 1.43 T magnetic field provided by the superconducting solenoid. The Forward (FTD) and Rear (RTD) Tracking Detectors are located at either end of the CTD and provide additional information on tracking and particle identification. The inner trackers are described in Section 3.4. The Small angle Rear Tracking Detector (SRTD), although technically part of the calorimeter, provides improved position resolution for particles and is particularly useful for the identification of the scattered lepton in the rear direction. Together, the tracking detectors provide an angular acceptance of $7.5° < \theta < 170°$ for charged particles.

Surrounding the superconducting magnet lies the ZEUS CALorimeter (CAL). The main calorimeter is the high resolution Uranium-scintillator sampling CALorimeter (UCAL) which is divided into three sections: the Forward (FCAL), Barrel (BCAL) and Rear (RCAL) CALorimeters. Outside the UCAL is the BAcking Calorimeter (BAC), which provides an energy measurement of late showering particles. Located between the layers of the FCAL and RCAL is the Hadron Electron Separator (HES) which can be used to distinguish between hadronic and electromagnetic objects. The ZEUS CAL and related components are described in Section 3.5.

Surrounding the UCAL and inside the iron yoke are the Forward (FMUI), Barrel (BMUI) and Rear (RMUI) Muon Identification chambers. Additional Forward, Barrel and Rear MUON chambers (FMUON, BMUON and RMUON) are located outside the iron yoke. These are drift chambers that are used to detect particles which have not been absorbed in the CAL.

Located in the rear direction is the C5 Counter. This is a lead-scintillator which monitors beam-related background and timing of bunches. Also in the rear direction, the VETO wall is located. Both of these components are used for the rejection of background events, which is explained further in Section 3.6.

[¶]The CTD was the central component during the 1996-1997 running period. In the long HERA shutdown of 2000-2002, a MicroVertex Detector (MVD) [125] was installed in the centre of ZEUS. This component provides significantly enhanced tracking and track resolution.

In the far rear direction is located the LUMInosity Monitor (LUMI). As well as providing a measurement of the collected luminosity, the LUMI is also used to identify small angle leptons and photons. This is described in more detail in Section 3.7.

3.4 The Inner Tracking Detectors

The ZEUS inner tracking system consists of three detectors: the FTD, CTD and RTD. These are designed to measure the momentum and direction of charged particles with a high precision, as well as providing a measure of the event vertex position. For this thesis, the CTD was used in the trigger selection and for event vertex-finding and jet reconstruction. The CTD is described in more detail in Section 3.4.1. For completeness, the FTD and RTD are also briefly described in Sections 3.4.2 and 3.4.3.

3.4.1 The Central Tracking Detector

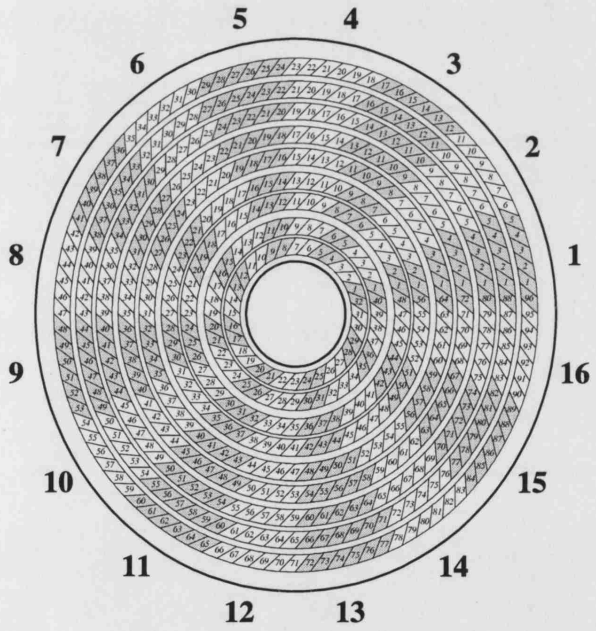

Figure 3.7: View of the CTD in the xy-plane, indicating the layout of the superlayers, sectors and cells. The numbers surrounding the cylinder give the sector number. The superlayers are numbered from 1-9 starting from the innermost layer.

The main tracking is performed by the CTD [126]. This is a cylindrical wire drift chamber with a polar angle coverage of $11° < \theta < 168°$. The CTD has an active length of 2.05 m and has inner and outer radii of 0.182 m and 0.794 m respectively. The chamber is flushed with a gas mixture composed of Ar(83%), CO_2(5%) and C_2H_6(12%), which is bubbled through C_2H_5OH. The gas mixture is maintained at close to atmospheric pressure.

The CTD consists of 72 radial layers, which are organised into 9 superlayers. Each superlayer contains between 32 and 96 drift cells, each of which are orientated at 45° to the radial direction. This is illustrated in Fig. 3.7, which shows a cross sectional view of the CTD in the xy-plane. In total, there are 576 drift cells and 4608 sense wires. These wires, which are made of gold-plated tungsten, are distributed evenly throughout the cells such that each individual cell comprises 8 sense wires. The CTD also contains a total of 19584 field wires which are kept at a high voltage to provide a uniform electric field. When a charged particle traverses the CTD, it ionises the gas. The electrons that are produced shower close to the positive sense wires, whilst the positive ions are repelled and drift towards the negative field wires. This gives a signal pulse on the wires which is measured and recorded via an electronic read-out. The drift field is orientated at a Lorentz angle of 45° to the radial axis so that the drift electrons travel along radially transverse paths in the $r\phi$-plane. This is important in left-right ambiguity breaking. The layout of a typical CTD drift cell, with the field lines indicated, is illustrated in Fig. 3.8

The odd-numbered (**axial**) superlayers contain drift wires which run parallel to the z-axis. The remaining even-numbered (**stereo**) superlayers contain wires which are orientated at a small stereo angle ($\sim \pm 5°$) with respect to the z-axis. This arrangement allows both $r\phi$ and z coordinates to be accurately measured. The nominal resolution for a track which has traversed all superlayers is $\sim 180\ \mu$m in $r\phi$ and ~ 2 mm in z. The measured event vertex is accurate to about 1 mm in xy and 4 mm in z.

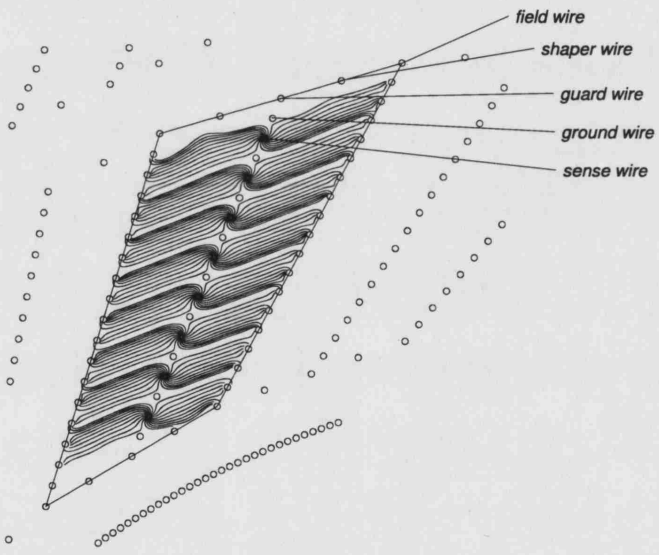

Figure 3.8: Layout of a drift cell in the CTD.

The inner three axial superlayers of the CTD are instrumented with a z-by-timing system. This estimates the z-position of a hit by measuring the difference in arrival time of the pulses on the sense wires at each end of the detector. Although the resolution achieved (~ 4 cm) is much cruder than that obtained using the full axial and stereo wire information, it is a relatively fast method and used predominantly for trigger purposes and track seed-finding.

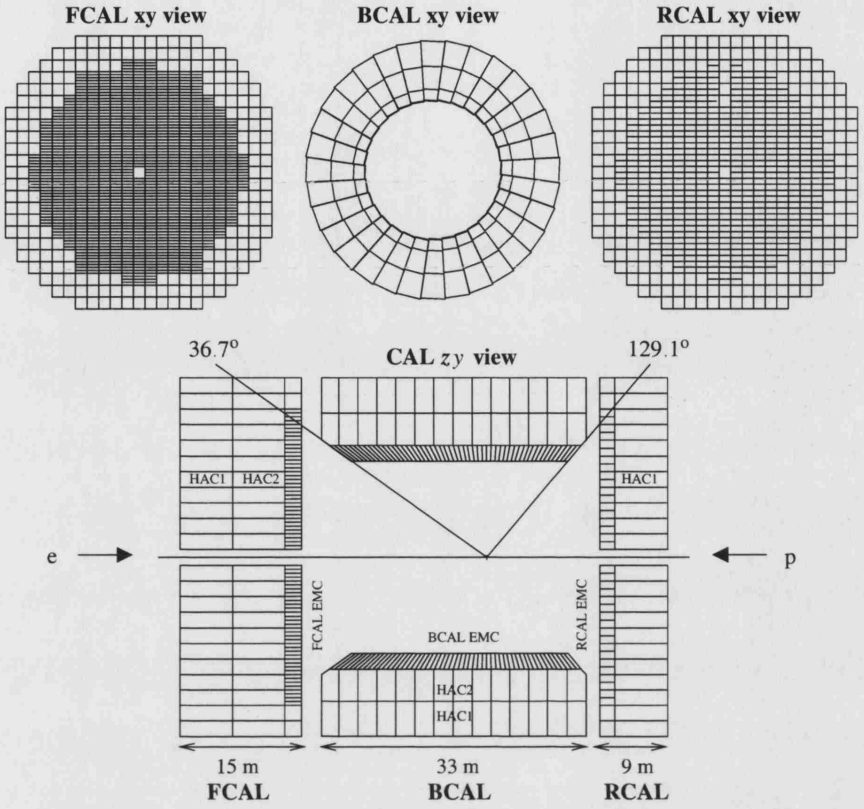

Figure 3.9: Schematic representation of the three sections of the UCAL.

As mentioned in Section 3.3, the CTD is contained within a superconducting solenoid which provides a magnetic field of 1.43 T. This field causes charged particles to travel in a circular path of radius, R, given by,

$$R \propto \frac{p_{\mathrm{T}}}{QB} \tag{3.2}$$

where Q is the charge on the particle, B is the strength of the magnetic field and p_{T} is the transverse momentum. This allows an accurate determination of the p_{T} of the charged particle. The transverse momentum resolution for full length tracks is $\sigma(p_{\mathrm{T}})/p_{\mathrm{T}} \approx 0.0058 p_{\mathrm{T}} \oplus 0.0065 \oplus 0.0014/p_{\mathrm{T}}$ [127] where p_{T} is in GeV. The first term is related to the number of CTD hit measurements and their resolution, while the second and third arise due to multiple scattering in material between the interaction point and the CTD.

3.4.2 The Forward Tracking Detector

The FTD covers the polar angle region from $7.5° < \theta < 28°$. It is composed of three planar drift chambers (FTD1, FTD2 and FTD3) which consist of three planes of wires organised in drift cells. These planes of wires are rotated by 120° with respect to each other to allow ambiguity breaking between multiple tracks. The chambers of the FTD are interleaved with Transition Radiation Detector (TRD) modules[‖]. There are four such modules, located in the gaps between FTD1 and 2 and between FTD2 and 3. These provide electron-hadron ($e - h$) separation for particles with momenta between 1 and 30 GeV, by detecting the transition radiation emitted when a particle passes through a barrier. The radiator consists of polypropylene fibres and the radiation is detected in a single layer drift chamber.

3.4.3 The Rear Tracking Detector

The RTD improves the accuracy of the tracking in the backward direction and covers the polar angle region $160° < \theta < 170°$. It is a planar drift chamber containing three layers of drift cells in the same format as the FTD.

3.5 ZEUS Calorimetry

The ZEUS CAL is used for measuring the energies of particles and is essential for the full reconstruction of jets and energy clusters. The CAL consists of the UCAL, SRTD, HES and PRES. Outside the UCAL is the BAC. Each of the calorimeter sub-components are described in the following subsections.

3.5.1 The Uranium Calorimeter

The main calorimetry is performed by the UCAL [129], which consists of alternate layers of 3.3 mm depleted uranium and 2.6 mm plastic scintillator material. The uranium absorber plates are an alloy consisting of ^{238}U(98.2%), Nb(1.7%) and ^{235}U(0.2%) which has a density of 18.5 gcm^{-3}. The thicknesses of the uranium and scintillator layers have been chosen such that the UCAL is **compensating**. Hadronic showers produce fewer photons than electromagnetic showers for initiating particles of the same energy. In the UCAL, neutrons from the hadronic shower are absorbed by the uranium, thereby producing additional photons. In this way, the UCAL *compensates*

[‖]The TRDs existed during the 1996-1997 running period. However, during the HERA shutdown of 2000-2002, the TRD was replaced with a Straw Tube Tracker (STT) [128]. This provides enhanced tracking efficiency in the forward direction for events with high multiplicity.

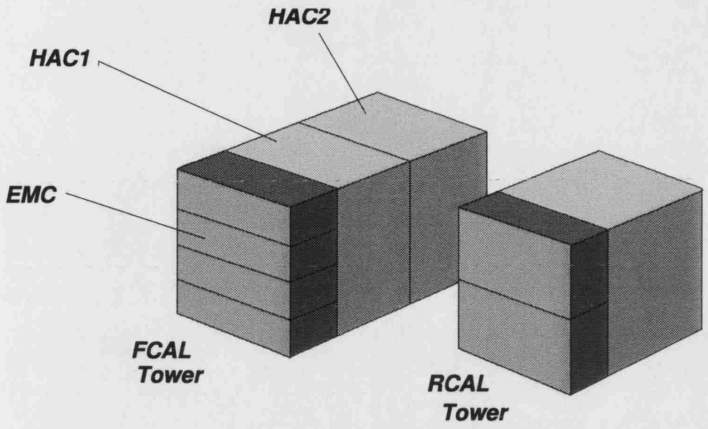

Figure 3.10: Schematic of an FCAL and RCAL tower in the UCAL. The layout of a BCAL tower is similar to that of an FCAL tower. Relative sizes are to scale.

so that the response to hadrons and electrons is equal ($e/h = 1 \pm 0.05$) when the initiating particles have the same energy. This is important in the reconstruction of jets which are composed of both electromagnetic and hadronic components in an unknown proportion. The UCAL is divided into three sections: the FCAL, BCAL and RCAL, which together cover 99.7% of the total solid angle. The layout of the three sections of the UCAL is shown in Fig. 3.9.

Each section of the UCAL is subdivided transversely into towers and longitudinally into ElectroMagnetic (EMC) and HAdronic (HAC) Calorimeter sections. The energy that may be absorbed by the calorimeter is a strong function of the polar angle and ranges from the proton-beam energy in the positive z-direction to the lepton-beam energy in the rear direction. Consequently, the depth of the UCAL sections have been designed to be different, being deeper in the forward region than in the rear. Specifically, the FCAL and BCAL have two hadronic sections (HAC1 and HAC2) whilst the RCAL has only one. Figure 3.10 shows a schematic view of an FCAL and RCAL tower showing the EMC and HAC divisions.

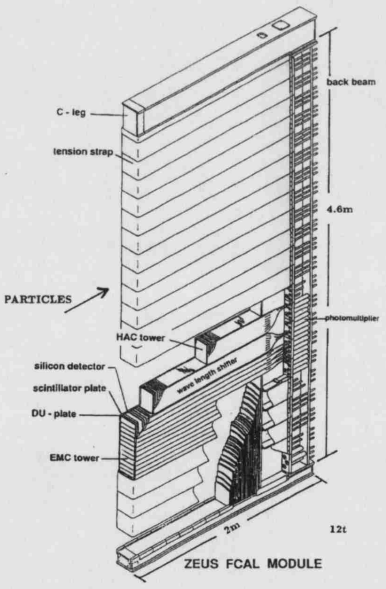

Figure 3.11: The structure of a typical FCAL module.

The smallest subdivision of the UCAL is called a cell. In the FCAL and BCAL, each tower contains 4 EMC cells with transverse dimensions of 5×20 cm^2 whilst in the RCAL each tower contains 2 EMC cells of transverse dimensions 10×20 cm^2. The EMC towers are innermost to the interaction point and have a depth of 1 absorption length (λ). The cells in the HAC towers have transverse dimensions of 20×20 cm^2 and depths of 6λ in the FCAL, 4λ in the BCAL and 3λ in RCAL. As a result of this design, 90% of all jets are expected to

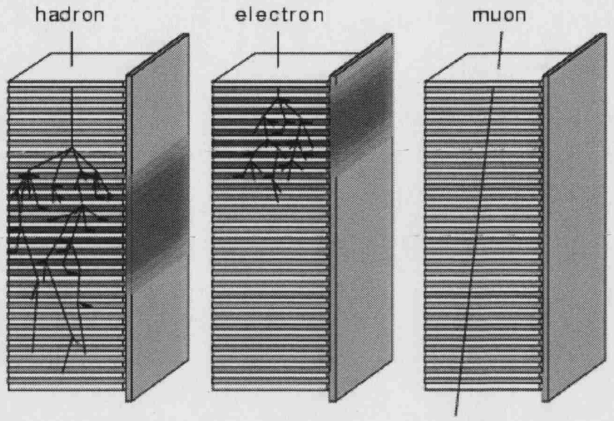

Figure 3.12: Typical shower profiles in the calorimeter for different types of particle. The uranium and scintillator layers of the UCAL and one of the wavelength shifter bars are shown.

deposit at least 95% of their energy in the UCAL. Some of the basic properties of the three sections of the UCAL are summarised in Tab. 3.2. Each calorimeter cell is read out by two PhotoMultiplier Tubes (PMTs) which are attached to the scintillator layers by wavelength shifter bars. The use of two PMTs for each cell ensures that the measurement is less dependent on the impact point of the particle. In total there are 6000 cells to be read out and 12000 read-out channels (2 PMTs per cell). Figure 3.11 shows the layout of a typical FCAL module, illustrating the EMC and HAC divisions as well as the position of the wavelength shifters and the PMTs.

The transverse and longitudinal segmentation of the UCAL is used to identify different types of particles. Three classes of particle, the typical shower developments of which are illustrated in Fig. 3.12, can be distinguished:

- **electrons and photons**
  These particles begin to shower as soon as they enter the calorimeter. They can be identified by the limited shower size in both the transverse and longitudinal directions.

- **hadrons**
  These begin to shower later than electrons and photons and so produce showers which are both broader and deeper than those for electromagnetic particles.

- **muons**
  These interact very little with the absorber material of the UCAL and lose most of their energy through ionisation. The deposited energy is largely independent

	FCAL	BCAL	RCAL
θ Coverage	$2.2° \rightarrow 39.9°$	$36.7° \rightarrow 129.1°$	$128.1° \rightarrow 176.5°$
η Coverage	$3.95 \rightarrow 1.01$	$1.10 \rightarrow -0.74$	$-0.72 \rightarrow -3.49$
Number of Cells	2172	2592	1152
Number of Modules	23	32	23
Towers/Module	11-23	14	11-23
Depth (m)	1.5	1.06	0.87
Radiation length (X_0)	25.9	24.6	24.3
Absorption length (λ)	7	5	4
EMC cell sizes (cm)	5×20	5×20	10×20
HAC cell sizes (cm)	20×20	20×20	20×20

Table 3.2: Some basic properties of the three sections of the UCAL.

of the momentum of the traversing muon. The energy deposition in the CAL is referred to as the Minimum Ionising Particle (MIP) signal.

The energy resolution of the UCAL, as measured under test-beam conditions at CERN [130], has been found to be $\sigma(E)/E = 18\%/\sqrt{E(\text{GeV})}$ for purely electromagnetic deposits and $\sigma(E)/E = 35\%/\sqrt{E(\text{GeV})}$ for hadrons. The timing resolution of a calorimeter cell is better than $\sigma_t = 1.5/\sqrt{E(\text{GeV})} \oplus 0.5$ ns

3.5.2 The Presampler

The PRES consists of two detectors located on the front surface of the FCAL (FPRES) and RCAL (RPRES) [131]. Together, these devices consist of 576 scintillator tiles with each tile having dimensions of $20 \times 20 \times 0.5$ cm^3. The presamplers measure the shower multiplicity of particles entering the UCAL. This enhances the ability to discriminate between electromagnetic and hadronic showers for particles with energy less than 5 GeV. In addition, the multiplicity is correlated to the energy loss of the particle in dead material in front of the UCAL. This means that the information from the presamplers can be used to correct for this energy loss.

3.5.3 The Hadron-Electron Separator

The HES is designed to provide separation between hadrons and electrons. It is located at 3 radiation lengths (X_0) inside the EMC section of the RCAL (RHES) and FCAL (FHES). In the ZEUS detector, this position corresponds to the electron

shower maximum, so that electromagnetic showers lead to larger energy deposits in the HES. The HES consists of a plane of 3 × 3 cm silicon diodes which significantly improve the segmentation of the FCAL and RCAL.

3.5.4 The Small Angle Rear Tracking Detector

The SRTD [132] is specifically designed to measure electrons scattered at small angles to the incident lepton-beam direction and to improve the measurement of their position and energy. The SRTD is located on the face of the RCAL, around the beam-pipe and consists of two layers of finely segmented silicon strips. The track resolution is $\sim$ 3 mm (compared to $\sim$ 1 cm in the calorimeter). The outer dimensions of the SRTD are 68×68 cm^2 and the total polar angle coverage is $162^\circ < \theta < 176^\circ$. This component is of particular importance for DIS since it is the region where most DIS electrons are scattered. In this analysis, the SRTD is used at the first level trigger (see Section 3.8.1) where the timing information from this component is used to reject proton beam-gas events.

3.5.5 The Backing Calorimeter

The ZEUS BAC surrounds the UCAL and lies outside the iron yoke. Most of the energy from a jet will be fully contained within the UCAL. However, there will be some leakage from the back of the component. For large jet energies, this becomes significant. Consequently, a method of estimating the extent of this leakage is required. The BAC is composed of iron plates with a thickness of 7.3 cm. The iron is instrumented with proportional counters, with which any energy that has leaked from the UCAL can be detected. In addition, the iron plates serve as a return path for the superconducting magnetic field. The energy resolution of the BAC is $\sigma(E)/E = 100\%/\sqrt{E(\mathrm{GeV})}$. This component can also be used to provide an additional tool for the identification of muons, which are expected to pass through the UCAL and BAC without much interaction.

3.6 Background Rejection

In addition to those processes originating from genuine lepton-proton interactions, there are several processes observed in the ZEUS detector that originate from other sources. These are referred to as **background** events. The ZEUS detector utilises several specialised sub-detectors and uses a variety of other techniques designed specifically for the identification and/or reduction of background. There are three main types of non-physics background that can occur in the ZEUS detector:

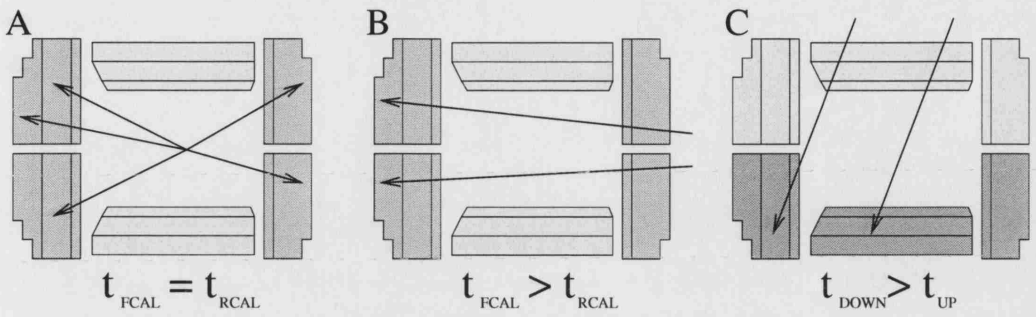

Figure 3.13: A: The signature of a lepton-proton interaction at the nominal interaction point, B: a typical signal from a proton beam-gas interaction and C: a typical signal from a cosmic muon event.

- interactions between beam particles and residual gas in the beam-pipe (or with the beam-pipe wall) produces so-called **beam-gas** events. These can occur either in the proton or the lepton beam. If such events occur close to or inside the detector, they may produce a signal. These type of events can also give rise to muons in the proton beam halo, via the decay of pions. These are referred to as **halo muons**.
- **synchrotron radiation** caused by the bending of the lepton beam in the HERA magnetic field is the main source of background from the lepton beam. However, the bending does not occur near the ZEUS detector and so the contribution to the overall background is limited.
- muons arising from cosmic-ray interactions can deposit energy into the detector giving rise to a signal.

In order to reduce these non-physics backgrounds, ZEUS employs a two-fold strategy. The first is simply to shield the detector as much as possible. The ZEUS detector is located at 25 m below ground level and it is surrounded by a $\sim$ 1 m thick layer of concrete and an iron yoke. This shielding considerably reduces background from cosmic-ray muons. The detector is also shielded against particles produced by the beams in the HERA tunnel. The iron VETO wall, which lies at $z = -7.5$ m, has a thickness of 0.87 m and has a 95×95 cm^2 hole for the beam-pipe, provides shielding from the proton beam halo.

The second strategy applied to reduce non-*ep* background is to reject the events at the trigger level. For example, the VETO wall is instrumented with scintillation counters on both sides. When it absorbs particles in the proton beam halo and from hadronic showers, it produces a signal. The coincidence in these counters is used to reject

halo muons at the trigger level. In addition, ZEUS has a series of collimators (C1-C6 counting from the forward to the rear). These are instrumented in order to provide an estimate of background rates within the experiment. Of particular importance is the C5 Counter, so-called because it is attached to HERA collimator number 5. This is located at $z = -3.15$ m and measures synchrotron radiation and timing of bunches.

Perhaps of most importance for the rejection of background events at trigger level, is the timing information from the UCAL, the SRTD and the C5 Counter. In ZEUS, the timing measurement of different components is calibrated in such a way that particles from a true lepton-proton collision at the nominal IP are produced at $t = 0$. This situation is illustrated in Fig. 3.13a). Beam-gas events have a flat vertex distribution and so will usually arrive at components at one end of the detector before the other. Such events can be identified using timing information from the RCAL, SRTD and C5 Counter. The difference in arrival time in the FCAL and RCAL can also be used to reject these events. A typical beam-gas event is illustrated in figure 3.13b). In the case of muons arising from cosmic ray interactions, there will be a difference in the time of arrival at the upper and lower halves of the BCAL. This situation is illustrated in Fig. 3.13c).

3.7 The Luminosity Monitor

The LUMI [133] is an essential component in the measurement of any cross section at ZEUS since the integrated luminosity must be known to a high precision in order to obtain the correct absolute normalisation. The luminosity at ZEUS is determined by monitoring the rate of hard photons from the lepton-proton bremsstrahlung (Bethe-Heitler) process $ep \rightarrow e'p\gamma$ [134], where the photon is emitted by the lepton and both are scattered at very small angles.

The LUMI consists of two separate sampling lead-scintillator calorimeters for the measurement of the small angle lepton and photon. Both detectors are positioned downstream of the lepton beam, with the electron calorimeter located at $z = -34$ m and the photon calorimeter at $z = -104$ m. Leptons with scattering angles of $\theta_e < 6$ mrad and energies $0.2E_e < E'_e < 0.8E_e$ are deflected out of the beam orbit by the HERA magnetic field from the bending dipoles (BH in Fig. 3.14). They leave the beam-pipe via an exit window located at $z = -27$ m to be detected by the electron calorimeter. In contrast, photons radiated within a cone of 0.5 mrad around the beam axis will leave the beam-pipe via a window at $z = -92$ m to be subsequently detected by the photon calorimeter. For photons with energy greater than 5 GeV, the acceptance is 98%. The energy resolution of both calorimeters is $\sigma(E)/E = 18\%/\sqrt{E(\mathrm{GeV})}$. However, the photon calorimeter is surrounded by a carbon filter of 1 radiation length thickness in order to shield the detector from direct synchrotron radiation. This degrades the

effective resolution to $\sigma(E)/E = 25\%/\sqrt{E(\mathrm{GeV})}$. The photon calorimeter also has a presampler to correct the measured energies for losses in dead material. A more detailed description of the LUMI can be found in [135].

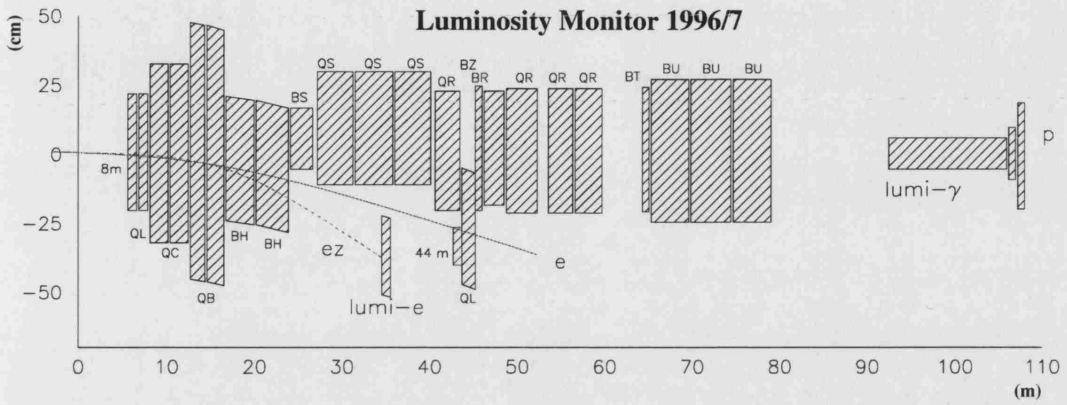

Figure 3.14: A schematic representation of the position of the electron and photon calorimeters of the luminosity monitor. All distances are measured from the nominal interaction point. Note the difference in scale in the x and y directions. In this diagram, the proton enters from the right and the lepton from the left. The 8 m and 44 m taggers are also shown.

The cross section for the Bethe-Heitler process is large ($\sim$ 15 mb) and higher order corrections are known to within 0.5% [136]. Integrating over final state scattering angles, the LO cross section is given by,

$$\frac{\mathrm{d}\sigma}{\mathrm{d}k} = 4\alpha r_e^2 \frac{E'_e}{kE_e}\left[\frac{E_e}{E'_e} + \frac{E'_e}{E_e} - \frac{2}{3}\right]\left[\log\frac{4E_pE_eE'_e}{Mmk} - \frac{1}{2}\right] \tag{3.3}$$

where k is the photon energy, E_e and E'_e are the initial and final lepton energies, E_p is the proton energy, M and m are the proton and lepton masses, respectively, α is the fine structure constant and r_e is the classical electron radius.

The original intention was to use information from both the electron and the photon calorimeters to determine the luminosity. However, the acceptance of the electron detector is poorly understood. Consequently, the bremsstrahlung cross section is determined from the count-rate of photons above a certain energy threshold (E_{T}^{th}) as measured in the photon calorimeter. The luminosity is then calculated as:

$$\mathcal{L} = \frac{R_{ep}(E_\gamma > E_{\mathrm{T}}^{th})}{\sigma_{ep}^{acc}(E_\gamma > E_{\mathrm{T}}^{th})}, \tag{3.4}$$

where $R_{ep}(E_\gamma > E_{\mathrm{T}}^{th})$ is the photon count rate and $\sigma_{ep}^{acc}(E_\gamma > E_{\mathrm{T}}^{th})$ is the acceptance corrected cross section for these photons to be produced. The accuracies of the

measured luminosity in 1996 and 1997 were 1.1% and 1.8%, respectively, with the largest uncertainty coming from the acceptance of the photon calorimeter.

Although the electron calorimeter is not used for the luminosity determination, it is used to measure incident leptons scattered at low angles (corresponding to low values of Q^2). Used in conjunction with the 8 m and 44 m taggers, this provides a means of tagging photoproduction events. The taggers are located at -8 m and -44 m from the nominal IP and are used to tag leptons with very small transverse momentum at the lepton vertex. Events tagged by these detectors have extremely low Q^2 values and are known to lie in a W range which is restricted by the energy and angle of the scattered lepton. The photon detector is used to measure the small angle photons from the ISR process.

3.8 The Trigger and Data Acquisition Systems

As previously mentioned, the interval between bunch crossings in the HERA accelerator is 96 ns. This corresponds to a nominal bunch crossing rate of $\sim$ 10 MHz of which only a small fraction are interesting ep events. This poses challenges for the Data AcQuisition (DAQ) and trigger systems. The interaction rate is dominated by beam-gas interactions, which contribute about $\sim 10 - 100$ kHz. In contrast, the rate of interesting ep events written to tape is of the order of a few to 10 Hz. In order to achieve the necessary rate reduction whilst efficiently selecting genuine ep events, the ZEUS experiment employs a three level trigger system [137]. A schematic diagram of the trigger and DAQ chain is shown in Fig. 3.15.

3.8.1 The First Level Trigger

The First Level Trigger (FLT) is a hardware trigger which reduces the signal to below 1 kHz. Each of the components used at the FLT have their own FLTs. Since most detector components cannot make a useful trigger decision in the 96 ns beam crossing interval, data is stored in a 4.4 μs pipeline (corresponding to exactly 46 bunch crossings) while a trigger decision is formed regarding a particular bunch crossing. The use of pipelines means that the whole process has zero dead-time. Different strategies are used for the pipelines of individual components. For example, the UCAL uses a switched capacitor array for analogue storage whilst the CTD uses a digital array. Each component participating in the FLT must make a **subtrigger** - or Local FLT (LFLT) - decision within $\sim$ 2 μs after the bunch crossing. This is then passed to the Global First Level Trigger (GFLT) where an overall decision must be made within the 4.4 μs timescale. At the FLT, decisions are made based on limited tracking information and global or regional energy sums in the ZEUS CAL. The FLT is the fastest but also the

least pure of the triggers. Approximately 98% of the events passed are background initiated.

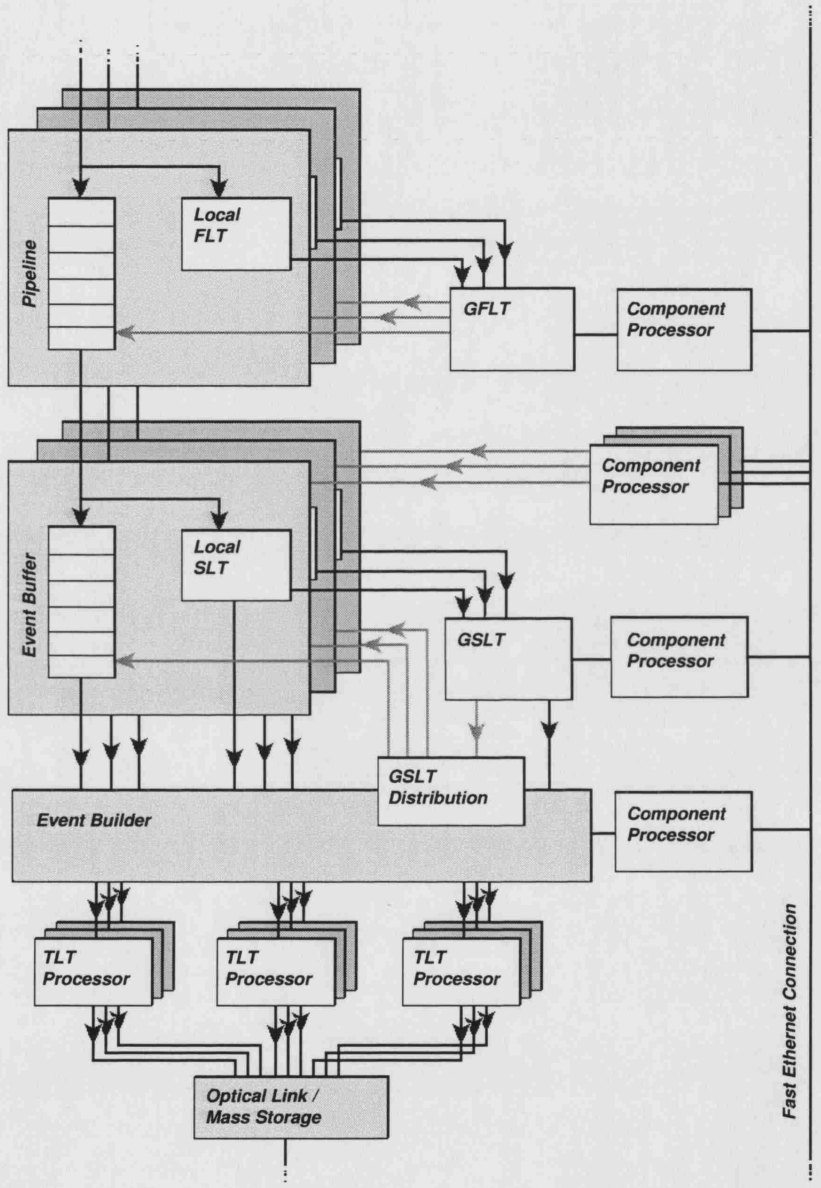

Figure 3.15: Data flow through the ZEUS trigger and DAQ systems.

3.8.2 The Second Level Trigger

Following acceptance by the GFLT, the data is transferred to the Second Level Trigger (SLT). This is a software trigger which uses parallel processing on transputer networks in order to reduce the $\sim$ 1 kHz output rate from the FLT to below 100 Hz. The component SLTs provide information on charged particle tracks and on the interaction vertex (CTD-SLT) and on calorimeter timing and global energy sums such as the transverse energy (E_{T}) or $E - p_z$ (CAL-SLT). Analogously to the FLT, the outputs of the Local SLT (LSLT) are passed to the Global SLT (GSLT) where a decision for the whole event is made in a few milliseconds. Since the time allowed for the decision to be made is much longer than for the FLT, more complete sub-component data is available for the decision and more sophisticated process algorithms are possible. The maximum output rate of the SLT is 60 Hz.

3.8.3 The Event Builder

Following acceptance by the GSLT, each component passes the accepted events to the EVent Builder (EVB). This stores the data from the components and combines it into one consistent record (the **event**) ready to be used by the Third Level Trigger (TLT). The EVB will build up to 75 events in parallel and has buffers which are able to store up to 72 further events.

3.8.4 The Third Level Trigger

The TLT is a software trigger running on a farm of processors which view the event as a whole. It uses a version of the offline reconstruction software, which is modified to reduce time overheads, in order to calculate the kinematics of the event. The TLT is able to make decisions concerning kinematic properties and is able to perform more refined vertex-finding and jet-finding. After this reconstruction, the TLT classifies *ep* events into physics categories according to various filters set by the physics working groups. The final output rate of the TLT is $\sim 1 - 10$ Hz. Events which have triggered a TLT slot are written to tape via a tape robot, over a dedicated connection to the DESY computing center (FLINK). Each event is typically 0.3 MB.

3.9 The Offline Reconstruction

Following the trigger selection, the data are processed using offline reconstruction software, in order to more completely reconstruct the kinematics of each event. All procedures which are too slow to be available at the TLT, such as the implementation

of complete calibration constants, are implemented in the offline reconstruction. The data are also passed through an additional filter, which makes selections based on physics criteria. The events selected by each filter are allocated a code, called a Data Storage Tape (DST) bit. The offline reconstruction procedure is discussed in more detail in Chapter 4.

Chapter 4

Event Reconstruction

In order to extract information on the properties of a particular event, certain measurable quantities must be precisely reconstructed. Following the trigger selection, only partial event information is available and a full reconstruction of events and event properties must be performed offline. In ZEUS, photoproduction events are defined by the requirement that no scattered lepton is detected in the UCAL. The kinematic reconstruction then relies completely on the measurement of hadrons in the final state. This chapter describes the techniques used to convert the information from the detector into a fully reconstructed data-set. The corresponding process used to reconstruct Monte Carlo events is also outlined.

4.1 Monte Carlo Reconstruction

In order to produce a physics measurement from the reconstructed ZEUS data, the effects of the detector and trigger system must be taken into account. In order to correct for these effects, samples of Monte Carlo are used to simulate the underlying lepton-proton interactions. The generated events are then passed through simulations of the ZEUS detector and trigger to form a sample of Monte Carlo which is in the same format as the real data stored on tape. The ZEUS Monte Carlo chain is illustrated in Fig. 4.1 and consists of the following programs:

- **ZDIS** (Zeus interface to Deep Inelastic Scattering) [138]
  Several different Monte Carlo programs are available for the generation of lepton-proton events*. These generators are collected into the ZDIS package which outputs the results of the generation (e.g. the four-momenta of the final state particles). The output is in a format compatible with the standard ZEUS analysis package (EAZE).

*The HERWIG and PYTHIA programs are used in this thesis.

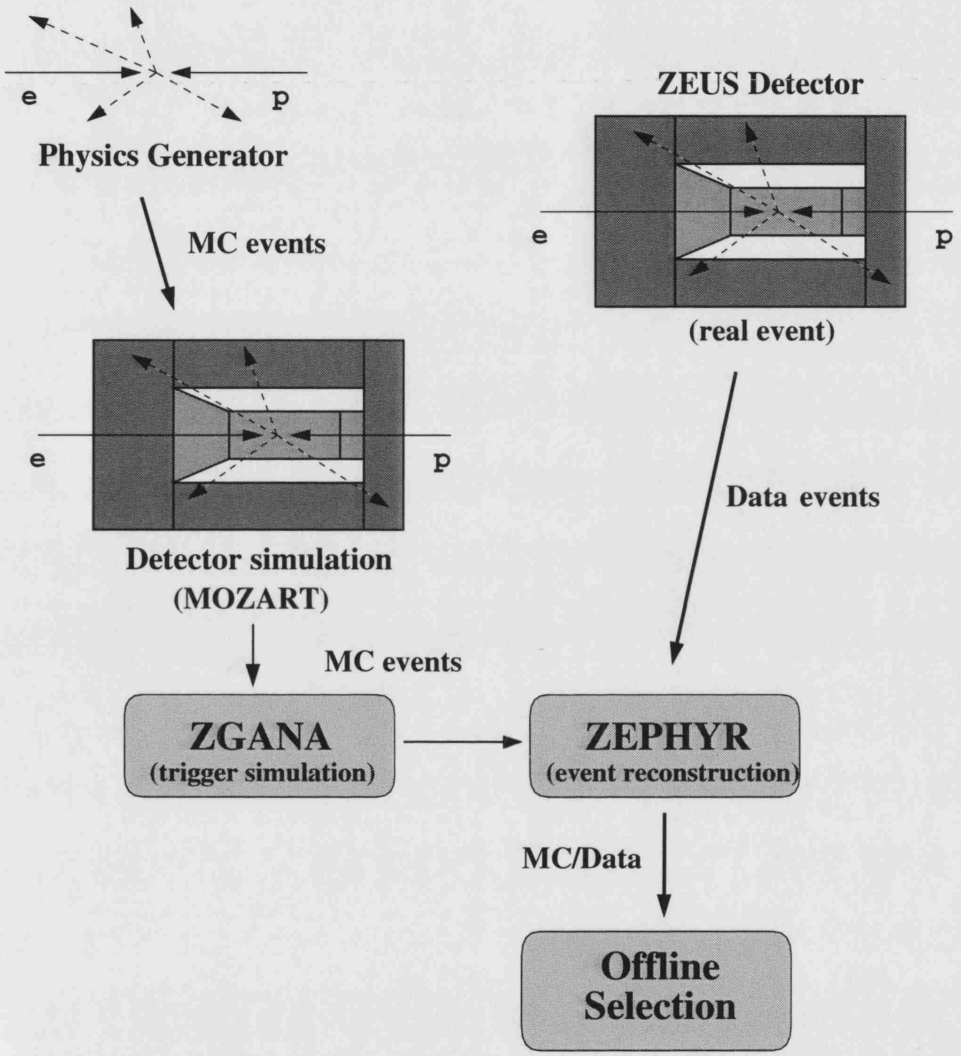

Figure 4.1: The ZEUS DAQ system and Monte Carlo software chain.

- **MOZART** (MOnte carlo for Zeus Analysis, Reconstruction and Trigger)
  The MOZART program is a simulation of the ZEUS detector. MOZART uses the GEANT [139] package to describe the detector geometry and contains a complete description of the positions and materials of the sub-components of the ZEUS detector. It also contains a full simulation of the magnetic field. MOZART simulates the passage of the final state particles of a ZDIS event, taking into account particle decays, interactions with material in the detector and detector response. The output from MOZART consists of tables of information regarding the details of the event (e.g. which CTD wires were hit, position and energies of calorimeter deposits etc.)

- **ZGANA** (ZG313 ANAlysis) [140]
  The ZGANA package is a complete simulation of the ZEUS three-level trigger.

Both the reconstructed Monte Carlo information and the original ZDIS four-vectors are stored. The relationship between the Monte Carlo reconstructed and generated distributions can then be used to correct the data for detector and trigger effects in order to produce a so-called hadron level measurement. The output tables from the detector and trigger simulation are formatted in exactly the same way as the information read out by the ZEUS detector for a real lepton-proton event. This means that the programs and methods used to reconstruct event information can be used on both real and Monte Carlo simulated data. Therefore, no distinction is made between data and Monte Carlo for the remainder of this chapter, unless otherwise stated.

4.2 The Offline Reconstruction Software

The ZEUS PHYsics Reconstruction (ZEPHYR) package contains the reconstruction code for each of the sub-components of the ZEUS detector. This package is used to reconstruct event information in the following stages:

- information from the inner tracking detectors (CTD, RTD, FTD), the calorimeter components (UCAL, BAC) and the LUMI are fully reconstructed;
- tracks found in the CTD, FTD and RTD are matched to energy clusters found in the UCAL and BAC;
- particles are identified using combined information from the CTD, CAL and HES.

For each event, a set of tables is filled which contains all the relevant information. Following the offline reconstruction, the data are passed through an additional filter

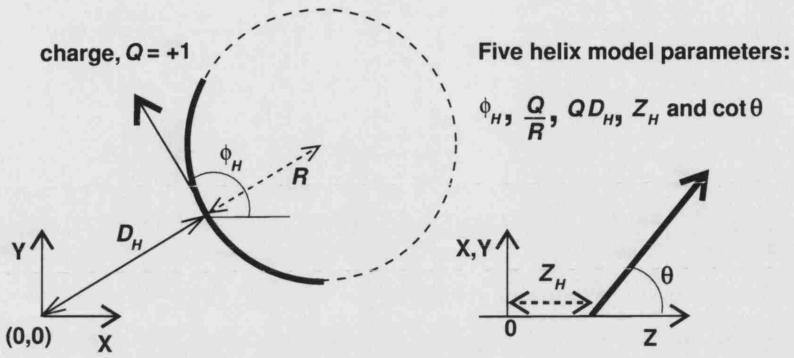

Figure 4.2: Illustration of the five helix parameter model.

which makes selections based on the reconstructed information. The events selected by each filter are added to the event record in the form of a Data Summary Tape (DST). For the analyses presented in this thesis, the most important information comes from the CTD and UCAL. The offline reconstruction of information from these components is described in more detail in the following sections.

4.2.1 The Tracking Reconstruction

ZEUS uses the VCTRAK [141, 142] package for the reconstruction of charged particle tracks[†]. In this code, tracks are reconstructed using information from the CTD, FTD, RTD and SRTD. The VCTRAK code performs reconstruction in two different modes. In the **regular** mode, information from all tracking detectors is used, while in the **CTD-only** mode, only information from the CTD is used. The advantage of the regular mode is that the information from the additional tracking detectors provides greater angular acceptance for track reconstruction. However, since the CTD is the best understood of all the tracking detectors, the CTD-only mode has been used in this thesis.

In the CTD-only mode, VCTRAK uses pattern recognition software to reconstruct tracks from hits to the sense wires in the CTD. The reconstruction begins by identifying track segments which are defined by the requirement of three adjacent hits in an axial superlayer. The VCTRAK program then connects the hits found in each superlayer to form complete tracks. The reconstruction begins from the outermost superlayer and is extrapolated inwards guided by an additional "virtual hit" at the beam-line. As the process of extrapolation continues, more hits are gathered which increases the precision with which the parameters of the track may be determined.

[†]A simplified version of VCTRAK, called VCTLT, is used at the TLT.

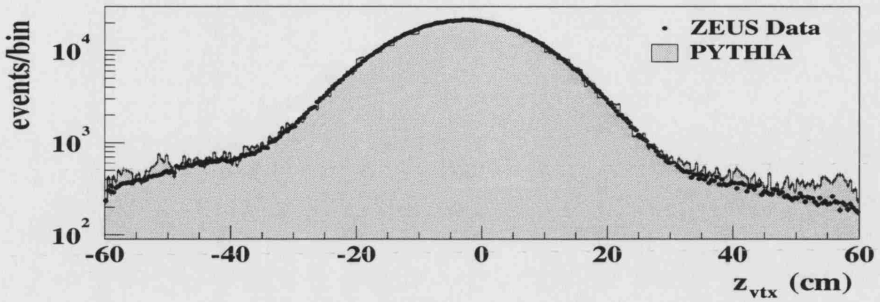

Figure 4.3: The $z_{\rm vtx}$ distribution. The points show the ZEUS data and the shaded histogram shows the prediction of the PYTHIA Monte Carlo following full detector and trigger simulation. All events have been required to satisfy the selection criteria described in Chapter 5, except for the cut on $z_{\rm vtx}$ which has been relaxed for this plot.

The series of axial hits form a trajectory in the xy-plane. If z-by-timing information is available from the axial layers, it is used to give an initial estimate of the z-position of the track. Following this, any hits in the stereo superlayers (which intercept the reconstructed trajectory) are used to provide more accurate information regarding the z-position. If a track is long, only the three innermost superlayers are used for the reconstruction. This accommodates curvature variation resulting from magnetic field inhomogeneity inside the CTD volume. This ensures a good quality of track and reduces the incidence of split tracks. For short tracks, which only have hits in the innermost axial superlayer, the reconstructed trajectories are extrapolated to the adjacent stereo superlayer in order to provide stereo information. The entire procedure is performed twice. In one case, only track candidates which extend into the innermost superlayer are accepted. These are classified as VCTPAR tracks. In the second case, tracks which have hits in at least two axial superlayers and the intervening stereo layer, but which have no information in the innermost superlayer, are stored. These are classified as VCTRHL tracks and are candidates for long-lived particle decays. In this thesis, only VCTPAR tracks are considered. The reconstructed tracks are fitted to a five parameter helix model [142] with the fit beginning from the innermost tracks. This model is illustrated in Fig. 4.2.

When all tracks have been fitted, the software attempts to establish the position of the primary interaction vertex by performing a χ^2-fit to all possible combinations of tracks. The most probable vertex is taken to be that with the smallest χ^2. All tracks which are consistent with the vertex are then re-fitted, constraining their origin to the primary event vertex. This re-fitting improves the momentum resolution of the tracks. Both the unfitted and fitted information is retained. The $z_{\rm vtx}$ distribution for the sample of hard photoproduction events defined in Chapter 5 is shown in Fig. 4.3.

4.2.2 The Calorimeter Reconstruction

The first stage in the calorimeter reconstruction is the suppression of noise (for more details, see Section 4.4.2). Following this, calorimeter cells are grouped together to form clusters. The characteristics of these clusters can be used to determine the nature of the originating particle. In this section, the **island-finding** algorithm is described.

4.2.2.1 Island Finding

In ZEUS, islands [143] are formed using calorimeter towers. Each tower is compared to its immediate and diagonally adjacent neighbours. The tower is then associated with its highest energy neighbour. If the tower being considered is itself the tower of highest energy, it is considered to be a "peak", which will be the centre for an island. As a result, all towers become uniquely associated with the nearest, highest-energy tower. All those associated with a particle peak are classified as islands. The island-finding algorithm is applied individually to each calorimeter section and are then joined across boundaries. The island algorithm is illustrated in Fig. 4.4.

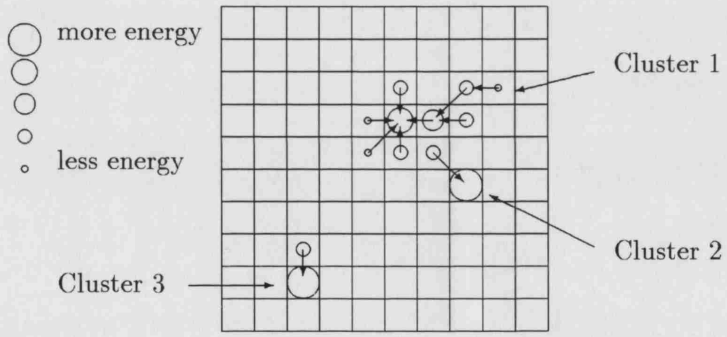

Figure 4.4: Schematic illustration of the island clustering algorithm.

The island-finding algorithm can also be performed on cells rather than towers. These are referred to as **cell-islands**. Cell-islands can also be further combined according to a probability function based on their angular separation to form **cone-islands**. The details of this clustering can be found elsewhere [144]. For the analyses presented in this thesis, cone-islands are used in the identification of electrons (Section 4.5) and in the reconstruction of the final hadronic state (Section 4.6).

4.2.3 Track Matching

It is also possible to match tracks to calorimeter energy deposits. The matching is performed by **swimming** the track out towards the calorimeter using a Runge-Kutta extrapolation, which uses a comprehensive map of the magnetic field. If a low

momentum track heading for the FCAL, BCAL or RCAL begins to spiral back towards the centre, the extrapolation to the face of the calorimeter is abandoned. The matching of tracks to calorimeter cells is used in the reconstruction of the hadronic final state (Section 4.6).

4.3 The EAZE Framework and ORANGE

EAZE is the standard ZEUS analysis package, which produces an output of an NTUPLE containing information about the event. The ORANGE (Overlying Routine for Analysis Ntuple GEneration) [145] is a software library which incorporates a set of standard analysis routines. It is available as a ZSMSM software package and can be compiled with all EAZE jobs. The routines incorporated into ORANGE give the best standard methods for reconstructing common variables.

4.4 Corrections

A number of corrections must be applied to the data in the offline reconstruction phase. This section describes the correction of the CTD B-field, the suppression of calorimeter noise and the calibration of the calorimeter energy scale. The corrections are applied by a set of standard routines that are stored in the ZEUS PHANTOM users library and which are called from within ORANGE.

4.4.1 CTD Magnetic Field

High statistics studies of particle mass peaks (e.g. J/ψ, D^*, K^0_s etc.) suggest that the magnetic field used by VCTRAK is too low by about 0.3%. In order to correct for this effect, the p_T of all tracks, which is proportional to B (see Eq. 3.2), is scaled by a factor of 1.003.

4.4.2 Calorimeter Noise Suppression

The reconstruction of the hadronic final state relies on a precise knowledge of information from the calorimeter. Events containing low levels of hadronic activity, or where the hadronic mass must be precisely determined, are sensitive to the effects of calorimeter noise. Noise in the calorimeter can arise from various sources. For example, the natural radioactivity of the uranium material causes small signals in the PMTs. This is a low level of noise and gives rise to only small energy deposits which are used

for calibration purposes. However, although the individual energy deposits are small, the cumulative energy sum can contribute significantly to the total measured energy. Other sources of noise include contributions from sparks in the PMTs and noise in the DAQ readout chain. Each noise source has its own characteristic signature.

The sources of noise have been studied [146–149] and standard routines which suppress the level of noise have been developed for each year of data-taking. The following four types of cut are implemented in order to reject noisy cells:

- removal of EMC (HAC) cells with $E_{\mathrm{EMC}} < 60$ MeV ($E_{\mathrm{HAC}} < 110$ MeV);
- removal of isolated EMC (HAC) cells with $E_{\mathrm{EMC}} < 80$ MeV ($E_{\mathrm{HAC}} < 140$ MeV).

  Since the majority of noise from the depleted uranium is concentrated at low energies, these cuts are effective at removing much of the noise due to this source.
- cuts on the relative energy **imbalance** obtained from the two PMTs in a cell such that $I_{\mathrm{cell}} < 0.7$ GeV, where $I_{\mathrm{cell}} = E_{\mathrm{PMT1}} - E_{\mathrm{PMT2}}$ is the difference in energy recorded by the two PMTs of a particular cell.

  This cut removes noise which arises predominantly from sparks in the PMTs.
- removal of noisy[‡] (or "hot") cells according to lists [150] provided each year.

  Noisy cells are due mainly to electronic malfunctions. If the noisy cell is known to have a malfunctioning PMT, the energy of the cell is set to two times the energy recorded from the working PMT provided that I_{cell} is not equal to zero. If $I_{\mathrm{cell}} = 0$ then the cell is ignored if the energy it measures in a normal ep event is less than the maximum energy for that cell.

4.4.3 Calorimeter Energy Scale

Studies of the energy response of the calorimeter to the scattered lepton in NC DIS events [151] have shown that there are differences in the energy scale of the calorimeter between data and Monte Carlo. To take account of this difference, corrections are applied to the energies of hadronic deposits in the calorimeter. The `RCALCORR` routine [152] applies these corrections following noise suppression. If there is no STRD or PRES information, the correction is applied to all cells in the calorimeter. Otherwise, it is applied only to those cells which are not identified with the electron candidate[§]. The corrections are applied *only* to the real ZEUS data since in the Monte Carlo, the calorimeter energy scale is precisely known. The energies in the FCAL and BCAL are scaled by global factors of 1.000 and 1.005 respectively, while the energies in the RCAL are scaled by cell-by-cell factors of between 1.000-1.0025.

[‡]Those which give a signal more often than the average or of higher energy than the average.
[§]The electron energy is preferentially corrected with information from the SRTD and PRES.

4.5 Electron Rejection

In order to reject events on the basis of identifying a scattered electron, a reliable method of electron-identification is required. In this thesis, electrons are identified offline using the SINISTRA95 [144] electron-finder[¶]. SINISTRA is a neural network which has been trained on low Q^2 NC DIS data and Monte Carlo to produce the best separation between electromagnetic and hadronic energy deposits by using the properties of shower profiles to establish the nature of the originating particle. SINISTRA uses calorimeter cone-islands as the input for the neural net. The output is then a number ($0 < P_e < 1$) which can be interpreted as the probability that the energy deposit is of electromagnetic origin. In this thesis, an energy deposit is considered to be a lepton candidate if $P_e > 0.9$. Such events are rejected as described in Section 5.4.

4.6 The Hadronic Final State

In ZEUS, the reconstruction of variables associated with the hadronic final state has previously relied only on information from the calorimeter. However, there are cases (e.g. low momentum charged particles) where tracking information is more reliable. An algorithm has been developed [153] which combines calorimeter information and tracking information from the CTD to form so-called **Energy Flow Objects** (EFOs), which are characterised by their energy and momentum. The use of both tracking *and* calorimeter information has several advantages. For example, the transverse momentum of tracks is less sensitive to energy losses in the inactive material in front of the CAL than is a measurement based on energy deposits in calorimeter cells. In addition, the use of tracking information allows the possibility of low energy particles (that do not reach the calorimeter) to be included in the reconstruction. The hadronic energy flow algorithm is discussed in more detail in Section 4.6.1.

In the cases where calorimeter information is more reliable than that of tracking, the EFOs are subject to energy loss and degradation of energy resolution. In addition, the energy response of the calorimeter in the ZEUS detector is not the same as its Monte Carlo simulated response. This gives rise to an energy scale uncertainty in the final measured distributions. A correction routine has been developed [154] which is designed to correct for lost energy, optimise the resolution and reduce the sensitivity of a measurement to the accurate simulation of the calorimeter energy response. The details of this correction routine are described further in Section 4.6.2.

[¶]A simplified version of this code is also used at the TLT.

4.6.1 The Hadronic Energy Flow Algorithm

To ensure the best quality data are used for the reconstruction, the noise suppression and calorimeter energy scale corrections are applied before the hadronic energy flow algorithm is implemented. The main steps in the routine then take place as follows:

- cell-islands are formed separately in the EMC, HAC1 and HAC2 sections of the calorimeter. Every calorimeter cell is assigned to a cell-island and the position of the island is determined from the logarithmically energy-weighted average of the positions of all the constituent cells. The cell-islands are then clustered into cone-islands by using a probability function based on their angular separation. The clustering is started from the outermost HAC2 section and moves inwards.
- high quality tracks originating from the primary vertex are matched to the cone-islands. A high quality track is defined as one which has traversed at least three CTD superlayers and which has a transverse momentum of $0.1 < p_{\mathrm{T}} < 30$ GeV. Each track is extrapolated to the surface of the calorimeter (as described in Section 4.2.3) and is considered to be matched to the island if the distance of closest approach is ≤ 20 cm or within the radius of the island.

Following the above procedures, three types of object remain:

- **tracks with no matching cone-islands**
  These are attributed to low energy charged pions. The energy is calculated using the momentum determined from the track.
- **cone-islands with no matching tracks**
  These are assumed to arise from neutral particles. The energy and momentum are calculated by assigning a momentum vector $\mathbf{p}$ such that $E^2 = |\mathbf{p}|^2$, where E is the energy measured by the calorimeter and $\mathbf{p}$ points from the interaction vertex to the cone-island position.
- **cone-islands which have been matched to tracks**
  These arise from charged particles which have sufficient energy to reach the calorimeter. In this case, a decision must be made regarding whether to use tracking or calorimeter information. If the cone-island has more than three tracks associated with it, then its energy and momentum are calculated using calorimeter information (as above). For all remaining objects, the tracking information will be used in preference to the cone-island energy *if* the following criteria are satisfied,

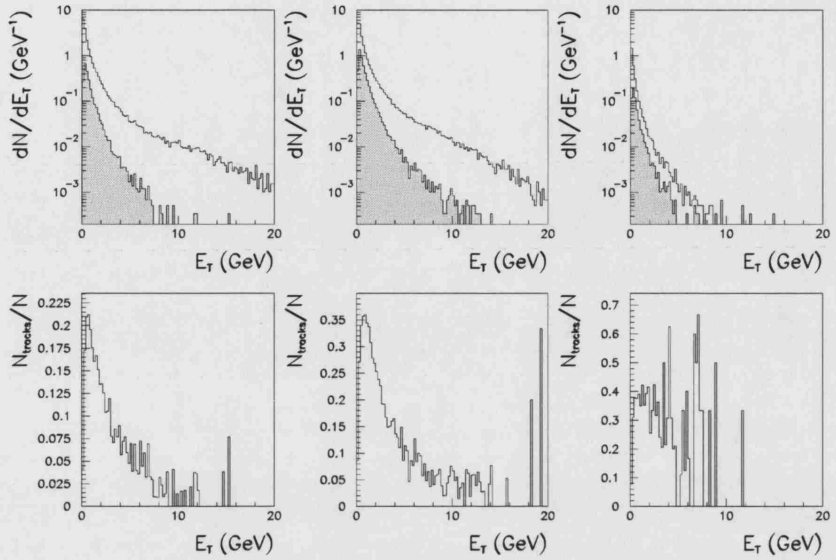

Figure 4.5: The average transverse energy distribution of ZUFOs in two jet photoproduction events in the FCAL, BCAL and RCAL. The shaded histogram indicates the amount of transverse energy measured with tracks. The lower figures show the fraction of the total transverse energy flow measured with tracks. Figure taken from [154].

- $\sigma(p)/p < \sigma(E)/E$. That is, the resolution of the track momentum is better than that of the island energy. This ensures that the highest possible precision is achieved for the reconstruction.
- $E/p < 0.8 + \sigma(E/p)$ where E is the calorimeter energy in GeV, p is the momentum measured by the CTD and $\sigma(E/p) = [(\sigma(E)/E)^2 + (\sigma(p)/p)^2]^{1/2}$. This ensures that the calorimeter energy is due only to the associated track and there are no additional neutral particles forming a contribution.

The resulting set of objects are called **ZEUS Unidentified Flow Objects** (ZUFOs).

4.6.2 Hadronic Energy Corrections

Track information is less sensitive to energy losses in inactive material than is calorimeter information. However, Fig. 4.5 shows that a large proportion of the final ZUFOs are reconstructed from calorimeter information. For these objects, a correction routine has been developed to correct for energy losses in dead material. In order to reduce the difference in energy scale between real and simulated data, the correction

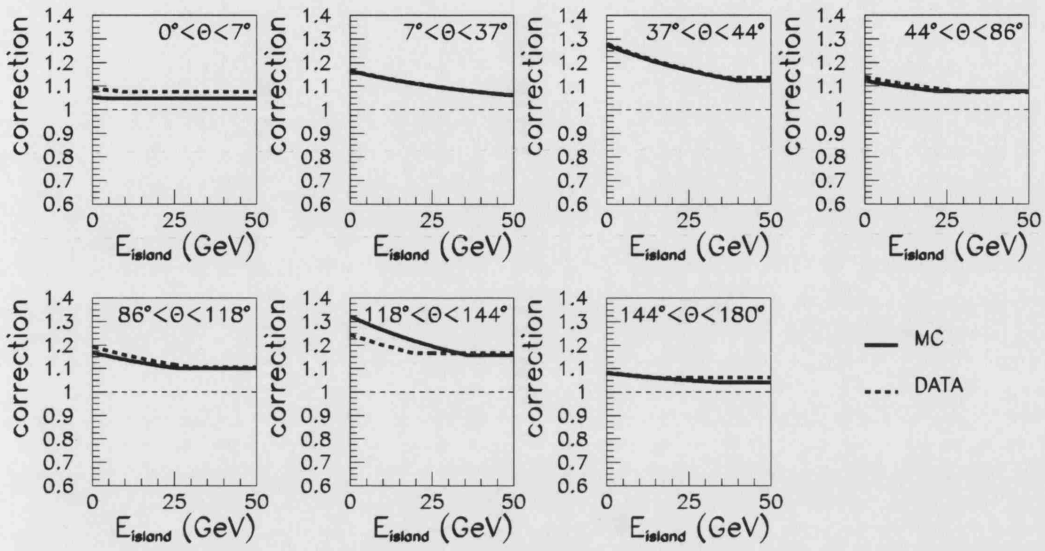

Figure 4.6: The hadronic energy correction factors as a function of E_{island} and θ for data and Monte Carlo. Figure taken from [154].

factors have been determined separately for data and Monte Carlo. The routine is applied only to the ZUFOs reconstructed from calorimeter information, the assumption being that the energy measurement determined from the momentum of tracks suffer from negligible energy loss.

The correction factors were determined using considerations of conservation of energy and momentum in high Q^2 NC DIS event, where the scattered electron is balanced by a collimated shower of hadronic particles. Since the energy of the scattered electron is better understood than the measurement of energy in the final hadronic state, the electron energy is used to constrain the hadronic energies. This is done by minimising the difference between the variables p_{T} and y as reconstructed from the both the electron and from the hadronic final state. The corrections were performed using two samples of data,

- **sample 1** consists of low y events for which most of the hadronic energy flow is in the forward direction. For this sample, the relative difference between the transverse momentum of the scattered electron and the final state hadron is minimised. The transverse momentum is reconstructed according to,

$$p_{\mathrm{T};e} = |E_e \sin\theta_e| \tag{4.1}$$

$$p_{\mathrm{T};h} = |\sum_{\mathrm{hadrons}} E \sin\theta| \tag{4.2}$$

- **sample 2** consists of high y events which are more sensitive to hadron energy deposits in the backward direction. For this sample, the relative difference between the values of y reconstructed from the electron and from the hadronic final state was minimised. The **electron-** and **Jaquet-Blondel** methods (see Section 4.9) were used for the reconstruction of y for the electron and hadronic final state, respectively.

Since the scattered electron also suffers from energy loss in dead material, its energy is first corrected using information from the RPRES. Full details of the correction procedure are given in [155]. The correction factors were then determined from a fit to a function of the form,

$$\sum_{\text{sample1}} \min\left[\left(\frac{p_{\mathrm{T};e} - p_{\mathrm{T};h}}{p_{\mathrm{T};e}}\right)^2, 0.2^2\right] + \sum_{\text{sample2}} \min\left[\left(\frac{y_e - y_{\mathrm{JB}}}{y_e}\right)^2, 0.2^2\right]. \qquad (4.3)$$

In order to prevent the poorly measured events in the tails of the distribution from having a significant influence on the results of the fit, relative differences of $> 20\%$ were truncated. The fit was applied separately to data and Monte Carlo and the resulting correction factors (as a function of cone-island energy and polar angle) are shown in Fig. 4.6. The final corrected energy is then simply given by the measured energy multiplied by the relevant correction factor.

The performance of the routine was tested [154] by applying the correction factors to photoproduction events generated by the HERWIG 5.9 Monte Carlo program. The transverse energies of the two highest-E_{T} hadron-level jets were required to satisfy $E_{\mathrm{T}} > 11$ GeV. Figure 4.7 shows the relative difference between the reconstructed and generated transverse energy as a function of jet pseudo-rapidity. The shaded band indicates the resolution. The results show that for jets reconstructed using ZUFOs, the

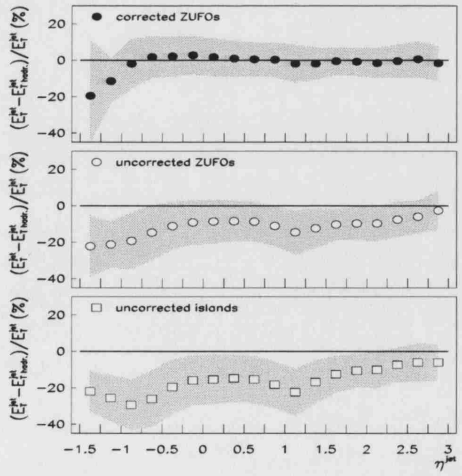

Figure 4.7: Comparison of the reconstructed and true jet E_{T} as a function of jet η. The lower plot shows the results for uncorrected cone-islands, the middle plot shows the results for uncorrected ZUFOs and the upper plot shows the results for corrected ZUFOs. The shaded band shows the resolution. Diagram taken from [154].

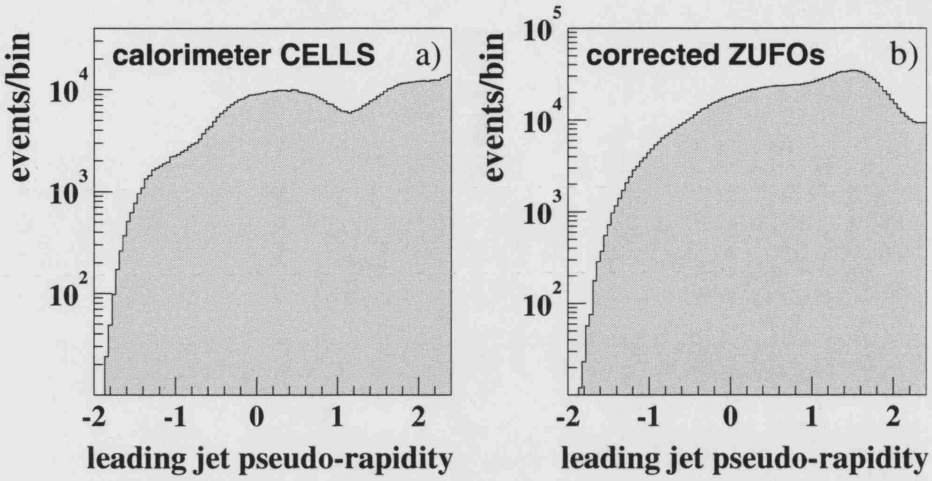

Figure 4.8: The pseudo-rapidity distribution of the highest transverse energy jet in a sample of two jet photoproduction data from 1996-1997. The results are shown for reconstructions performed using a) calorimeter cells and b) corrected ZUFOs.

resolution is improved and the shift from zero is reduced. Following application of the correction routine, the resolution is further improved and for $\eta^{\text{jet}} > -1$, the transverse energy differs from the generated value by $< 1\%$. The biases in the distribution at the transition regions between the RCAL/BCAL ($\eta \sim -1$) and the BCAL/FCAL ($\eta \sim 1$) are also smoothed. This is also shown in Fig. 4.8 which compares the pseudo-rapidity distributions of the highest transverse energy jet in a sample of two jet photoproduction, for jets reconstructed using calorimeter cells and corrected ZUFOs.

4.6.3 Calorimeter Energy Scale

The scale difference between the calorimeter response to data and Monte Carlo for the corrected ZUFOs has been studied [154]. Figure 4.9 shows the relative difference in the transverse momentum reconstructed from the hadronic final state and that reconstructed according to the **double angle method** [156], as a function of hadronic angle. The relative difference between data and Monte Carlo is also shown. For uncorrected cone islands, the energy response in data is up to 4% lower than in Monte Carlo. For uncorrected ZUFOs (not shown) the energy scale uncertainty is $\sim 3\%$, while for corrected ZUFOs, the data and Monte Carlo agree to within $\sim 2-3\%$. This is also indicated in Fig. 4.10 (left) which shows the results for corrected ZUFOs as a function of jet transverse energy. More recent studies [157], using the ZEUS 1996-1997 data (that is, the data-set used in this thesis), have investigated the energy scale uncertainty using corrected ZUFOs with $E_{\text{T}}^{\text{jet}} > 6$ GeV. The results, summarised in Fig. 4.10 (right), show that for jets with $E_{\text{T}} > 7$ GeV the energy scale uncertainty is $\sim 1\%$ while at lower jet transverse energies a 3% uncertainty can be assumed.

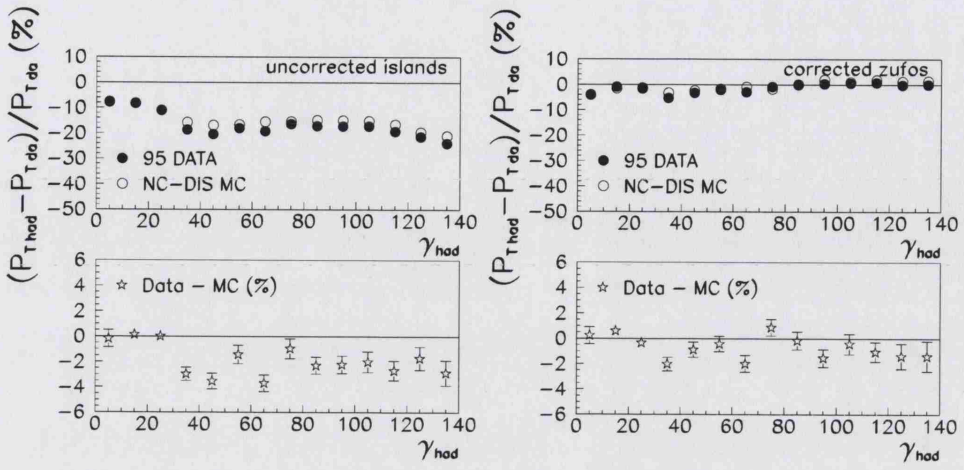

Figure 4.9: The relative difference between the p_T reconstructed from the hadronic final state and that reconstructed using the double angle method as a function of γ_h. The results from uncorrected islands are shown on the left and the results from corrected ZUFOs are shown on the right. The lower plots show the relative difference between data and Monte Carlo. Errors are statistical only. Diagram taken from [154].

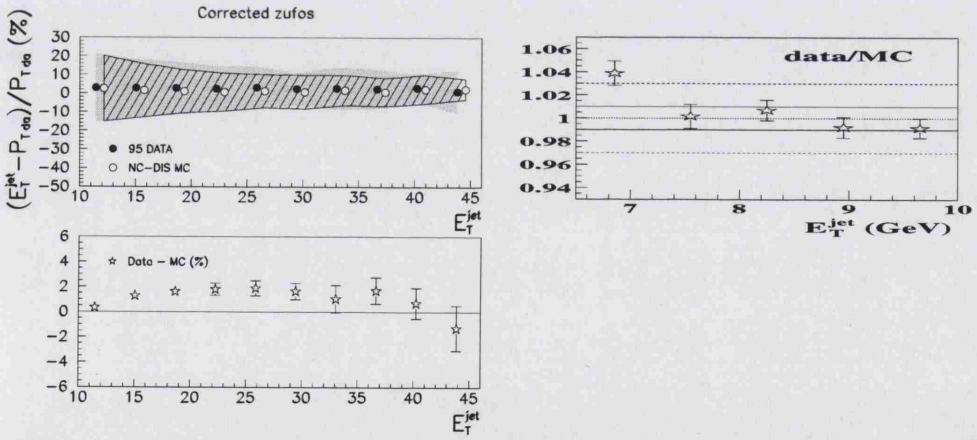

Figure 4.10: The jet-energy-scale uncertainty as a function of E_T^{jet} for corrected ZUFOs. Left: The relative difference between E_T^{jet} and p_T reconstructed using the double angle method for (ZEUS 1995) data and Monte Carlo. The shaded and cross-hatched bands show the resolution for data and Monte Carlo respectively. The lower plot shows the difference between data and Monte Carlo. Diagram taken from [154]. Right: The ratio of (ZEUS 1996-1997) data and Monte Carlo. The solid lines indicate a 1% uncertainty and the dashed lines indicate a 3% uncertainty. Diagram created from [157].

4.7 Jet Algorithms

In order to determine the underlying dynamics of hadronic interactions, final state particles are grouped into jets. According to LPHD, the properties of these jets should closely correspond to those of the outgoing partons from which the jets were formed. However, a jet is not a fundamental QCD object and it is necessary to establish an exact definition. A jet algorithm is required to satisfy the following:

- **infra-red safety**
  The same results should be obtained for the classification of any given event and an exactly similar event but with an arbitrary number of infinitely soft partons with arbitrary directions added to it. If this condition is not satisfied, it will cause infra-red divergences in the theory. Experimentally, this means that the results should not be influenced by the emission of very low energy particles.

- **collinear safety**
  The same results should be obtained for the classification of any event and an exactly similar event but with any massless partons replaced by an arbitrary number of collinear, massless partons with the same total momentum. In theoretical calculations, this would give rise to collinear divergences, which only disappear when no distinction is made between a single particle with energy E and N collinear particles whose energies sum to the same value such that $E_1 + E_2 + ... + E_N = E$ and contributions from each are integrated over. Experimentally, this means that the results should be largely independent of the granularity of the detector (e.g. the final result should be the same whether an energy deposit is spread over one or two calorimeter cells).

If either of these conditions is violated, even for some small class of events, the results will be divergent in perturbation theory. Therefore, it is necessary to create an algorithm which can identify jet-like objects while satisfying the above conditions. A jet algorithm that is both infra-red and collinear safe can be used to gain information on the underlying hard parton dynamics. Such algorithms are generally applied to a set of objects which represent the final state e.g. partons, hadrons, calorimeter cells (or clusters of cells), ZUFOs etc.

Two types of algorithm are available to define jets: the **cone** algorithm and the **clustering** algorithm. In this thesis, both cone and clustering algorithms are used. The EUCELL [158] cone algorithm is used for the selection of two jet photoproduction events at the TLT and the $k_\perp$ algorithm [159] is used in the offline selection (see Chapter 5) and in the cross section definitions. The details of the jet algorithms used in this thesis are reviewed in Appendix D.

4.8 Jet Kinematics and Reconstruction

In a lepton-hadron (or hadron-hadron) collision, the centre-of-mass of the resulting hadronic system is usually boosted in the longitudinal direction with respect to the incoming beam particles. Therefore, it is particularly useful to classify the final hadronic state in terms of variables which have a simple transformation under boosts in the z-direction. For this reason, jets are usually described in terms of their transverse momentum p_{T}, rapidity y and azimuthal angle ϕ. The four-momentum p^{μ} and rapidity y of a jet of mass m are given by,

$$p^{\mu} = (E, p_x, p_y, p_z) = (m_{\mathrm{T}} \cosh y, p_{\mathrm{T}} \cos\phi, p_{\mathrm{T}} \sin\phi, m_{\mathrm{T}} \sinh y) \tag{4.4}$$

$$y = \frac{1}{2} \log\left(\frac{E + p_z}{E - p_z}\right) \tag{4.5}$$

where the transverse mass is defined as $m_{\mathrm{T}} = [p_{\mathrm{T}}^2 + m^2]^{1/2}$ and the transverse momentum is given by $p_{\mathrm{T}} = [p_x^2 + p_y^2]^{1/2}$. Under a longitudinal boost, the rapidity is changed only by the addition of a constant. That is, *rapidity differences are boost invariant.* This is shown in Appendix B. In practice, single jets are normally considered to be massless. In the $m \rightarrow 0$ limit, p_{T} and y can be replaced by E_{T} and η such that,

$$p_{\mathrm{T}} \simeq E_{\mathrm{T}} = E \sin\theta, \tag{4.6}$$

$$\eta = -\log\left(\tan\frac{\theta}{2}\right), \tag{4.7}$$

where $\tan\theta = \frac{E_{\mathrm{T}}}{p_z}$. Jets are more often defined in terms of $(E_{\mathrm{T}}, \eta, \phi)$ than $(p_{\mathrm{T}}, y, \phi)$ since E_{T} and θ are the quantities which are directly measured in a detector.

4.8.1 Jet Resolutions

The measured (reconstructed) values of the jet quantities $(E_{\mathrm{T}}, \eta, \phi)$ will deviate from the corresponding hadron (true) values. Such deviations arise as a result of inactive material in front of the calorimeter, the finite resolution of the CTD and CAL and the effects of the magnetic field on the trajectories of low energy charged particles. In order to study the differences between the generated and reconstructed properties of the jets, a sample of two jet photoproduction with $Q^2 < 1$ GeV^2 and $0.2 < y < 0.85$ has been generated using the PYTHIA Monte Carlo. At the hadron level, events with at least two jets satisfying $E_{\mathrm{T}}^{1,2}(\mathrm{true}) > 4$ GeV with all jets lying in the pseudo-rapidity range $-3.0 < \eta^{1,2}(\mathrm{true}) < 3.0$ were selected. At the detector level, a sample of clean

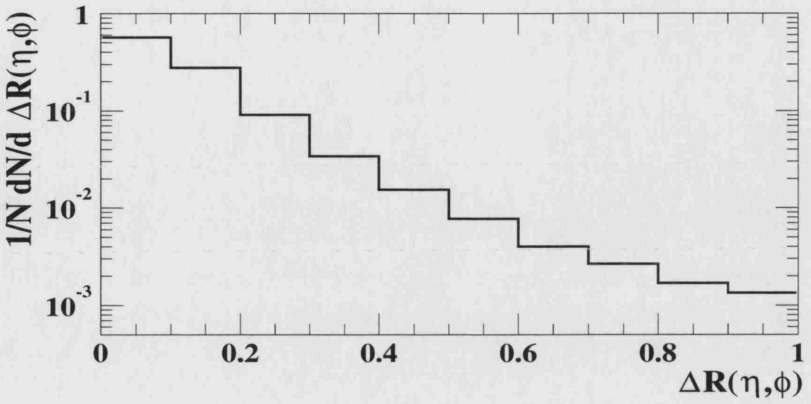

Figure 4.11: The $\eta - \phi$ distance between matching true and reconstructed jets.

photoproduction events were selected as detailed in Chapter 5. In addition, each event was required to contain at least two jets with $E_{\mathrm{T}}^{1,2}(\mathrm{rec.}) > 5$ GeV with all jets lying in the pseudo-rapidity range $-2.4 < \eta^{1,2}(\mathrm{rec.}) < 2.4$. The true and reconstructed jets are considered to be matched in $\eta - \phi$ space if,

$$\Delta R(\eta, \phi) = [(\eta^{\mathrm{jet}}(\mathrm{rec.}) - \eta^{\mathrm{jet}}(\mathrm{true}))^2 + (\phi^{\mathrm{jet}}(\mathrm{rec.}) - \phi^{\mathrm{jet}}(\mathrm{true}))^2]^{1/2} < 1. \qquad (4.8)$$

If more than one pair of jets are found to be matched in any given event, then the pair of jets with the smallest value of $\Delta R(\eta, \phi)$ are taken to be the matched jets. The distribution of ΔR for matched jets is shown in Fig. 4.11.

Figures 4.12 - 4.14 show the variation on the mean value of the quantities $\phi^{\mathrm{jet}}(\mathrm{rec.}) - \phi^{\mathrm{jet}}(\mathrm{true})$, $\eta^{\mathrm{jet}}(\mathrm{rec.}) - \eta^{\mathrm{jet}}(\mathrm{true})$ and $E_{\mathrm{T}}^{\mathrm{jet}}(\mathrm{rec.})/E_{\mathrm{T}}^{\mathrm{jet}}(\mathrm{true})$ with respect to $\eta^{\mathrm{jet}}(\mathrm{rec.})$, $\phi^{\mathrm{jet}}(\mathrm{rec.})$ and $E_{\mathrm{T}}^{\mathrm{jet}}(\mathrm{rec.})$ for each matching pair of jets. The results are shown for both the case where the reconstruction is performed using calorimeter cells and when it is performed using corrected ZUFOS. In each figure, the error bars represent the root-mean-square (r.m.s) spread on the distribution and therefore give an indication of the resolution. The results are shown for direct and resolved events separately.

Figure 4.12 shows that there is no systematic variation in the reconstruction of any of the jet quantities as a function of $\phi^{\mathrm{jet}}(\mathrm{rec.})$. The deviation of the mean values of $\phi^{\mathrm{jet}}(\mathrm{rec.}) - \phi^{\mathrm{jet}}(\mathrm{true})$ and $\eta^{\mathrm{jet}}(\mathrm{rec.}) - \eta^{\mathrm{jet}}(\mathrm{true})$ from zero is $\lesssim 0.01$. The results also show that the variation of the mean and r.m.s values are independent of whether the reconstruction is performed using calorimeter cells and ZUFOs. In contrast, the variation of the mean value of $E_{\mathrm{T}}^{\mathrm{jet}}(\mathrm{rec.})/\mathrm{E}_{\mathrm{T}}^{\mathrm{jet}}(\mathrm{true})$ indicates a shift of $\sim -15\%$ when the reconstruction is performed using calorimeter cells, while for corrected ZUFOs, the deviation from unity is $\lesssim 2\%$ for direct events and $\lesssim 4\%$ for resolved. In both cases, the ratio $E_{\mathrm{T}}^{\mathrm{jet}}(\mathrm{rec.})/\mathrm{E}_{\mathrm{T}}^{\mathrm{jet}}(\mathrm{true})$ is marginally higher for resolved events than direct events.

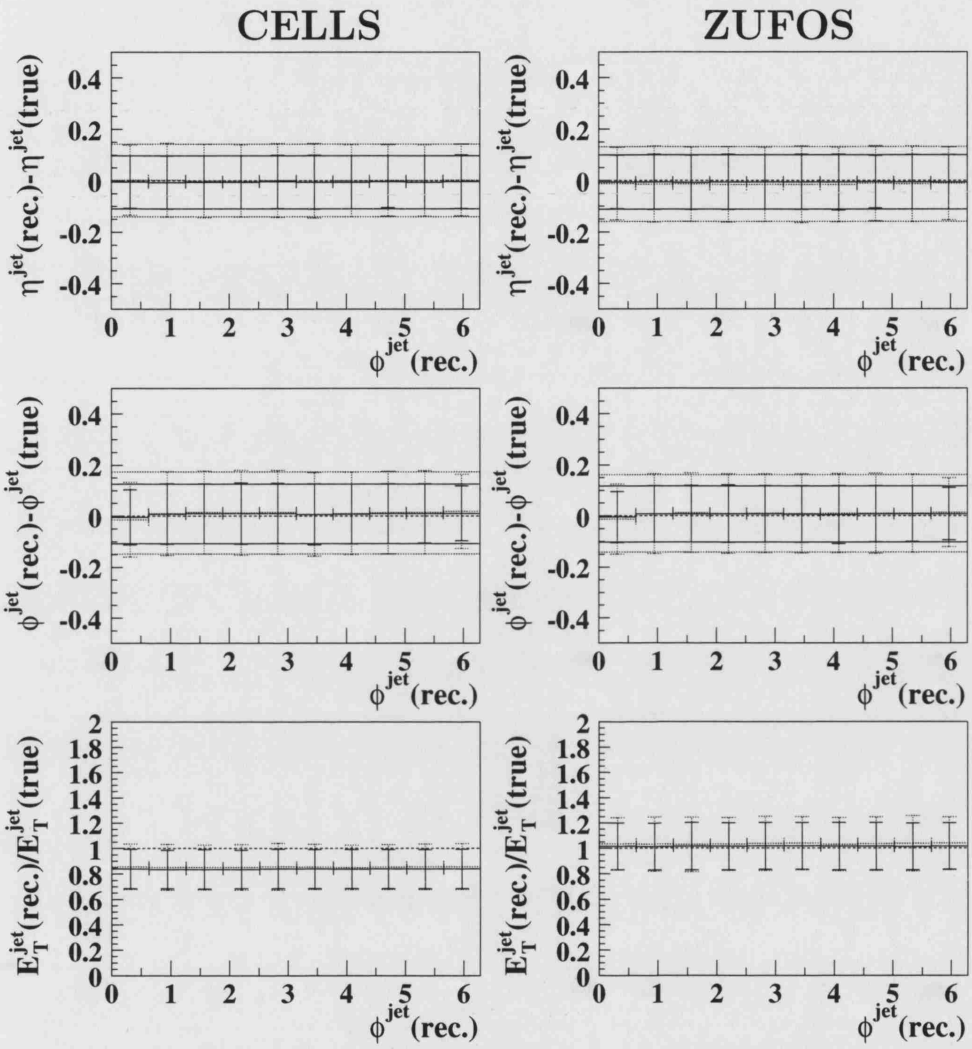

Figure 4.12: The relative difference between the true and reconstructed values of $\eta^{\rm jet}$, $\phi^{\rm jet}$ and $E_{\rm T}^{\rm jet}$ as a function of $\phi^{\rm jet}$ for a sample of two jet photoproduction generated using the PYTHIA Monte Carlo. The vertical error bars give the r.m.s of the distribution in each bin. The left and right columns show the results from jets reconstructed using calorimeter cells and corrected ZUFOs respectively. The solid and dotted markers show the contribution from direct and resolved photoproduction, respectively. The solid and dotted horizontal lines show the typical r.m.s for the direct and resolved samples. The horizontal dashed lines indicate where the results would lie if the reconstructed values were exactly equal to the generated values.

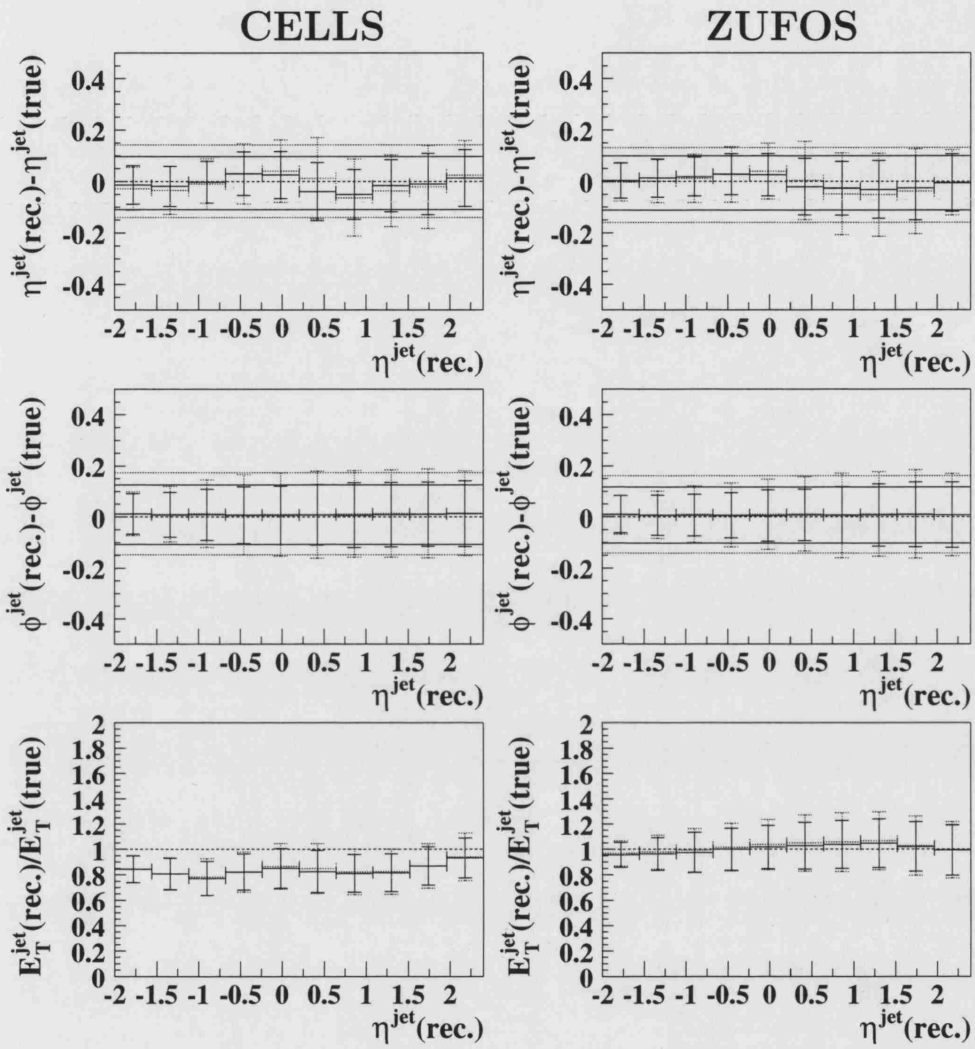

Figure 4.13: The relative difference between the true and reconstructed values of $\eta^{\rm jet}$, $\phi^{\rm jet}$ and $E_{\rm T}^{\rm jet}$ as a function of $\eta^{\rm jet}$ for a sample of two jet photoproduction generated using the PYTHIA Monte Carlo. The vertical error bars give the r.m.s of the distribution in each bin. The left and right columns show the results from jets reconstructed using calorimeter cells and corrected ZUFOs respectively. The solid and dotted markers show the contribution from direct and resolved photoproduction, respectively. The solid and dotted horizontal lines show the typical r.m.s for the direct and resolved samples. The horizontal dashed lines indicate where the results would lie if the reconstructed values were exactly equal to the generated values.

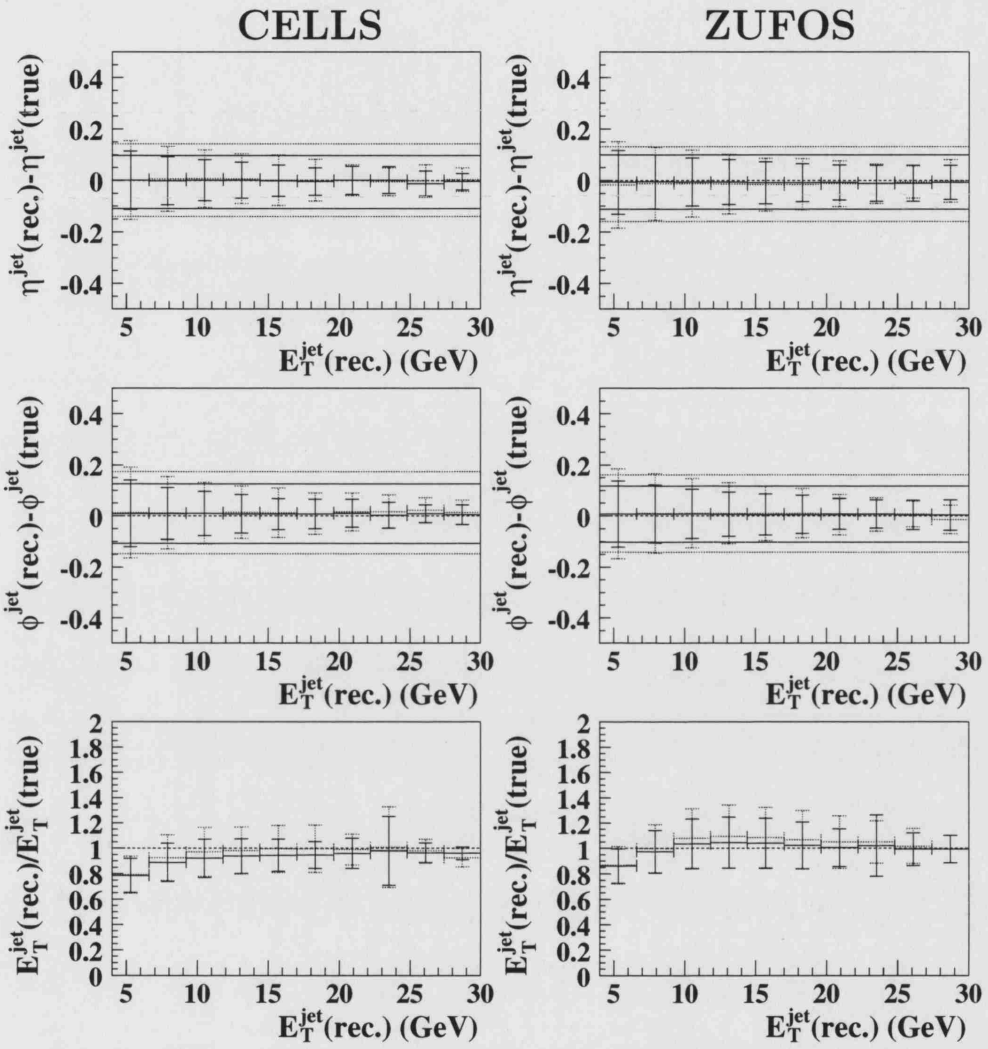

Figure 4.14: The relative difference between the true and reconstructed values of η^{jet}, ϕ^{jet} and $E_{\text{T}}^{\text{jet}}$ as a function of $E_{\text{T}}^{\text{jet}}$ for a sample of two jet photoproduction generated using the PYTHIA Monte Carlo. The vertical error bars give the r.m.s of the distribution in each bin. The left and right columns show the results from jets reconstructed using calorimeter cells and corrected ZUFOs respectively. The solid and dotted markers show the contribution from direct and resolved photoproduction, respectively. The solid and dotted horizontal lines show the typical r.m.s for the direct and resolved samples. The horizontal dashed lines indicate where the results would lie if the reconstructed values were exactly equal to the generated values.

Figure 4.13 shows that there is some systematic variation of the mean value of $\eta^{\text{jet}}(\text{rec.}) - \eta^{\text{jet}}(\text{true})$ with respect to $\eta^{\text{jet}}(\text{rec.})$. However, the variation is smaller than the resolution and is significantly less apparent when the reconstruction is performed using ZUFOs as opposed to calorimeter cells. The quantity $\phi^{\text{jet}}(\text{rec.}) - \phi^{\text{jet}}(\text{true})$ shows little deviation from the nominal value of zero, although the resolution appears to worsen slightly at more forward $\eta^{\text{jet}}(\text{rec.})$. When the reconstruction is performed using calorimeter cells, the quantity $E_{\text{T}}^{\text{jet}}(\text{rec.})/\text{E}_{\text{T}}^{\text{jet}}(\text{true})$ again shows a significant shift from unity. This deviation is largest at $\eta^{\text{jet}}(\text{rec.}) \sim -1$ and $\eta^{\text{jet}}(\text{rec.}) \sim 1$ which correspond to the RCAL/BCAL and BCAL/FCAL boundaries where there are large amounts of inactive material. For the corrected ZUFOs jets, the value of $E_{\text{T}}^{\text{jet}}(\text{rec.})/\text{E}_{\text{T}}^{\text{jet}}(\text{true})$ is closer to unity across the entire range of $\eta^{\text{jet}}(\text{rec.})$ and the large shifts at $\eta^{\text{jet}}(\text{rec.}) \sim -1$ and $\eta^{\text{jet}}(\text{rec.}) \sim 1$ are less apparent.

Figure 4.14 shows that the resolution of all the jet quantities improve as the transverse energy of the jets increases. For the quantities $\phi^{\text{jet}}(\text{rec.}) - \phi^{\text{jet}}(\text{true})$ and $\eta^{\text{jet}}(\text{rec.}) - \eta^{\text{jet}}(\text{true})$, the value of the mean is close to zero over the whole $E_{\text{T}}^{\text{jet}}$ range. However, the quantity $E_{\text{T}}^{\text{jet}}(\text{rec.})/\text{E}_{\text{T}}^{\text{jet}}(\text{true})$ shows large variations as a function of $E_{\text{T}}^{\text{jet}}(\text{rec.})$. For jets reconstructed using calorimeter cells, the shift from unity is significantly larger for low- than for high-transverse-energy jets reaching a maximum of $\sim 20\%$. For corrected ZUFOs, this behaviour is less apparent and the deviation from the mean is generally $\lesssim 5\%$.

4.9 Reconstruction of y and Q^2

There are many methods that can be used to reconstruct the variables y and Q^2. In this section the two of relevance to the current work are discussed; namely the **electron** and the **Jacquet-Blondel** methods. For a more detailed review, see [155].

4.9.1 The Electron Method

Both y and Q^2 can be calculated using the momentum of the scattered lepton,

$$y_e = 1 - \frac{E'_e}{2E_e}(1 - \cos\theta_e) \tag{4.9}$$

$$Q^2_e = 2E_e E'_e(1 + \cos\theta_e) \tag{4.10}$$

where E_e and E'_e are the incoming and scattered lepton energies respectively and θ_e is the scattered lepton angle with respect to the proton-beam direction. This method assumes that there are no additional emissions from the lepton i.e. that it entered

the hard scatter with the beam energy, E_e, and it left with the measured energy E'_e. Consequently, the result is sensitive to both initial- and final-state electromagnetic radiative corrections.

From Eq. 4.10, it is apparent that θ_e will be large in low Q^2 events. This means that the lepton continues to travel in a direction close to its original path. For this reason, the experimental definition of photoproduction in ZEUS is the absence of the scattered lepton in the UCAL. This corresponds to $\theta_e \gtrsim 177°$ and $Q^2 \lesssim 1$ GeV^2. Substituting these large values of θ_e into Eq. 4.9 gives that,

$$y_e = \frac{(E_e - E'_e)}{E_e} \approx \frac{E_\gamma}{E_e}. \tag{4.11}$$

Therefore, y is the fraction of the electron energy carried by the exchanged photon.

4.9.2 The Jacquet-Blondel Method

Since photoproduction in ZEUS is defined in terms of an anti-tag condition on the lepton, it is necessary to also be able to calculate the value of y without requiring the presence of the lepton in the detector. The Jacquet-Blondel [160] method calculates the values of y and Q^2 using the final hadronic state. Consequently, this method can be used even when the scattered lepton is not measured. Summing over all final state particles (except for the lepton) gives

$$y_{\rm JB} = \frac{\sum_i (E_i - p_{zi})}{2E_e} \approx \frac{\sum_i E_i(1 - \cos\theta_i)}{2E_e} \tag{4.12}$$

$$Q^2_{\rm JB} = \frac{(\sum_i p_{xi})^2 + (\sum_i p_{yi})^2}{1 - y_{\rm JB}}. \tag{4.13}$$

If the sum is over all final state hadrons, then the above relations are exact. However, experimentally, the sum runs over all calorimeter cells. If the scattered lepton is found in the detector, the cluster of cells identified with the scattered lepton are excluded from the sum. If it is not possible to remove such cells, as in the case of low energy electrons which have not been identified by the electron-finder, then values of $y_{\rm JB}$ which approach unity will be observed. This allows events with an unidentified lepton to be rejected. The position of each cell is determined from the nominal cell centre corrected for the position of the event vertex as reconstructed from tracks in the ZEUS CTD. This definition is relatively insensitive to loss of particles in the forward beam-pipe. These particles would largely come from the proton remnant which do not contribute in the limit of small polar angle.

Since the Jaquet-Blondel method measures the energy transferred *to* the hadronic system, it is unaffected by FSR. However, since the calculation of $y_{\rm JB}$ involves E_e, it is sensitive to ISR.

4.10 Parton Momentum Fractions

At LO, the fractional momentum of the incoming partons from the proton and photon can be reconstructed from the momentum of the two outgoing partons from the hard scatter according to,

$$x_\gamma^{\mathrm{LO}} = \frac{\sum_i E_{\mathrm{T}}^i \exp(-\eta^i)}{2E_\gamma} \tag{4.14}$$

$$x_p^{\mathrm{LO}} = \frac{\sum_i E_{\mathrm{T}}^i \exp(\eta^i)}{2E_p} \tag{4.15}$$

where the sum runs over the two outgoing partons. The quantities E_{T}^i and η^i are the transverse energy and pseudo-rapidity of parton i in the laboratory frame. Equations 4.14 and 4.15 are derived in Appendix B. Also note that, in the collinear approximation, $E_\gamma = yE_e$.

As a result of confinement, parton energies cannot be measured experimentally. Instead, the jets can be used to define observable quantities x_γ^{OBS} and x_p^{OBS} which are correlated to the parton level quantities x_γ and x_p. These observables are formed by simply replacing the sum over partons by a sum over jets so that,

$$x_{\gamma;\mathrm{NJ}}^{\mathrm{OBS}} = \frac{\sum_i E_{\mathrm{T}}^i \exp(-\eta^i)}{2yE_e} \tag{4.16}$$

$$x_{p;\mathrm{NJ}}^{\mathrm{OBS}} = \frac{\sum_i E_{\mathrm{T}}^i \exp(\eta^i)}{2E_p} \tag{4.17}$$

where the sum now runs over the N jets within the accepted pseudo-rapidity range. Provided all events are treated consistently in both theory and experiment, these definitions are valid to all orders of perturbation theory. The same definitions can also be used at detector level, where the jet quantities are reconstructed using the methods described in previous sections and the value of y is replaced by y_{JB}.

At LO, direct photoproduction events contribute purely at $x_\gamma^{\mathrm{LO}} = 1$, while resolved events populate the region at lower x_γ^{LO}. Beyond LO, the distinction between direct and resolved processes becomes ambiguous. As a result of both higher order and hadronisation effects, the direct contribution of x_γ^{OBS} will not lie exactly at unity. At the detector level, the distribution will be further affected by detector smearing. However, it is still possible to choose a working experimental definition which allows the discrimination of direct and resolved photon events. In this thesis, events with $x_{\gamma;\mathrm{NJ}}^{\mathrm{OBS}} < 0.75$ are considered to be **resolved-enhanced** and those with $x_{\gamma;\mathrm{NJ}}^{\mathrm{OBS}} > 0.75$ are **direct-enhanced**. This separation between direct and resolved events is used in both

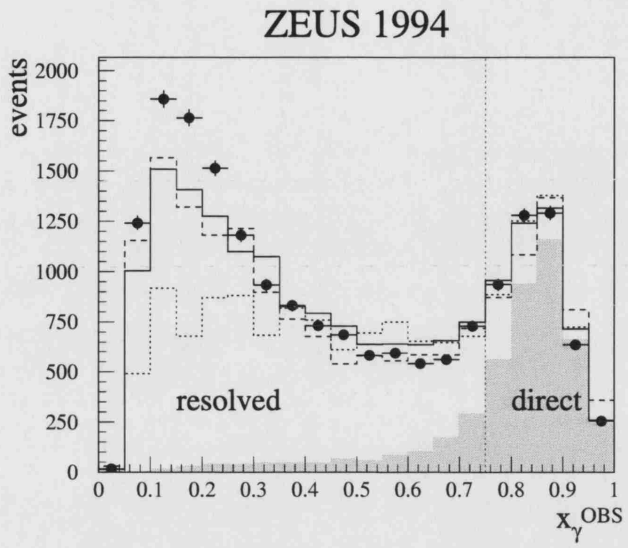

Figure 4.15: The 1994 ZEUS measurement of $x_{\gamma;2J}^{OBS}$. The uncorrected data are shown by the solid points. The solid, dotted and dashed histograms show the predictions of HERWIG (with and without multi-parton interactions) and PYTHIA (with MPI). The shaded region indicates the events generated as direct photoproduction from the HERWIG Monte Carlo. The vertical line indicates the experimental cut used to separate resolved- and direct-enhanced regions.

data and theoretical calculations. It is useful to note also, that events with large x_γ^{OBS} correspond to the kinematic region where most of the energy of the photon is available to probe the proton at low x_p.

Figure 4.15 shows the distribution of $x_{\gamma;2J}^{OBS}$ for a sample of two jet photoproduction events from ZEUS 1994 data. The Monte Carlo predictions underestimate the number of events at low $x_{\gamma;2J}^{OBS}$, although inclusion of multi-parton interactions in the models is shown to improve the agreement with the data. The vertical line indicates the experimental separation between the direct- and resolved-enhanced regions.

Chapter 5

Jet Photoproduction Selection

For the analyses presented in this thesis, a sample of ZEUS data from the 1996-1997 HERA running period was used. In this chapter, the criteria for the selection of jet photoproduction events are described in detail. The first stage is the selection of runs for which the ZEUS detector was running both efficiently and reliably. Following this, the selection of photoproduction events is carried out in two stages. The first stage is an online selection using the ZEUS first, second and third level triggers whilst in the second stage a more refined offline selection is performed. The criteria that must be satisfied at both stages are designed to minimise the level of background contamination, whilst maximising the number of genuine jet photoproduction events selected.

5.1 Run Selection

Runs were selected using the EVTAKE routine [161]. This is a code which selects runs, provided the following criteria are satisfied for the particular run under consideration:

- the LUMI monitor is fully functional;
- the magnetic field is on;
- the CTD is at full high voltage with no large dead regions;
- the UCAL is operational without a significant number of dead channels.

The luminosity delivered by HERA during 1996-1997 corresponds to 53.5 pb^{-1}. Following the EVTAKE selection, the total data sample corresponds to an integrated luminosity of 38.6 ± 0.6 pb^{-1} [161]. The EVTAKE luminosities for several years of data-taking are shown in Fig. 5.1.

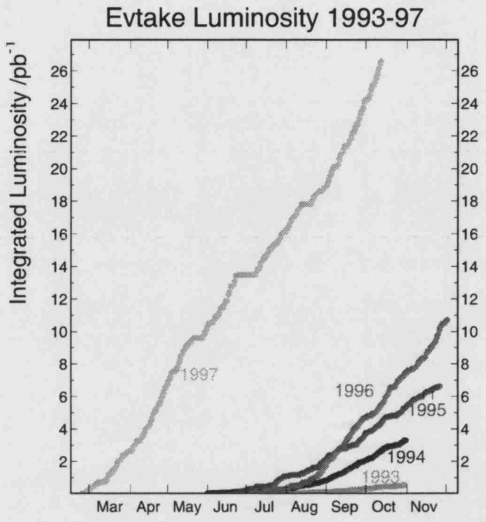

Figure 5.1: The integrated luminosity for EVTAKE runs from 1993-1997.

5.2 Rejection Methods

In order to select a sample of clean photoproduction events, it is necessary to consider the methods by which contaminating background events may be rejected. Different types of background have characteristic features that may be used in order to minimise their contribution to the final event sample. There are several sources of potential background which can be broadly classified into two groups:

- **non-physics background**
  - beam-gas interactions from the lepton and proton beams;
  - halo muons travelling collinear to the proton beam;
  - cosmic ray muons.

  These type of backgrounds can be efficiently rejected by demanding an interaction vertex close to the nominal IP and by requiring the timing information to be consistent with a true lepton-proton collision. This is illustrated in Fig. 5.2 which shows the correlation between $z_{\rm vtx}$ and $t_{\rm FCAL}$ for a LUMI-tagged sample of photoproduction events. The distribution shows that the events are peaked near $z_{\rm vtx} \sim t_{\rm FCAL} \sim 0$.

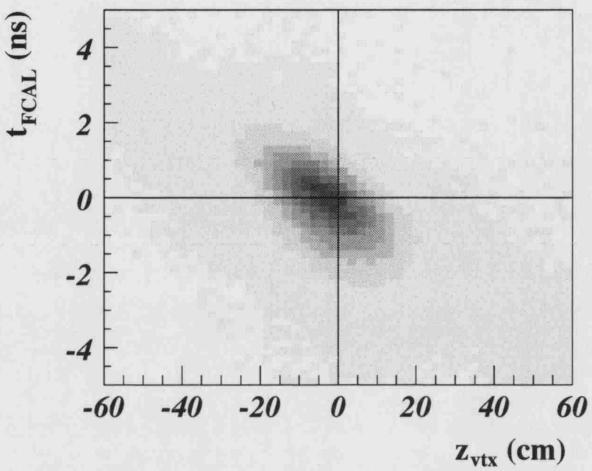

Figure 5.2: The distribution of $z_{\rm vtx}$ versus $t_{\rm FCAL}$.

- **physics background**
  - NC DIS events. These events can be rejected by a cut on the $(E - p_z)$ of the event. In an NC DIS event, $(E - p_z) = 2E_e$ (as measured in the calorimeter). However, in photoproduction events the scattered lepton escapes undetected. Therefore, this quantity is generally much lower than for DIS events since it is then only equal to $2E_\gamma$. The majority of the remaining NC DIS events can be rejected when a scattered lepton candidate is detected in the calorimeter.
  - CC DIS events. These are rejected by a cut on the missing transverse momentum in the event, which is carried away by the neutrino.

Figure 5.3 shows examples of events which would enter the final jet photoproduction sample if not for the application of the specific cut used to reject that type of background. In the following sections, the online and offline selection criteria are described in more detail.

5.3 Online Event Selection

The three level trigger system employed by ZEUS has been described in general terms in Section 3.8. In this section, the specific trigger logic used for the selection of jet photoproduction events (at each trigger level) is explicitly described.

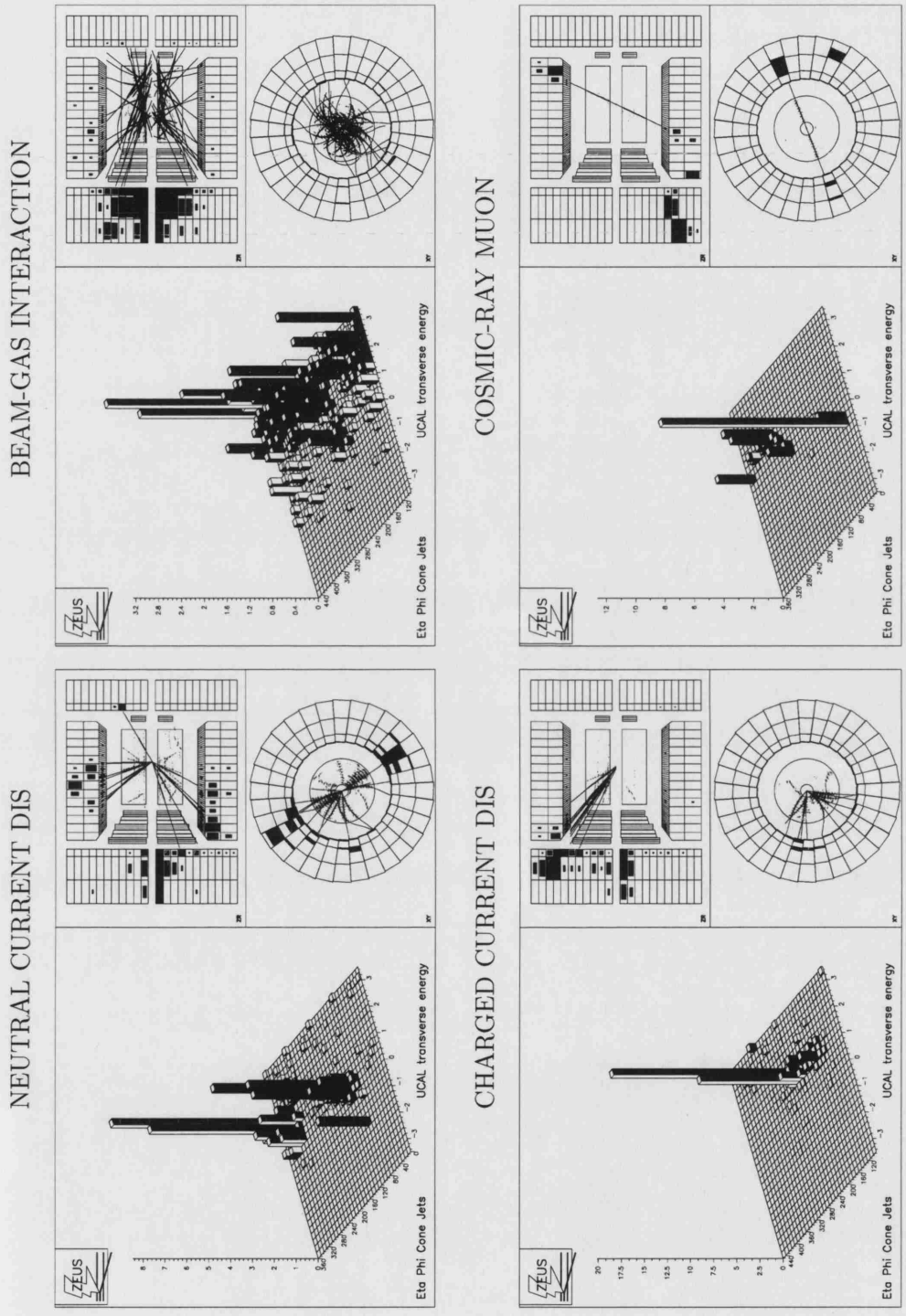

Figure 5.3: Examples of backgrounds to the two jet photoproduction selection.

5.3.1 First Level Trigger

The short decision time required by the FLT means that only limited information about event properties is available. The criteria in the FLT triggers are based primarily on global or regional energy sums in the UCAL, together with simple tracking requirements from the CTD FLT and vetoes from additional components. At the FLT, various different combinations of requirements are implemented as various trigger **slots**, which correspond to selection bits in the FLT data words. The distribution of trigger logic between slots is chosen so that the logic of each can be cross-checked using the information from additional, independent slots.

The primary trigger for these analyses is FLT slot42. In order to select jet photoproduction candidate events, the following requirements are made for this slot:

- at least one good track found by the CTD FLT, where a good track is defined as one coming from the nominal interaction region such that the z-position of the vertex satisfies -50 cm $< z_{\text{vtx}} <$ 80 cm;
- a CAL FLT energy requirement;
  - total energy in the CAL, `CAL_E` > 14.968 GeV,
  - `OR` total EMC energy, `EMC_E` > 10.068 GeV,
    These "total" energies are calculated excluding the three inner rings around the FCAL beam-hole and the inner ring around the RCAL beam-hole, corresponding to -3.66 $< \eta <$ 2.2.
  - `OR` total BCAL EMC energy, `BEMC_E` > 3.404 GeV,
  - `OR` total RCAL EMC energy, `REMC_E` > 2.032 GeV,
    This also excludes the inner ring around the RCAL beam-pipe.

In addition, beam-gas events are rejected at the FLT by veto requirements based on information from the C5 Counter, the VETO wall and the SRTD:

- the timing information from the C5 Counter is used to veto events that have beam-gas timing and no physics timing in one or both of the scintillation counters,
- information from the VETO wall is used to reject events where a coincidence is observed between the inner and outer plane of the component. This indicates that the interaction took place outside of the detector,
- the SRTD timing information is used to veto events which have beam-gas timing and no physics timing in one or both of the RTD planes,

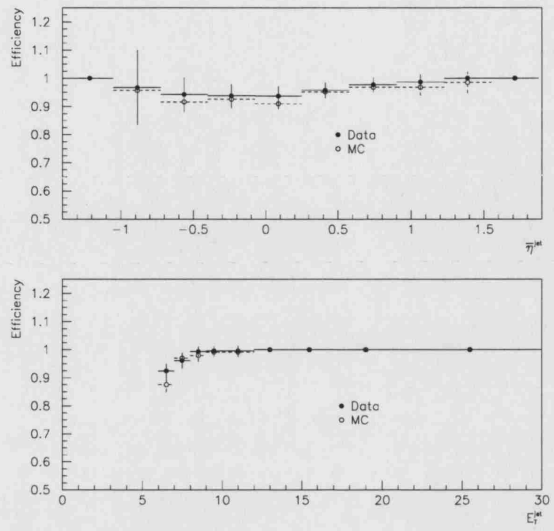

Figure 5.4: Efficiency of the FLT slot42 as a function of $E_{\mathrm{T}}^{\mathrm{jet}}$ and $\bar{\eta}$ from [82].

- events should have `TrKclass>2`. These are events with a relatively high ratio of vertex to total tracks. The exact value of the ratio is dependent on the number of vertex and non-vertex tracks, but is $\gtrsim 25 - 30\%$.

In order to study the efficiency of the FLT slot, it is necessary to choose an independent FLT trigger, which subsequently feeds into the same SLT and TLT. Demanding that the rest of the trigger chain be common to both FLT slots ensures that no bias is introduced as a result of differences in subsequent trigger requirements. The FLT slot used for this analysis was studied [82] using an independent sample of events from the LUMI branch of the FLT. The LUMI trigger branch requires the observation of the scattered lepton in the LUMI $-$ e detector, together with some low energy CAL thresholds. In addition, there should be little or no corresponding energy in the LUMI $-$ γ detector. The fraction of events passing the LUMI branch, which also pass the CAL triggers, was measured. The results of this study are shown in Fig. 5.4 and show that the efficiency of the FLT is well simulated by the MC.

5.3.2 Second Level Trigger

At the SLT, more complete detector information is available than at the FLT and there is time for more sophisticated algorithms to be used. This allows more complete physical quantities, such as the total $E - p_z$ measured in the CAL, to be reconstructed. In addition, the extra time available allows the vertex position to be calculated

from tracks reconstructed from CTD hit information using more sophisticated track reconstruction algorithms than are available at the FLT.

At the SLT, the HPP01 slot was used to select jet photoproduction candidates. This is the high-E_T trigger, designed specifically for hard photoproduction events. The selection criteria at this slot are defined as follows:

- at least 1 vertex track AND $|z_{vtx}| < 60$ cm;
- $\sum E - p_z > 8.0$ GeV, where E and p_z are the energy and longitudinal momentum of the event, determined from the energy deposits in the calorimeter.
- $\sum E_T^{box} > 8.0$ GeV, where E_T^{box} is the sum of the transverse energy in the CAL excluding the first inner ring around the FCAL beam-pipe (outside a value of $\eta \sim 3$).
- $\sum E - p_z > 12.0$ GeV OR $\sum p_z/E < 0.95$.

The efficiency of the SLT can be studied using a similar technique as for the FLT. The SLT slot used for this thesis was studied [82] using the LUMI SLT. The FLT and TLT slots were the same as those used for the CAL trigger chain. The LUMI SLT has the same requirements as the LUMI FLT, with the additional criterion that the energy in the LUMI $-$ e detector is greater than 5.0 GeV. The fraction of the sample of events passing the CAL FLT and LUMI SLT, and which also pass the HPP01 slot, was measured. The results of this study are shown in Fig. 5.5 and indicate a reasonable agreement between data and Monte Carlo.

5.3.3 Third Level Trigger

At the TLT, yet more time is available and algorithms can be used that are more complex than those available at either the FLT or the SLT. The use of more sophisticated algorithms allows a more detailed discrimination of events.

In this thesis, the HPP14 slot was used at the TLT. After the TLT selection, events go through a complete offline reconstruction and pass through additional offline filters. For this thesis, DST bit77 was used. This is the Hard PhotoProduction (HPP) low-E_T two jet filter, which uses a simplified version of the EUCELL cone algorithm (called EUTLT) in order to identify jets. The DST bits effectively correspond to a pass-through of the associated TLT bits and so the distinction between the TLT and DST trigger is nominal. In order for events to pass the HPP two jet trigger, events are required to satisfy the following criteria:

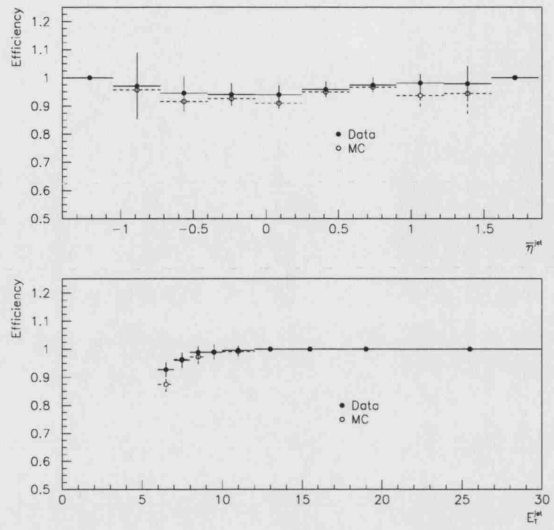

Figure 5.5: Efficiency of the SLT from [82].

- the event has an interaction vertex with a reconstructed z-position (relative to the nominal IP) satisfying $|z_{\text{vtx}}| < 60$ cm;
- there must be less than six bad tracks, where a bad track is one for which any of the following conditions are *not* satisfied,
  - number of degrees of freedom > 20,
  - OR $p_{\text{T}} \geq 0.2$ GeV,
  - OR -3.13 $< \eta <$ 1.75,
  - OR number of hits in the CTD axial superlayers > 5,
  - OR number of hits in the CTD stereo superlayers > 5,
  - OR distance of closest approach to the vertex, in z is ≤ 75 cm,
- 5.0 GeV $< E - p_z <$ 75.0 GeV AND $p_z/E < 1.0$
- $E_{\text{T}}^{\text{cone}} > 5.0$ GeV, where $E_{\text{T}}^{\text{cone}}$ is the summed transverse energy in the CAL outside a 10° cone (corresponding to $\eta < 2.44$) around the FCAL beam-pipe.

In addition, the EUTLT jet-finder is required to identify at least two jets with:

- $E_{\text{T}} > 4.0$ GeV,
- $|\eta| < 2.5$ GeV.

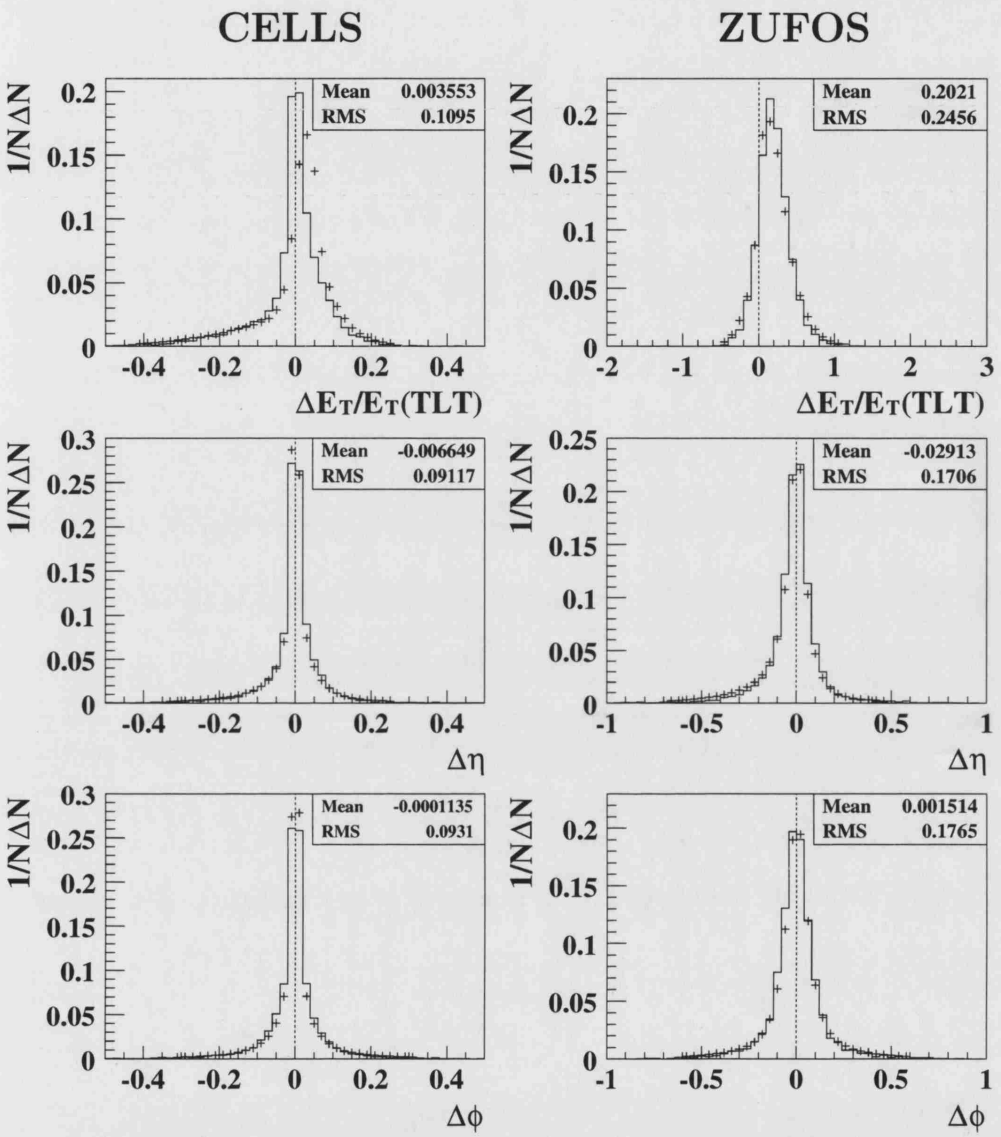

Figure 5.6: The TLT jet resolutions as a function of $\Delta E_{\mathrm{T}}/E_{\mathrm{T}}(\mathrm{TLT})$, $\Delta\eta$ and $\Delta\phi$. The points show the ZEUS data and the histogram shows the prediction of the PYTHIA Monte Carlo. The TLT jets are reconstructed using the EUTLT jet algorithm. The left and right columns correspond to offline jets reconstructed using the $k_\perp$ algorithm on calorimeter cells and corrected ZUFOs respectively. The values of the mean and r.m.s correspond to the data.

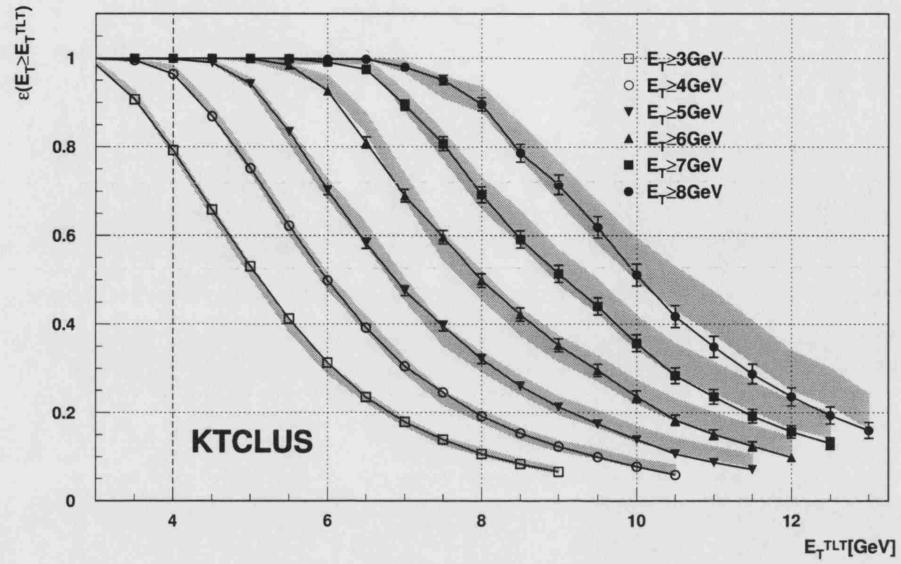

Figure 5.7: The efficiency of the two jet TLT as a function of the TLT jet E_{T} threshold for a variety of offline jet thresholds. The dashed line shows the actual TLT threshold of 4 GeV. The shaded band shows the prediction of HERWIG following the full detector and trigger simulation. Diagram taken from [162].

Figure 5.6 shows the TLT jet resolutions for the ZEUS data compared to the prediction of the PYTHIA Monte Carlo. The resolutions are defined by $\Delta E_{\mathrm{T}} = E_{\mathrm{T}}(\mathrm{offline}) - E_{\mathrm{T}}(\mathrm{TLT})$, $\Delta\eta = \eta(\mathrm{offline}) - \eta(\mathrm{TLT})$ and $\Delta\phi = \phi(\mathrm{offline}) - \phi(\mathrm{TLT})$. Events were required to have two jets with $E_{\mathrm{T}} > 4.0$ GeV at the TLT level and two jets with $E_{\mathrm{T}} > 4.0, 4.8$ GeV ($E_{\mathrm{T}} > 5.0, 6.0$ GeV) at the offline stage for calorimeter cells (corrected ZUFOs). Both TLT and offline jets are required to lie in the pseudo-rapidity range $-2.4 < \eta < 2.4$. The results are shown for jets reconstructed using calorimeter cells and corrected ZUFOs. The Monte Carlo gives a good description of $\Delta\eta$ and $\Delta\phi$ for offline jets reconstructed using both calorimeter cells and corrected ZUFOs. However, the resolutions for offline jets reconstructed using corrected ZUFOs are approximately twice as large as those from calorimeter cells. The distribution of $\Delta E_{\mathrm{T}}/E_{\mathrm{T}}(\mathrm{TLT})$ is shifted slightly with respect to the Monte Carlo for offline jets reconstructed using calorimeter cells indicating that the offline jet E_{T} is slightly higher relative to the TLT jet E_{T} in data compared to Monte Carlo. For offline jets reconstructed using corrected ZUFOs, the description by the Monte Carlo is marginally better. However, the overall shift in the distribution from zero is $\sim 20\%$. This is as expected since the transverse energies of the ZUFOS have already been corrected for energy loss in inactive material while the TLT jets have not.

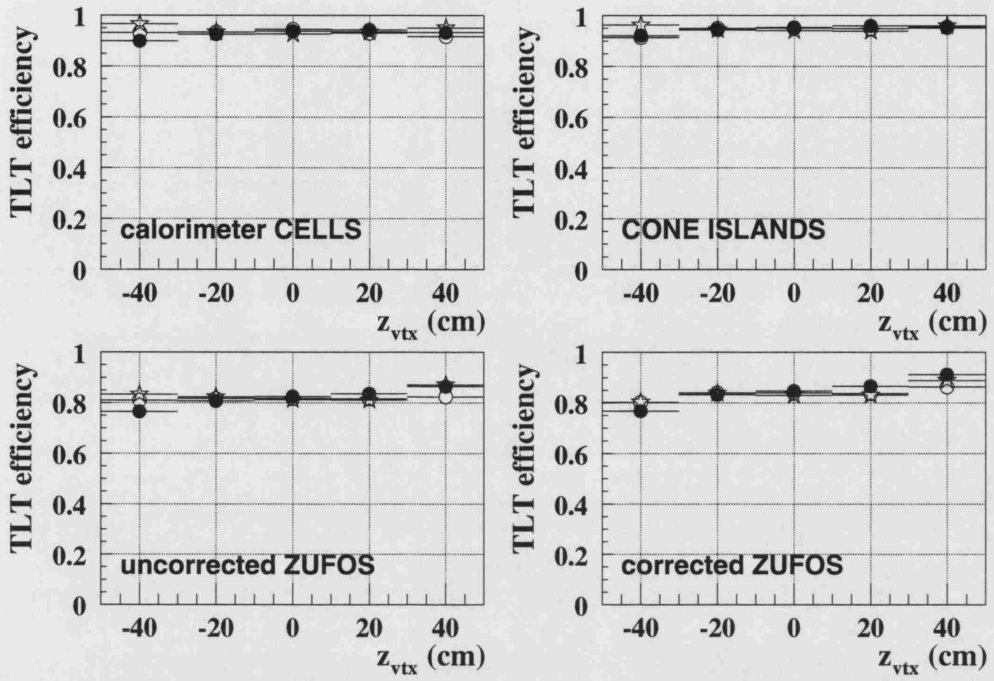

Figure 5.8: Efficiency of the TLT as a function of $z_{\rm vtx}$. The solid points show the ZEUS data and the open circles and stars respectively show the predictions of PYTHIA and HERWIG following full detector and trigger simulation. The selection criteria imposed on the reconstructed jets is stated in the text.

The efficiency of the TLT can be studied using an independent trigger as a monitor. For the two jet TLT, a sample of events which pass DST bit27 is used to provide a sample of two jet events which is unbiased by the jet-finding. This corresponds to the $D^* \rightarrow K\pi\pi$ Tracking Trigger and is based on events coming from the Charm Tracking TLT which uses a simplified version of the full offline tracking (VCTLT). The majority of events with two high-$E_{\rm T}$ jets which pass this trigger will *not* be due to charm events but, rather, will be due to background from light quark events. Therefore, it is considered reasonable to use this trigger bit in order to provide a sample which is largely unbiased by the jet-finding. Of course, the efficiencies calculated by this method will be biased by the D^*-finding. However, this is deemed acceptable since the purpose of this study is to assess the level of agreement between data and Monte Carlo. For both TLT triggers, events are required to pass the FLT and SLT slots used in this thesis. Then, the efficiency of the two jet TLT is given by, $\epsilon_{\rm b77} = \frac{N_{\rm b77} \cap N_{\rm b27}}{N_{\rm b27}}$ where $N_{\rm b77}$ and $N_{\rm b27}$ are the number of events passing the Two-Jet and Charm Tracking TLT's respectively. The jet-finding efficiency of the TLT Two-Jet trigger as a function of the TLT jet $E_{\rm T}$ threshold has been previously studied [162] using this method. Figure 5.7 shows the results of this study for a variety of offline jet $E_{\rm T}$ thresholds. The offline jets were

reconstructed by applying the $k_\perp$ algorithm to calorimeter cells. The results show that at the real TLT threshold of $E_T > 4$ GeV, the efficiency for tagging events with two offline jets with $E_T > 4$ GeV is $\sim 95\%$. This efficiency increases to 100% for offline jets with transverse energies greater than ~ 5 GeV. The shaded band shows the prediction of HERWIG following full detector and trigger simulation. The results indicate that the overall jet efficiency is well modelled across the TLT threshold cut.

The efficiency of the Two-Jet TLT has also been studied here. For this study, offline jets have been reconstructed using the $k_\perp$ algorithm on calorimeter cells, cone islands, uncorrected ZUFOs and corrected ZUFOs. Photoproduction events have been selected which contain two jets satisfying $-2.4 < \eta^{1,2} < 2.4$ and $E_T^{1,2} > 4.00, 4.80$ GeV (calorimeter cells and cone islands), $E_T^{1,2} > 4.25, 5.10$ GeV (uncorrected ZUFOs) and $E_T^{1,2} > 5.00, 6.00$ GeV (corrected ZUFOs). The differences between the chosen E_T thresholds for each reconstruction method are based on the jet resolutions and approximately correspond to the same region of phase-space. The TLT efficiencies as a function of z_{vtx} are shown in Fig. 5.8. In each case, the solid points show the ZEUS data and the open stars and circles show the results of the HERWIG and PYTHIA Monte Carlo. In each case, the efficiency of the TLT is $\gtrsim 80\%$ and the description of the data by the Monte Carlo is good in all cases.

5.4 Offline Event Selection

Following the trigger selection, there remains a small contamination from beam-gas interactions, cosmic-ray background and CC and NC DIS events. In order to obtain a clean sample of photoproduction events, the following requirements are made offline:

$$\begin{aligned} &\text{NO positron with } (y_e < 0.85 \text{ AND } E_e > 5 \text{ GeV}); \\ &0.2 < y_{JB} < 0.85; \\ &\not{p}_T / E_T^{1/2} = \left[\frac{(\sum p_x)^2 + (\sum p_y)^2}{\sum E_T}\right]^{1/2} < 2 \text{ GeV}^{1/2}; \\ &t^u_{BCAL} - t^l_{BCAL} > -6 \text{ ns}; \\ &\text{-40 cm} < z_{vtx} < 40 \text{ cm}. \end{aligned}$$

In order to determine this set of offline cuts, the following samples of data were studied:

- Events where a positron has been identified in the LUMI $-$ e calorimeter with energy 5 GeV $< E_e^{LUMI} <$ 20 GeV, with little or no corresponding energy in the LUMI $-$ γ detector such that $E_\gamma^{LUMI} < 2$ GeV. This is called a **LUMI tagged sample**;

  LUMI tagged events correspond to clean photoproduction events.

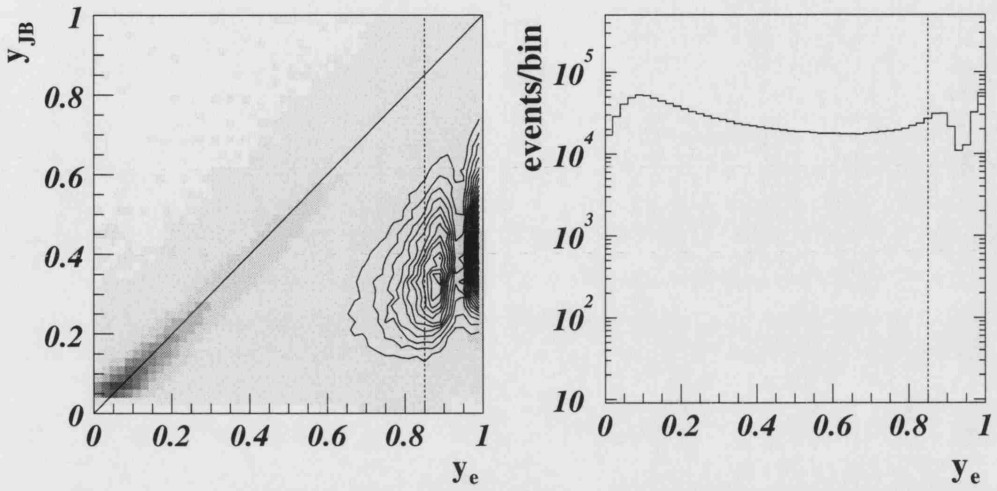

Figure 5.9: Left: The correlation between y_e and y_{JB} for the sample of events with an identified positron (shaded boxes) and the subsample of those events which are also LUMI tagged (contours). Right: The distribution of y_e for the DST sample of events. In both plots, the dashed line indicates the cut imposed in the final data selection.

- Events from unpaired proton bunches;
- Events from unpaired positron bunches;
- Events with neither protons nor positrons;

  Events from unpaired bunches correspond to beam-gas interactions while events with neither positrons or protons can be used to estimate the contribution from cosmic-ray interactions. Note that events with unpaired protons, unpaired positrons and empty bunches occur $\sim \frac{1}{35}$, $\sim \frac{1}{14}$ and $\sim \frac{1}{14}$ of the total. Therefore, in all histograms that follow, these samples are multiplied by factors of 35, 14 and 14, respectively, in order to estimate the background contribution due to beam-gas and cosmic-ray muons.

- Events where a positron was identified in the calorimeter;
- Events where a positron with $y_e < 0.85$ was found in the calorimeter.

  These samples allow a study of the contribution from DIS events where the low y_e events form the majority of NC DIS candidates.

A major source of contamination arises from higher Q^2 NC DIS events. In order to reject events on the basis of finding the scattered positron in the detector, it is necessary to have confidence in the unambiguous identification of that positron. Figure 5.9 (left) shows the correlation between y_e and y_{JB}. The shaded boxes represent all events with an identified positron candidate while the contours show the distribution of the subset of those events in which the scattered positron has been identified in the LUMI-e detector. There is a strong correlation between y_e and y_{JB} up to $y_e \sim 0.6$. However, above this value there is a wide spread in the distribution, indicating that only very rarely has the positron been correctly identified. This is due to the fact that positrons from high-y events are low in energy. A significant number of LUMI-tagged events enter into this histogram. These events are largely due to electromagnetic showers from π^0 and η mesons. This means that the rejection of an event purely on the basis of identifying a positron in the calorimeter would reject a significant number of genuine photoproduction events and unnecessarily reduce the available statistics. In order to maintain a high photoproduction selection efficiency, probable NC DIS events are rejected by requiring *no* scattered positron (as found by the electron finder `SINISTRA`) satisfying the requirements that $y_e < 0.85$ and $E_e > 5$ GeV. Above the 5 GeV threshold, the electron finder approaches 100% efficiency. The y_e cut also provides an additional check since positrons with $E_e < 5$ GeV tend to lie at high y_e.

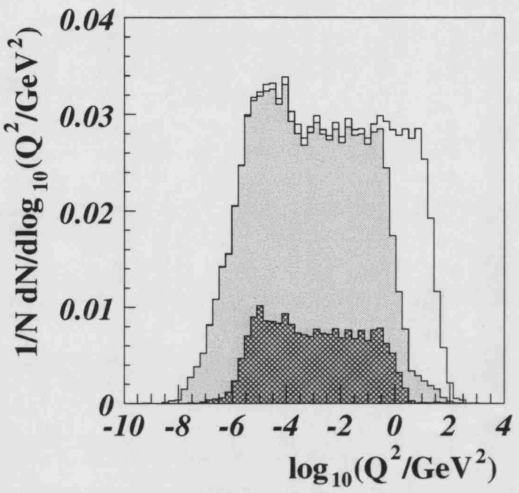

Figure 5.10: The Q^2 distribution from the PYTHIA Monte Carlo before (empty histogram) and after (shaded histogram) DIS electron rejection and after all offline selection cuts (cross-hatched histogram).

Figure 5.9 (right) shows the y_e distribution for the DST selected sample of events. The depletion of events at $y_e \sim 0.9$ corresponds to the cross-over between the regions dominated by the true and fake positron candidates.

Figure 5.10 shows the effect of applying the y_e cut on the Q^2 distribution according to the PYTHIA Monte Carlo. The results show that the rejection of positron candidates significantly reduces the number of high Q^2 events in the sample. The distribution of Q^2 following all online and offline selection cuts is also shown by the cross-hatched histogram.

The cut on y_e is not sufficient to reject all NC DIS events. For example, it does not remove events where the positron is correctly identified to have $y_e > 0.85$. Neither

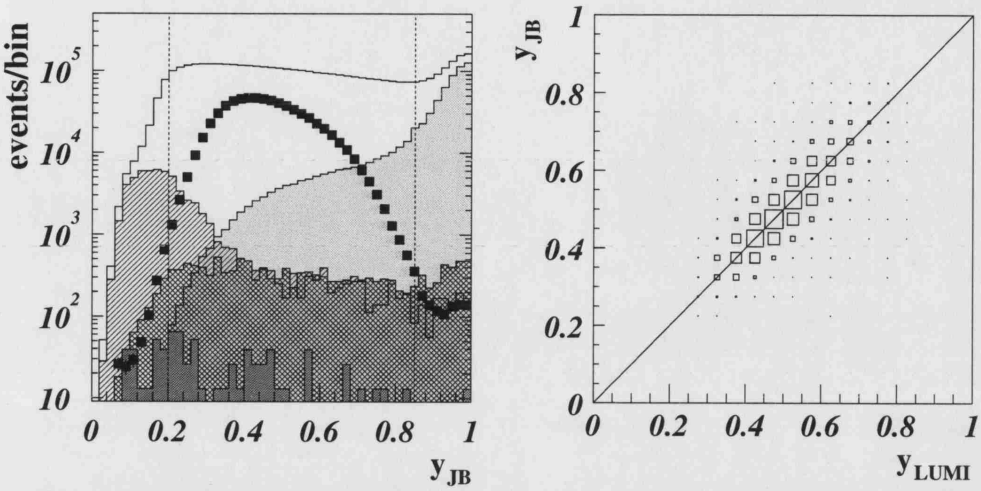

Figure 5.11: Left: The distribution of y_{JB} for the DST selected sample of events (empty histogram), the LUMI tagged sample (solid squares), events with an identified positron with $y_e < 0.85$ (light shaded histogram), events from unpaired proton bunches (diagonally hatched histogram), events from unpaired positron bunches (cross-hatched histogram) and events from empty bunches (dark shaded histogram). The dashed lines indicate the offline selection cuts used for the final data sample. Right: The correlation between y_{JB} and y_{LUMI} for the LUMI-tagged sample of events.

does it remove events for which the scattered positron entered the detector but was not identified. Figure 5.11 (left) shows the y_{JB} distribution. For events where the scattered positron entered the UCAL, $E - p_z \rightarrow 2E_e$ and the value of y_{JB} will be close to unity. This is illustrated by the sample of events with a positron candidate with $y_e < 0.85$ (light shaded histogram). Events where $y_{\mathrm{JB}} > 0.85$ were therefore rejected from the sample in order to eliminate the remaining NC DIS events. A lower cut of $0.2 < y_{\mathrm{JB}}$ was also imposed to reject beam-gas events which are boosted forwards and consequently lie at low values of y_{JB} (hatched histogram). The cuts are indicated by the dashed lines in the figure. For events where the positron is detected in the LUMI-e detector, the value of y can be calculated directly according to $y_{\mathrm{LUMI}} = (E_e - E'_e)/E_e$ where E_e and E'_e are the initial and scattered positron energies. The correlation between y_{JB} and y_{LUMI} (following all selection cuts) is shown in Fig. 5.11 (right). The strong correlation between the two reconstructed values of y confirms that there is little background in the data.

CC DIS events are rejected by a cut on the missing transverse momentum carried away by the neutrino. Since the incoming proton and positron beams have no transverse component, the total transverse energy of an NC DIS or photoproduction event should

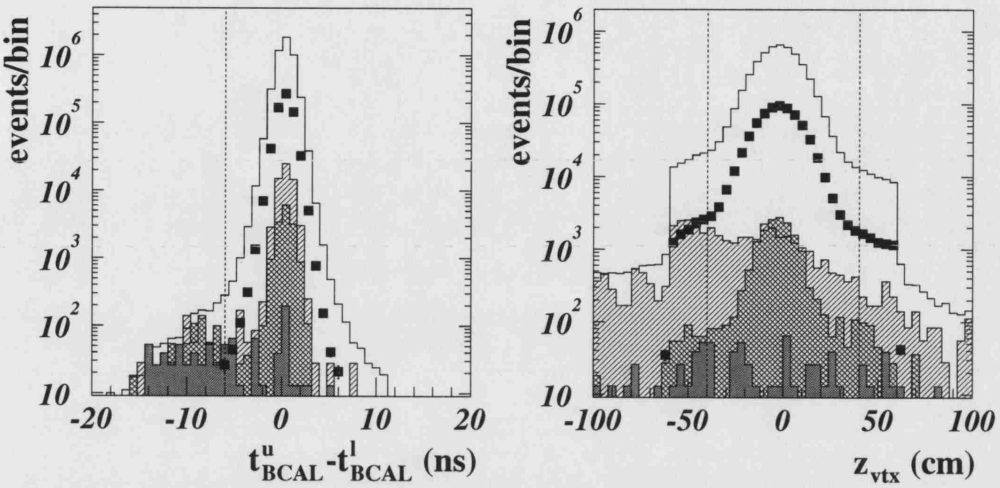

Figure 5.12: The distributions of (left) $t^{\mathrm{u}}_{\mathrm{BCAL}} - t^{\mathrm{l}}_{\mathrm{BCAL}}$ and (right) z_{vtx} for the DST selected sample of events (empty histogram), the LUMI tagged sample (solid squares), events from unpaired proton bunches (diagonally hatched histogram), events from unpaired positron bunches (cross-hatched histogram) and events from empty bunches (dark shaded histogram). The dashed lines indicate the offline selection cuts used for the final data sample.

be zero. This means that the missing transverse momentum $\not{p}_{\mathrm{T}}$ should be exactly zero. However, since the resolution of the calorimeter is finite, a distribution arises. The width of the distribution is largely due to statistical fluctuations in the energy losses due to inactive material and is therefore proportional to $E_{\mathrm{T}}^{1/2}$. A cut of $\not{p}_{\mathrm{T}}/E_{\mathrm{T}}^{1/2} < 2$ $\mathrm{GeV}^{1/2}$ has been imposed in order to reject CC DIS events. This requirement also reduces the number of cosmic-ray background events.

Figure 5.12 (left) shows the difference in signal time between the upper and lower halves of the BCAL. For cosmic-ray muons that pass through the top of the detector first, this time difference should be ~ -10 ns, while for a true lepton-proton collision at the IP it should be ~ 0. The hatched, cross-hatched and dark-shaded histograms show that there is an excess of beam-gas and cosmic events at $t^{\mathrm{u}}_{\mathrm{BCAL}} - t^{\mathrm{l}}_{\mathrm{BCAL}} \lesssim -6$ ns. Such events have been rejected from the final data sample.

The z_{vtx} distribution is shown in Fig. 5.12 (right). The background due to beam-gas and cosmic-ray muons is approximately uniform, while the sample of photoproduction corresponding to the LUMI-tagged sample shows a gaussian distribution centred at $z_{\mathrm{vtx}} \sim 0$ cm. The fall-off in the distribution away from $z_{\mathrm{vtx}} \sim 0$ cm is due to the finite size of the beam spot and the physical dimensions of the tracking detectors, while the sharp fall-off at $|z_{\mathrm{vtx}}| \sim 60$ cm is due to the vertex requirements applied at trigger level.

In order to reject the region due almost entirely to background events, the requirement -40 cm $< z_{\text{vtx}} <$ 40 cm has been imposed.

5.4.1 Jet Selection

Following all online and offline cuts, the longitudinally invariant $k_\perp$ algorithm is applied to the ZUFOs. The resulting sample of clean photoproduction events has $Q^2 \lesssim 1$ GeV^2 with an estimated median of $\sim 10^{-3}$ GeV^2 [163]. This is illustrated by the cross-hatched histogram in Fig. 5.10 which shows the distribution of Q^2 following all online and offline selection cuts. Any additional selection requirements specific to the two analyses in this thesis are detailed in the relevant chapters.

5.5 Background Contamination

The final data sample will still contain a small amount of background, both from non-*ep* collisions and also from NC DIS events where the scattered positron entered the detector but was not identified. The contribution from beam-gas and cosmic rays, entering the final event sample defined in this chapter, has been estimated using the data samples corresponding to non-matched proton and empty bunches. The estimated contribution from these sources is $< 0.3\%$. The contribution from NC DIS events was estimated using the DJANGOH [164] Monte Carlo and was found to be $< 0.3\%$ for jet transverse energies below ~ 20 GeV and rises to between $4 - 10\%$ for high E_{T}. Since the contribution is small, no background subtraction has been performed in this thesis.

5.6 Example Events

Figure 5.13 shows two examples of events which satisfy all selection criteria described in this chapter. On the right of each diagram are shown the zr- and xy-projections of the central tracker and calorimeter. In the zr-projection, the proton enters from the right and the lepton from the left. On the left is a lego plot of the $\eta - \phi$ space over which the jet-finding is performed. The observed energy deposits have been identified as jets by the EUTLT jet-finder at the TLT. The vertical scale gives the transverse energy deposited in the calorimeter cells ($E_{\text{T}}^{cell} = E^{cell} \sin\theta^{cell}$) at each point in the $\eta - \phi$ plane. The transverse momentum of the largest transverse energy deposits (visible in the upper and lower halves of the BCAL in the zr-projection and as the collimated energy deposits on the lego plot) are approximately balanced. This feature shows that these events are not CC DIS. In addition, neither of the diagrams show any obvious energy deposits that could be attributed to the scattered positron. This indicates that

DIRECT PHOTOPRODUCTION

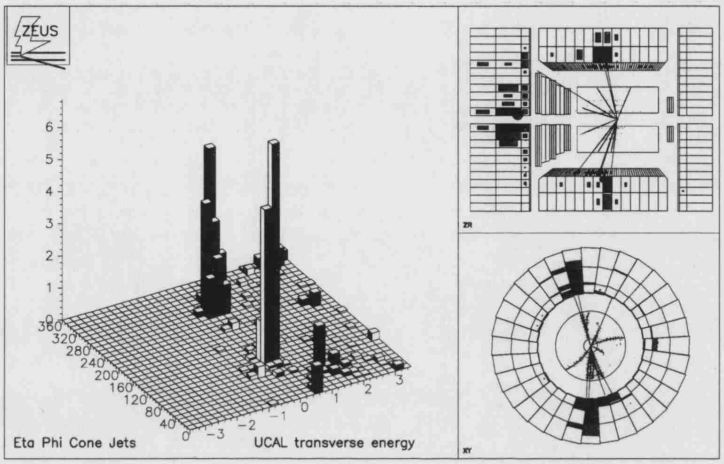

RESOLVED PHOTOPRODUCTION

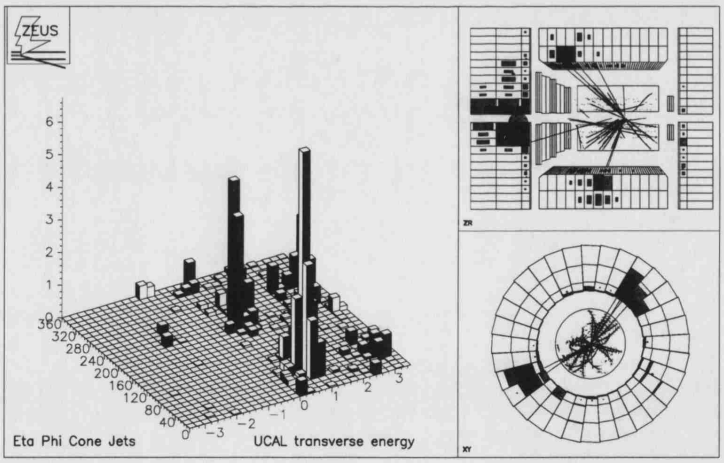

Figure 5.13: Direct and resolved two jet photoproduction candidates in ZEUS.

the positron has been lost down the beam-pipe and that the events are therefore at low Q^2: the kinematic region of photoproduction. Furthermore, the high transverse energies of the jets shown in the lego plots, indicate that they originated from a *hard* partonic scattering. Additional energy deposits are also visible in the forward (proton) direction. These deposits are relatively close to the beam direction and so are at low transverse momentum. This is attributed to the proton remnant. In the top diagram, no similar deposits are seen in the backward direction and so this event is classified as a direct photoproduction candidate. In contrast, the bottom diagram shows extra energy deposits in the backward directions. The low transverse energy deposit in the RCAL is attributed to the photon remnant, characterising this event as resolved photoproduction.

Chapter 6

Unfolding to the Cross Section

In order to study the underlying physics of a particular process, the **true** distribution must be inferred. In this context, a true distribution corresponds to that which represents the processes occurring at the level of the final-state hadrons. It is also possible to correct to the parton level using Monte Carlo to determine hadronisation correction factors. However, this is highly model dependent and is not performed in this thesis. As a result of finite detector resolution and imperfect trigger and reconstruction efficiencies, the observed data do not directly correspond to the true sample of data. In order to determine the true distribution, it is necessary to correct for these effects. In this chapter, the method used to correct the data is described and the formula used to extract the cross section is defined.

6.1 Correction Method

If $\mathbf{x}$ is a state vector which describes all the event characteristics, then the true distribution may be represented by a continuous function $t(\mathbf{x}) \equiv t(x_1, x_2, ..., x_{n_t})$. Similarly, the measured distributions may be represented by $m(\mathbf{x'}) \equiv m(x'_1, x'_2, ..., x'_{n_m})$, where $\mathbf{x'}$ is the corresponding measured state vector. In general, these two distributions are related by some **transfer function**, $T(\mathbf{x'};\mathbf{x})$, so that,

$$m(\mathbf{x'}) = \int \mathrm{d}^{n_t}\mathbf{x} T(\mathbf{x'};\mathbf{x}) t(\mathbf{x}). \tag{6.1}$$

This relationship can be used to determine the true distribution $t(\mathbf{x})$ provided $m(\mathbf{x'})$ and $T(\mathbf{x'};\mathbf{x})$ are known. The determination of $t(\mathbf{x})$ is known as **unfolding** to the true distribution. Performing rigorous multi-dimensional unfolding, where the distributions depend on many variables, is extremely complex and requires very high statistics. In

order to simplify the method, unfolding is usually restricted to the one-dimensional case where Eq. 6.1 reduces to,

$$m(x') = \int \mathrm{d}x T(x';x)t(x). \tag{6.2}$$

In this case, the distribution of the measured variable x' is assumed to be unaffected by variations in any other variable. In reality, this will not necessarily be the case and any influence that additional variables do have on the distribution are assigned as systematic uncertainties on the final cross section.

In practice, distributions are measured in discrete bins. Hence, the distributions themselves can be written as vectors such that $m(x') \rightarrow \mathbf{m} = [m_1, m_2, ..., m_{n_m}]$ and $t(x) \rightarrow \mathbf{t} = [t_1, t_2, ..., t_{n_t}]$. T then becomes a **transfer matrix** such that,

$$\mathbf{m} = T\mathbf{t}. \tag{6.3}$$

Equivalently, the elements of $\mathbf{m}$ are written as,

$$m_i = \sum_j T_{ij} t_j. \tag{6.4}$$

The elements t_j are the number of events generated in the true bin j and m_i are the number of elements measured in bin i. The elements of T represent the fraction of events generated in bin j which are measured in bin i such that,

$$T_{ij} = \frac{u_{ij}}{t_j} = \frac{m_i \cap t_j}{t_j}. \tag{6.5}$$

The unfolding procedure now involves obtaining the vector $\mathbf{t}$ given a measured distribution $\mathbf{m}$ and an estimate of the transfer matrix, T. In practice, the elements of T are evaluated using a sample of simulated Monte Carlo data. Then, both the generated (true) and reconstructed (measured) distributions are known and an estimate of T can be obtained. There are several possible unfolding methods which use different techniques to evaluate T. In this thesis, the **bin-by-bin method** is adopted.

6.1.1 Bin-by-Bin Unfolding

Bin-by-bin unfolding is one of the simplest methods of obtaining the true distribution from the measured distribution. The number of true events generated in a given bin i, and satisfying the cross section criteria is denoted t_i. Similarly, the number of measured events that are reconstructed in bin i are labelled m_i. The number of events generated in bin i which are *also* reconstructed in that same bin are labelled $u_i \equiv u_{ii}$. The **purity**, π_i, and **efficiency**, ϵ_i in each bin i are then defined as,

$$\pi_i = \frac{u_i}{m_i}, \tag{6.6}$$

$$\epsilon_i = \frac{u_i}{t_i}. \tag{6.7}$$

According to their definitions, π_i is the fraction of events *measured* in bin i which were also *generated* in that bin and ϵ_i is the number of events *generated* in bin i that are also *reconstructed* in that bin. The uncertainties on the purity and efficiency are given by,

$$\Delta\pi_i = \left[\frac{(1-\pi_i)\pi_i}{m_i}\right]^{1/2}, \tag{6.8}$$

$$\Delta\epsilon_i = \left[\frac{(1-\epsilon_i)\epsilon_i}{t_i}\right]^{1/2}. \tag{6.9}$$

The **correction factor**, C_i, for bin i is calculated according to,

$$C_i = \frac{\pi_i}{\epsilon_i} = \frac{t_i}{m_i} \tag{6.10}$$

with an uncertainty given by,

$$\Delta C_i = \left[\frac{t_i}{m_i^3}(t_i + m_i - 2u_i)\right]^{1/2}. \tag{6.11}$$

The expressions for the errors on π_i, ϵ_i and C_i are derived in Appendix E. The unfolded number of events in bin i is then given by,

$$t_i^{\text{unfolded}} = C_i m_i^{\text{data}}. \tag{6.12}$$

When using this unfolding method, it is necessary that the bin-width of the measured distribution is significantly larger then the resolution of that variable in order to avoid long-range migrations between bins. In general, the analyses presented in this thesis have used the basic requirement that the bin-width is at least a factor of two larger than the resolution of the variable in that bin.

A useful variable to define how stable the distribution is with respect to migrations between the bins is the **stability** $\mathcal{S}_i$ where,

$$\mathcal{S}_i = \pi_i \frac{m_i}{u} = \frac{u_i}{u} \tag{6.13}$$

where u is the number of events that were generated in bin i and reconstructed somewhere in the final event sample (not necessarily in bin i). The error on the stability is given by,

$$\Delta\mathcal{S}_i = \left[\frac{(1-\mathcal{S}_i)\mathcal{S}_i}{u}\right]^{1/2}. \tag{6.14}$$

6.2 The Monte Carlo Sample

For the analyses presented in this thesis, the PYTHIA 6.1 Monte Carlo generator is used for the unfolding procedure. All Monte Carlo samples are passed through a full simulation of the ZEUS detector, the details of which are described in Section 4.1, and both **detector-level** and **hadron-level** information are retained.

For the unfolding procedure, direct and resolved events are generated separately. However, *a priori*, the relative fractions of direct and resolved that should be combined to form a complete sample of photoproduction events is not known. In order to determine these fractions, the direct and resolved samples are individually normalised to the total number of events in the uncorrected data sample. The whole Monte Carlo sample is then fitted to the uncorrected $x_{\gamma;\mathrm{NJ}}^{\mathrm{OBS}}$ distribution using a single parameter χ^2-fit of the form,

$$N_i = \alpha N_i^{\mathrm{resolved}} + (1-\alpha) N_i^{\mathrm{direct}}. \tag{6.15}$$

The N_i^{resolved} and N_i^{direct} are the number of resolved and direct events in each bin i and α is the fraction of resolved events in the total sample obtained from the fit. This is in contrast to the models used as comparisons to the final measured distributions, which are combined according to the generated Monte Carlo cross sections.

6.3 The Cross Section Calculation

The cross section differential in variable x is given by,

$$\frac{\mathrm{d}\sigma_i}{\mathrm{d}x} = \frac{N_i(x) C_i(x)}{\mathcal{L}^{\mathrm{int}} \Delta_i x}. \tag{6.16}$$

After passing all selection cuts, $N_i(x)$ is the number of observed events in bin i, $\Delta_i x$ is the bin width of x in bin i and $\mathcal{L}^{\mathrm{int}} = \int \mathcal{L} \mathrm{d}t$ is the integrated luminosity of the total data sample. During the 1996-1997 data-taking period, $\mathcal{L}^{\mathrm{int}} = 38.6 \pm 0.6$ pb^{-1} [161].

Chapter 7

Multi-Jets in Photoproduction

In this chapter, a study of **Multi-Jets in Photoproduction** is presented. Measurements of inclusive, two jet and three jet final states in photoproduction have already been carried out at HERA [7–19]. In this analysis, cross sections for the photoproduction of four or more jets are presented for the first time. Following a brief introduction, the measured variables are defined. The kinematic region in which the cross sections have been measured, and the event selection criteria, are then described. The Monte Carlo sample that has been used to unfold for detector effects is discussed and compared to kinematic quantities important to this analysis. Following a discussion of the correction procedure and systematic uncertainties, the corrected cross sections are presented and the results are discussed. Finally, the data presented in this chapter are used, in conjunction with other measurements, to provide constraints on Monte Carlo parameters; particularly those relevant to the modelling of the underlying event.

7.1 Introduction

Jet photoproduction studies have so-far established the existence of direct and resolved events [7], provided stringent tests of pQCD at and beyond LO [8–13] and provided information on the structure of real and virtual photons [14–16], the underlying event [17] and the structure of jets [18]. The study of three-jet production [19] has also provided tests of pQCD and provided information on the dominant jet production mechanisms. Figure 7.1 shows the ZEUS measurement [19] of the three jet cross section differential in the three jet invariant mass, $m_{3\mathrm{J}}$. The data are compared to $\mathcal{O}(\alpha\alpha_s^2)$ pQCD predictions - the highest order currently available - and to the predictions of Leading Logarithm (LL) Monte Carlo. The shape of the distribution is well described by both the fixed order theory and the Monte Carlo models, although the normalisation of the Monte Carlo underestimate the data by $\sim 20 - 40\%$. This

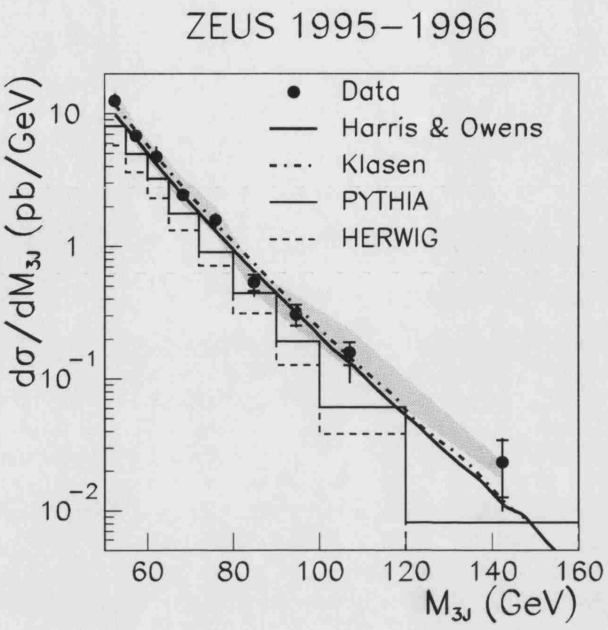

Figure 7.1: The three jet cross section differential in m_{3J} from [19].

shows that parton shower models are able to give an adequate description of the shape of the distributions, suggesting that only the normalisation is significantly affected by higher order contributions.

There are several reasons why the extension to four jet production studies is of particular interest. Firstly, such measurements can provide tests of pQCD at even higher orders in α_s. At LO, four jet photoproduction is an intrinsically $\mathcal{O}(\alpha\alpha_s^3)$ process. No fixed order QCD calculations of this order currently exist for photoproduction processes. However, measurements of multi-jet final states can also provide sensitive tests of parton shower extensions to fixed order theories. This is particularly important since very high order processes soon become impractical to calculate. The understanding of multi-jet final states will also be of great importance at the next generation of colliders, such as the LHC. For example, new particle searches in the Higgs and SUSY* sectors, require the simulation of $2 \to 4$, $2 \to 6$ and even $2 \to 10$ jet processes and a full understanding of the QCD Standard Model background will be vital. In addition, the study of multi-jets (and of four jet events in particular), provides an ideal testing ground to search for the effects of multi-parton interactions (see Section 2.12.1). Understanding this process will also be important for future colliders. For example, at the LHC, the cross section for the production of four jets arising from two separate scatters is expected to dominate the single scattering process for $p_T < 20$ GeV [166].

*For a good review on SUperSYmmetry (SUSY) see, for example, [165].

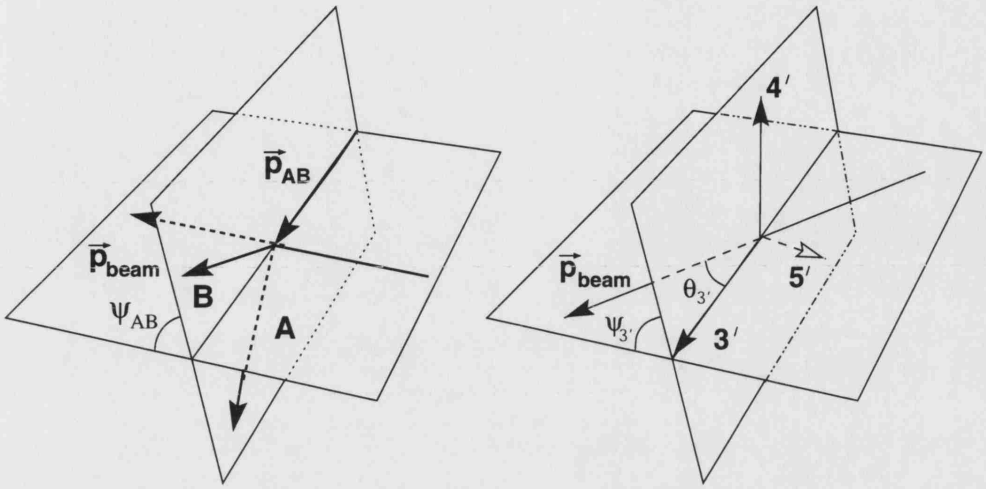

Figure 7.2: Schematic diagram of the four jet rest frame.

In this analysis, cross sections for the photoproduction of four moderately high transverse energy jets are measured in two different kinematic regions, which are separated by a cut on the four jet invariant mass, $m_{4\mathrm{J}}$. The high transverse energies mean that the cross sections are calculable in pQCD. However, the low mass region may also be sensitive to the underlying event. The selection of four jets in the event should also maximise the sensitivity to contributions from multi-parton interactions that are sufficiently hard to produce a second pair of jets.

7.2 Definition of the Variables

Multi-jet events can be characterised by a set of kinematic variables which span the multi-jet parameter space, allow the interpretation of the data within the context of pQCD and facilitate comparisons between events containing different numbers of jets in the final state [167]. For a four jet event, the variables are defined according to the following convention:

1. The incoming particles are labelled 1 and 2 where $E_1 > E_2$ and the four jets of highest energy are labelled 3, 4, 5 and 6.

2. The four highest transverse energy jets are boosted to the four jet centre-of-mass frame, re-ordered in energy and re-labelled (if necessary) such that $E_3 > E_4 > E_5 > E_6$.

3. The pair of jets with the smallest two jet invariant mass are combined, by adding their vectors, to form a separate (A+B)-system. These jets are labelled such that the energies of the two jets (in the four jet rest frame) satisfy $E_\mathrm{A} > E_\mathrm{B}$.

4. The three remaining **pseudo-jets** are re-labelled 3′, 4′ and 5′ and re-ordered in energy such that $E_{3'} > E_{4'} > E_{5'}$ in the three body rest frame.

The (A+B)- and the pseudo-three-jet systems are illustrated in Fig. 7.2. The system of four (massless) jets is described by 7 independent variables[†]:

- The four jet invariant mass is defined as,

$$m_{4\mathrm{J}} = E_3 + E_4 + E_5 + E_6. \tag{7.1}$$

- The (A+B)-system is described by two independent parameters,

$$\cos\psi_{\mathrm{AB}} = \frac{(\mathbf{p}_{\mathrm{AB}} \times \mathbf{p}_{\mathrm{beam}}).(\mathbf{p}_{\mathrm{A}} \times \mathbf{p}_{\mathrm{B}})}{|\mathbf{p}_{\mathrm{AB}} \times \mathbf{p}_{\mathrm{beam}}||\mathbf{p}_{\mathrm{A}} \times \mathbf{p}_{\mathrm{B}}|} \tag{7.2}$$

$$X_{\mathrm{A}} = \frac{E_{\mathrm{A}}}{E_{\mathrm{A}} + E_{\mathrm{B}}} \tag{7.3}$$

  where $p_{\mathrm{AB}} = p_{\mathrm{A}} + p_{\mathrm{B}}$ is the four vector of the (A+B)-system. The quantity p_{beam} is defined as $p_{\mathrm{beam}} = p_1 - p_2 = (E_e - E_p, 0, 0, E_e + E_p)$ where E_p and E_e are the proton and lepton beam energies respectively. Note that, like all the vectors associated with the four jets, p_{beam} is evaluated in the four jet centre-of-mass system. The angular variable ψ_{AB} is the angle between (i) the plane containing the (A+B)-system and the average beam direction and (ii) the plane containing jets A and B. X_{A} is an energy-sharing variable defined in the four jet rest frame, which expresses the fraction of the total (A+B)-system energy that is carried by the highest energy jet of that system.

- The pseudo-three-jet system is described by four independent variables,

$$\cos\theta_{3'} = \frac{\mathbf{p}_{\mathrm{beam}} \cdot \mathbf{p}_{3'}}{|\mathbf{p}_{\mathrm{beam}}||\mathbf{p}_{3'}|} \tag{7.4}$$

$$\cos\psi_{3'} = \frac{(\mathbf{p}_{\mathrm{beam}} \times \mathbf{p}_{3'}).(\mathbf{p}_{4'} \times \mathbf{p}_{5'})}{|\mathbf{p}_{\mathrm{beam}} \times \mathbf{p}_{3'}||\mathbf{p}_{4'} \times \mathbf{p}_{5'}|} \tag{7.5}$$

[†]A general N-jet system is described by 4N independent parameters. However, momentum conservation provides 3 constraints. In addition, it is possible to rotate the N-body system around the incoming beam direction without losing any interesting information. Consequently, 4N-4 parameters are necessary to completely describe the system. For a four jet system, 5 of these parameters are related to the masses of the jets (2 for jets A and B and 3 for pseudo-jets 3′, 4′ and 5′). Under the assumption that single jets (and pseudo-jets) are massless (as is assumed in this thesis) a further 5 constraints are imposed so that there are a total of 7 independent parameters.

$$X_{3'} = \frac{2E_{3'}}{E_3 + E_4 + E_5 + E_6} = \frac{2E_{3'}}{m_{4\mathrm{J}}} \tag{7.6}$$

$$X_{4'} = \frac{2E_{4'}}{E_3 + E_4 + E_5 + E_6} = \frac{2E_{4'}}{m_{4\mathrm{J}}}. \tag{7.7}$$

The quantity $\theta_{3'}$ is the angle between the highest energy pseudo-jet and the average beam direction. The $\psi_{3'}$ variable is the angle between (i) the pseudo-three-jet plane and (ii) the plane containing the beam and the highest energy pseudo-jet. As a result of colour coherence (see Section 2.13) these planes are expected to approximately coincide, leading to a distribution peaked at $\psi_{3'} \sim 0$ and π. The quantities $X_{3'}$ and $X_{4'}$ are energy-sharing variables which represent the fraction of the total available energy carried by the highest- and second-highest-energy pseudo-jet. These variables are normalised so that $X_{3'} + X_{4'} + X_{5'} = 2$ and conservation of energy requires that $\frac{2}{3} < X_{3'} < 1$, $\frac{1}{2} < X_{4'} < 1$ and $0 < X_{5'} < \frac{2}{3}$.

In the limit $E_6 \to 0$, the variables reduce to the three jet equivalents $m_{3\mathrm{J}}$, $\cos\theta_3$, ψ_3, X_3 and X_4. Furthermore, as $E_5 \to 0$ (and then, by definition, $E_6 \to 0$) the situation reduces to the two jet case described by the variables $m_{2\mathrm{J}}$ and $\cos\theta^*$. The variables $\cos\theta^*$ and $\cos\theta_3$ have been measured at HERA in previous two [168–170] and three jet [19, 171] analyses. These definitions ensure that direct comparisons can be made between distributions for events containing different numbers of jets.

In addition, the energy sharing variables, $X_{3'}$ and $X_{4'}$, and the angular variable, $\cos\theta_{3'}$, may be particularly sensitive to the effects of multi-parton interactions in four jet events. This is considered in detail in Section 7.12.2.

7.3 Definition of the Cross Section

Cross section measurements have been carried out in the kinematic region defined by,

$$Q^2 < 1 \text{ GeV}^2$$
$$0.2 < y < 0.85$$
$$E_{\mathrm{T}}^{1,2,3,4} > 6, 6, 5, 5 \text{ GeV}$$
$$\text{-}2.4 < \eta^{1,2,3,4} < 2.4$$
$$\text{-}0.8 < \cos\theta_{3'} < 0.8$$
$$X_{3'} < 0.95$$

where the superscripts 1, 2, 3 and 4 denote the four highest transverse energy jets in order of decreasing E_{T}, as measured in the laboratory frame. This defines the **inclusive** sample of events. A **high mass** sample has also been defined by the additional requirement that $m_{4\mathrm{J}} > 50$ GeV.

The Q^2 range is set by the calorimeter acceptance and the event selection criteria. The restriction on y corresponds to a proton-photon centre-of-mass energy in the range $134 < W_{\gamma p} < 277$ GeV. All jets are identified using the $k_\perp$ algorithm in the longitudinally invariant, inclusive mode [172]. This is particularly suited to the study of multi-jet final states since it suffers from no ambiguities due to overlapping jets. The transverse energy requirements on the jets ensure that the fundamental process is calculable in pQCD and the pseudo-rapidity requirements ensure that the jets are fully contained in the calorimeter.

The requirement on $\cos\theta_{3'}$ reduces the bias introduced by the minimum transverse energy requirements, which restrict the number of jets produced close to the beam-line. The value of $X_{3'}$ is also restricted in order to increase the fraction of the total energy available to the lowest energy pseudo-jet. For the high mass sample, the requirement on $m_{4\mathrm{J}}$ increases the average transverse energies of the jets. This reduces kinematic bias imposed by the minimum transverse energy requirements. It is also expected to reduce the sensitivity of the measurement to contributions from the underlying event, such as multi-parton interactions. Note also, that the cross section criteria for the high mass sample are exactly equivalent to the three jet cross section definition in a previous measurement [171], allowing direct comparisons to be made between the two.

In this analysis, differential cross sections are measured for the inclusive and high mass regions as a function of $m_{4\mathrm{J}}$ (inclusive only), ψ_{AB}, X_{A}, $\cos\theta_{3'}$, $\psi_{3'}$, $X_{3'}$, $X_{4'}$, $x_{\gamma;4\mathrm{J}}^{\mathrm{OBS}}$ and y. In addition, the $\cos\theta_{3'}$ cross sections have been measured in the regions $x_{\gamma;4\mathrm{J}}^{\mathrm{OBS}} < 0.75$ and $x_{\gamma;4\mathrm{J}}^{\mathrm{OBS}} > 0.75$ to further investigate the distribution of this variable in the direct- and resolved-enhanced regions. The corresponding normalised cross sections have also been measured. This is useful for the purpose of shape comparisons since systematic uncertainties which may be large in the total cross sections, are often reduced in the normalised cross sections.

7.4 Event Selection

The hadronic final state has been reconstructed using corrected ZUFOs (see Section 4.6.2). It has already been shown (Section 4.8.1), that corrected ZUFOs produce a close correspondence between the values of reconstructed hadronic quantities and the true values. This means that the criteria that define the cross section can also sensibly be used to define the event sample at the detector level. Specifically, events with at

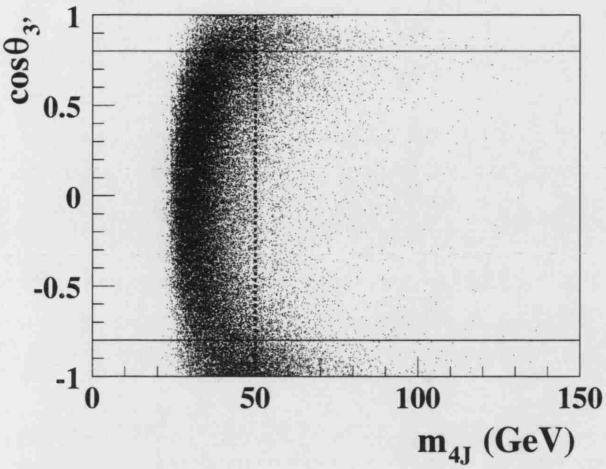

Figure 7.3: The distribution of $\cos\theta_{3'}$ versus $m_{4\mathrm{J}}$. The horizontal solid lines indicate the cuts imposed on the value of $\cos\theta_{3'}$. The dashed line indicates the cut on $m_{4\mathrm{J}}$ which defines the high mass sample.

least two jets with $E_{\mathrm{T}} > 6$ GeV and a further two jets with $E_{\mathrm{T}} > 5$ GeV and with all jets lying in the pseudo-rapidity range -2.4 $< \eta <$ 2.4 are selected. The range of y_{JB} is restricted to $0.2 < y_{\mathrm{JB}} < 0.85$ (as has already been described in Section 5.4).

The distribution of $\cos\theta_{3'}$ with respect to $m_{4\mathrm{J}}$, for events satisfying these jet criteria, is shown in Fig. 7.3. The results show that the minimum invariant mass is ~ 20 GeV (a constraint set by the transverse energy requirements on the jets). In addition, the results show that there is a reduction in the number of events at low $m_{4\mathrm{J}}$ and large absolute $\cos\theta_{3'}$. This bias is also due to the minimum transverse energy requirements, which restrict the phase space available for jets produced close to the beam-line. In order to reduce this bias, the additional requirement that -0.8 $< \cos\theta_{3'} <$ 0.8 has been imposed. This cut is illustrated by the solid lines in the plot.

Figure 7.4 shows the distribution of $m_{4\mathrm{J}}$ in bins of $|\cos\theta_{3'}|$. The solid points show the distribution for the sample of events selected in this analysis, with all selection criteria imposed except for the $\cos\theta_{3'}$ requirement, which has been relaxed for this plot. The hollow points show the distribution for a loose sample of four jet events containing two jets with $E_{\mathrm{T}} > 4.5$ GeV and two jets with $E_{\mathrm{T}} > 3.5$ GeV. Also shown is the ratio of these distributions. These results illustrate the effectiveness of a cut on $m_{4\mathrm{J}}$ at reducing the effect of the jet E_{T} thresholds. At low $m_{4\mathrm{J}}$, the distributions are very different and show the sensitivity to the E_{T} cuts. However, at high $m_{4\mathrm{J}}$ the distributions have a similar mass dependence, indicating that the jet E_{T} requirements no longer affect the shape of the distribution. The value of $m_{4\mathrm{J}}$ at which the shape of the distributions become similar rises as a function of $|\cos\theta_{3'}|$. For the region $|\cos\theta_{3'}| > 0.8$, the shape of the distributions never fully coincide. This is illustrated more clearly by the ratio of the high-E_{T} cut to low-E_{T} cut region. In contrast, for $|\cos\theta_{3'}| < 0.8$, the ratio is approximately flat and at the level of $\sim 50\%$ for $m_{4\mathrm{J}} > 50$ GeV. Therefore, the combined requirements on $|\cos\theta_{3'}|$ and $m_{4\mathrm{J}}$ select a sample which is largely unbiased

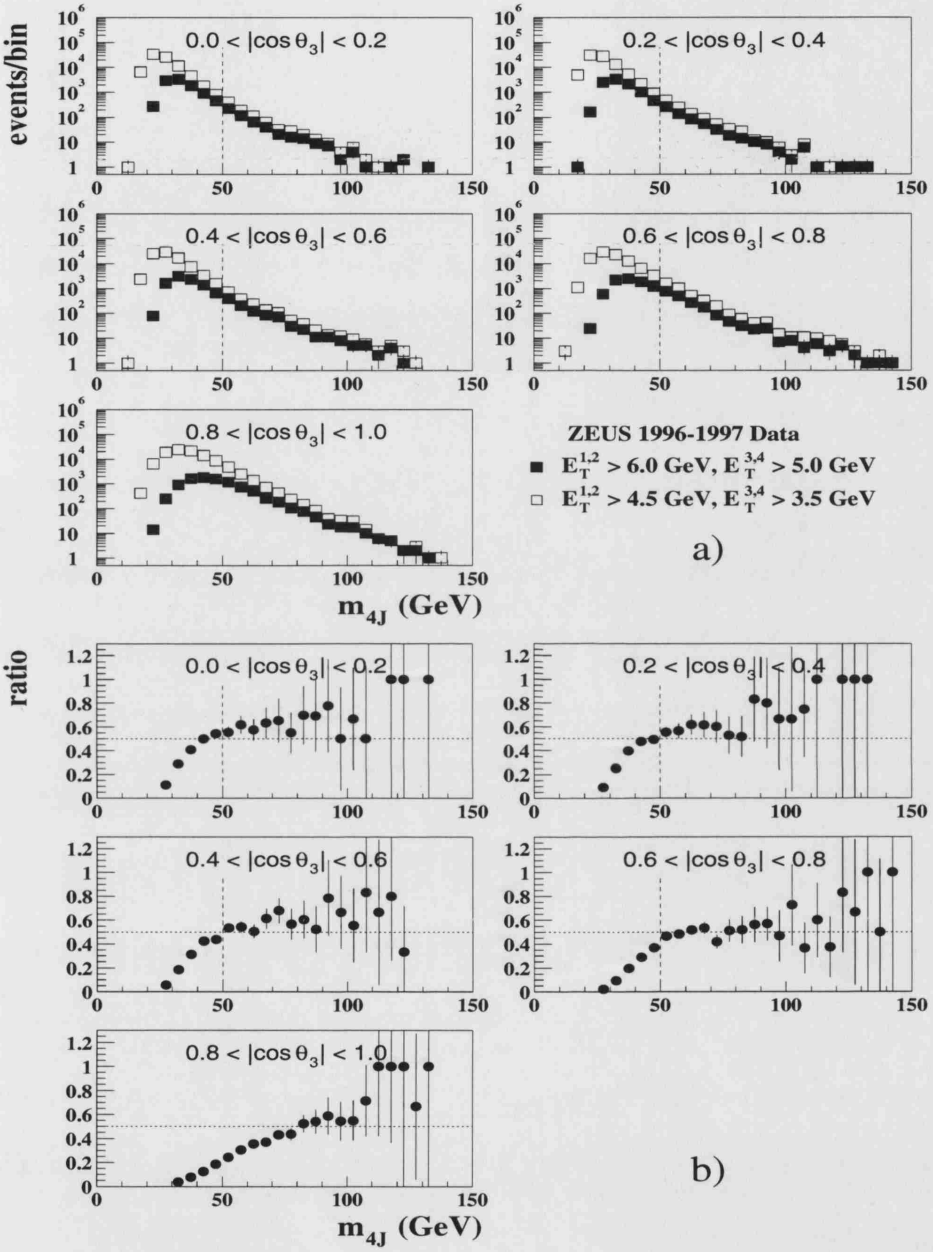

Figure 7.4: a) The distribution of $m_{4\mathrm{J}}$ in bins of $|\cos\theta_{3'}|$. The solid squares indicate those events passing the four jet selection cuts ($E_{\mathrm{T}}^{1,2} > 6.0$ GeV, $E_{\mathrm{T}}^{3,4} > 5.0$ GeV) and the hollow squares show a loose sample of four jet events ($E_{\mathrm{T}}^{1,2} > 4.5$ GeV, $E_{\mathrm{T}}^{3,4} > 3.5$ GeV). b) The ratio of the two distributions shown in a). The dotted lines show the 50% threshold. In both a) and b), the dashed lines indicate the cut on $m_{4\mathrm{J}}$ which defines the high mass sample.

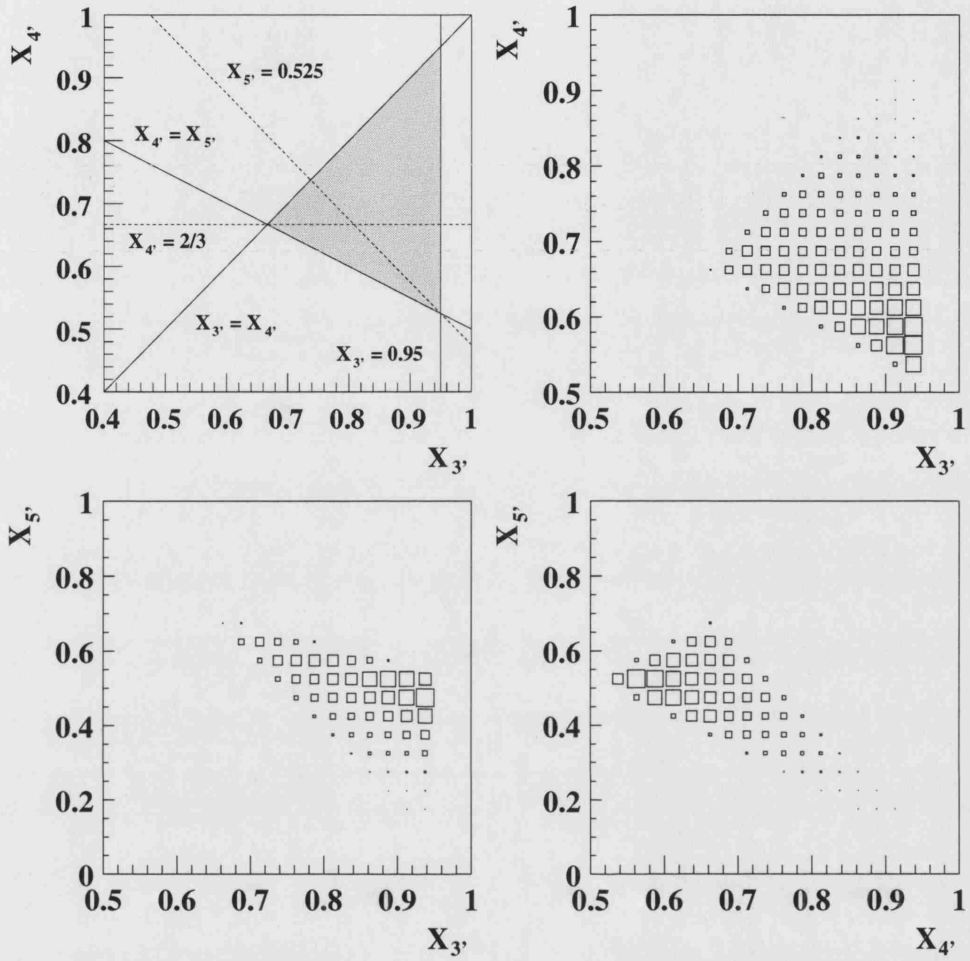

Figure 7.5: Top Left: Illustration of the phase space available to the energy sharing variables $X_{3'}$, $X_{4'}$ and $X_{5'}$. The phase space restricted by requiring that $X_{3'} > X_{4'} > X_{5'}$ and $X_{3'} < 0.95$ is indicated by the shaded area. The dashed lines show the values at which the available phase space for each quantity is maximised. Top Right: The distribution of $X_{3'}$ versus $X_{4'}$. Bottom Left: The distribution of $X_{3'}$ versus $X_{5'}$. Bottom Right: The distribution of $X_{4'}$ versus $X_{5'}$.

by the jet E_{T} cuts. The cut on $m_{4\mathrm{J}}$ also has the effect of increasing the average transverse energy of the jets in the event. Therefore, this cut is also expected to reduce the sensitivity to long-range, non-perturbative, physics.

A cut of $X_{3'} < 0.95$ has also been imposed in order to increase the fraction of energy available to the lowest energy pseudo-jet. The regions of phase space available to the variables $X_{3'}$, $X_{4'}$ and $X_{5'}$, following all selection cuts, are shown in Fig. 7.5.

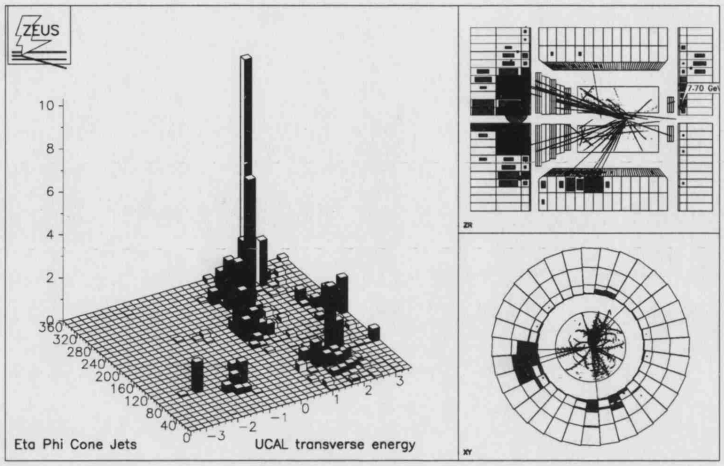

Figure 7.6: A resolved four jet event in the ZEUS detector.

Following all selection cuts, the inclusive sample contains 30413 (1996:1997=8373:22040) events and the high mass sample contains 3267 (1996:1997 = 922:2345) events. An example of a resolved four jet photoproduction event in the ZEUS detector is shown in Fig. 7.6. The large transverse energy deposits due to the jets, as well as the proton and photon remnant, are visible.

7.5 The Monte Carlo Sample

The PYTHIA 6.1 Monte Carlo has been used to correct the data for detector and acceptance effects. The model used for the final unfolding includes a simulation of multi-parton interactions. Here, the simplest model, corresponding to MSTP(82)=1, has been used[‡]. For comparison at the detector level, a sample of Monte Carlo which includes no simulation of multi-parton interactions was also generated. The PYTHIA samples without and with a simulation of multi-parton interactions will be referred to as PYTHIA and PYTHIA + MPI, respectively. For each model, the parton densities of the proton were generated according to the GRV-LO parameterisation and those of the photon according to the WHIT2 parameterisation. In each model, a value of $p_{\mathrm{T}}^{\mathrm{min}} = 2.0$ GeV was taken to be the minimum transverse momentum of the primary scatter and for the PYTHIA + MPI model, a value of $p_{\mathrm{T}}^{\mathrm{mi}} = 1.5$ GeV was taken to be the minimum transverse momentum of all secondary scatters. The important parameters for each model are summarised in Tab. 7.1. Each Monte Carlo sample has been passed through a full simulation of the ZEUS detector and trigger. Only the PYTHIA + MPI model is used for the final data correction.

[‡]This model generates multi-parton interactions assuming the same probability in all events (no impact parameter dependence) and an abrupt cut-off at the user-defined value of $p_{\mathrm{T}}^{\mathrm{mi}}$ (in GeV).

Generator	Process	MPI included	PDF(p)	PDF(γ)	$p_T^{min/mi}$ (GeV)	No. of events
PYTHIA	Direct	-	GRV-LO	-	2.0 -	25246
	Resolved	×	GRV-LO	WHIT2	2.0 -	5096
		√	GRV-LO	WHIT2	2.0 1.5	30936

Table 7.1: Parameters of the Monte Carlo samples used for the correction of the data. The last column refers to the number of events passing the inclusive selection cuts in each Monte Carlo sample.

Model	Sample	Resolved Fraction
PYTHIA	Inclusive	80%
PYTHIA + MPI		89%
PYTHIA + MPI (re-weighted)		91%
PYTHIA	High Mass	68%
PYTHIA + MPI		61%

Table 7.2: Resolved fraction in the generated Monte Carlo sample.

7.5.1 The $x_{\gamma;4J}^{OBS}$ and y_{JB} Distributions

For each Monte Carlo sample, direct and resolved events were generated separately and combined in the ratio obtained from a χ^2-fit to the uncorrected $x_{\gamma;4J}^{OBS}$ distribution. The fit was performed separately for the inclusive and high mass samples. For the inclusive sample, the model with no simulation of multi-parton interactions has been fitted only to the range $0.7 < x_{\gamma;4J}^{OBS} < 1.0$[§], in order to give the best description of the high $x_{\gamma;4J}^{OBS}$ region. Table 7.2 lists the resolved contribution for each Monte Carlo sample.

The uncorrected $x_{\gamma;4J}^{OBS}$ and y_{JB} distributions, for the inclusive and high mass samples, are shown in Figs. 7.7 and 7.8 respectively. In each case, the dashed and solid histograms show the predictions of the PYTHIA and PYTHIA + MPI samples.

The inclusive $x_{\gamma;4J}^{OBS}$ distribution shows a clear enhancement at low $x_{\gamma;4J}^{OBS}$ relative to the PYTHIA Monte Carlo, indicating the need for additional energy flow in the low x_γ region. The PYTHIA + MPI model gives a significantly improved description of the data. In contrast, the y_{JB} distribution is adequately described by PYTHIA, while the model with a simulation of multi-parton interactions is peaked at much higher values of y_{JB} relative to the data. The observed discrepancy is due to the fact that $x_{\gamma;4J}^{OBS}$ has an

[§]For the $x_{\gamma;4J}^{OBS}$ plot, the normalisation is also only to the range $0.7 < x_{\gamma;4J}^{OBS} < 1.0$

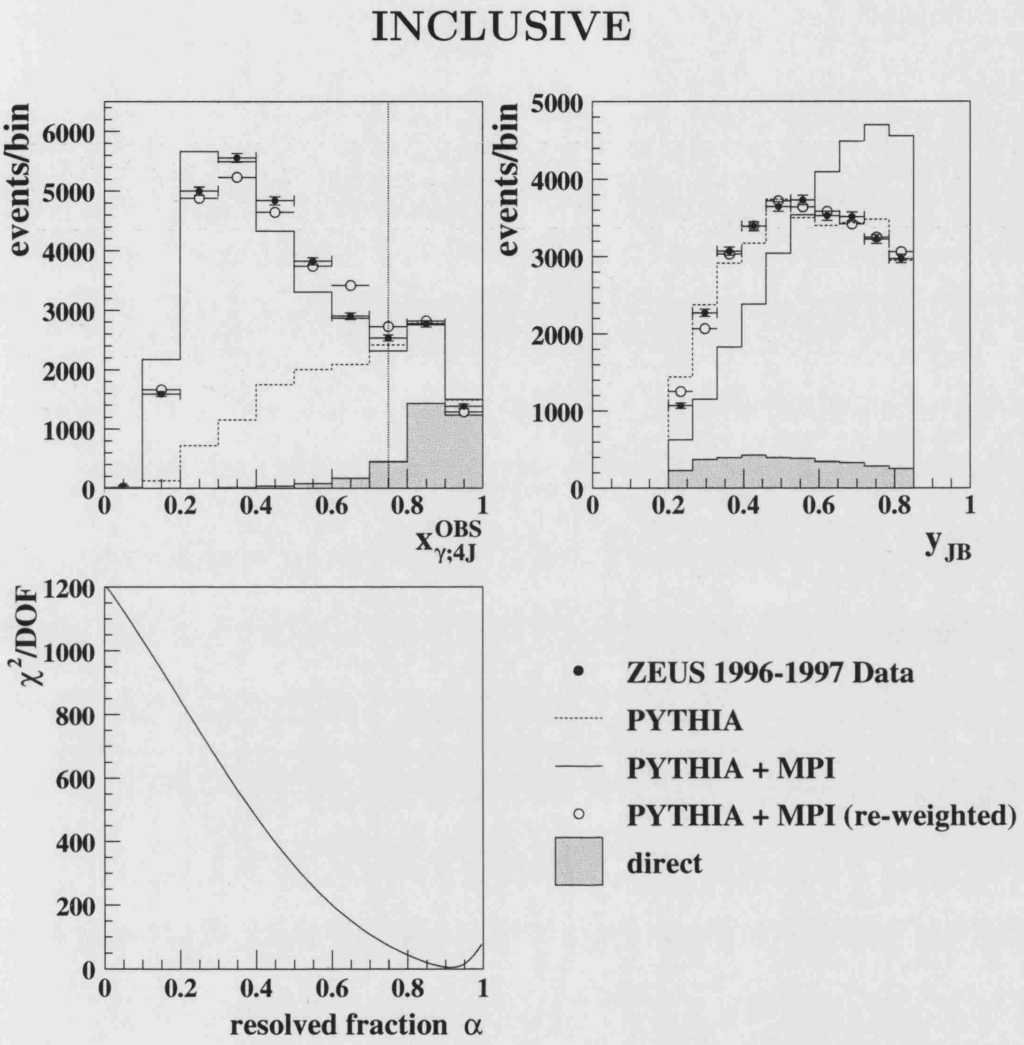

Figure 7.7: Top Left: The distribution of $x^{\mathrm{OBS}}_{\gamma;4\mathrm{J}}$. Top Right: The distribution of y_{JB}. In each case, the solid points show the uncorrected ZEUS data and the dashed and solid histograms show the predictions of the PYTHIA and PYTHIA + MPI Monte Carlo samples, respectively. The shaded histogram shows the distribution of events generated as direct photoproduction from the (re-weighted) PYTHIA + MPI sample. The open circles indicate the (re-weighted) Monte Carlo sample used for the final unfolding. The vertical dotted line on the $x^{\mathrm{OBS}}_{\gamma;4\mathrm{J}}$ plot indicates the separation between the direct- and resolved-enhanced regions. All errors are statistical only. Bottom Left: The results of the one-parameter χ^2-fit to the uncorrected $x^{\mathrm{OBS}}_{\gamma;4\mathrm{J}}$ distribution for the final sample (corresponding to the open circles in all other plots).

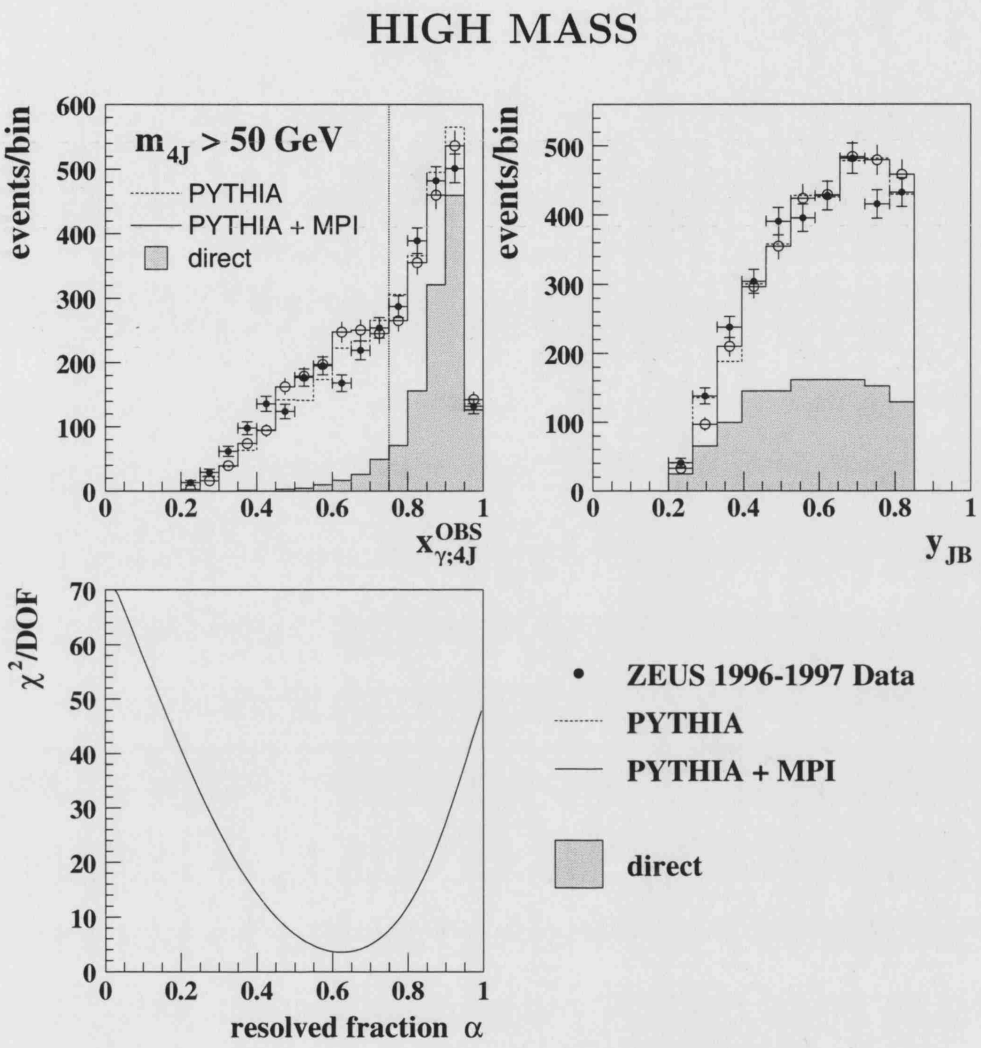

Figure 7.8: Top Left: The distribution of $x_{\gamma;4J}^{\mathrm{OBS}}$. Top Right: The distribution of y_{JB}. In each case, the solid points show the uncorrected ZEUS data and the dashed and solid histograms show the predictions of the PYTHIA and PYTHIA + MPI Monte Carlo samples, respectively. The shaded histogram shows the distribution of events generated as direct photoproduction from the PYTHIA + MPI sample. The open circles indicate the Monte Carlo sample used for the final unfolding (in this case identical to the solid histogram). The vertical dotted line on the $x_{\gamma;4J}^{\mathrm{OBS}}$ plot indicates the separation between the direct- and resolved-enhanced regions. All errors are statistical only. Bottom Left: The results of the one-parameter χ^2-fit to the uncorrected $x_{\gamma;4J}^{\mathrm{OBS}}$ distribution for the final sample (corresponding to the open circles in all other plots).

inverse dependence on y (see Eq. 4.16). While the model with multi-parton interactions gives enhanced energy flow in the forward direction (and increases the number of events at low $x_{\gamma;4J}^{OBS}$), the effect on the y_{JB} distribution is to provide an enhancement at high y. In order to improve the description of the data, the PYTHIA + MPI Monte Carlo sample has been re-weighted. The details of the re-weighting procedure are outlined in Section 7.5.2. Following the re-weighting, the direct and resolved samples were fitted again to the uncorrected $x_{\gamma;4J}^{OBS}$ distribution to obtain the final photoproduction sample used for the unfolding. The results are shown by the open circles on the $x_{\gamma;4J}^{OBS}$ and y_{JB} plots. The results of the one-parameter χ^2-fit for the re-weighted sample is also shown in Fig. 7.7.

The high mass distribution of $x_{\gamma;4J}^{OBS}$ is peaked at $x_{\gamma;4J}^{OBS} \sim 0.9$ and has a tail extending down to ~ 0.2. The energy flow at low $x_{\gamma;4J}^{OBS}$ is highly suppressed relative to the inclusive sample. Furthermore, both the models with and without a simulation of multi-parton interactions give an adequate description of the data. This suggests that the high mass sample is relatively insensitive to the effects of multi-parton interactions. The distribution of y_{JB} is also adequately described by both Monte Carlo samples.

7.5.2 Monte Carlo Re-Weighting

The Monte Carlo sample with and without a simulation of multi-parton interactions share a common sample of direct photoproduction events. Therefore, the differences between the PYTHIA and PYTHIA + MPI models arise purely from the resolved sector. Since the model without a simulation of multi-parton interactions gives a reasonable description of the inclusive y_{JB} distribution, the resolved + MPI sample has been re-weighted to have the same y_{JB} distribution as the resolved sample. Note that no re-weighting has been applied to the direct sample. Figure 7.9 shows the ratio of (resolved) to (resolved + MPI) events as a function of y_{JB} for the PYTHIA Monte Carlo. The selection cuts imposed on y_{JB} have been relaxed for this plot. The solid, dotted and dashed curves show a second-, third- and fourth-order polynomial fit to the distribution, respectively. The second-order polynomial has been used for the final re-weight function since it is the lowest order fit that gives a reasonable description of the distribution. The re-weighting has been applied only to the inclusive sample since the Monte Carlo already gives an adequate description of the high mass sample.

The nominal cross section measurements have been performed using the re-weighted Monte Carlo sample (shown by the open circles in Figs. 7.7 and 7.8). However, the cross sections obtained from the Monte Carlo before re-weighting have been used as a cross check on the final results. This is discussed in Section 7.11. In all figures that follow, the PYTHIA + MPI model refers to the sample after re-weighting.

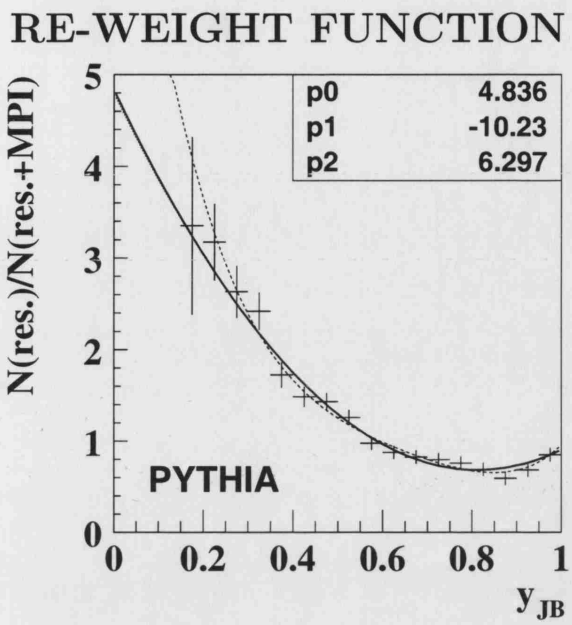

Figure 7.9: The distribution of the ratio of resolved events with and without a simulation of multi-parton interactions as a function of y_{JB} from the PYTHIA Monte Carlo. The solid, dotted and dashed curves show the results of a second-, third- and fourth-order polynomial fit to the distribution. The text box shows the parameters of the second-order polynomial which is used as the final re-weight function. The cuts imposed on y_{JB} have been relaxed for this plot.

7.6 Description of Data by Monte Carlo

In order for the Monte Carlo samples described in Section 7.5 to be used with confidence to unfold for detector effects, it is essential that they provide an adequate description of the data. In particular, the quantities that are used to define the data sample should be reasonably well modelled in order that they do not introduce any unexpected systematic bias into the extraction of the cross section. In this section, the description of the data by the Monte Carlo, for a variety of detector level jet and kinematic quantities, is discussed. In each of the plots, the data is shown by the solid points and the PYTHIA and PYTHIA + MPI Monte Carlo samples are shown by the open stars and open circles, respectively. In each case, the Monte Carlo has been normalised to the total number of events in the data.

7.6.1 Jet Quantities

The E_{T} distributions of the four highest transverse energy jets are shown in Figs. 7.10 and 7.11 for the inclusive and high mass samples, respectively. Also shown are the distributions of the total E_{T} (containing all of the four highest transverse energy jets) and the quantity $E_{\mathrm{T}}^{\mathrm{sum}} = \sum_{i=1}^{4} E_{\mathrm{T}}^{i}$. The event selection criteria require that $E_{\mathrm{T}}^{1,2} > 6$ GeV and $E_{\mathrm{T}}^{3,4} > 5$ GeV. In general, jet transverse energy distributions may be expected to fall approximately exponentially from the threshold values. However, the restrictions imposed on $|\cos\theta_{3'}|$ and $m_{4\mathrm{J}}$ in this analysis restrict the phase space available for low

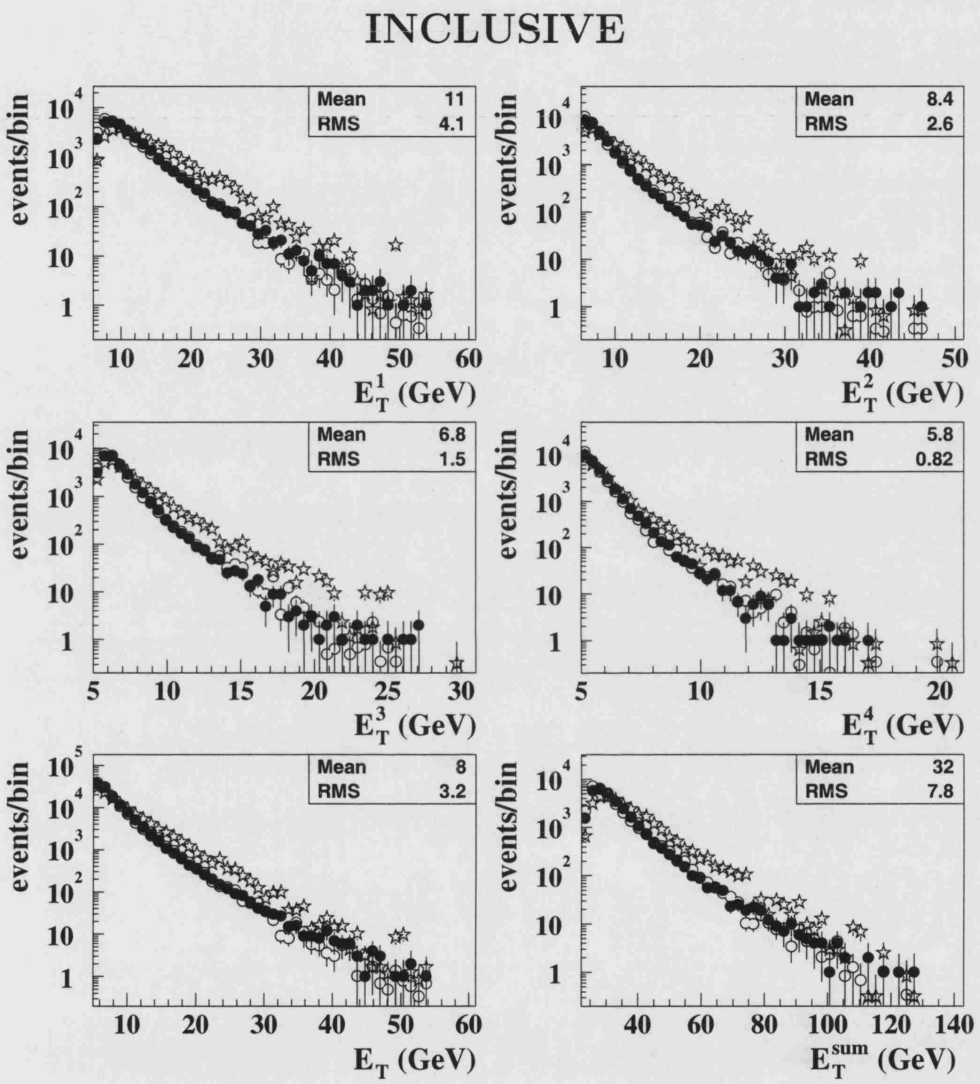

Figure 7.10: The transverse energy distributions of the four highest transverse energy jets for the inclusive sample of events. The solid points show the uncorrected ZEUS data. The open stars and open circles show the predictions of the PYTHIA and PYTHIA + MPI Monte Carlo samples, respectively. Errors are statistical only.

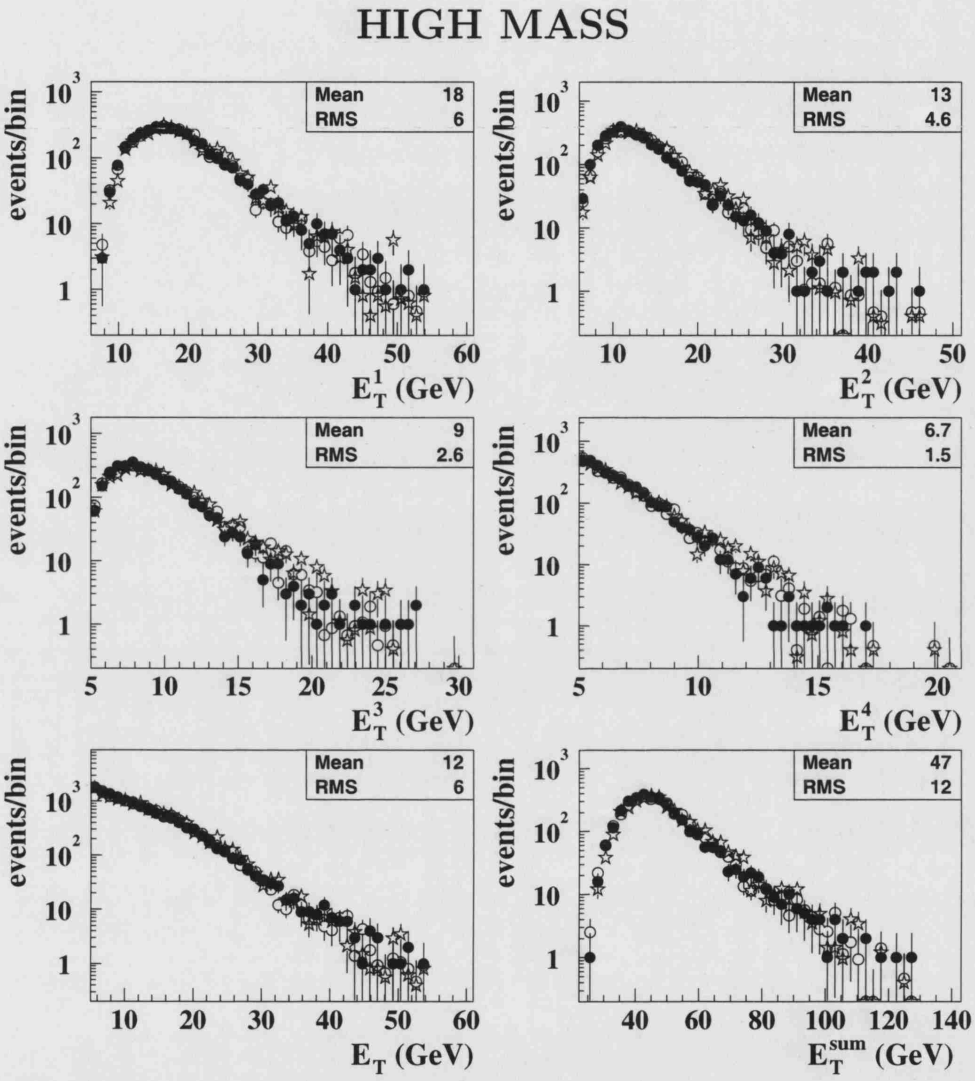

Figure 7.11: The transverse energy distributions of the four highest transverse energy jets for the high mass sample of events. The solid points show the uncorrected ZEUS data. The open stars and open circles show the predictions of the PYTHIA and PYTHIA + MPI Monte Carlo samples, respectively. Errors are statistical only.

E_T jet production. Since the resulting transverse energy distributions do not peak at threshold, the angular distributions should be relatively insensitive to the E_T selection criteria. As a result of the cut imposed on m_{4J} for the high mass sample, the transverse energies of the jets in this sample peak at higher values and have higher mean values than those in the inclusive sample. This is the reason why the high mass sample is expected to be less sensitive to the underlying event. The PYTHIA + MPI Monte Carlo gives a reasonable description of the jet transverse energy distributions, for both the inclusive and high mass samples. The PYTHIA sample is also able to describe the high mass distributions but is not able to adequately describe the E_T dependence of the jets for inclusive events over the measured range. More specifically, taking into account the fact that the Monte Carlo samples have been normalised to the data, the PYTHIA model *is* able to give an adequate description of the data at high jet transverse energies but produces insufficient activity at low E_T^{jet}.

The jet pseudo-rapidity distributions of the four highest transverse energy jets are shown in Figs. 7.12 and 7.13 for the inclusive and high mass samples respectively. In both cases the data are concentrated in the $\eta > 0$ region. This is due to the fact that, for the majority of QCD subprocesses, the z boost is in the forward (proton) direction. Also shown is the distribution of $\bar{\eta} = \frac{1}{4}(\eta^1 + \eta^2 + \eta^3 + \eta^4)$. For both the inclusive and high mass distributions, the value of $\bar{\eta}$ is peaked at around 1. However, for the inclusive sample, this quantity extends back to lower values of $\bar{\eta}$ than in the high mass case. The PYTHIA + MPI sample gives a reasonable description of both the inclusive and high mass distributions. The PYTHIA sample also gives an adequate description of the high mass sample. However, for the inclusive sample, the PYTHIA Monte Carlo has lower average values of the jet pseudo-rapidity and $\bar{\eta}$ than the data. This is particularly apparent for the highest and second highest transverse energy jets.

Studies of two jet photoproduction (satisfying $E_T > 6$ GeV and $\eta < 1.6$) at ZEUS [173] have found a third, low energy cluster, associated with the photon remnant, with mean transverse energies of ~ 2 GeV and pseudo-rapidities peaked at $\eta \sim -2$. Since all of the four highest transverse energy jets found in this analysis have a mean $E_T \gtrsim 6$ GeV (even for the inclusive sample) and pseudo-rapidities that extend back only as far as $\eta \sim -1.5$, the jets in this analysis are not associated with the photon remnant.

The distributions of m_{4J} are shown in Fig. 7.14. Although the high mass events are contained within the inclusive set, the inclusive and high mass distributions are shown separately since the normalisation of the Monte Carlo to the respective data sample is different in each case. For the inclusive sample, the distribution of the data rises to a maximum at $m_{4J} \sim 30$ GeV and then falls approximately exponentially. The PYTHIA + MPI Monte Carlo gives an adequate description of the data. The fact that the PYTHIA sample can only describe the data at high values of m_{4J} is shown explicity in the equivalent high mass plot. Here, the data falls exponentially from the threshold at $m_{4J} = 50$ GeV and both Monte Carlo samples give an adequate description of the data.

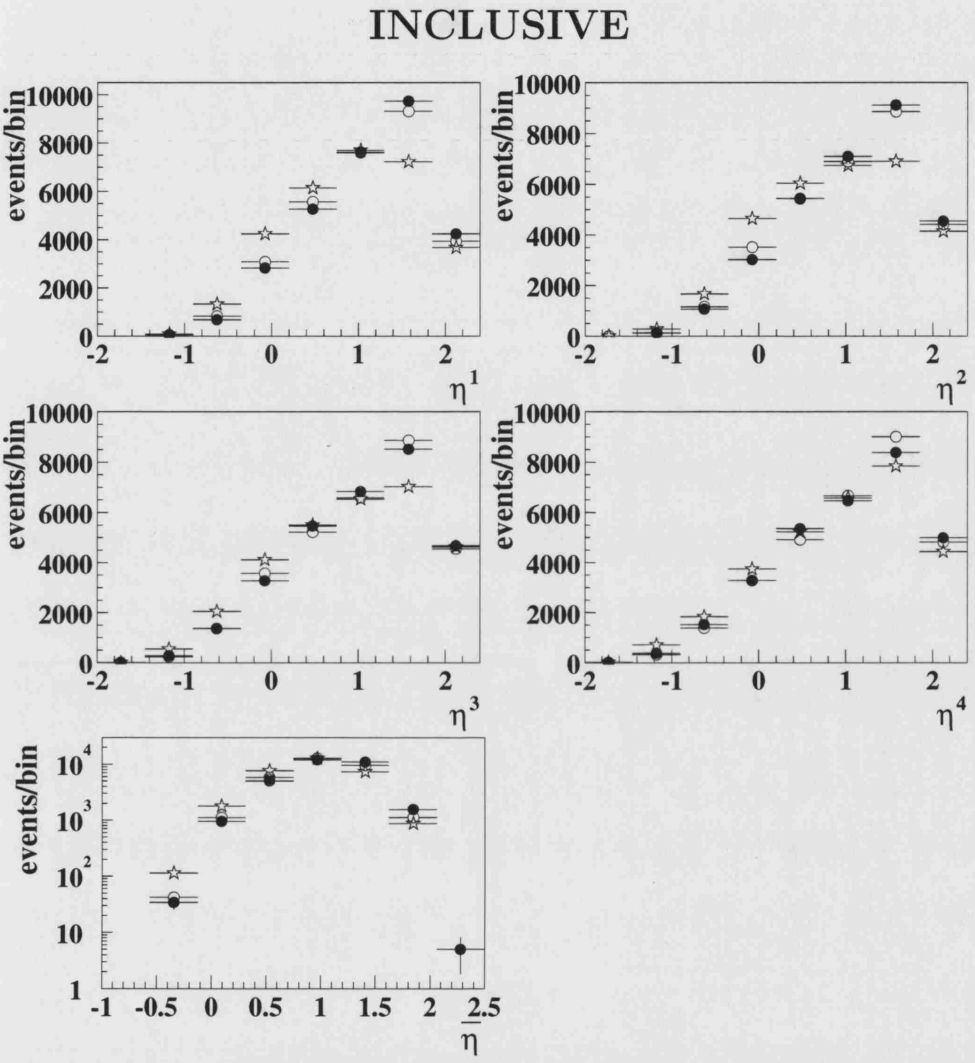

Figure 7.12: The pseudo-rapidity distributions of the four highest-transverse-energy jets for the inclusive sample of events. The solid points show the uncorrected ZEUS data. The open stars and open circles show the predictions of the PYTHIA and PYTHIA + MPI Monte Carlo samples, respectively. Errors are statistical only. The horizontal error bars indicate the width of the bins.

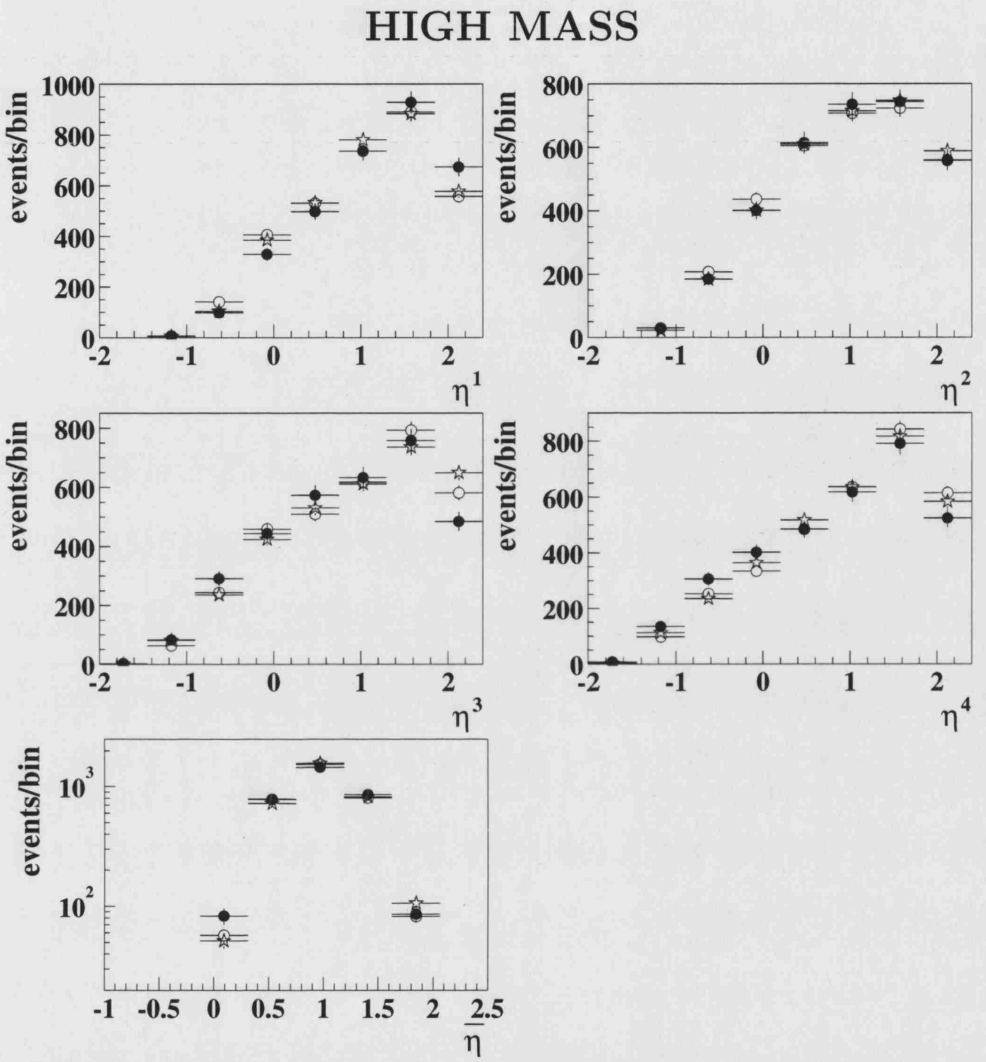

Figure 7.13: The pseudo-rapidity distributions of the four highest-transverse-energy jets for the high mass sample of events. The solid points show the uncorrected ZEUS data. The open stars and open circles show the predictions of the PYTHIA and PYTHIA + MPI Monte Carlo samples, respectively. Errors are statistical only. The horizontal error bars indicate the width of the bins.

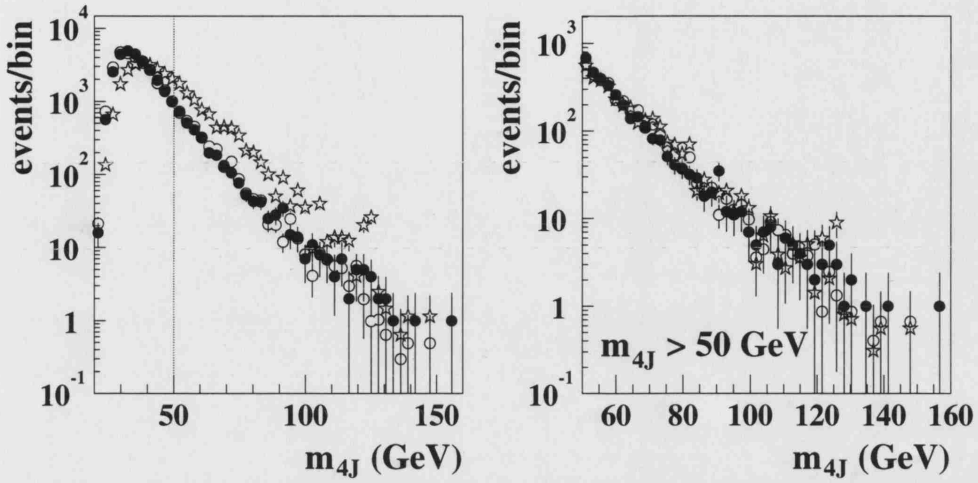

Figure 7.14: The distribution of m_{4J} for the inclusive (left) and high mass (right) samples. The solid points show the uncorrected ZEUS data. The open stars and open circles show the predictions of the PYTHIA and PYTHIA + MPI Monte Carlo samples, respectively. Errors are statistical only.

7.6.2 Jet Profiles

The study of jet profiles gives a sensitive test of the description of the data by the Monte Carlo. Jet profiles give the distribution of the transverse energy around the jet axis. The construction of a jet profile is described in detail in Section 8.8.2.

Figure 7.15 shows the $\delta\eta$ jet profiles for the four highest transverse energy jets in the inclusive sample of events. Each profile is shown separately for the regions $x_{\gamma;4J}^{OBS} < 0.75$ (resolved-enhanced) and $x_{\gamma;4J}^{OBS} > 0.75$ (direct-enhanced). The uncorrected ZEUS data are shown by the solid points and the predictions of the PYTHIA and PYTHIA + MPI Monte Carlo samples are shown by the dashed and solid lines, respectively. In the resolved enhanced region, the PYTHIA sample is unable to correctly describe either the height of the collimated jet core or that of the jet energy pedestal. Specifically, the average transverse energies of the jets in the PYTHIA sample lie above the data, while the energy pedestal is underestimated, particularly in the forward direction where the discrepancy is $\sim$ 1 GeV per unit $\delta\eta$. In contrast, the PYTHIA + MPI Monte Carlo gives a reasonable description of the jet core and the backwards energy pedestal. However, there remains a small discrepancy of $\lesssim 0.5$ GeV per unit $\delta\eta$ in the forward direction. This is possibly due to insufficient multi-parton interactions generated in the Monte Carlo and/or possible contributions from a soft underlying event, which is not included in the model. In the direct enhanced region, the difference between the PYTHIA and PYTHIA + MPI models is minimal and both give a reasonable

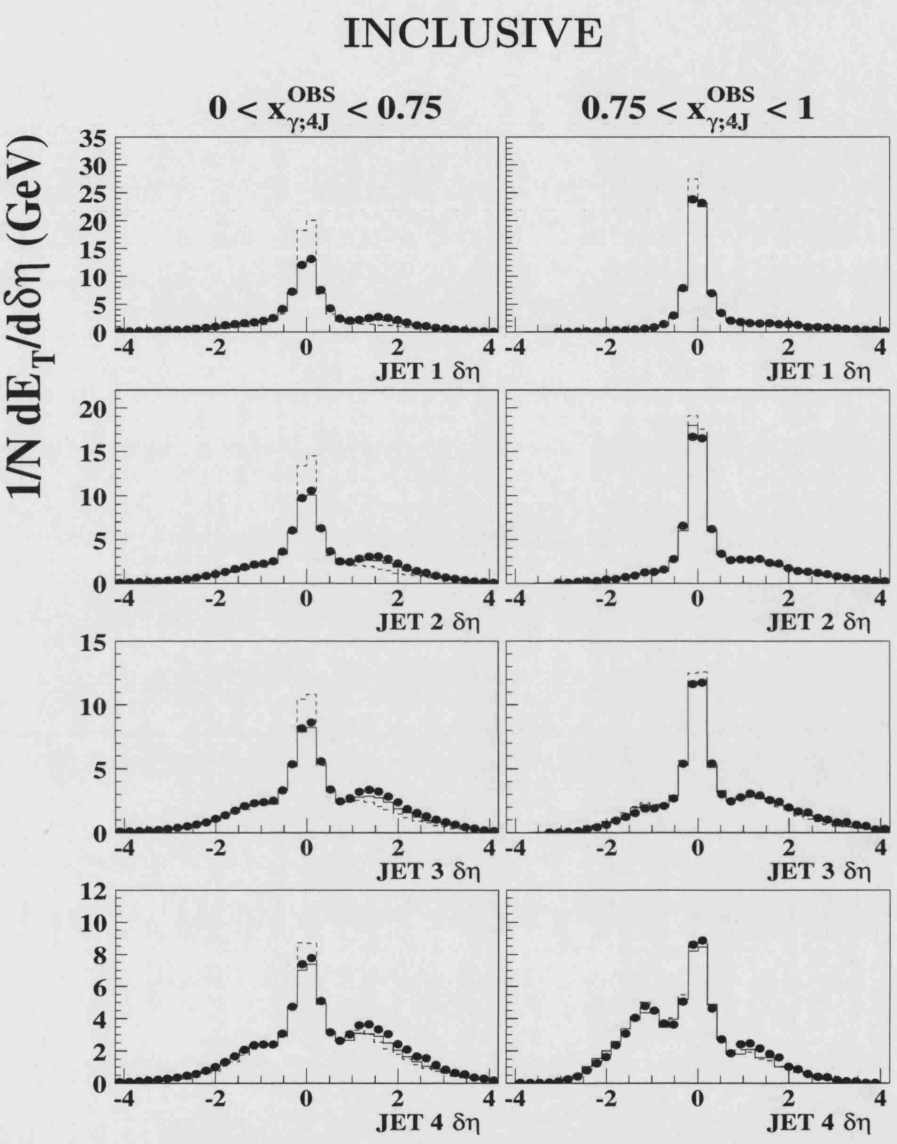

Figure 7.15: The transverse energy jet profiles of the four highest transverse energy jets as a function of $\delta\eta$ for the inclusive sample. The left and right columns show the profiles for the $x_{\gamma;4J}^{\mathrm{OBS}} < 0.75$ and $x_{\gamma;4J}^{\mathrm{OBS}} > 0.75$ regions respectively. The uncorrected ZEUS data are shown by the solid points. The dashed and solid histograms show the predictions of the PYTHIA and PYTHIA + MPI Monte Carlo samples, respectively.

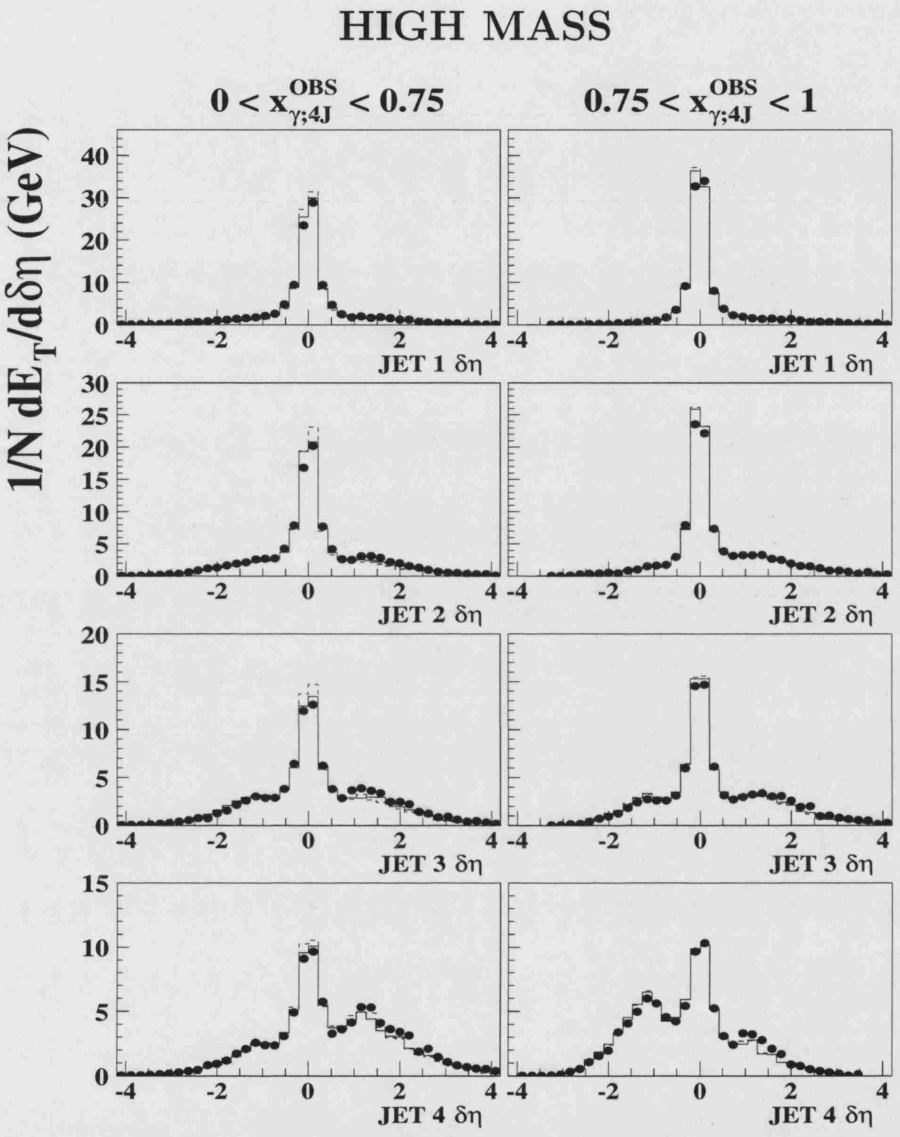

Figure 7.16: The transverse energy jet profiles of the four highest transverse energy jets as a function of $\delta\eta$ for the high mass sample. The left and right columns show the profiles for the $x_{\gamma;4J}^{OBS} < 0.75$ and $x_{\gamma;4J}^{OBS} > 0.75$ regions respectively. The uncorrected ZEUS data are shown by the solid points. The dashed and solid histograms show the predictions of the PYTHIA and PYTHIA + MPI Monte Carlo samples, respectively.

description of the data. Note also, that the mean transverse energies of the jets are higher in the direct-enhanced relative to the resolved-enhanced region.

The $\delta\eta$ profiles for the high mass sample are shown in Fig. 7.16. There is little difference between the PYTHIA and PYTHIA + MPI models in either the resolved or direct-enhanced regions. This indicates again the relative insensitivity of the high mass sample to the effects of multi-parton interactions. Both Monte Carlo samples give a reasonable description of the data, although a small excess in the data, above the model predictions, is observed in the forward direction; particularly for the third and fourth jets. The higher average transverse energies of the jets relative to the inclusive sample are apparent.

7.7 Cumulative Efficiencies

It is informative to study the efficiency at each stage of the event selection. In this context, the efficiency is defined as the fraction of events passing all hadron-level selection criteria, that are also reconstructed and accepted as events at the detector-level. Figure 7.17 shows the efficiency at each stage of the event selection as a function of $m_{4\mathrm{J}}$. The results are shown for the PYTHIA + MPI Monte Carlo sample. In each case, the solid points show the results for the inclusive sample of events and the hollow circles show the results for the high mass sample. The chosen bin widths reflect the resolution on $m_{4\mathrm{J}}$ (this is discussed further in Section 7.8).

The efficiency at the FLT is $\gtrsim 95\%$ over the range of $m_{4\mathrm{J}}$. The efficiencies of the SLT and TLT are also $\sim 95\%$, giving a cumulative efficiency of $\gtrsim 85\%$ at the TLT. The offline event selection represents all cleaning cuts described in Section 5.4. The cumulative efficiency at this stage is $\gtrsim 75\%$. The two jet efficiency corresponds to the nominal selection of two jets, as described in Section 5.4.1. At this stage, the cumulative efficiency remains above 70%. The high efficiency at this stage of the selection is due to the fact that four jets have been selected at the hadron level. Therefore, the probability that at least two jets are reconstructed and accepted as events at the detector level is high. The final stage is the selection of four jets and the additional requirements on $X_{3'}$, $\cos\theta_{3'}$ and $m_{4\mathrm{J}}$ (the latter for the high mass sample only). This is the most restrictive stage of the event selection. The selection of events satisfying the $X_{3'}$ and $\cos\theta_{3'}$ criteria results in only a small reduction in efficiency, with the largest reduction arising from the requirement of four jets. This is largely due to the jet transverse energy resolution. For the high mass sample, the selection of events with $m_{4\mathrm{J}} > 50$ GeV also reduces the efficiency for events close to the $m_{4\mathrm{J}}$ threshold cut. The efficiency increases as a function of $m_{4\mathrm{J}}$ due to the higher average transverse energies for high mass events.

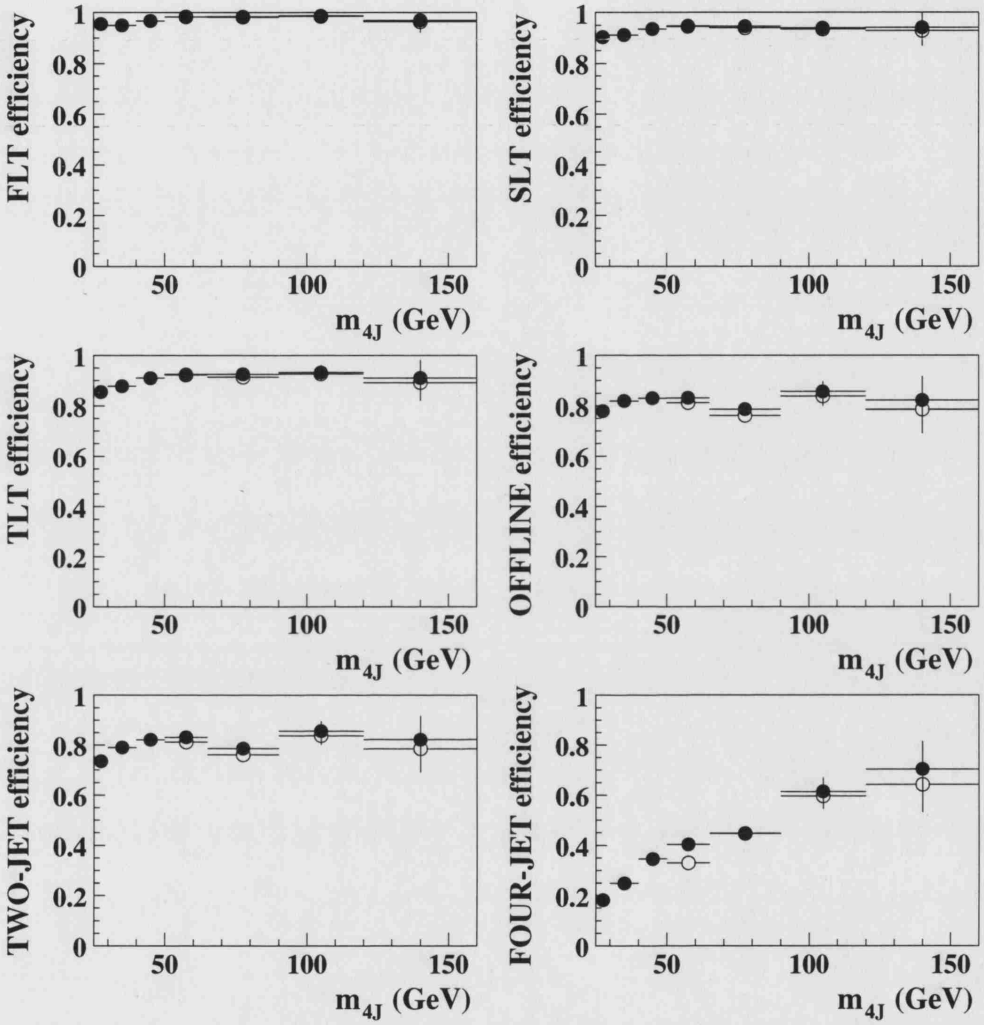

Figure 7.17: The cumulative efficiencies as a function of m_{4J} at each stage of the event selection according to the PYTHIA + MPI Monte Carlo. The results for the inclusive sample are shown by the solid points and the results for the high mass sample are shown by the open circles. From top left to bottom right: The efficiency up to the FLT, SLT, TLT, offline selection (see Section 5.4), two jet photoproduction selection (see Section 5.4.1) and the final event sample (defined in Section 7.4).

7.8 Pull and Resolution

The reconstruction quality of event variables must be assessed in order to establish whether the *reconstructed* values give an adequate description of the *true* values. In order to quantify this, two variables are defined: the **pull** $\mathcal{P}$ and **resolution** $\mathcal{R}$. For any variable X, the pull gives the deviation of the reconstructed value from the true value and the resolution gives the spread on that distribution. In this thesis, the pull for all dimensionless quantities has been taken to be the absolute difference between the reconstructed and true values so that $\mathcal{P}_{\mathrm{X}} = \langle \mathrm{X(rec.)} - \mathrm{X(true)} \rangle$ with a resolution given by $\mathcal{R}_{\mathrm{X}} = \sigma\left(\mathrm{X(rec.)} - \mathrm{X(true)}\right)$. For dimensionful quantities, the pull has been defined as the fractional difference so that $\mathcal{P}_{\mathrm{X}} = \left\langle \frac{\mathrm{X(rec.)}-\mathrm{X(true)}}{\mathrm{X(true)}} \right\rangle$ and $\mathcal{R}_{\mathrm{X}} = \sigma\left(\frac{\mathrm{X(rec.)}-\mathrm{X(true)}}{\mathrm{X(true)}}\right)$.

The pull and resolution can be calculated in a number of ways. For example, the value of $\mathcal{P}$ could be taken to be the absolute mean of the distribution of $\mathrm{X(rec.)} - \mathrm{X(true)}$ (or $(\mathrm{X(rec.)} - \mathrm{X(true)})/\mathrm{X(true)}$) with $\mathcal{R}$ being given by the r.m.s spread. This is called the **r.m.s method**. However, the results of this method are particularly sensitive to tails in the distribution and to any bias imposed by kinematic restrictions. An alternative method is the **Gaussian-fit method**. In this case, a Gaussian function is fitted to the distribution of $\mathrm{X(rec.)} - \mathrm{X(true)}$ (or $(\mathrm{X(rec.)} - \mathrm{X(true)})/\mathrm{X(true)}$). The mean of the fit is then taken to be the value of $\mathcal{P}$ while the width gives the value of $\mathcal{R}$. This method is less influenced by tails and kinematic boundaries.

In this section, the Gaussian-fit method is used to evaluate the pulls and resolutions of several kinematic quantities, including the cross-section variables. The pulls and resolutions have been estimated using the PYTHIA + MPI Monte Carlo sample. Events were required to pass the event selection cuts for the inclusive sample at both detector and hadron level.

7.8.1 Reconstruction of the Hadronic Final State

The reconstruction qualities of the jet variables $(E_{\mathrm{T}}, \eta, \phi)$ are illustrated in Fig. 7.18. For these plots, true and reconstructed jets have been matched as described in Section 4.8.1. Each distribution includes all of the four highest transverse energy jets in the event. The results show a clear correlation between the true and reconstructed values of the variables. The pull of the quantity $E_{\mathrm{T}}^{\mathrm{jet}}$ is $\sim 2\%$, showing that the detector and hadron level values are comparable. This supports the use of corrected ZUFOs for the reconstruction. The resolution on this quantity is 16%. The pull of the jet η and ϕ are also small, and the resolutions are 0.06 and 0.08 for η and ϕ respectively.

Figure 7.19 illustrates the quality of reconstruction of the variables $m_{4\mathrm{J}}$, $x_{\gamma;4\mathrm{J}}^{\mathrm{OBS}}$ and y. The reconstructed value of y has been calculated using the Jaquet-Blondel method. A

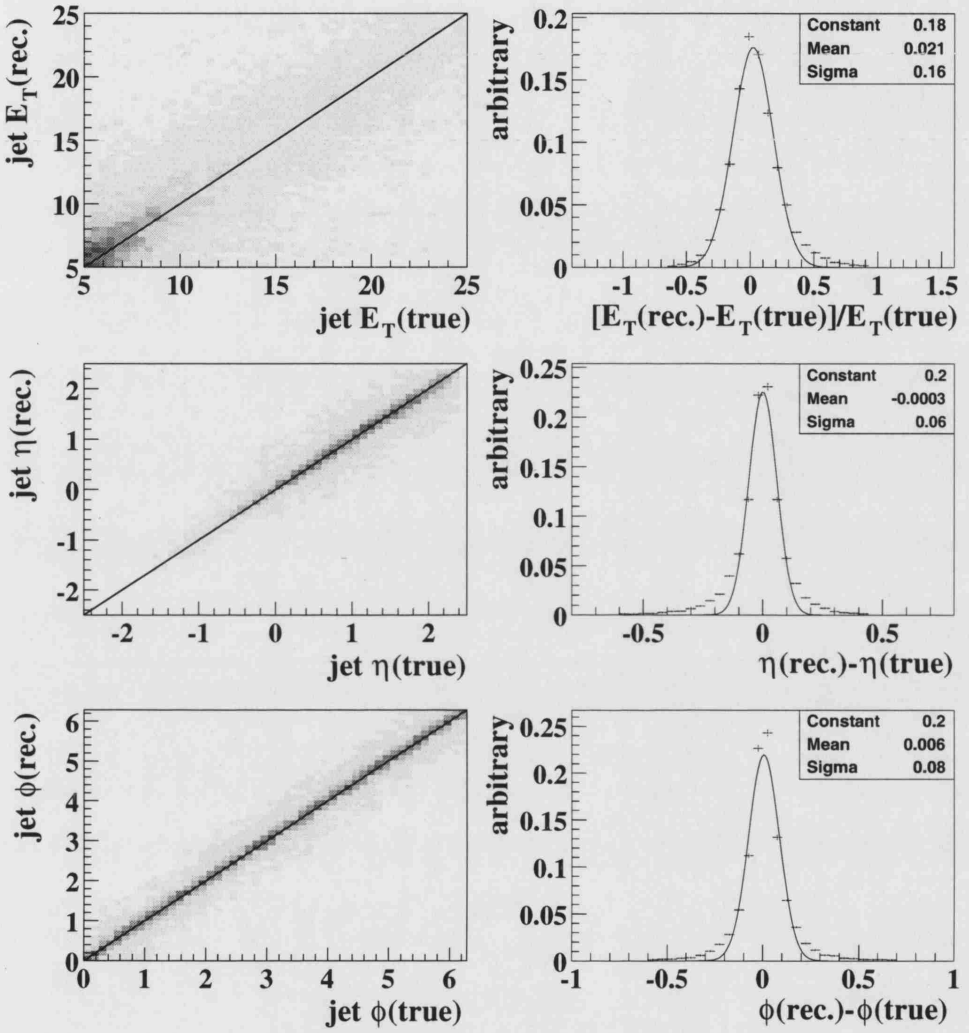

Figure 7.18: Left: The correlations between the true and reconstructed values of the jet variables (E_T,η,ϕ). Right: The bias and resolutions of the jet variables. The curve shows a Gaussian fit to the distribution and the text box gives the parameters of the fit. In each case, the area under the distribution is normalised to unity. For both the correlations and the resolutions, the results are from the PYTHIA + MPI Monte Carlo and the plots include the four highest-transverse-energy jets in the event.

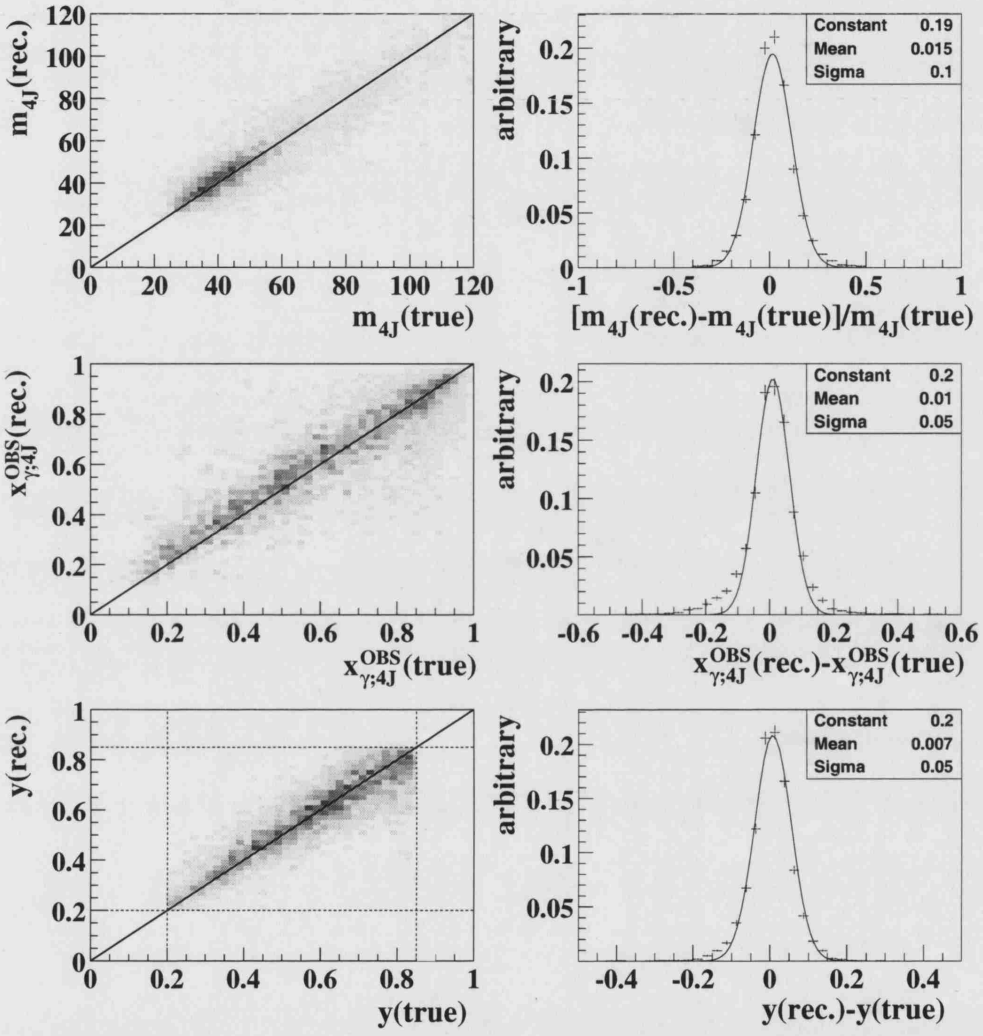

Figure 7.19: The pull and resolution of $m_{4\mathrm{J}}$, $x_{\gamma;4\mathrm{J}}^{\mathrm{OBS}}$ and y from the PYTHIA + MPI Monte Carlo. The curve shows a Gaussian fit to the distribution and the text box gives the parameters of the fit. In each case, the area under the distribution is normalised to unity.

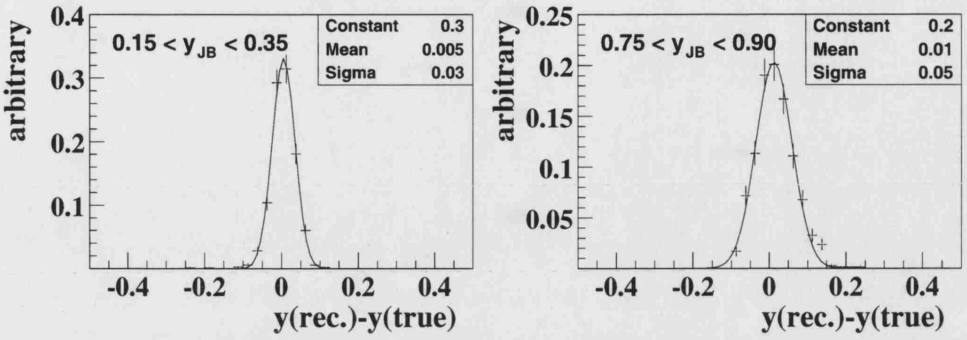

Figure 7.20: The pull and resolution of y across the cuts on y_{JB} from the PYTHIA + MPI Monte Carlo. The curve shows a Gaussian fit to the distribution and the text box gives the parameters of the fit. In each case, the area under the distribution is normalised to unity.

strong correlation between the true and reconstructed quantities is observed. The pull on $m_{4\mathrm{J}}$ is $< 2\%$ and the resolution is $\sim 10\%$. The pulls and resolutions of $x_{\gamma;4\mathrm{J}}^{\mathrm{OBS}}$ and y are also small. The y resolution has also been studied in the regions $0.15 < y_{\mathrm{JB}} < 0.35$ and $0.75 < y_{\mathrm{JB}} < 0.9$ (see Fig. 7.20). The values of the pulls and resolutions from these plots are relevant to those events which may migrate across the cuts placed on y_{JB}. The results show that the pull is 0.005 at low y and 0.01 at high y with resolutions of 0.03 and 0.05 respectively.

7.8.2 Binning the Data

Several factors must be taken into account when choosing the width of the bins for the final measured cross sections. In order to obtain the most information about the shape of the variable, there should ideally be as many bins as possible. However, in a real measurement, there are limited statistics. In addition, the resolution of the variables must be taken into consideration to avoid long-range migrations between bins. The pull and resolution of the four jet centre-of-mass observables are shown in Fig. 7.21. The results are shown on a $\log_{10}$ scale in order to accentuate the details. In each case, the pulls are close to zero and the resolutions are less than the widths of the bins chosen for the final cross section measurement.

7.8.2.1 Bin Stabilities

Figure 7.22 shows the stability (see Eq. 6.13) of the measured distributions with respect to migrations between bins. The solid histogram shows the results for the inclusive sample and the points show the results for the high mass sample. The results show that the bin stabilities are typically $> 20\%$ for both the inclusive and high mass samples.

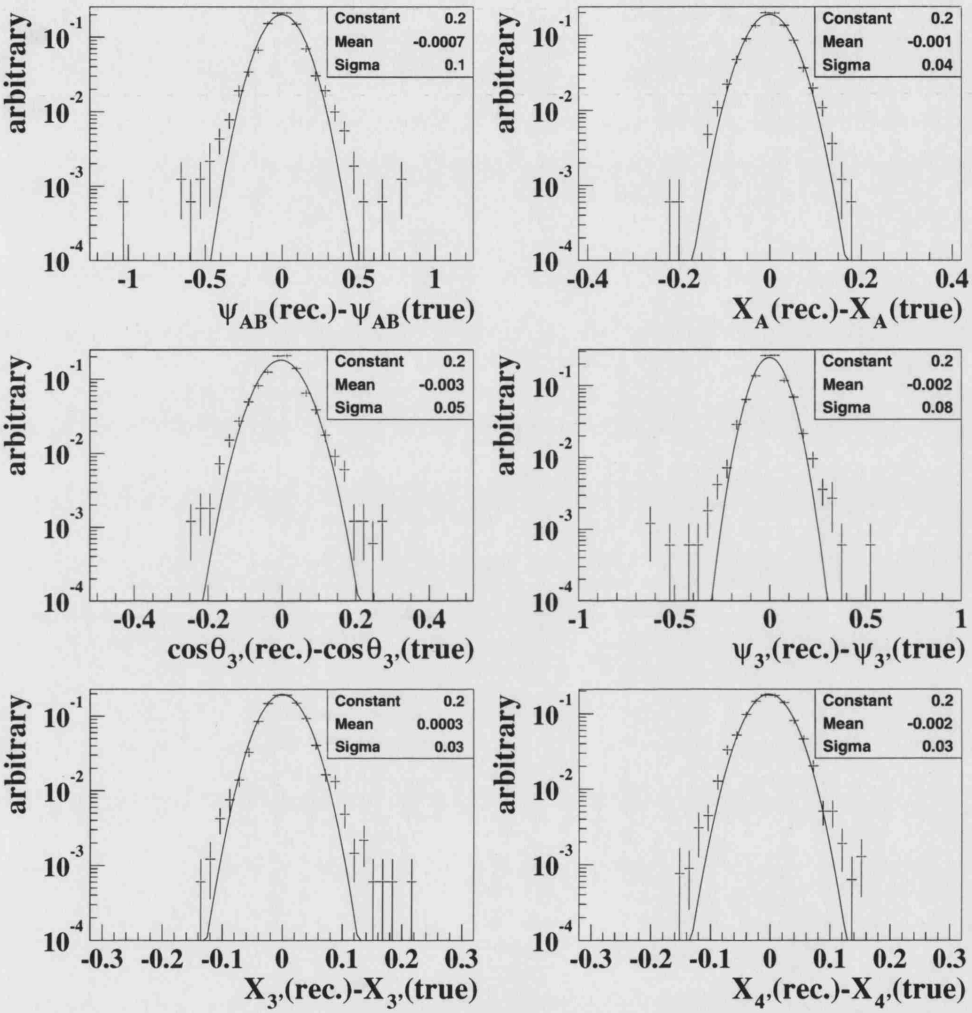

Figure 7.21: The pull and resolution of ψ_{AB}, X_{A}, $\cos\theta_{3'}$, $\psi_{3'}$, $X_{3'}$ and $X_{4'}$ from the PYTHIA + MPI Monte Carlo sample. The curve shows a Gaussian fit to the distribution and the text box gives the parameters of the fit. In each case, the area under the distribution is normalised to unity.

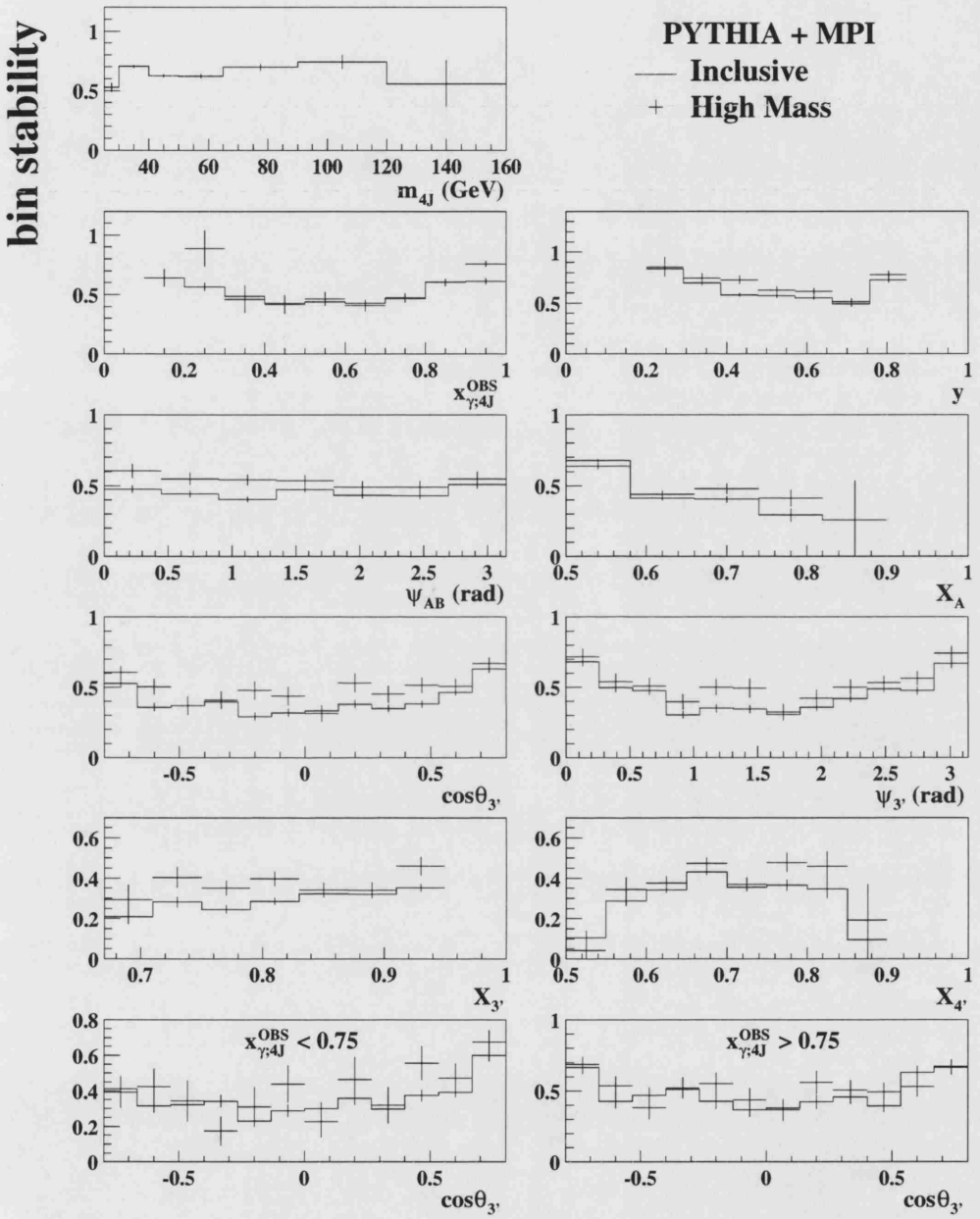

Figure 7.22: The bin stabilities for the cross section variables m_{4J}, $x^{OBS}_{\gamma;4J}$, y, ψ_{AB}, X_A, $\cos\theta_{3'}$, $\psi_{3'}$, $X_{3'}$ and $X_{4'}$. All results are from the PYTHIA + MPI Monte Carlo sample. The solid histogram and points show the results for the inclusive and high mass samples respectively.

7.9 The Correction Procedure

In order to quantify the systematic uncertainties and to facilitate comparisons with hadron level distributions, the data must be unfolded for detector effects. Measured distributions can be corrected from detector to hadron level by applying bin-by-bin correction factors. The correction factors are given by the ratio of the bin purity to the bin efficiency.

It has already been shown that the inclusive distributions are sensitive to the inclusion of multi-parton interactions in the models, while the high mass distributions are not. As a result of the significantly improved description of the inclusive data by the PYTHIA + MPI relative to the PYTHIA Monte Carlo sample, the former has been used to determine the correction factors in this analysis. Figures 7.23-7.25 show the bin purities, bin efficiencies and bin-by-bin correction factors according to the PYTHIA + MPI sample. In each case, the solid histogram shows the results for the inclusive sample and the points show the results for the high mass sample.

The bin purities (see Eq. 6.6) for the cross section variables are shown in Fig. 7.23. The bin purities for the high mass sample are typically between 10 and 20%, while those of the inclusive sample are generally lower and typically between 3 and 5%. The higher purities for the high mass sample is due to the fact that the jets tend to be of higher transverse energy. This means that jets passing the detector level cuts are likely to have a corresponding true E_{T} which also pass the hadron level requirements. For similar reasons, the purity rises as a function of $x_{\gamma;4\mathrm{J}}^{\mathrm{OBS}}$ since events with high $x_{\gamma;4\mathrm{J}}^{\mathrm{OBS}}$ also tend to produce jets of higher transverse energy.

The bin efficiencies (see Eq. 6.7) are shown in Fig. 7.24. The values are typically $\gtrsim 10\%$ for the inclusive sample and $\gtrsim 15\%$ for the high mass sample. The higher efficiencies of the high mass sample is due to the fact that high transverse energy jets are more efficiently selected. An increase in efficiency as a function of $x_{\gamma;4\mathrm{J}}^{\mathrm{OBS}}$ is also observed.

The correction factors according to the PYTHIA + MPI model, for each of the cross section variables, are shown in Fig 7.25. The factors for the inclusive sample are generally smaller than for the high mass sample since the mass cut of 50 GeV produces a larger relative increase in the purity than in the efficiency. This is also illustrated by the general rise in the correction factor as a function of $m_{4\mathrm{J}}$. The correction factors as a function of the other cross section variables are, in general, reasonably flat.

The uncorrected distributions have been multiplied by the correction factors shown in this section and the final cross sections have been calculated using Eq. 6.16. The results are shown in subsequent sections.

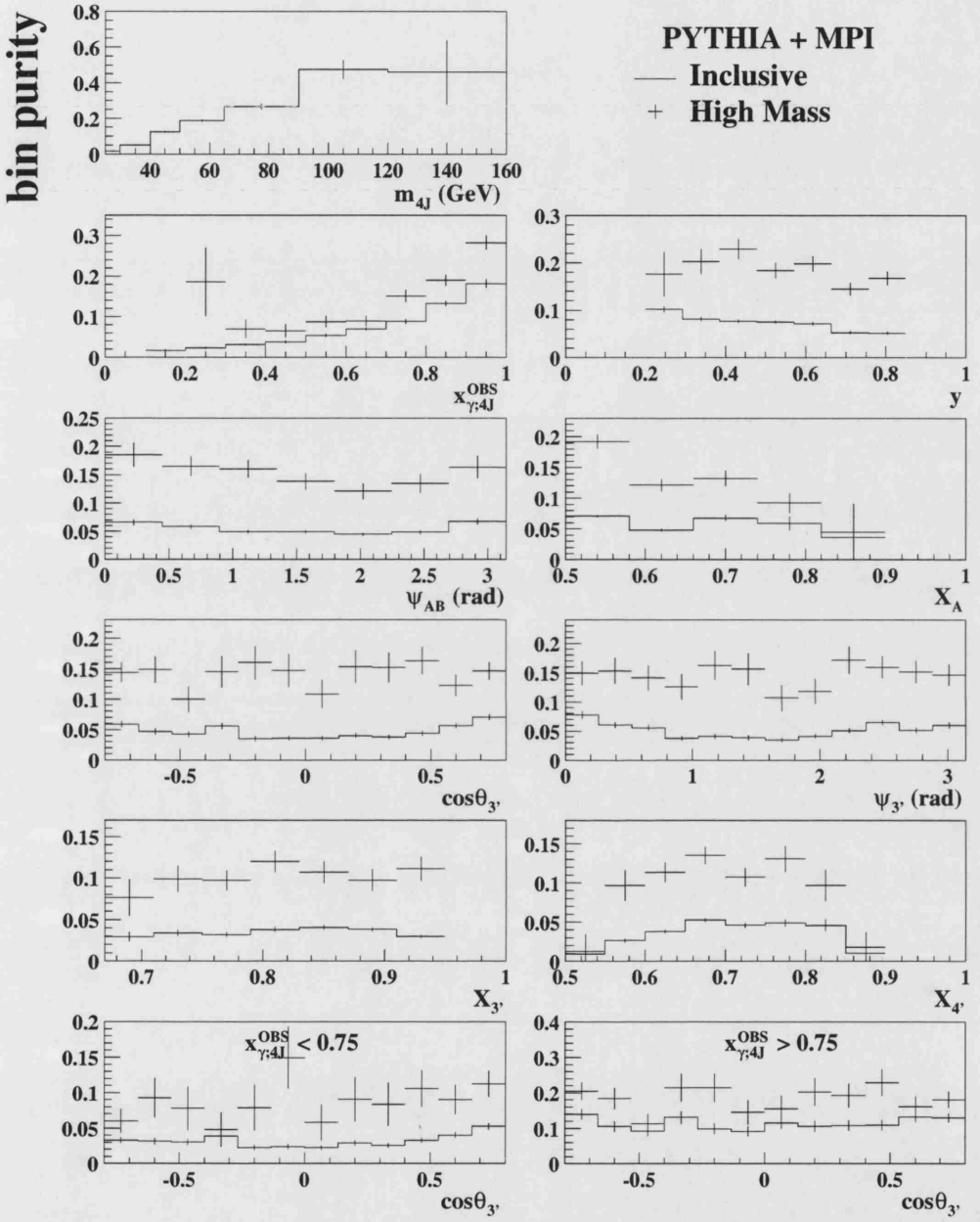

Figure 7.23: The bin purities for the cross section variables $m_{4\mathrm{J}}$, $x_{\gamma;4\mathrm{J}}^{\mathrm{OBS}}$, y, ψ_{AB}, X_{A}, $\cos\theta_{3'}$, $\psi_{3'}$, $X_{3'}$ and $X_{4'}$. All results are from the PYTHIA + MPI Monte Carlo sample. The solid histogram and points show the results for the inclusive and high mass samples respectively.

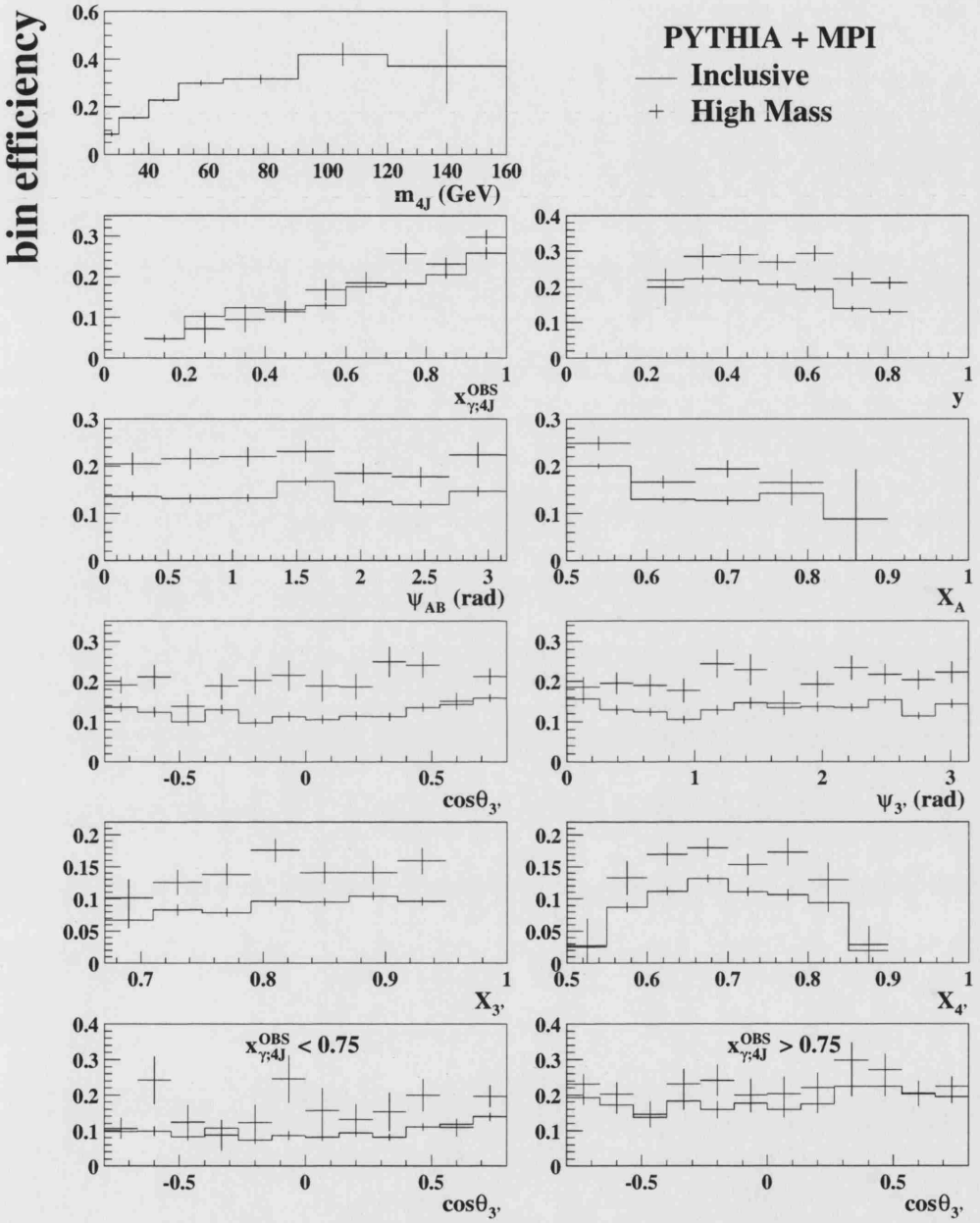

Figure 7.24: The bin efficiencies for the cross section variables $m_{4\mathrm{J}}$, $x_{\gamma;4\mathrm{J}}^{\mathrm{OBS}}$, y, ψ_{AB}, X_{A}, $\cos\theta_{3'}$, $\psi_{3'}$, $X_{3'}$ and $X_{4'}$. All results are from the PYTHIA + MPI Monte Carlo sample. The solid histogram and points show the results for the inclusive sample and high mass samples respectively.

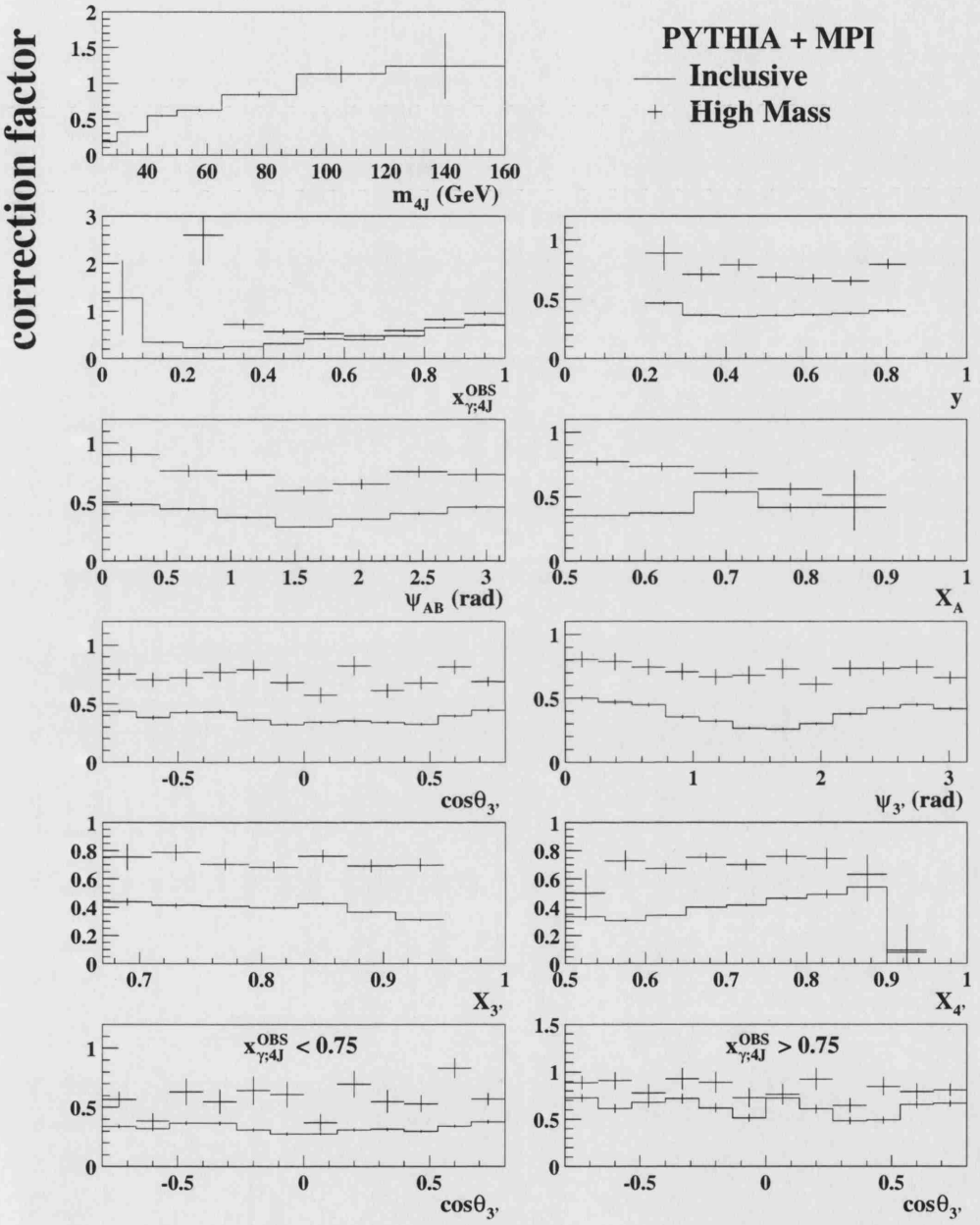

Figure 7.25: The correction factors for the cross section variables $m_{4\mathrm{J}}$, $x_{\gamma;4\mathrm{J}}^{\mathrm{OBS}}$, y, ψ_{AB}, X_{A}, $\cos\theta_{3'}$, $\psi_{3'}$, $X_{3'}$ and $X_{4'}$. All results are from the PYTHIA + MPI Monte Carlo sample. The solid histogram and points show the results for the inclusive sample and high mass samples respectively.

7.10 Comparison of Normalised Cross Sections

Figure 7.26 shows the normalised cross sections differential in $x_{\gamma;4J}^{OBS}$, y, ψ_{AB}, X_A, $\cos\theta_{3'}$, $\psi_{3'}$, $X_{3'}$ and $X_{4'}$. Also shown are the normalised cross sections differential in $\cos\theta_{3'}$ for the regions $x_{\gamma;4J}^{OBS} < 0.75$ and $x_{\gamma;4J}^{OBS} > 0.75$. The solid and dashed histograms show the results for the inclusive and high mass samples, respectively. The purpose of this section is to study the differences in shape between the inclusive and high mass cross sections and so, for clarity, no error bars are shown.

The $x_{\gamma;4J}^{OBS}$ distribution for the inclusive sample has a maximum at ~ 0.55 and another at ~ 0.85. The depletion of events at $x_{\gamma;4J}^{OBS} \sim 0.7$ corresponds to the cross-over between resolved and direct dominated events (see also Fig. 7.30a)). In contrast, the high mass cross section rises from the minimum at 0.2 to reach a maximum at high $x_{\gamma;4J}^{OBS}$. Comparison of the shape of the cross sections shows that the inclusive sample has a much higher proportion of events at low $x_{\gamma;4J}^{OBS}$, relative to the high mass sample. This means that inclusive events have a larger probability that multi-parton interactions will occur and influence the properties of the hadronic final state.

The inclusive y cross section peaks at ~ 0.5 while the corresponding high mass distribution rises up to the kinematic threshold of $y = 0.85$. This shows that the fraction of the lepton beam energy carried by the interacting photon tends to be larger in high mass events, which is expected, since the jets are generally of higher transverse energy.

The angular variable ψ_{AB} and the energy sharing variable X_A describe the (A+B)-system. There are no equivalent variables in the three- or two-jet cases. The ψ_{AB} variable represents the angle in the four jet rest frame between the plane containing jets A and B, and that containing the beam and the (A+B)-vector $p_{AB} = p_A + p_B$. The ψ_{AB} distributions for both the inclusive and high mass samples show a suppression of the phase space available for four jet production at $\psi_{AB} = 0$ and π. This arises from restrictions on the minimum possible angular separation imposed by the jet algorithm and the minimum transverse energy requirements. Taking into account this suppression, the data suggest that the ψ_{AB} distribution is approximately flat indicating that the orientation of jets A and B is uniform in phase space. This, in turn, implies that their orientation is decorrelated from the hard scatter. The distribution of X_A in the inclusive and high mass regions fall steeply from the minimum value of 0.5. This shows that jets A and B tend to carry approximately equal fractions of energy. However, the average value of X_A is slightly lower in the inclusive sample than for high mass events.

The $\cos\theta_{3'}$ variable gives the angle of the highest energy pseudo-jet with respect to the beam. The equivalent variables in the two and three jet cases depend *only* on the orientation of the highest energy jet. However, in the four jet case, the highest energy

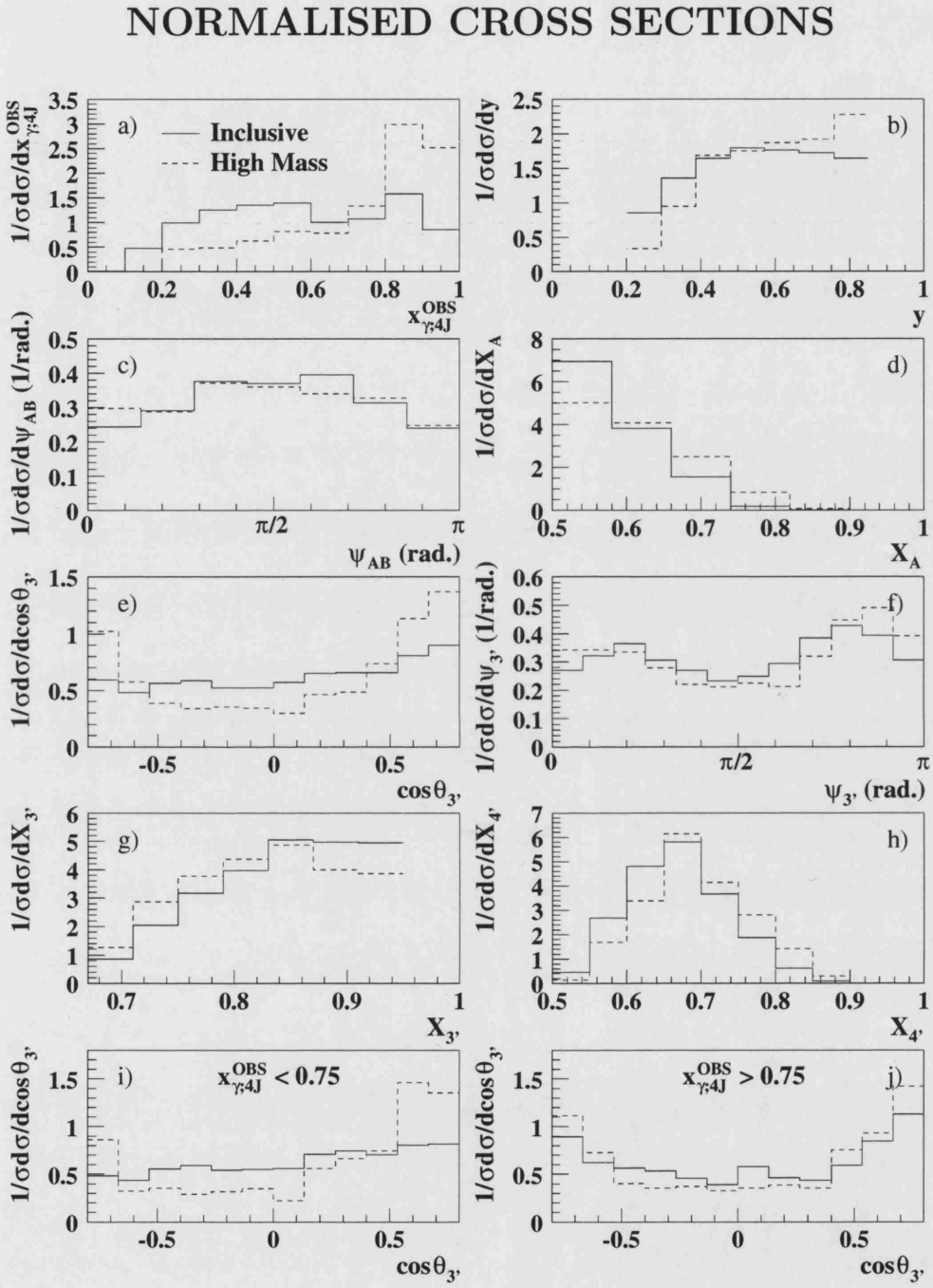

Figure 7.26: The normalised cross sections differential in $x^{\mathrm{OBS}}_{\gamma;4\mathrm{J}}$, y, ψ_{AB}, X_{A}, $\cos\theta_{3'}$, $\psi_{3'}$, $X_{3'}$ and $X_{4'}$. The dashed and solid histograms show the inclusive and high mass cross sections respectively.

pseudo-jet may be the combined (A+B)-system. This means that the distribution of $\cos\theta_{3'}$ may also be expected to be sensitive to the orientation of the lower energy jets. The inclusive $\cos\theta_{3'}$ distribution is relatively flat, although a slight asymmetry is apparent in favour of the proton direction. This may be due to residual bias from the jet E_{T} and η requirements. The corresponding high mass distribution is very different and peaks strongly at $\cos\theta_{3'} \pm 0.8$. This indicates that the highest energy pseudo-jet in the centre-of-mass frame is likely to be produced at small, rather than large, angles to the beam direction, as in Rutherford scattering. This behaviour is also observed in previous measurements of the three jet variable $\cos\theta_3$ [19, 171] which also required a high invariant mass of the multi-jet system. As for the inclusive case, an asymmetry towards the forward direction is apparent. The inclusive and high mass distributions of $\cos\theta_{3'}$ in the regions $x_{\gamma;4\mathrm{J}}^{\mathrm{OBS}} < 0.75$ and $x_{\gamma;4\mathrm{J}}^{\mathrm{OBS}} > 0.75$ are also shown. In the resolved-enhanced region, the inclusive distribution is relatively flat. However, in the direct-enhanced region, the data are peaked at $\cos\theta_{3'} \pm 0.8$. The corresponding high mass distributions show that the distribution peaks at small scattering angles in both the resolved-enhanced and the direct-enhanced regions. These results suggest that the flatness of the inclusive $\cos\theta_{3'}$ distribution shown in Fig. 7.26e) may arise partially as a result of the influence of the underlying event, since this shape is only present in the low mass, resolved-enhanced region.

The $\psi_{3'}$ variables gives the angle in the centre-of-mass frame between the plane containing the three pseudo-jets and that containing the highest energy pseudo-jet and the beam. The distribution is therefore expected to be sensitive to the lower energy jets in the event. As for the ψ_{AB} distribution, a suppression of phase space is apparent at 0 and π. Taking this into account, the data suggest that the distribution is peaked at $\psi_{3'} = 0$ and π. This is a configuration in which the lowest energy pseudo-jet tends to lie close to the plane containing the highest energy pseudo-jet and the beam in the centre-of-mass. The production of the lowest energy pseudo-jet at large angles is suppressed. This results from the effects of QCD coherence as determined in a previous three jet analysis [19]. Coherence effects arise due to the interference of soft gluon radiation amplitudes which results in a restriction of the phase space available for soft gluon emission. Both the inclusive and high mass distributions show similar features.

The inclusive $X_{3'}$ distribution rises up to ~ 0.85 and then remains approximately flat, indicating that the highest energy pseudo-jet tends to take a large fraction of the available energy. The high mass distribution has a lower average value of $X_{3'}$ relative to inclusive events. Both the inclusive and high mass distributions of $X_{4'}$ peak at ~ 0.65. However, the inclusive distribution has a lower average value that the high mass distribution. This is correlated to the higher average value of $X_{3'}$. Note also, that the lowest energy pseudo-jet also carries a significant proportion of the total available energy.

7.11 Systematic Uncertainties and Cross-Checks

In order to estimate the sensitivity of the measured cross sections to migrations across the kinematic boundaries and to the modelling of the data, several systematic checks and cross-checks have been performed. These have been broadly separated into three separate categories:

1. **Model Dependence**
   All systematics associated with the uncertainty in the correct modelling of the data come under this category. The nominal cross section has been obtained using the PYTHIA + MPI Monte Carlo sample for the unfolding. Direct and resolved events have been added in the ratio that gives the best fit to the uncorrected $x_{\gamma;4J}^{OBS}$ distribution.

   (a) For the inclusive sample, the cross section measurements have been checked using the PYTHIA + MPI sample before re-weighting for the unfolding. For the y and $x_{\gamma;4J}^{OBS}$ cross sections this has been taken as a systematic uncertainty on the final measurement. For all other variables, this has been treated as a consistency check only. The reasons for this are explained later in this section.

   (b) The dependence of the unfolding on the fraction of direct and resolved events used in the photoproduction sample has also been tested by combining the resolved and direct events in the ratio of the generated Monte Carlo cross sections, rather than in the ratio obtained from the χ^2-fit. This can have a significant effect particularly since direct and resolved events have different resolutions for the various kinematic variables. This has been used as a consistency check only.

2. **Kinematic Selection**
   The effects on the cross section of events migrating in and out of the kinematic range of interest were investigated by systematically varying the cuts that define the detector level event sample. The z_{vtx} cut was varied by ± 10 cm, the $\not{p}_T / E_T^{1/2}$ cut was varied by ± 0.2 GeV$^{1/2}$ and the y_e cut was varied by 0.05. All other cuts were varied by $\pm 1\sigma$ the resolution on the variable of interest. The changes to the cuts were applied to both data and Monte Carlo and the results have been assigned as uncorrelated systematic uncertainties.

3. **Calorimeter Energy Scale**
   There is an uncertainty associated with the difference between data and Monte Carlo in the simulation of the energy scale of the calorimeter (see Section 4.4.3). For jets with transverse energy less than 7 GeV, this was taken to be $\pm 3\%$ while

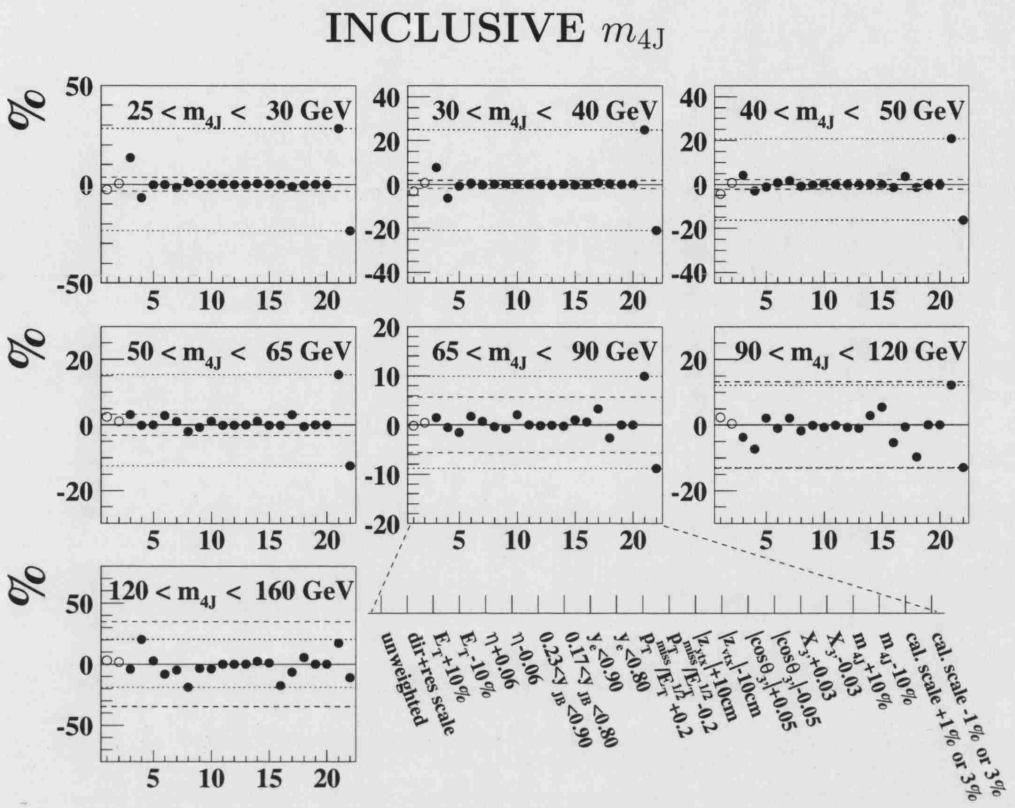

Figure 7.27: The percentage difference between the check result (numbers 1-22 in Tab. 7.3) and nominal result for the inclusive $d\sigma/dm_{4J}$ cross section. The solid line indicates the nominal value. The dashed lines show the percentage statistical uncertainty on the nominal result. The dotted lines indicate the largest systematic uncertainty in each bin (upper and lower separately). Also shown is an enlarged version of the x-axis which labels each check.

for jets of higher energy, an uncertainty of $\pm 1\%$ was used. The value of y_{JB} was varied by $\pm 3\%$ in every event, independent of the jet transverse energies. This change was applied only to data and is assigned as a correlated systematic uncertainty.

Note also that there is a 1.6% uncertainty in the determination of the luminosity for the data obtained in this thesis. This has not been assigned as a systematic uncertainty in the final measurement.

The checks that are listed under points 1-3, above, are summarised in Tab. 7.3. The checks have been performed for the measurement of both the total and normalised cross sections. The results for the total cross section differential in m_{4J} are presented in Fig. 7.27. The results for all other cross sections are shown in Appendix F. In each

Check Number	Nominal Selection	Check Selection
MODEL DEPENDENCE		
1	PYTHIA + MPI (re-weighted)	PYTHIA + MPI
RATIO OF DIRECT AND RESOLVED		
2	Fraction from χ^2-Fit	Generated Cross Section Fraction
KINEMATIC CUTS		
3	$E_{\mathrm{T}}^{1,2,3,4} > 6.0, 6.0, 5.0, 5.0$ GeV	$E_{\mathrm{T}}^{1,2,3,4} > 6.96, 6.96, 5.80, 5.80$
4		$E_{\mathrm{T}}^{1,2,3,4} > 5.04, 5.04, 4.20, 4.20$
5	$-2.40 < \eta^{1,2,3,4} < 2.40$	$-2.34 < \eta^{1,2,3,4} < 2.46$
6		$-2.46 < \eta^{1,2,3,4} < 2.34$
7	$0.20 < y_{\mathrm{JB}} < 0.85$	$0.23 < y_{\mathrm{JB}} < 0.90$
8		$0.17 < y_{\mathrm{JB}} < 0.80$
9	$y_e < 0.85$	$y_e < 0.90$
10		$y_e < 0.80$
11	$\not{p}_{\mathrm{T}} / E_{\mathrm{T}}^{1/2} < 2.0$ GeV$^{1/2}$	$\not{p}_{\mathrm{T}} / E_{\mathrm{T}}^{1/2} < 2.2$ GeV$^{1/2}$
12		$\not{p}_{\mathrm{T}} / E_{\mathrm{T}}^{1/2} < 1.8$ GeV$^{1/2}$
13	$\lvert z_{\mathrm{vtx}} \rvert < 40$ cm	$\lvert z_{\mathrm{vtx}} \rvert < 50$ cm
14		$\lvert z_{\mathrm{vtx}} \rvert < 30$ cm
15	$-0.8 < \cos\theta_{3'} < 0.8$	$-0.75 < \cos\theta_{3'} < 0.85$
16		$-0.85 < \cos\theta_{3'} < 0.75$
17	$X_{3'} < 0.95$	$X_{3'} < 0.98$
18		$X_{3'} < 0.92$
ADDITIONAL CUTS FOR HIGH-MASS EVENTS ONLY		
19	$m_{4\mathrm{J}} > 50$ GeV	$m_{4\mathrm{J}} > 55$ GeV
20		$m_{4\mathrm{J}} > 45$ GeV
CALORIMETER ENERGY SCALE		
21	$E_{\mathrm{T}}^{\mathrm{jet}}$, y_{JB}	$E_{\mathrm{T}}^{\mathrm{jet}} + 1/3\%$, $y_{\mathrm{JB}} + 3\%$
22		$E_{\mathrm{T}}^{\mathrm{jet}} - 1/3\%$, $y_{\mathrm{JB}} - 3\%$

Table 7.3: The nominal event selection and reconstruction criteria compared to those used for the estimation of the systematic uncertainties. Numbers 1-22 correspond to the points (from left to right) in each bin of the plots shown in Fig. 7.27.

case, all checks are presented as a percentage difference between the the check and the nominal cross section values. In each plot, the solid and dashed lines respectively indicate the nominal value and the statistical uncertainty on the nominal result. The dotted lines indicate the largest systematic in each bin (upper and lower separately). The numbers on the x-axis correspond to the numbers in the left-hand column of Tab. 7.3. Only the solid points are taken as systematic uncertainties on the final measurement. The remaining checks (hollow points) are used only as cross-checks.

The cross sections differential in the four jet centre-of-mass observables show only a small change relative to the nominal when the Monte Carlo before re-weighting is used for the unfolding. However, significant changes are observed for the cross section differential in y, such that the shape of the resulting distribution is marginally altered. This is shown more clearly in Fig. 7.28, which compares the unfolded cross sections for several variables before and after Monte Carlo re-weighting. The change in the y cross section is shown to be significant, particularly at low and high y, probably due to the effects of long-range migrations between bins which are different in the Monte Carlo samples before and after re-weighting. The value of $x_{\gamma;4\mathrm{J}}^{\mathrm{OBS}}$ is correlated to that of y. Therefore, in order to be conservative when assigning the systematic uncertainties, the difference due to the re-weighting has been assigned as a systematic in both the $x_{\gamma;4\mathrm{J}}^{\mathrm{OBS}}$ and y cross sections. For all other variables, the effect of the Monte Carlo re-weighting has only a small effect on the extracted cross section. This is illustrated by the $\cos\theta_{3'}$ and $\psi_{3'}$ distributions, shown in Fig. 7.28. The cross sections differential in all other centre-of-mass observables show a similar level of agreement.

For both the inclusive and high mass cross sections, the largest systematic uncertainty arises from the changes to the jet transverse energy cuts and the calorimeter energy scale uncertainty. Also significant in the high mass cross sections, are the changes due to varying the cuts on $m_{4\mathrm{J}}$. The results from all other checks, generally lie within the statistical uncertainty on the measurement.

As an additional consistency check, the four jet cross sections obtained from the 1996 and 1997 data individually have been compared. Figure 7.29 shows the cross section differential in $X_{3'}$ for the inclusive and high mass samples. The results show that the cross sections for the individual years are consistent within the independent statistical uncertainties and that the ratios of the two cross sections are approximately flat and centred on unity. The cross sections differential in all other measured variables show similar agreement.

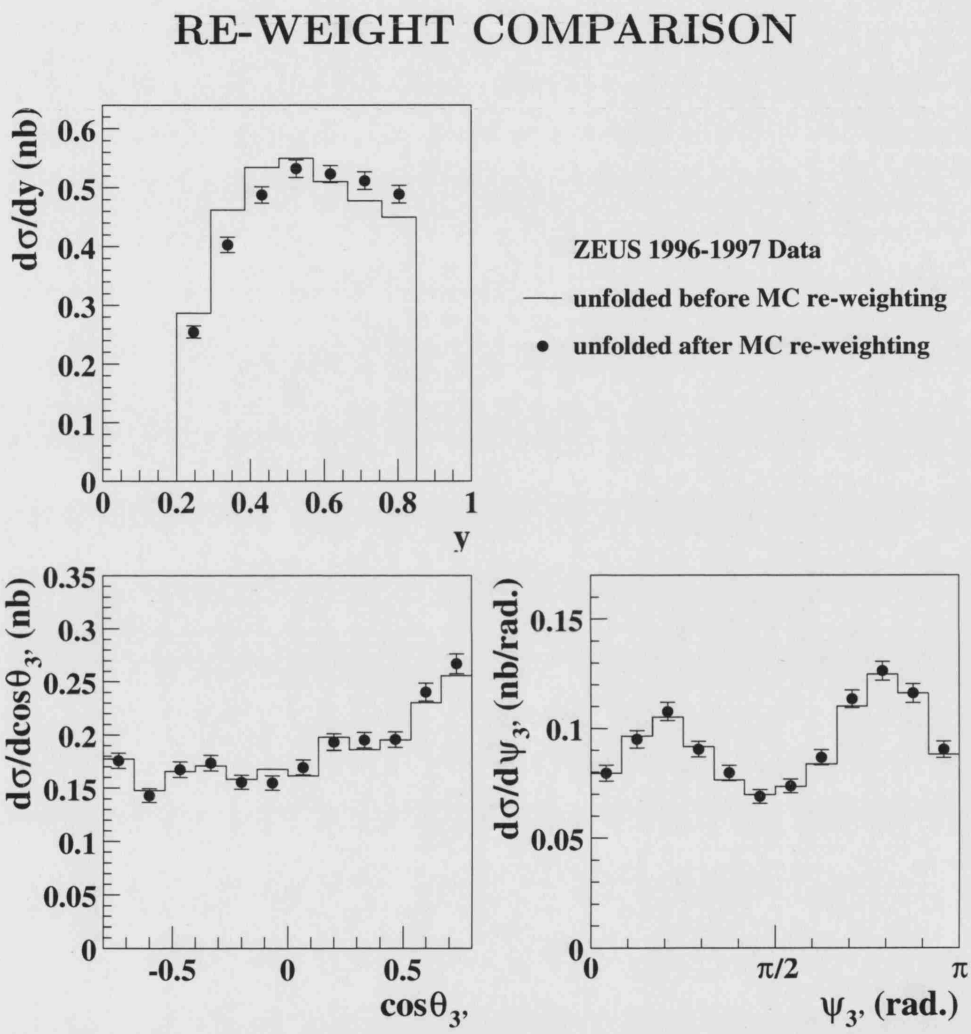

Figure 7.28: The inclusive cross sections differential in y, $\cos\theta_{3'}$ and $\psi_{3'}$. The histogram and solid points show the cross section resulting from using the PYTHIA + MPI for the unfolding before and after re-weighting respectively. The nominal measurement corresponds to the solid points.

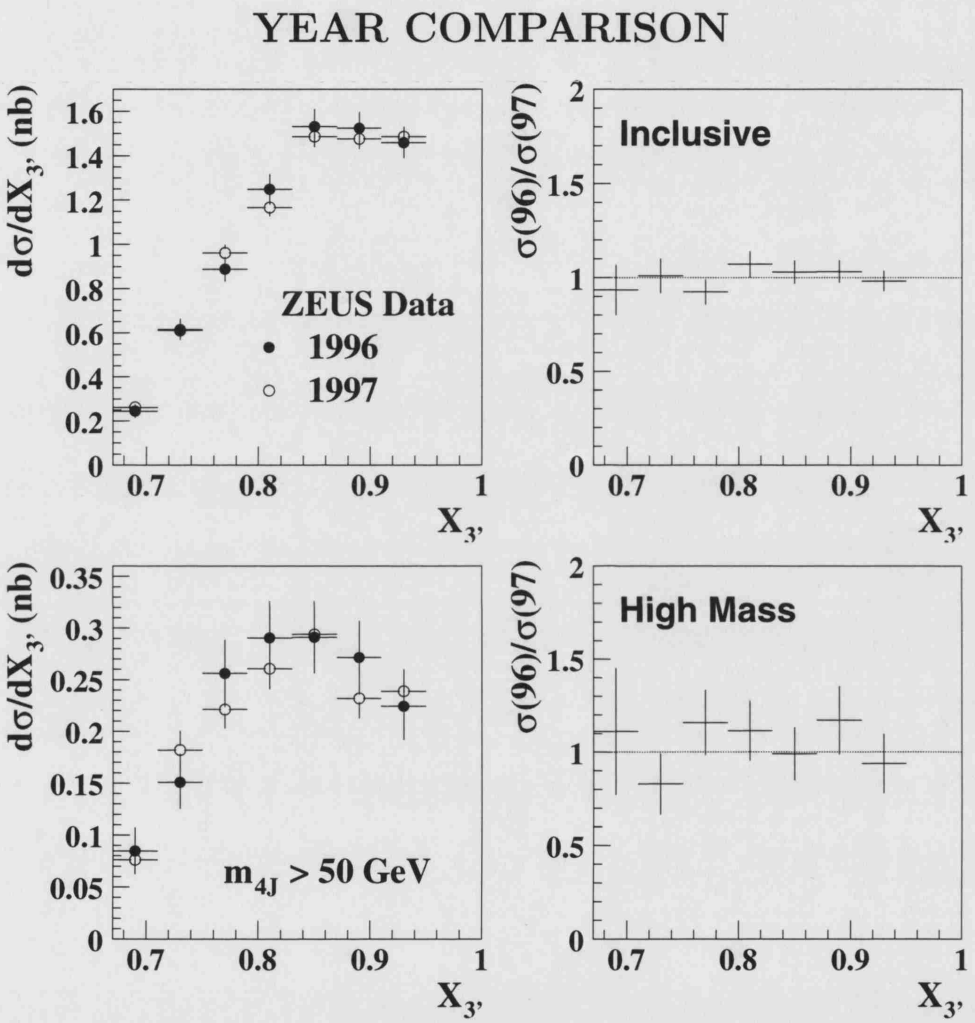

Figure 7.29: Left: The cross section differential in $X_{3'}$ for the inclusive and high mass samples. The solid points and open circles show the corrected ZEUS data from 1996 and 1997 data, respectively. Right: The ratio of the 1996:1997 cross sections.

7.12 Results and Discussion

At LO, four jet photoproduction is an intrinsically $\mathcal{O}(\alpha\alpha_s^3)$ process. There are no fixed order pQCD calculations currently available for such processes. However, parton shower models, which use the LO matrix elements for $2 \rightarrow 2$ scattering, together with a simulation of initial- and final-state QCD radiation, can model multi-parton final states by approximating the effects of higher order matrix elements. Such models allow, in addition, a full simulation of the hadronisation process and include options to simulate the effects of an underlying event.

The HERWIG 6.4 and PYTHIA 6.206 Monte Carlo generators have been used to simulate four jet photoproduction events for comparison with the data of this analysis. Direct and resolved events have been generated separately and combined according to their relative cross sections. In LL Monte Carlo generators, the normalisation of the predicted cross sections have large uncertainties due to higher order corrections and uncertainties in the scale at which α_s should be evaluated (see also Sections 2.15 and A.1). In an attempt to sensibly constrain the normalisation, the cross section predictions from all models have been scaled by factors which have been determined from precise high-E_{T} jet measurements. Further details regarding the choice of normalisation are given in Section 7.14. Unless otherwise stated, the proton and photon PDFs for all models have been generated using the CTEQ5L and SaS2D sets, respectively. Throughout the rest of this chapter, the measured cross sections are compared to the predictions of a number of different HERWIG and PYTHIA models. The main parameters and the relevant scale factors, for each model shown, are summarised in Tab. 7.4 for HERWIG and Tab. 7.5 for PYTHIA.

7.12.1 Standard Parton Shower Models

In this section, the data are compared to the predictions of standard HERWIG and PYTHIA in order to assess the ability of the models to describe the measured distributions from this analysis. The models shown in this section will be referred to simply as HERWIG and PYTHIA, the parameters of which are summarised in Tabs. 7.4 and 7.5 respectively. Neither the HERWIG nor the PYTHIA models shown in this section include a simulation of multi-parton interactions. Note that the *default* setting in PYTHIA does include a simulation of multi-parton interactions according to the simplest available model (MSTP(82)=1). However, in this section the model shown has been generated with the same parameters as that of default HERWIG. This has been done in order to assess the slightly different underlying physics models present in the two generators, without any additional uncertainties present from the inclusion of multi-parton interactions.

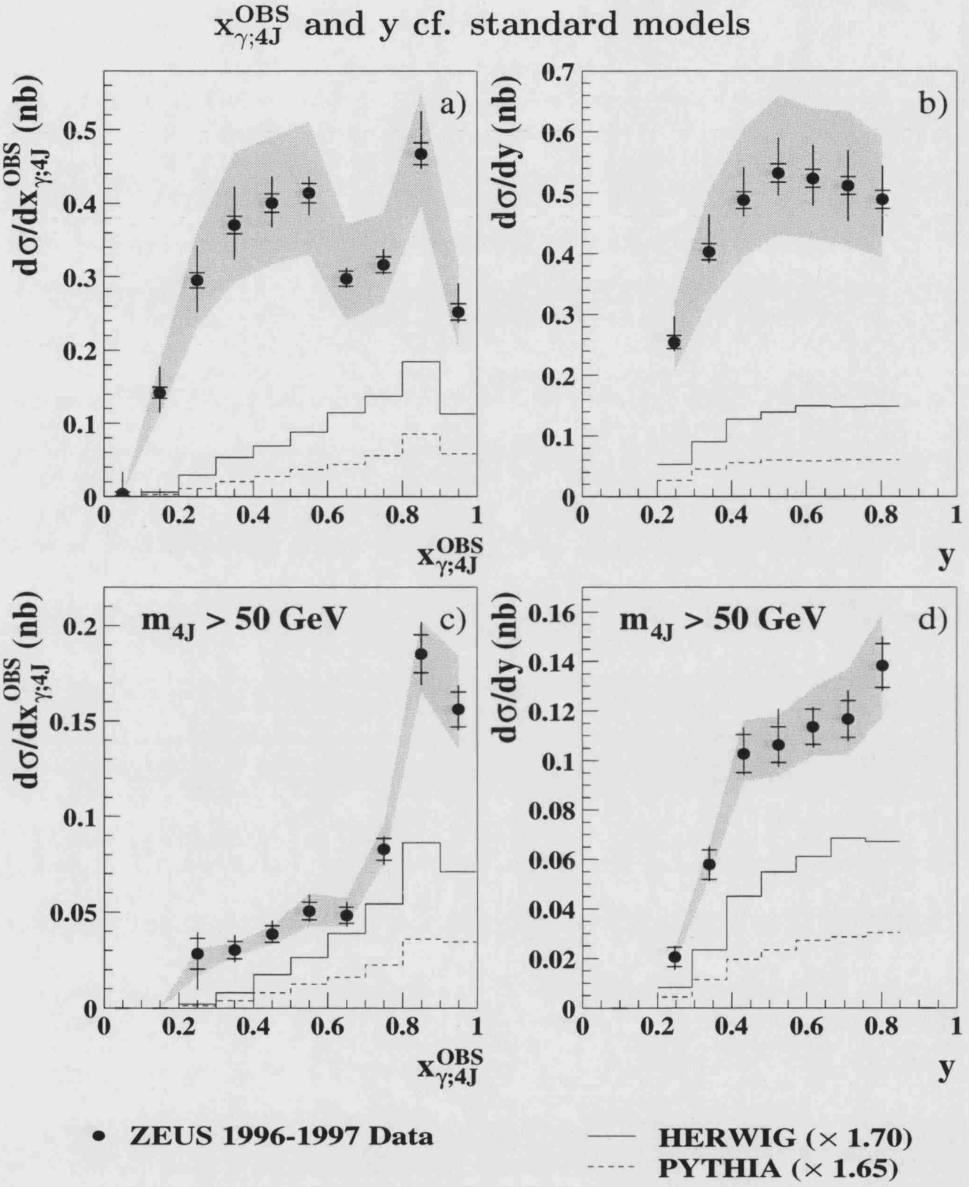

Figure 7.30: The total cross sections differential in $x_{\gamma;4J}^{\mathrm{OBS}}$ and y. The results for the inclusive sample are shown in a) and b) and those for the high mass sample are shown in c) and d). The solid points show the corrected ZEUS data. The inner error bars show the statistical uncertainty and the outer error bars show the statistical and uncorrelated systematic uncertainties combined in quadrature. The shaded band represents the calorimeter energy scale uncertainty. Compared to the data are the predictions of HERWIG and PYTHIA.

Figure 7.30 shows the cross sections differential in $x_{\gamma;4J}^{OBS}$ and y for the inclusive and high mass samples. Both HERWIG and PYTHIA underestimate the measured cross sections, even after scaling by the factors listed in Tabs. 7.4 and 7.5. Furthermore, the inclusive cross section is underestimated by a larger amount than the high mass cross section. This shows that neither the rate of four jet production, relative to that of high-E_T two jet production, nor the rate of high-to-low mass four jet photoproduction is properly described by the models.

The inclusive $x_{\gamma;4J}^{OBS}$ distribution peaks at ~ 0.55 and ~ 0.85. However, the predictions of HERWIG and PYTHIA peak only at high $x_{\gamma;4J}^{OBS}$, and are unable to describe the enhancement at low values. This shows the need for additional energy flow in the low $x_{\gamma;4J}^{OBS}$ region. The shape of the y cross section is also inadequately described by the models. In particular, the data rise to a maximum at $\sim 0.5-0.6$ and then show a fall-off as a function of increasing y, while the models are consistent with a rise up to kinematic limit of $y = 0.85$. The high mass distributions are also inadequately described. In particular, the amount of activity in the high $x_{\gamma;4J}^{OBS}$ region is underestimated relative to the activity in the resolved region. This may suggest that the ratio of resolved to direct events is incorrectly predicted. Since this is the first time that a measurement has been performed in this particular kinematic region, it is not surprising that these variables are not well described and this information should be used to improve future modelling of the data. However, the large discrepancy at low $x_{\gamma;4J}^{OBS}$ in the inclusive distribution cannot be accounted for by a change to the ratio of direct and resolved events and must, therefore, arise from a different source. Most importantly, the results indicate the need for an increased cross section at low $x_{\gamma;4J}^{OBS}$.

The dynamics of four jet production can be investigated by studying the four jet centre-of-mass observables, defined in Section 7.2. It has already been shown that the normalisation of the cross section is significantly underestimated by the models. However, it is also useful to study the description of the shape of the measured variables.

In order to study the description of the shapes of the four jet centre-of-mass observables, the normalised cross sections have been measured. The results for the inclusive cross sections are shown in Fig. 7.31. The shape of the distributions are generally not well described by either HERWIG or PYTHIA. In particular, the average values of X_A and $X_{4'}$ are overestimated by the models, while that of $X_{3'}$ is underestimated. In addition, the model predictions for $\cos\theta_{3'}$, show a significant enhancement in the forward and backward direction, which is not obvious in the data. It is also apparent that HERWIG is more strongly peaked at $\cos\theta_{3'} \pm 0.8$ than PYTHIA. In the $\psi_{3'}$ distribution, the suppression at $\sim \pi/2$ arises due to the effects of QCD coherence. In parton shower models, this is implemented as angular ordering. The results show that the general trend of the data are reasonably described by both models. However, the effects of coherence appear to be slightly stronger in HERWIG than in PYTHIA, with the data favouring the latter model.

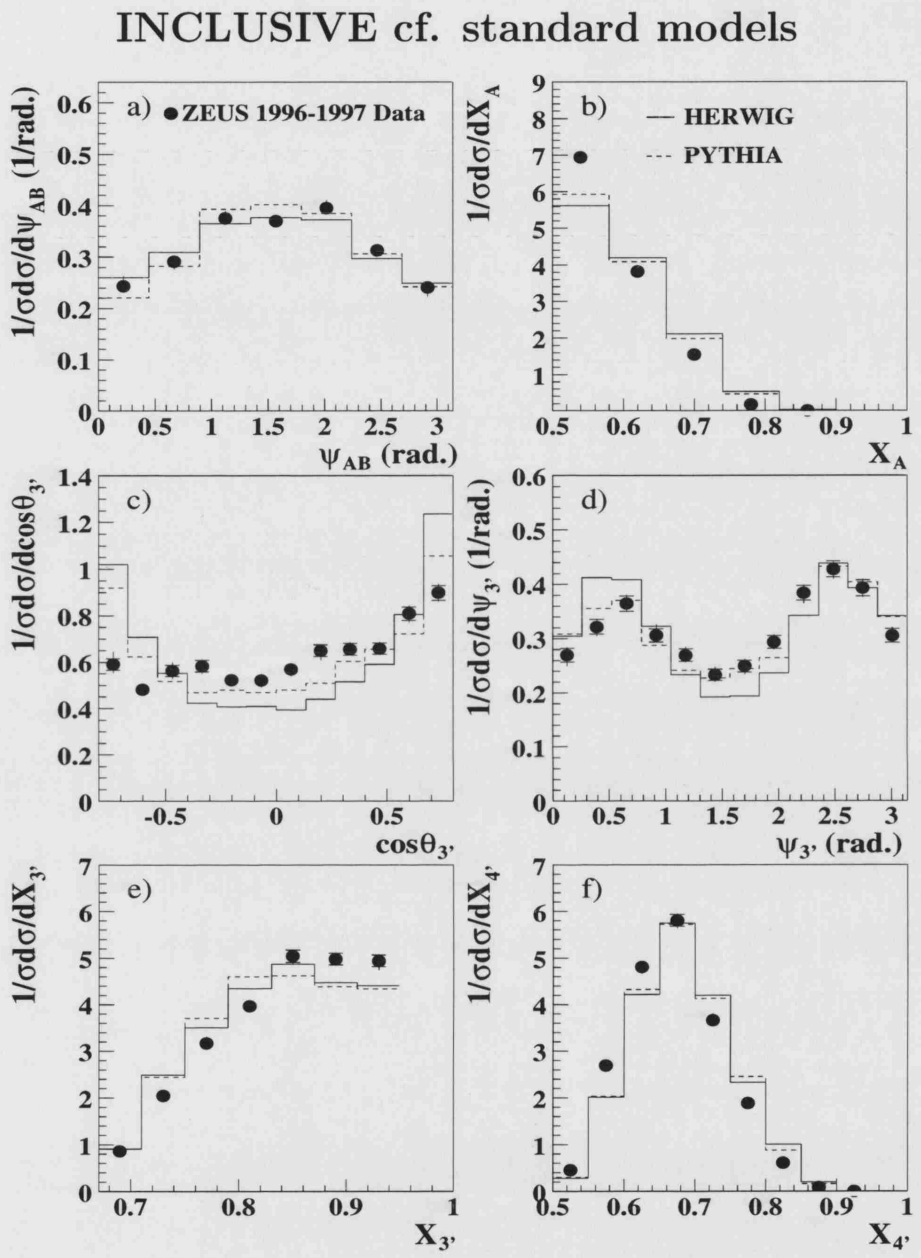

Figure 7.31: The normalised cross sections differential in $\psi_{\rm AB}$, $X_{\rm A}$, $\cos\theta_{3'}$, $\psi_{3'}$, $X_{3'}$ and $X_{4'}$ for the inclusive sample. The solid points show the corrected ZEUS data. The inner error bars show the statistical uncertainty and the outer error bars show the statistical and uncorrelated systematic uncertainties combined in quadrature. In the cases that the error bars are not visible, the uncertainties are smaller than the size of the point. Compared to the data are the predictions of HERWIG and PYTHIA.

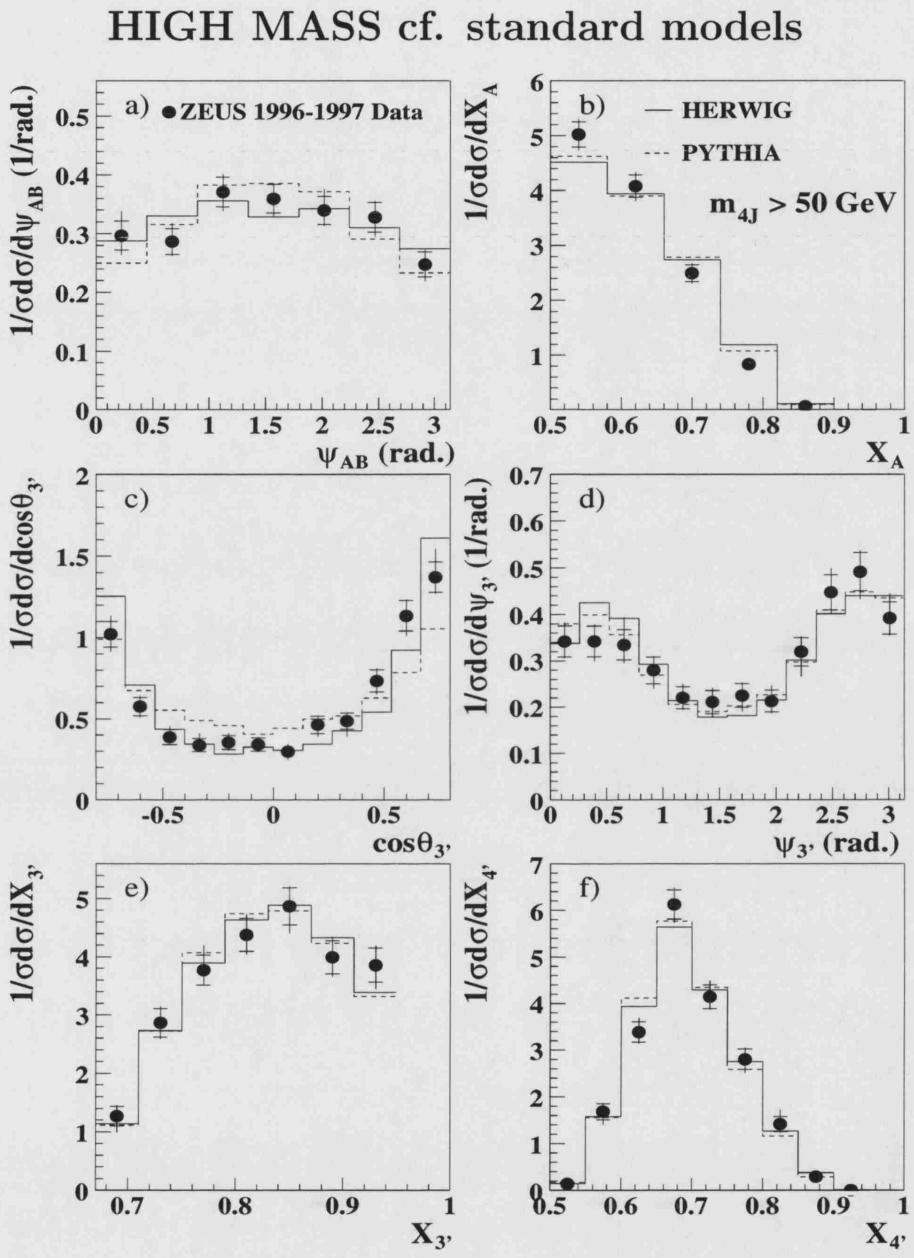

Figure 7.32: The normalised cross sections differential in $\psi_{\rm AB}$, $X_{\rm A}$, $\cos\theta_{3'}$, $\psi_{3'}$, $X_{3'}$ and $X_{4'}$ for the high mass sample. The solid points show the corrected ZEUS data. The inner error bars show the statistical uncertainty and the outer error bars show the statistical and uncorrelated systematic uncertainties combined in quadrature. In the cases that the error bars are not visible, the uncertainties are smaller than the size of the point. Compared to the data are the predictions of HERWIG and PYTHIA.

The corresponding high mass cross sections are shown in Fig. 7.32. The description of the data by both HERWIG and PYTHIA is reasonable with the largest difference between the two models arising in the $\cos\theta_{3'}$ distribution. For this variable, the PYTHIA model gives a distribution which is less peaked at $\cos\theta_{3'} \pm 0.8$ than in HERWIG. The data appear to be slightly better described by the HERWIG model, although the statistics are not sufficient to fully distinguish between the two.

In summary, the magnitude of both the inclusive and the high mass cross sections are inadequately described by the HERWIG and PYTHIA models shown in this section, even after constraining the normalisation to precise high-E_T two jet data. While the shape of the high mass distributions are reasonably well described by standard parton shower models, the inclusive energy sharing and angular variables are not. The results of this section, particularly the differences between data and Monte Carlo in both shape and normalisation for the inclusive sample, along with the need for additional flow in the low $x_{\gamma;4J}^{OBS}$ region, motivates the study of models which include simulations of an underlying event.

7.12.2 The Underlying Event Model

In photoproduction, the concept of an underlying event is only relevant for resolved photon events since the secondary scatters (whether soft or hard) require the presence of a photon, as well as a proton, remnant. In HERWIG, two underlying event models are available. The first is the so-called Soft Underlying Event (SUE) model. This is a simulation of soft collisions between beam clusters containing spectator partons. The probability of a soft scatter occurring is controlled by the parameter PRSOF. Secondly, the Jimmy [81] package, used in conjunction with HERWIG allows the simulation of multi-parton interactions. Multi-parton interactions form a hard, partonic contribution to the underlying event. In addition, the secondary scatters may be sufficiently hard to produce an additional pair of jets. The PYTHIA program also allows the generation of multi-parton interactions [174] and the simplest available model is the default in PYTHIA. The multi-parton interaction models available in HERWIG and PYTHIA are described in more detail in Appendix C.

In this section, the measured differential cross sections are compared to a number of different underlying event models. For HERWIG, both a soft underlying event model and a multi-parton interaction model have been generated. These models will be referred to as HERWIG + $SUE_{0.3}$ and HERWIG + Jimmy respectively. In the soft underlying event model the value of PRSOF= 0.3[¶] has been chosen in accordance with a recent H1 tuning [170]. For PYTHIA, a simple model with MSTP(82)=1 has been generated. This model will be referred to as PYTHIA + MPI(1). The values of p_T^{min} and p_T^{mi} for this model are motivated by a previous HERA tuning [175].

[¶]The default value in HERWIG is PRSOF=1.0.

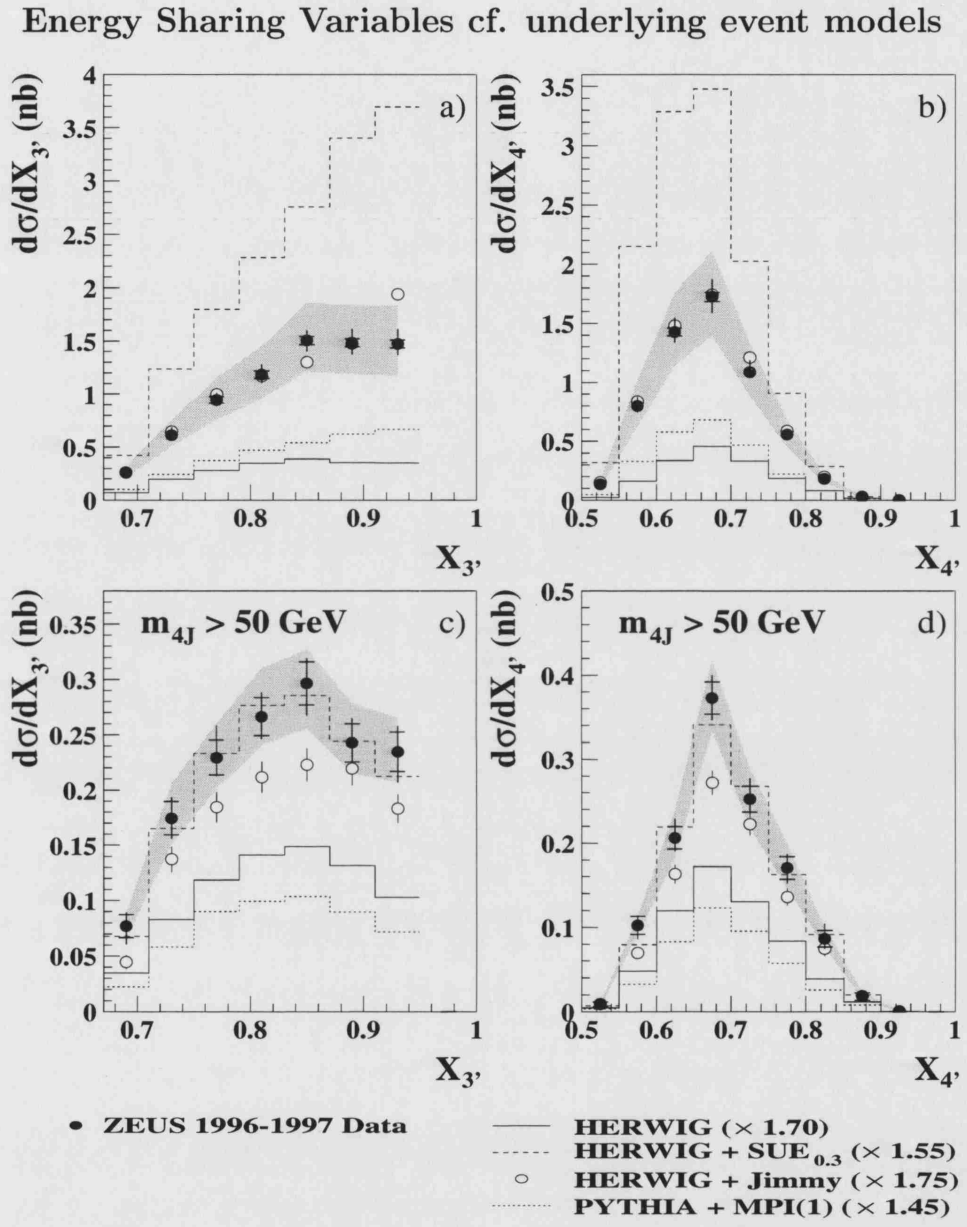

Figure 7.33: The inclusive and high mass cross section differential in $X_{3'}$ and $X_{4'}$. The results for the inclusive sample are shown in a) and b) and those for the high mass sample in c) and d). The solid points show the corrected ZEUS data. The inner error bars show the statistical uncertainty and the outer error bars show the statistical and systematic uncertainties combined in quadrature. The shaded band indicates the calorimeter energy scale uncertainty. Compared to the data are the predictions of HERWIG, HERWIG + $\text{SUE}_{0.3}$, HERWIG + Jimmy and PYTHIA + MPI(1).

Figure 7.33 shows the inclusive and high mass cross sections differential in $X_{3'}$ and $X_{4'}$. Compared to the data are the predictions of HERWIG, HERWIG + $\text{SUE}_{0.3}$, HERWIG + Jimmy and PYTHIA + MPI(1). The inclusive cross sections show an extremely strong sensitivity to the underlying event. While it has already been shown that the prediction of HERWIG lies below the data, the cross section for the soft underlying event model lies significantly above the measured points. In contrast, the prediction of the HERWIG + Jimmy, following scaling by the relevant factor listed in Tab. 7.4, is in close correspondence with the measurement. The PYTHIA + MPI(1) model gives a reasonable description of the shape, although the normalisation of the data is underestimated by this model. The high mass sample shows a reduced sensitivity to the underlying event model, although some differences in the magnitude of the predicted cross sections from the different models are still apparent.

To assess the extent to which the shapes of the measured cross sections are described by the different models, the normalised cross sections have been studied. Figure 7.34 shows the normalised cross sections differential in the four jet centre-of-mass observables for the inclusive sample of events. It has already been shown that the HERWIG model with no simulation of an underlying event, is not able to adequately describe the shape of the energy sharing variables X_{A}, $X_{3'}$ and $X_{4'}$, or of the angular variables $\cos\theta_{3'}$. The HERWIG + $\text{SUE}_{0.3}$ model is also disfavoured by the data. In particular, the shape of the pseudo-three-jet angular distributions show an enhancement at $\psi_{3'} \sim \pi/2$ and $\cos\theta_{3'} \sim 0$. The soft underlying event model produces additional soft energy flow, which is distributed approximately uniformly in η and ϕ. The shape of the angular distributions according to this model may, therefore, tend towards that expected from jets produced uniformly in phase space. The energy sharing distributions are also inadequately described by HERWIG + $\text{SUE}_{0.3}$ model, showing the opposite trend in behaviour to standard HERWIG. Specifically, the measured distribution of $X_{3'}$ has a lower average value than the prediction of the soft underlying event model and this is correlated to the higher average value of $X_{4'}$ relative to the model prediction. The multi-parton interaction model, HERWIG + Jimmy, is shown to give a significantly improved description of the data. Firstly, the description of the shape of the energy sharing variables, particularly that of $X_{4'}$, is significantly improved. In addition, the shape of the predicted $\cos\theta_{3'}$ distribution is relatively flat and slowly rising in accordance with the trend of the data. These features are also apparent in the PYTHIA + MPI(1) model. The distribution of $\cos\theta_{3'}$ has also been measured in the regions $x_{\gamma;4\text{J}}^{\text{OBS}} < 0.75$ and $x_{\gamma;4\text{J}}^{\text{OBS}} > 0.75$. The results show that all underlying event models give a reasonable description of the data in the direct-enhanced region. However, only the multi-parton interaction models are able to adequately reproduce the trend of the data in the resolved-enhanced region.

The corresponding high mass normalised cross sections are shown in Figs. 7.35. Comparison of these distributions with the model predictions shows that there is a

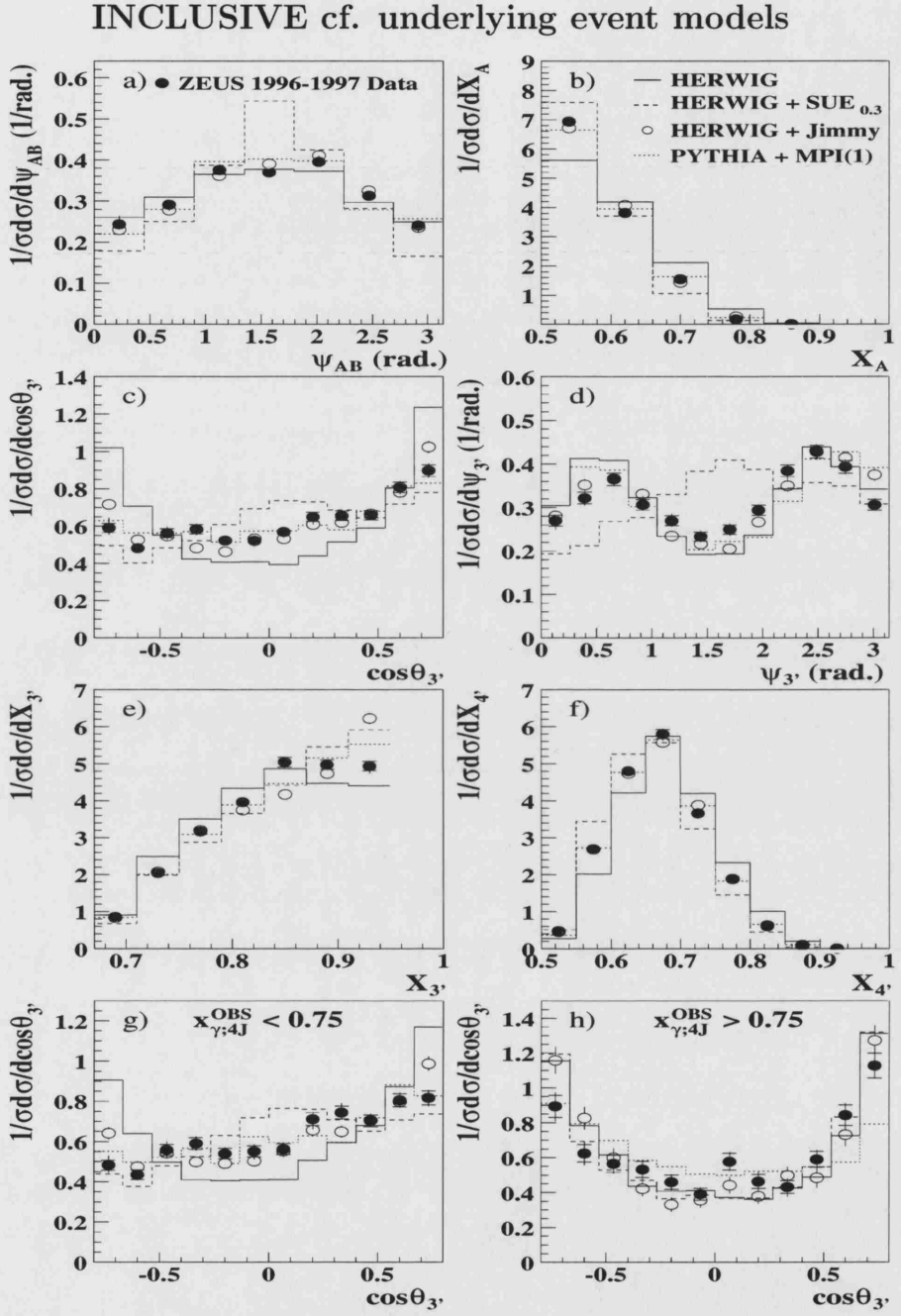

Figure 7.34: The normalised cross sections differential in ψ_{AB}, X_{A}, $\cos\theta_{3'}$, $\psi_{3'}$, $X_{3'}$ and $X_{4'}$ for the inclusive sample. The solid points show the corrected ZEUS data. The inner error bars show the statistical uncertainty and the outer error bars show the statistical and uncorrelated systematic uncertainties combined in quadrature. Compared to the data are the predictions of HERWIG, HERWIG + $\mathrm{SUE}_{0.3}$, HERWIG + Jimmy and PYTHIA + MPI(1).

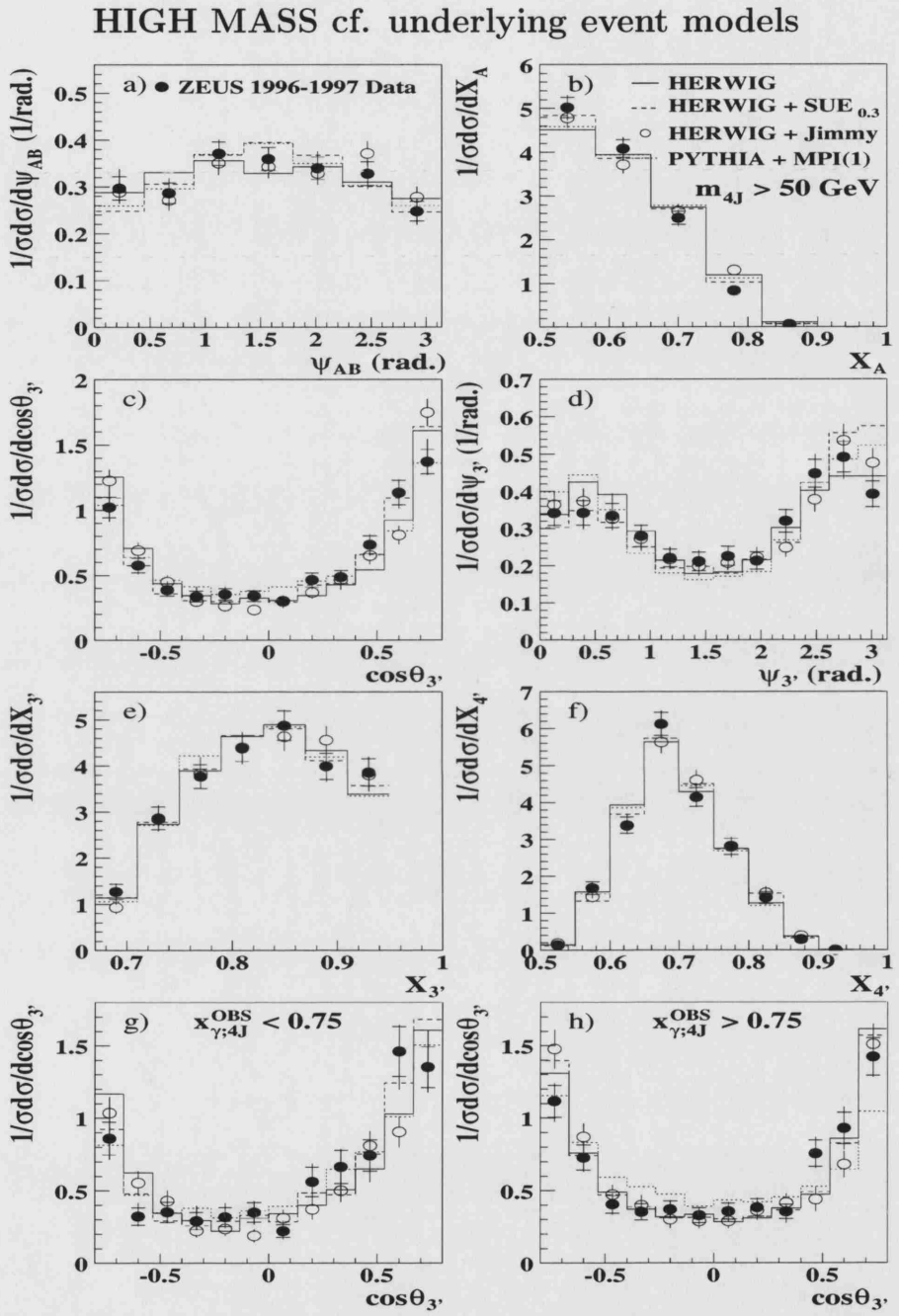

Figure 7.35: The normalised cross sections differential in ψ_{AB}, X_{A}, $\cos\theta_{3'}$, $\psi_{3'}$, $X_{3'}$ and $X_{4'}$ for the high mass sample. The solid points show the corrected ZEUS data. The inner error bars show the statistical uncertainty and the outer error bars show the statistical and uncorrelated systematic uncertainties combined in quadrature. Compared to the data are the predictions of HERWIG, HERWIG + $\mathrm{SUE}_{0.3}$, HERWIG + Jimmy and PYTHIA + MPI(1).

much reduced sensitivity in the high mass sample to the influence of long distance physics. The shape of all distributions are well described by the different models. Even the soft underlying event model, which showed a dramatic difference in shape when compared to the inclusive data, is able to give an adequate description of the high mass distributions.

The features that are observed in the measured distributions, particularly those of the energy sharing variables and the angular variable $\cos\theta_{3'}$, may be understood by considering the effects of the underlying event on the event energy and topology.

First, the effect on the fractional energy share will be considered. Energy from the underlying event will contribute to the energies of the jets themselves. Furthermore, as a result of the positive z-boost arising in the majority of QCD subprocesses, the underlying event energy will contribute more to jets in the forward, than those in the backward direction. Indeed, the large discrepancy in the forward direction between data and Monte Carlo (when no underlying event is included) has already been observed in the jet profiles shown in this chapter (see Fig. 7.15). For the inclusive sample, even a small energy contribution from the underlying event may cause a large fractional increase in the total energies of the pseudo-jets. Furthermore, the inclusive $\cos\theta_{3'}$ distribution exhibits a slight asymmetry in favour of the proton direction which shows that the highest energy pseudo-jet is slightly more likely to be in the forward, than in the backward, direction. It is therefore probable that the underlying event will contribute more to pseudo-jet $3'$ than to $4'$. If this is the case, than the average value of $X_{3'}$ would increase relative to models which contain no underlying event. This is supported by comparing the distributions of HERWIG + $\text{SUE}_{0.3}$ and HERWIG + Jimmy with that of default HERWIG in Figs. 7.34e) and f). The increase in the average value of $X_{3'}$ when an underlying event is included, is also correlated to a lower average value of $X_{4'}$. Comparison of the data with the models suggests that the soft underlying event model adds too much energy to pseudo-jet $3'$, consequently predicting a lower value of $X_{4'}$ than the data. Both HERWIG + Jimmy and PYTHIA + MPI(1) give an improved description of the distributions of $X_{3'}$ and $X_{4'}$, relative to HERWIG and HERWIG + $\text{SUE}_{0.3}$.

The shape of the $\cos\theta_{3'}$ distribution may also be a direct consequence of the effects of the underlying event. This may be understood by considering the fact that the highest energy pseudo-jet may either be simply a single jet, or it may be the combined (A+B)-system. In the case where it is a single jet, the distribution will reflect the orientation of one of the highest energy jets in the event and may be expected, therefore, to have a distribution similar to the three jet equivalent i.e. will favour small scattering angles. However, in the case where pseudo-jet $3'$ is the (A+B)-system, a different topology may arise. The *least* likely components of the combined system are the two highest transverse energy jets since they will have a large two jet invariant mass and the

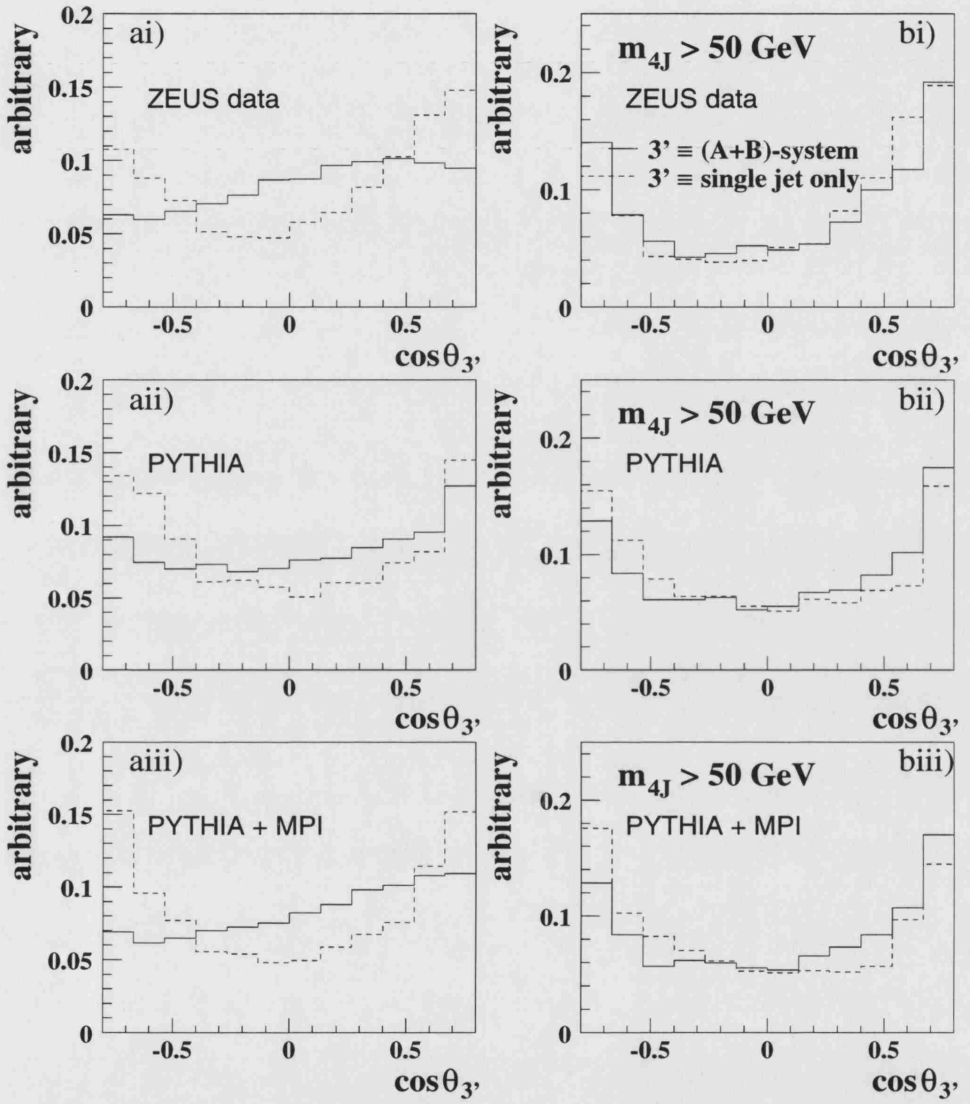

Figure 7.36: The distribution of $\cos\theta_{3'}$ separated into the case in which pseudo-jet $3'$ is equivalent to a single jet (dashed histogram) and the case where it is equivalent to the (A+B)-system (solid histogram). Figures ai), aii) and aiii) show the results for the inclusive sample from uncorrected ZEUS data, PYTHIA and PYTHIA + MPI respectively. Figures bi), bii) and biii) show the results for the high mass sample from uncorrected ZEUS data, PYTHIA and PYTHIA + MPI respectively. All distributions are shown at the detector level.

(A+B)-system is, by definition, the system with the lowest two jet mass. This means that the combined system will usually contain at least one of the lower energy jets and will, therefore, be sensitive to their orientation. In the case that the multi-jet system is produced via QCD radiation, the softest jets will tend to lie approximately collinear to the jet from which the initiating gluon was emitted. In this case, the distribution of $\cos\theta_{3'}$ will look similar to that where 3′ is simply a single jet. However, there will also be cases where the jet arising from QCD radiation will have a large p_T relative to the jet from which the initiating gluon was emitted. In this case, the axis of the (A+B)-system will not necessarily lie at small angles to the beam. In addition, multi-parton interactions introduce the possibility that the combined (A+B)-system consists of two jets which are randomly orientated with respect to each other. That is, in the presence of multi-parton interactions, the (A+B)-system is most likely to consist of one jet from the primary scatter and another from the seconday scatter, with the two scatters being uncorrelated in angle. Note that it is unlikely that both jets in the (A+B)-system originate from the same scatter, since the jets produced will have a large invariant mass. This means again that the axis of the highest energy pseudo-jet will not necessarily favour small angles and would, in fact, give rise to a much flatter distribution.

To investigate this, the distribution of $\cos\theta_{3'}$ has been studied and has been separated into two types of event: those in which pseudo-jet 3′ is simply a single jet and those in which it is the combined (A+B)-system. The results for the inclusive sample are shown in Figs. 7.36ai)-aiii) and those for the high mass sample in Figs. 7.36bi)-biii). The results of Figs. 7.36i), ii) and iii) respectively show the distributions from uncorrected ZEUS data, the PYTHIA and the PYTHIA + MPI Monte Carlo samples. The Monte Carlo results are from the samples shown earlier in this chapter (defined in Section 7.5) and are shown at the detector level to provide a direct comparison with the data. The results indicate that, in the case where the highest energy pseudo-jet is a single jet, the distribution does indeed favour small scattering angles. For the high mass sample, the distribution when the (A+B)-system forms the highest energy pseudo-jet, is also peaked at $\cos\theta_{3'} \pm 0.8$. However, the inclusive distributions show a much flatter $\cos\theta_{3'}$ distribution when the (A+B)-system forms the highest energy pseudo-jet. This is more apparent in PYTHIA + MPI than in PYTHIA since the additional contribution from multi-parton interactions would increase the number of events in which the (A+B)-axis is at large angles to the beam.

The results of this section have shown that both the shape and the normalisation of the inclusive cross sections are sensitive to inclusion of the underlying event. This shows that, not only does the energy from the underlying event increase the rate of low mass four jet production, but it may also change the topology of the event. This is due to the fact that the jet transverse energies of jets in the inclusive sample are usually low enough, that contributions from the underlying event can change the energy ordering

and fractional energy share of the jets. In contrast, the results for the high mass cross sections suggest that the effect of the underlying event in this kinematic region simply shifts the jet transverse energies towards higher values, while the fundamental properties of the hadronic final state, such as the shape of the angular distributions and fractional energy share, remain unaffected. For this reason, the high mass cross sections are considered suitable for comparisons with pQCD calculations when they become available.

7.12.3 Parton-to-Hadron Corrections

All currently available fixed order calculations predict the cross sections at the parton level and include no model of the hadronisation process. The highest order pQCD calculation currently available is $\mathcal{O}(\alpha\alpha_s^2)$, which is LO for three jet and NLO for two jet photoproduction. However, in preparation for the availability of $\mathcal{O}(\alpha\alpha_s^3)$ calculations, it is useful to estimate the size of the parton-to-hadron corrections.

Figure 7.37 compares the parton and hadron level predictions for the high mass cross sections, according to the HERWIG model. The solid and dashed histograms show the hadron and parton level distributions, respectively, and the points show the ratio of the parton-to-hadron level distributions. The size of the parton-to-hadron corrections are shown to be large (up to $\sim 50\%$) at high $x_{\gamma;4\mathrm{J}}^{\mathrm{OBS}}$. For all other variables, the correction factors are approximately flat and at the level of $\sim 10-20\%$.

7.13 Ratio of Four-To-Three Jet Cross Sections

In an event which contains three and only three jets, the third jet must arise from QCD ISR and/or FSR. However, the possibility of secondary hard scatters between the partons in the beam remnants introduces an additional jet production mechanism. In the presence of multi-parton interactions, the rate of four jet production would be expected to exceed the predictions of standard models which do not include the possibility of secondary partonic scatters.

The four jet high mass cross section measured in this analysis is defined in the same kinematic region as a previous three jet photoproduction measurement [171]. For both analyses, the ZEUS 1996-1997 data were used. The data from both analyses have been used to study the rate of four jet photoproduction relative to that for producing three jets. Only a simple calculation of the ratio has been performed, including only statistical uncertainties, which have been calculated assuming the two measurements are completely correlated.

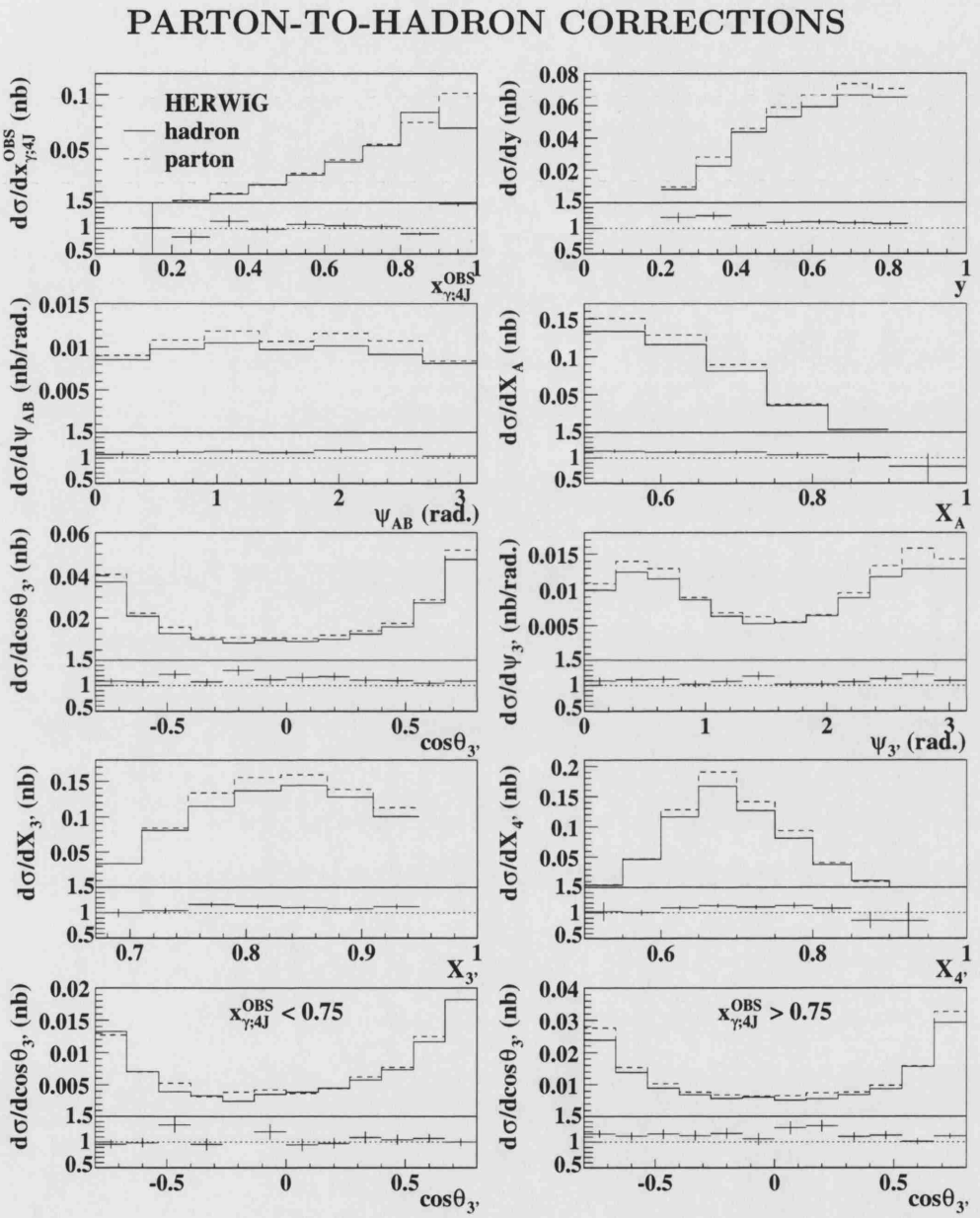

Figure 7.37: The high mass cross sections according to the predictions of HERWIG. The solid and dashed histograms show the hadron and parton level distributions respectively. The solid points show the ratio of the parton-to-hadron level distributions.

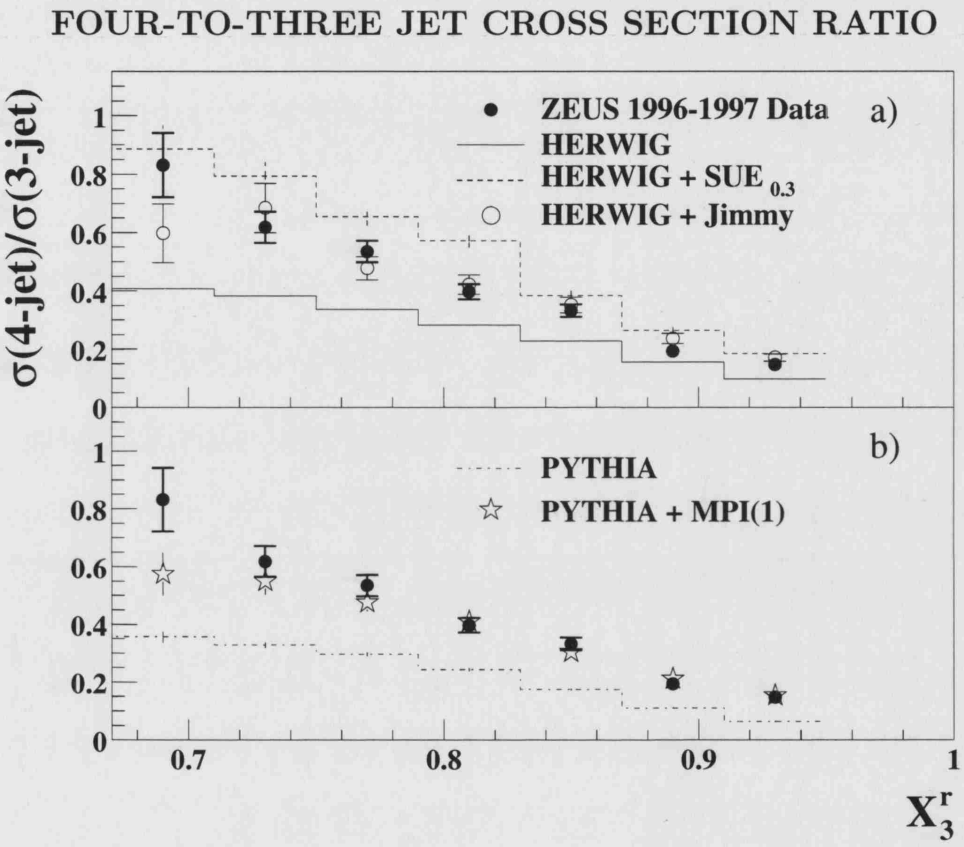

Figure 7.38: The ratio of the four-to-three jet cross sections. The solid points show the ratio of the four jet high mass cross section differential in $X_{3'}$ (from this analysis) to the three jet cross section differential in X_3 (from [171]). Errors are statistical only. In a), the data are compared to the predictions of HERWIG, HERWIG + $SUE_{0.3}$ and HERWIG + Jimmy. In b), the data are compared to the predictions of PYTHIA and PYTHIA + MPI(1).

Figure 7.38 shows the ratio of the high mass four jet cross section differential in $X_{3'}$ to that of the three jet cross section differential in X_3. Note that the variable $X_{3'}$ is exactly equal to the three jet equivalent X_3 in the limit that $E_6 \to 0$. For notational purposes in this section, the variable will be denoted as X_3^γ. The data are shown by the solid points. In Fig. 7.38a), the predictions of HERWIG, HERWIG + $\text{SUE}_{0.3}$ and HERWIG + Jimmy are compared to the ZEUS data. The measured ratio shows a clear excess above the prediction of standard HERWIG, while the soft underlying event model produces a rate which is, in general, higher than the data. In contrast, the models which include a simulation of multi-parton interactions provide a significantly improved description, with nearly all points lying within the statistical uncertainty on the measurement. The same general conclusion can be drawn from Fig. 7.38b) which shows the same data compared to PYTHIA and PYTHIA + MPI(1). These results suggest that the relative rate of four-to-three jet production cannot be described by models which produce multi-parton final states through the simulation of QCD radiation only. However, the measurement presented here is very simple, and includes no assessment of the systematic uncertainties (although many such uncertainties may be reduced in the ratio). A full measurement of the rate of four jet production, perhaps as a function of jet E_{T} or η, will be of interest to future analyses.

7.14 Tuning the Monte Carlo

Precision tests of QCD calculations, and their experimental tests at hadronic colliders, are inherently difficult. However, the interpretation of all physics results from hadronic experiments, including particle searches beyond the Standard Model, electroweak precision measurements and the study of heavy quarks, all rely on a detailed understanding of QCD. In order to properly interpret the data from both past and present colliders (e.g. LEP, HERA and the Tevatron) and to make predictions for future colliders (e.g. LHC, Next Linear Collider (NLC)), it is essential that the free parameters in existing QCD Monte Carlo models are tuned to current data. The JETWEB [20] package is a World Wide Web interface to a Monte Carlo validation and tuning facility. The aim of the package is to allow rapid and reproducible comparisons to be made between measurements from several high energy colliders and general purpose Monte Carlo simulations[‖].

The data from this analysis has been included in the JETWEB database, along with a variety of measurements from other experiments at LEP [176, 177], HERA [11, 13, 16–19, 23, 79, 168–170, 178–182] and the Tevatron [183–186]. The measurements include studies of photon structure, jet shapes and substructure, the underlying event

[‖]Only the HERWIG and PYTHIA Monte Carlo generators are currently included.

and multi-jet production (including a selection of results from this analysis). In this section, a selection of current results from JETWEB is presented. This concentrates mainly on the tuning of the underlying event parameters, to which the multi-jet data of this analysis is particularly relevant.

There are several other model parameters (in addition to those relevant to the underlying event) which can be systematically varied in JETWEB e.g. the fragmentation parameters, the intrinsic k_T of the proton/photon and the proton/photon PDFs. Since this section mainly concerns the tuning of the underlying event model, all parameters not directly related to the underlying event have been kept fixed. Specifically, the default fragmentation parameters have been used while the intrinsic k_T of the proton and photon has been taken to be 0 GeV in all HERWIG models and 1 GeV in PYTHIA. All models use the CTEQ5L proton (the most recent parameterisation available in PDFLIB [187]) and the SaS2D photon PDF sets. The choice of photon PDF is motivated by the current results from JETWEB, which suggest that this set gives the best overall χ^2/DOF to the fitted data. It is also known to be consistent with fits to current F_2^γ data. However, it should be noted that different PDF sets may require different tunings.

The multi-jet data of this analysis has already placed general constraints on the underlying event model and the inclusive data has been shown to strongly favour a contribution from multi-parton interactions. However, it is important, when constraining the parameters of the models in this way, to ensure that the description of other data is not detrimentally affected.

In addition to the multi-jet data of this analysis, there are several measurements that are of particular importance to the tuning of the Monte Carlo. Very precise high-E_T jet measurements [169] have recently been carried out at HERA, the results of which should be expected to be relatively insensitive to the underlying event model, but will provide strong constraints on other model parameters such as the parton densities. In addition, such measurements have been used to set the normalisation of the Monte Carlo. These scale factors have been applied to all models shown in Section 7.12 and throughout the remainder of this chapter. By using precise data to constrain the normalisation, the effects of varying the model parameters on the normalisation, as well as the shape of the data, can be investigated. In this section, several HERWIG and PYTHIA models are studied. In each case, the normalisation is set by the high-E_T data. These model predictions are also compared to data from LEP and Tevatron.

Figure 7.39a)-c) shows examples of measurements from HERA, LEP and the Tevatron, respectively. In each case, the experimental data are shown by the solid points. All errors are statistical only. Figure 7.39a) shows the ZEUS measurement [169] of the high-E_T cross section differential in E_T^{jet1} for two jet photoproduction. This is an example of a measurement that serves to set the normalisation of the Monte Carlo.

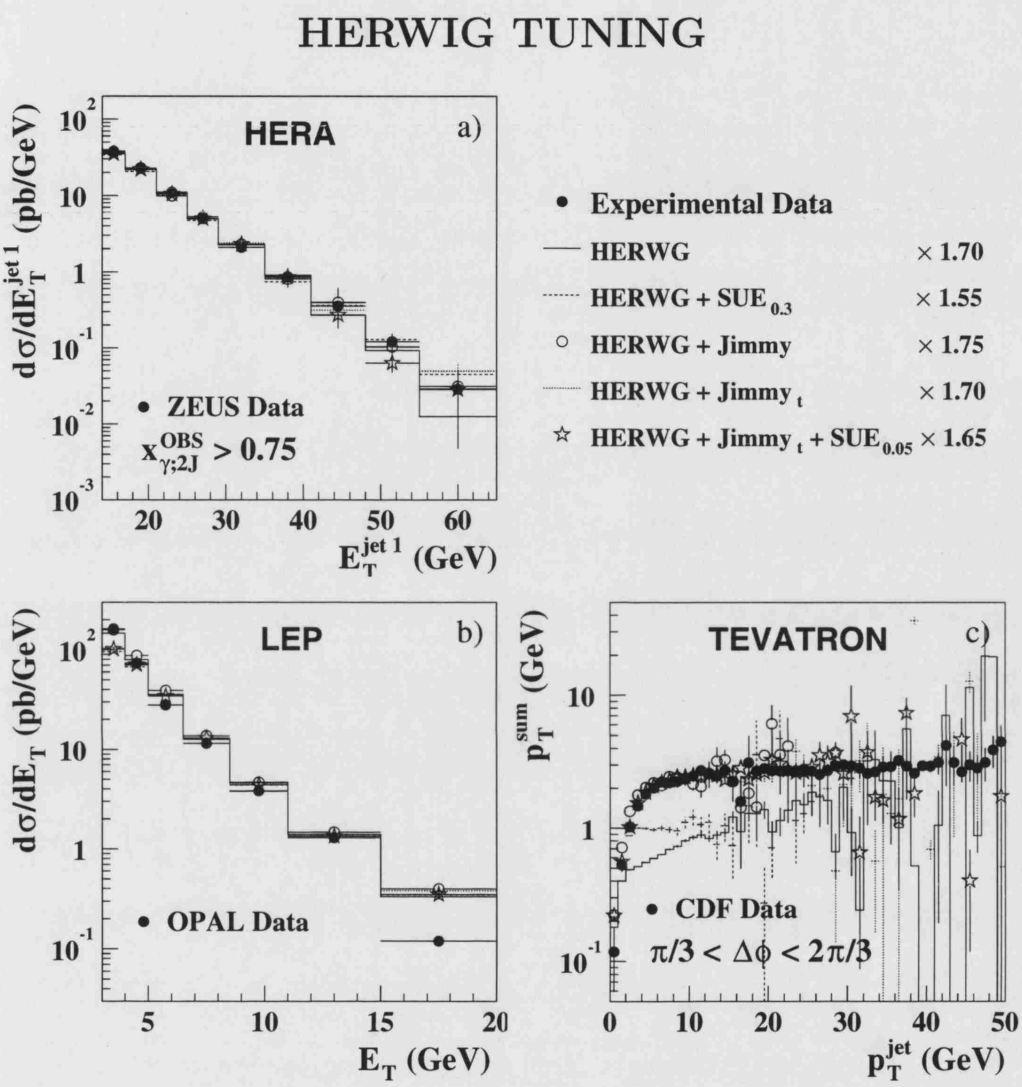

Figure 7.39: a) The cross section differential in $E_{\mathrm{T}}^{\mathrm{jet1}}$ for photoproduction events containing at least two jets with $E_{\mathrm{T}}^{\mathrm{jet1,2}} > 14, 11$ GeV, $1 < \eta^{\mathrm{jet1}} < 2.4$ and $0 < \eta^{\mathrm{jet2}} < 1$ for $x_{\gamma;2\mathrm{J}}^{\mathrm{OBS}} > 0.75$ as measured by the ZEUS Collaboration at HERA [169]. b) The cross section differential in $E_{\mathrm{T}}^{\mathrm{jet}}$ for events with $|\eta| < 2$ as measured by the OPAL Collaboration at LEP [177]. c) The distribution of the scalar sum of $p_{\mathrm{T}}^{\mathrm{sum}}$ as a function $p_{\mathrm{T}}^{\mathrm{jet}}$ in the region $\pi/3 < \Delta\phi < 2\pi/3$ as measured by the CDF Collaboration at the Tevatron [183]. The quantities $p_{\mathrm{T}}^{\mathrm{sum}}$ and $\Delta\phi$ are defined in the text. Compared to the data in each case are the predictions of the HERWIG Monte Carlo models listed in Tab. 7.4. Monte Carlo results taken from [20].

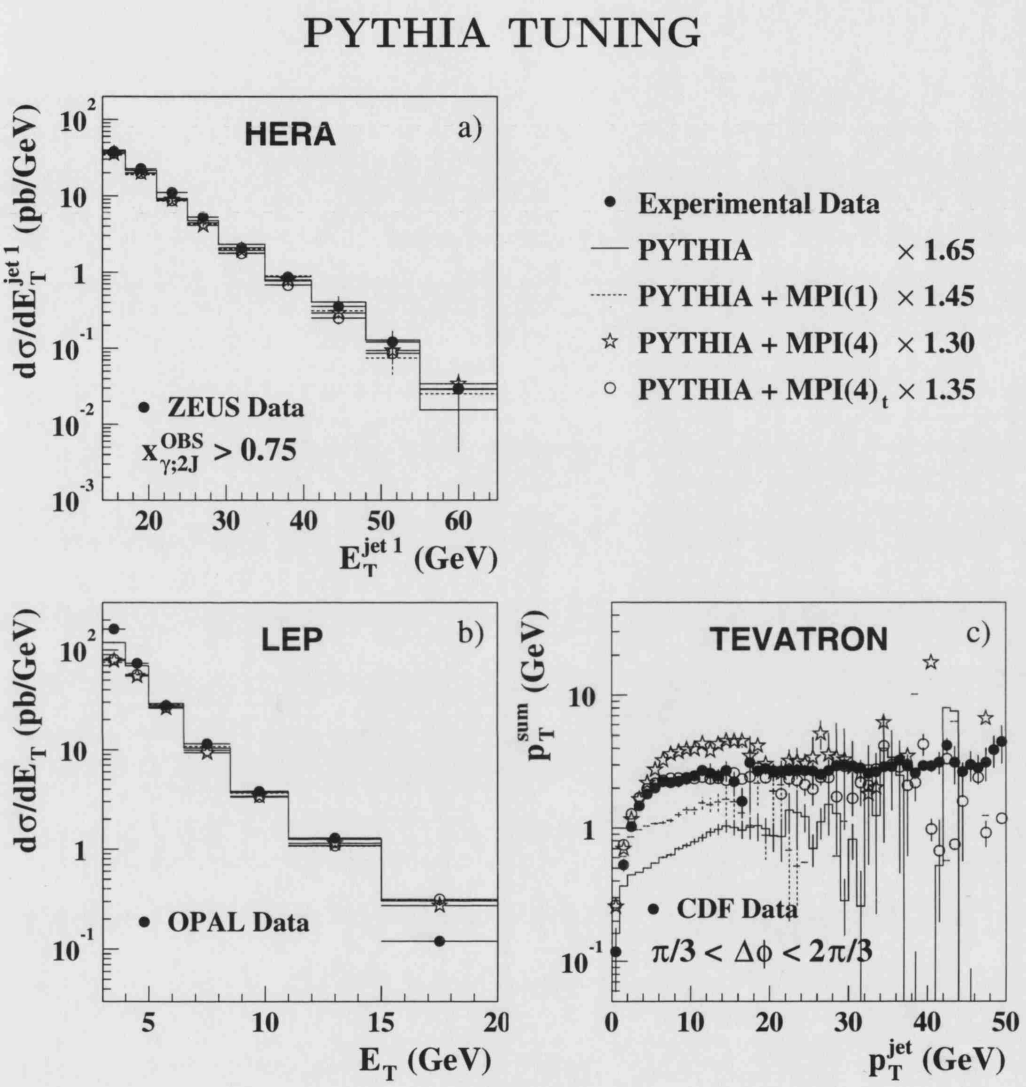

Figure 7.40: a) The cross section differential in $E_{\mathrm{T}}^{\mathrm{jet1}}$ for photoproduction events containing at least two jets with $E_{\mathrm{T}}^{\mathrm{jet1,2}} > 14, 11$ GeV, $1 < \eta^{\mathrm{jet1}} < 2.4$ and $0 < \eta^{\mathrm{jet2}} < 1$ for $x_{\gamma;2\mathrm{J}}^{\mathrm{OBS}} > 0.75$ as measured by the ZEUS Collaboration at HERA [169]. b) The cross section differential in $E_{\mathrm{T}}^{\mathrm{jet}}$ for events with $|\eta| < 2$ as measured by the OPAL Collaboration at LEP [177]. c) The distribution of the scalar sum of $p_{\mathrm{T}}^{\mathrm{sum}}$ as a function $p_{\mathrm{T}}^{\mathrm{jet}}$ in the region $\pi/3 < \Delta\phi < 2\pi/3$ as measured by the CDF Collaboration at the Tevatron [183]. The quantities $p_{\mathrm{T}}^{\mathrm{sum}}$ and $\Delta\phi$ are defined in the text. Compared to the data in each case are the predictions of the PYTHIA Monte Carlo models listed in Tab. 7.5. Monte Carlo results taken from [20].

Generator	Underlying Event Model	$p_{\mathrm{T}}^{\mathrm{min/mi}}$ (GeV)		R_p	R_γ	PRSOF	Scale Factor
HERWIG	NONE	2.0	-	-	-	-	1.70
HERWIG	$\mathrm{SUE}_{0.3}$	3.0	-	1.0	1.0	0.3	1.55
HERWIG	JIMMY	1.8	1.8	1.0	1.0	-	1.75
HERWIG	JIMMY_t	3.0	3.0	3.0	1.0	-	1.70
HERWIG	JIMMY_t + $\mathrm{SUE}_{0.05}$	3.0	3.0	3.0	1.0	0.05	1.65

Table 7.4: Parameters of the HERWIG Monte Carlo models shown in Fig. 7.39. The values of $p_{\mathrm{T}}^{\mathrm{min}}$ and $p_{\mathrm{T}}^{\mathrm{mi}}$ respectively correspond to the minimum transverse momentum of the primary and all secondary scatters. The scale factor by which the proton and photon radii are scaled, are given by $1/\sqrt{R_p}$ and $1/\sqrt{R_\gamma}$, respectively. The value of PRSOF gives the probability of a soft interaction in the HERWIG soft underlying event model.

Figure 7.39b) shows a cross section measurement [177] from two jet production in photon-photon collisions from the OPAL Collaboration at LEP. Figure 7.39c) shows a measurement [183] from the CDF Collaboration. Shown is the distribution of $p_{\mathrm{T}}^{\mathrm{sum}} = \langle \sum p_{\mathrm{T}}^{i} \rangle$ as a function of the transverse momentum of the highest p_{T} jet in the event. The quantity p_{T}^{i} is the transverse momentum of charged particle i. Only the region $\pi/3 < \Delta\phi < 2\pi/3$ (the so-called **transverse region**) is shown where $\Delta\phi$ is the distance in ϕ between the jet centre and charged particle i.

Compared to the data in Fig. 7.39 are the predictions of five HERWIG models. The important model parameters, including the applied scale factors, are listed in Tab. 7.4. Note that for the measurement presented in Fig. 7.39c), no scale factor is applied to the Monte Carlo since this is a profile plot and not a cross section. The solid histogram shows the default HERWIG model with no simulation of an underlying event. The dashed lines show the prediction of HERWIG + $\mathrm{SUE}_{0.3}$ and the open circles show the HERWIG + Jimmy model, using a value of $p_{\mathrm{T}}^{\mathrm{min}} = p_{\mathrm{T}}^{\mathrm{mi}} = 1.8$ GeV. The results show that all three models give a reasonable description of the HERA high-E_{T} and OPAL data. However, the CDF data is shown to be very sensitve to the underlying event model. HERWIG and HERWIG + $\mathrm{SUE}_{0.3}$ fail to describe the level of activity in the transverse region. In contrast, the HERWIG + Jimmy model enhances the level of underlying activity and gives a reasonable description of the data.

The fact that the HERWIG + Jimmy model provides a reasonable description of the data shown in Fig. 7.39, as well as providing a good description of the multi-jet data, lends further support to the use of multi-parton interaction in the models. However, two limitations of this particular choice of model are apparent. Firstly, it was shown

Generator	Underlying Event Model	PARP(84)	$p_{\mathrm{T}}^{\mathrm{min/mi}}$ (GeV)		Scale Factor
PYTHIA	NONE	-	2.0	-	1.65
PYTHIA	MPI(1)	-	2.0	1.5	1.45
PYTHIA	MPI(4)	0.2	3.0	1.9	1.30
PYTHIA	MPI(4)$_t$	0.4	3.0	1.9	1.35

Table 7.5: Parameters of the PYTHIA Monte Carlo models shown in Fig. 7.40. The values of $p_{\mathrm{T}}^{\mathrm{min}}$ and $p_{\mathrm{T}}^{\mathrm{mi}}$ respectively correspond to the minimum transverse momentum of the primary and all secondary scatters. The value of i in the notation MPI(i) refers to the value of MSTP(82) in PYTHIA. The parameter PARP(84) specifies the radius of the core of the double gaussian in the MPI(4) multi-parton interaction model.

in Section 7.12.2 that, while the shapes of both the inclusive and high mass multi-jet cross sections are well described by the HERWIG + Jimmy model, the normalisation of the high mass distributions are slightly underestimated. Secondly, while HERWIG + Jimmy provides an improved description of the CDF data relative to the default and the soft underlying event models, a small excess above the data is observed at low $p_{\mathrm{T}}^{\mathrm{jet}}$.

The latter observation has motivated an independent tuning [188]** to the data shown in Fig. 7.39c). The tuned model, referred to here as HERWIG + Jimmy$_t$††, uses the Jimmy package for the simulation of multi-parton interactions, with values of $p_{\mathrm{T}}^{\mathrm{min}} = p_{\mathrm{T}}^{\mathrm{mi}} = 3.0$ GeV and a reduction of the proton radius by a factor of $1/\sqrt{3}$. The results are shown by the dotted lines in Fig. 7.39 and are shown to give a good description of the Tevatron data. The open stars show the results of an extended tuning, based on the parameters of the HERWIG + Jimmy$_t$, which has been performed for this analysis. This model, referred to as HERWIG + Jimmy$_t$ + SUE$_{0.05}$, uses exactly the same Jimmy parameters as the CDF tuned model just described. However, in addition, a small amount of soft underlying event has been added (PRSOF=0.05). The choice of PRSOF is motivated by the multi-jets data (which will be discussed further in Section 7.14.1) and it should be noted that the model also produces a good agreement with all the data shown in Fig. 7.39 and does not significantly affect the description of the CDF data by, for example, producing levels of activity that are too high.

Figure 7.40 shows the same data as Fig. 7.39, this time compared to several PYTHIA models. The important parameters are listed in Tab. 7.5. The solid and dashed lines

**The original tuning was performed using the CTEQ4L proton PDF which indicates an even larger excess at low $p_{\mathrm{T}}^{\mathrm{jet}}$ than that observed with the CTEQ5L parameterisation used in this thesis.

††The subscript $_t$ stands for "tuned".

respectively correspond to PYTHIA and PYTHIA + MPI(1). The open stars and open circles, referred to as PYTHIA + MPI(4) and PYTHIA + MPI(4)$_t$ respectively, show the results of two impact parameter dependent multi-parton interaction models (corresponding to MSTP(82)=4). Both models assume a double Gaussian matter distribution. The main difference between these two models is the choice of the parameter PARP(84), which regulates the size of the double Gaussian core. The parameters of PYTHIA + MPI(4)$_t$ have been motivated by an independent tuning [189] to the CDF data shown in this section. The impact parameter dependent multi-parton interaction model used here is described in more detail in Section C.2.1.2. Figures 7.40a) and b) show that, after scaling by the appropriate factors, all models give a reasonable description of the HERA high-E_T and OPAL data. In contrast, the CDF data again shows sensitivity to the underlying event model. PYTHIA and PYTHIA + MPI(1) significantly underestimate the data while PYTHIA + MPI(4) gives too much underlying event activity at low to intermediate p_T^{jet}. PYTHIA + MPI(4)$_t$, which has been tuned to these data, produces a reasonable agreement.

7.14.1 The Multi-Jet Data

Generator	Underlying Event Model	χ^2/DOF high-E_T only	χ^2/DOF all-E_T	χ^2/DOF all-E_T (inc. Multi-Jet)
HERWIG	NONE	1.60	9.39	12.79
	SUE$_{0.3}$	2.09	5.18	13.53
	Jimmy	1.90	5.13	4.92
	Jimmy$_t$	2.46	5.83	6.17
	Jimmy$_t$ + SUE$_{0.05}$	2.27	4.79	4.58
PYTHIA	NONE	2.14	15.59	20.30
	MPI(1)	2.50	7.35	9.49
	MPI(4)	3.32	5.85	5.82
	MPI(4)$_t$	2.20	6.58	9.45

Table 7.6: The χ^2/DOF values of the JETWEB fits for each of the models shown in this chapter. The first and second columns list the generator and underlying event model type. The third column gives the χ^2/DOF value for fits to the high-E_T data only. The fourth column gives the χ^2/DOF value for fits to all-E_T data (using only the subset of included measurements which are published and recommended [20]) and the fifth column gives the new χ^2/DOF for all-E_T data after inclusion of the multi-jets data into the fit.

It is important to test whether the tunings that have been found to produce a reasonable agreement with the HERA, LEP and Tevatron data, shown in the previous section, are also able to describe the multi-jet data of this analysis.

Figure 7.41 shows the total cross sections differential in $X_{3'}$ and $X_{4'}$ for the inclusive and high mass samples. Compared to the data are the predictions of HERWIG + Jimmy$_t$, HERWIG + Jimmy$_t$ + SUE$_{0.05}$ and PYTHIA + MPI(4)$_t$. The results show that both HERWIG + Jimmy$_t$ and PYTHIA + MPI(4)$_t$ significantly underestimate the normalisation of the measured cross section. The difference in normalisation between the HERWIG + Jimmy model (compared to the data in Section 7.12.2) and HERWIG + Jimmy$_t$ arises largely from the different values of $p_{\mathrm{T}}^{\mathrm{min}}$ and $p_{\mathrm{T}}^{\mathrm{mi}}$. The lower value of $p_{\mathrm{T}}^{\mathrm{min}} = p_{\mathrm{T}}^{\mathrm{mi}} = 1.8$ GeV in HERWIG + Jimmy, compared to $p_{\mathrm{T}}^{\mathrm{min}} = p_{\mathrm{T}}^{\mathrm{mi}} = 3.0$ GeV in HERWIG + Jimmy$_t$, leads to a higher predicted cross section, particularly for the inclusive sample, since reducing this parameter gives rise to more multi-parton interactions. However, the higher value of 3.0 GeV chosen for HERWIG + Jimmy$_t$ was found to be necessary in order to properly describe the CDF data in the low $p_{\mathrm{T}}^{\mathrm{jet}}$ region. The difference in normalisation can be compensated for by introducing a small amount of soft underlying event, as shown by the HERWIG + Jimmy$_t$ + SUE$_{0.05}$ model. The results show that a reasonable agreement is obtained in both shape and normalisation of the inclusive and high mass data.

The normalised cross sections of the four jet centre-of-mass observables are compared to the predictions of HERWIG + Jimmy$_t$ + SUE$_{0.05}$ and PYTHIA + MPI(4) in Figs 7.42 and 7.43. While the PYTHIA + MPI(4)$_t$ model is not able to adequately describe the normalisation, it is still informative to study the description of the shape. In general, the normalised distributions of HERWIG + Jimmy$_t$ are similar to that of HERWIG + Jimmy$_t$ + SUE$_{0.05}$ and so are not shown. The inclusive distributions shown in Fig. 7.42 illustrate that the HERWIG + Jimmy$_t$ + SUE$_{0.05}$ model gives a reasonable description of the shape of all variables. The PYTHIA + MPI(4)$_t$ model also gives an adequate description of the shape of X_{A}, $X_{3'}$, $X_{4'}$ and ψ_{AB}. The $\cos\theta_{3'}$ distribution shown in Fig. 7.42c) is also reasonably described. However, the distribution of the same variable in the direct-enhanced region, shown in Fig. 7.42h), is less peaked at $\cos\theta_{3'} \pm 0.8$ relative to the data. In addition, this model produces a $\psi_{3'}$ distribution which is too strongly suppressed at $\psi_{3'} \sim \pi/2$. The corresponding high mass distributions are shown in Fig. 7.43. The shapes of the distributions are, in general, adequately described by both the HERWIG + Jimmy$_t$ + SUE$_{0.05}$ and PYTHIA + MPI(4)$_t$ models within the available statistics. However, the $\cos\theta_{3'}$ distribution for $x_{\gamma;4\mathrm{J}}^{\mathrm{OBS}} > 0.75$ again appears to favour HERWIG + Jimmy$_t$ + SUE$_{0.05}$ rather than the PYTHIA + MPI(4)$_t$ model, the latter of which is significantly less peaked in the forward and backward direction, than the data. The less signifiacnt enhancement at $\cos\theta_{3'} = \pm 0.8$ in PYTHIA compared to HERWIG has been shown throughout this chapter to be a feature of PYTHIA itself, and is not due to the choice of underlying event model *per se*.

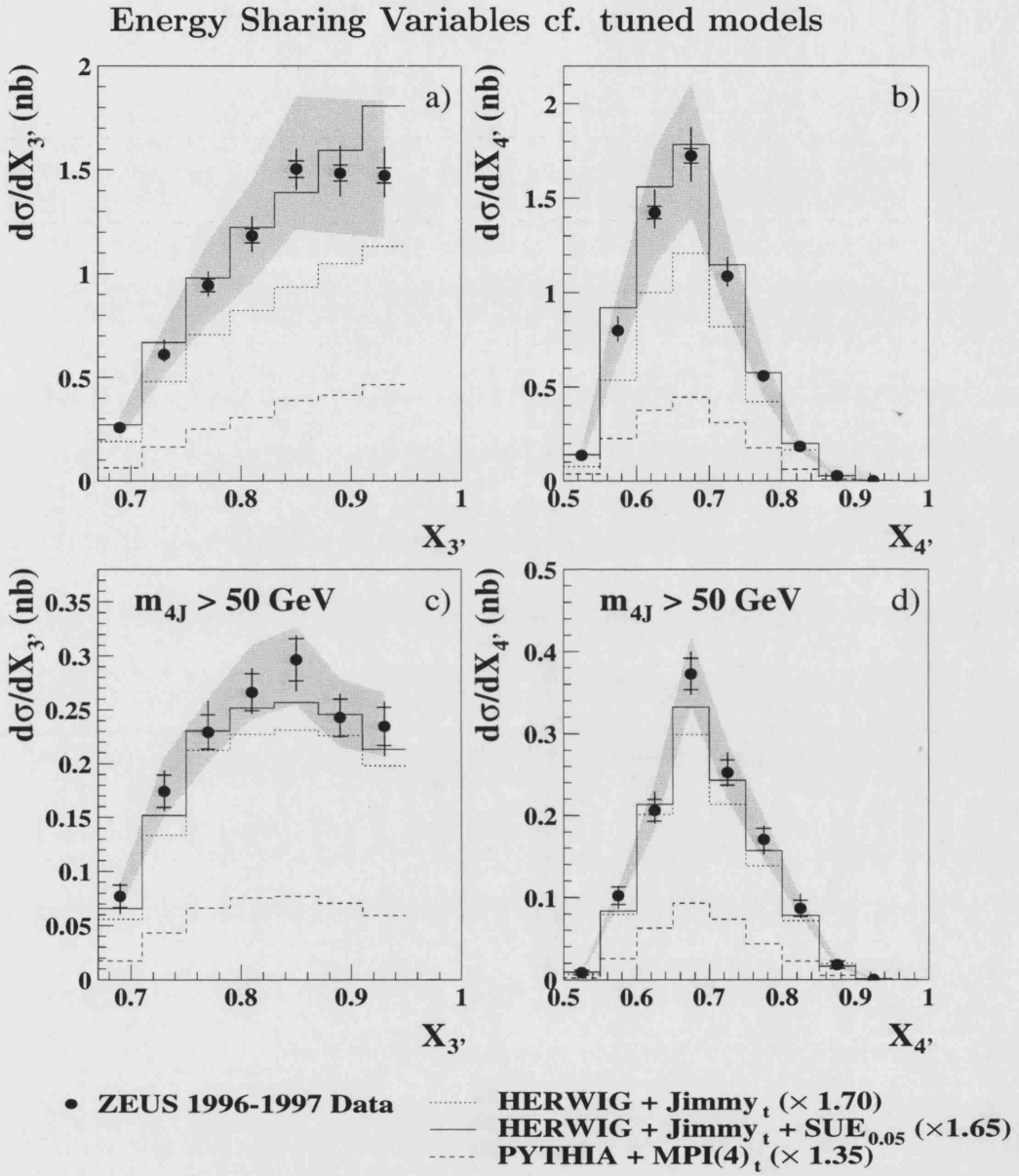

Figure 7.41: The total cross sections differential in $X_{3'}$ and $X_{4'}$ for the inclusive and high mass samples. The results for the inclusive sample are shown in a) and b) and those for the high mass sample are shown in c) and d). The solid points show the corrected ZEUS data. The inner error bars show the statistical uncertainty and the outer error bars show the statistical and uncorrelated systematic uncertainties combined in quadrature. The shaded band shows the calorimeter energy scale uncertainty. Compared to the data are the predictions of HERWIG + Jimmy$_t$ + SUE$_{0.05}$ and PYTHIA + MPI(4).

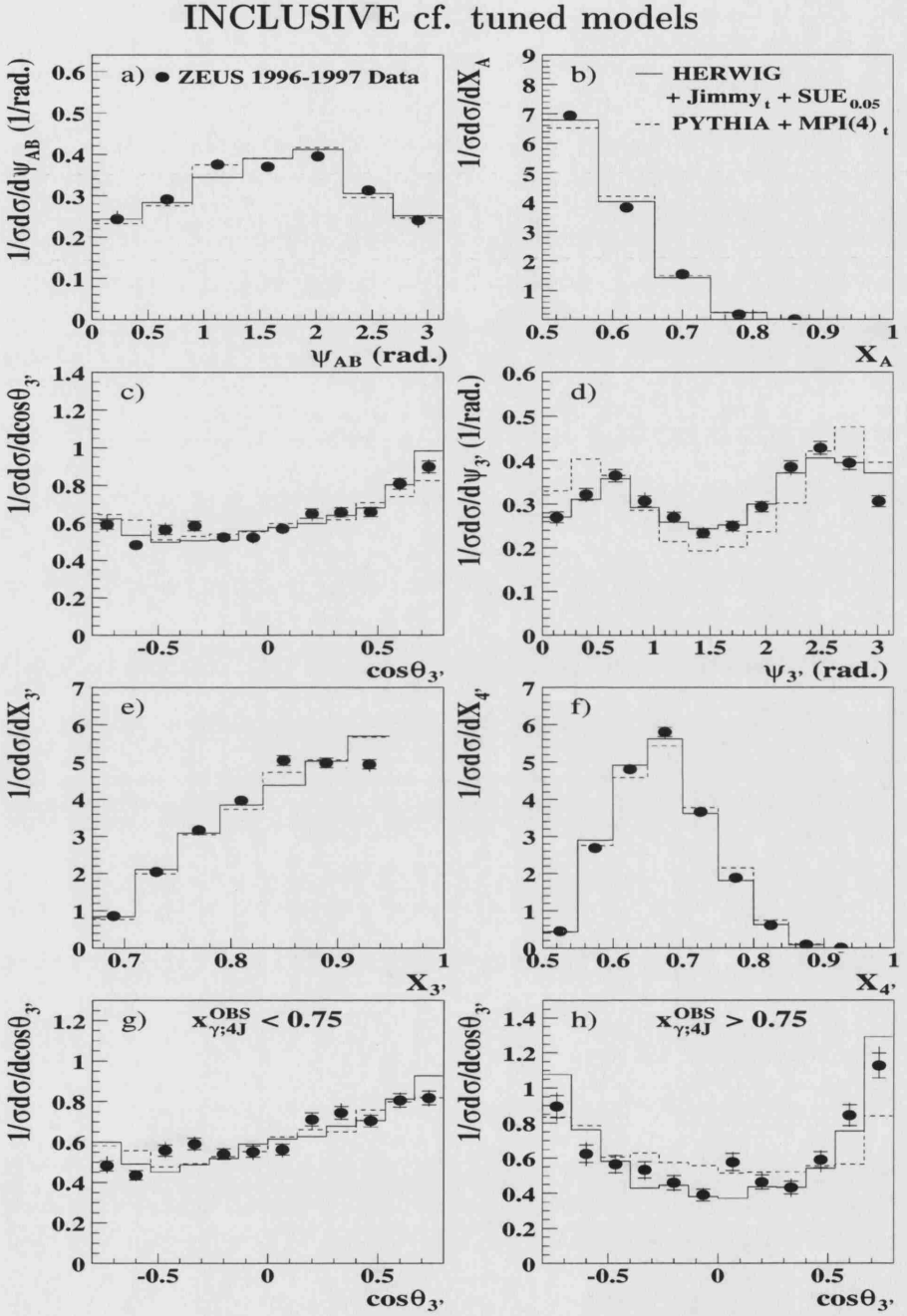

Figure 7.42: The normalised cross sections differential in ψ_{AB}, X_{A}, $\cos\theta_{3'}$, $\psi_{3'}$, $X_{3'}$ and $X_{4'}$ for the inclusive sample. The solid points show the corrected ZEUS data. The inner error bars show the statistical uncertainty and the outer error bars show the statistical and uncorrelated systematic uncertainties combined in quadrature. Compared to the data are the predictions of HERWIG + Jimmy$_t$ + SUE$_{0.05}$ and PYTHIA + MPI(4).

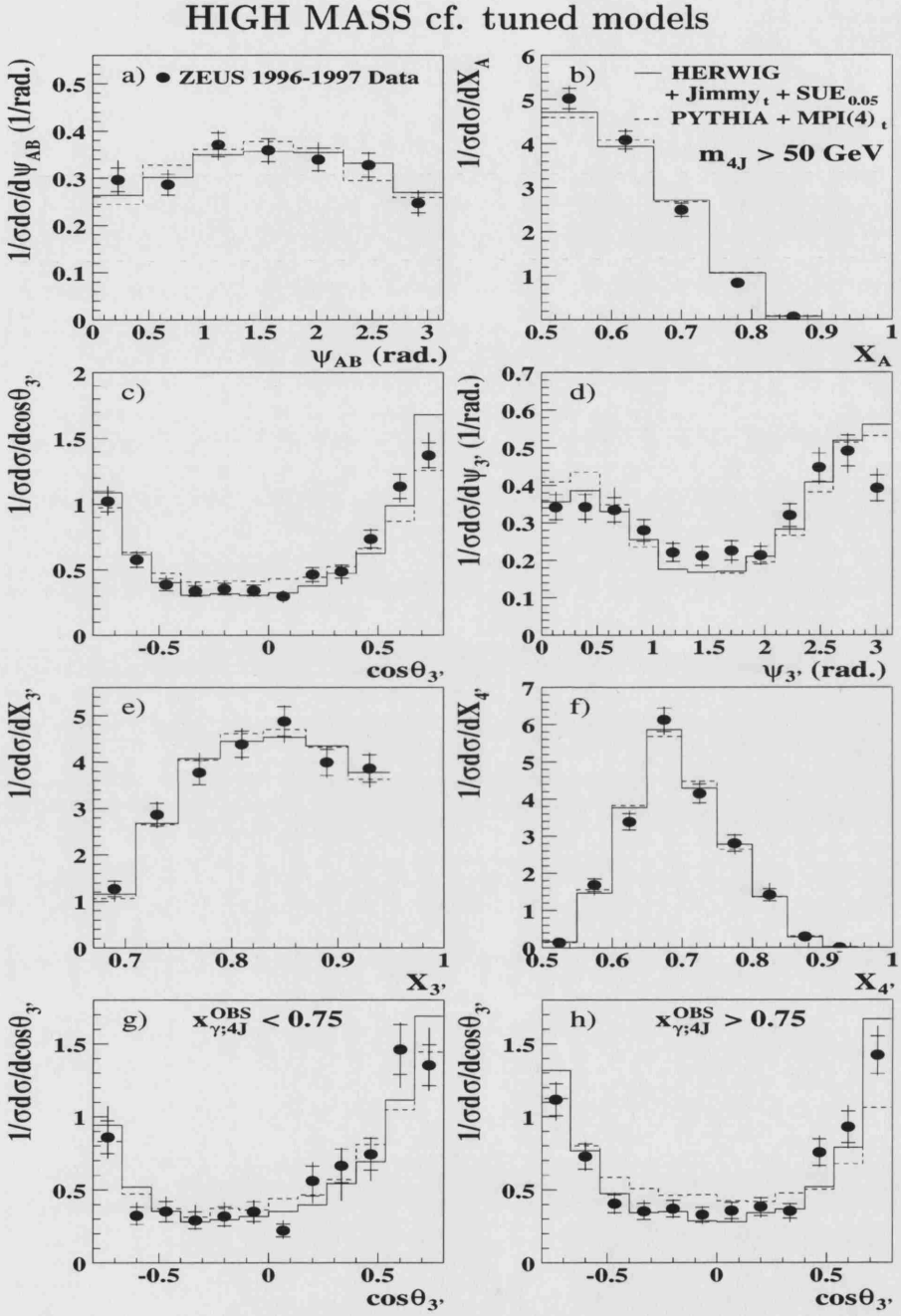

Figure 7.43: The normalised cross sections differential in ψ_{AB}, X_{A}, $\cos\theta_{3'}$, $\psi_{3'}$, $X_{3'}$ and $X_{4'}$ for the high mass sample. The solid points show the corrected ZEUS data. The inner error bars show the statistical uncertainty and the outer error bars show the statistical and uncorrelated systematic uncertainties combined in quadrature. Compared to the data are the predictions of HERWIG + Jimmy$_t$ + SUE$_{0.05}$ and PYTHIA + MPI(4)$_t$.

It is informative to study how consideration of the multi-jet measurement affects the quality of the overall fit to the data included in JETWEB. The χ^2/DOF for all HERWIG and PYTHIA models shown in this and previous sections are listed in Tab. 7.6. The first and second columns in the table list the generator and underlying event model type while the third shows the value of the χ^2/DOF resulting from fits to only high-E_{T} data. The fourth column gives the χ^2/DOF values resulting from the fits to all data which is both published and recommended [20] in JETWEB. Finally, the fifth column gives the χ^2/DOF from fits to all data, which also includes the multi-jets measurement from this analysis. The results show that the HERWIG + Jimmy$_t$ + SUE$_{0.05}$ model gives the best χ^2/DOF for the fit to all-E_{T} data. Furthermore, inclusion of the multi-jet data in the χ^2 calculation improves the value further. However, it should be noted that the generated luminosity of the models currently on JETWEB are not equal in all cases. Therefore, only general conclusions should be drawn from the information shown in Tab. 7.6.

In summary, a variety of HERWIG and PYTHIA models have been compared to a selection of data from the JETWEB database, including results from this analysis. Both the CDF data and the multi-jet data from this analysis are exceedingly sensitive to the underlying event model and are therefore very useful in tuning the parameters of current QCD models. A tuning for HERWIG has been found that gives a good description of a wide variety of data, in both shape and normalisation, including the multi-jets data of this analysis. A tuning for PYTHIA, based on a study [189] of the CDF data shown in this section, has also been studied. However, this model is not able to properly account for the magnitude of the multi-jet cross sections and neither is it able to adequately describe the shape of the inclusive $\psi_{3'}$ distribution. The fact that no PYTHIA model has yet been found that adequately describes the wide variety of data included in JETWEB is not surprising since there are many tunable parameters, only some of which have so far been studied. The results summarised here demonstrate the need for an improved understanding of the underlying event, and indicate the importance of the multi-jet data in constraining the model parameters.

Chapter 8

Rapidity Gaps and Energy Flow Between Jets in Photoproduction

In this chapter, a study of **Rapidity Gaps and Energy Flow Between Jets** is presented. Following a brief review of previous measurements related to this study, the method used to conduct the measurement is described. The cross section definition and event selection criteria are then stated. The Monte Carlo sample that has been used to extract a detector independent measurement is described and compared to the kinematic quantities important for this analysis. The uncorrected distributions of the measured cross section variables are also studied, and are used to extract a detector dependent measurement of the gap fraction. Following a discussion of the correction procedure and of the systematic uncertainties, the cross sections and corrected gap fractions are presented and compared to theoretical predictions. Finally, the results are discussed.

8.1 Introduction

In Section 2.14, the process of diffractive scattering and the importance of understanding the gap-producing mechanism within the context of QCD was discussed. This forms the basis of the gaps-between-jets analysis presented here.

An excess of events with rapidity gaps between jets, over that expected from typical QCD processes, have previously been observed at the Tevatron [21, 22] and in photoproduction at HERA [23–25]. The Tevatron has observed an excess of $\sim 3\%$ ($\sim 1\%$) at $\sqrt{s} = 630$ GeV ($\sqrt{s} = 1800$ GeV) over standard QCD processes, while HERA reports an excess of $7 - 10\%$. A summary of the HERA results to date, are shown in Figs. 8.1 and 8.2. The observed excess has been interpreted as evidence for the exchange of a strongly interacting colour singlet object. At HERA, the gaps-between-jets approach can only be used in photoproduction since a strongly interacting colour

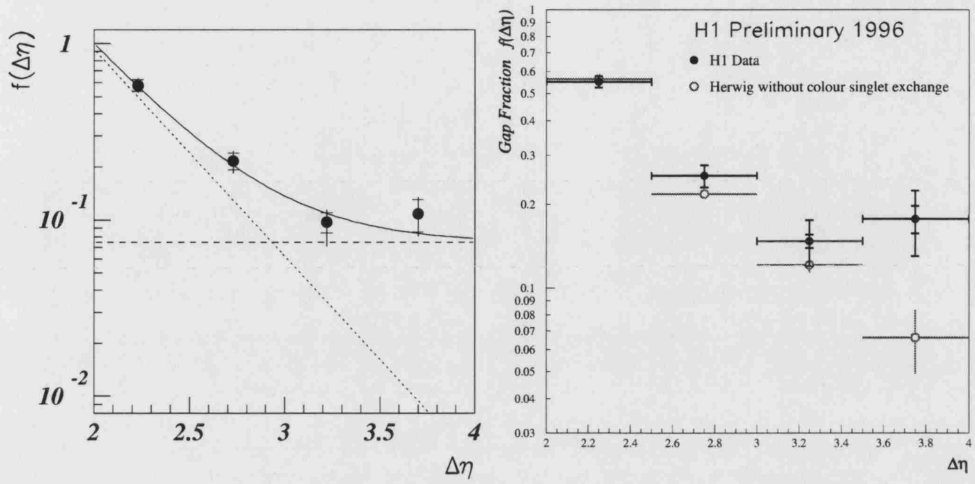

Figure 8.1: Left: The gap fraction $f(\eta)$ as measured by ZEUS [23], with a fit to the data of the form $f = C(\alpha, \beta)e^{(\alpha\Delta\eta)} + \beta$. Right: The gap fraction $f(\eta)$ as measured by H1 [24] compared to the HERWIG Monte Carlo. A gap is defined in terms of the multiplicity of particles between the two highest-transverse-energy jets.

singlet object can couple only to hadronic objects (e.g. proton, resolved photon). Furthermore, the differences in the reported excesses, both between experiments at different colliders and at different centre-of-mass energies at the same collider, may be due to the decreasing gap survival probability at increasing s (see Section 2.14.4).

One of the challenges of this type of measurement is in obtaining a reliable experimental definition of a gap. The studies presented in [21–24] relied on gap definitions based on particle multiplicities in the region between the two highest-transverse-energy jets in the event. However, such definitions are not infra-red safe i.e. even the softest gluon carries colour and so the definition of the colour content of the event is problematic. Neither is the definition collinear safe. For example, a gap may be defined as the absence of any particles with transverse momentum above some threshold p_{T}^{th}. If a particle with $p_{\mathrm{T}} > p_{\mathrm{T}}^{th}$ exists in the central rapidity region, then the event is not identified as a gap candidate. However, the same results will not be obtained if, before detection, the original particle splits into N collinear particles each with $p_{\mathrm{T}}^{i} < p_{\mathrm{T}}^{th}$ ($p_{\mathrm{T}} = \sum p_{\mathrm{T}}^{i}$).

A solution to these problems has been provided by Oderda and Sterman [190] who suggested that rapidity gap events could be defined in terms of the energy flow, Q_{C}, in the region between the jets. The observable Q_{C} is both infra-red and collinear safe. Rapidity gap events are then classified as those with "small" Q_{C} (i.e. below some energy threshold cut). The cross section can be treated using factorisation theorems and in the limit that $Q_{\mathrm{C}} >> \Lambda_{\mathrm{QCD}}$, the measured cross sections will be perturbatively calculable. If, in addition, the transverse energies of the jets are required to be much larger than

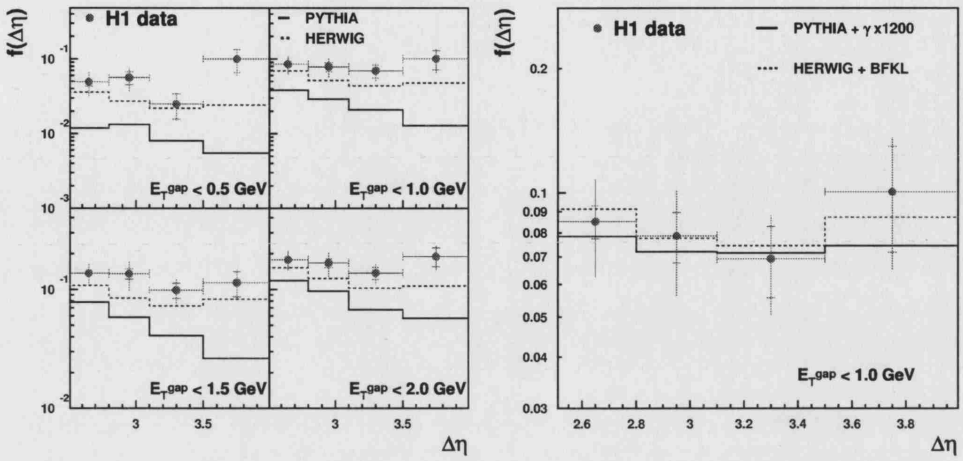

Figure 8.2: The gap fraction $f(\eta)$ compared to (left) HERWIG and PYTHIA and (right) HERWIG and PYTHIA including a simulation of colour singlet exchange. A gap is defined in terms of the energy flow between the two highest-transverse-energy jets.

Q_C so that $E_T >> Q_C >> \Lambda_{QCD}$, then there are two hard scales and logarithms in their ratio, E_T/Q_C, can be summed. This re-summation allows the concept of hard colour singlet exchange to be generalised. In the Regge limit, the dominant exchange is purely colour singlet. This method is complementary to the BFKL approach, because both deal with the re-summation of gluon radiation. Oderda [191] calculated the fraction of events with $Q_C < 350$ MeV and showed that a reasonable agreement with the ZEUS data of [23] was obtained.

The proposal by Oderda and Sterman has been translated into an experimental framework [25]. This method (defined in Section 8.3) has also formed the basis of the gap definition used in this thesis.

8.2 The Gap Fraction

An observable that allows the discrimination of events containing a gap is the **gap fraction**, f. This is calculated as the ratio of the two jet gap cross section to the two jet inclusive cross section,

$$f = \frac{\sigma_{\text{gap}}}{\sigma}. \tag{8.1}$$

From both a theoretical and experimental standpoint, this is a particularly useful quantity since many uncertainties present in the measurement of the absolute cross

sections will cancel in the ratio, and the dependence of the measurement on the kinematics of jet production should be reduced. The gap fraction as a function of $\Delta\eta$, $f(\Delta\eta)$, is the quantity shown in Figs. 8.1 and 8.2.

The gap cross section is expected to have two contributions, $\sigma_{\rm gap} = \sigma^{\rm ND}_{\rm gap} + \sigma^{\rm D}_{\rm gap}$. The quantity $\sigma^{\rm ND}_{\rm gap}$ is the contribution to the total cross section from both multiplicity fluctuations in standard photoproduction processes and from electroweak exchange, while $\sigma^{\rm D}_{\rm gap}$ is the diffractive contribution to the total cross section arising from the exchange of a strongly interacting colour singlet object. As discussed in Section 2.14, the cross section from electroweak exchange is very small and should not contribute largely to the cross section. Therefore, the contribution from $\sigma^{\rm ND}_{\rm gap}$ is expected to dominate at small gap separations but will fall exponentially as a function of $\Delta\eta$ so that at large jet separations the $\sigma^{\rm D}_{\rm gap}$ component will dominate. This is illustrated by the results shown in Fig. 8.1. The height of the plateau region allows the discrimination between strong and electroweak processes.

8.3 Gap Definition

Rapidity gap events are defined according to the definition presented in [25]. This method is defined in the following way:

1. Jet-finding is performed on the final state particles using the $k_\perp$ algorithm in the inclusive mode. This algorithm is the best suited to this analysis since it is both infra-red and collinear safe and suffers from no ambiguities due to overlapping jets.

2. The two highest transverse energy jets within the specified pseudo-rapidity range are taken to be the leading jet pair. To ensure a high momentum transfer, t, events are selected only if these jets are separated by some minimum $\Delta\eta$. The most forward of the pair is called the **leading** jet and the most backward is called the **trailing** jet.

3. The remaining jets in the event are referred to as **mini-jets**. The transverse energy of all mini-jets lying in the pseudo-rapidity region between the two leading jets is summed to form the quantity $E_{\rm T}^{\rm gap}$ such that,

$$E_{\rm T}^{\rm gap} = \sum E_{\rm T}^{\rm mini-jet}; \;\; \eta^{\rm jet}_{\rm TRAILING} < \eta^{\rm mini-jet} < \eta^{\rm jet}_{\rm LEADING}. \tag{8.2}$$

4. A rapidity gap event is then defined to be one in which $E_{\rm T}^{\rm gap} < E_{\rm T}^{\rm cut}$ where $E_{\rm T}^{\rm cut}$ is a transverse energy threshold parameter. Although $E_{\rm T}^{\rm gap}$ must be small, it is also required to satisfy $E_{\rm T}^{\rm cut} >> \Lambda_{\rm QCD}$ in order to be calculable in pQCD.

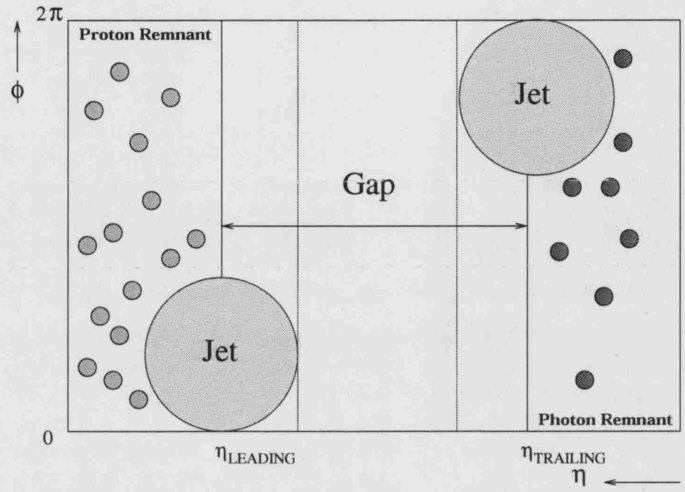

Figure 8.3: Experimental signature of a rapidity gap in photoproduction at HERA.

This definition of a gap has many advantages over previous definitions based on particle multiplicities. Theoretically, the definition has the advantage of being infrared and collinear safe since it is defined in terms of the energy flow between the jets. Furthermore, this energy flow is defined as the scalar sum of the transverse energies of $k_\perp$ clustered objects. Secondly, the fact that the transverse energy flow is defined as a sum of $k_\perp$ clustered jets, rather than as the sum of the energies of the particles themselves, significantly reduces the sensitivity of the measurement to hadronisation effects. While colour singlet events produce no hadronic activity between the jets, there may still be some QCD radiation from the colour connections between the jet centres and the beam remnants. This radiation may "spill" into the central rapidity region. However, in the above definition, activity at the edges of the gap region are more likely to be included in mini-jets whose centres lie outside the central rapidity region and so their energies will not be included in the energy sum.

Experimentally, this definition is also advantageous. For example, jet energies can be calibrated more easily than those of individual particles. Secondly, previous definitions using particle multiplicities have considered only the region between the inner jet edges. However, using a jet algorithm to sum the energy means that the gap region extends to the centres of the jets. This is illustrated in Fig. 8.3. Therefore, a wider region of $\eta - \phi$ space is available over which the gap signature may be observed. Along with this comes a corresponding increase in the available statistics. In the HERA measurements of [23, 24], an excess was observed only for separations of $\Delta\eta \gtrsim 3.2$. However, in the latest H1 measurement [25] (which uses the above gap definition) an excess over the predictions of standard photoproduction models was already observed at values of $\Delta\eta \gtrsim 2.5$.

8.4 Definition of the Cross Section

The measured cross sections are defined in the following kinematic region,

$$Q^2 < 1 \text{ GeV}^2$$
$$0.2 < y < 0.85$$
$$E_{\text{T}}^{1,2} > 6.0, 5.0 \text{ GeV}$$
$$-2.4 < \eta < 2.4$$
$$2.5 < \Delta\eta < 4.0 \quad *$$
$$|\bar{\eta}| = \tfrac{1}{2}|\eta^1 + \eta^2| < 0.75$$

where 1 and 2 label the highest and second-highest transverse energy jet, respectively. The above criteria refer to the true (or hadron-level) quantities and define the **inclusive** cross section measurement. In addition, **gap** cross sections are defined by the additional requirement that,

$$E_{\text{T}}^{\text{gap}} < E_{\text{T}}^{\text{cut}}; \quad E_{\text{T}}^{\text{cut}} = 0.5, 1.0, 1.5, 2.0 \text{ GeV}.$$

As for the multi-jets analysis, the Q^2 region is set by the event selection criteria and the calorimeter acceptance and the restrictions on y correspond to photon-proton centre-of-mass energies in the range $134 < W_{\gamma p} < 277$ GeV. All jets are identified using the $k_\perp$ algorithm in the inclusive mode. Therefore, there is no ambiguity between overlapping jets and all particles are assigned to only one jet. The moderately high transverse energy requirements on the jets ensure that the fundamental process is calculable in pQCD. The asymmetric cut reduces the regions of phase space where the NLO QCD calculations may suffer from incomplete cancellations between real and virtual contributions [192]. These requirements will allow the measured distributions to be compared to pQCD calculations when they become available. The pseudo-rapidity requirements apply to all jets and mini-jets and ensures that they are completely contained in the calorimeter. The lower limit on $\Delta\eta$ means that the jets are well separated and ensures a large parton-parton centre-of-mass energy, $\hat{s}$, while the upper limit is a natural constraint imposed by the acceptance of the detector. The constraint on $|\bar{\eta}|$ ensures that a large fraction of the photon energy participates in the hard interaction. These events are better simulated by the Monte Carlo generators since there is less uncertainty in the photon PDFs. In addition, this requirement means that there is less likelihood of multi-parton interactions. This reduces the contribution from (possibly large) non-perturbative corrections. In addition, this requirement means that

*Note that the reference to $\Delta\eta$ here and throughout this chapter, really refers to $|\Delta\eta|$.

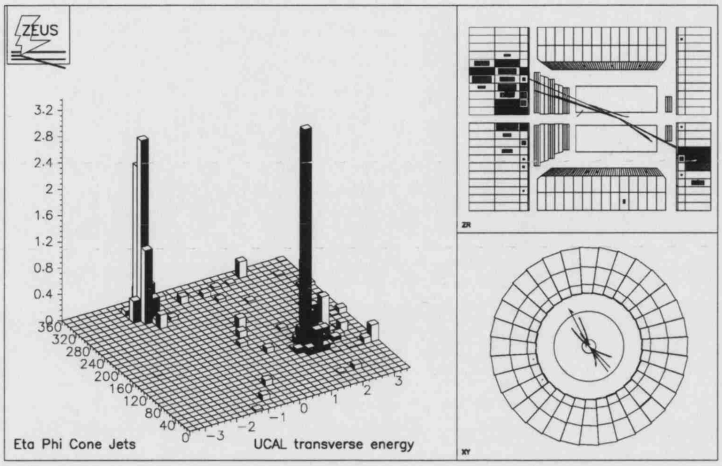

Figure 8.4: A rapidity gap candidate in the ZEUS detector.

events are more uniformly distributed throughout pseudo-rapidity space. For the gap events, the requirement that $E_{\mathrm{T}}^{\mathrm{cut}} > \Lambda_{\mathrm{QCD}}$ means that the gap cross sections are also calculable in pQCD.

In this analysis, inclusive cross sections are measured differentially in $E_{\mathrm{T}}^{\mathrm{gap}}$, $\Delta\eta$, $x_{\gamma;2\mathrm{J}}^{\mathrm{OBS}}$, $\log_{10}(x_{p;2\mathrm{J}}^{\mathrm{OBS}})$ and y. Gap cross sections and gap fractions are also measured differentially in $\Delta\eta$, $x_{\gamma;2\mathrm{J}}^{\mathrm{OBS}}$, $\log_{10}(x_{p;2\mathrm{J}}^{\mathrm{OBS}})$ and y for $E_{\mathrm{T}}^{\mathrm{cut}} = 0.5$, 1.0, 1.5 and 2.0 GeV. In addition, the gap fractions as a function of $\Delta\eta$ for $x_{\gamma;2\mathrm{J}}^{\mathrm{OBS}} < 0.75$ and $x_{\gamma;2\mathrm{J}}^{\mathrm{OBS}} > 0.75$ have been measured to allow further investigation of the distributions in the resolved- and direct-enhanced regions.

8.5 Event Selection

This analysis has been performed using the ZEUS 1996-1997 data-set, corresponding to 38.6 pb^{-1} of integrated luminosity. At the detector level, events containing at least two jets, with the highest-transverse-energy jet satisfying $E_{\mathrm{T}} > 5.1$ GeV and the second-highest-transverse-energy jet satisfying $E_{\mathrm{T}} > 4.25$ GeV, have been selected. The reduction by 15% relative to the cross section definition is chosen partially to take into account the pull on the jet transverse energies (see Section 8.7.1) and partially to increase the efficiency of selection. All jets are required to have reconstructed pseudo-rapidities in the range $-2.4 < \eta < 2.4$ and the two leading jets are required to satisfy $|\bar{\eta}| < 0.75$. The requirement that $2.5 < \Delta\eta < 4.0$ has also been imposed to ensure a large separation between the jets. The gap samples are defined by an additional requirement on the transverse energy flow in the region between the leading pair of jets, $E_{\mathrm{T}}^{\mathrm{gap}}$, where $E_{\mathrm{T}}^{\mathrm{cut}}$ is taken to have four different values: 0.6, 1.2, 1.8 and 2.4

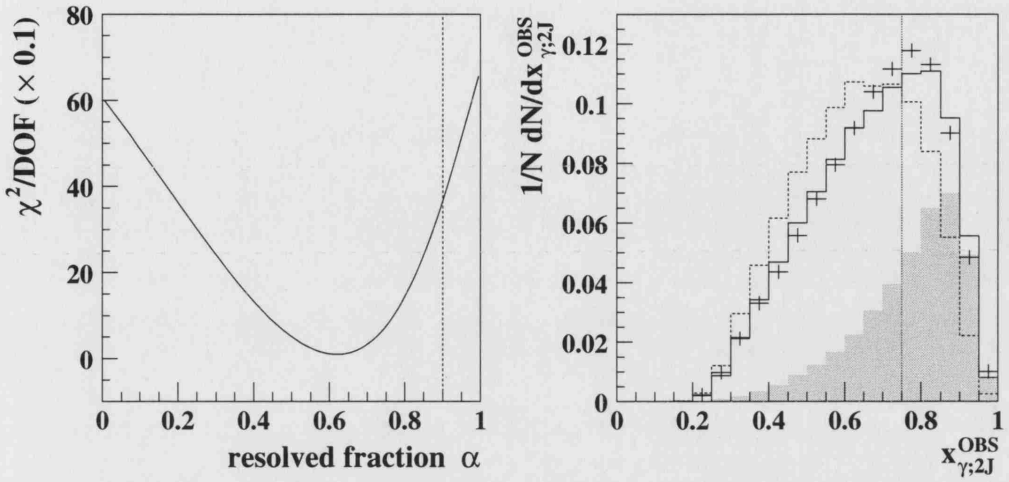

Figure 8.5: Left: The results of the one-parameter χ^2-fit to the uncorrected $x_{\gamma;2J}^{\mathrm{OBS}}$ distribution. The dashed line shows the resolved fraction taken from the generated Monte Carlo cross sections. Right: The distribution of $x_{\gamma;2J}^{\mathrm{OBS}}$ compared to the PYTHIA photoproduction Monte Carlo. The solid line indicates the distribution for a resolved fraction obtained from a χ^2-fit to the $x_{\gamma;2J}^{\mathrm{OBS}}$ distribution and the dashed lines show the results for a resolved fraction taken from the generated Monte Carlo cross section. The shaded histogram shows the distribution of events generated as direct photoproduction. The vertical dotted line indicates the separation between direct-enhanced and resolved-enhanced regions.

GeV. The 20% increase in the values of the $E_{\mathrm{T}}^{\mathrm{cut}}$ variable relative to the cross section definition increases the efficiency of selection.

The numbers of events passing the final selection cuts were 70472 for the inclusive sample, and 1899, 4337, 7596 and 11394 for the gap samples corresponding to $E_{\mathrm{T}}^{\mathrm{cut}} = 0.6, 1.2, 1.8$ and 2.4 GeV respectively.

Figure 8.4 shows an example of an event passing the gap event selection criteria. The high transverse energy jets are approximately back-to-back in ϕ and separated by a large region in pseudo-rapidity. The low levels of hadronic activity ($E_{\mathrm{T}}^{\mathrm{gap}} = 0.18$ GeV in this event) between the jet axes characterise this as a gap event.

8.6 The Monte Carlo Sample

The PYTHIA 6.1 Monte Carlo program has been used to generate hard photoproduction events for the purpose of correcting the data for detector and acceptance effects. This sample has been passed through a full simulation of the ZEUS detector and trigger. The parton distributions of the proton were generated according to the GRV-LO

parameterisation and those of the photon according to the WHIT2 parameterisation. The minimum transverse momentum of the two outgoing partons from the hard scatter was taken to be $p_T^{min} = 2.0$ GeV. The sample also includes a simulation of multi-parton interactions[†] and a value of $p_T^{mi} = 1.5$ GeV was taken to be the minimum transverse momentum of all secondary scatters.

Direct and resolved events were generated separately and combined in the ratio obtained from a χ^2- fit to the inclusive $x_{\gamma;2J}^{OBS}$ distribution. The results of this fit, and the uncorrected $x_{\gamma;2J}^{OBS}$ distribution for data and Monte Carlo, are shown in Fig. 8.5. For comparison, the distribution for the case where direct and resolved events are combined in the ratio of the generated Monte Carlo cross section is also shown. Table 8.1 gives the resolved contribution for each case.

Generator	Combination Method	Resolved Fraction
PYTHIA	χ^2 Fit Fraction to $x_{\gamma;2J}^{OBS}$	63%
	Generated Cross Section Fraction	90%

Table 8.1: Resolved fraction in the generated Monte Carlo sample.

The $x_{\gamma;2J}^{OBS}$ distribution peaks at $x_{\gamma;2J}^{OBS} \sim 0.75$ showing that, in general, the interacting parton from the photon carries a large proportion of the total photon momentum. The shaded histogram shows the contribution from direct events (for the case where the fraction has been taken from the χ^2-fit). This shows that although the average value of $x_{\gamma;2J}^{OBS}$ is high, a large proportion of resolved events still contribute. The vertical dotted line at $x_{\gamma;2J}^{OBS} = 0.75$ indicates the separation between events which are dominated by direct events and those that are dominated by resolved photon events. These are called the direct-enhanced and the resolved-enhanced regions. However, there clearly remains a contribution to each region from each type of event.

8.6.1 Colour Singlet Exchange

PYTHIA includes no simulation of strongly interacting colour singlet exchange. Therefore, the colour singlet exchange process has been simulated using high-t γ exchange[‡]. Such events contain only LO resolved processes of quark-quark scattering mediated by a photon. As for the photoproduction sample, the GRV-LO and WHIT2 PDFs were used for the proton and photon respectively. A value of $p_T^{min} = 2.0$ GeV was used for the minimum transverse momentum of the hard scatter. No additional simulation of multi-parton interactions was included in this sample.

[†]The simplest multi-parton interaction model was chosen, corresponding to MSTP(82)=1.

[‡]The t in "high-t γ" refers to the usual Mandelstam variable, $t = (p_a - p_c)^2$.

Generator	Process	MPI	PDF(p)	PDF(γ)	p_T^{min} p_T^{mi} (GeV)	No. of events
PYTHIA	Direct	-	GRV-LO	-	2.0 -	2417857
	Resolved	$\surd$	GRV-LO	WHIT2	2.0 1.5	4033279
	High-t γ	$\times$	GRV-LO	WHIT2	2.0 -	379462

Table 8.2: Parameters of the Monte Carlo samples used for the correction of the data.

In order to provide the best description of the data, from the generated Monte Carlo (see subsequent sections), the high-t γ sample has been added to the photoproduction sample in a 2% contribution to form a PYTHIA mixed sample of events. This choice of normalisation is described further in Section 8.11. Note that the high-t γ process is not considered to be a candidate for the gap-producing mechanism since the cross section is very small ($\mathcal{O}(\alpha/\alpha_s)^2 \sim 0.001$). However, the purpose of this Monte Carlo sample is to attempt to provide as good a description of the data as possible, so that the unfolding procedure may be used with confidence. Therefore, the underlying dynamics of the process are less important than is the ability of the Monte Carlo to simply reproduce the distributions.

8.6.2 Summary

Table 8.2 lists the important parameters relevant to the Monte Carlo samples described in this section. From the generated events, three separate Monte Carlo samples have been defined: the PYTHIA **photoproduction sample** (containing direct and resolved events combined in the ratio given by the χ^2-fit), the PYTHIA **high-t γ sample** (containing LO quark-quark scattering only) and the **mixed sample**, or PYTHIA + high-t γ sample, (containing 98% photoproduction and 2% high-t γ). These Monte Carlo samples are used in subsequent sections to draw conclusions from the data and unfold for detector effects.

8.7 Reconstruction of the Hadronic Final State

For the selection of gap events, it is essential that an adequate reconstruction of low energy particles can be performed. The corrected ZUFOs method (described in detail in Section 4.6 and used for the multi-jets analysis) was developed for the energy correction of high transverse energy clusters and jets. Therefore, it is not neceesarily the most appropriate method of reconstruction for this analysis since it does not properly correct

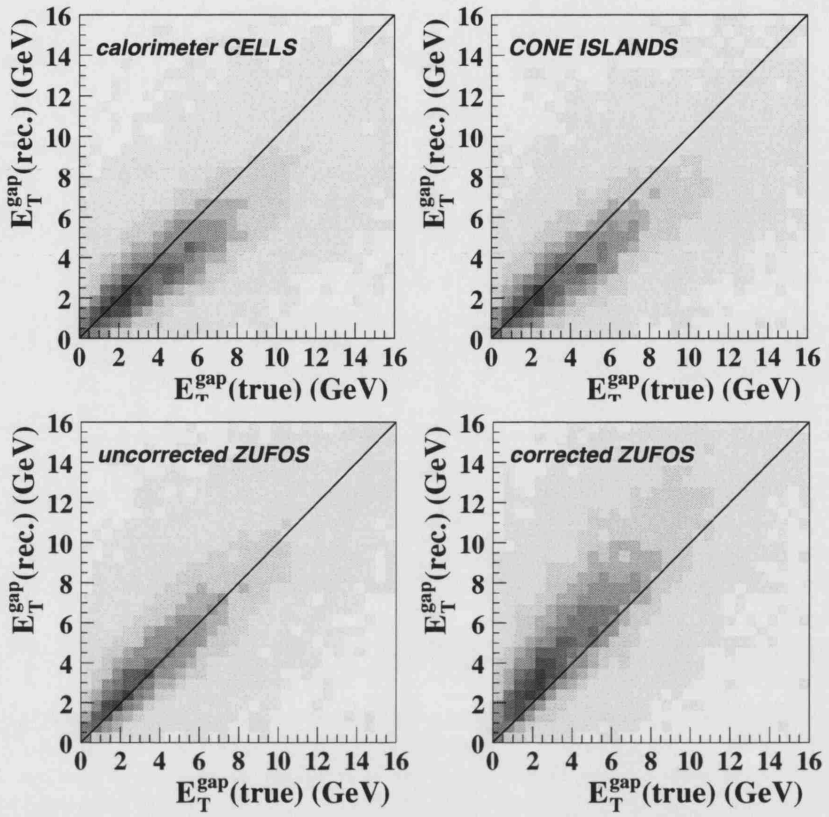

Figure 8.6: The correlation between the true and reconstructed values of $E_{\mathrm{T}}^{\mathrm{gap}}$ for reconstructions performed using calorimeter cells, calorimeter cone islands, uncorrected ZUFOs and corrected ZUFOs.

low energy, isolated clusters and may be invalid for the correction of low transverse energy jets. To study the suitability of various methods, the reconstruction quality of the variable $E_{\mathrm{T}}^{\mathrm{gap}}$ has been studied using calorimeter cells, cone islands, uncorrected ZUFOs and corrected ZUFOs. Cone islands are briefly discussed in Section 4.2.2.1 and in this context, they are equivalent to uncorrected ZUFOs for which only calorimeter information has been used (i.e. no tracking information). There are several factors that may influence the reconstruction quality, each of which will have a differing importance depending on the actual method of reconstruction. Firstly, the effects of calorimeter noise may have a significant effect. While the noise suppression routines described in Section 4.4.2 have been applied, small levels of noise may remain. In absolute terms, the effect of noise should be approximately constant as a function of $E_{\mathrm{T}}^{\mathrm{gap}}$. Secondly, particles will be subjected to $\sim 15-20\%$ energy loss in inactive material before being detected in the calorimeter. Finally, very low energy particles may be sufficiently bent by the magnetic field that they will not reach the calorimeter.

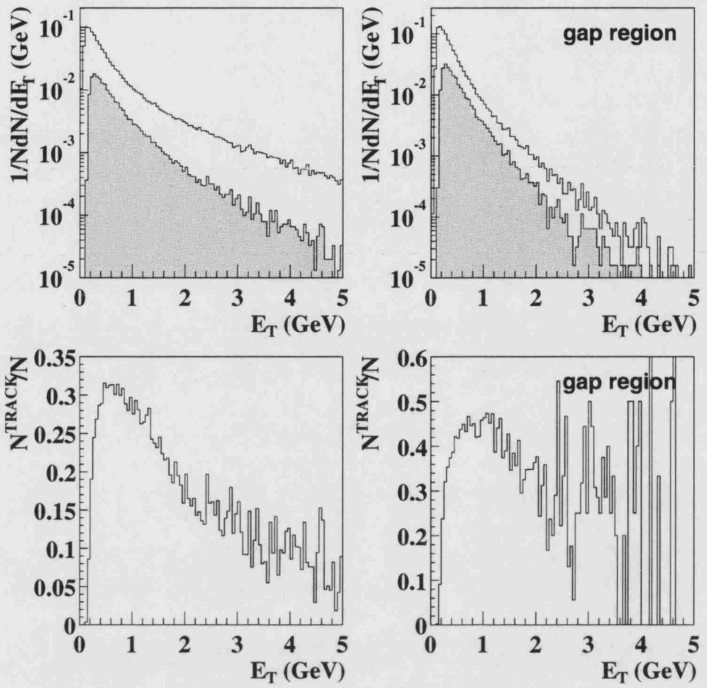

Figure 8.7: The average transverse energy distribution of ZUFOs from a sample of ZEUS data for the inclusive sample of events. The shaded histogram indicates the amount of transverse energy measured with tracks. The lower figures show the fraction of the total transverse energy flow measured with tracks. The figures on the left show the results for all ZUFOs in the event (including the leading and trailing jets) and those on the right show the results for only those ZUFOs in the gap region.

The correlations between the true and reconstructed values of $E_{\mathrm{T}}^{\mathrm{gap}}$ for each reconstruction method are shown in Fig. 8.6. Both the calorimeter cells and cone islands rely only on information from the calorimeter. In general, the reconstructed value of $E_{\mathrm{T}}^{\mathrm{gap}}$ is lower than the true value due to energy loss in inactive material and non-detection of very low energy particles. At very low $E_{\mathrm{T}}^{\mathrm{gap}}$, the reconstructed and true value are very close. The effect of noise is proportionally larger at low $E_{\mathrm{T}}^{\mathrm{gap}}$ and this counteracts the other effects. For the uncorrected ZUFOs, the detector- and hadron-level values are well reconstructed over the whole range of the variable. At low energy, tracking information is often more reliable. This is illustrated in Fig. 8.7 which shows the distribution of the ZUFO transverse energies for the inclusive sample of events. The results show that the fraction of the transverse energy calculated using tracks is generally higher at low E_{T}. The use of tracking information also means that the effect on the measurement of noise in the calorimeter is reduced. For the corrected ZUFOs, the reconstructed value of $E_{\mathrm{T}}^{\mathrm{gap}}$ is generally larger than the true value. This shows that,

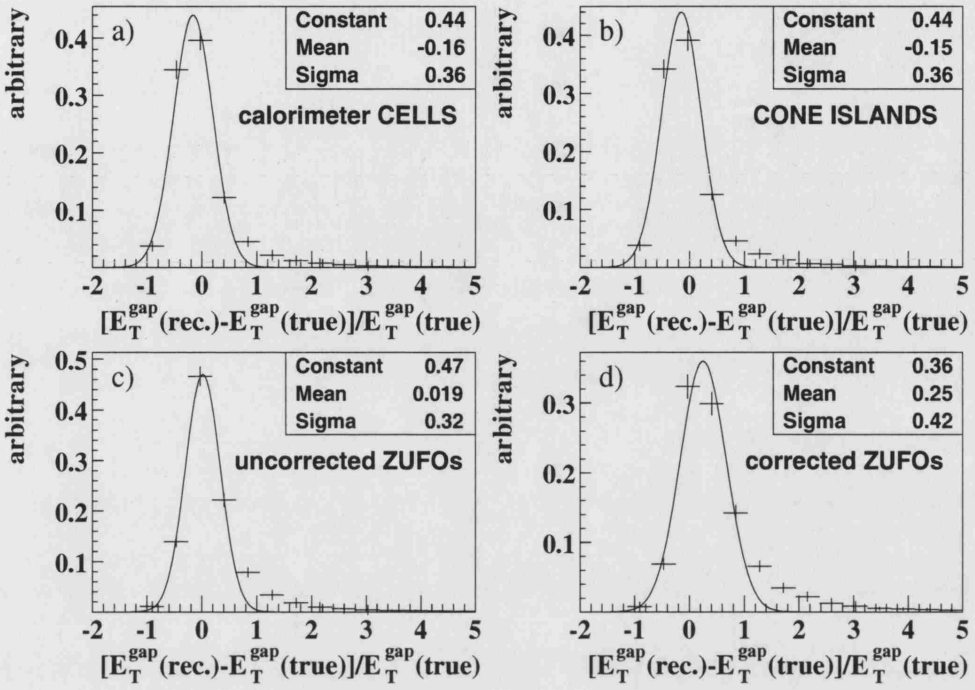

Figure 8.8: The resolution of $E_{\mathrm{T}}^{\mathrm{gap}}$ for reconstructions performed using a) calorimeter cells b) calorimeter cone islands c) uncorrected ZUFOs and d) corrected ZUFOs. The results are from the PYTHIA photoproduction Monte Carlo. The curve shows a Gaussian fit to the peak of the distribution and the values in the text box are the parameters of the fit.

for the proportion of ZUFOs which use calorimeter information, the correction factors are too large.

To quantify the quality of the reconstruction, the resolutions of $E_{\mathrm{T}}^{\mathrm{gap}}$ for each reconstruction method are shown in Fig. 8.8. A Gaussian function has been fitted to the peak of the distribution in order to estimate the values of the pulls and resolutions. For calorimeter cells and cone islands the pull is $\sim -15\%$. In contrast, uncorrected ZUFOs give a pull of $< 2\%$. For corrected ZUFOs the reconstructed value of $E_{\mathrm{T}}^{\mathrm{gap}}$ is generally larger than the true value with a pull of $\sim 25\%$. The corrected ZUFOs also have the poorest resolution which shows that the corrections are degrading the resolution for very low energy objects.

As a result of the conclusions from this section, this analysis uses uncorrected ZUFOs for the reconstruction of the hadronic final state. The results using calorimeter cells are also used as a cross-check on the stability of the measurement to the reconstruction method.

8.7.1 Pull and Resolution

For the inclusive sample of events, Fig. 8.9 shows the distributions of X(rec.)-X(true) or [X(rec.)-X(true)]/X(true) for a variety of calorimeter and jet quantities for events satisfying both the detector and hadron level requirements. The results have been obtained using the PYTHIA photoproduction Monte Carlo using uncorrected ZUFOs for the reconstruction of the hadronic final state. In order to quantify the quality of the reconstruction, a Gaussian function has been fitted to the peak of the distribution.

For the y distribution, the reconstructed value has been calculated using the Jacquet-Blondel method. This distribution has been separated into low and high y regions to study the pull and resolution over the cut boundaries. The results show that the reconstructed value is lower than the true value by ~ 0.05 at low y and ~ 0.02 at high y. The resolutions are similar at both low and high y, and have values of $\sim 0.04 - 0.05$.

For the jet quantities (E_T,η,ϕ), hadron and detector level jets have been matched as described in Section 4.8.1. The distributions contain both the leading and trailing jets. The reconstructed jet transverse energies are, on average, $\sim 10\%$ lower than the hadron-level values. The jet η and ϕ distributions are well reconstructed with the pulls being less than 0.005 and the resolutions $\sim 0.06 - 0.07$. The value of $\bar{\eta}$ is also well reconstructed and has a resolution of ~ 0.06.

8.8 Monte Carlo Description of Data

In order for the Monte Carlo samples described in Section 8.6 to be used with confidence to unfold for detector effects, it is essential that they provide an adequate description of the data. In particular, the quantities that are used to define the data sample should be reasonably well modelled in order that they do not introduce any unexpected systematic bias into the extraction of the cross section. In this section, the description of the data by the Monte Carlo, for a variety of detector (particularly jet) quantities and kinematic variables, is discussed. For this study, the events from both the data and the Monte Carlo have been required to pass the final selection cuts for the inclusive sample (see Section 8.5). In each of the plots, the data is shown by the solid points and the PYTHIA photoproduction and high-t γ Monte Carlo samples are shown by the open circles and open stars respectively. In general, the distribution of the mixed sample is very similar to that of the photoproduction sample and so is not shown unless explicitly stated. In each case, the Monte Carlo has been normalised to the total number of events in the inclusive sample.

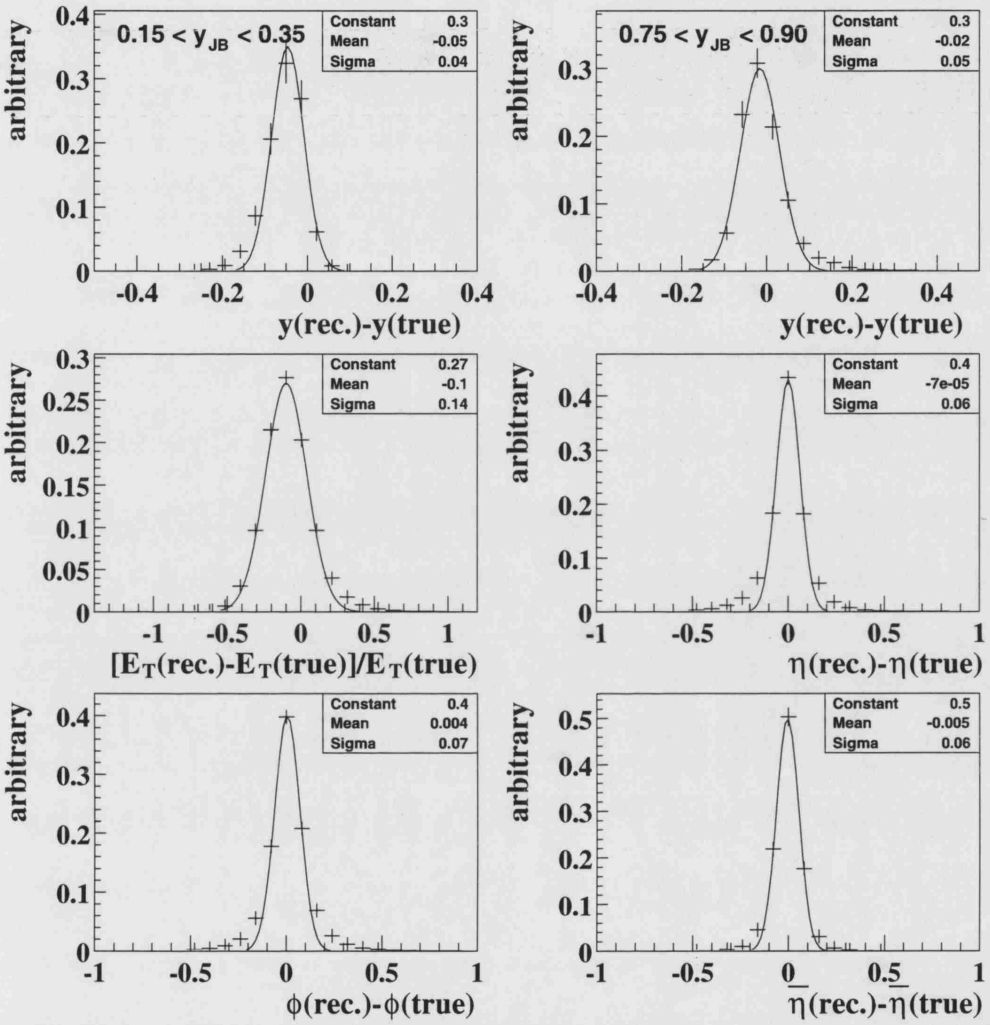

Figure 8.9: The resolutions of calorimeter and jet quantities for the inclusive sample of events according to the PYTHIA photoproduction Monte Carlo. For the jet E_T, η and ϕ, the plot contains the two highest transverse energy jets in the event. The curve shows a Gaussian fit to the peak of the distribution and the values in the text box are the parameters of the fit.

8.8.1 Jet Quantities

Figure 8.10 shows the transverse energy and pseudo-rapidity distributions for the leading and trailing jets. The E_T distributions fall approximately exponentially from the threshold value. The leading jet has a higher average transverse energy and the distribution extends to higher values of E_T in comparison to the trailing jet. This may be due to the higher jet energy pedestal in the forward direction. The transverse energy distributions are adequately described by the PYTHIA photoproduction Monte Carlo, although the model lies below the data at high jet transverse energies. The leading jet transverse energy is also reasonably described by the high-t γ sample. However, the transverse energy spectrum of the trailing jet is harder in the high-t γ sample than in the data.

The pseudo-rapidity of the leading jet peaks at $\eta \sim 1.75$. This corresponds to energy deposits in the FCAL. In contrast, the pseudo-rapidities of the trailing jet peak near the BCAL/RCAL interface at $\eta \sim -1$. These distributions are reasonably well described by the PYTHIA photoproduction and high-t γ Monte Carlo samples. However, the high-t γ sample has a slightly higher average value of the leading jet pseudo-rapidity and a lower average value of the trailing jet pseudo-rapidity relative to the data.

The distribution of the average pseudo-rapidity (or boost), $\bar{\eta}$, shows that the data are strongly boosted in the proton direction, with the distribution peaking at $\bar{\eta} \sim 0.5$. The data are adequately described by both the PYTHIA photoproduction and high-t γ Monte Carlo sample. The $\Delta\eta$ distribution is steeply falling. It is well described by the photoproduction Monte Carlo. However, the high-t γ sample has a shallower fall-off, showing a larger number of events with large jet separation.

Figures 8.11 and 8.12 shows the transverse energy distributions of the leading and trailing jets in four bins of $\Delta\eta$. As the separation, $\Delta\eta$, increases, the transverse energy spectrum becomes softer. This is particularly apparent for the trailing jet. The PYTHIA photoproduction sample gives a reasonable description of the data.

8.8.2 Jet Profiles

The study of jet profiles gives a sensitive test of the description of the data by the Monte Carlo. Jet profiles give the distribution of the transverse energy around the jet axis. For each jet, the measured transverse energy can be found as a function of the quantity $\delta\eta = \eta^{\mathrm{ZUFO}} - \eta^{\mathrm{jet}}$ ($\delta\phi = \phi^{\mathrm{ZUFO}} - \phi^{\mathrm{jet}}$) within a radius $|\delta\phi| < 1$ ($|\delta\eta| < 1$). The quantity η^{ZUFO} (ϕ^{ZUFO}) is the position in pseudo-rapidity (azimuth) of a particular ZUFO while η^{jet} (ϕ^{jet}) is the position of the jet axis. The jet profile geometry of the trailing jet is shown in Fig. 8.13. The profiles themselves are formed by plotting the

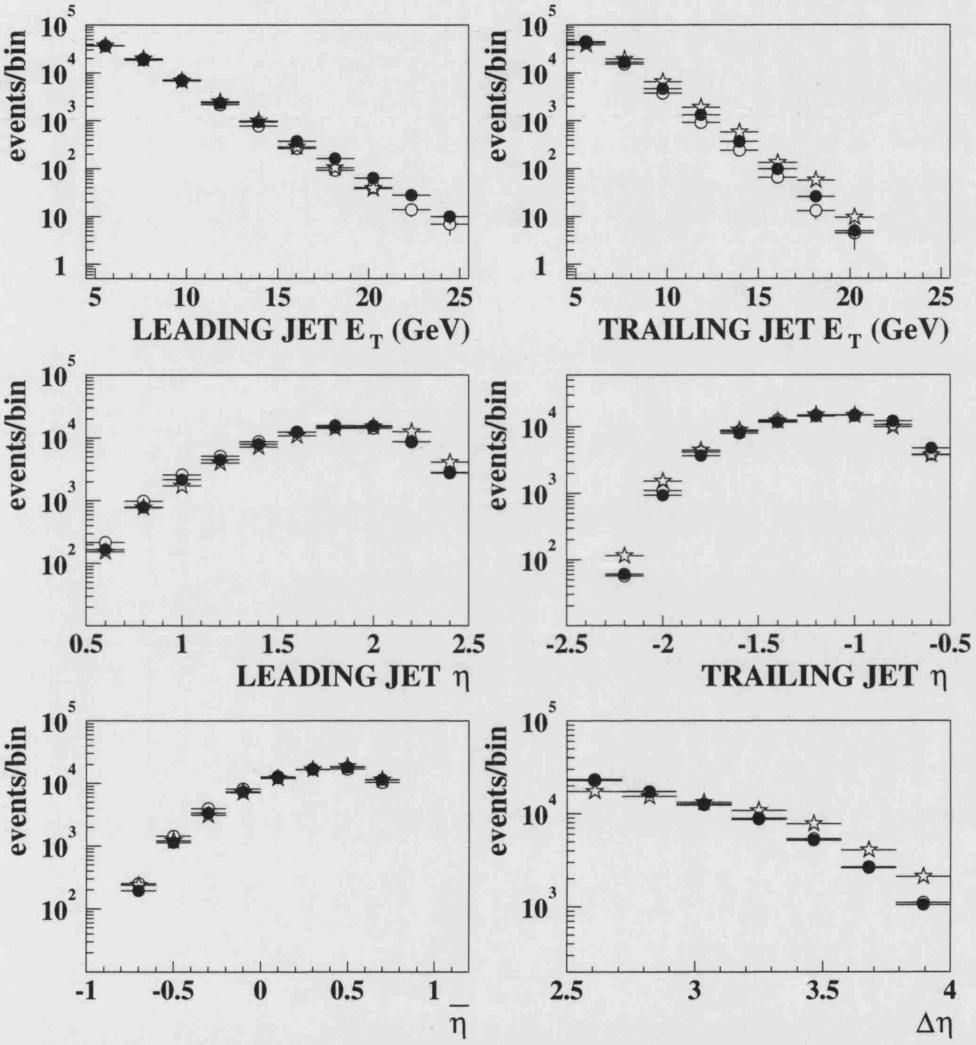

Figure 8.10: The transverse energy and pseudo-rapidity distributions for the leading and trailing jets for the inclusive sample of events. The uncorrected ZEUS data are shown by the solid points. The prediction of the PYTHIA photoproduction and high-t γ samples are shown by the open circles and open stars respectively.

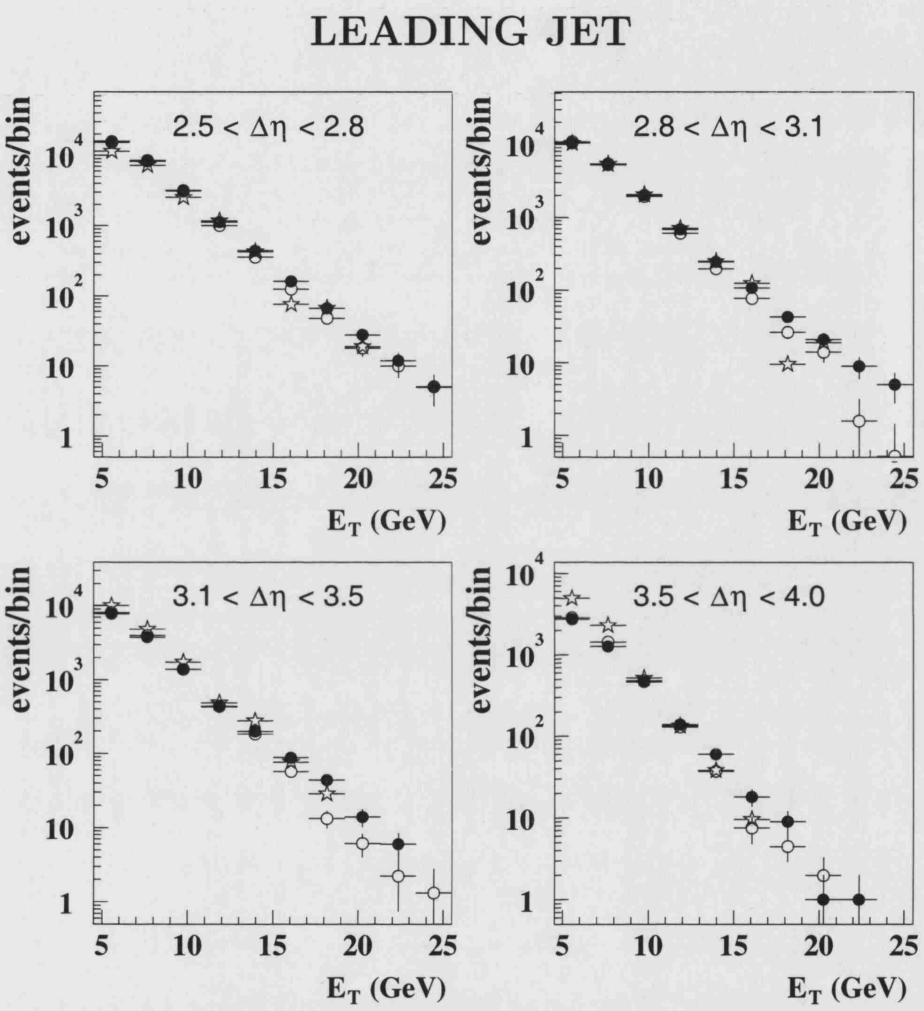

Figure 8.11: The transverse energy distributions of the leading jet in bins of $\Delta\eta$. The uncorrected ZEUS data are shown by the solid points. The prediction of the PYTHIA photoproduction and high-t samples are shown by the open circles and open stars, respectively.

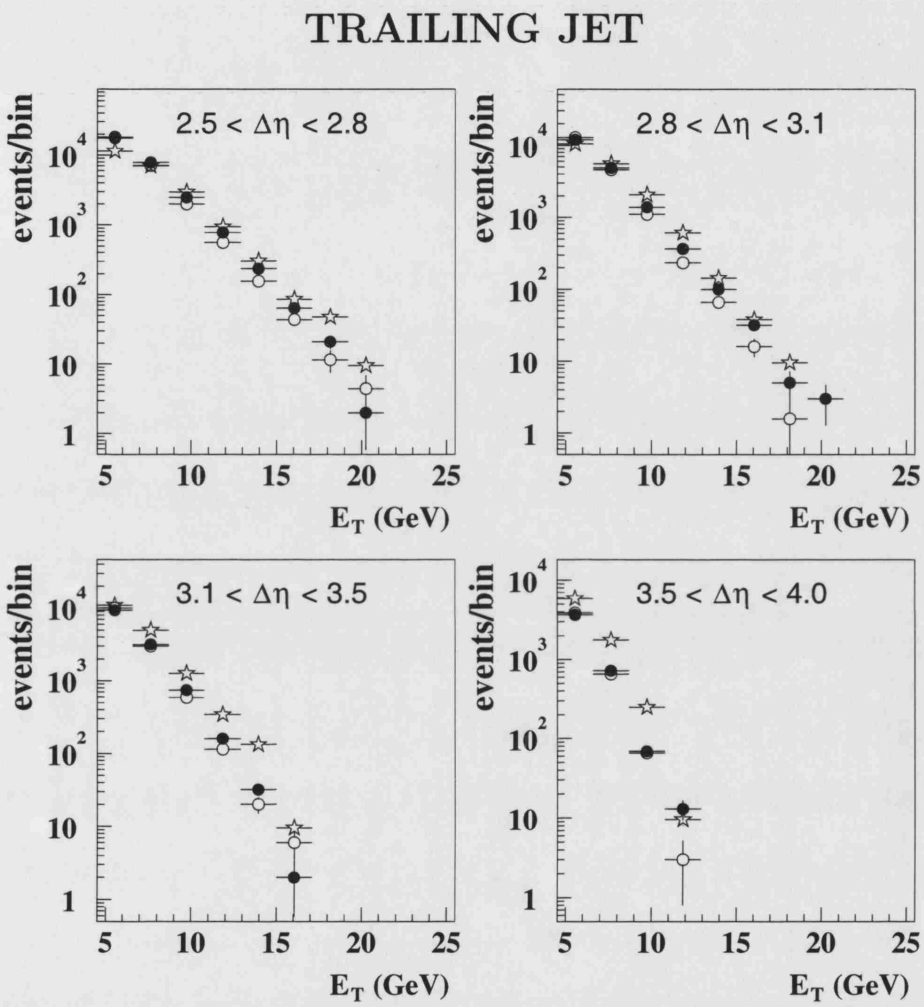

Figure 8.12: The transverse energy distributions of the trailing jet in bins of $\Delta\eta$. The uncorrected ZEUS data are shown by the solid points. The prediction of the PYTHIA photoproduction and high-t samples are shown by the open circles and open stars, respectively.

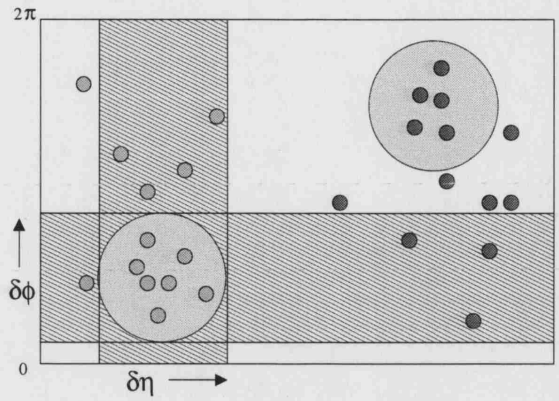

Figure 8.13: The jet profile geometry for the trailing jet. The jets are shown as the large circles and the individual final-state particles are shown by the small circles. The shaded bands indicate the regions included in the $\delta\eta$ and $\delta\phi$ jet profiles.

quantities $\delta\eta$ ($\delta\phi$) weighted by the transverse energy of the appropriate ZUFO, $E_{\mathrm{T}}^{\mathrm{ZUFO}}$, and divided by the bin width.

The jet profiles of the leading and trailing jets for the inclusive sample of events are shown in Fig. 8.14. The uncorrected ZEUS data are shown by the solid points and the predictions of the PYTHIA photoproduction and high-t γ samples are shown by the solid and dashed histograms respectively. The PYTHIA photoproduction sample gives a reasonable description, both of the collimated jet core, and of the pedestal energy. For the leading jet, there remains a small discrepancy of < 0.5 GeV per unit $\delta\eta$ in the forward direction. This is possibly due to insufficient multi-parton interactions generated in the model. The energy pedestal of the leading jet is, on average, ~ 1 GeV higher than that for the trailing jet, as illustrated by the $\delta\phi$ profiles. The jet profiles for the PYTHIA high-t γ sample are more highly collimated than those of the data, with a significantly lower jet energy pedestal. The high degree of collimation is mainly due to the fact that this sample contains only quark jets in the final state. In contrast, the photoproduction sample also contains gluon jets which tend to be broader than those due to quarks [193]. The lower energy pedestal is also expected and is due to the fact that the exchange of the (colour singlet) photon gives rise to less radiation into the central rapidity region than the quark and gluon propagators that dominate standard photoproduction processes.

Figure 8.15 shows the jet profiles for the gap sample of events with $E_{\mathrm{T}}^{\mathrm{gap}} < 1.2$ GeV. Comparison with the profiles for the inclusive sample in Fig. 8.14 illustrates the suppression of energy flow in the region between the leading and trailing jets. The distributions are well described by the PYTHIA photoproduction sample. The high degree of collimation and the lower energy pedestal is still apparent in the high-t γ

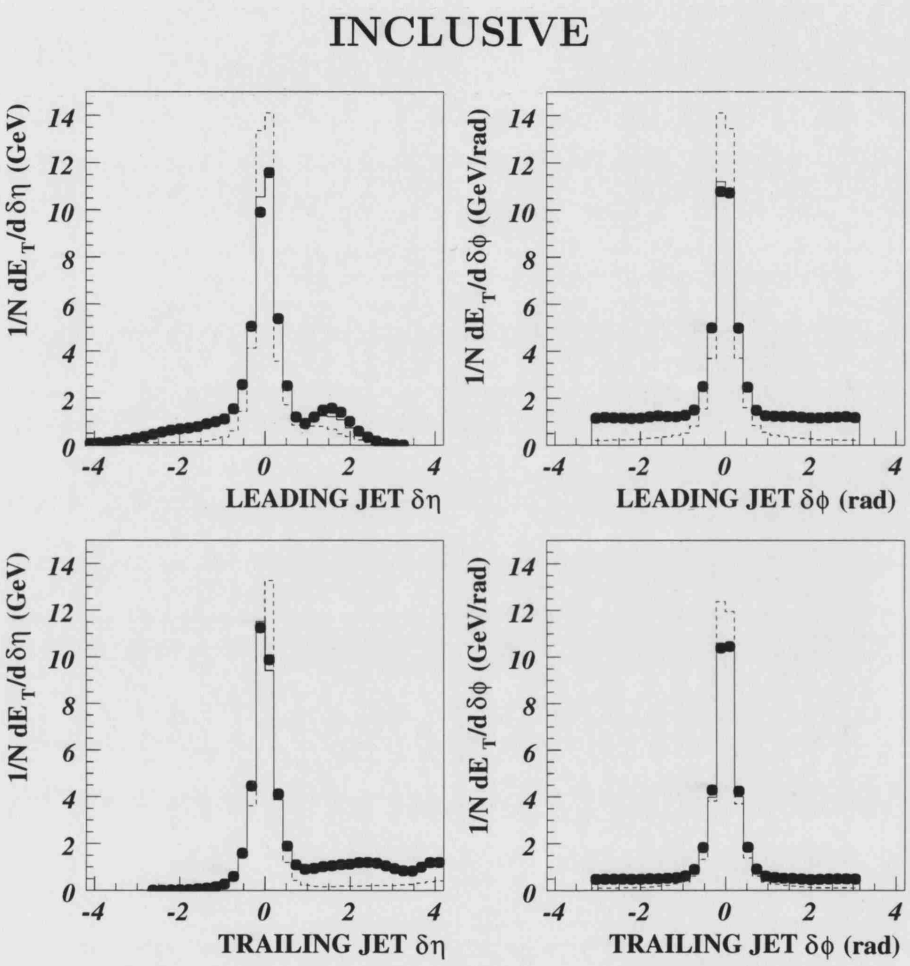

Figure 8.14: The transverse energy jet profiles for the leading and trailing jets as a function of $\delta\eta$ and $\delta\phi$ for the inclusive sample of events. The uncorrected ZEUS data are shown by the solid points. The prediction of the PYTHIA photoproduction sample is shown by the solid histogram and the prediction of the high-t γ sample is shown by the dashed histogram.

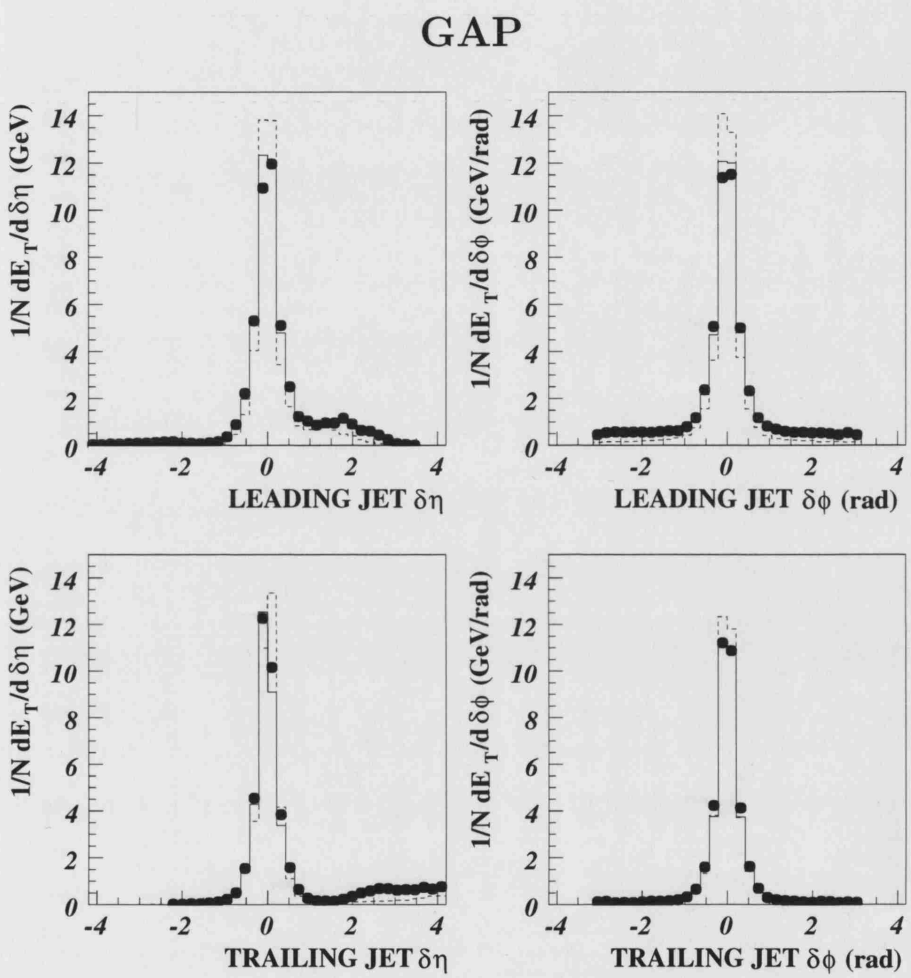

Figure 8.15: The transverse energy jet profiles for the leading and trailing jets as a function of $\delta\eta$ and $\delta\phi$ for the gap sample of events with $E_{\mathrm{T}}^{\mathrm{cut}} = 1.2$ GeV. The uncorrected ZEUS data are shown by the solid points. The prediction of the PYTHIA photoproduction sample is shown by the solid histogram and the prediction of the high-t γ sample is shown by the dashed histogram.

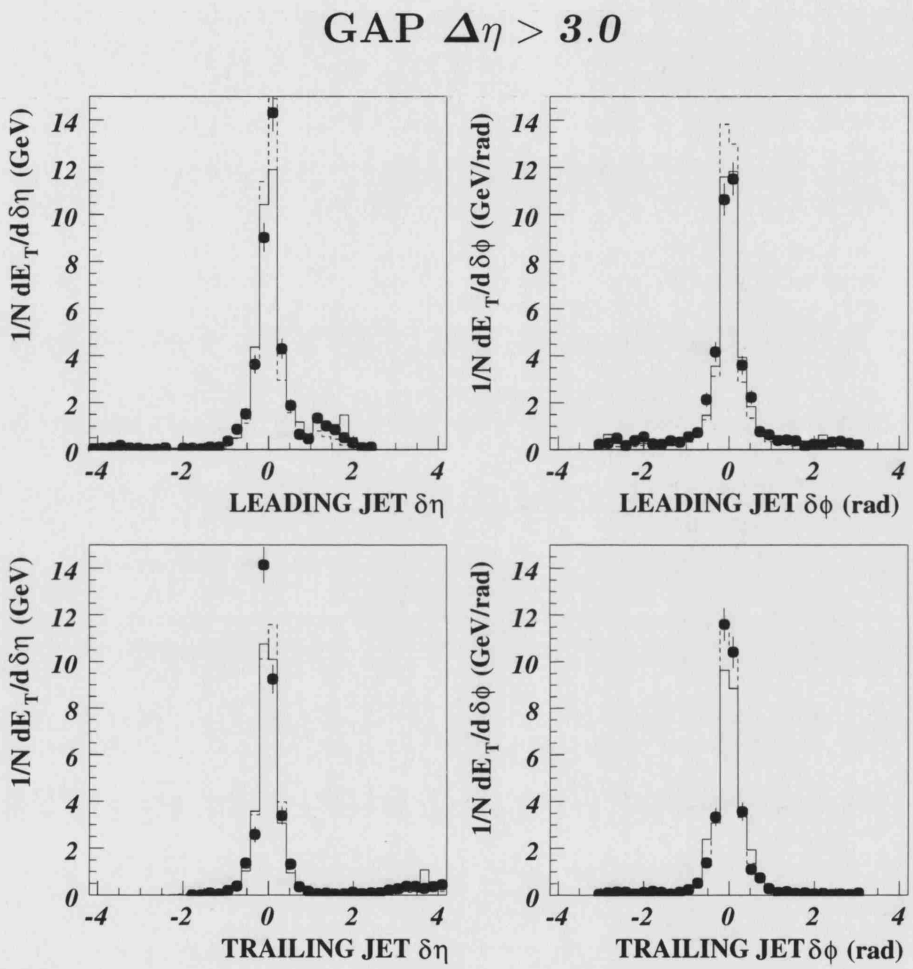

Figure 8.16: The transverse energy jet profiles for the leading and trailing jets as a function of $\delta\eta$ and $\delta\phi$ for the subsample of the gap with $E_T^{cut} = 1.2$ GeV that also satisfies $\Delta\eta > 3.0$. The uncorrected ZEUS data are shown by the solid points. The prediction of the PYTHIA photoproduction sample is shown by the solid histogram and the prediction of the high-t γ sample is shown by the dashed histogram.

sample, particularly for the leading jet. In Fig. 8.16, the profiles for the subsample of the gap events with $\Delta\eta > 3.0$ is shown. The distributions are well reproduced by both the PYTHIA photoproduction and high-t γ Monte Carlo samples and the difference in the degree of collimation of the jets is less apparent.

8.9 Cumulative Efficiencies

It is interesting to study the efficiency at each stage of the event selection. In this context, the efficiency is defined as the fraction of the events passing the hadron-level selection that are also reconstructed and accepted as events at the detector-level (somewhere in the final event sample). Figure 8.17 shows the efficiencies at each stage of the event selection as a function of $\Delta\eta$. The results are shown for the PYTHIA photoproduction sample. The results from the PYTHIA mixed sample have also been checked and found to be consistent. In each case, the solid points show the results for the inclusive sample of events, while the open circles show the results for the gap sample with $E_{\mathrm{T}}^{\mathrm{cut}} = 1.0$ GeV. The results for all gap samples show similar trends.

The efficiency at the FLT is $\gtrsim 85\%$ over the whole range of $\Delta\eta$ while the efficiency at the SLT is close to 100%. At the TLT, the efficiency is $\sim 75\%$, giving an overall cumulative efficiency of $\gtrsim 60\%$ at this stage of the event selection. The offline event selection represents all cleaning cuts described in Section 5.4. This has a cumulative efficiency of $\gtrsim 50\%$ following all offline cleaning cuts. The largest reduction in efficiency at the offline selection stage arises from the rejection of DIS electrons through the requirements on y_e. The reason for this is illustrated in Fig. 5.9, which shows the distribution of y_e for a LUMI tagged sample of photoproduction. The plot shows that the cut on $y_e < 0.85$ rejects some genuine photoproduction events. However, this cut has been imposed in order to ensure a corresponding increase in purity. The selection of two jet photoproduction events corresponds to the nominal selection criteria described in Section 5.4.1. This stage is relatively inefficient, largely as a result of the poor resolution on the jet transverse energies. However, this efficiency is independent of whether or not the event contains a gap. This indicates that the jets themselves are similar in both gap and non-gap events. The final stage is the additional selection criteria on $\bar{\eta}$, $\Delta\eta$ and $E_{\mathrm{T}}^{\mathrm{gap}}$ (the latter for the gap sample only). Here, for the first time, the efficiency depends on whether the event contains a gap. In general, the $\bar{\eta}$ and $\Delta\eta$ requirements have little effect on the overall efficiency. However, the $\Delta\eta$ requirement does reduce the efficiency in the first bin due to the fact that migrations to (from) this bin can only occur from (towards) larger $\Delta\eta$. The low efficiency of the gap sample is due to the poor resolution on the quantity $E_{\mathrm{T}}^{\mathrm{gap}}$.

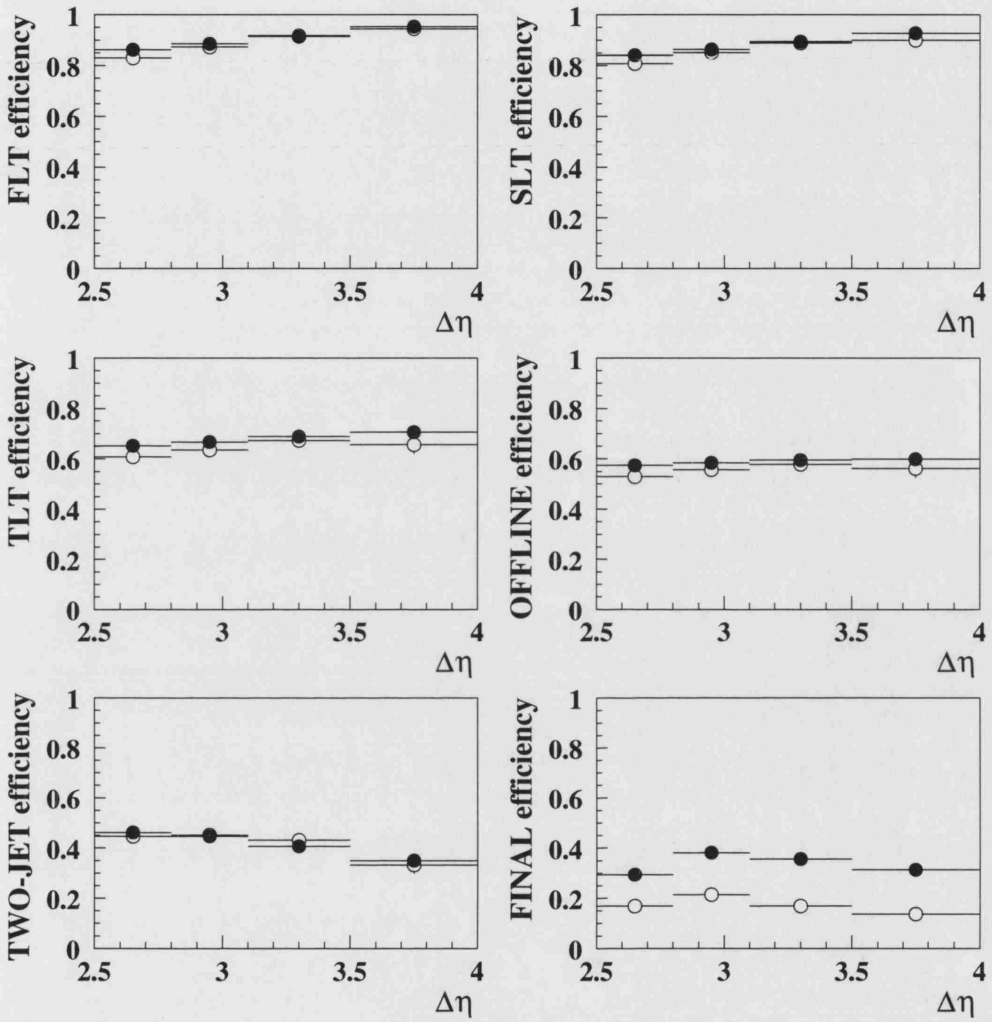

Figure 8.17: The cumulative efficiencies at each stage of the event selection according to the PYTHIA photoproduction Monte Carlo. The results for the inclusive sample are shown by the solid points and the results for the gap sample with $E_{\mathrm{T}}^{\mathrm{cut}} = 1.0$ GeV are shown by the open circles. From top left to bottom right: The efficiency up to the FLT, SLT, TLT, offline selection (see Section 5.4), two jet photoproduction selection (see Section 5.4.1) and the final event sample (defined in Section 8.5).

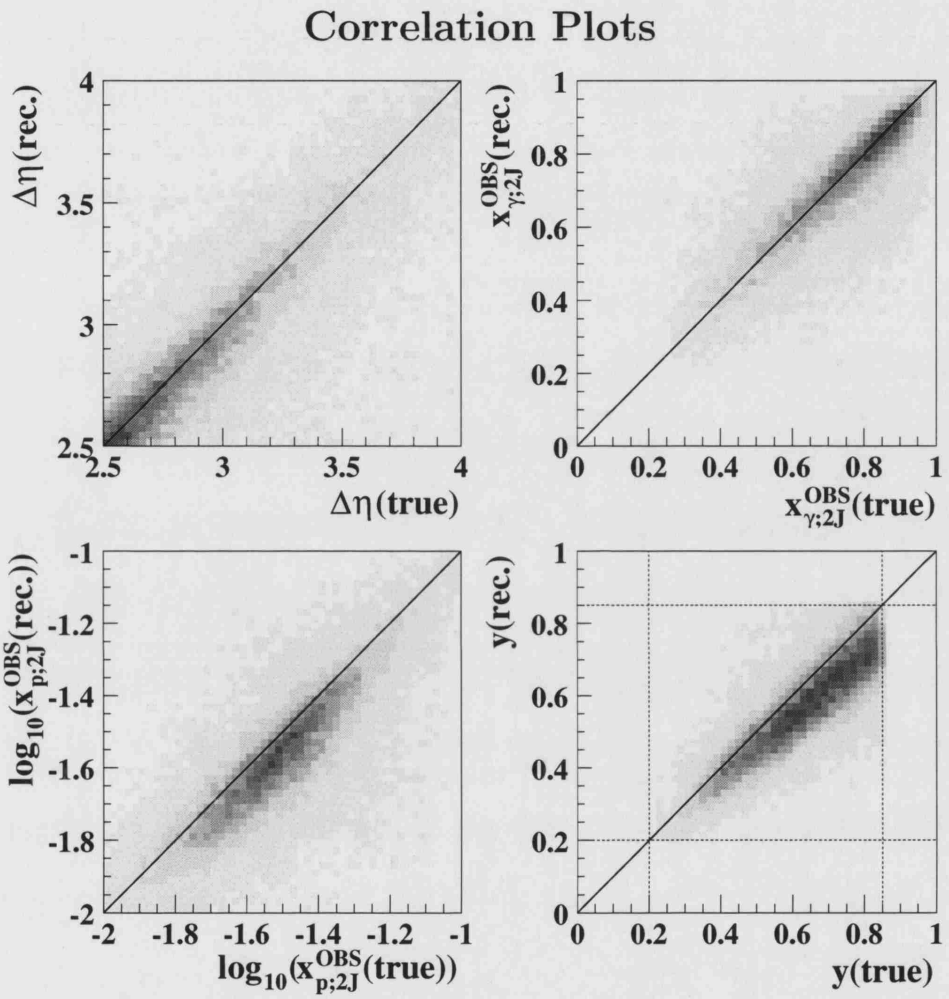

Figure 8.18: The correlations between the true and reconstructed values of the cross section variables $\Delta\eta$, $x_{\gamma;2\mathrm{J}}^{\mathrm{OBS}}$, $\log_{10}(x_{p;2\mathrm{J}}^{\mathrm{OBS}})$ and y from the PYTHIA photoproduction Monte Carlo sample. The diagonal lines illustrate the case for which $X(\mathrm{rec.}) \equiv X(\mathrm{true})$. The dashed lines on the y correlation plot indicate the cuts imposed on this variable. In each case, the darkest shading represents the highest density of points.

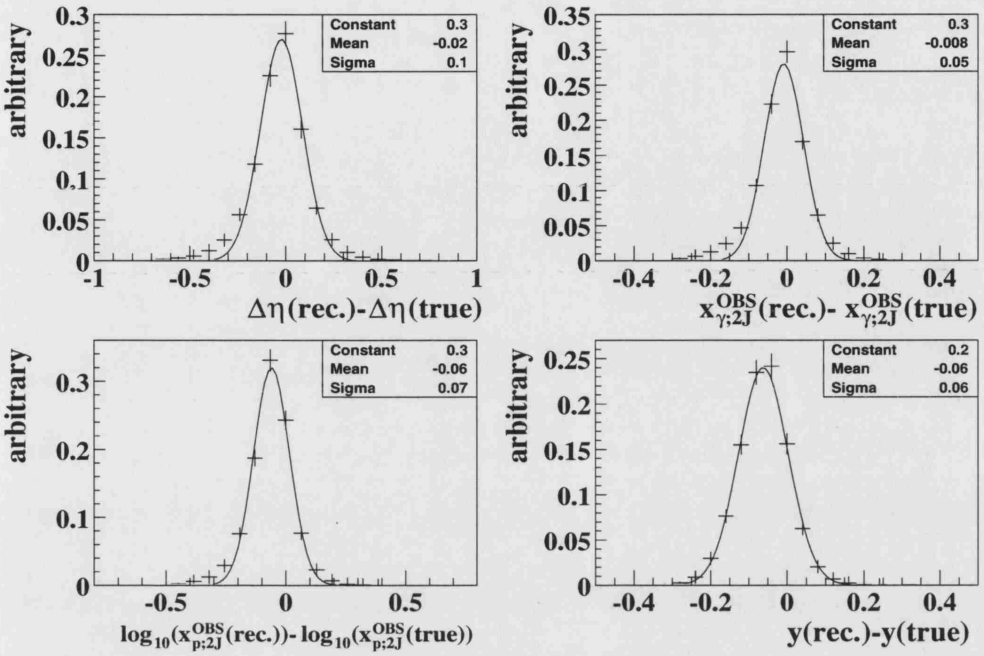

Figure 8.19: The pull and resolution of the cross section variables $\Delta\eta$, $x_{\gamma;2\mathrm{J}}^{\mathrm{OBS}}$, $\log_{10}(x_{p;2\mathrm{J}}^{\mathrm{OBS}})$ and y. All results are from the PYTHIA photoproduction Monte Carlo sample. The curve shows a Gaussian fit to the peak of the distribution and the values in the text box give the parameters of the fit.

8.10 Pull and Resolution

The correlations between the true and reconstructed values of the variables $\Delta\eta$, $x_{\gamma;2\mathrm{J}}^{\mathrm{OBS}}$, $\log_{10}(x_{p;2\mathrm{J}}^{\mathrm{OBS}})$ and y from the PYTHIA photoproduction Monte Carlo are shown in Fig. 8.18. The results show a strong correlation indicating that the cross section variables are, in general, well reconstructed. To quantify this further, the Gaussian-fit method (described in Section 7.8) has been used to estimate the pull and resolution on the cross section variables. The results from the PYTHIA photoproduction Monte Carlo are shown in Fig. 8.19. The results from the mixed sample have also been checked and found to be consistent. In each case, the curve shows a Gaussian fit to the peak of the distribution. The parameters of the fit are given in the text box on each figure, with the mean and sigma representing the pull and resolution, respectively. The results show that the pulls on $\Delta\eta$ and $x_{\gamma;2\mathrm{J}}^{\mathrm{OBS}}$ are ≤ 0.02, while those on $\log_{10}(x_{p;2\mathrm{J}}^{\mathrm{OBS}})$ and y are around $\sim 0.06 - 0.07$.

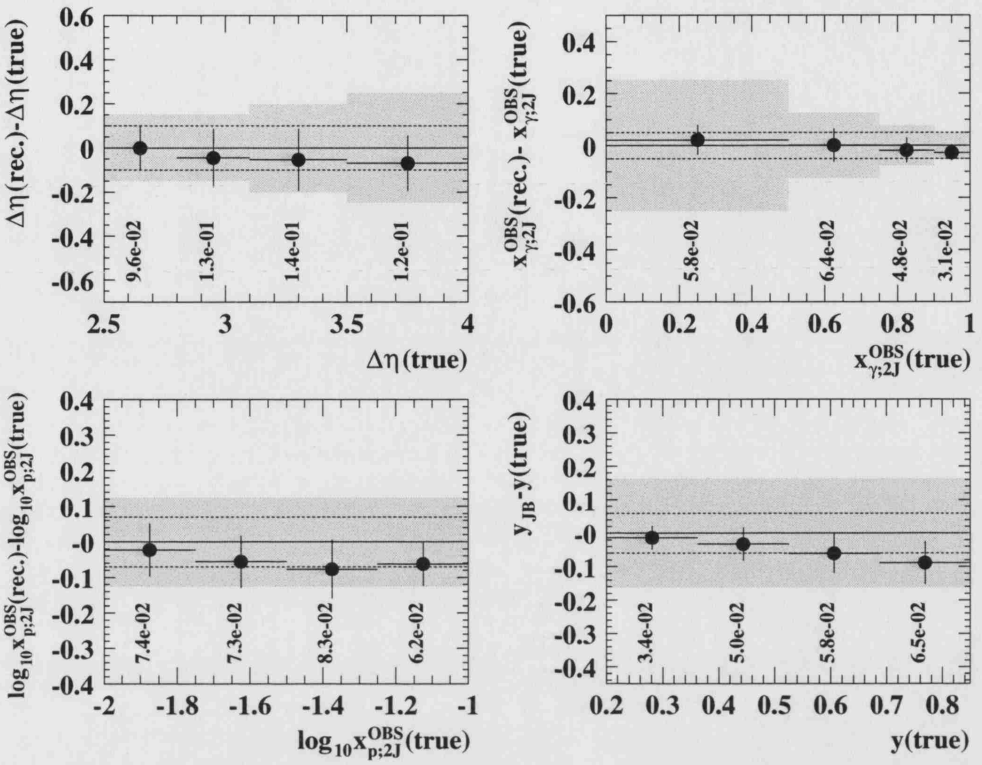

Figure 8.20: The results of a binned Gaussian fit to the distribution X(rec.)-X(true) for the cross section variables X = $\Delta\eta$, $x_{\gamma;2\mathrm{J}}^{\mathrm{OBS}}$, $\log_{10}(x_{p;2\mathrm{J}}^{\mathrm{OBS}})$ and y. The results from the PYTHIA photoproduction Monte Carlo sample are shown. The positions of the points show the value of the pull and the vertical error bars and text indicate the resolution in each bin used for the final measurement. The horizontal error bars indicate the width of the bins. The shaded band indicates the chosen bin widths and the dashed lines show the resolution of the whole distribution (see Fig. 8.19).

8.10.1 Binning of the Data

In order to ensure that the unfolding process is not significantly affected by long range migrations between bins, the chosen bin widths should be larger than the value of the resolution in each bin. Figure 8.20 shows the binned mean value of the X(rec.)-X(true) distributions as a function of X(true) for each of the cross section variables X = $\Delta\eta$, $x_{\gamma;2\mathrm{J}}^{\mathrm{OBS}}$, $\log_{10}(x_{p;2\mathrm{J}}^{\mathrm{OBS}})$ and y. The points give the pull (mean of the fit) and the vertical error bars and text give the resolution (width of the fit) in each bin. For comparison, the dashed lines show the value of the resolution for the whole distribution (see Fig. 8.19) and the shaded region indicates the widths of the bins chosen for the final cross section measurement.

The pull of $\Delta\eta$ shows a systematic dependence on the value of the variable, with the deviation from the true value increasing as a function of $\Delta\eta$. The $\Delta\eta$ resolution remains approximately constant as a function of the variable. In contrast, the $x_{\gamma;2J}^{OBS}$ distribution shows that the resolution improves as a function of increasing $x_{\gamma;2J}^{OBS}$. This is due to the fact that higher values of $x_{\gamma;2J}^{OBS}$ are correlated with higher jet transverse energies and such jets can be better reconstructed in the detector. For similar reasons, the quality of reconstruction of the variable $\log_{10}(x_{p;2J}^{OBS})$ also improves with increasing $x_{p;2J}^{OBS}$. The results for the y distribution show that the resolution generally worsens as a function of increasing y. For every variable, the chosen bin width is at least a factor of two larger than the value of the resolution in that bin. However, the values of the pull are reasonably large at high $\log_{10}(x_{p;2J}^{OBS})$ and high y. To check that this does not have a significant effect on the measured cross sections, the inclusive cross sections have been checked using corrected ZUFOs (see Section 8.13). This is useful since the pulls on hadronic quantities such as jet E_T, y and $x_{p;2J}^{OBS}$ are small for corrected ZUFOs (refer to Section 7.8). Therefore, while this method is not suitable for the reconstruction of gap events, it can provide a useful test of the stability of the measurement to long-range migrations between bins for the inclusive sample.

8.10.2 Bin Stabilities

Figure 8.21 shows the stability (see Eq. 6.13) of the measured distributions with respect to migrations between bins. The solid squares show the results for the inclusive sample and the open squares show the results for the gap sample with $E_T^{cut}(\text{true}) = 1.0$ GeV ($E_T^{cut}(\text{rec.}) = 1.2$ GeV). The results for all gap samples show similar features. The stabilities are $\gtrsim 40\%$ in all bins for all measured variables and the results are relatively independent of whether or not the event contains a gap.

8.11 The Uncorrected Results

It has already been established that the PYTHIA photoproduction Monte Carlo sample provides an adequate description of the data for a variety of quantities. In this section, the uncorrected results are presented. Firstly, the detector level distributions of the quantities used to define a gap (mini-jet multiplicity and E_T^{gap}) are studied. Secondly, the detector level distributions of the variables to be measured ($\Delta\eta$, $x_{\gamma;2J}^{OBS}$, $\log_{10}(x_{p;2J}^{OBS})$ and y) are presented in the same bins as the final cross section measurements (as established in Section 8.10.1). The data is compared to the PYTHIA photoproduction, high-t γ and mixed samples. In each figure, the uncorrected ZEUS data are shown by the solid points and the PYTHIA photoproduction, high-t γ and mixed samples are shown by the open circles, open stars and dashed lines respectively. In each plot, the Monte Carlo predictions have been normalised to the total number of events in the inclusive sample of data, irrespective of whether that event contains a gap.

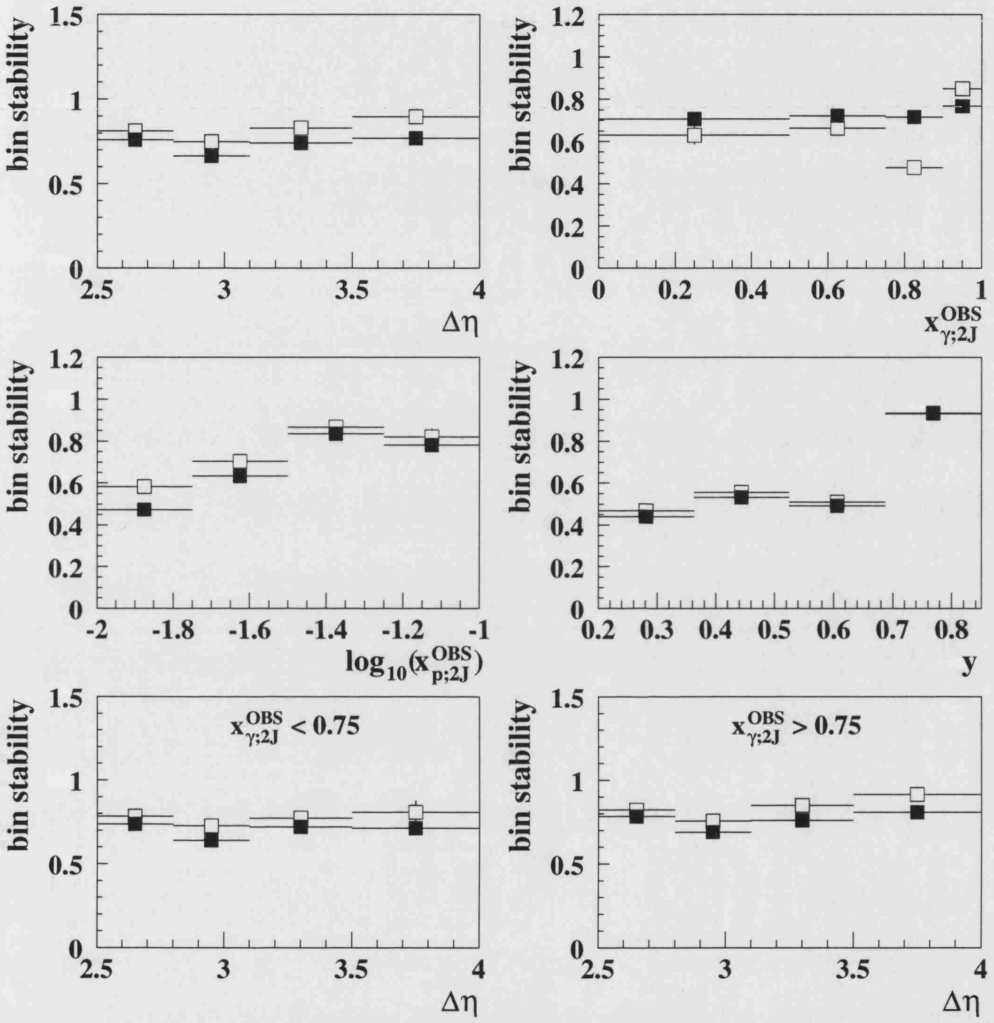

Figure 8.21: The bin stabilities of $\Delta\eta$, $x^{\rm OBS}_{\gamma;2J}$, $\log_{10}(x^{\rm OBS}_{p;2J})$ and y calculated from the PYTHIA photoproduction Monte Carlo sample. The solid squares show the results for the inclusive sample and the open squares show the results for the gap sample of events with $E_{\rm T}^{\rm cut} = 1.0$ GeV. The horizontal error bars indicate the widths of the bins.

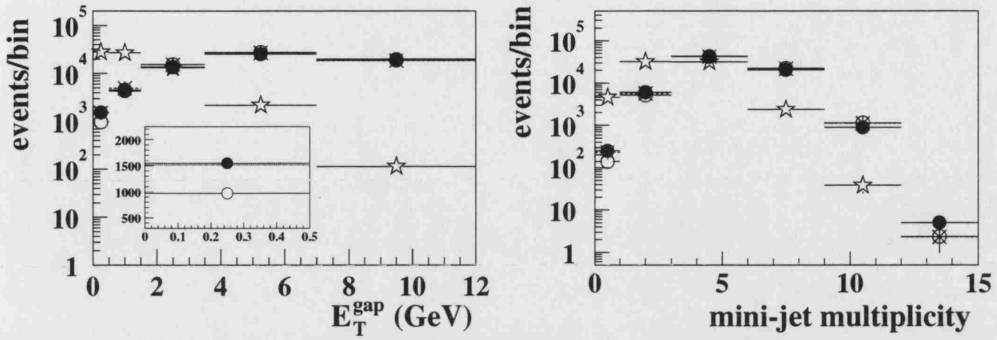

Figure 8.22: The distributions of E_T^{gap} and the mini-jet multiplicity for the inclusive sample of events. The ZEUS data are shown by the solid points. The prediction of the PYTHIA photoproduction, high-t γ and mixed samples are shown by the open circles, open stars and dashed lines respectively. The horizontal error bars indicate the width of the bins. The inset is an enlarged version of the region $E_T^{gap} < 0.5$ GeV.

8.11.1 Energy Flow and Multiplicity

The E_T^{gap} and mini-jet multiplicity distributions are shown in Fig. 8.22. The mean value of E_T^{gap} is ~ 5 GeV. The photoproduction Monte Carlo gives a reasonable description of the shape of the distribution although slightly underestimates the data for low values of E_T^{gap}. The PYTHIA high-t γ sample shows a larger number of events with small E_T^{gap}. The 2% contribution from electroweak colour singlet exchange used to produce the mixed sample was chosen to approximately agree with the data in the region $E_T^{gap} < 0.5$ GeV, as illustrated by the inset which shows an enlarged version of the first bin of the plot. The dashed lines show that the resulting mixed sample gives a good description of the data over the whole range of the variable.

On average, ~ 5 mini-jets are found between the two highest transverse energy jets in the event. The shape of the mini-jet multiplicity distribution is reasonably well described by the PYTHIA photoproduction model although there is some indication that the data lie in excess of the model at very low multiplicity. The high-t γ sample predicts a larger number of events with low mini-jet multiplicities than is shown by the data. The data are well described by the mixed Monte Carlo over the whole range of the distribution.

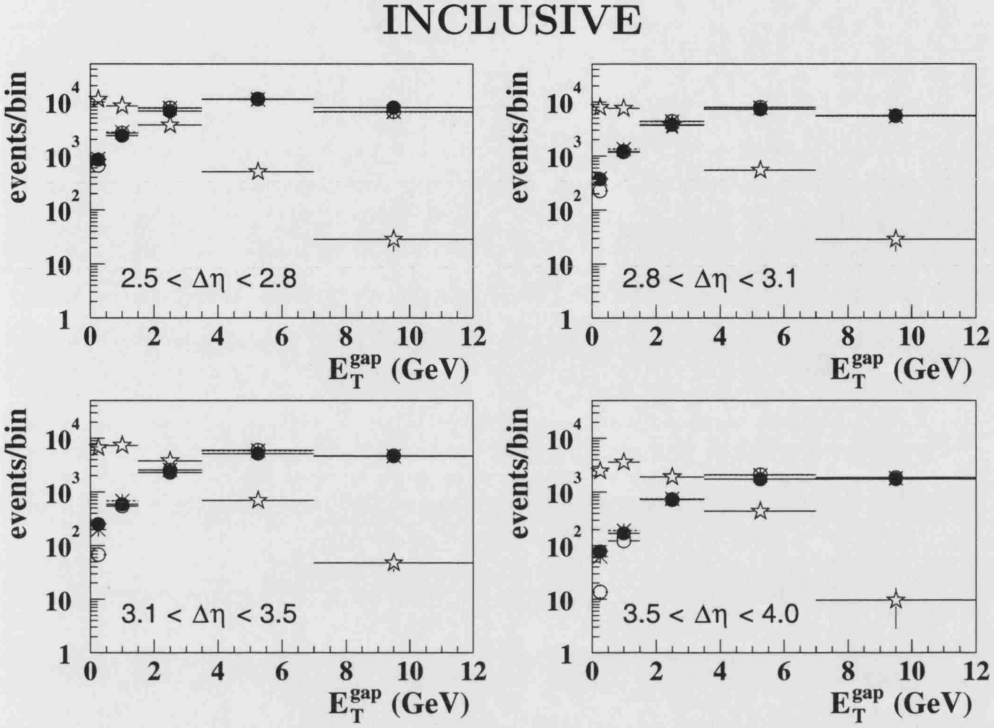

Figure 8.23: The distribution of E_T^{gap} in bins of $\Delta\eta$. The ZEUS data are shown by the solid points. The prediction of the PYTHIA photoproduction, high-t γ and mixed samples are shown by the open circles, open stars and dashed lines respectively. The horizontal error bars indicate the widths of the bins.

To further investigate the quantities that define gap events in this analysis, the E_T^{gap} and mini-jet distributions have been separated into four bins of $\Delta\eta$. The relevant distributions are shown in Figs. 8.23 and 8.24. For the E_T^{gap} distribution, the data are reasonably well described for $2.5 < \Delta\eta < 2.8$. However, at larger values of $\Delta\eta$, the data begin to lie in excess of the photoproduction model at small E_T^{gap}. The mixed sample again provides a significantly improved description, particularly for $E_T^{gap} < 0.5$ GeV. Similar features are observed for the multiplicity distributions. In particular, as $\Delta\eta$ increases, a discrepancy between the data and the PYTHIA photoproduction Monte Carlo becomes apparent at low multiplicities, with the data lying in excess of the models. This is particularly visible for $\Delta\eta \gtrsim 3.0$. The PYTHIA mixed sample provides an improved description of the data, indicating the need for additional colour singlet exchange in the models.

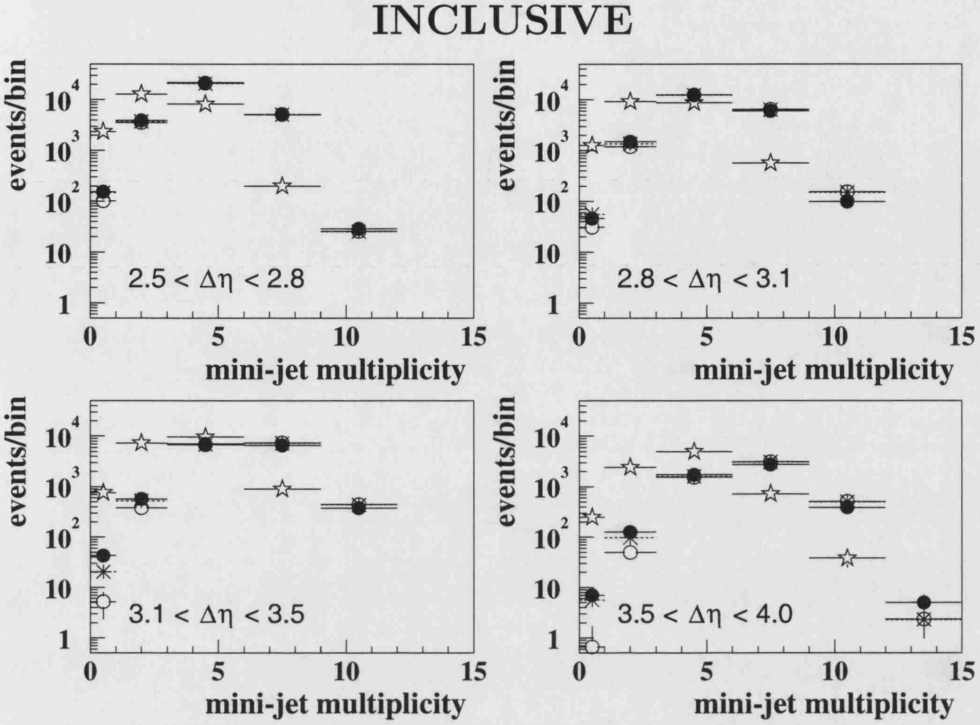

Figure 8.24: The total mini-jet multiplicity in bins of $\Delta\eta$ for the inclusive sample of events. The ZEUS data are shown by the solid points. The prediction of the PYTHIA photoproduction, high-t γ and mixed samples are shown by the open circles, open stars and dashed lines respectively. The horizontal error bars indicate the widths of the bins.

8.11.2 The Inclusive Sample

The inclusive distributions of $\Delta\eta$, $x_{\gamma;2\mathrm{J}}^{\mathrm{OBS}}$, $\log_{10}(x_{p;2\mathrm{J}}^{\mathrm{OBS}})$ and y_{JB} are shown in Fig. 8.25. The $\Delta\eta$ distribution falls from the threshold value of $\Delta\eta = 2.5$ to the limit $\Delta\eta = 4.0$. The PYTHIA photoproduction model gives a good description of the data. The high-t γ sample also shows a falling distribution. However, the fall-off is less steep than the data. The distribution of $x_{\gamma;2\mathrm{J}}^{\mathrm{OBS}}$ has a maximum occurring at $x_{\gamma;2\mathrm{J}}^{\mathrm{OBS}} \sim 0.75$. This is well reproduced by the photoproduction sample. In contrast, the high-t γ sample peaks at higher values of $x_{\gamma;2\mathrm{J}}^{\mathrm{OBS}}$. The minimum value of $x_{p;2\mathrm{J}}^{\mathrm{OBS}}$ is set by the minimum requirement on $\Delta\eta$ since this is equivalent to a restriction on the parton-parton centre-of-mass energy. This is illustrated in Fig. 8.26 which shows the distribution of $x_{p;2\mathrm{J}}^{\mathrm{OBS}}$ for a variety of cuts on $\Delta\eta$. The shape of the $\log_{10}(x_{p;2\mathrm{J}}^{\mathrm{OBS}})$ distribution in Fig. 8.25 is well described by the PYTHIA photoproduction Monte Carlo. The high-t γ distribution is also similar in shape. The y_{JB} distribution has a maximum at ~ 0.6 and is reasonably well described by both the photoproduction and high-t samples.

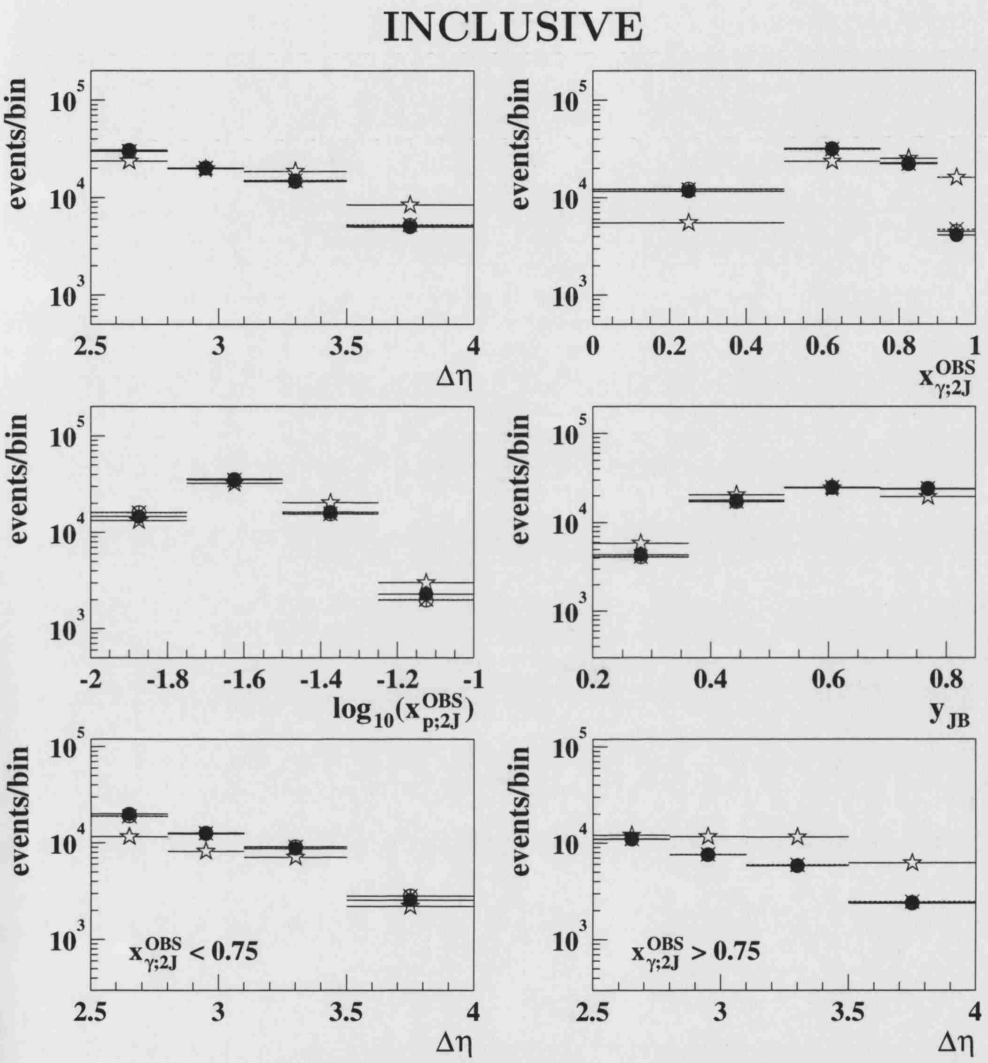

Figure 8.25: The distributions of $\Delta\eta$, $x_{\gamma;2J}^{\rm OBS}$, $\log_{10}(x_{p;2J}^{\rm OBS})$ and $y_{\rm JB}$ for the inclusive sample of events. The ZEUS data are shown by the solid points. The prediction of the PYTHIA photoproduction, high-t γ and mixed samples are shown by the open circles, open stars and dashed lines respectively. The horizontal error bars indicate the widths of the final cross section bins.

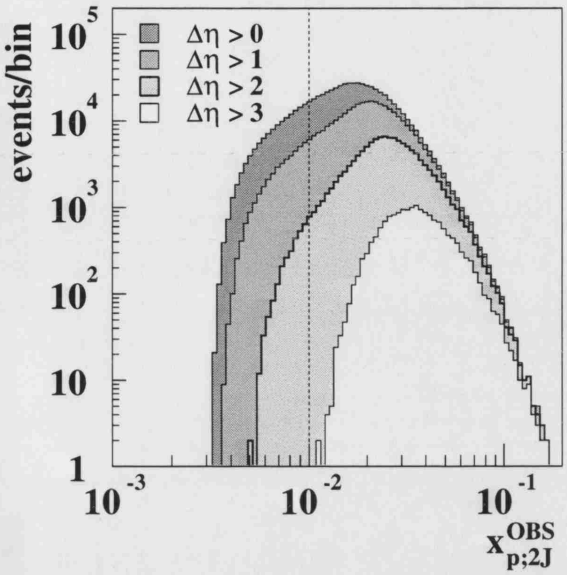

Figure 8.26: The distribution of $x_{p;2J}^{OBS}$ for a variety of $\Delta\eta$ cuts from the 1996-1997 (uncorrected) ZEUS data-set. All inclusive selection cuts are imposed, as described in Section 8.5, except for the cut on $\Delta\eta$ which is as stated on the plot. The dashed line indicates the value of the minimum bin edge used for the measurement of the $\log_{10}(x_{p;2J}^{OBS})$ cross section.

The distribution of $\Delta\eta$ has been further investigated by separating into direct- and resolved-enhanced regions. The description by the PYTHIA photoproduction Monte Carlo is good in both cases. For the resolved-enhanced region, the high-t γ sample lies below the data for $\Delta\eta \lesssim 3.0$, but gives a reasonable description at very large values of $\Delta\eta$. It is interesting to note the reasonable description for $\Delta\eta \gtrsim 3$, since the resolved-enhanced region at high $\Delta\eta$ is the region that would be most sensitive to the effects of colour singlet exchange. However, in the direct-enhanced region, the high-t γ sample lies significantly above the data.

For each of the variables $\Delta\eta$, $x_{\gamma;2J}^{OBS}$, $\log_{10}(x_{p;2J}^{OBS})$ and y_{JB}, the prediction of the PYTHIA mixed sample is shown to have no significant effects on the shape of the distribution relative to the photoproduction sample.

8.11.3 The Gap Sample

The distributions of $\Delta\eta$, $x_{\gamma;2J}^{OBS}$, $\log_{10}(x_{p;2J}^{OBS})$ and y_{JB} for the gap sample of events with $E_T^{cut} = 1.2$ GeV are shown in Fig. 8.27. Note that the features described in this section are generally the same for all four gap samples (corresponding to $E_T^{cut} = 0.6, 1.2, 1.8$ and 2.4 GeV). As for the inclusive case, the $\Delta\eta$ distribution for the gap sample is steeply falling as a function of increasing $\Delta\eta$. The PYTHIA photoproduction sample is able to describe the distribution up to $\Delta\eta \sim 3$, thereafter falling below the data. The high-t γ sample has a significantly higher number of gap events than the data. The mixed sample gives a good description of the data over the whole range of $\Delta\eta$.

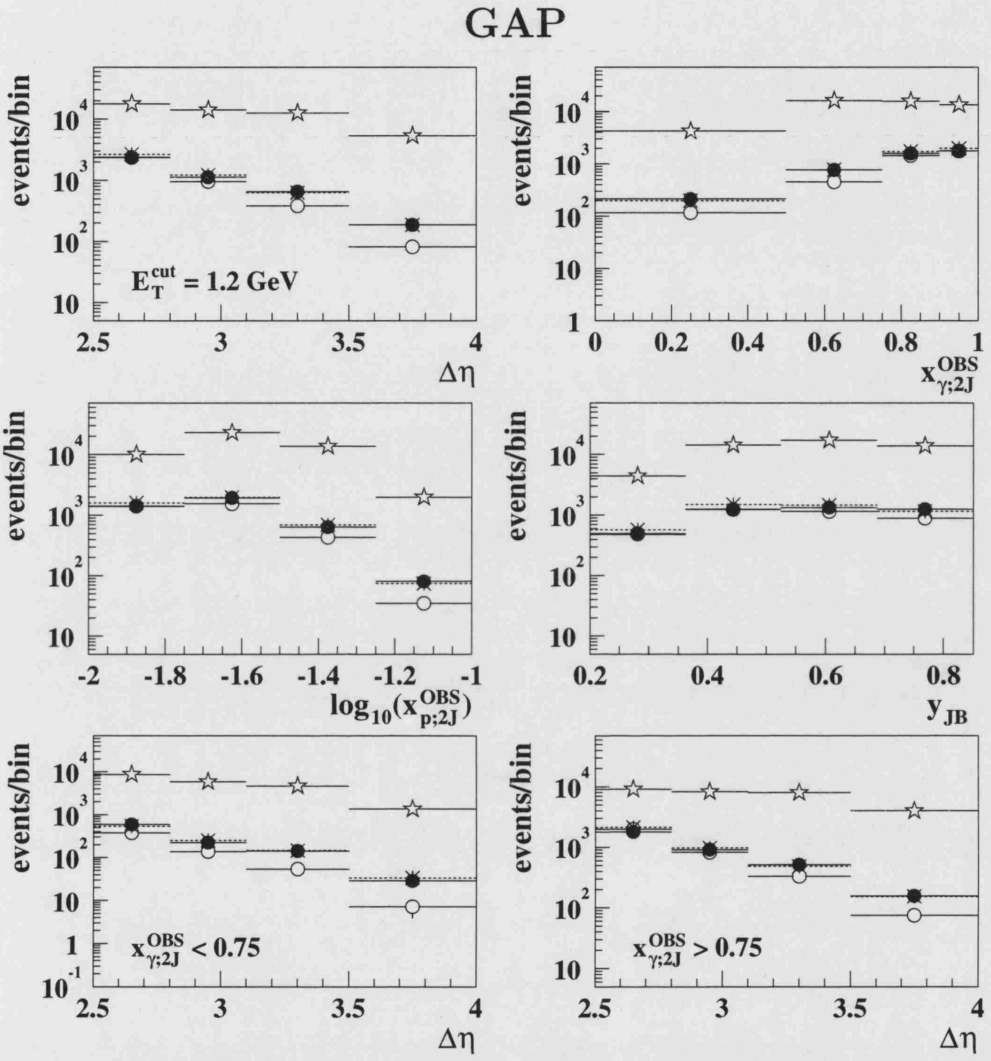

Figure 8.27: The distributions of $\Delta\eta$, $x_{\gamma;2\mathrm{J}}^{\mathrm{OBS}}$, $\log_{10}(x_{p;2\mathrm{J}}^{\mathrm{OBS}})$ and y_{JB} for the gap sample of events with $E_{\mathrm{T}}^{\mathrm{cut}} = 1.2$ GeV. The ZEUS data are shown by the solid points. The prediction of the PYTHIA photoproduction, high-t γ and mixed samples are shown by the open circles, open stars and dashed lines respectively. The horizontal error bars indicate the widths of the final cross section bins.

The distribution of $x_{\gamma;2J}^{OBS}$ shows a general rise, with the maximum occurring at $x_{\gamma;2J}^{OBS} \sim 1$. This is in contrast to the corresponding inclusive distribution, where the maximum occurs at lower values of $x_{\gamma;2J}^{OBS}$. The PYTHIA photoproduction sample gives a reasonable description of the data at high $x_{\gamma;2J}^{OBS}$, although the model lies below the data at low $x_{\gamma;2J}^{OBS}$. This would be expected if the discrepancy is due to a colour singlet object, which can couple only to the resolved photon. The high-t γ sample also shows a generally rising distribution, although possibly falls at very high $x_{\gamma;2J}^{OBS}$. The mixed sample gives a reasonable description of the data, with the effect of adding the colour singlet contribution being most significant at low $x_{\gamma;2J}^{OBS}$.

The $\log_{10}(x_{p;2J}^{OBS})$ distribution has a similar shape to the corresponding inclusive distribution although the rise to the maximum is shallower and the fall-off from the maximum is steeper. The distribution is reasonably described by the photoproduction sample for $x_{p;2J}^{OBS} \lesssim 0.03$, thereafter falling below the data. The high-t γ sample has a similar shape to the data but, as in all the gap distributions, has a larger number of gap events overall. The mixed sample gives a good description of the shape and normalisation of the data.

The distribution of y_{JB} is reasonably well described by the photoproduction Monte Carlo and the addition of a 2% contribution from colour singlet exchange has only a small effect. The difference in the photoproduction and mixed Monte Carlos is marginally more apparent at high y_{JB}, which corresponds to large $W(= ys)$ and is also correlated to low $x_{\gamma;2J}^{OBS}$.

The distributions of $\Delta\eta$ for $x_{\gamma;2J}^{OBS} < 0.75$ and $x_{\gamma;2J}^{OBS} > 0.75$ are also shown. In the resolved-enhanced region, the photoproduction sample lies below the data over the whole range of $\Delta\eta$. The high-t γ sample shows a less steeply falling distribution and when combined with the photoproduction sample to produce the mixed sample, the data is well described. Similarly, in the direct enhanced region, the $\Delta\eta$ distribution is also steeply falling. The PYTHIA photoproduction sample still lies below the data, although this is not manifest until $\Delta\eta \gtrsim 3$ and the overall excess in the data is less significant than in the resolved-enhanced region. Again, the mixed sample gives a good description of the data.

8.11.4 The Gap Fraction

By taking the ratio of Figs. 8.27 and 8.25, a detector dependent measurement of the gap fraction has been obtained. The results are shown in Figs. 8.28.

The gap fraction as a function of $\Delta\eta$ lies above the prediction of the PYTHIA photoproduction sample for $\Delta\eta \gtrsim 3.0$. The high-t γ sample shows a relatively flat distribution, while the mixed sample gives a good description of the shape

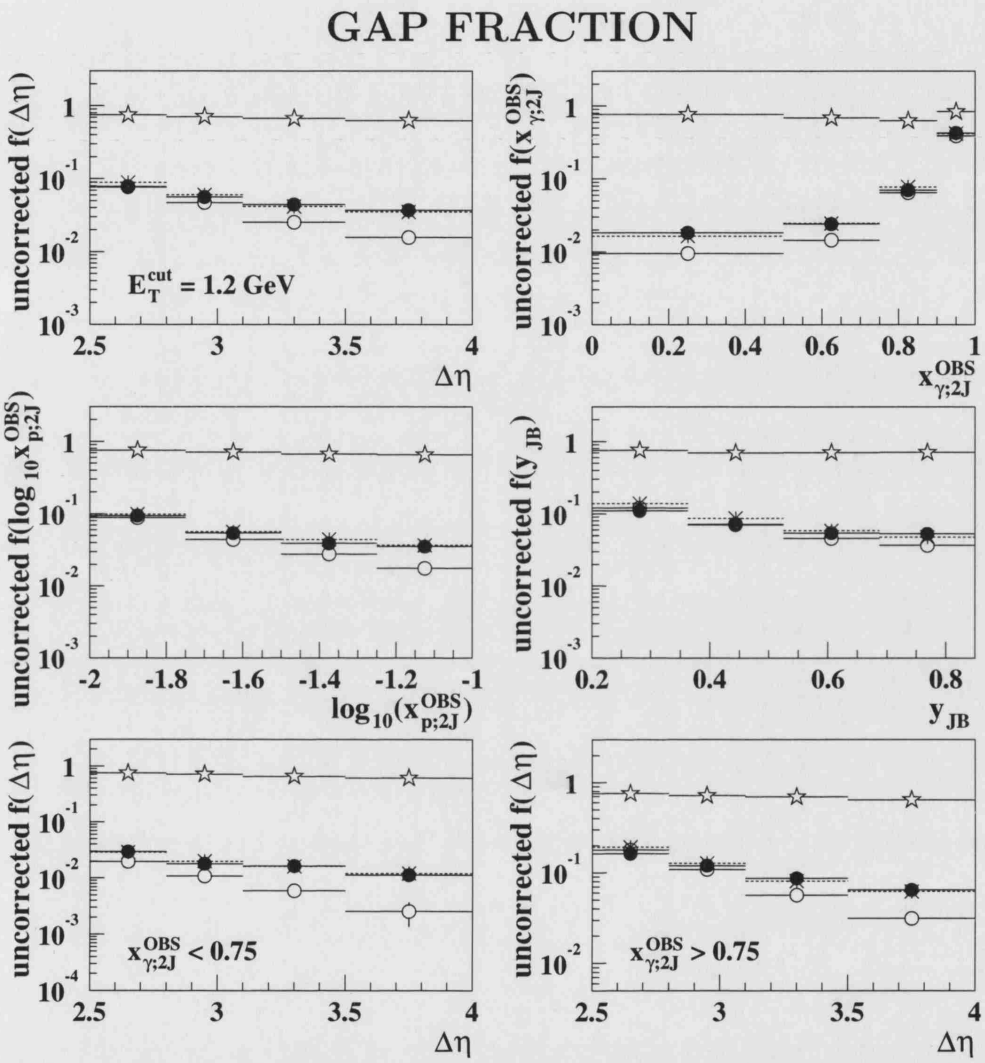

Figure 8.28: The uncorrected gap fractions for $\Delta\eta$, $x_{\gamma;2J}^{\rm OBS}$, $\log_{10}(x_{p;2J}^{\rm OBS})$ and $y_{\rm JB}$ with $E_{\rm T}^{\rm cut} = 1.2$ GeV. The ZEUS data are shown by the solid points. The prediction of the PYTHIA photoproduction, high-t γ and mixed samples are shown by the open circles, open stars and dashed lines respectively. The horizontal error bars indicate the widths of the final cross section bins.

and normalisation of the data over the whole range of $\Delta\eta$. This shows that a two component behaviour is favoured: the exponential fall-off from standard photoproduction processes, combined with the approximately constant distribution from colour singlet exchange.

The gap fraction as a function of $x_{\gamma;2J}^{OBS}$ shows a rising distribution with a maximum at $x_{\gamma;2J}^{OBS} \sim 1$. This may be explained in terms of the fact that direct photon events have quark propagators which have less probability of radiating into the region between the jets than the gluon propagators which dominate resolved events [25]. In addition, gaps produced in high $x_{\gamma;2J}^{OBS}$ events have less probability of being destroyed by multi-parton interactions. Therefore, it is events at high $x_{\gamma;2J}^{OBS}$ which are more likely overall to have a gap, even though the colour singlet exchange process would occur only in resolved photoproduction. The PYTHIA photoproduction model lies below the data for low values of $x_{\gamma;2J}^{OBS}$. The high-t γ distribution shows a flat distribution and this leads to a good description of the data by the PYTHIA mixed sample.

The gap fraction as a function of $\log_{10}(x_{p;2J}^{OBS})$ shows a falling distribution as $x_{p;2J}^{OBS}$ increases. The PYTHIA photoproduction distribution falls below the data for $x_{p;2J}^{OBS} \sim 0.03$. The shape of the distribution is correlated to the shape of the $x_{\gamma;2J}^{OBS}$ distribution. In particular, for a fixed parton-parton centre-of-mass energy, larger values of $x_{\gamma;2J}^{OBS}$ are correlated with smaller values of $x_{p;2J}^{OBS}$ and visa versa. This is also why the excess over the photoproduction Monte Carlo at small $x_{\gamma;2J}^{OBS}$ is observed at large $x_{p;2J}^{OBS}$. The high-t γ model is relatively flat as a function of $\log_{10}(x_{p;2J}^{OBS})$. As for the $\Delta\eta$ and $x_{\gamma;2J}^{OBS}$ distributions, the mixed sample gives a good description of the data.

The gap fraction as a function of y_{JB} shows a falling distribution. The PYTHIA photoproduction model gives an adequate description of the data although lies marginally below at large values of y_{JB}. The mixed sample gives a reasonable description over the whole range of the variable.

The gap fraction as a function of $\Delta\eta$ for $x_{\gamma;2J}^{OBS} < 0.75$ and $x_{\gamma;2J}^{OBS} > 0.75$ shows that the fraction for the direct-enhanced region is higher overall than that for the resolved-enhanced region in both the data and the PYTHIA photoproduction sample. This is due to the increasing gap fraction as a function of increasing $x_{\gamma;2J}^{OBS}$, as discussed above. In contrast, the value of the gap fraction for the high-t sample is relatively independent of the x_γ region. As for the gap distributions, the mixed Monte Carlo sample gives a good description of the gap fractions.

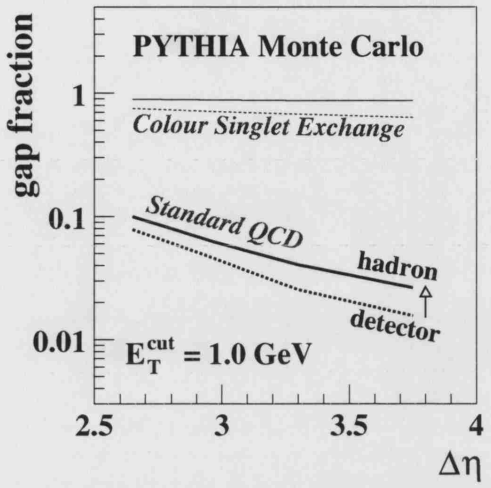

Figure 8.29: The distribution of $f(\Delta\eta)$. The solid and dashed lines show the distribution at hadron and detector level, respectively. The thick and thin lines correspond to the PYTHIA photoproduction and high-t γ Monte Carlo samples, respectively.

8.11.5 Summary

In this section, it has been shown that the data exhibits an excess of events with a rapidity gap compared to the predictions of standard photoproduction processes as implemented in PYTHIA. The excess is particularly apparent at large values of $\Delta\eta$ ($\gtrsim 3.0$) and low values of $x_{\gamma;2J}^{OBS}$ (which are also correlated with large values of $x_{p;2J}^{OBS}$ for a fixed centre-of-mass energy $\sqrt{s}$). The uncorrected gap fraction $f(\Delta\eta)$, supports a two component behaviour: an exponential fall at low $\Delta\eta$ and a flatter distribution at high $\Delta\eta$. This behaviour can be described by the inclusion of a colour singlet exchange process. The PYTHIA mixed sample of events (containing 98% photoproduction and 2% high-t γ exchange) is able to describe the gap fractions as a function of $\Delta\eta$, $x_{\gamma;2J}^{OBS}$, $\log_{10}(x_{p;2J}^{OBS})$ and y_{JB} in both normalisation and shape. However, the high-t γ exchange process should not be considered as a candidate for the colour singlet exchange process since the cross section is too small. In order to facilitate comparisons with theoretical predictions and to verify that the excess in the data over the predictions of standard photoproduction Monte Carlo is not simply a remnant of detector effects, the data must be unfolded. As an illustration of the effects of detector acceptance and smearing, the distribution of $f(\Delta\eta)$ for the gap sample of events with $E_T^{cut} = 1.0$ GeV is shown in Fig. 8.29. The results are shown for both the PYTHIA photoproduction and high-t γ samples (thick and thin curves, respectively), and at both hadron and detector level (solid and dashed lines, respectively). The effect of the detector is largest at large $\Delta\eta$ (which is dominated by low E_T^{gap} events). In this region, the effects of noise are more significant and the mini-jets are low in energy which makes their accurate reconstruction more difficult.

In the following section, the correction procedure is described. For the final correction, the PYTHIA mixed Monte Carlo sample has been used because of the significantly improved description of the data relative to the photoproduction sample.

8.12 The Correction Procedure

Detector-independent measurements are obtained by unfolding the uncorrected distributions (shown in Section 8.11) using bin-by-bin correction factors obtained with Monte Carlo. These factors are calculated as the ratio of the bin purities to the bin efficiencies. Equivalently, the correction factors can simply be calculated as the ratio of the hadron to detector level distributions. In this section, the bin purities, efficiencies and correction factors are presented for the inclusive and gap samples of events. These quantities have been calculated using the PYTHIA mixed Monte Carlo. Unless otherwise stated, the solid points correspond to the inclusive sample and the hollow circles correspond to the gap sample with $E_{\mathrm{T}}^{\mathrm{cut}} = 1.0$ GeV.

8.12.1 Bin Purities

The bin purities (Eq. 6.6) for each of the cross section variables are shown in Fig. 8.30. In this analysis, the general requirement that the purity should be $\gtrsim 10\%$ has been imposed. This minimum value is indicated by the dotted line. However, for the inclusive sample the purities are generally $> 20\%$. The increase in the purity as a function of $x_{\gamma;2\mathrm{J}}^{\mathrm{OBS}}$ is due to the fact that the jets in these events tend to be of higher transverse energy and so have more detected jets which are also above the hadron level threshold. Similarly, the purity shows a general increase as a function of $\log_{10}(x_{p;2\mathrm{J}}^{\mathrm{OBS}})$.

8.12.2 Bin Efficiencies

The bin efficiencies (Eq. 6.7) are shown for each of the cross section variables in Fig. 8.31. For the inclusive sample, the bin efficiencies are $> 13\%$ in every bin and typically $\gtrsim 20\%$. For the gap sample, the efficiencies are lower due to the poor resolution of $E_{\mathrm{T}}^{\mathrm{gap}}$. The lowest bin efficiency is $\sim 5\%$.

8.12.3 Correction Factors

The correction factors (Eq. 6.10) for the measured cross section variables are shown in Figs. 8.32. For $\Delta\eta$, the factors are reasonably flat as a function of the measured variable. In contrast, they rise as a function of $x_{\gamma;2\mathrm{J}}^{\mathrm{OBS}}$ and $\log_{10}(x_{p;2\mathrm{J}}^{\mathrm{OBS}})$. This is due to the fact that the purity rises more than the efficiency as a function of these variables. In contrast, the factors fall slightly as a function of y. The correction factors for the inclusive sample are generally smaller than for the gap sample. For illustration, the effective correction factors for the gap fractions are shown in Fig. 8.33. These factors are relatively flat and generally lie in the range 1-2.

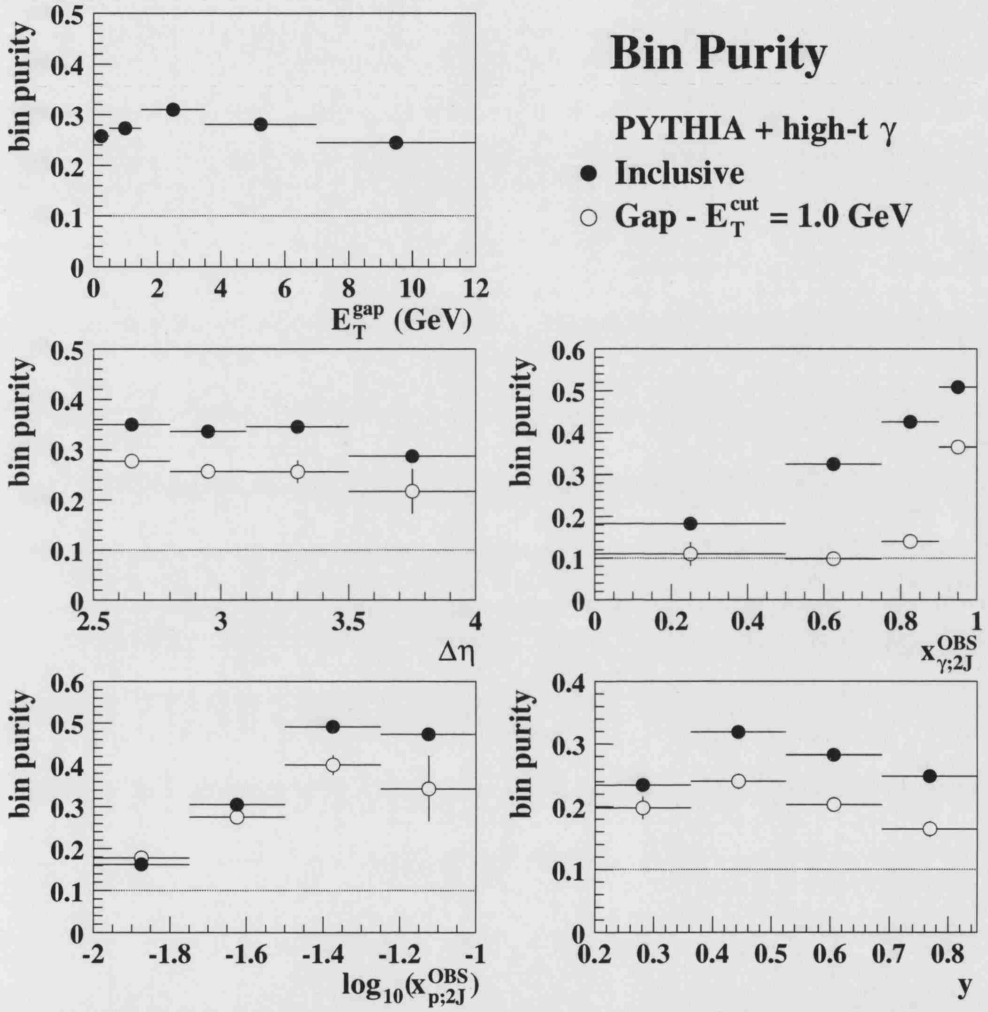

Figure 8.30: The bin purities of $E_{\mathrm{T}}^{\mathrm{gap}}$, $\Delta\eta$, $x_{\gamma;2\mathrm{J}}^{\mathrm{OBS}}$, $\log_{10}(x_{p;2\mathrm{J}}^{\mathrm{OBS}})$ and y calculated from the PYTHIA mixed Monte Carlo sample. The solid points show the results for the inclusive sample and the open circles show the results for the gap sample of events with $E_{\mathrm{T}}^{\mathrm{cut}} = 1.0$ GeV. The horizontal error bars indicate the widths of the final cross section bins.

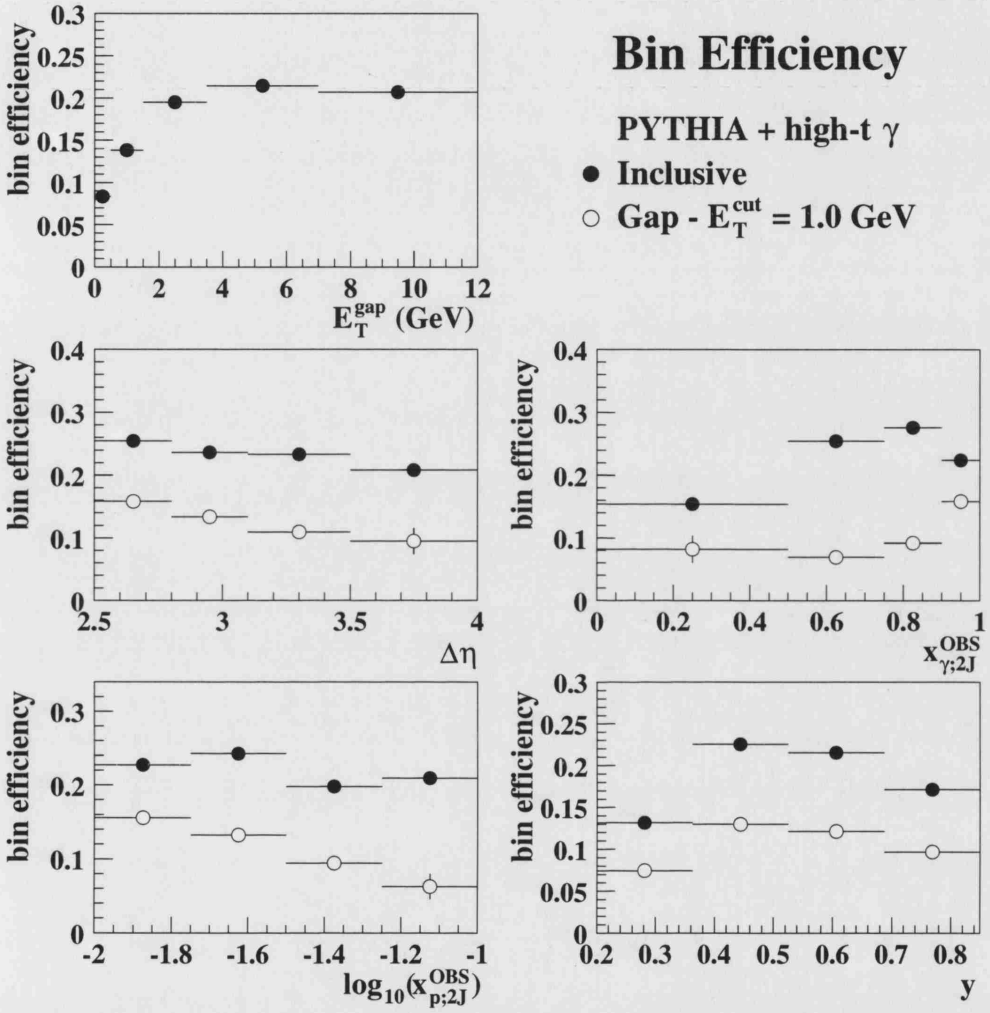

Figure 8.31: The bin efficiencies of $E_{\mathrm{T}}^{\mathrm{gap}}$, $\Delta\eta$, $x_{\gamma;2\mathrm{J}}^{\mathrm{OBS}}$, $\log_{10}(x_{p;2\mathrm{J}}^{\mathrm{OBS}})$ and y calculated from the PYTHIA mixed Monte Carlo sample. The solid points show the results for the inclusive sample and the open circles show the results for the gap sample of events with $E_{\mathrm{T}}^{\mathrm{cut}} = 1.0$ GeV. The horizontal error bars indicate the width of the bin.

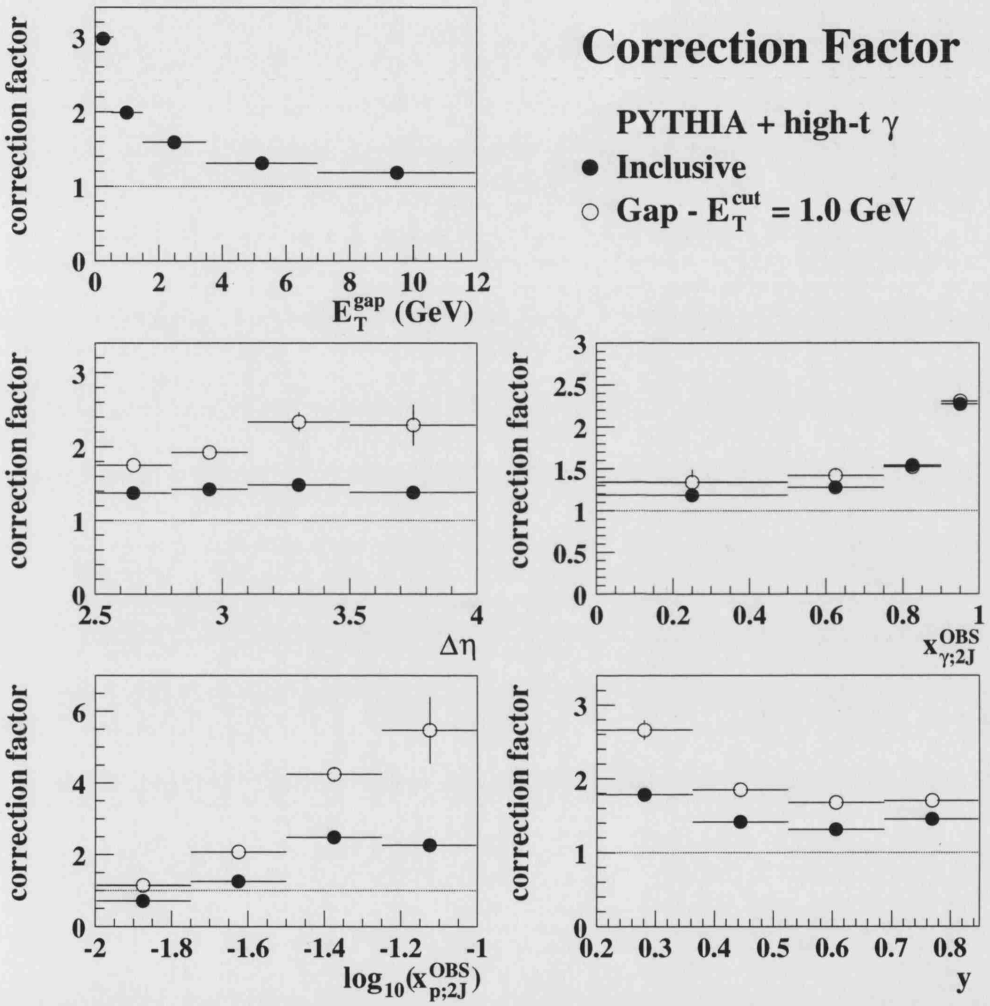

Figure 8.32: The correction factors for $E_{\mathrm{T}}^{\mathrm{gap}}$, $\Delta\eta$, $x_{\gamma;2\mathrm{J}}^{\mathrm{OBS}}$, $\log_{10}(x_{p;2\mathrm{J}}^{\mathrm{OBS}})$ and y calculated from the PYTHIA mixed Monte Carlo sample. The solid points show the results for the inclusive sample and the open circles show the results for the gap sample of events with $E_{\mathrm{T}}^{\mathrm{cut}} = 1.0$ GeV. The horizontal error bars indicate the widths of the final cross section bins.

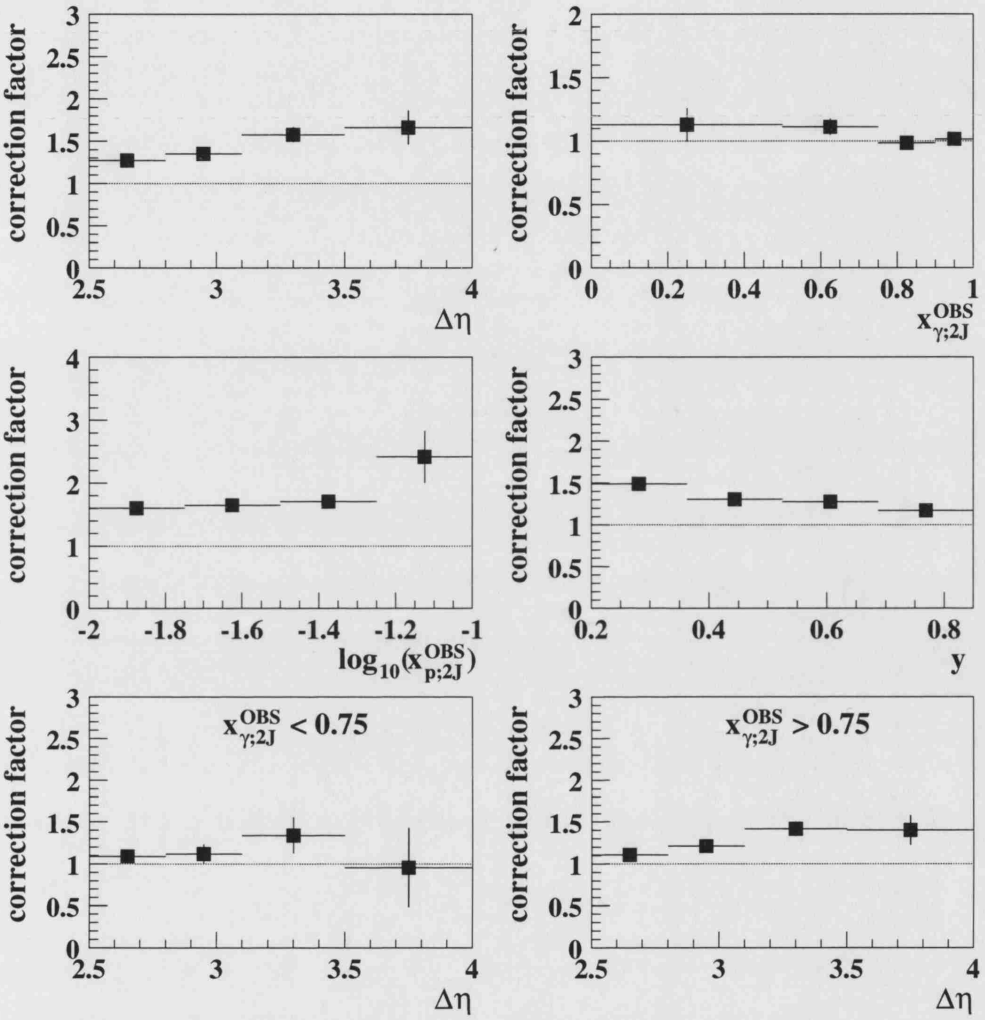

Figure 8.33: The effective gap fraction correction factors for $\Delta\eta$, $x^{\mathrm{OBS}}_{\gamma;2\mathrm{J}}$, $\log_{10}(x^{\mathrm{OBS}}_{p;2\mathrm{J}})$, y and $\Delta\eta$ in the regions $x^{\mathrm{OBS}}_{\gamma;2\mathrm{J}} < 0.75$ and $x^{\mathrm{OBS}}_{\gamma;2\mathrm{J}} > 0.75$ calculated from the PYTHIA mixed Monte Carlo sample. The solid squares show the results for the fractions corresponding to $E_{\mathrm{T}}^{\mathrm{cut}} = 1.0$ GeV. The horizontal error bars indicate the widths of the final cross section bins.

8.13 Systematic Uncertainties and Cross-Checks

The nominal cross section (defined in Section 8.4) has been calculated using the detector-level event selection criteria described in Section 8.5. In order to estimate the sensitivity of the measured cross sections and cross section ratios to changes in the selection criteria and the method used to extract the cross section, several systematic checks and additional consistency checks have been performed. These have been broadly separated into four categories:

1. **Reconstruction Method**
   The nominal measurement has used uncorrected ZUFOs for the reconstruction of the final hadronic state. It has been shown that this is the best method of reconstructing low energy particles and isolated clusters. The reconstruction method has been checked using two other methods:

   (a) To study the effect of possible long-range migrations between bins in the measurement of the hadronic variables $x_{\gamma;2\mathrm{J}}^{\mathrm{OBS}}$, $\log_{10}(x_{p;2\mathrm{J}}^{\mathrm{OBS}})$ and y, the inclusive cross sections have been re-calculated using corrected ZUFOs for the reconstruction. This check is applied only to the inclusive cross sections since it has already been shown that the correction routine is not applicable at the low energies required for the reconstruction of gap events.

   (b) As an additional cross-check, the inclusive and gap cross sections, as well as the gap fractions, have been re-calculated using calorimeter cells for the reconstruction of the hadronic final state.

   These checks are to test the stability of the chosen reconstruction method. They are used as consistency checks only and are not assigned as systematic uncertainties on the final measurement.

2. **Model Dependence**
   The nominal cross section has been obtained using the PYTHIA mixed Monte Carlo sample for the unfolding. This sample contains 98% photoproduction and 2% high-t γ exchange. For the photoproduction sample, direct and resolved events have been added in the ratio that gives the best fit to the uncorrected inclusive $x_{\gamma;2\mathrm{J}}^{\mathrm{OBS}}$ distribution.

   (a) To assess the dependence on the addition of a colour singlet exchange to the Monte Carlo sample, the unfolding procedure has also been carried out using the PYTHIA photoproduction sample alone.

(b) The ratio of direct to resolved events is not known *a priori*. To assess the dependence on the relative fractions of direct and resolved events, the cross sections have been calculated using the ratio obtained from the predicted cross sections in the Monte Carlo. This can have a significant effect, particularly since direct and resolved events have different resolutions.

These changes have also been treated as consistency checks and are not assigned as systematics on the final measurement.

3. **Kinematic Selection**
   The effects on the cross section of events migrating in and out of the kinematic region of interest have been studied by systematically varying the cuts that define the detector level event selection. The z_{vtx} cut has been varied by ± 10 cm, the $\not{p}_{\text{T}}/E_{\text{T}}^{1/2}$ cut has been varied by 0.2 $\text{GeV}^{1/2}$ and the cut on y_e has been varied by 0.05. All remaining cuts have been varied by $\pm 1\sigma$ the resolution on the variable of interest. The changes to the cuts were applied to both data and Monte Carlo and the results have been assigned as uncorrelated systematic uncertainties.

4. **Calorimeter Energy Scale**
   An uncertainty of $\pm 3\%$ has been assigned to the jet transverse energies and y_{JB}. The variation has been applied only to data and the results assigned as a correlated systematic uncertainty on the final results.

Note also that the uncertainty in the determination of the luminosity for the 1996-1997 data-taking period is 1.6%. Assigning this as an uncertainty results in only a small change to the measured cross sections (and cancels out completely in the gap fraction). This has not been assigned as a systematic on the final result.

The checks that have been performed are summarised in Table 8.3.

Figures 8.34 to 8.46 show the cross section and gap fraction measurements as a function of $E_{\text{T}}^{\text{gap}}$ (inclusive cross-section only), $\Delta\eta$, $x_{\gamma;2\text{J}}^{\text{OBS}}$, $\log_{10}(x_{p;2\text{J}}^{\text{OBS}})$ and y. In each figure, the numbers on the x-axis indicate the value at the centre of the bin. The open squares show the nominal cross section measurement. This is also indicated by the solid lines. The open diamonds and open stars show the results from the corrected ZUFOs (shown only for the inclusive cross sections) and calorimeter cells cross-checks. The open triangles show the results from the model dependence checks and the solid points show the results for each of the systematic variations, with the points from left to right corresponding to checks 5 to 24 in Tab. 8.3. For comparison, and to illustrate the size of the correction factors, the hollow circles show the results for the uncorrected data. For each of the cross section points shown on the plot, the vertical error bars show the statistical uncertainty on the final measurement which is the propagated error arising

from both data and Monte Carlo statistics. For clarity, the largest systematic in each bin is indicated by the dashed lines (upper and lower separately).

The results show that the measurement of the inclusive cross sections using corrected ZUFOs are consistent with the nominal measurement within systematic uncertainties. The largest discrepancy between the two methods of reconstruction arises in the low $E_{\mathrm{T}}^{\mathrm{gap}}$ bins, where the correction routine is known to be invalid. However, even in this region, the two measurements are broadly consistent. In all cases, the results using calorimeter cells are consistent with the nominal measurement within the combined systematic uncertainties. The results using the PYTHIA photoproduction Monte Carlo for the unfolding and from changing the ratio of direct and resolved result in only very small changes from the nominal measurement.

For the inclusive cross section, the systematic uncertainties are dominated by the calorimeter energy scale uncertainty. Variations in the jet E_{T} and y_{JB} cuts also cause non-negligible changes to the cross section. For the gap cross sections and gap fractions, the largest systematic uncertainties arise from the changes to $E_{\mathrm{T}}^{\mathrm{cut}}$. Changes to the cuts on the jet transverse energies and y_{JB} are also significant. All other systematic uncertainties are, in general, within the statistical uncertainty on the measurement.

In all plots shown in subsequent sections, the position and statistical uncertainty on the nominal cross section points (hollow squares) are taken to be the final measured values. The (uncorrelated) systematic uncertainty is taken to be the quadratic sum of the deviation of all uncorrelated systematic cross sections from the nominal value. The calorimeter energy scale uncertainty is shown as the shaded band on all inclusive and gap cross section plots. The uncertainty due to the calorimeter energy scale is small in the gap fraction and is not shown on the gap fraction plots.

Check Number	Nominal Selection	Check Selection
RECONSTRUCTION METHOD		
1	Uncorrected ZUFOs	Corrected ZUFOs (inc. only)
2		Calorimeter Cells
MODEL DEPENDENCE		
3	PYTHIA mixed	PYTHIA photoproduction
4	Fraction from χ^2-Fit	Generated cross section fraction
KINEMATIC CUTS		
5	$E_{\mathrm{T}}^{1,2} > 5.10, 4.25$ GeV	$E_{\mathrm{T}}^{1,2} > 5.80, 4.85$
6		$E_{\mathrm{T}}^{1,2} > 4.40, 3.65$
7	$-2.40 < \eta^{1,2} < 2.40$	$-2.34 < \eta^{1,2} < 2.46$
8		$-2.46 < \eta^{1,2} < 2.34$
9	$\lvert\bar{\eta}\rvert < 0.75$	$\lvert\bar{\eta}\rvert < 0.81$
10		$\lvert\bar{\eta}\rvert < 0.69$
11	$2.5 < \Delta\eta < 4.0$	$2.4 < \Delta\eta < 3.9$
12		$2.6 < \Delta\eta < 4.1$
13	$0.20 < y_{\mathrm{JB}} < 0.85$	$0.24 < y_{\mathrm{JB}} < 0.90$
14		$0.16 < y_{\mathrm{JB}} < 0.80$
15	$\not{p}_{\mathrm{T}} / E_{\mathrm{T}}^{1/2} < 2.0$ GeV$^{1/2}$	$\not{p}_{\mathrm{T}} / E_{\mathrm{T}}^{1/2} < 2.2$
16		$\not{p}_{\mathrm{T}} / E_{\mathrm{T}}^{1/2} < 1.8$
17	$y_e < 0.85$	$y_e < 0.90$
18		$y_e < 0.80$
19	$\lvert z_{\mathrm{vtx}}\rvert < 40$ cm	$\lvert z_{\mathrm{vtx}}\rvert < 50$ cm
20		$\lvert z_{\mathrm{vtx}}\rvert < 30$ cm
ADDITIONAL CUTS FOR GAP EVENTS ONLY		
21	$E_{\mathrm{T}}^{\mathrm{cut}} = 0.6, 1.2, 1.8, 2.4$ GeV	$E_{\mathrm{T}}^{\mathrm{cut}} = 0.78, 1.56, 2.34, 3.12$ GeV
22		$E_{\mathrm{T}}^{\mathrm{cut}} = 0.42, 0.84, 1.26, 1.68$ GeV
CALORIMETER ENERGY SCALE		
23	E_{T}, y_{JB}	$E_{\mathrm{T}} + 3\%$, $y_{\mathrm{JB}} + 3\%$
24		$E_{\mathrm{T}} - 3\%$, $y_{\mathrm{JB}} - 3\%$

Table 8.3: The nominal event selection and reconstruction criteria compared to those used for the estimation of the systematic uncertainties. Numbers 1-4 are consistency checks and are not assigned as systematics on the final measurement. Numbers 5-24 correspond to the solid points (from left to right) in each bin of the plots shown in Figs. 8.35 - 8.46.

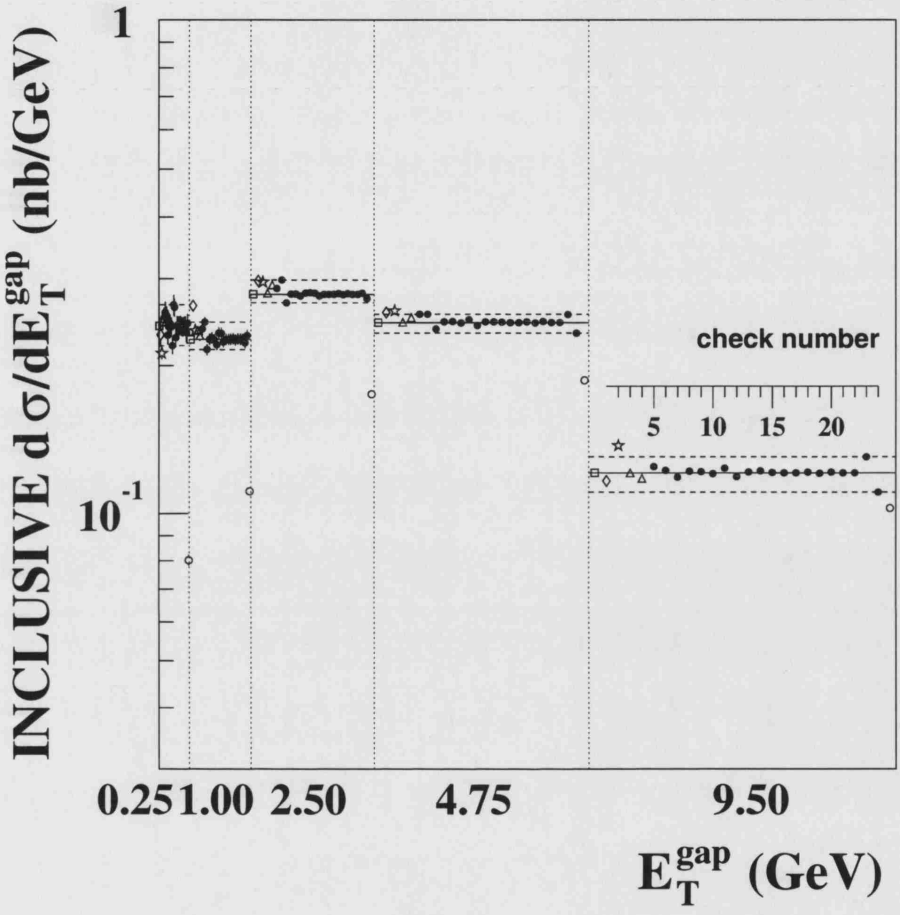

Figure 8.34: The inclusive cross section differential in $E_{\mathrm{T}}^{\mathrm{gap}}$. The open squares (and solid lines) represent the nominal cross section points. The open diamonds and open stars indicate the corrected ZUFOs and calorimeter cells cross-check and the open triangles show the checks on the model dependence. The solid points show the results for each of the systematic changes listed in Table 8.3. The open circles show the detector level distribution. The dashed lines indicate the largest systematic variation (lower and upper separately) and the dotted lines indicate the bin edges.

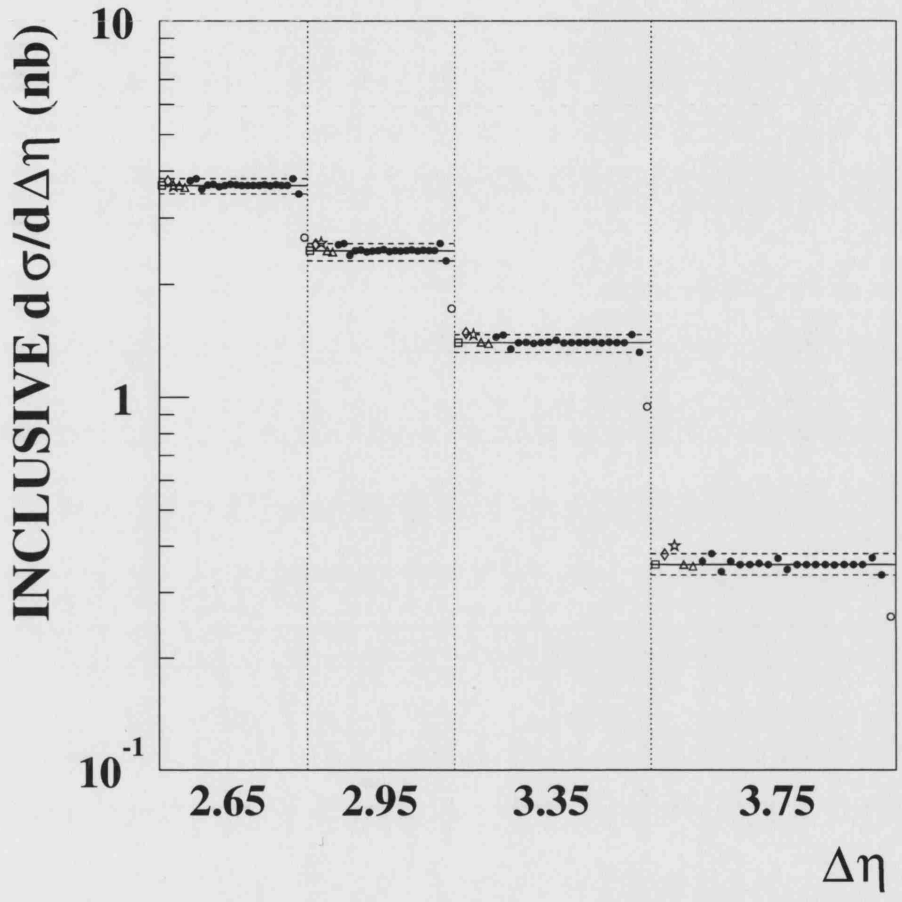

Figure 8.35: The inclusive cross section differential in $\Delta\eta$. The open squares (and solid lines) represent the nominal cross section points. The open diamonds and open stars indicate the corrected ZUFOs and calorimeter cells cross-check and the open triangles show the checks on the model dependence. The solid points show the results for each of the systematic changes listed in Table 8.3. The open circles show the detector level distribution. The dashed lines indicate the largest systematic variation (lower and upper separately) and the dotted lines indicate the bin edges.

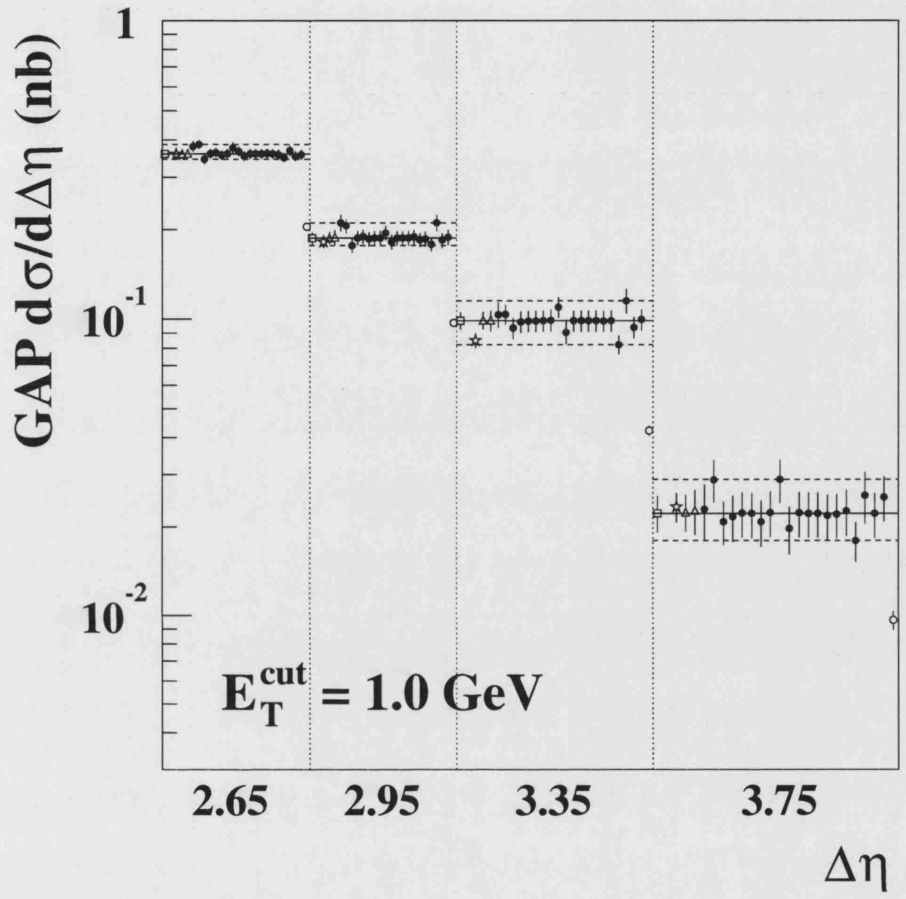

Figure 8.36: The gap cross section differential in $\Delta\eta$. The open squares (and solid lines) represent the nominal cross section points. The open diamonds and open stars indicate the corrected ZUFOs and calorimeter cells cross-check and the open triangles show the checks on the model dependence. The solid points show the results for each of the systematic changes listed in Table 8.3. The open circles show the detector level distribution. The dashed lines indicate the largest systematic variation (lower and upper separately) and the dotted lines indicate the bin edges.

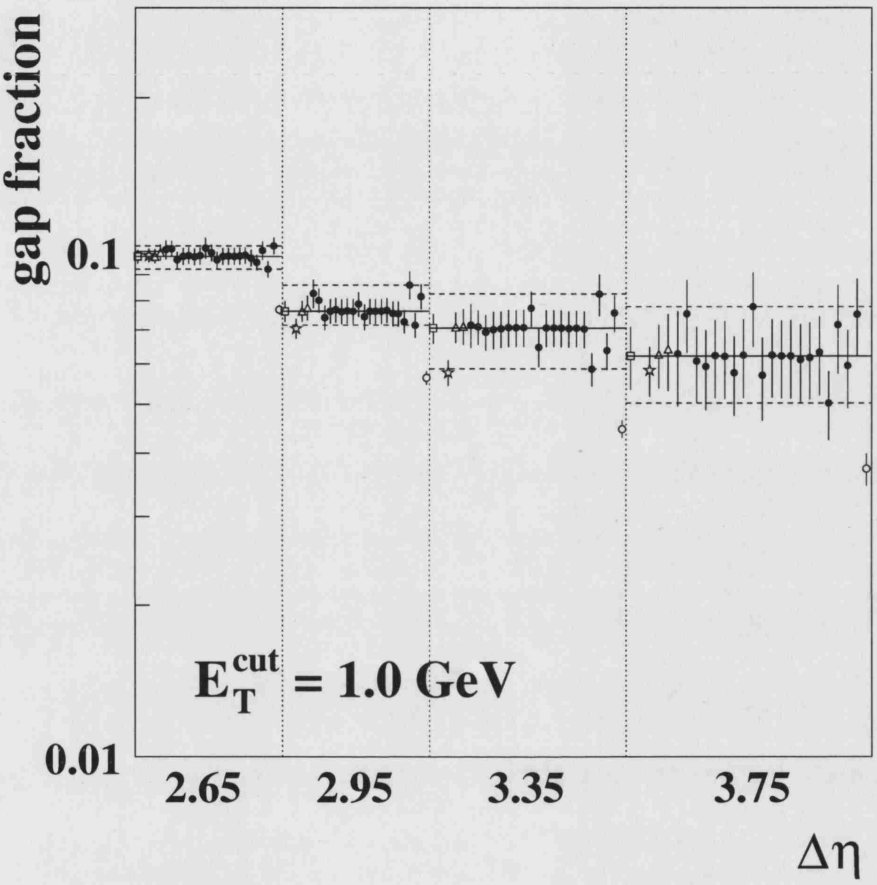

Figure 8.37: The gap fraction differential in $\Delta\eta$. The open squares (and solid lines) represent the nominal cross section points. The open diamonds and open stars indicate the corrected ZUFOs and calorimeter cells cross-check and the open triangles show the checks on the model dependence. The solid points show the results for each of the systematic changes listed in Table 8.3. The open circles show the detector level distribution. The dashed lines indicate the largest systematic variation (lower and upper separately) and the dotted lines indicate the bin edges.

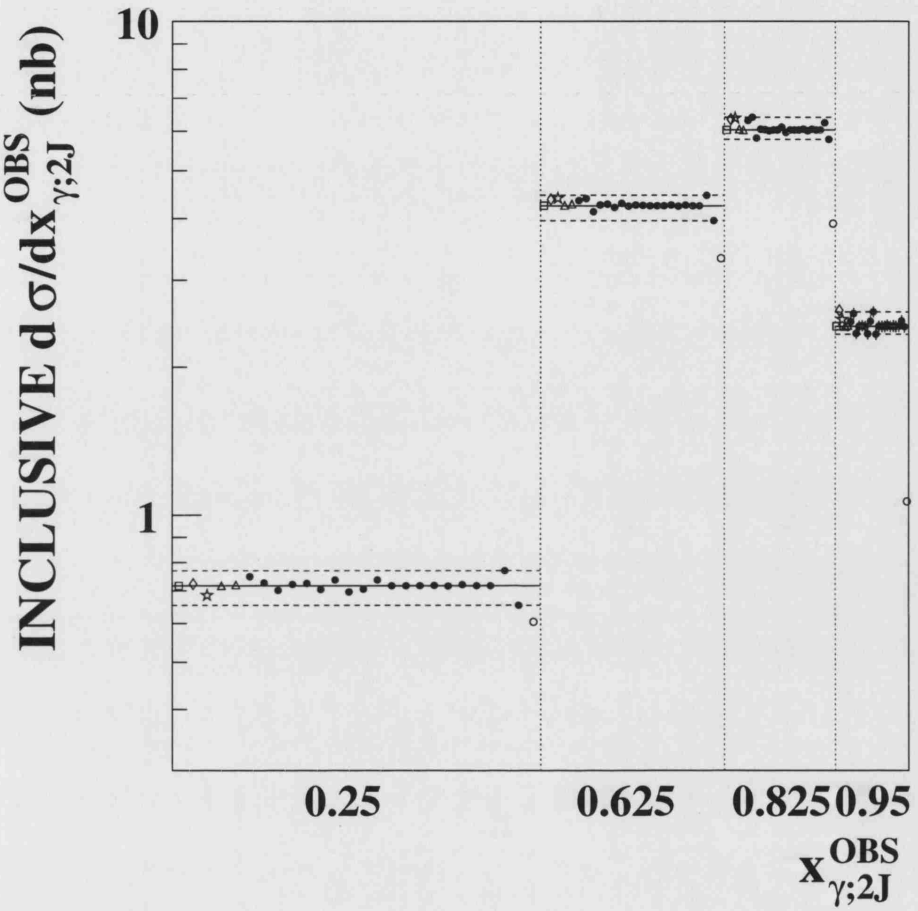

Figure 8.38: The inclusive cross section differential in $x_{\gamma;2\mathrm{J}}^{\mathrm{OBS}}$. The open squares (and solid lines) represent the nominal cross section points. The open diamonds and open stars indicate the corrected ZUFOs and calorimeter cells cross-check and the open triangles show the checks on the model dependence. The solid points show the results for each of the systematic changes listed in Table 8.3. The open circles show the detector level distribution. The dashed lines indicate the largest systematic variation (lower and upper separately) and the dotted lines indicate the bin edges.

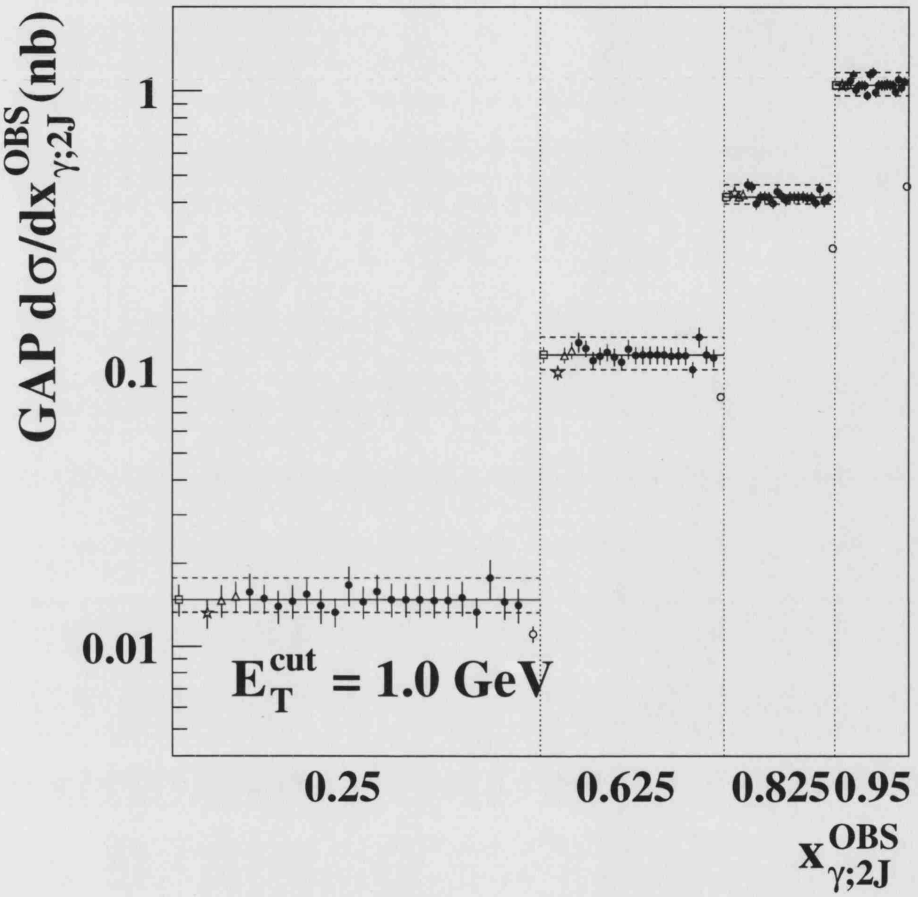

Figure 8.39: The gap cross section differential in $x^{\mathrm{OBS}}_{\gamma;2\mathrm{J}}$. The open squares (and solid lines) represent the nominal cross section points. The open diamonds and open stars indicate the corrected ZUFOs and calorimeter cells cross-check and the open triangles show the checks on the model dependence. The solid points show the results for each of the systematic changes listed in Table 8.3. The open circles show the detector level distribution. The dashed lines indicate the largest systematic variation (lower and upper separately) and the dotted lines indicate the bin edges.

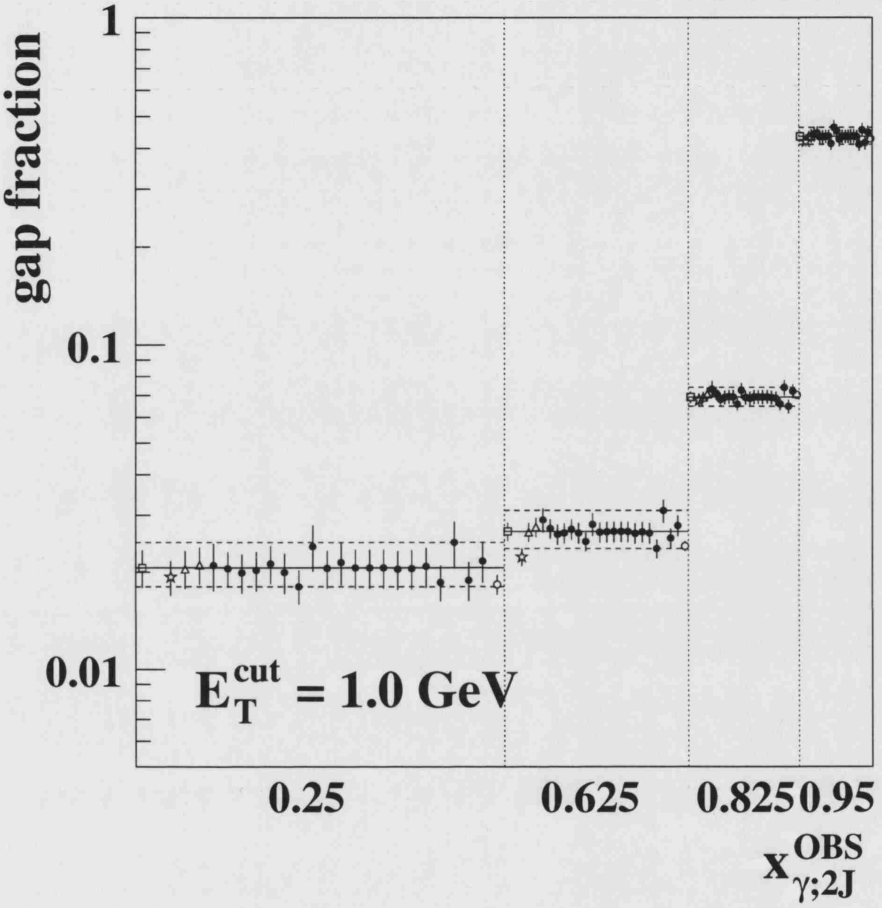

Figure 8.40: The gap fraction differential in $x_{\gamma;2J}^{\mathrm{OBS}}$. The open squares (and solid lines) represent the nominal cross section points. The open diamonds and open stars indicate the corrected ZUFOs and calorimeter cells cross-check and the open triangles show the checks on the model dependence. The solid points show the results for each of the systematic changes listed in Table 8.3. The open circles show the detector level distribution. The dashed lines indicate the largest systematic variation (lower and upper separately) and the dotted lines indicate the bin edges.

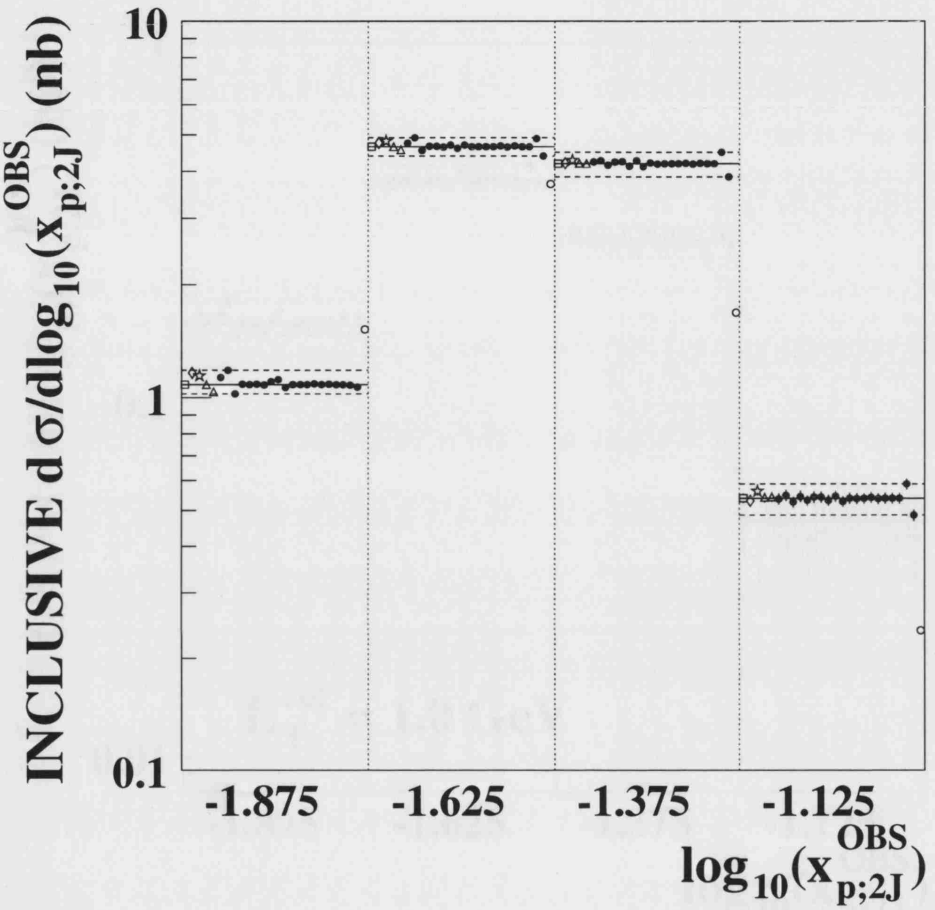

Figure 8.41: The inclusive cross section differential in $\log_{10}(x_{p;2\mathrm{J}}^{\mathrm{OBS}})$. The open squares (and solid lines) represent the nominal cross section points. The open diamonds and open stars indicate the corrected ZUFOs and calorimeter cells cross-check and the open triangles show the checks on the model dependence. The solid points show the results for each of the systematic changes listed in Table 8.3. The open circles show the detector level distribution. The dashed lines indicate the largest systematic variation (lower and upper separately) and the dotted lines indicate the bin edges.

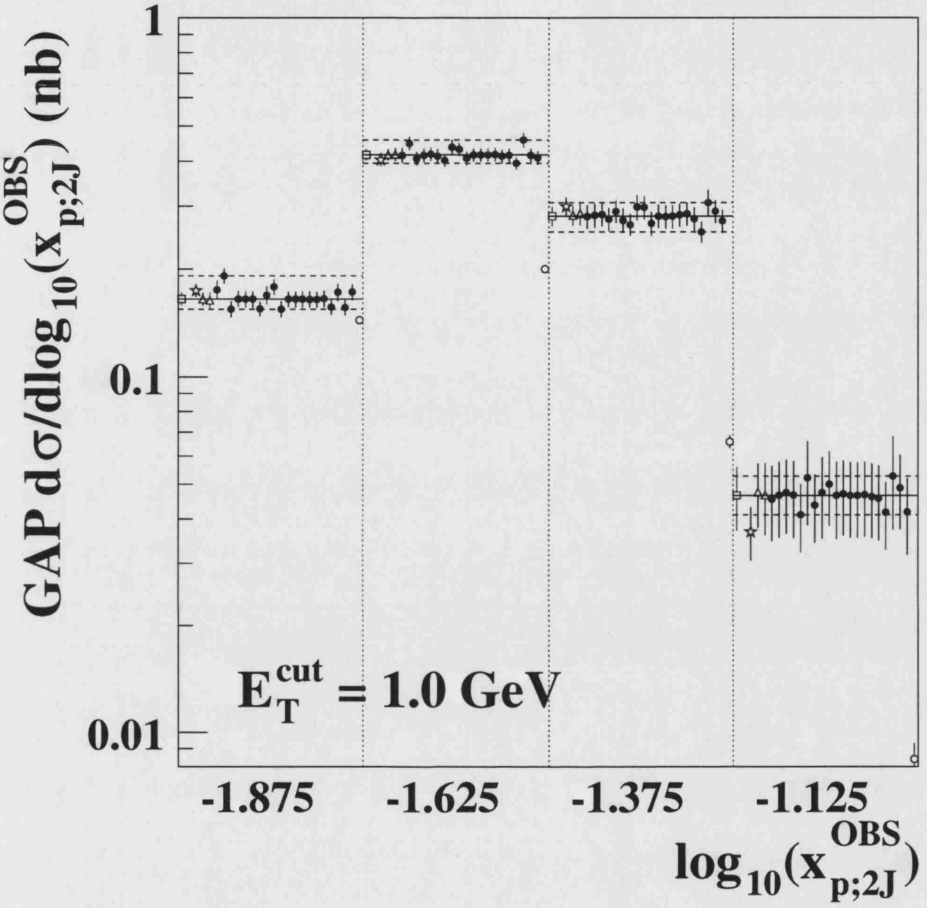

Figure 8.42: The gap cross section differential in $\log_{10}(x_{p;2J}^{\mathrm{OBS}})$. The open squares (and solid lines) represent the nominal cross section points. The open diamonds and open stars indicate the corrected ZUFOs and calorimeter cells cross-check and the open triangles show the checks on the model dependence. The solid points show the results for each of the systematic changes listed in Table 8.3. The open circles show the detector level distribution. The dashed lines indicate the largest systematic variation (lower and upper separately) and the dotted lines indicate the bin edges.

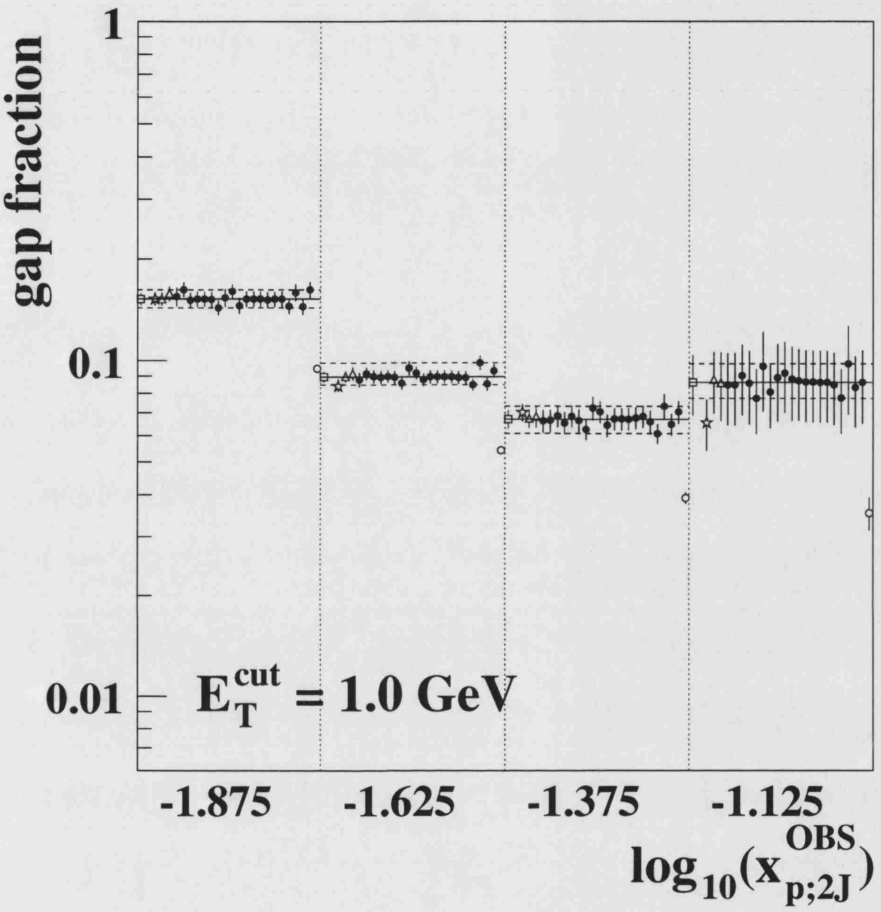

Figure 8.43: The gap fraction differential in $\log_{10}(x_{p;2J}^{\mathrm{OBS}})$. The open squares (and solid lines) represent the nominal cross section points. The open diamonds and open stars indicate the corrected ZUFOs and calorimeter cells cross-check and the open triangles show the checks on the model dependence. The solid points show the results for each of the systematic changes listed in Table 8.3. The open circles show the detector level distribution. The dashed lines indicate the largest systematic variation (lower and upper separately) and the dotted lines indicate the bin edges.

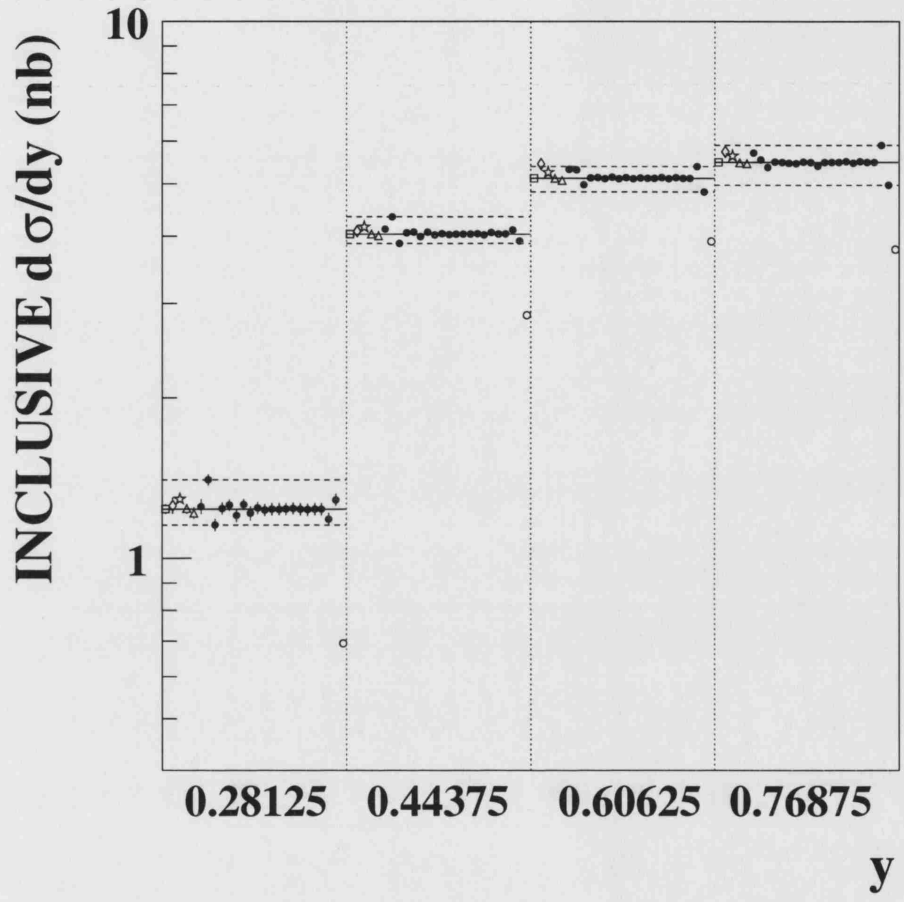

Figure 8.44: The inclusive cross section differential in y. The open squares (and solid lines) represent the nominal cross section points. The open diamonds and open stars indicate the corrected ZUFOs and calorimeter cells cross-check and the open triangles show the checks on the model dependence. The solid points show the results for each of the systematic changes listed in Table 8.3. The open circles show the detector level distribution. The dashed lines indicate the largest systematic variation (lower and upper separately) and the dotted lines indicate the bin edges.

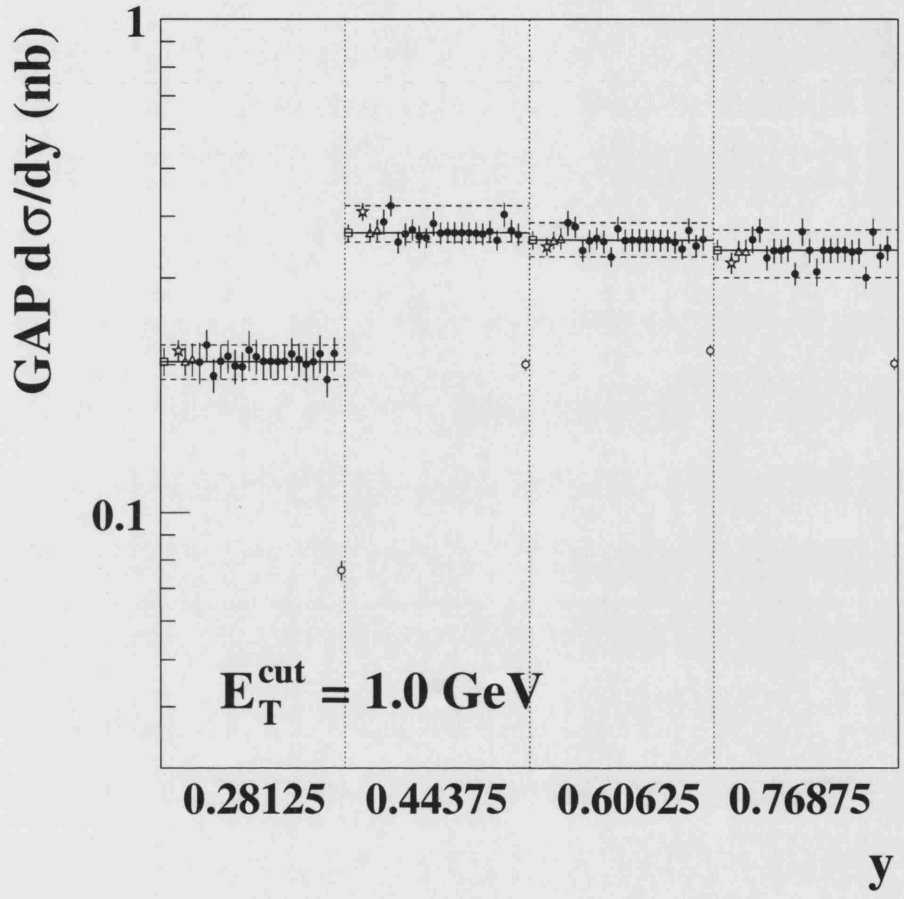

Figure 8.45: The gap cross section differential in y. The open squares (and solid lines) represent the nominal cross section points. The open diamonds and open stars indicate the corrected ZUFOs and calorimeter cells cross-check and the open triangles show the checks on the model dependence. The solid points show the results for each of the systematic changes listed in Table 8.3. The open circles show the detector level distribution. The dashed lines indicate the largest systematic variation (lower and upper separately) and the dotted lines indicate the bin edges.

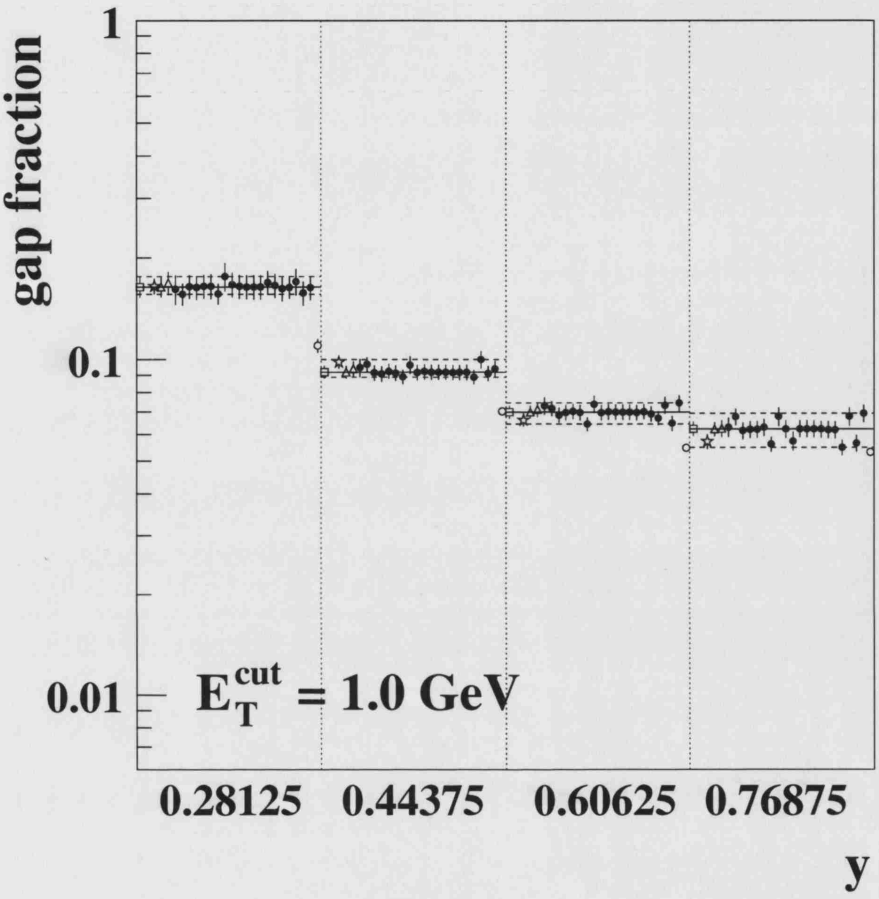

Figure 8.46: The gap fraction differential in y. The open squares (and solid lines) represent the nominal cross section points. The open diamonds and open stars indicate the corrected ZUFOs and calorimeter cells cross-check and the open triangles show the checks on the model dependence. The solid points show the results for each of the systematic changes listed in Table 8.3. The open circles show the detector level distribution. The dashed lines indicate the largest systematic variation (lower and upper separately) and the dotted lines indicate the bin edges.

8.14 Results and Discussion

In this section, the measured cross sections and gap fractions are presented and discussed. Tables of all results are given in Appendix H. The HERWIG 6.4 and PYTHIA 6.206 Monte Carlo generators have been used to simulate photoproduction events for comparison with the data. The CTEQ5L and SaS2D PDF parameterisations have been used for the proton and photon respectively. Both the HERWIG and PYTHIA models include a simulation of the underlying event. For HERWIG, the model parameters are motivated by the JETWEB tuning described in this thesis (Section 7.14) while, for PYTHIA, the simplest multi-parton interaction model has been used. The specific model parameters correspond to HERWIG + Jimmy$_t$ + SUE$_{0.05}$ in Tab. 7.4 and PYTHIA + MPI(1) in Tab. 7.5. For ease of reference, the main parameters are summarised again in Tab. 8.4. For each model, direct and resolved events were generated separately and combined according to their relative cross sections. The predicted cross sections from the HERWIG and PYTHIA samples have initially been scaled by factors of 1.65 and 1.45, respectively. This choice is motivated by the JETWEB tuning which constrains the normalisation of the Monte Carlo cross sections using high-E_{T} measurements. However, it will be shown that the prediction of HERWIG requires an additional scaling by a factor of 1.4 in order to produce agreement with the inclusive cross section measurements.

Model	Underlying Event Model	$p_{\mathrm{T}}^{\mathrm{min}}/p_{\mathrm{T}}^{\mathrm{mi}}$ GeV	PRSOF	$R(p)$	$R(\gamma)$
HERWIG	Jimmy$_t$ + SUE$_{0.05}$	3.0 3.0	0.05	3.0	1.0
PYTHIA	MPI(1)	2.0 1.5	-	-	-

Table 8.4: Parameters of the Monte Carlo models compared to the corrected data.

In addition to the simulations of standard QCD processes, a sample of colour singlet exchange events has also been generated using the Leading Logarithmic Approximation (LLA) BFKL process, as implemented in HERWIG[§]. The proton and photon PDFs and all underlying event parameters are the same as those for HERWIG + Jimmy$_t$ + SUE$_{0.05}$. The free parameters in Eq. 2.79 have been chosen to be $\alpha_s^{pre.} = \alpha_s^{den.} = 0.18$. The choice of $\alpha_s^{den.}$ gives $\omega_0 = 0.48$ according to the definition in Section 2.14.3. These choices are motivated by previous gaps-between-jets studies [25, 194] and the study of high-t double dissociative diffraction [195]. The BFKL sample was added to the HERWIG photoproduction sample according to the generated cross section. The

[§]A version of the code has been used which includes the full Mueller-Tang calculation, with no asymptotic approximation [149].

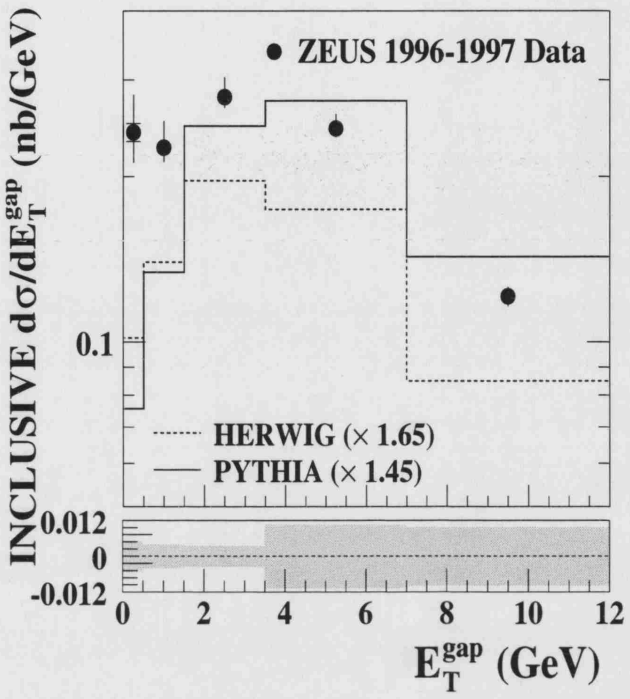

Figure 8.47: The inclusive cross section differential in $E_{\mathrm{T}}^{\mathrm{gap}}$. The solid points show the corrected ZEUS data. The inner error bars show the statistical uncertainty and the outer error bars show the statistical and systematic uncertainties combined in quadrature. The shaded band indicates the calorimeter energy scale uncertainty. The data are compared to the predictions of the HERWIG and PYTHIA photoproduction samples.

predictions of the resulting HERWIG + BFKL model gives the results expected from standard QCD with the addition of strongly interacting colour singlet exchange.

Figure 8.47 shows the measured cross section differential in $E_{\mathrm{T}}^{\mathrm{gap}}$. In this figure, the data are compared to the predictions of the HERWIG and PYTHIA photoproduction samples. Following application of the stated scale factors, the cross section prediction of PYTHIA is larger than that of HERWIG. PYTHIA fails to describe the shape of the distribution, even at large $E_{\mathrm{T}}^{\mathrm{gap}}$. Both models lie below the data for $E_{\mathrm{T}}^{\mathrm{gap}} \lesssim 2$ GeV.

Figure 8.48 displays the same data again, but this time compared to the predictions of HERWIG and HERWIG + BFKL. As well as the stated factor of 1.65, an additional scale factor of 1.40 has been applied to the predicted photoproduction cross section in order to produce agreement with the data in the high $E_{\mathrm{T}}^{\mathrm{gap}}$ region. The results show that the shape of the distribution is well described by HERWIG for values of $E_{\mathrm{T}}^{\mathrm{gap}} > 2$ GeV. However, the excess above the data at low $E_{\mathrm{T}}^{\mathrm{gap}}$ remains visible. The

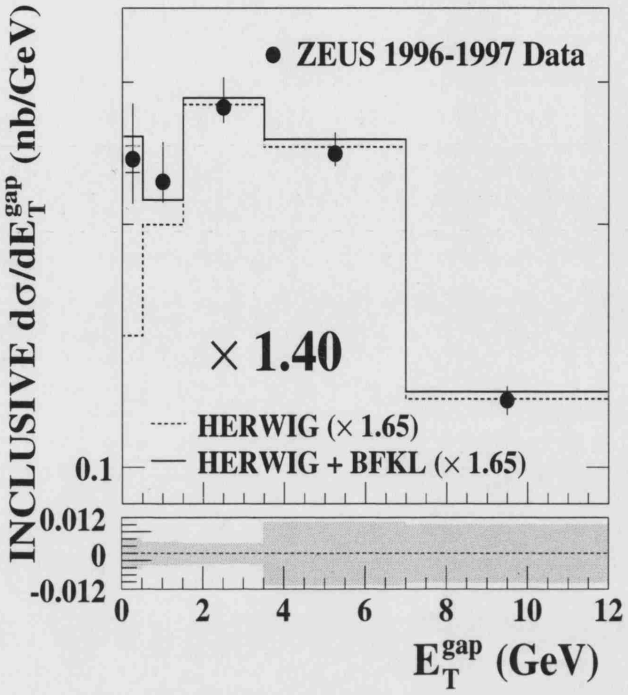

Figure 8.48: The inclusive cross section differential in $E_{\mathrm{T}}^{\mathrm{gap}}$. The solid points show the corrected ZEUS data. The inner error bars show the statistical uncertainty and the outer error bars show the statistical and systematic uncertainties combined in quadrature. The shaded band indicates the calorimeter energy scale uncertainty. The data are compared to the predictions of HERWIG and HERWIG + BFKL.

prediction of HERWIG + BFKL is shown to give a good agreement with the shape of the distribution over the whole range of the measured variable. The observed excess over the predictions of standard photoproduction processes, and the good description by the BFKL model, motivates differential measurements in the low $E_{\mathrm{T}}^{\mathrm{gap}}$ region.

8.14.1 The Differential Cross Sections

Figures 8.49 and 8.50 show the inclusive and gap cross sections differential in $\Delta\eta$, $x_{\gamma;2\mathrm{J}}^{\mathrm{OBS}}$, $\log_{10}(x_{p;2\mathrm{J}}^{\mathrm{OBS}})$ and y. For illustrative purposes, the gap cross sections are shown only for $E_{\mathrm{T}}^{\mathrm{cut}} = 1.0$ GeV. The measured cross sections are compared to the predictions of the HERWIG and PYTHIA standard photoproduction samples. In all figures, the predictions from HERWIG are multiplied by a total factor of 1.65×1.40 to produce agreement with the inclusive cross section measurements. The original stated factor of 1.45 is kept for the PYTHIA model.

The inclusive and gap cross sections differential in $\Delta\eta$ are shown in Figs. 8.49a) and 8.50a) respectively. Both distributions fall steeply as a function of increasing $\Delta\eta$. The results show that the PYTHIA sample gives a good description of the shape of the inclusive data. The normalisation, following scaling by the factor determined from high-E_{T} jet measurements, is also well described. HERWIG falls slightly more steeply than PYTHIA as a function of increasing $\Delta\eta$, lying below the data for $\Delta\eta \gtrsim 3.5$. The gap cross section shows that the data lie in excess of the models, although it is apparent that HERWIG predicts a larger gap cross section than PYTHIA. The difference in the predicted number of gap events between the two models arises mainly from the different hadronisation models in the two Monte Carlo generators. This is discussed in more detail in Section 8.15.1.

Figure 8.49b) shows the inclusive $x_{\gamma;2\mathrm{J}}^{\mathrm{OBS}}$ cross section. The distribution rises to a maximum at $x_{\gamma;2\mathrm{J}}^{\mathrm{OBS}} \sim 0.8$ illustrating that, in general, a large fraction of the photon momentum participates in the hard interaction. This is due to the pseudo-rapidity requirements $|\eta| < 2.4$, $|\Delta\eta| > 2.5$ and $|\bar{\eta}| < 0.75$, which reject events in which both jets lie in the forward direction. Such configurations are rare unless a large fraction of the photon momentum participates in the interaction. Neither HERWIG nor PYTHIA are able to describe the shape of the measured distribution. A similar discrepancy has also been observed in a previous HERA measurement [25] of rapidity gaps-between-jets. Figure 8.50b) shows the corresponding gap cross section, which is strongly peaked at high values of $x_{\gamma;2\mathrm{J}}^{\mathrm{OBS}}$. This is due to two main reasons. Firstly, direct photon events are dominated by quark propagators, which give rise to less QCD radiation from the internal propagator than the gluon propagators which dominate resolved events. In addition, events at high $x_{\gamma;2\mathrm{J}}^{\mathrm{OBS}}$ have a lower probability of multi-parton interactions occurring, which may destroy the gap.

The shape of the inclusive $\log_{10}(x_{p;2\mathrm{J}}^{\mathrm{OBS}})$ cross section, shown in Fig. 8.49c), is well described by both HERWIG and PYTHIA. Only a small kinematic range of $x_{p;2\mathrm{J}}^{\mathrm{OBS}}$ is available since the minimum $\Delta\eta$ requirements set a limit on the minimum possible parton-parton centre-of-mass energy. Figure 8.50c) shows that the gap cross section has a lower average value of $x_{p;2\mathrm{J}}^{\mathrm{OBS}}$ than the corresponding inclusive cross section. This is correlated to the shape of the $x_{\gamma;2\mathrm{J}}^{\mathrm{OBS}}$ distribution since for a fixed parton-parton centre-of-mass energy, a low value of $x_{p;2\mathrm{J}}^{\mathrm{OBS}}$ must mean correspondingly larger value of $x_{\gamma;2\mathrm{J}}^{\mathrm{OBS}}$.

Finally, the inclusive y distribution, shown in Fig. 8.49d), rises to a maximum at the kinematic limit of $y = 0.85$ showing that, in general, a large fraction of the lepton beam energy is carried by the interacting photon. The predictions of HERWIG and PYTHIA rise more steeply than the data. The corresponding gap cross section, shown in Fig. 8.50d), has a lower average value of y than the inclusive distribution, which is again correlated to the shape of the $x_{\gamma;2\mathrm{J}}^{\mathrm{OBS}}$ distribution, since the two variables are inversely related (see Eq. 4.16).

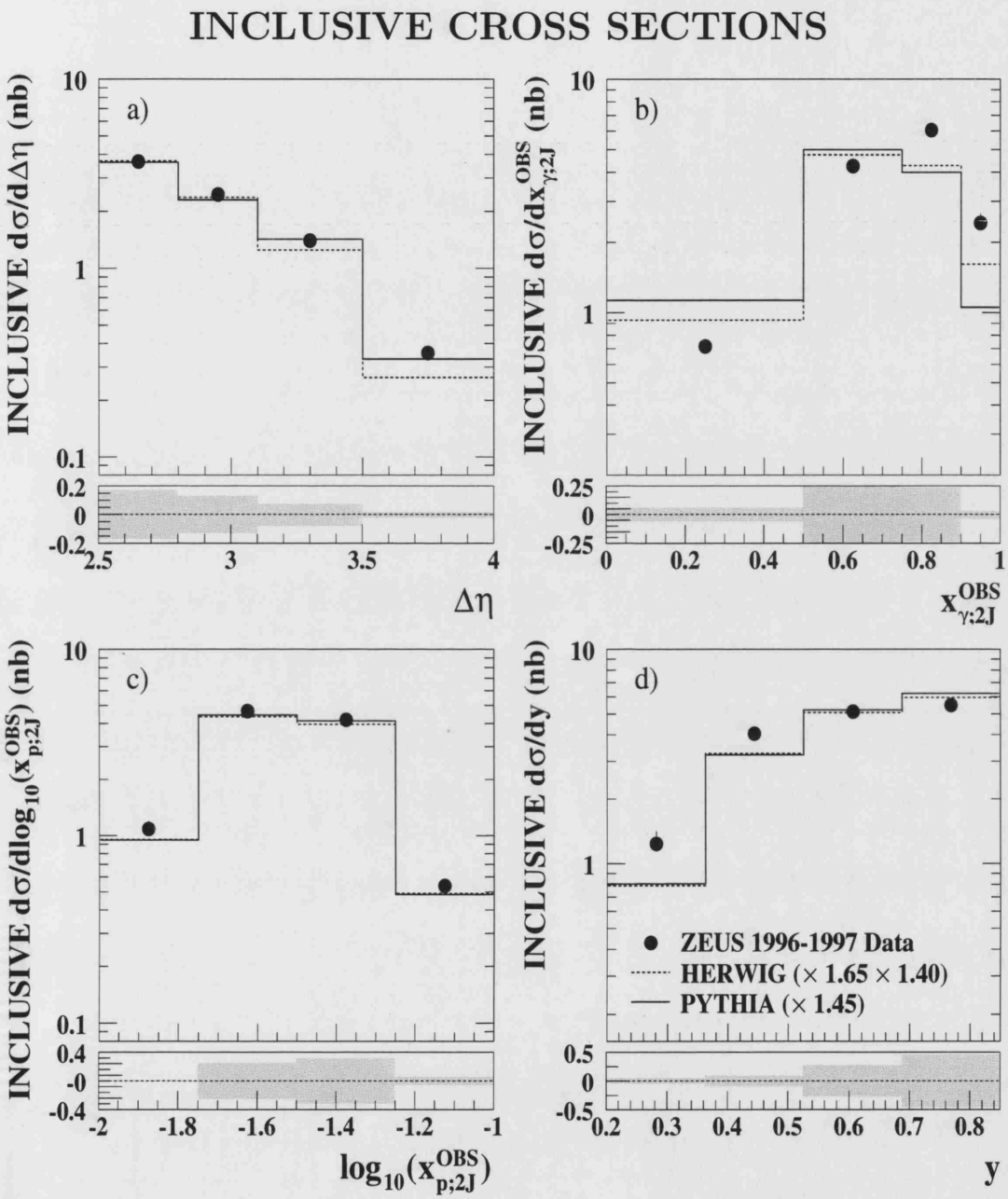

Figure 8.49: The inclusive cross sections differential in $\Delta\eta$, $x_{\gamma;2J}^{OBS}$, $\log_{10}(x_{p;2J}^{OBS})$ and y. The solid points show the corrected ZEUS data. The inner error bars show the statistical uncertainty and the outer error bars show the statistical and systematic uncertainties combined in quadrature. The shaded band indicates the calorimeter energy scale uncertainty. The dashed and solid histograms show the predictions of HERWIG and PYTHIA respectively.

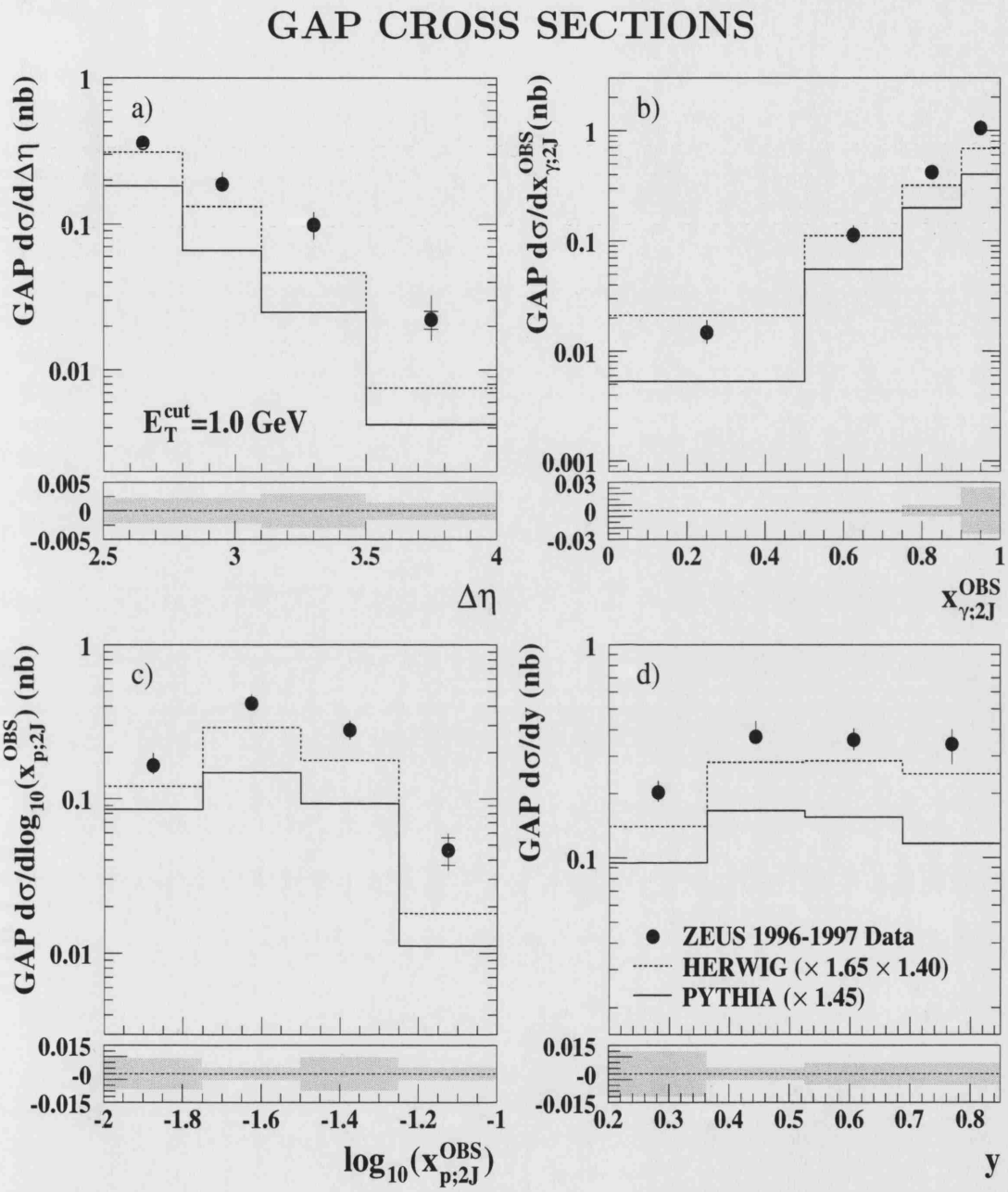

Figure 8.50: The gap cross sections differential in $\Delta\eta$, $x_{\gamma;2\mathrm{J}}^{\mathrm{OBS}}$, $\log_{10}(x_{p;2\mathrm{J}}^{\mathrm{OBS}})$ and y. The solid points show the corrected ZEUS data. The inner error bars show the statistical uncertainty and the outer error bars show the statistical and systematic uncertainties combined in quadrature. The shaded band indicates the calorimeter energy scale uncertainty. The dashed and solid histograms show the predictions of HERWIG and PYTHIA respectively.

8.14.2 The Gap Fraction

In order to further investigate the observed excess of the data over the predictions of the standard QCD Monte Carlos, the gap fractions have been measured. Gap fraction measurements are particularly useful since the dependence on the dynamics of jet production is reduced. In addition, the interpretation of the results is independent of the choice of normalisation of the Monte Carlo cross section.

Figure 8.51 shows the measured gap fractions differential in $\Delta\eta$ for the four values of $E_{\mathrm{T}}^{\mathrm{cut}}$. Taking into account only standard photoproduction processes, the gap fraction is naïvely expected to fall exponentially as a function of increasing $\Delta\eta$. This behaviour is observed in both the HERWIG and PYTHIA photoproduction samples. The data show a large excess above the predictions of the photoproduction models. This excess is most apparent at small $E_{\mathrm{T}}^{\mathrm{gap}}$ and large $\Delta\eta$, where the effects of colour-singlet exchange would be expected to dominate that of standard QCD. However, a significant excess does persist even to the highest values of $E_{\mathrm{T}}^{\mathrm{cut}}$ measured in this analysis. Addition of BFKL colour singlet exchange gives a significantly improved description of the data.

The gap fractions differential in $x_{\gamma;2\mathrm{J}}^{\mathrm{OBS}}$ are shown in Fig. 8.52. A strongly interacting colour singlet object can couple only to the resolved photon. Therefore, while the absolute value of the gap fraction may be expected to be highest at large $x_{\gamma;2\mathrm{J}}^{\mathrm{OBS}}$ (for reasons already discussed), the *excess* above the model predictions would be expected to be most apparent at small $x_{\gamma;2\mathrm{J}}^{\mathrm{OBS}}$. This is exactly the behaviour illustrated by the PYTHIA model. However the prediction of HERWIG is approximately consistent with the data and, consequently, the BFKL model lies above the measured points. The fact that an excess over the prediction of HERWIG is observed in the $\Delta\eta$ distributions but not in the $x_{\gamma;2\mathrm{J}}^{\mathrm{OBS}}$ distribution is likely to be an artifact of the inadequate description of the $x_{\gamma;2\mathrm{J}}^{\mathrm{OBS}}$ cross section. The inclusive cross section suggests that the models predict a ratio of resolved to direct events which is incorrect for this kinematic region. Both the creation of a gap via strongly interacting colour singlet exchange, and the destruction of a gap via multi-parton interactions, occur only in resolved photoproduction. Therefore, an incorrect description of the proportion of resolved events may have a large effect in the prediction of the gap fraction, particularly at low $x_{\gamma;2\mathrm{J}}^{\mathrm{OBS}}$. Therefore, the information from the $x_{\gamma;2\mathrm{J}}^{\mathrm{OBS}}$ cross sections should be used to improve future modelling of the data.

Figure 8.53 shows the measured gap fraction differential in $\log_{10}(x_{p;2\mathrm{J}}^{\mathrm{OBS}})$. The decrease in the measured gap fraction as a function of increasing $\log_{10}(x_{p;2\mathrm{J}}^{\mathrm{OBS}})$ is correlated to the strong rise of the $x_{\gamma;2\mathrm{J}}^{\mathrm{OBS}}$ fraction. The clear excess in the data over the predictions of standard QCD is again apparent, and the BFKL model produces a reasonable agreement with the data for all values of $E_{\mathrm{T}}^{\mathrm{cut}}$.

The gap fractions differential in y are shown in Fig. 8.54. The excess in the data over the standard QCD predictions, is most apparent at high y. The HERWIG + BFKL model gives a reasonable description of the data at intermediate to high y, although lies slightly above the data in the low y region.

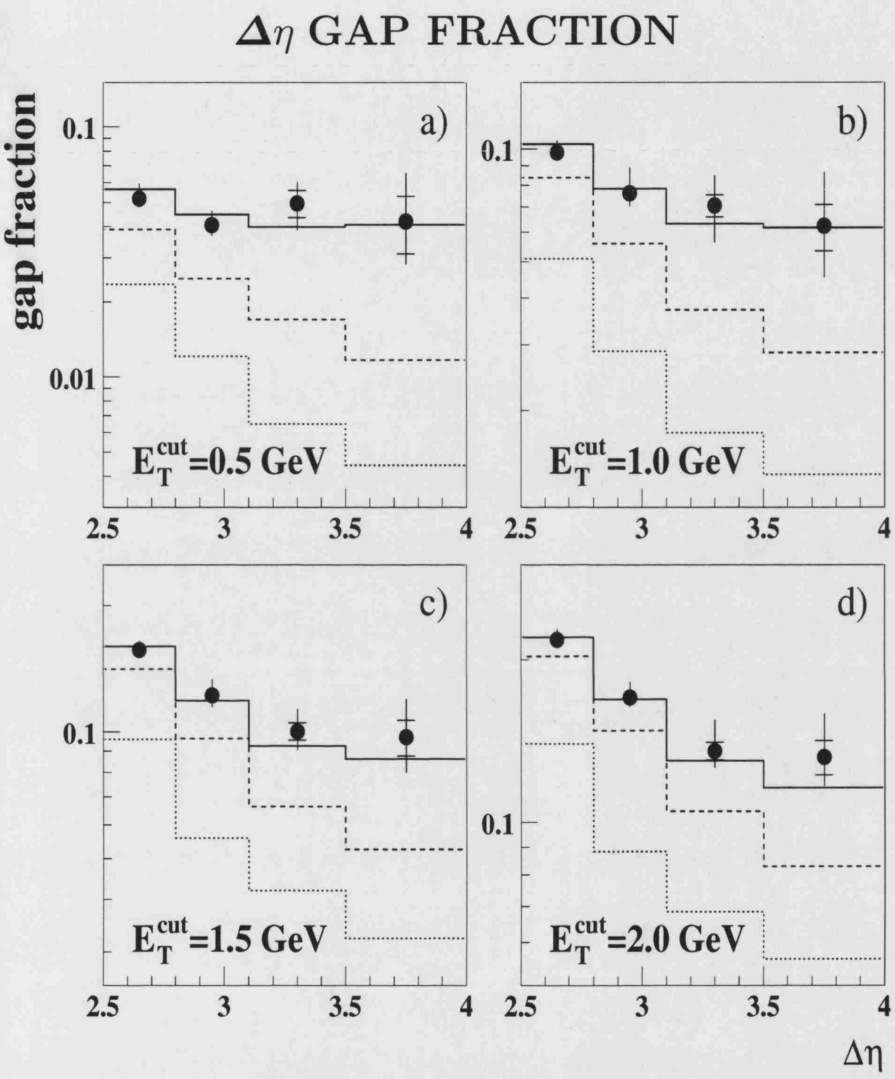

Figure 8.51: The distribution of $f(\Delta\eta)$ for E_T^{cut} = 0.5, 1.0, 1.5 and 2.0 GeV. The solid points show the corrected ZEUS data. The inner error bars show the statistical uncertainty and the outer error bars show the statistical and uncorrelated systematic uncertainties combined in quadrature. The dotted, dashed and solid lines show the predictions of PYTHIA, HERWIG and HERWIG + BFKL respectively.

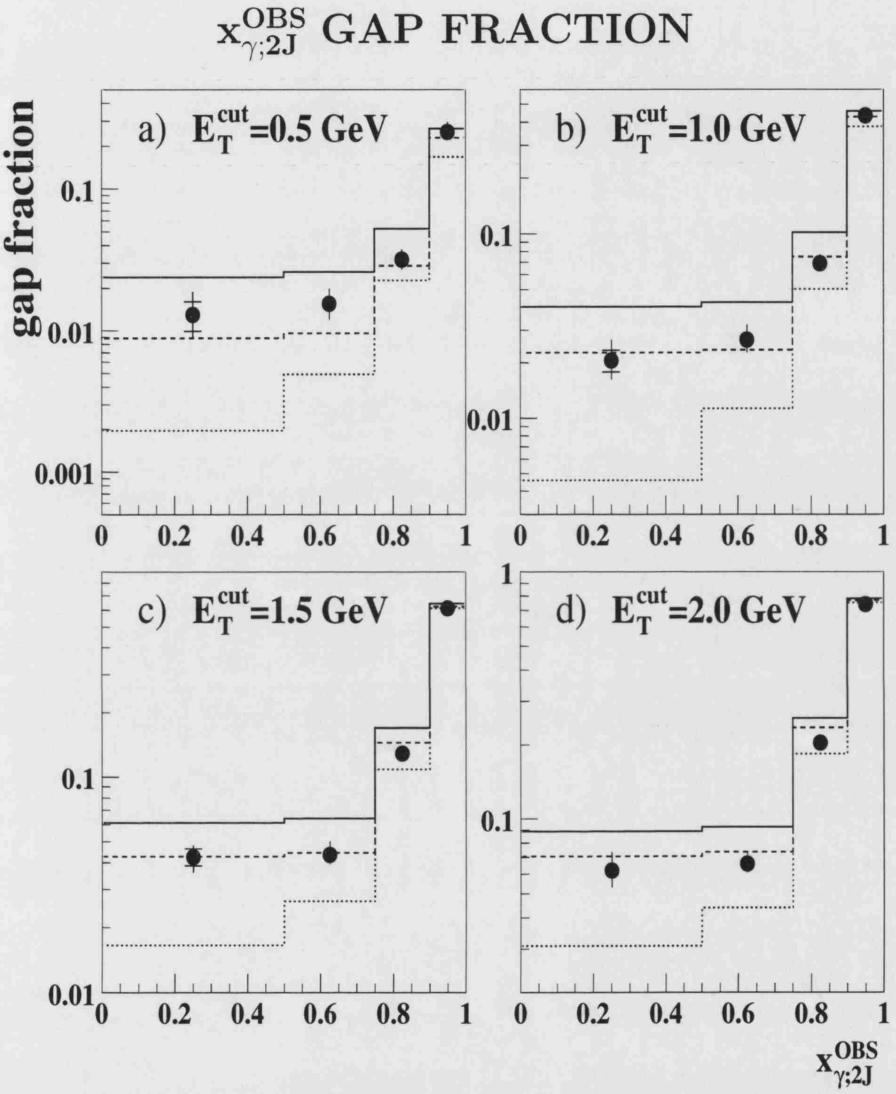

Figure 8.52: The distribution of $f(x_{\gamma;2J}^{\mathrm{OBS}})$ for $E_{\mathrm{T}}^{\mathrm{cut}} = 0.5$, 1.0, 1.5 and 2.0 GeV in the range $2.5 < \Delta\eta < 4.0$. The solid points show the corrected ZEUS data. The inner error bars show the statistical uncertainty and the outer error bars show the statistical and uncorrelated systematic uncertainties combined in quadrature. The dotted, dashed and solid lines show the predictions of PYTHIA, HERWIG and HERWIG + BFKL respectively.

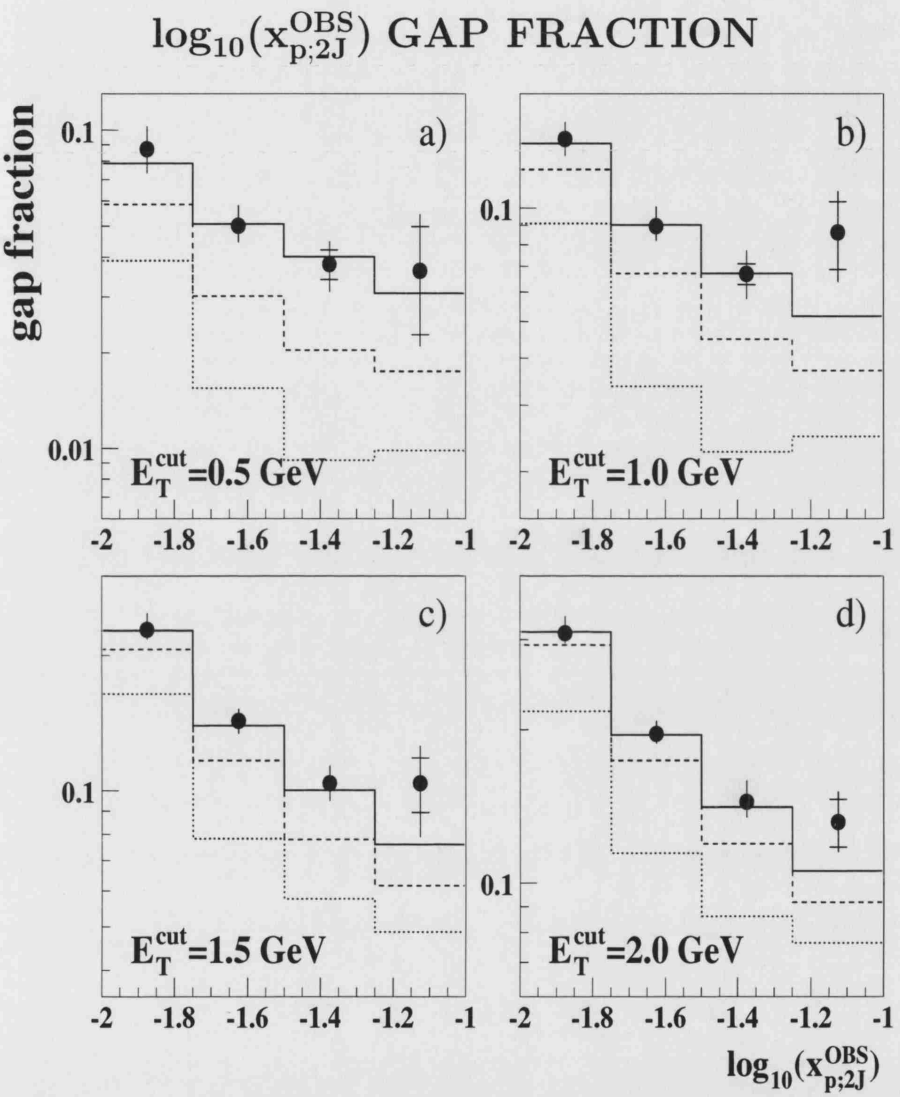

Figure 8.53: The distribution of $f(\log_{10}(x_{p;2\mathrm{J}}^{\mathrm{OBS}}))$ for $E_{\mathrm{T}}^{\mathrm{cut}} = 0.5$, 1.0, 1.5 and 2.0 GeV in the range $2.5 < \Delta\eta < 4.0$. The solid points show the corrected ZEUS data. The inner error bars show the statistical uncertainty and the outer error bars show the statistical and uncorrelated systematic uncertainties combined in quadrature. The dotted, dashed and solid lines show the predictions of PYTHIA, HERWIG and HERWIG + BFKL respectively.

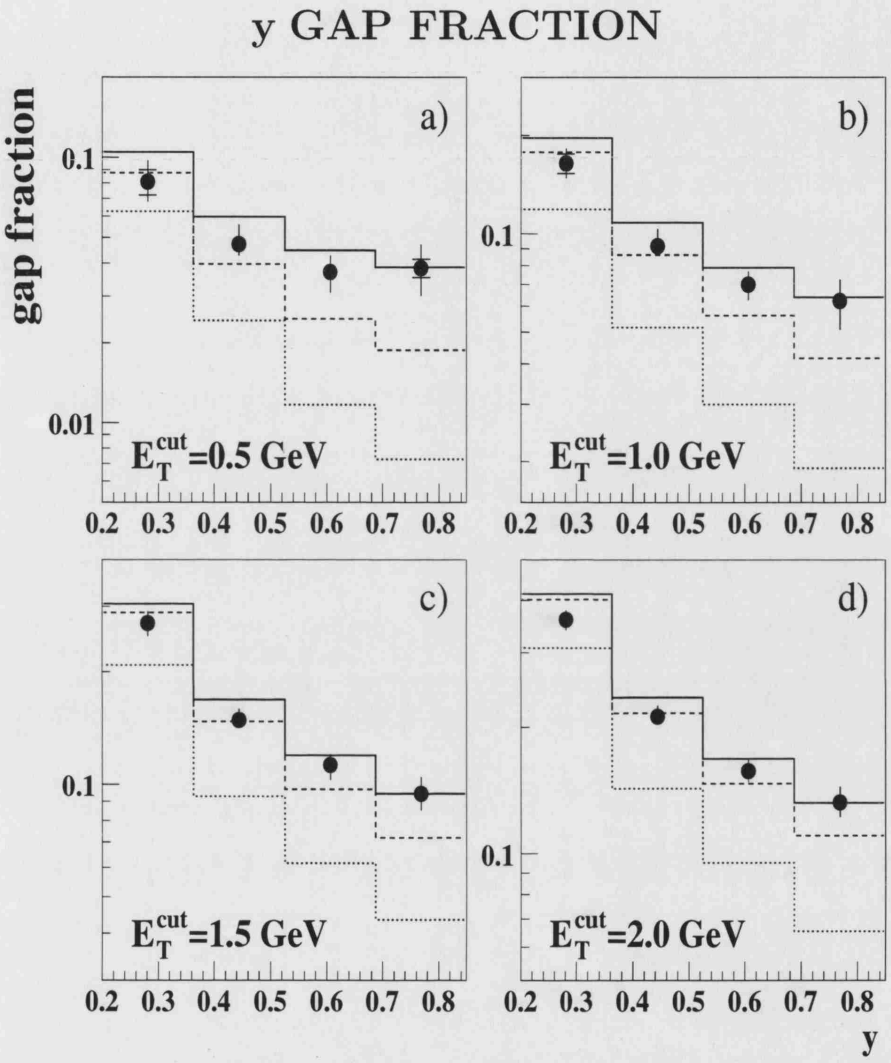

Figure 8.54: The distribution of $f(y)$ for E_T^{cut} = 0.5, 1.0, 1.5 and 2.0 GeV in the range $2.5 < \Delta\eta < 4.0$. The solid points show the corrected ZEUS data. The inner error bars show the statistical uncertainty and the outer error bars show the statistical and uncorrelated systematic uncertainties combined in quadrature. The dotted, dashed and solid lines show the predictions of PYTHIA, HERWIG and HERWIG + BFKL respectively.

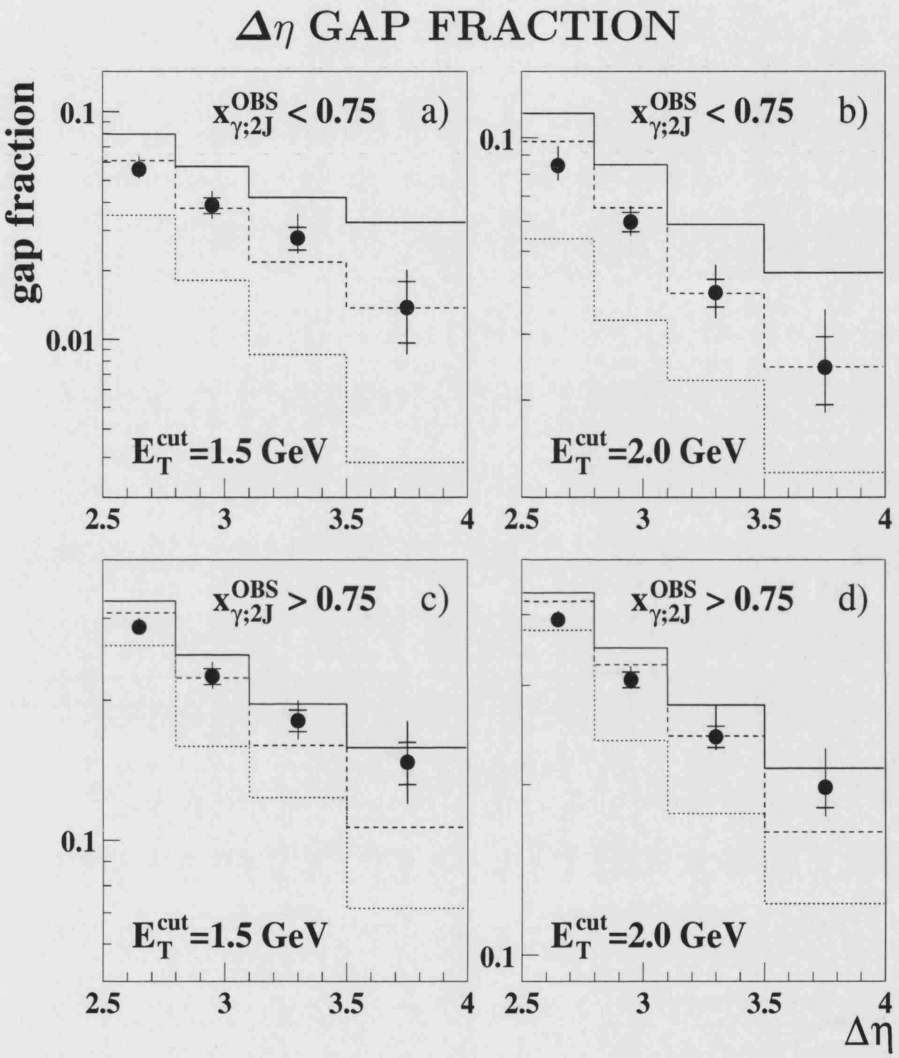

Figure 8.55: The distribution of $f(\Delta\eta)$ in the regions $x_{\gamma;2J}^{\rm OBS} < 0.75$ and $x_{\gamma;2J}^{\rm OBS} > 0.75$ for $E_{\rm T}^{\rm cut} = 1.5$ and 2.0 GeV in the range $2.5 < \Delta\eta < 4.0$. The solid points show the corrected ZEUS data. The inner error bars show the statistical uncertainty and the outer error bars show the statistical and uncorrelated systematic uncertainties combined in quadrature. The dotted, dashed and solid lines show the predictions of PYTHIA, HERWIG and HERWIG + BFKL respectively.

To investigate the $\Delta\eta$ distribution in the direct- and resolved-enhanced region, the gap fraction differential in $\Delta\eta$ has been measured for $x_{\gamma;2J}^{OBS} < 0.75$ and $x_{\gamma;2J}^{OBS} > 0.75$. The results, shown in Fig. 8.55 for $E_T^{cut} = 1.5$ and 2.0 GeV, illustrate that the PYTHIA model lies below the data in all cases. The results also show that, as for the gap fraction differential in $x_{\gamma;2J}^{OBS}$, the prediction of HERWIG + BFKL lies above the data in the resolved-enhanced region. In the direct region, the HERWIG + BFKL model lies above the for data $\Delta\eta < 3.0$ and is approximately consistent with the measurement for $\Delta\eta > 3.0$.

8.15 Gap Survival

The formation of a gap by any mechanism is greatly complicated by the effects of hadronisation and the underlying event. Of particular importance is the possibility that the rapidity gap signature may be destroyed by multi-parton interactions between spectator partons in the colliding beam particles. Detailed comparisons of measured data, and their subsequent interpretation, must therefore include a treatment of such processes. In this analysis, an attempt to treat the effects of the underlying event as correctly as possible, at least within the framework of current understanding, has been made by using sets of tuned underlying event model parameters. In the models shown so-far, the default fragmentation parameters have been used in both HERWIG and PYTHIA. In this section, the sensitivity of the model predictions to changes in the fragmentation and underlying event model, is qualitatively assessed.

8.15.1 Fragmentation

The fragmentation process can only be described by phenomenological models. Different choices of fragmentation model can produce large differences in the gap fraction prediction. Indeed, the large differences already observed in the predictions of HERWIG and PYTHIA arise largely from the different fragmentation schemes: the cluster model [115] in HERWIG and the string model [116] in PYTHIA. This is illustrated in Fig. 8.56 which compares the parton and hadron level gap fraction predictions for standard photoproduction from HERWIG and PYTHIA. The results show that at the parton level, the distributions are reasonably similar, while at the hadron level there are large differences which become even more significant as a function of increasing $\Delta\eta$.

The cluster model of HERWIG and the (Lund Symmetric) string model of PYTHIA are just two of the fragmentation models available. The PYTHIA generator includes options to simulate the fragmentation process in a number of different ways. Several models are studied in this section to assess the sensitivity of the gap fraction prediction

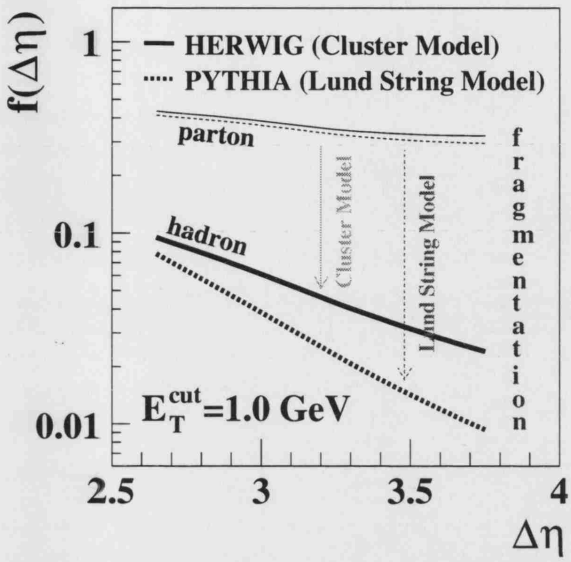

Figure 8.56: The distribution of $f(\Delta\eta)$ for $E_{\mathrm{T}}^{\mathrm{cut}} = 1.0$ GeV. The solid and dashed curves show the predictions of HERWIG and PYTHIA, respectively. The thin (upper pair) and thick (lower pair) curves show the parton- and hadron-level predictions, respectively. All models use a value of $p_{\mathrm{T}}^{\mathrm{min}} = 2.4$ and include no simulation of multi-parton interactions or the soft underlying event.

on the fragmentation model. For simplicity, the models include no simulation of the underlying event.

Figure 8.57 shows the gap fraction differential in $\Delta\eta$ for $E_{\mathrm{T}}^{\mathrm{cut}} = 1.5$ GeV. Four different Monte Carlo models, each of which use a different fragmentation scheme, have been generated. The open stars show the cluster model of HERWIG and the open triangles show the prediction of the Lund Symmetric [116] string model, which is the default in PYTHIA. The open diamonds show again the prediction of the string model, but using the Field-Feynman [196] fragmentation function. For comparison, the open crosses show the prediction of the independent fragmentation model [197] using the Lund Symmetric fragmentation function. The HERWIG model is approximately consistent with the data for $\Delta\eta \lesssim 3$, thereafter lying below the measured points. This model gives a higher gap fraction prediction then the tuned model shown in the previous section. However, since the fragmentation parameters are the same in both models, this is due entirely to the differences in the value of $p_{\mathrm{T}}^{\mathrm{min}}$[¶] and the underlying event model. The sensitivity to the underlying event is discussed in the next subsection.

It has already been shown that the prediction of the Lund string model, which is the default fragmentation model in PYTHIA, lies significantly below that of the HERWIG cluster model. However, the results of Fig. 8.57b) also show that the Field-Feynman string and independent fragmentation models lie below the default PYTHIA model, and significantly below that of default HERWIG.

The independent fragmentation model, in its original form, is known to have problems due to violation of momentum conservation [6]. It also suffers from difficulties when the

[¶]The value of $p_{\mathrm{T}}^{\mathrm{min}}$ is taken to be = 2.4 GeV in all models shown in this section.

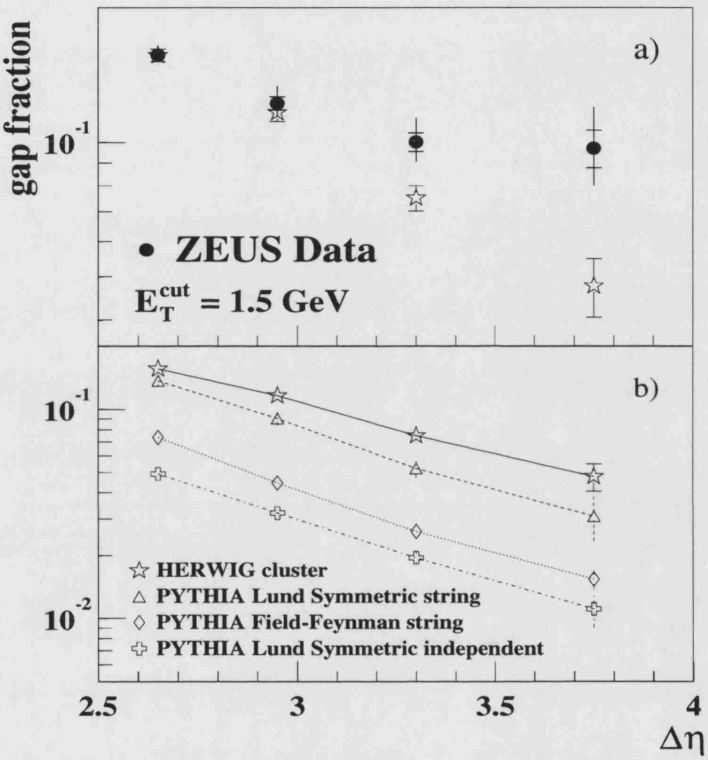

Figure 8.57: The gap fraction as a function of $\Delta\eta$ for $E_T^{cut} = 1.5$ GeV. a) The ZEUS data are compared to the prediction of the HERWIG cluster model (open stars). b) The cluster model is compared to the predictions of the Lund Symmetric string model (open triangles), the Field-Feynman string model (open diamonds) and the Lund Symmetric independent (open crosses) fragmentation model.

jets become close together in angle. However, there is no reason, *a priori* to discount either the string or cluster model and the results of this section show that there are large uncertainties in the gap fraction prediction resulting from the treatment of the fragmentation process. Constraints on the fragmentation process have, to date, been provided mainly by e^+e^- annihilation experiments. The results shown here indicate that further constraints are necessary if the data from this analysis is to be properly interpreted.

8.15.2 The Underlying Event

The HERWIG generator has been used to study the uncertainties in the predicted gap fraction arising from the treatment of the underlying event. The default cluster fragmentation parameters have been used in all models shown in this section.

Figure 8.58 shows the gap fraction as a function of $\Delta\eta$ for $E_{\mathrm{T}}^{\mathrm{cut}} = 1.5$ GeV. Compared to the data are the predictions of three different HERWIG models: the default model, which includes no simulation of the underlying event, a soft underlying event model and the tuned HERWIG model with parameters listed in Tab. 8.14. The three models respectively correspond to HERWIG, HERWIG + $\mathrm{SUE}_{0.3}$ and HERWIG + Jimmy_t + $\mathrm{SUE}_{0.05}$ in Tab. 7.4. In addition, a model with parameters corresponding to those of HERWIG + Jimmy in Tab. 7.4 has also been studied. The results were found to be very similar to the HERWIG + Jimmy_t + $\mathrm{SUE}_{0.05}$ model and so are not shown here.

Figure 8.58a) shows that the gap fraction prediction does indeed depend on the choice of underlying event model parameters. As expected, the model with no simulation of an underlying event gives the highest prediction and is consistent with the data for $\Delta\eta \lesssim 3$. The soft underlying event model gives the smallest gap fraction prediction and lies significantly below the data over the whole range of $\Delta\eta$. In Fig. 8.58b), the same data are displayed again. In this figure, the model comparisons include a simulation of the BFKL process which is added according to the generated cross sections. For all three models, addition of the BFKL process produces a closer agreement with the data at large $\Delta\eta$. However, the tuned model gives the best description of the data over the whole range of $\Delta\eta$. Note also that the shape of the predicted gap fraction is very similar for all underlying event model parameters, illustrated by the lines joining the points in Fig. 8.58. This suggests that the gap survival probability can be considered as a constant multiplicative factor.

The sensitivity to the effects of the underlying event may be reduced by requiring higher transverse energies of the two highest-E_{T} jets. Such a requirement would also reduce uncertainties associated with the photon PDF. Figure 8.58c) shows the gap fraction prediction of the HERWIG models shown in a), but with jet transverse energy requirements of $E_{\mathrm{T}}^{1,2} > 10,8$ GeV for the two highest-E_{T} jets. The results show a

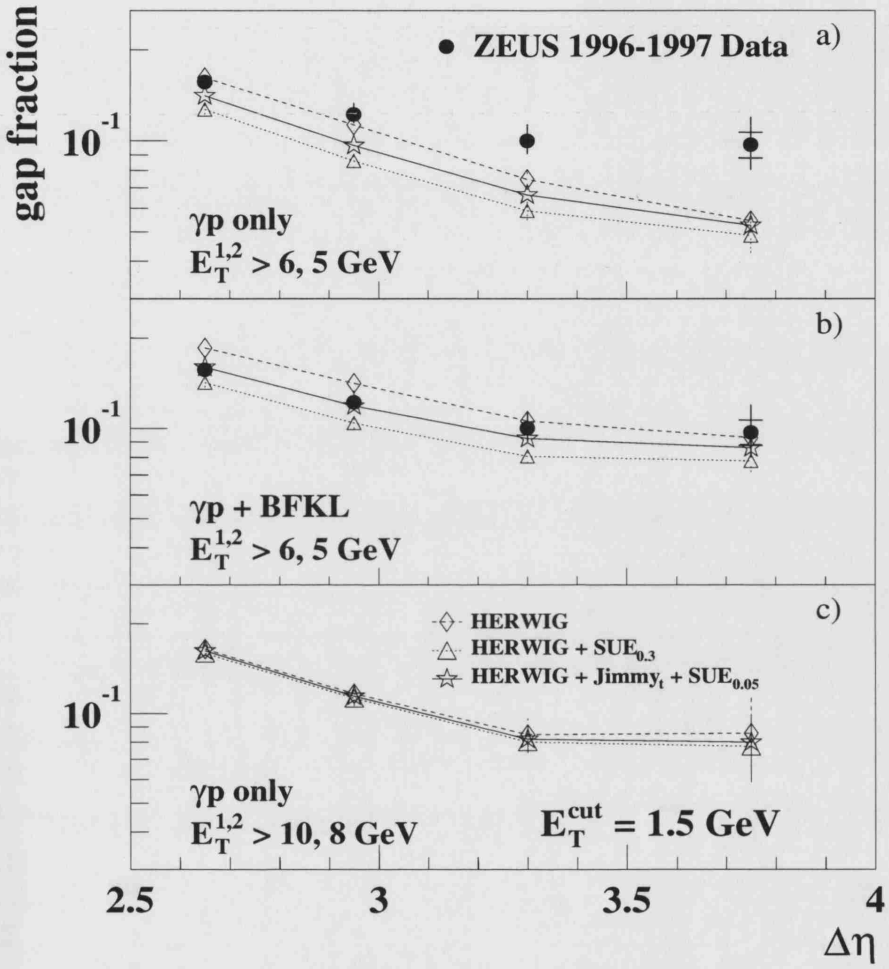

Figure 8.58: The gap fraction as a function of $\Delta\eta$ for $E_T^{cut} = 1.5$ GeV. The solid points show the corrected ZEUS data. The inner error bars show the statistical uncertainty and the outer error bars show the statistical and uncorrelated systematic uncertainties combined in quadrature. In a) the data are compared to the predictions of HERWIG, HERWIG + $SUE_{0.3}$ and HERWIG + $Jimmy_t$ + $SUE_{0.05}$ (standard photoproduction only). In b) the data are compared to the same models but with the addition of the BFKL process. In c) the photoproduction models are shown again but with the requirement $E_T^{1,2} > 10, 8$ GeV for the two highest transverse energy jets. Full details of the models parameters are given in Tab. 7.4.

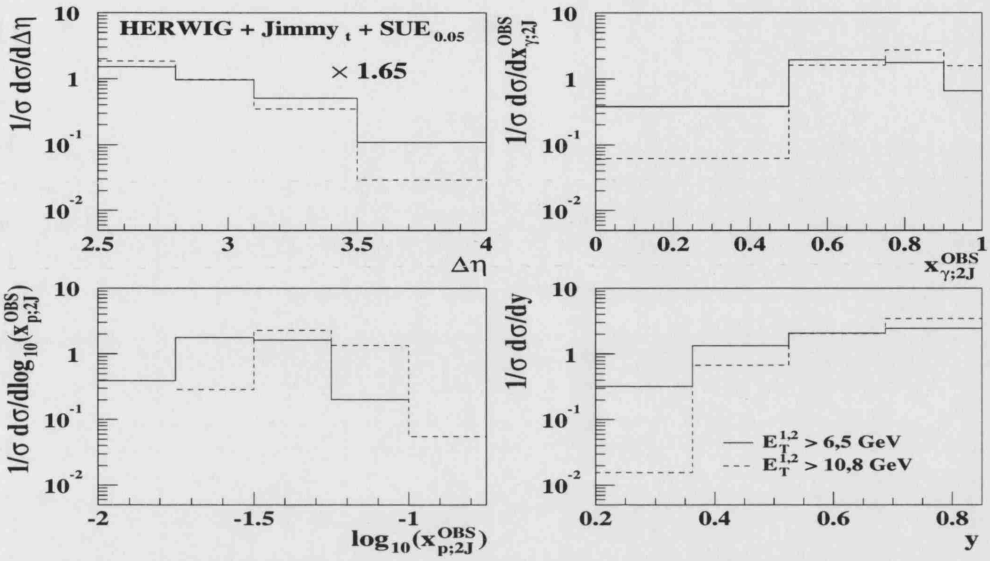

Figure 8.59: The inclusive cross sections according to the HERWIG + Jimmy$_t$ + SUE$_{0.05}$ Monte Carlo model. The solid histogram shows the prediction for the cross section definition of this analysis, while the dashed histogram shows the prediction for jet transverse energy requirements of $E_{\mathrm{T}}^{1,2} > 10,8$ GeV. The cross sections have been scaled by a factor of 1.65 only.

much reduced sensitivity to the underlying event model. For the 1996-1997 data-set, such a high transverse energy requirement would severely limit the available statistics. However, with the increase in luminosity expected from HERA II running, a high-E_{T} measurement will be possible and is recommended for future analyses.

It should also be reiterated that $\Delta\eta \simeq \log\left(\hat{s}/-\hat{t}\right)$ (see Eq. 2.79) where $\hat{s}$ is the parton-parton centre-of-mass energy squared and $\hat{t}$ is the momentum transfer squared. Since $|\hat{t}| \sim E_{\mathrm{T}}^2$ (see Section B.2), then in order to maintain a large separation, $\Delta\eta$, the increase in the average values of $|\hat{t}|$ must be compensated for by a corresponding increase in $\hat{s}$. This is illustrated in Fig. 8.59 which shows the inclusive cross section predictions according to the HERWIG + Jimmy$_t$ + SUE$_{0.05}$ model. The solid histogram shows the predictions for $E_{\mathrm{T}}^{1,2} > 6,5$ GeV (the cross section definition of this analysis) while the dashed histogram shows the predictions for $E_{\mathrm{T}}^{1,2} > 10,8$ GeV. The results show that the higher jet transverse energy requirements give rise to higher average values of $x_{\gamma;2\mathrm{J}}^{\mathrm{OBS}}$, $x_{p;2\mathrm{J}}^{\mathrm{OBS}}$ and y, all of which contribute to a larger parton-parton centre-of-mass energy $\hat{s}$. The larger proton beam energy used in HERA from 1998 onwards (920 GeV compared to 820 GeV for the 1996-1997 running period used in this analysis) will also provide a small enhancement in the average parton-parton centre-of-mass energy and this should be utilised in future analyses.

8.15.3 Estimation of the Gap Survival Probability

The concept of gap survival relates to the probability that a gap produced at the parton level will not survive to be measured at the hadron level. Of particular importance are the effects of hadronisation and the underlying event, and especially the destruction of a gap via multi-parton interactions. It has been suggested [103] that the gap fraction at the hadron level $f(\Delta\eta)$ is related to that at the parton level $\hat{f}(\Delta\eta)$ via a linear relationship $f(\Delta\eta) = \mathcal{S} \cdot \hat{f}(\Delta\eta)$. The quantity $\mathcal{S}$ is known as the gap survival probability. Estimates of $\mathcal{S}$ in hadron-hadron collisions at the Tevatron range from about 5-30% [103, 198]. Previous studies [194] of the effects of multi-parton interactions have shown that the value of $\mathcal{S}$ at HERA is likely to be considerably larger than that at the Tevatron. This is due to the different colliding beam particles, the lower centre-of-mass energy and the large fraction of the photon momentum that participates in the hard interaction, each of which reduce the probability that the gap signature will be destroyed by the effects of multi-parton interactions.

The HERWIG and PYTHIA Monte Carlo models have been used to study the effects of hadronisation and the underlying event on colour singlet exchange processes in general and, more particularly, to extract an estimate of the gap survival probability for the BFKL process. For simplicity, the value of $\mathcal{S}$ has been separated into two parts: that relating to the hadronisation process ($\mathcal{S}_{had}$) and that relating to the underlying event ($\mathcal{S}_{ue}$). For this study, the quantities $\mathcal{S}_{had}$ and $\mathcal{S}_{ue}$ are assumed to be independent, giving a total gap survival factor of $\mathcal{S} = \mathcal{S}_{had}\mathcal{S}_{ue}$.

Figure 8.60 illustrates the effects of hadronisation and the underlying event on the colour singlet exchange process. On the left of the figure are the predicted gap fractions. The dotted, dashed and solid lines respectively show the predictions at parton level, hadron level (with no underlying event) and hadron level (including underlying event). The different curves will be referred to as **parton**, **hadron** and **hadron$_{ue}$** respectively. On the right of the figure the open triangles, open circles and solid stars respectively show the values of $\mathcal{S}_{had}$, $\mathcal{S}_{ue}$, and $\mathcal{S}$. These quantities are calculated from the ratio of **hadron:parton**, **hadron$_{ue}$:hadron** and **hadron$_{ue}$:parton** respectively.

The results for the BFKL process show that both hadronisation and the underlying event reduce the expected gap fraction. The values of $\mathcal{S}_{had}$ and $\mathcal{S}_{ue}$ are approximately constant as a function of $\Delta\eta$ and have a value of just over 80%. This gives an overall gap survival factor of $\sim 67\%$. The results are found to be consistent for all values of $E_{\mathrm{T}}^{\mathrm{cut}}$, and give a value of $\mathcal{S} = 65\% - 70\%$ in each case. The flatness of the ratio as a function of $\Delta\eta$ supports the idea that the gap survival factor may be considered simply as a multiplicative factor.

In order to assess the sensitivity to the nature of the colour singlet exchange process, the effects of hadronisation and the underlying event on the high-t γ exchange process

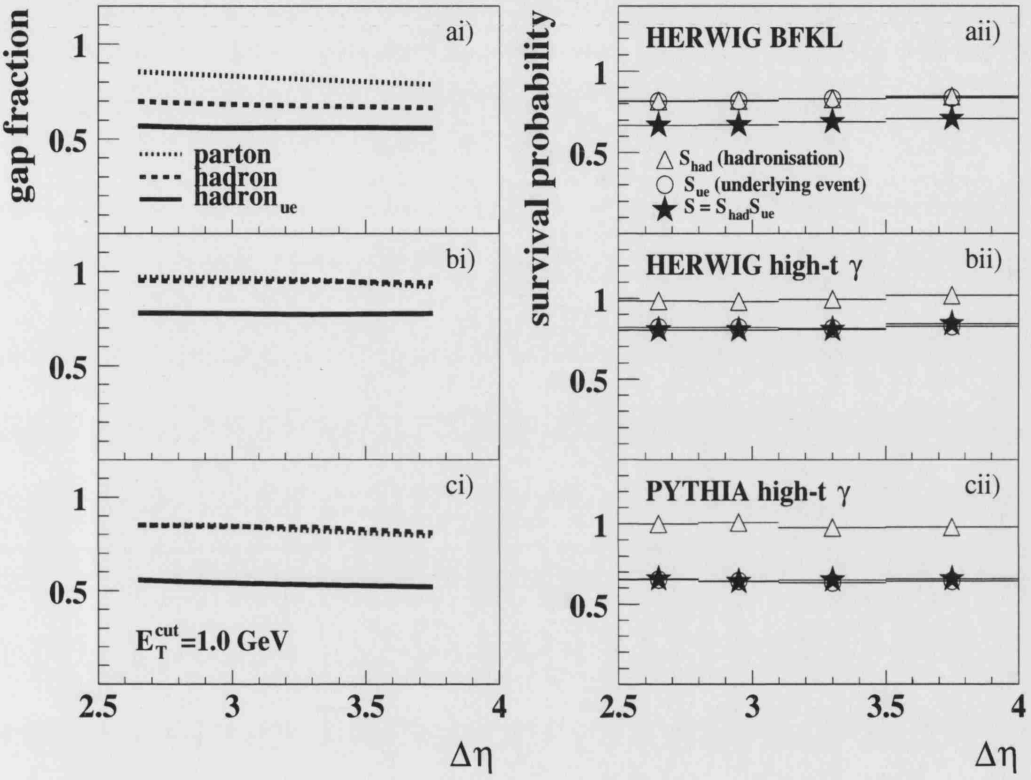

Figure 8.60: The effects of hadronisation and the underlying event on the colour singlet gap fraction prediction. Figures ai), bi) and ci) respectively show the predictions of HERWIG BFKL, HERWIG high-t γ and PYTHIA high-t γ. In each case, the dotted, dashed and solid lines show the distributions at the parton-level, hadron-level and hadron-level including underlying event. Figures aii), bii) and cii), show the estimates of $\mathcal{S}_{had}$, $\mathcal{S}_{ue}$ and $\mathcal{S} = \mathcal{S}_{had}\mathcal{S}_{ue}$ which are obtained from taking the ratios of (**hadron:parton**), (**hadron$_{ue}$:hadron**) and (**hadron$_{ue}$:parton**) respectively.

has also been studied. Both HERWIG and PYTHIA have been used to simulate this process. The results of Fig. 8.60b) and c) show that the hadronisation process has little or no effect on the predicted gap fraction i.e. $\mathcal{S}_{had} \sim 1$. This is due to the fact that the high-t sample contains only LO quark-quark scattering. This would lead to less QCD radiation than in events mediated by a BFKL pomeron, which couples preferentially to gluons. The different values of $\mathcal{S}_{ue}$ between HERWIG ($\sim 80\%$) and PYTHIA ($\sim 65\%$) arises simply due to the different treatment of the underlying event, most particularly the different values of $p_{\mathrm{T}}^{\mathrm{min}}$ and $p_{\mathrm{T}}^{\mathrm{mi}}$ used in the models.

Chapter 9

Summary

This thesis presents two studies involving the hard photoproduction of jets: a study of **Multi-Jets in Photoproduction** and a study of **Rapidity Gaps Between Jets**. The data were taken from e^+p collisions during the 1996-1997 HERA running period and correspond to an integrated luminosity of 38.6 pb^{-1}. The $k_\perp$ clustering algorithm was employed to define the jets. A bin-by-bin correction procedure was used to unfold the data to obtain hadron level cross sections. The measured distributions have been compared to leading log parton shower models. In the following sections, a brief summary of each analysis is given.

9.1 Multi-Jets in Photoproduction

Cross sections for the photoproduction of four high transverse energy jets have been measured. This is the highest order process in QCD to have been measured at HERA. The so-called **inclusive** cross section was defined by requiring at least four jets with $|\eta| < 2.4$, two of which were required to satisfy $E_{\rm T} > 6$ GeV with a further two satisfying $E_{\rm T} > 5$ GeV in the laboratory frame. Additional selection criteria of $|\cos\theta_{3'}| < 0.8$ and $X_{3'} < 0.95$ were imposed to reduce the effects of the jet transverse energy thresholds. The **high mass** cross section was defined by the additional requirement that $m_{4\rm J} > 50$ GeV. This requirement also reduces bias imposed by the jet transverse energy selection and allows direct comparisons to be made with previous three jet measurements. Furthermore, the requirement of a high invariant mass of the four jet system reduces the sensitivity to the effects of the underlying event.

The measured differential cross sections have been compared to the predictions of the HERWIG and PYTHIA Monte Carlo generators. These models employ only the $2 \rightarrow 2$ photoproduction matrix elements, but are able to approximate multi-parton final states through the modelling of initial- and final-state parton showers. The generators also

include phenomenological models of the hadronisation process and allow the option of simulating an underlying event. Comparison of the measured data with the predictions from these models yield the following conclusions:

- The inclusive distributions are extremely sensitive to the underlying event model in both shape and normalisation. Inclusion of only a soft underlying event is ruled out by the shape of the angular distributions. Addition of multi-parton interactions, which introduce a hard, partonic scattering component to the underlying event, significantly improves the agreement with the data.
- The shape of the high mass differential cross sections are well described by the parton shower models and there is little sensitivity to the inclusion of an underlying event. Therefore, in this kinematic region, the dynamics should be relatively insensitive to the effects of non-perturbative physics and the high mass distributions are considered suitable for comparison with higher order pQCD calculations when they become available.
- The rate of four jet production, relative to that of three jet, exceeds that expected from standard Monte Carlo generators which produce multi-parton final states only through the simulation of initial and final state QCD radiation. Models including a simulation of multi-parton interactions - which introduces an additional mechanism for the photoproduction of four jets - are able to adequately describe the data.
- The inclusive and high mass data have been used to tune the Monte Carlo model parameters. This tuning has been performed with the present data, in conjunction with other measurements from LEP, HERA and the Tevatron, and has largely concentrated on varying the parameters of the underlying event. A tuning has been found which gives reasonable agreement with the multi-jet data in both shape and normalisation, while maintaining a good description of data from other experiments.

This is the first study of four jet final states in photoproduction and provides information on the underlying dynamics of multi-jet production. Furthermore, the results provide important tests of the ability of parton shower extensions to fixed order pQCD to reproduce particular aspects of multi-jet final states such as the orientation of jets and the distribution of energy. The results are ready for comparison with $\mathcal{O}(\alpha\alpha_s^3)$ pQCD calculations when they become available. This will provide stringent tests of higher order QCD in the future.

9.2 Rapidity Gaps Between Jets

Differential cross sections for the photoproduction of two high transverse energy jets separated by a large region in pseudo-rapidity have been measured. The so-called **inclusive** cross section has been defined by requiring two jets satisfying $|\eta^{1,2}| < 2.4$ and $E_T^{1,2} < 6,5$ GeV. Additionally, the jets were required to satisfy $|\bar{\eta}| = \frac{1}{2}|\eta^1 + \eta^2| < 0.75$ and $2.5 < |\Delta\eta| < 4.0$. The **gap** cross sections were defined by the additional criteria that $E_T^{gap} < E_T^{cut}$ where $E_T^{cut} = 0.5$, 1.0, 1.5 and 2.0 GeV and the quantity E_T^{gap} is the scalar sum of the transverse energy of all mini-jets between the two leading jets. The gap fractions, which are defined as the ratio of the gap cross sections to the inclusive cross section, have also been measured.

The measured distributions have been compared to the predictions of the HERWIG and PYTHIA Monte Carlo generators. Comparison of the data with the predictions of these models yields the following conclusions:

- The data show an excess over the predictions of standard photoproduction processes. Provided the shape of the inclusive differential cross section is correctly described, the observed excess can be explained by the addition of colour singlet exchange according to the LLA BFKL process with a fixed value of $\alpha_s^{pre.} = 0.18$ and values of $\alpha_s^{den.} = 0.18$ and $\omega_0 = 0.48$. However, the models exhibit a strong sensitivity to the hadronisation and underlying event models. These, non-perturbative effects must be more fully understood before a proper interpretation of the results is possible.

- A Monte Carlo study of the effects of hadronisation and the underlying event on the BFKL process produces an estimate for the gap survival probability of $\mathcal{S} \sim 65\% - 70\%$. The high-$t$ γ exchange process has also been studied and the value of $\mathcal{S}$ is found to be highly dependent on the nature of the colour singlet exchange process, as well as the parameters of the underlying event. These differences arise from the differing amounts of QCD radiation arising from objects which couple predominantly to quarks or to gluons.

This measurement uses both an improved gap definition and an improved reconstruction technique for the hadronic final state, compared to the previous ZEUS measurement. In addition, the data used in this analysis represent an increase of ~ 6 in luminosity compared to all previous HERA measurements. The results have confirmed the excess over the predictions of standard QCD, as observed in previous gaps-between-jets analyses. This excess can be interpreted as evidence for the exchange of a strongly interacting colour singlet object. However, the models are sensitive to non-perturbative aspects of the event such as hadronisation and the underlying event. Future measurements, including more data, will be able to increase the transverse energy thresholds of

the two highest transverse energy jets. This should reduce the sensitivity of the measurement to the effects of the underlying event, resulting in smaller model uncertainties and thereby enabling further progress in understanding this area of physics.

Appendix A

Running Couplings

From renormalisation arguments (see [6] for example), the running of a coupling constant α with some external energy scale μ^2 is given by the renormalisation group equation,

$$\frac{\mathrm{d}\alpha}{\mathrm{d}\log\mu^2} = \beta(\alpha) \tag{A.1}$$

where $\alpha = \alpha(\mu^2)$. The renormalised coupling depends on the scale μ_0 at which the theory is chosen to be renormalised. Note that μ_0 is an arbitrary parameter. It is not defined in QCD, although a choice of scale is necessary to render physical constants finite in the the theory at the quantum level. Integration of Eq. A.1 with a choice of μ_0 gives,

$$\begin{aligned}
\int_{\mu_0^2}^{\mu^2} \mathrm{d}\log\mu^2 &= \int_{\alpha(\mu_0^2)}^{\alpha(\mu^2)} \frac{\mathrm{d}\alpha}{\beta(\alpha)} \\
\log\mu^2 - \log\mu_0^2 &= F(\alpha(\mu^2)) - F(\alpha(\mu_0^2)) \\
\alpha(\mu^2) &= F^{-1}\left(F(\alpha(\mu_0^2)) + \log\frac{\mu^2}{\mu_0^2}\right).
\end{aligned} \tag{A.2}$$

Any dependence on the renormalisation scale μ_0 can be removed by the introduction of a dimensionful constant Λ so that,

$$\log\Lambda^2 \equiv \log\mu_0^2 - F(\alpha(\mu_0^2)). \tag{A.3}$$

Then, Eq. A.2 becomes,

$$\alpha(\mu^2) = F^{-1}\left(\log\frac{\mu^2}{\Lambda^2}\right) \tag{A.4}$$

where Λ must be evaluated experimentally. The scale μ^2 is often taken to be the four-momentum transfer Q^2 in lepton-hadron collisions, or the centre-of-mass energy, $\sqrt{s}$ in lepton-lepton collisions.

A.1 The Running of $\alpha_s(Q^2)$

The running of the strong coupling constant α_s is determined by the QCD (or Callan-Symanzik) β-function [199] given by,

$$\beta(\alpha_s) = -b_0\alpha_s^2[1 + b_1\alpha_s + b_2\alpha_s^2 + \mathcal{O}(\alpha_s^3)]. \tag{A.5}$$

The coefficients are given by,

$$\begin{aligned} b_0 &= \frac{11C_A - 2n_f}{12\pi} = \frac{33 - 2n_f}{12\pi} \\ b_1 &= \frac{17C_A^2 - 5C_An_f - 3C_Fn_f}{12\pi(11C_A - 2n_f)} = \frac{153 - 19n_f}{12\pi(33 - 2n_f)} \\ b_2 &= \frac{2857C_A^3 + (54C_F^2 - 615C_FC_A - 1415C_A^2)n_f + (66C_F + 79C_A)n_f^2}{288\pi^2(11C_A - 2n_f)} \\ &= \frac{77139 - 15099n_f + 325n_f^2}{288\pi^2(33 - 2n_f)} \end{aligned} \tag{A.6}$$

where n_f is the number of active light flavours at the scale Q^2*. The β-function coefficients are extracted from the higher order (loop) corrections to the bare vertices of the theory. The coefficients b_0, b_1 and b_2 respectively correspond to the one-loop, two-loop and three-loop calculations. An example of a one-loop correction is shown in Fig. 2.1.

At LO, only the one-loop term is retained and Eq. A.1 becomes,

$$\frac{\mathrm{d}\alpha_s(Q^2)}{\mathrm{d}\log Q^2} = -b_0\alpha_s^2(Q^2). \tag{A.7}$$

Integrating Eq. A.7 gives,

$$\begin{aligned} \int_{\alpha_s(\mu_0^2)}^{\alpha_s(Q^2)} \frac{\mathrm{d}\alpha_s}{-b_0\alpha_s^2} &= \int_{\mu_0^2}^{Q^2} \mathrm{d}\log Q^2 \\ \frac{1}{b_0}\left[\frac{1}{\alpha_s}\right]_{\alpha_s(\mu_0^2)}^{\alpha_s(Q^2)} &= \log Q^2 - \log\mu_0^2 \\ \frac{1}{\alpha(Q^2)} - \frac{1}{\alpha(\mu_0^2)} &= b_0\log\frac{Q^2}{\mu_0^2} \\ \alpha_s(Q^2) &= \frac{\alpha(\mu_0^2)}{1 + [\alpha(\mu_0^2)b_0]\log(Q^2/\mu_0^2)} \end{aligned} \tag{A.8}$$

*This result corresponds to the $\overline{\mathrm{MS}}$ renormalisation scheme.

Substitution of $\log \Lambda^2 = \log \mu_0^2 - \frac{1}{b_0 \alpha_s(\mu_0^2)}$ into Eq. A.8 gives,

$$\alpha_s(Q^2) = \frac{1}{b_0 \log(Q^2/\Lambda^2)}. \quad \text{(A.9)}$$

For $n_f \leq 16$, b_0 is positive, which means that as the energy scale Q^2 increases, the value of α_s decreases. This shows the effects of the non-Abelian nature of QCD. This can be contrasted to the LO formula for QED. In this case, the one-loop β-function is given by

$$\beta_{\text{QED}} = \frac{1}{3\pi}\alpha^2. \quad \text{(A.10)}$$

Equation A.2 therefore becomes,

$$\alpha(Q^2) = \frac{\alpha(\mu_0^2)}{1 - [\alpha(\mu_0^2)/(3\pi)] \log(Q^2/\mu_0^2)} \quad \text{(A.11)}$$

demonstrating the QED behaviour that as Q^2 increases, so too does the value of α.

It should also be noted from Eq. A.9, that a change of the scale Q by an arbitrary factor of order unity e.g. $Q \to Q/2$, induces a variation in α_s that is of the order α_s^2. This variation is not controllable since it is beyond the accuracy at which Eq. A.9 is valid. Therefore, in LO perturbation theory, α_s is not unambiguously defined.

Appendix B

Kinematics

The kinematics of lepton-proton scattering at HERA are discussed in more detail in this section. In particular, a more detailed discussion of the Lorentz invariant quantities Q^2, x and y is given. In addition, the boost invariance of the rapidity y is discussed and expressions for the observables $x_{\gamma;\mathrm{NJ}}^{\mathrm{OBS}}$ and $x_{p;\mathrm{NJ}}^{\mathrm{OBS}}$ are derived. Finally, an expression for the dependence of the gap fraction, f, on the rapidity separation, Δy, is derived.

B.1 The Lorentz Invariants

The Lorentz invariant quantities Q^2, x and y will be derived in this section, with reference to Fig. B.1 which shows the general lepton-proton scattering process occurring at HERA. In this diagram, k and k' represent the incoming and outgoing lepton four-momenta respectively. The four-momentum of the interacting parton from the proton is given by ξp and the hadronic product carries a four-momentum p' and is scattered through an angle γ_h.

The virtuality Q^2 is defined as the negative of the square of the four-momentum transfer, $Q^2 = -q^2$. This can also be written in terms of the scattering angle of the lepton, θ_e. Neglecting the mass of the lepton,

$$\begin{aligned} Q^2 &= -(k-k')^2 \\ &= -(k^2 + k'^2 - 2k\cdot k') \\ &= 2k\cdot k' \\ &= 2E_e E_{e'}(1+\cos\theta_e) \end{aligned} \tag{B.1}$$

Conservation of four-momentum leads to the expressions,

$$\begin{aligned} k+\xi p &= k'+p' \\ p' &= k-k'+\xi p = q+\xi p \end{aligned} \tag{B.2}$$

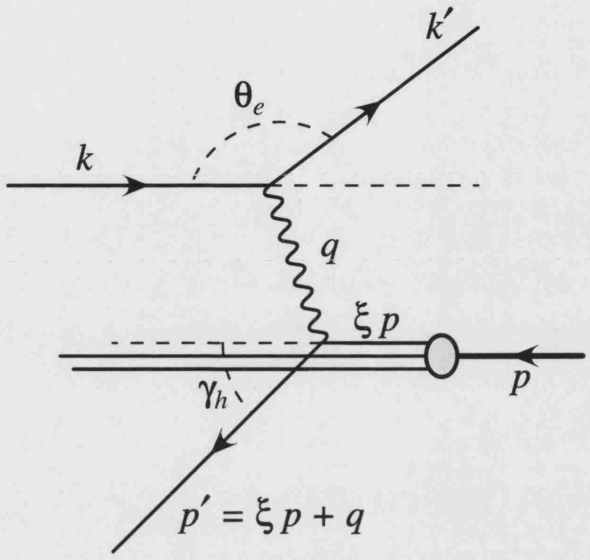

Figure B.1: The kinematics of lepton-proton scattering at HERA.

Neglecting all masses, this leads to the expression,

$$\begin{aligned} 0 \approx (p')^2 &= (q + \xi p)^2 \\ &= q^2 + (\xi p)^2 + 2\xi q \cdot p \\ &= q^2 + 2\xi q \cdot p. \end{aligned} \tag{B.3}$$

Identifying the fraction of the total proton momentum interaction carried by the interacting parton, x, with the variable ξ, leads to the commonly used form,

$$x = \frac{-q^2}{2q \cdot p} = \frac{Q^2}{2q \cdot p}. \tag{B.4}$$

The Lorentz invariant y is defined as,

$$y = \frac{p \cdot q}{p \cdot k}. \tag{B.5}$$

Writing this explicitly in terms of energy and three-momentum gives,

$$y = \frac{E_p E_\gamma - \mathbf{p} \cdot \mathbf{q}}{E_p E_e - \mathbf{p} \cdot \mathbf{k}}. \tag{B.6}$$

In the rest frame of the proton, $\mathbf{p} = \mathbf{0}$ and the expression reduces to $y = \frac{E_\gamma}{E_e}$.

Alternatively, Eq. B.6 can be written as,

$$y = \frac{E_p E_\gamma (1 - \cos\theta_{p\gamma})}{E_p E_e (1 - \cos\theta_{pe})} \tag{B.7}$$

where $\theta_{p\gamma}$ is the opening angle between the incoming proton and the photon, and θ_{pe} is the opening angle between the incoming proton and lepton. In the photoproduction regime, $Q^2 \rightarrow 0$ GeV^2 and the photon is emitted collinear to the lepton direction i.e. $\theta_{p\gamma} = \theta_{pe}$ and, $y = \frac{E_\gamma}{E_e}$.

B.2 Momentum Transfer

In a general t-channel photoproduction process, the Mandelstam variable t is equal to the momentum transferred between the interacting partons. This is equivalent to the invariant mass of the propagator. In a t-channel process, the incoming partons are labelled a and b while the outgoing partons have been labelled c and d, so that t is given by,

$$t = (a - c)^2. \tag{B.8}$$

An expression for t will now be derived in the centre-of-mass frame of the hard subprocess. In this frame, the four-momenta of the incoming and outgoing partons are given by,

$$\begin{aligned} a &= (E, 0, 0, E) \\ b &= (E, 0, 0, -E) \\ c &= (E, p_x, p_y, E\cos\theta) \\ d &= (E, -p_x, -p_y, -E\cos\theta). \end{aligned} \tag{B.9}$$

Substitution of these expressions into equation B.8, and neglecting all masses leads to,

$$\begin{aligned} -t &= p_{\mathrm{T}}^2 + E^2(1 - \cos\theta)^2 \\ |t| &\geq |p_{\mathrm{T}}^2|. \end{aligned} \tag{B.10}$$

B.3 Rapidity and Boost Invariance

The four-momentum of a particle of mass m may be written as,

$$p^\mu = (E, p_x, p_y, p_z) = (m_{\mathrm{T}}\cosh y, p_{\mathrm{T}}\cos\phi, p_{\mathrm{T}}\sin\phi, m_{\mathrm{T}}\sinh y). \tag{B.11}$$

where $p_{\mathrm{T}} = [p_x^2 + p_y^2]^{1/2}$, ϕ is the azimuthal angle with respect to the z-axis and y is the rapidity. The transverse mass is defined as $m_{\mathrm{T}} = [p_{\mathrm{T}}^2 + m^2]^{1/2}$.

From Eq. B.11, it is possible to write,

$$E = [p_{\mathrm{T}}^2 + m^2]^{1/2}\cosh y = [p_{\mathrm{T}}^2 + m^2]^{1/2}\frac{e^{-y} + e^{y}}{2} \tag{B.12}$$

$$p_z = [p_T^2 + m^2]^{1/2} \sinh y = [p_T^2 + m^2]^{1/2} \frac{e^{-y} - e^y}{2}. \tag{B.13}$$

Adding and subtracting Eqs. B.12 and B.13 gives,

$$E + p_z = [p_T^2 + m^2]^{1/2} e^y \tag{B.14}$$

$$E - p_z = [p_T^2 + m^2]^{1/2} e^{-y}. \tag{B.15}$$

Therefore,

$$\begin{aligned} \frac{E + p_z}{E - p_z} &= e^{2y} \\ \Rightarrow \quad y &= \frac{1}{2} \log \left(\frac{E + p_z}{E - p_z} \right). \end{aligned} \tag{B.16}$$

If a system is subject to a boost in the z-direction, it undergoes a Lorentz Transformation according to,

$$\begin{pmatrix} E' \\ p'_x \\ p'_y \\ p'_z \end{pmatrix} = \begin{pmatrix} \gamma & 0 & 0 & -\beta\gamma \\ 0 & 1 & 0 & 0 \\ 0 & 0 & 1 & 0 \\ -\beta\gamma & 0 & 0 & \gamma \end{pmatrix} \begin{pmatrix} E \\ p_x \\ p_y \\ p_z \end{pmatrix} \tag{B.17}$$

Therefore,

$$E' = \gamma E - \beta\gamma p_z \tag{B.18}$$

$$p'_z = -\beta\gamma E + \gamma p_z. \tag{B.19}$$

and so,

$$\begin{aligned} y' &= \frac{1}{2} \log \left(\frac{E' + p'_z}{E' - p'_z} \right) \\ &= \frac{1}{2} \log \left(\frac{(E + p_z)(\gamma - \beta\gamma)}{(E - p_z)(\gamma + \beta\gamma)} \right) \\ &= \frac{1}{2} \log \left(\frac{E + p_z}{E - p_z} \right) + \frac{1}{2} \log \left(\frac{1 - \beta}{1 + \beta} \right) \\ &= y + \frac{1}{2} \log \left(\frac{1 - \beta}{1 + \beta} \right) \end{aligned} \tag{B.20}$$

B.3.1 Pseudo-Rapidity

In the limit that $m \to 0$,

$$|\mathbf{p}| \to E = (E\sin\theta\cos\phi, E\sin\theta\sin\phi, E\cos\theta). \tag{B.21}$$

Therefore,

$$\begin{aligned} E + p_z &\to E(1+\cos\theta) \\ E - p_z &\to E(1-\cos\theta) \end{aligned} \tag{B.22}$$

and so,

$$y \to \eta = \frac{1}{2}\log\left(\frac{1+\cos\theta}{1-\cos\theta}\right). \tag{B.23}$$

From the **Double Angle Formulae**,

$$\begin{aligned} \cos 2\psi &= \cos^2\psi - \sin^2\psi \\ &= 2\cos^2\psi - 1 \\ &= 1 - 2\sin^2\psi \end{aligned} \tag{B.24}$$

$$\sin 2\psi = 2\sin\psi\cos\psi. \tag{B.25}$$

Therefore,

$$\begin{aligned} \cos\frac{\theta}{2} &= \left[\frac{1}{2}(1+\cos\theta)\right]^{1/2} \\ \sin\frac{\theta}{2} &= \left[\frac{1}{2}(1-\cos\theta)\right]^{1/2} \end{aligned} \tag{B.26}$$

and so,

$$\tan\frac{\theta}{2} = \left[\frac{1-\cos\theta}{1+\cos\theta}\right]^{1/2}. \tag{B.27}$$

Substitution into Eq. B.23 gives,

$$\begin{aligned} \eta &= \frac{1}{2}\log\left(\tan\frac{\theta}{2}\right)^{-2} \\ \Rightarrow\ \eta &= -\log\left(\tan\frac{\theta}{2}\right). \end{aligned} \tag{B.28}$$

B.4 Parton Momentum Fractions

In a lepton-proton scattering event, the quantity x_γ (x_p) represents the fraction of the total momentum of the photon (proton) taking part in the hard interaction. LO expressions for these quantities can be derived using conservation of four-momentum arguments.

Conservation of energy gives,

$$\begin{aligned} x_\gamma E_\gamma + x_p E_p &= \sum_{i=1}^{2} E^i \\ &= \sum_{i=1}^{2} E^i \sin\theta_i \frac{1}{\sin\theta_i} \\ &= \sum_{i=1}^{2} E^i_{\mathrm{T}} \frac{1}{\sin\theta_i} \end{aligned} \tag{B.29}$$

where the sum is over the two outgoing partons.

Similarly, conservation of momentum leads to the expression,

$$x_\gamma |\mathbf{p}_\gamma| \cos(\pi - \theta) + x_p |\mathbf{p}_p| \cos\theta = \sum_{i=1}^{2} |\mathbf{p}^i| \cos\theta_i. \tag{B.30}$$

In the approximation that the photon and proton are collinear to the beam-line ($\theta = 0$),

$$-x_\gamma |\mathbf{p}_\gamma| + x_p |\mathbf{p}_p| = \sum_{i=1}^{2} |\mathbf{p}^i| \cos\theta_i. \tag{B.31}$$

In the massless limit $|\mathbf{p}| \to E$ and so,

$$\begin{aligned} -x_\gamma E_\gamma + x_p E_p &= \sum_{i=1}^{2} E^i \cos\theta_i \\ &= \sum_{i=1}^{2} E^i \sin\theta_i \frac{1}{\tan\theta_i} \\ &= \sum_{i=1}^{2} E^i_{\mathrm{T}} \frac{1}{\tan\theta_i} \end{aligned} \tag{B.32}$$

Using the Double Angle Formulae of Eqs. B.24 and B.25,

$$\frac{1}{\sin\theta_i} - \frac{1}{\tan\theta_i} = \frac{1-\cos\theta_i}{\sin\theta_i} = \frac{2\sin^2\frac{\theta_i}{2}}{2\sin\frac{\theta_i}{2}\cos\frac{\theta_i}{2}} = \tan\frac{\theta_i}{2} \tag{B.33}$$

$$\frac{1}{\sin\theta_i}+\frac{1}{\tan\theta_i}=\frac{1+\cos\theta_i}{\sin\theta_i}=\frac{2\cos^2\frac{\theta_i}{2}}{2\sin\frac{\theta_i}{2}\cos\frac{\theta_i}{2}}=\left[\tan\frac{\theta_i}{2}\right]^{-1} \tag{B.34}$$

The final expressions for x_γ and x_p are obtained using the above relationships.

Taking the difference of Eqs. B.29 - B.32 gives,

$$\begin{aligned} 2x_\gamma E_\gamma &= \sum_{i=1}^{2} E_{\mathrm{T}}^i\left[\frac{1}{\sin\theta_i}-\frac{1}{\tan\theta_i}\right] \\ &= \sum_{i=1}^{2} E_{\mathrm{T}}^i\left[\tan\frac{\theta_i}{2}\right]. \end{aligned} \tag{B.35}$$

But $\eta=-\log\tan\left(\frac{\theta}{2}\right)$ leading to the expression,

$$x_\gamma = \frac{\sum_{i=1}^{2} E_{\mathrm{T}}^i\exp(-\eta^i)}{2E_\gamma}. \tag{B.36}$$

Since $E_\gamma = yE_e$, where y is the fraction of the electron energy carried by the photon, this expression may also be written,

$$x_\gamma = \frac{\sum_{i=1}^{2} E_{\mathrm{T}}^i\exp(-\eta^i)}{2yE_e}. \tag{B.37}$$

Similarly, the sum of Eqs. B.29 + B.32 gives,

$$\begin{aligned} 2x_p E_p &= \sum_{i=1}^{2} E_{\mathrm{T}}^i\left[\frac{1}{\sin\theta_i}+\frac{1}{\tan\theta_i}\right] \\ &= \sum_{i=1}^{2} E_{\mathrm{T}}^i\left[\frac{1}{\tan\frac{\theta_i}{2}}\right] \end{aligned} \tag{B.38}$$

leading to,

$$x_p = \frac{\sum_{i=1}^{2} E_{\mathrm{T}}^i\exp(\eta^i)}{2E_p}. \tag{B.39}$$

B.5 Gap Fraction Expectation

In standard QCD processes, rapidity gap events may be produced through multiplicity fluctuations. Let g is the number of events with a rapidity gap and P be the probability for a particle to be radiated into a small rapidity interval dy. Since, for non-diffractive events, this probability can be assumed to be constant, the number of events with a gap may be expected to decrease according to,

$$\mathrm{d}g = -gP\mathrm{d}y. \tag{B.40}$$

Integrating both sides gives,

$$g = k \exp(-P\Delta y) \tag{B.41}$$

where k is a constant of integration. Therefore, in standard QCD, the number of gap events may be expected to fall exponentially as a function of increasing interval in rapidity, Δy. Experimentally, the pseudo-rapidity is used which, as shown in Section B.3.1, is equivalent to y in the limit $m \to 0$.

Appendix C

Monte Carlo Event Generators

The HERWIG [118] and PYTHIA [119] Monte Carlo generators have been used for the simulation of photoproduction events in this thesis. Both programs assume the factorisation of the scattering process into a hard scattering amplitude (which contains only the LO matrix elements), initial- and final-state perturbative radiation, non-perturbative fragmentation in the final state and parton evolution in the initial state. Generically, the generation of a complete photoproduction event takes place in the same way for both HERWIG and PYTHIA with the main steps taking place as follows,

- **incoming partons**
  Two incoming beam particles are characterised by a set of PDFs which describe the fraction of energy associated with each parton, as well as their flavour. One parton from each of the beam particles initiates a shower of partons. The remainder contribute to the beam remnants (or take part in multi-parton interactions).

- **initial-state showers**
  The parton that initiates the shower begins a sequence of branchings (e.g. $q \rightarrow qg$) which are governed by the DGLAP evolution equations. Initially, the partons have a low space-like virtuality which increases with each successive radiation of a time-like parton.

- **elementary hard subprocess**
  One incoming parton from each of the two showers enters the hard sub-process. It is the nature of this that determines the main characteristics of the event.

- **final-state showers**
  The outgoing partons from the elementary sub-process have a virtuality Q^2_{max} which is controlled by the nature of the hard scattering process. The partons undergo branchings to create final-state showering, with the virtuality of the

partons decreasing with each successive emission, until a minimum virtuality Q_0^2 is reached.

- **hadronisation**
  Colour neutral hadrons are created from the outgoing quarks and gluons from the final state shower.

- **decay of unstable particles**
  The colour neutral particles produced in the hadronisation process decay into stable final state hadrons.

Differences between HERWIG and PYTHIA lie mainly in their treatment of the perturbative radiation and the non-perturbative fragmentation. A more detailed description of the individual programs is given in the following sections.

C.1 The HERWIG Generator

The HERWIG (Hadron Emissions Reactions With Interfering Gluons) Monte Carlo is a general purpose generator which attempts to provide as complete an implementation of the underlying perturbative QCD process as possible. In particular, the HERWIG Monte Carlo calculates the LO matrix elements and incorporates a detailed implementation of the perturbative parton shower, including effects of coherence and interfering gluons. The non-perturbative hadronisation process is simulated using the simplest universal model available. The aim of HERWIG is to describe the largest possible number of processes with the fewest possible number of parameters. As a result, the HERWIG program has a large predictive power.

In HERWIG, it is the nature of the hard subprocess that determines the partonic structure and other characteristics of the event as a whole. The factorisation scale of the hard subprocess is given by,

$$\mu^2 = \frac{2stu}{s^2 + t^2 + u^2}, \tag{C.1}$$

where s, t and u are the Mandelstam variables. The resulting cross-section is divergent in the limit $p_{\mathrm{T}}^2 \rightarrow 0$ GeV^2, where p_{T} is the transverse momentum of the outgoing partons. Therefore, a minimum transverse momentum cut, $p_{\mathrm{T}}^{\mathrm{min}}$, is introduced. In principle, the Monte Carlo prediction should be largely independent of the choice of $p_{\mathrm{T}}^{\mathrm{min}}$ provided that the transverse energy of the selected jets satisfy $E_{\mathrm{T}}^{\mathrm{jet}} >> p_{\mathrm{T}}^{\mathrm{min}}$.

The incoming and outgoing partons undergo showering processes in which hadrons are formed from partons. These showers are generated by a **coherent branching**

algorithm. Each individual parton splits into many partons according to the DGLAP splitting functions, thereby forming leading log parton showers. These partons are ordered in terms of the opening angle between them, such that the angle decreases with each successive branching. This allows a more correct treatment of the effects of coherent radiation and interfering gluons [200]. For outgoing (time-like) partons, the evolution is continued down to some **hadronic scale** which is of the order of the mass of typical light mesons. In contrast, initial state (space-like) parton showering is generated using the **backward evolution** scheme. Here, both ends of the evolution have fixed scales. The showering proceeds from the elementary sub-process at a hard scale which is set by colour coherence and continues backwards until the hadron scale, Q_0^2, is reached. At each stage in the evolution, the properties of the emitted partons (e.g. x, Q^2, flavour) are matched to the PDF parameters of the initial beam particles. For the initial state shower, the opening angle refers to the angle between the direction of the incoming particle and the emitted parton.

In direct photoproduction events, the full $2 \rightarrow 3$ matrix elements are used. However, for resolved events the initial photon spectrum radiated from the incoming lepton is generated using the EPA. In these, resolved events, the backwards evolution means that at each stage of the branching towards the initial state, the parton is given the opportunity to have resulted directly from a $\gamma \rightarrow q\bar{q}$ splitting. In this way, anomalous splittings can be generated dynamically. The factorisation scale for anomalous splittings is chosen to be consistent with that for hadronic photon events.

Following the parton shower, the transition from partons to hadrons proceeds via a non-perturbative framework called the **cluster model** [115]. This groups the partons together into colour-singlet objects. At the fragmentation scale, all gluons are split into $q\bar{q}$ pairs. These pairs are then *clustered* into colour-singlet objects via the colour connections generated in the parton shower. Each cluster is then fragmented into two hadrons or the lightest hadron for its flavour if the cluster is not massive enough to create two hadronic objects. In the final stage, unstable particles are allowed to decay producing the final-state stable hadrons.

C.1.1 Multi-Parton Interactions

HERWIG uses the Jimmy [81] package for the simulation of multi-parton interactions. The formulation begins by considering the scattering of two overlapping hadronic objects which are flattened by Lorentz contraction. Since the different parts of the hadronic object are then causally separated, the probability of an interaction between a particular pair of partons is considered to be uncorrelated to an interaction between any other pair. For a fixed impact parameter between the colliding objects, the number of interactions then follows a Poisson distribution. Since the average number of

interactions occurring in a central collision will be greater than if only the peripheries overlap, a model which describes the distribution of partons on the hadronic object is also required. This approach, which combines the assumption of a Poisson distribution at each fixed impact parameter, with an impact-parameter dependent overlap function, is called an **eikonal model**.

The mean number of partonic scatters produced in a hadronic interaction is given by,

$$\langle n(b,s)\rangle = \mathcal{L}_{\text{parton}} \oplus \hat{\sigma}_{\text{H}} \tag{C.2}$$

where b is the impact parameter, s is the centre-of-mass energy squared, $\mathcal{L}_{\text{parton}}$ is the parton luminosity and $\hat{\sigma}_{\text{H}}$ is the cross section for a pair of partons (with $p_{\text{T}} > p_{\text{T}}^{\text{min}}$) to produce a pair of jets. The parton luminosity is given by,

$$d\mathcal{L}_{\text{parton}} = A(b) n_i(x_i) n_j(x_j) dx_i dx_j \tag{C.3}$$

where i, j denote the two colliding hadronic objects and $n_i(x_i)$ is the number density of partons in hadron i which carry a fraction x_i of the hadron energy. For the proton, the number density is equal to the proton parton density ($n_p(x_p) = f_p(x_p)$). In the case of a resolved photon, $n_\gamma(x_\gamma) = f_\gamma(x_\gamma)/P_{res}$. The factor $P_{res} = \kappa 4\pi\alpha/f_\rho^2$ is the probability that the photon fluctuates into a hadronic state with parton density $f_\gamma(x_\gamma)$. Assuming ρ-dominance ($\kappa = 1$), $P_{res} \approx 1/300$. The function $A(b)$ is the overlap function which specifies the relative density of the partonic content of the the interacting hadrons (in the region where they overlap). In HERWIG it is assumed that the partons taking part in the interaction are distributed according to the electric form factors of the hadrons. Note that for the photon, the form factor of the pion is used. Then, $A(b)$ is given by the Fourier transform of the product of the two form factors. The parton luminosity integrated over all impact parameter space is simply the product of the parton number densities. The form of $A(b)$ must then satisfy,

$$\int A(b)\pi d^2 b = 1. \tag{C.4}$$

For a γp collider, the mean number of jet pairs produced can be written as,

$$\langle n(b,s)\rangle = \frac{A(b)}{P_{res}} \sigma_{\text{H}}(s) \tag{C.5}$$

where $\sigma_{\text{H}}(s)$ is the inclusive cross section for $\gamma p \rightarrow$ jets, given by,

$$\sigma_{\text{H}}(s) = \int_{p_{\text{T}}^{\text{min2}}}^{s/4} \mathrm{d}p_{\text{T}}^2 \int_{4p_{\text{T}}^2/s}^{1} \mathrm{d}x_\gamma \int_{4p_{\text{T}}^2/x_\gamma s}^{1} \mathrm{d}x_p \sum_{ij} f_{i/\gamma}(x_\gamma, p_{\text{T}}^2) f_{j/p}(x_p, p_{\text{T}}^2) \frac{\mathrm{d}\hat{\sigma}_{ij}(x_\gamma x_p s, p_{\text{T}})}{\mathrm{d}p_{\text{T}}^2}. \tag{C.6}$$

All separate scatters are assumed to be independent i.e. they obey Poisson statistics. In this case, the probability of there being m (and *only* m) partonic interactions in any given collision, is given by,

$$P_m(b) = \frac{\langle n(b,s)\rangle^m}{m!}\exp(-\langle n(b,s)\rangle). \tag{C.7}$$

Taking the sum of all probabilities for $m = 1 \rightarrow \infty$ and integrating over b gives the total (non-diffractive)* cross-section for $\gamma p \rightarrow$ partons with $p_{\mathrm{T}} > p_{\mathrm{T}}^{\mathrm{min}}$,

$$\begin{aligned}\sigma_{\mathrm{ND}}(s) &= \pi P_{res}\int \mathrm{d}^2b\Sigma_{m=1}^{\infty}P_m(b) \\ &= \pi P_{res}\int \mathrm{d}^2b[1-\exp(-\langle n(b,s)\rangle)].\end{aligned} \tag{C.8}$$

The mean number of jet pairs produced per event can be calculated from,

$$\begin{aligned}\langle n(s)\rangle &= \frac{\int \mathrm{d}^2b\sum_{m=1}^{\infty} mP_m}{\int \mathrm{d}^2b\sum_{m=1}^{\infty}P_m} \\ &= \frac{\int \mathrm{d}^2b\langle n(b,s)\rangle}{\int \mathrm{d}^2b[1-\exp(-\langle n(b,s)\rangle)]} \\ &= \frac{\sigma_{\mathrm{H}}(s)}{\sigma_{\mathrm{ND}}(s)}.\end{aligned} \tag{C.9}$$

This means that σ_{H} is larger than σ_{ND} by a factor which is equal to the mean number of partonic interactions per event. This is due to the fact that σ_{H} incorporates all jet pairs produced (including those occurring in the same event). Note also that, while σ_{ND} is always less than the total γp cross section, σ_{H} does not need to be.

The result of the model described above is dependent on the value of $p_{\mathrm{T}}^{\mathrm{min}}$. In HERWIG, the same value is used for the minimum transverse momentum of the primary and all secondary interactions. In order to ensure physical results, energy conservation is imposed so that, following the backward evolution of all hard scatters in an event, the energy remaining in the hadron remnants is greater than zero. In addition, if during the backward evolution of the first scatter, the splitting $q\bar{q} \leftarrow \gamma$ is arrived at before the evolution cut-off scale, the event is classified as an "anomalous" event and no multi-parton interactions are allowed.

*Note that an alternative eikonal model, called the Dual Topological Unitarization (DTU) approach includes pomeron terms to incorporate diffractive topology in the description. This model is used, for example, in PHOJET [85].

C.2 The PYTHIA Generator

The PYTHIA Monte Carlo is named after the oracle at Delphi. Like HERWIG, the PYTHIA program is a general purpose generator which uses the LO matrix elements to generate the elementary hard sub-process. However, in contrast to HERWIG, PYTHIA incorporates detailed models for the non-perturbative aspects of the event generation and consequently has a large number of free parameters. The simulation of an event is divided into the same steps as in HERWIG. However, there are significant differences in the implementation of both the perturbative and non-perturbative phases of the two generators.

In the perturbative part, there are two main differences. Firstly, PYTHIA uses the WWA to generate the initial photon spectrum of radiation from the incoming lepton. In addition, the factorisation scale is the mean transverse mass of the outgoing partons from the hard sub-process, m_{T}^2, such that,

$$\mu^2 = m_{\mathrm{T}}^2 = \frac{1}{2}(m_1^2 + p_{\mathrm{T}1}^2 + m_2^2 + p_{\mathrm{T}2}^2), \tag{C.10}$$

where m_i^2 and $p_{\mathrm{T}i}^2$ are the mass and transverse momentum of parton i, respectively.

The development of initial and final state parton showers is conceptually the same in both HERWIG and PYTHIA. However, in PYTHIA the evolution is ordered in the virtuality of the radiated partons rather than in terms of the opening angle. This ordering does not imply coherence and so this is dealt with separately.

The Monte Carlo generators also differ in the non-perturbative fragmentation stage. In PYTHIA, the partons are hadronised using the **Lund Symmetric String Fragmentation** model [116] as implemented in JETSET [201]. In this model, the partons are connected by *strings*, the strength of which is $\sim$ 1 GeVfm^{-1}. As the partons separate from each other, the string gains energy until it finally breaks to produce quark-anti-quark pairs. When the energy of a particular string is too small for further separation, hadrons are created from the partons at the end of the strings. As in HERWIG, the final stage is the decay of unstable hadrons.

C.2.1 Multi-Parton Interactions

There are two main types of multi-parton interaction model available in PYTHIA [174]: a simple model and an impact parameter dependent model. These models are described in more detail below.

C.2.1.1 The Simple Model

The primary assumption is that the partonic scatterings in an event are ordered in a decreasing series in p_{T}. The mean number of partonic interactions, $\langle n(s)\rangle$, is again given by the ratio $\langle n(s)\rangle = \sigma_{\mathrm{H}}(p_{\mathrm{T}}^{\mathrm{min}})/\sigma_{\mathrm{ND}}(s)$ where σ_{H} is the total cross section for $\gamma p \rightarrow$ *jets* and σ_{ND} is the inelastic, non-diffractive cross section. All hadronic collisions are assumed to be equivalent (no impact parameter dependence) and all parton-parton interactions take place independently of one another. The number of scatterings per event then follow a Poisson distribution with mean $\langle n(s)\rangle$. Assuming the hadronic objects undergo non-diffractive, inelastic collisions, the probability that a parton-parton interaction occurs at p_{T} is defined as,

$$P(p_T^2) = \frac{1}{\sigma_{\mathrm{ND}}(s)} \frac{\mathrm{d}\sigma_{\mathrm{H}}(p_{\mathrm{T}}^2)}{\mathrm{d}p_{\mathrm{T}}^2} \tag{C.11}$$

where $\frac{\mathrm{d}\sigma_{\mathrm{H}}(p_{\mathrm{T}}^2)}{\mathrm{d}p_{\mathrm{T}}^2}$ is obtained by analogy with Eq. C.6.

The probability that the hardest scatter occurs at p_{T1} is given by,

$$P(p_{\mathrm{T1}})\exp\left(-\int_{p_{\mathrm{T1}}^2}^{s/4} P(p_{\mathrm{T}}')\mathrm{d}p_{\mathrm{T}}'^2\right). \tag{C.12}$$

This is the probability that a scatter occurs at p_{T1} multiplied by the probability that there are *no* scatters with $p_{\mathrm{T}} > p_{\mathrm{T1}}$. It can then be shown that the probability for an n^{th} scatter to occur at $p_{\mathrm{T}n} < p_{\mathrm{T}n-1} < \ldots < p_{\mathrm{T1}} < s/4$ is,

$$P(p_{\mathrm{T}n}^2)\frac{1}{(n-1)!}\left(\int_{p_{\mathrm{T}n}^2}^{s/4} P(p_{\mathrm{T}}'^2)\mathrm{d}p_{\mathrm{T}}'^2\right)^{n-1} \exp\left(-\int_{p_{\mathrm{T}n}^2}^{s/4} P(p_{\mathrm{T}}'^2)\mathrm{d}p_{\mathrm{T}}'^2\right). \tag{C.13}$$

The total probability that a scatter occurs at a particular p_{T}^2 then sums to the original $P(p_{\mathrm{T}}^2)$ given by Eq. C.11. The formalism for multi-parton interactions then retains the correct pQCD expression for the scattering probability at any given p_{T}^2.

The average number of partonic interactions per event is given by,

$$\begin{aligned}
\langle n(s)\rangle &= \int_{p_{\mathrm{T}}^{2\mathrm{min}}}^{s/4} P(p_{\mathrm{T}}'^2)\mathrm{d}p_{\mathrm{T}}'^2 \\
&= \frac{1}{\sigma_{\mathrm{ND}}} \int_{p_{\mathrm{T}}^{2\mathrm{min}}}^{s/4} \frac{\mathrm{d}\sigma_{\mathrm{H}}(p_{\mathrm{T}}'^2)}{\mathrm{d}p_{\mathrm{T}}'^2}\mathrm{d}p_{\mathrm{T}}'^2 \\
&= \frac{\sigma_{\mathrm{H}}(p_{\mathrm{T}}^{2\mathrm{min}})}{\sigma_{\mathrm{ND}}(s)}.
\end{aligned} \tag{C.14}$$

For each event, the partonic interactions are generated according to the probabilities from Eq. C.12 (starting from the maximum $s/4$). In addition to the p_{T}^2 of an interaction, it is also necessary to generate the other flavour and kinematic variables. For the hardest scatter, the usual PDFs determine the flavour and energy distribution. However, the parton distributions for all other scatters must depend on all preceding flavours and values of x. The properties of hadrons are not well enough understood to be able to write down such a correlated probability distribution. In order to take account the energy already used in harder scatters, the parton distributions for the n^{th} scatter are evaluated at,

$$x_{n'} = \frac{x_n}{\sum_{i=1}^{n-1} x_n}. \tag{C.15}$$

In a fraction of $\exp(-\langle n(s)\rangle)$ of events, there will be no hard scattering above $p_{\mathrm{T}}^{\mathrm{min}}$. Therefore, PYTHIA includes options to generate soft interactions. However, in this thesis, these options are not used and every event is required to have a hard interaction with a sharp cut-off at $p_{\mathrm{T}} = p_{\mathrm{T}}^{\mathrm{min}}$. The values of $p_{\mathrm{T}}^{\mathrm{min}}$ and $p_{\mathrm{T}}^{\mathrm{mi}}$ can be set separately in PYTHIA.

In events with multi-parton interactions, the treatment of the beam remnant is slightly modified. Initially, the hard scatter is generated, along with its associated initial and final state radiation, and then any secondary scatters. Only then is the beam remnant attached to the initiating partons of the hardest scatter, taking into account the energy and momentum already removed from the beam remnants from the multi-parton interactions.

C.2.1.2 The Impact Parameter Dependent Model

The simple model assumes that the initial state is the same in all collisions. However, each hadronic collision is characterised by a varying impact parameter, b. This means that a function, which specifies the distribution of partons on the hadronic object, must be introduced. Several different matter distribution functions are available in PYTHIA. In this thesis, only the double Gaussian is used, since this allows the greatest freedom for tuning the parameters. The double Gaussian function is given by,

$$\beta(r) \propto \frac{1-\beta}{a_1^3}\exp\left(-\frac{r^2}{a_1^2}\right) + \frac{\beta}{a_2^3}\exp\left(-\frac{r^2}{a_2^2}\right) \tag{C.16}$$

This corresponds to a distribution with a small core of radius a_2 and containing a fraction β of the total hadronic matter, embedded in a larger hadron of radius a_1[†]. The parameter β regulates the core density and a_2/a_1 regulates the core size.

[†]The parameters PARP(83) and PARP(84) correspond to the values of β and a_2/a_1 respectively.

For a collision with impact parameter b, the time integrated overlap $\mathcal{O}(b)$ between the matter distributions of the colliding hadrons is given by,

$$\begin{aligned}\mathcal{O}(b) &\propto \int \mathrm{d}t \int \mathrm{d}^3x \rho(x,y,z)\rho(x+b,y.z+t) \\ &\propto \frac{(1-\beta)^2}{2a_1^2}\exp\left(\frac{-b^2}{2a_1^2}\right) + \frac{2\beta(1-\beta)}{a_1^2+a_2^2}\exp\left(\frac{-b^2}{a_1^2+a_2^2}\right) + \frac{\beta^2}{2a_2^2}\exp\left(\frac{-b^2}{2a_2^2}\right)\end{aligned} \tag{C.17}$$

The larger the overlap $\mathcal{O}(b)$, the more likely it is to have interactions between partons in the two colliding hadrons. In fact, the average number of interactions is related to the overlap $\mathcal{O}(b)$ via a linear relationship,

$$\langle \tilde{n}(b) \rangle = k\mathcal{O}(b). \tag{C.18}$$

where $\tilde{n} = 0, 1, 2, ...$ is the number of interactions when two hadrons pass each other with impact parameter b. The constant of proportionality, k, is related to the hadronic cross section and therefore increases with centre-of-mass energy.

As for the HERWIG model, the number of interactions is assumed to be distributed according to Poisson statistics. The probability that two hadrons in a collision with impact parameter b undergo a collision is,

$$P(b) = 1 - \exp(-\langle \tilde{n}(b) \rangle) = 1 - \exp(-k\mathcal{O}(b)). \tag{C.19}$$

and the average number of interactions per event at impact parameter b is given by,

$$\langle n(b) \rangle = \frac{\langle \tilde{n}(b) \rangle}{P(b)} = \frac{k\mathcal{O}(b)}{1 - \exp(-k\mathcal{O}(b))}. \tag{C.20}$$

The relation $\langle n \rangle = \sigma_{\mathrm{H}}/\sigma_{\mathrm{ND}}$ must still hold true when integrated over all $P(b)$ so that,

$$\begin{aligned}\langle n \rangle &= \frac{\int \langle n(b) \rangle P(b) \mathrm{d}^2b}{\int P(b) \mathrm{d}^2b} \\ &= \frac{\int k\mathcal{O}(b) \mathrm{d}^2b}{\int (1 - \exp(-k\mathcal{O}(b))) \mathrm{d}^2b} \\ &= \frac{\sigma_{\mathrm{H}}}{\sigma_{\mathrm{ND}}}.\end{aligned} \tag{C.21}$$

In this model, it is still possible to use a sharp cut-off at some specified value of $p_{\mathrm{T}}^{\mathrm{min}}$. However, now each event is required to have at least one interaction, while in the simple model, events without interactions were set to $p_{\mathrm{T}} = 0$. In the impact parameter dependent model, it is the default to assume a gradual turn-off so that a semi(hard) interaction can be rather soft part of the time. The matrix elements roughly diverge like $\alpha_s(p_{\mathrm{T}}^2)\mathrm{d}p_{\mathrm{T}}^2/p_{\mathrm{T}}^4$ for $p_{\mathrm{T}} \to 0$. Therefore, they are regularised by replacing the $1/p_{\mathrm{T}}^4$ pole by $1/(p_{\mathrm{T}}^2 + p_{\mathrm{T0}}^2)$ and using $p_{\mathrm{T}}^2 + p_{\mathrm{T0}}^2$ as the argument in α_s rather than just p_{T}^2.

C.3 Other Monte Carlo Generators

In order to study background contamination to the photoproduction process from NC and CC DIS events, small samples of additional Monte Carlo were used. The NC and CC samples were generated using the DJANGOH [164] program. This connects the event generator LEPTO [202] (which can be used for both NC and CC processes) to HERACLES [203] which simulates electroweak radiative corrections, and ARIADNE [204], used for the simulation of the fragmentation.

Appendix D

Jet Algorithms

D.1 Cone Algorithms

A cone algorithm defines a jet as a cone with a maximal radius R_{cone} in $\eta - \phi$ space. At each stage of the jet-forming, an object i is combined with the jet if,

$$\Delta R^2 = [(\eta_i - \eta^{\text{jet}})^2 + (\phi_i - \phi^{\text{jet}})^2] \leq R^2_{\text{cone}}. \tag{D.1}$$

The jet E_{T} and (η, ϕ) coordinates are then defined by the **Snowmass Accord** [205],

$$\begin{aligned} E_{\text{T}}^{\text{jet}} &= \sum\nolimits_i E_{\text{T},i} \\ \eta^{\text{jet}} &= \frac{1}{E_{\text{T}}^{\text{jet}}} \sum\nolimits_i E_{\text{T},i}\eta_i \\ \phi^{\text{jet}} &= \frac{1}{E_{\text{T}}^{\text{jet}}} \sum\nolimits_i E_{\text{T},i}\phi_i \end{aligned} \tag{D.2}$$

where the sum runs over every object i within the jet cone.

The jet-finding process is iterative and requires some initial pre-cluster, or **seed**, as the input for the algorithm. The jet variables are calculated from these seeds according to Eq. D.2, and the (η, ϕ) coordinates of the jets are taken to be the new set of seeds. This process continues until the sample of enclosed objects is stable. Any overlapping objects are then treated to form a final set of jets. The detailed properties of seed finding and jet merging are not defined within the Snowmass Convention and so they may be different for each cone algorithm. For example, in the PUCELL algorithm [206], overlapping jets are combined if the energy in the overlap region consists of $> 75\%$ of the total energy of the lowest energy jet involved. Otherwise, the energy in the overlap region is assigned to the nearest jet. In contrast, EUCELL (see Section D.1.1) has no merging criteria for overlapping jets. This means that jets from different cone algorithms with identical cone radii may not be the same.

D.1.1 The EUCELL Algorithm

In the EUCELL algorithm, the hadrons or cells are clustered using a grid in $\eta - \phi$ space. The sizes of the cells that make up the grid are determined such that $\Delta\eta^{\text{gridcell}} \approx \Delta\phi^{\text{gridcell}} \approx R/2$. Potential pre-clusters are formed by sliding a 3×3 cell "window" over the grid. If the total summed transverse energy of any 3×3 section is above some energy threshold, E_{T}^{th}, it is taken to be a seed for the jet algorithm. A cone of radius R_{cone} is then placed around the pre-cluster and an iterative process is performed until some stable situation (or some maximum number of iterations) is reached. At the TLT, values of $E_{\text{T}}^{th} = 1.0$ GeV and $R^{\text{cone}} = 1$ are used. The cone with the highest transverse energy, independent of which pre-cluster it derives from, is accepted as a jet. The objects contained within this jet cone are then excluded from further jet-finding. This process is repeated until no further cones exist with an energy above E_{T}^{th}. EUCELL has no need for a jet-merging scheme, since no overlapping jets will be produced. Every object is associated to a jet such that the highest transverse energy jet in that part of the $\eta - \phi$ plane is produced. However, in reality, jets from separate partons may overlap, but the EUCELL recombination is designed in such a way that all the energy in the overlap region is associated with the highest transverse energy jet.

D.2 The $k_\perp$ Clustering Algorithm

The $k_\perp$ algorithm was initially designed for use in e^+e^- experiments. For lepton-hadron and hadron-hadron experiments, the algorithm is used in a modified form called KTCLUS [207].

The $k_\perp$ algorithm requires the specification of a distance measure to determine *which* particles will be merged together, as well as a recombination scheme which defines *how* they will be merged. In this thesis KTCLUS is run in the laboratory frame in the inclusive mode of Ellis and Soper [172], which is invariant under longitudinal boosts and has a recombination scheme similar to the Snowmass Convention. This is the so-called p_{T}-mode* which treats single jets as massless objects.

To decide which particles should be merged, the quantities,

$$d_i = E_{\text{T},i}^2 \tag{D.3}$$

$$d_{ij} = \min(E_{\text{T},i}^2, E_{\text{T},j}^2)[(\eta_i - \eta_j)^2 + (\phi_i - \phi_j)^2]/R^2 \tag{D.4}$$

*An alternative is the E_{T}-mode which combines four-vectors.

are formed for each particle i and each pair of particles ij. R is a radius parameter which has been set to unity throughout this thesis, but is retained in this discussion for illustrative purposes. If the smallest of all the d values is d_{ij}, then particles i and j are merged into a single object k. However, if the smallest value is a d_i then this particle is considered "complete" and is removed from further clustering. This process is then repeated until all the objects have been removed, producing an $E_{\rm T}$ ordered list of objects. These objects are accepted as jets if their transverse energy is above some user-defined threshold.

The scheme for merging the objects is similar to the Snowmass Convention,

$$\begin{aligned} E_{{\rm T},ij} &\equiv E_{{\rm T},i} + E_{{\rm T},j} \\ \eta_{ij} &\equiv \frac{E_{{\rm T},i}\eta_i + E_{{\rm T},j}\eta_j}{E_{{\rm T},ij}} \\ \phi_{ij} &\equiv \frac{E_{{\rm T},i}\phi_i + E_{{\rm T},j}\phi_j}{E_{{\rm T},ij}}. \end{aligned} \tag{D.5}$$

Neighbouring objects are combined if, for any given state (and at any stage of the jet clustering) two particles i and j (where $E_{{\rm T},i} < E_{{\rm T},j}$) satisfy,

$$d_i = E^2_{{\rm T},i} > d_{ij} = E^2_{{\rm T},i}[(\eta_i - \eta_j)^2 + (\phi_i - \phi_j)^2]/R^2. \tag{D.6}$$

If an object is separated from all other objects by > 1 in the $\eta - \phi$ plane, it is considered complete. It is therefore either a well isolated jet, or part of the hadron remnant. In either case, it should take no further part in the clustering.

Note also, that the combination criterion may be rewritten as,

$$\Delta R^2 \equiv (\eta_i - \eta_j)^2 + (\phi_i - \phi_j)^2 \leq R^2 \tag{D.7}$$

which is similar to the merging criterion for the generic cone algorithm. Rewriting Eq. D.7 in terms of the jet variables, the following condition is obtained,

$$(\eta_i - \eta^{\rm jet})^2 + (\phi_i - \phi^{\rm jet})^2 \leq \frac{(E_{\rm T}^{\rm jet} - E_{{\rm T},i})^2}{\left(E_{\rm T}^{\rm jet}\right)^2} R^2. \tag{D.8}$$

With this recombination scheme, the $k_\perp$ algorithm acts exactly as a cone algorithm, except the cone radius is variable and depends on $E_{\rm T}$. Thus, the *effective cone radius* $R_{k_\perp}$ for any given particle, is smaller than the corresponding cone radius $R_{\rm cone}$ and is given by,

$$R^2_{k_{\rm T}} = \frac{(E_{\rm T}^{\rm jet} - E_{{\rm T},i})^2}{E_{\rm T}^{\rm jet2}} R^2_{\rm cone}. \tag{D.9}$$

D.3 Theoretical Considerations

It has already been outlined that cone algorithms have several limitations. In particular, the treatment of overlapping jets is not defined within the Snowmass Convention, and neither is the question of seed-finding for the initial jets. This leads to theoretical ambiguity with respect to jet-merging in the final state and the process is not infra-red safe above NLO without modification. In contrast, the seed-finding and jet-merging criteria are completely determined for the $k_\perp$ algorithm for any given final state. The $k_\perp$ algorithm assigns all objects to jets in a well prescribed manner and the issue of overlapping jets does not arise. This means that the algorithm is completely infra-red and collinear safe. Several additional factors that should be considered are listed below.

- **Dependence on the level at which the algorithm is applied**
  In order to facilitate comparisons between data and Monte Carlo, a suitable algorithm should not depend on the type of object to which it is applied. However, cone algorithms are sensitive to the number of objects in the final state. An example of a problematic configuration is shown in Fig. D.1. In this case, two jets are produced which are separated by slightly less than $2R$ in $\eta - \phi$ space. At the detector or hadron level, where the number of objects is large (Fig. D.1 (left)), the jets will be recognised as two separate objects. However, at the parton level, the number of outgoing objects is small (typically 2-3) as shown in (Fig. D.1 (right)). Intuitively, the partons should be considered as two separate jets. However, since they both fit into a single cone of radius R they would be combined into a single object. Solutions to this problem have been devised [208, 209] by the introduction of a parameter R_{sep}. This is the maximum separation between two particles that are still allowed to be combined into one jet. However, the value of R_{sep} must be tuned to data.

- **Separation of hadronic remnants**
  In a hadronic event, the final state will contain beam remnant jets as well as the hard jets produced in the interaction. Any remnant should be kept separate from the jets and should minimally influence the jet-finding. In a cone algorithm, this is achieved by restricting the maximum size of the jet. In the $k_\perp$ algorithm, it is achieved by treating the remnant as a separate object[†] by factoring all jets below some scale into the hadronic remnants following clustering.

[†]Note that the original form of the $k_\perp$ algorithm does not treat the remnants as separate objects.

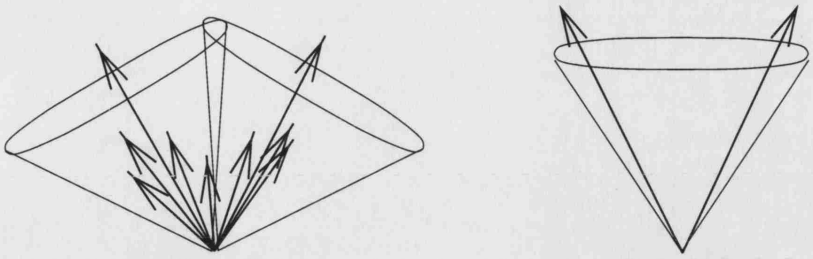

Figure D.1: Illustration of the assignment of jets in the cone algorithm. On the left there are many objects and so the assignment of jets is unambiguous. On the right, only a few objects are present which can lead to a wrong assignment.

- **Dependence on the frame of measurement**
  A jet algorithm should be as independent as possible from the frame in which it is measured (e.g. laboratory, partonic centre-of-mass frame etc.). In lepton-hadron collisions, these frames are generally related by a boost in the z-direction. Therefore, the requirement of boost invariance is usually satisfied by considering only the transverse energy in an $\eta - \phi$ plane. Since E_{T} and ϕ remain unchanged by a boost in the z-direction and η is changed only by the addition of a constant, the form of the E_{T} distribution in $\eta - \phi$ is the same in all frames. The $k_{\perp}$ algorithm is well defined in E_{T}, η and ϕ and so the property of boost invariance of the jet-finding is satisfied.

Appendix E

Derivation of Errors

E.1 Purity, Efficiency and Correction Factors

The purity, π, efficiency, ϵ, and correction factor, C, were defined in Section 6.1.1 in terms of the number of events generated in bin i, t_i, the number of measured events, m_i, and the number of events both generated and measured in a bin, u_i. These variables make the interpretation of these quantities clear, however, they are not statistically independent. In order to calculate the errors on these quantities, correctly taking into account these correlations, the problem is recast in terms of statistically independent variables a, b and c. Where a is the number of events generated and measured in the same bin, b is the number of events generated in the bin but not detected in it, and c is the number of events not generated in the bin but detected in it. Therefore,

$$t = a + b \; ; \; m = a + c \; ; \; u = a \; ;$$

and

$$\pi = \frac{a}{a+c};$$
$$\epsilon = \frac{a}{a+b};$$
$$C = \frac{a+b}{a+c}.$$

E.1.1 Purity

The error on the purity is then given by,

$$\begin{aligned}\delta\pi^2 &= \left(\frac{\delta\pi}{\delta a}\right)^2 \cdot V_a + \left(\frac{\delta\pi}{\delta c}\right)^2 \cdot V_c \\ &= \left[\frac{1}{a+c} - \frac{a}{(a+c)^2}\right]^2 \cdot V_a + \left[\frac{a}{(a+c)^2}\right]^2 \cdot V_c \\ &= \frac{c^2 \cdot V_a^2 + a^2 \cdot V_c}{(a+c)^4},\end{aligned}$$

where V_a is the variance of the mean of a. Rewriting this in terms of the original variables gives:

$$\delta\pi = \left[\frac{m^2 \cdot V_u + u^2 \cdot V_m - 2 \cdot m \cdot u \cdot V_u}{m^4}\right]^{1/2}. \tag{E.1}$$

When the events are weighted the numbers of events in, for example, the sample m is given by the sum of the weights, $\sum w_i(m)$, and the variance, V_m, is given by $\sum w_i(m)^2$. * For unweighted events, like those in this thesis, this reduces to the more commonly given form:

$$\delta\pi = \left[\frac{(1-\pi)\cdot\pi}{m}\right]^{1/2}. \tag{E.2}$$

E.1.2 Efficiency

Similarly, the error on the efficiency is given by,

$$\delta\epsilon = \left[\frac{t^2 \cdot V_u + u^2 \cdot V_t - 2 \cdot t \cdot u \cdot V_u}{t^4}\right]^{1/2}, \tag{E.3}$$

which for unweighted events again reduces to the more commonly given form:

$$\delta\epsilon = \left[\frac{(1-\epsilon)\cdot\epsilon}{t}\right]^{1/2}. \tag{E.4}$$

E.1.3 Correction Factor

Finally, the error on the correction factor is given by:

$$\begin{aligned}\delta C^2 &= \left(\frac{\delta\pi}{\delta a}\right)^2 \cdot V_a + \left(\frac{\delta\pi}{\delta b}\right)^2 \cdot V_b + \left(\frac{\delta\pi}{\delta c}\right)^2 \cdot V_c \\ &= \left[\frac{1}{a+c} - \frac{a+b}{(a+c)^2}\right]^2 \cdot V_a + \left[\frac{1}{a+c}\right]^2 \cdot V_b + \left[\frac{a+b}{(a+c)^2}\right]^2 \cdot V_b \\ &= \frac{(c-b)^2 \cdot V_a + (a+c)^2 \cdot V_b + (a+b)^2 \cdot V_c}{(a+c)^4}.\end{aligned}$$

*The variance of a sum of weights from Poisson sources is $\sum_i w_i^2$.

Which, in terms of the original variables, is:

$$\delta C = \left[\frac{m^2 \cdot V_t + t^2 \cdot V_m - 2 \cdot m \cdot t \cdot V_u}{m^4}\right]^{1/2}. \tag{E.5}$$

For unweighted events this again reduces to the more commonly given form:

$$\delta C = \left[\frac{t}{m^3}[t + m - 2 \cdot u]\right]^{1/2}. \tag{E.6}$$

E.2 Error on the Gap Fraction

The gap fraction (at the level of the number of events) can be expressed as,

$$f = \frac{g}{i} = \frac{g}{g+n}$$

where i is the number of events in the inclusive sample, g is the number of events which also contain a rapidity gap and n is the number of events which *do not* contain a gap.

This can equivalently be written,

$$\log f = \log g - \log(g+n). \tag{E.7}$$

Differentiating gives,

$$\begin{aligned}
\frac{\delta f}{f} &= \frac{\delta g}{g} - \frac{\delta g}{g+n} - \frac{\delta n}{g+n} \\
&= \delta g\left(\frac{1}{g} - \frac{1}{g+n}\right) - \delta n\left(\frac{1}{g+n}\right) \\
&= \frac{\delta g}{g}(1-f) - \frac{\delta n}{n}(f-1) \\
\frac{\delta f}{f} &= (1-f)(\delta g/g + \delta n/n). \qquad \text{(E.8)}
\end{aligned}$$

The quantities g and n can be assumed to be independent and Poisson distributed,

$$\Rightarrow \quad \sigma_f = f \cdot (1-f) \cdot \sqrt{(\sigma_g/g)^2 + (\sigma_n/n)^2}. \tag{E.9}$$

Since $\sigma_g = \sqrt{g}$ and $\sigma_n = \sqrt{n}$,

$$\sigma_f = f \cdot (1-f) \cdot \sqrt{1/g + 1/n} \tag{E.10}$$

Appendix F

Multi-Jets in Photoproduction

Systematic Uncertainties

Appendix F

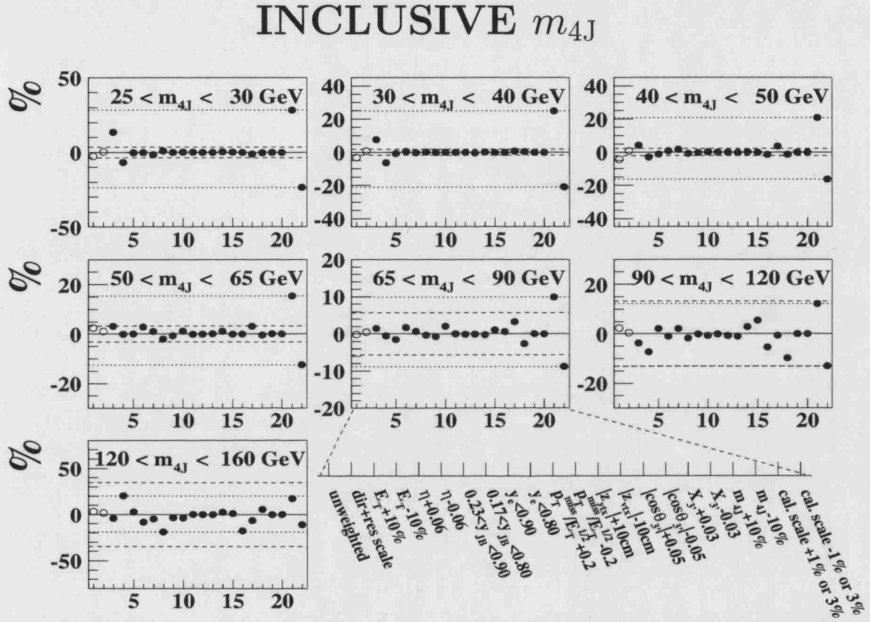

Figure F.1: The percentage difference between the check result (numbers 1-22 in Tab. 7.3) and nominal result for the inclusive $\mathrm{d}\sigma/\mathrm{d}m_{4\mathrm{J}}$ cross section. The solid line indicates the nominal value. The dashed lines show the percentage statistical uncertainty on the nominal result. The dotted lines indicate the largest systematic uncertainty in each bin (upper and lower separately). Also shown is an enlarged version of the x-axis which labels each check.

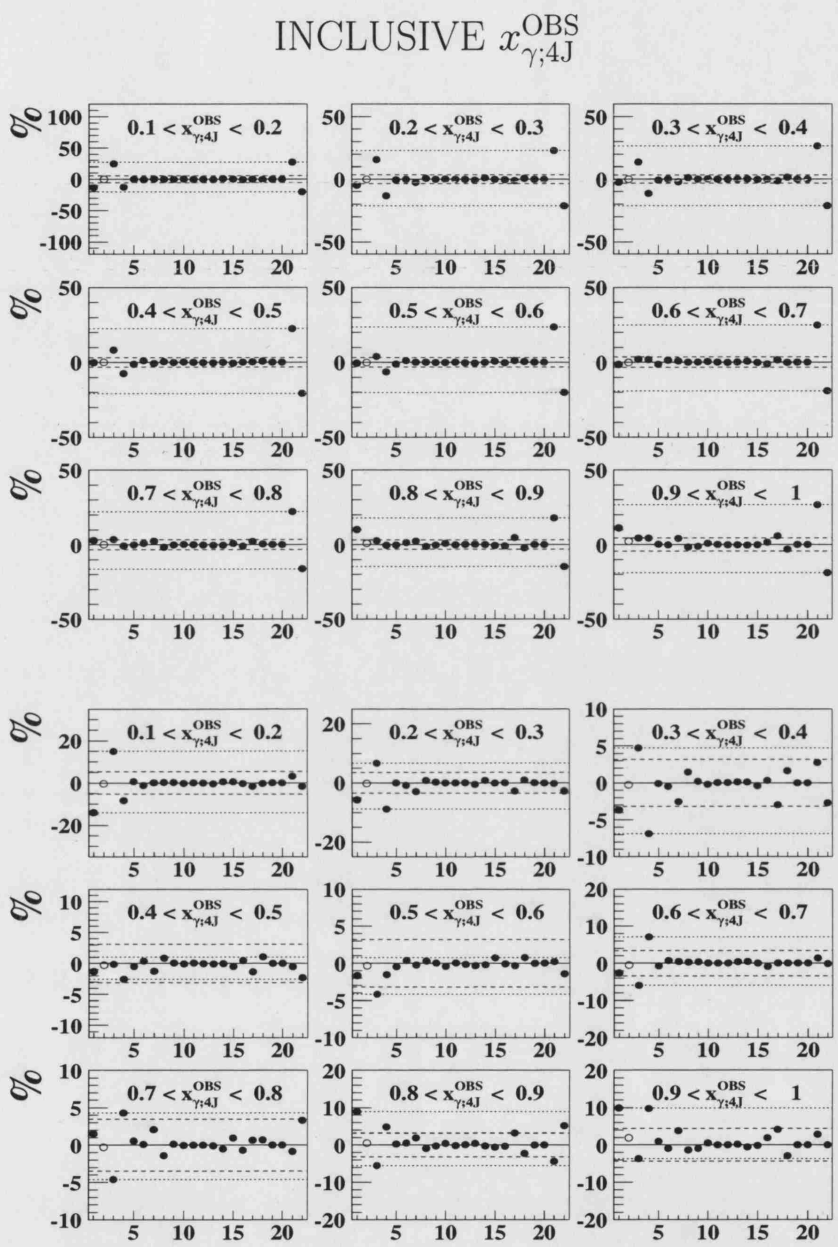

Figure F.2: The percentage difference between the check result (numbers 1-22 in Tab. 7.3) and nominal result for the inclusive $x_{\gamma;4J}^{OBS}$ cross section. The upper figure shows the results for the total cross section and the lower figure shows the results for the normalised cross section. The solid line indicates the nominal value. The dashed lines show the percentage statistical uncertainty on the nominal result. The dotted lines indicate the largest systematic uncertainty in each bin (upper and lower separately).

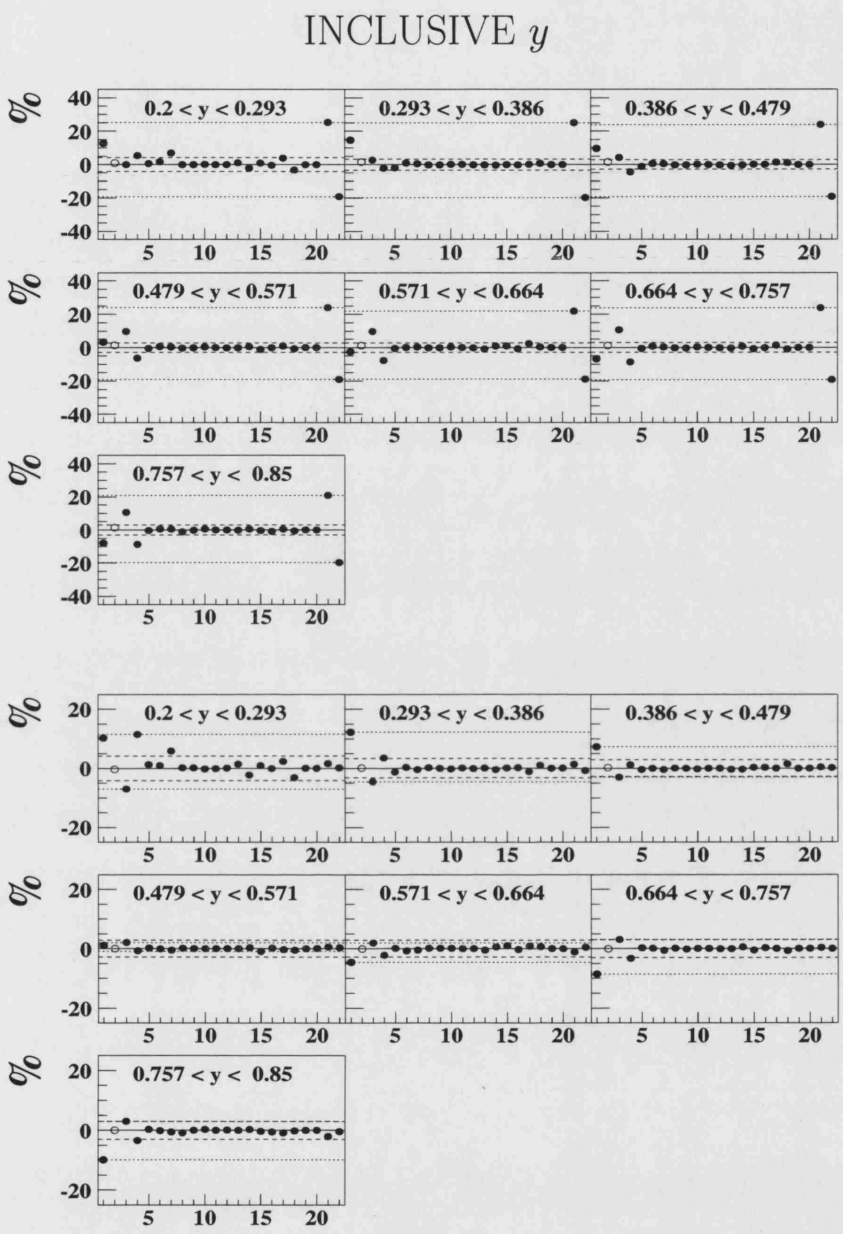

Figure F.3: The percentage difference between the check result (numbers 1-22 in Tab. 7.3) and nominal result for the inclusive y cross section. The upper figure shows the results for the total cross section and the lower figure shows the results for the normalised cross section. The solid line indicates the nominal value. The dashed lines show the percentage statistical uncertainty on the nominal result. The dotted lines indicate the largest systematic uncertainty in each bin (upper and lower separately).

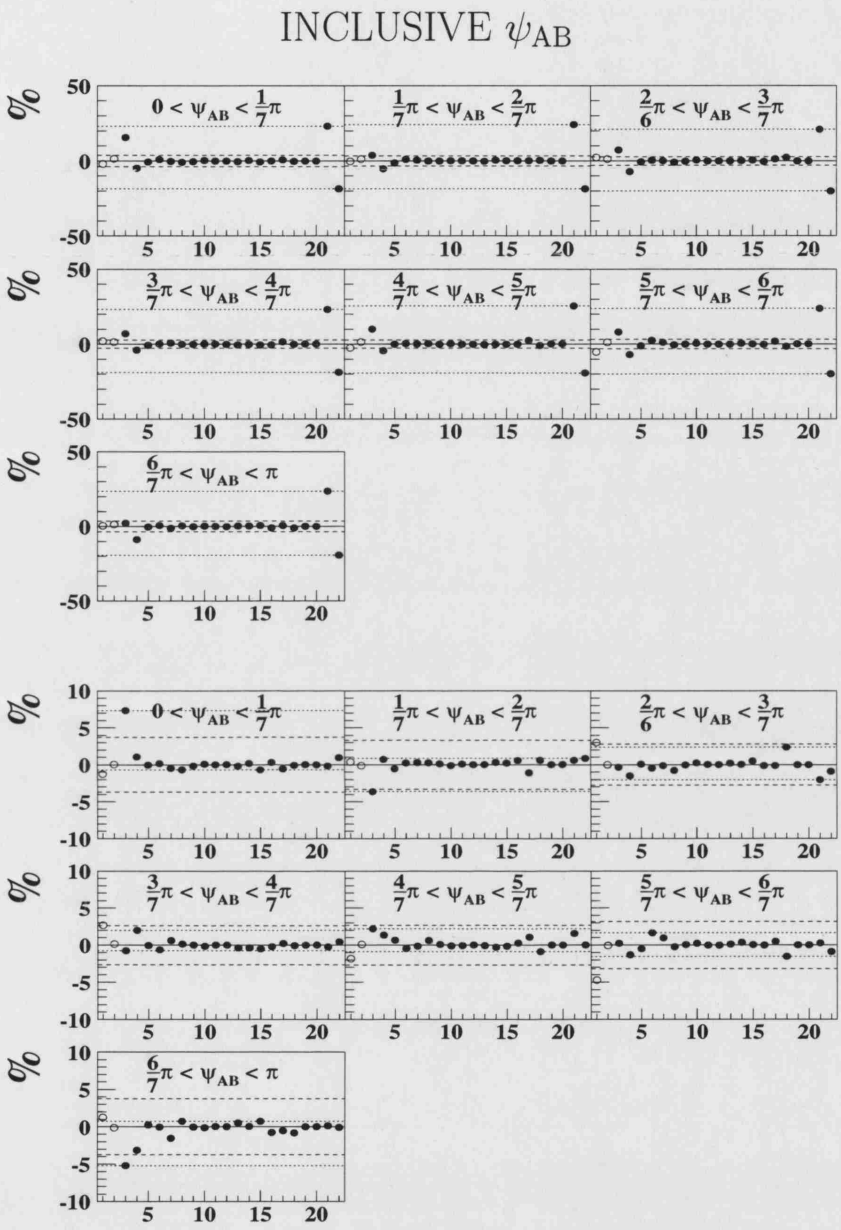

Figure F.4: The percentage difference between the check result (numbers 1-22 in Tab. 7.3) and nominal result for the inclusive ψ_{AB} cross section. The upper figure shows the results for the total cross section and the lower figure shows the results for the normalised cross section. The solid line indicates the nominal value. The dashed lines show the percentage statistical uncertainty on the nominal result. The dotted lines indicate the largest systematic uncertainty in each bin (upper and lower separately).

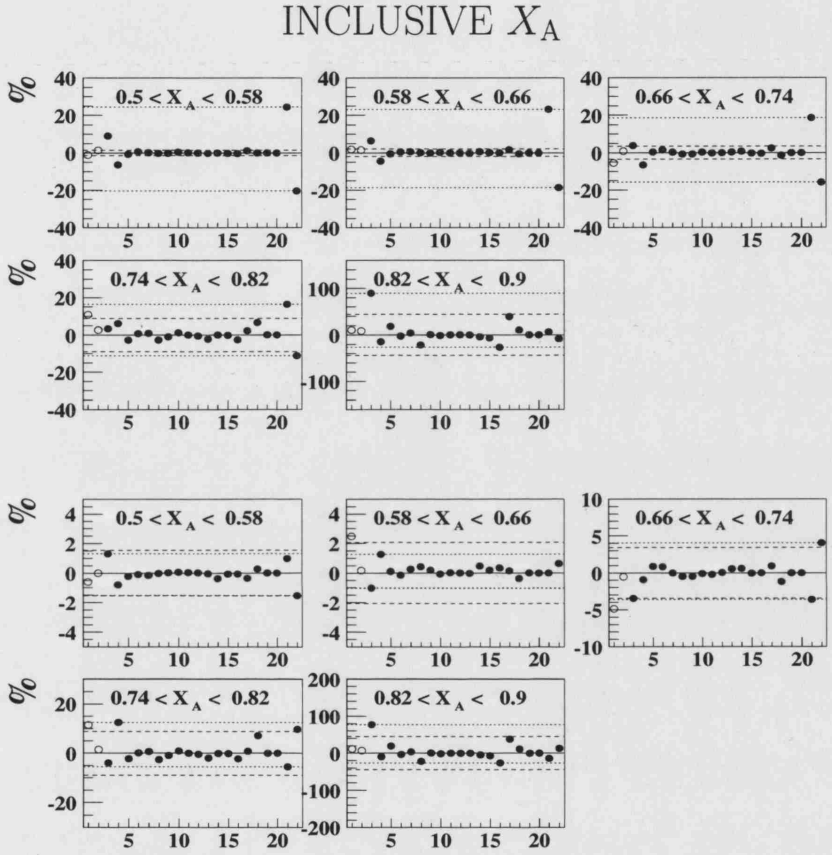

Figure F.5: The percentage difference between the check result (numbers 1-22 in Tab. 7.3) and nominal result for the inclusive X_A cross section. The upper figure shows the results for the total cross section and the lower figure shows the results for the normalised cross section. The solid line indicates the nominal value. The dashed lines show the percentage statistical uncertainty on the nominal result. The dotted lines indicate the largest systematic uncertainty in each bin (upper and lower separately).

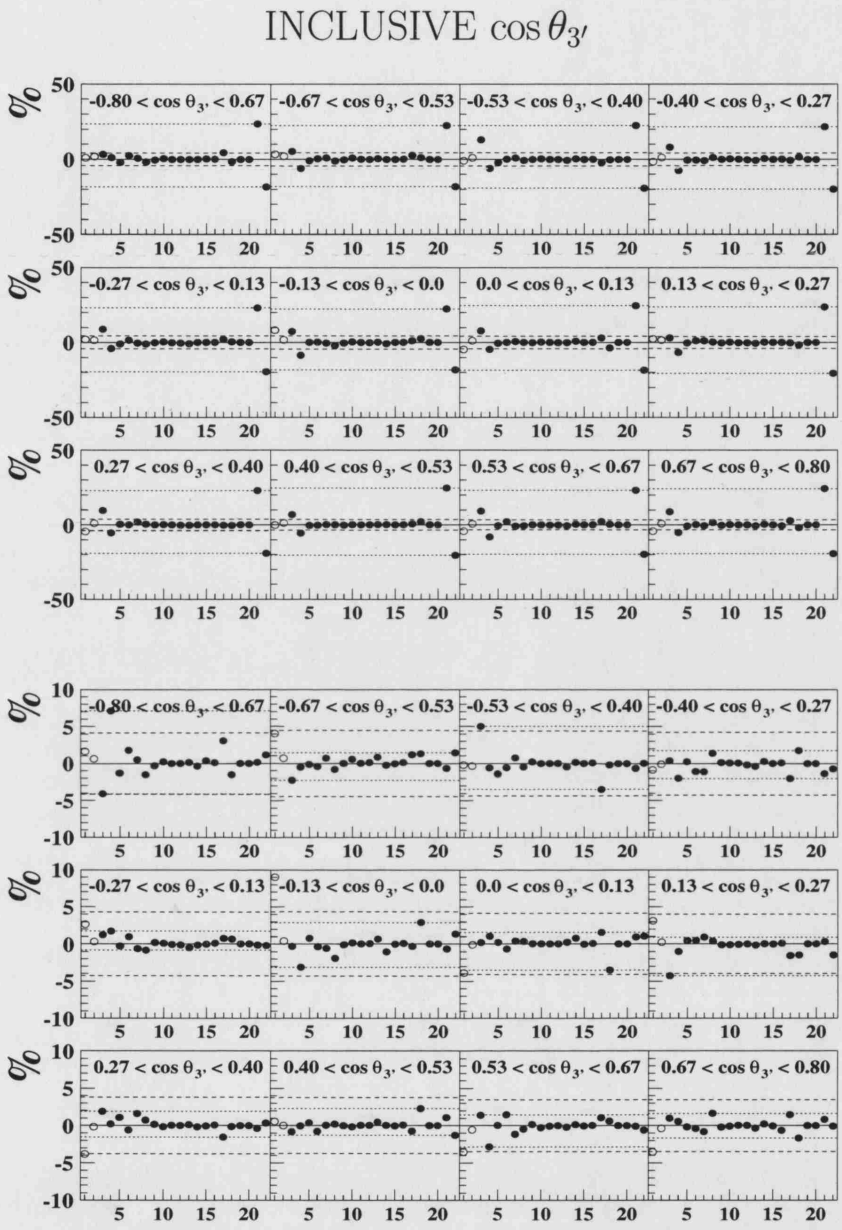

Figure F.6: The percentage difference between the check result (numbers 1-22 in Tab. 7.3) and nominal result for the inclusive $\cos\theta_{3'}$ cross section. The upper figure shows the results for the total cross section and the lower figure shows the results for the normalised cross section. The solid line indicates the nominal value. The dashed lines show the percentage statistical uncertainty on the nominal result. The dotted lines indicate the largest systematic uncertainty in each bin (upper and lower separately).

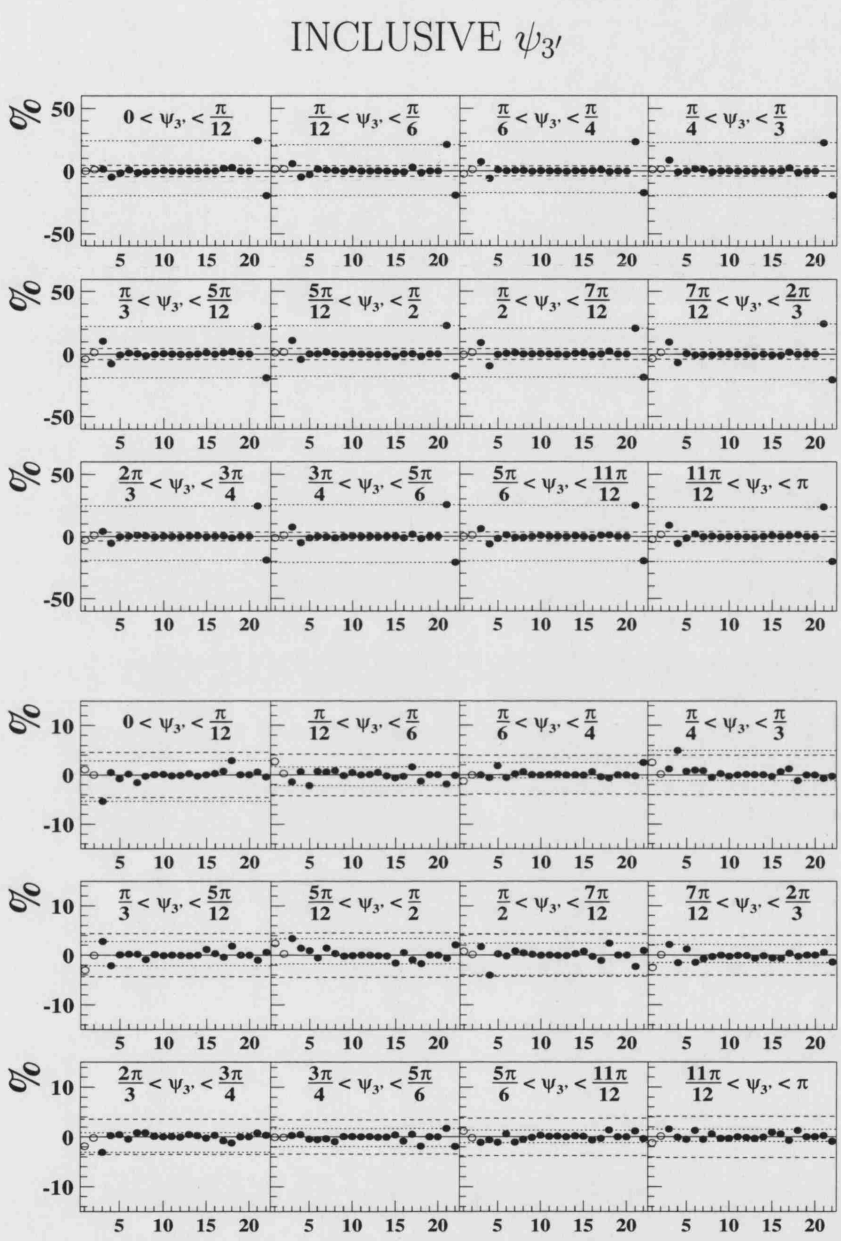

Figure F.7: The percentage difference between the check result (numbers 1-22 in Tab. 7.3) and nominal result for the inclusive $\psi_{3'}$ cross section. The upper figure shows the results for the total cross section and the lower figure shows the results for the normalised cross section. The solid line indicates the nominal value. The dashed lines show the percentage statistical uncertainty on the nominal result. The dotted lines indicate the largest systematic uncertainty in each bin (upper and lower separately).

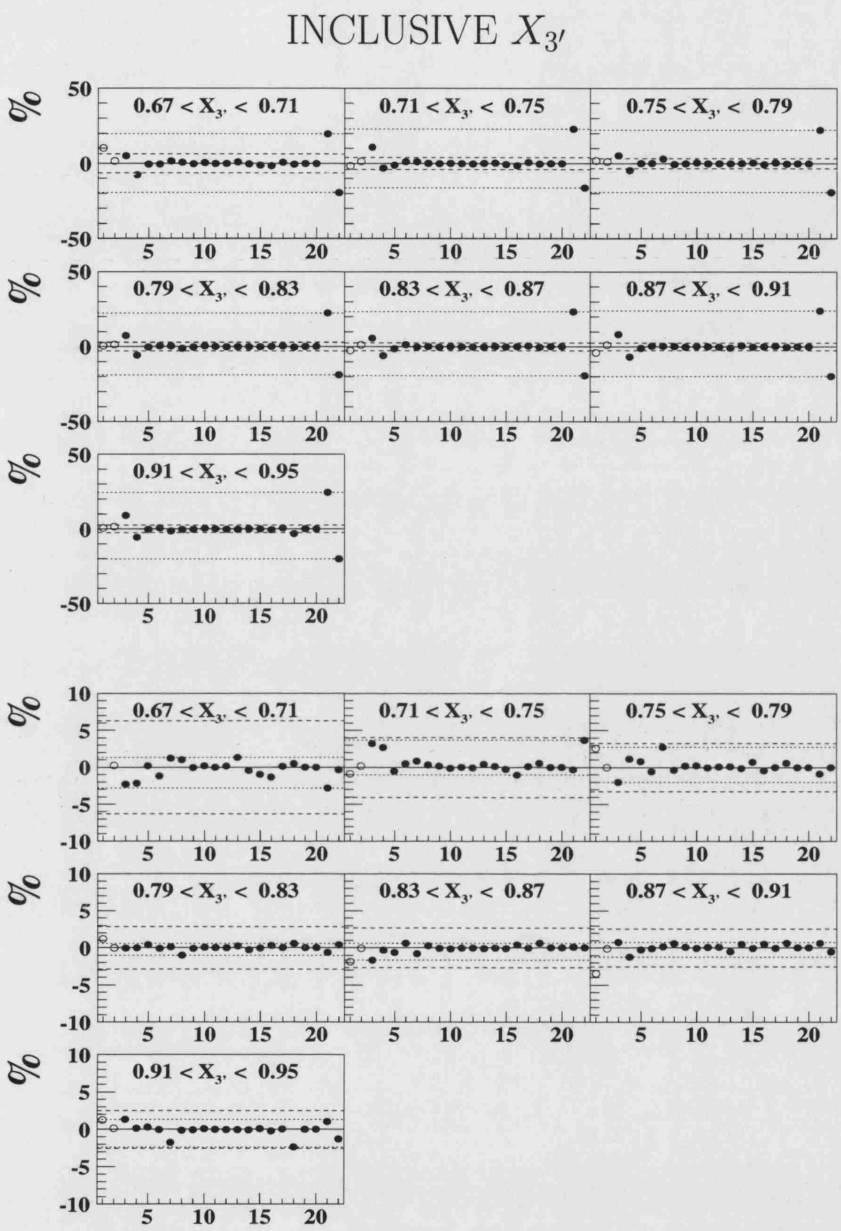

Figure F.8: The percentage difference between the check result (numbers 1-22 in Tab. 7.3) and nominal result for the inclusive $X_{3'}$ cross section. The upper figure shows the results for the total cross section and the lower figure shows the results for the normalised cross section. The solid line indicates the nominal value. The dashed lines show the percentage statistical uncertainty on the nominal result. The dotted lines indicate the largest systematic uncertainty in each bin (upper and lower separately).

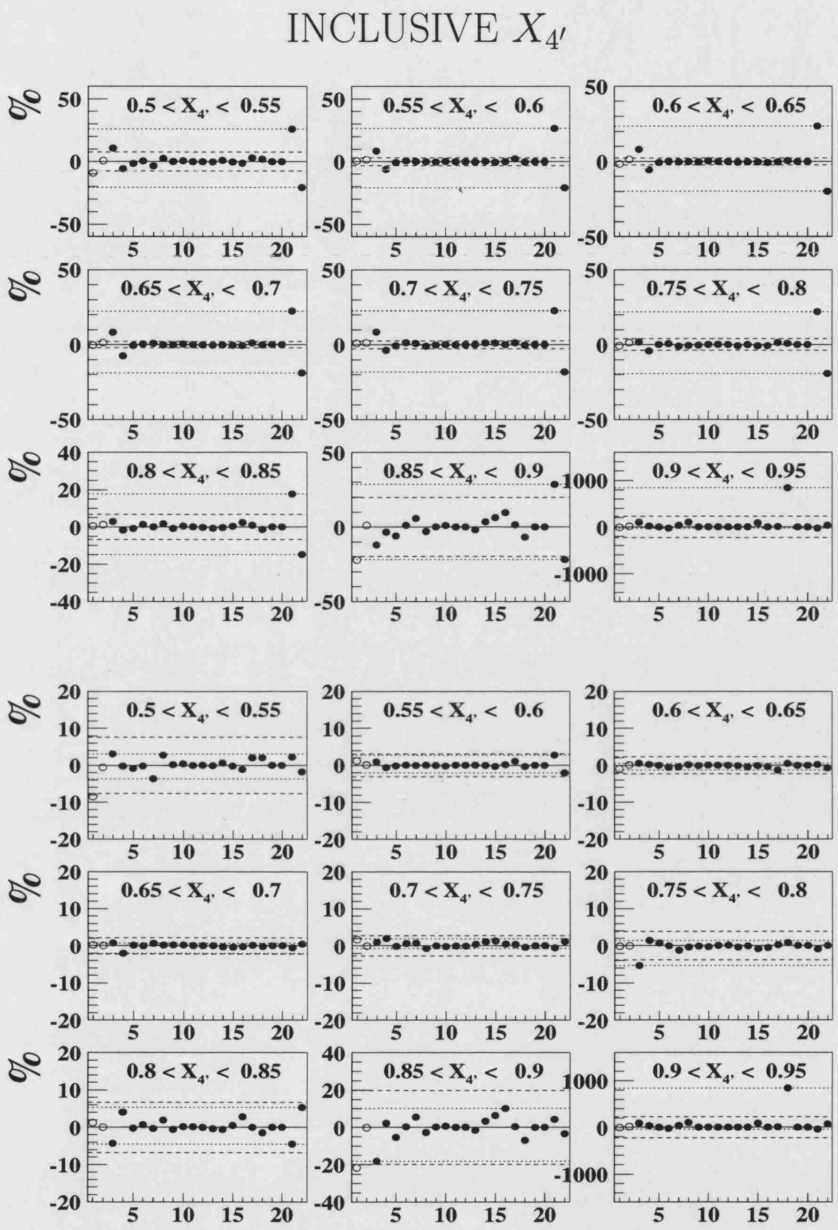

Figure F.9: The percentage difference between the check result (numbers 1-22 in Tab. 7.3) and nominal result for the inclusive $X_{4'}$ cross section. The upper figure shows the results for the total cross section and the lower figure shows the results for the normalised cross section. The solid line indicates the nominal value. The dashed lines show the percentage statistical uncertainty on the nominal result. The dotted lines indicate the largest systematic uncertainty in each bin (upper and lower separately).

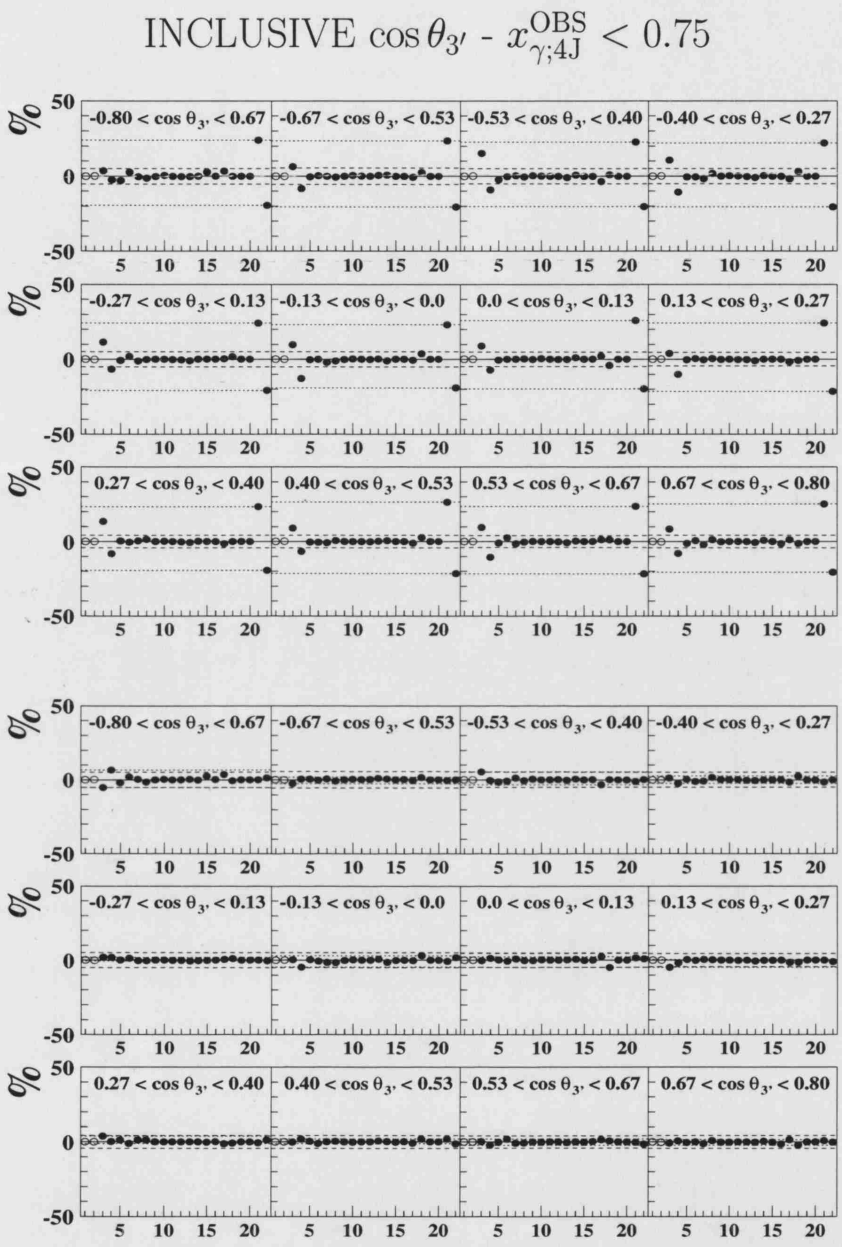

Figure F.10: The percentage difference between the check result (numbers 1-22 in Tab. 7.3) and nominal result for the inclusive $\cos\theta_{3'}$ cross section in the region $x_{\gamma;4J}^{OBS} < 0.75$. The upper figure shows the results for the total cross section and the lower figure shows the results for the normalised cross section. The solid line indicates the nominal value. The dashed lines show the percentage statistical uncertainty on the nominal result. The dotted lines indicate the largest systematic uncertainty in each bin (upper and lower separately).

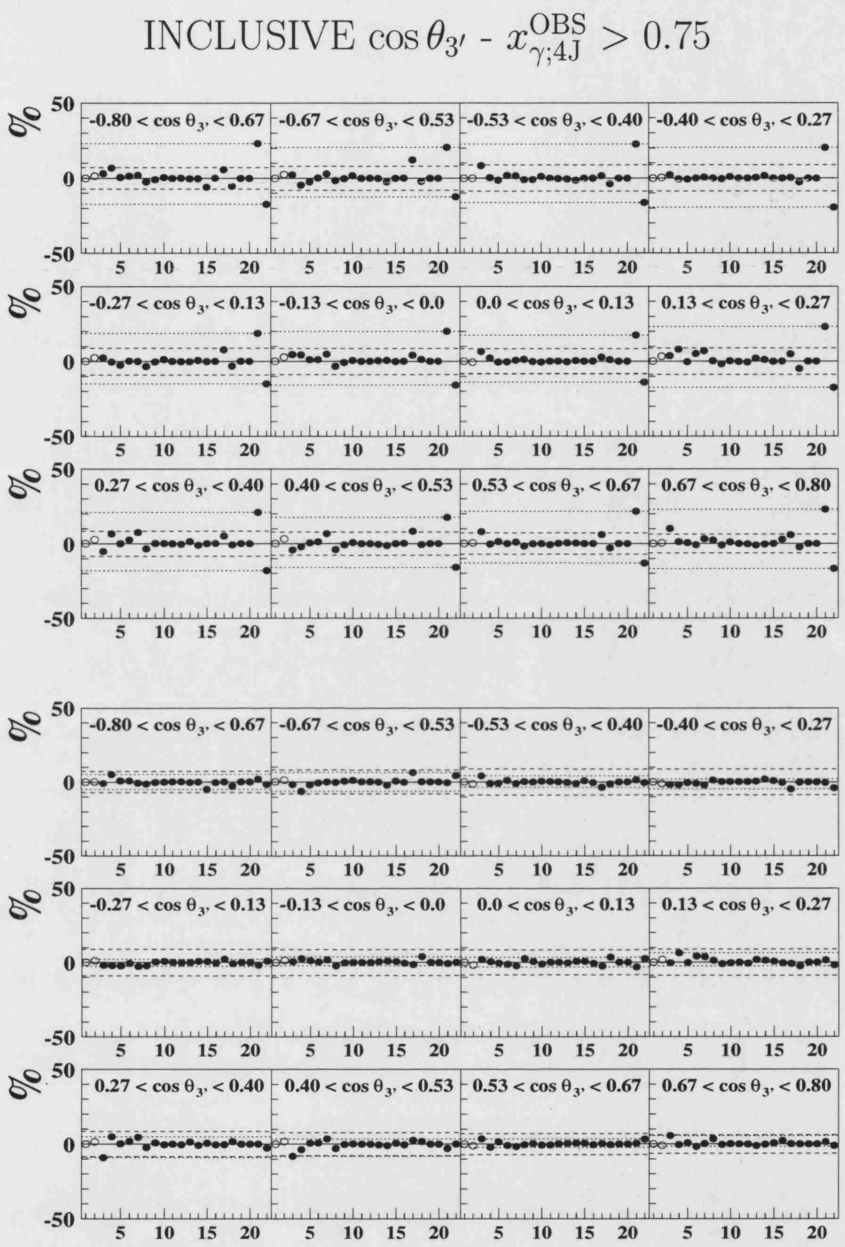

Figure F.11: The percentage difference between the check result (numbers 1-22 in Tab. 7.3) and nominal result for the inclusive $\cos\theta_{3'}$ cross section in the region $x_{\gamma;4J}^{OBS} > 0.75$. The upper figure shows the results for the total cross section and the lower figure shows the results for the normalised cross section. The solid line indicates the nominal value. The dashed lines show the percentage statistical uncertainty on the nominal result. The dotted lines indicate the largest systematic uncertainty in each bin (upper and lower separately).

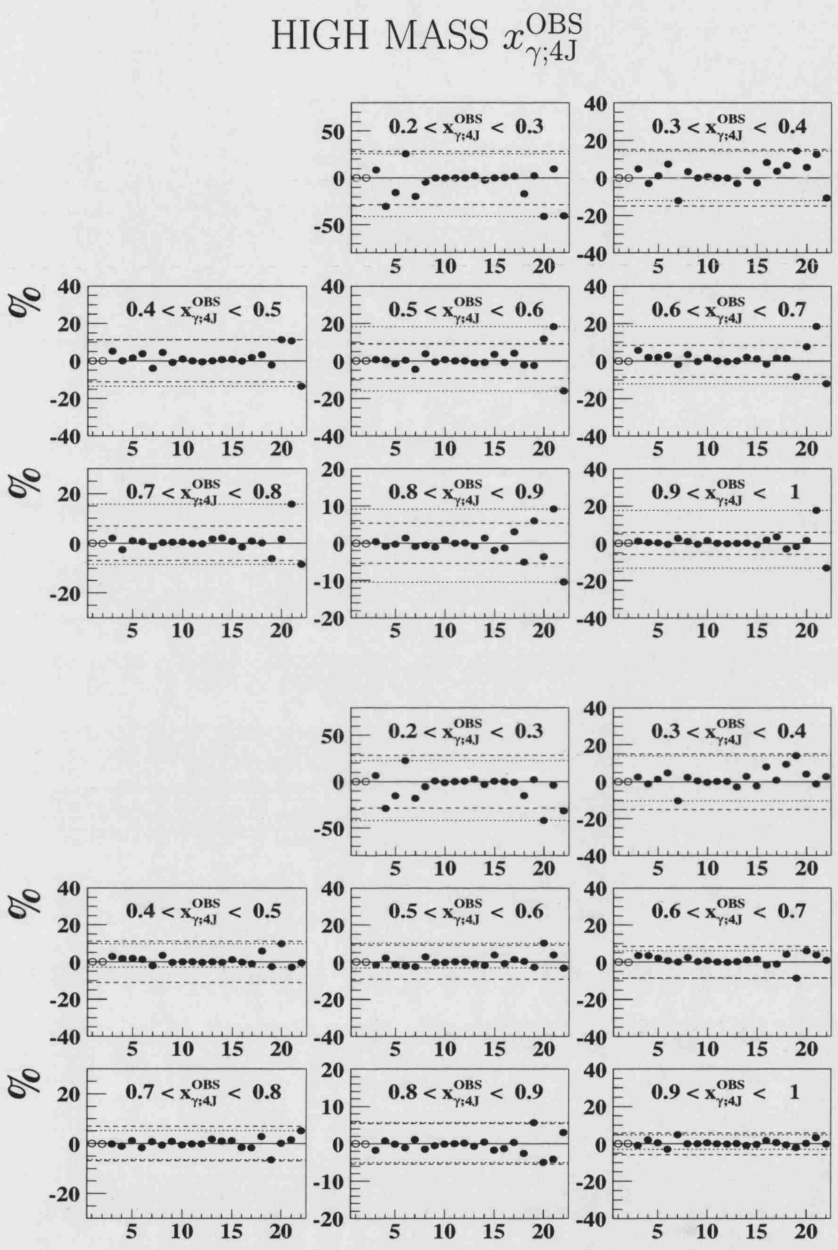

Figure F.12: The percentage difference between the check result (numbers 1-22 in Tab. 7.3) and nominal result for the high mass $x_{\gamma;4J}^{OBS}$ cross section. The upper figure shows the results for the total cross section and the lower figure shows the results for the normalised cross section. The solid line indicates the nominal value. The dashed lines show the percentage statistical uncertainty on the nominal result. The dotted lines indicate the largest systematic uncertainty in each bin (upper and lower separately).

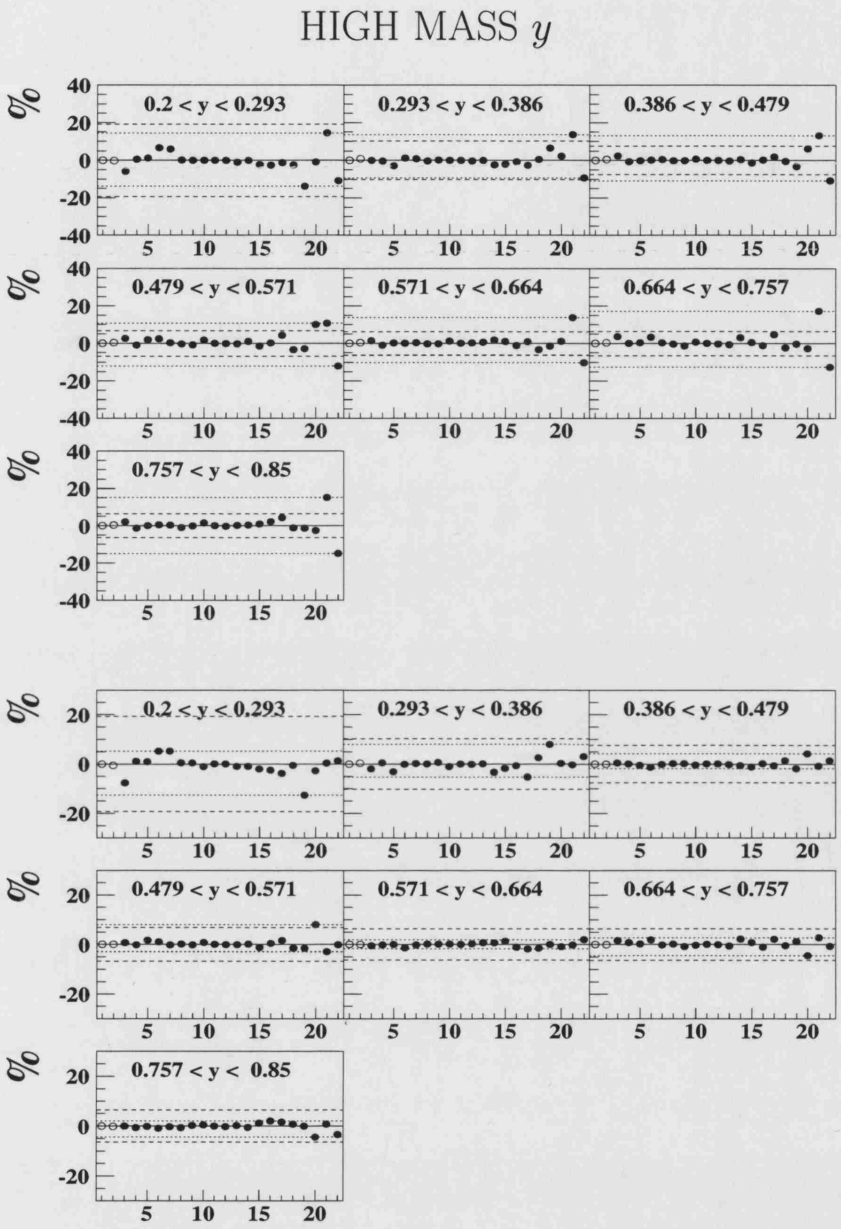

Figure F.13: The percentage difference between the check result (numbers 1-22 in Tab. 7.3) and nominal result for the high mass y cross section. The upper figure shows the results for the total cross section and the lower figure shows the results for the normalised cross section. The solid line indicates the nominal value. The dashed lines show the percentage statistical uncertainty on the nominal result. The dotted lines indicate the largest systematic uncertainty in each bin (upper and lower separately).

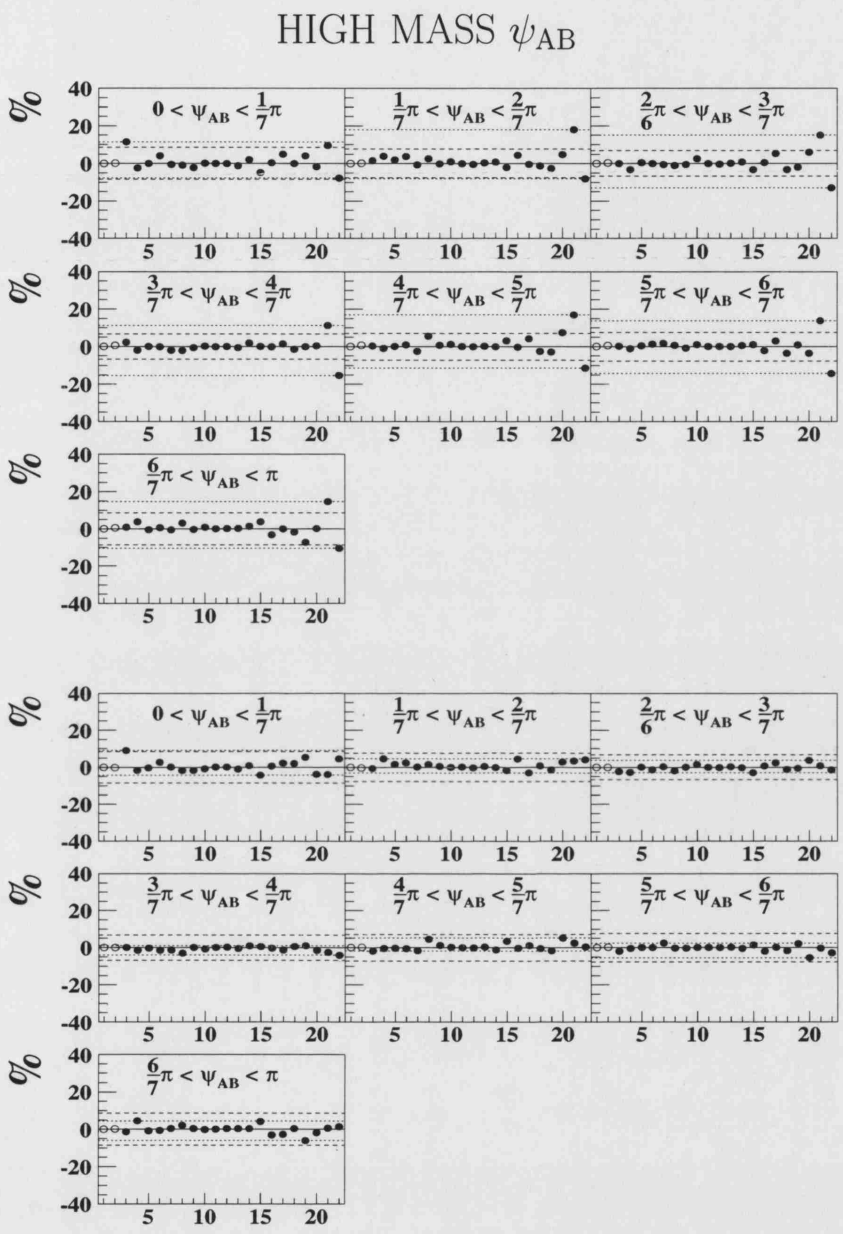

Figure F.14: The percentage difference between the check result (numbers 1-22 in Tab. 7.3) and nominal result for the high mass ψ_{AB} cross section. The upper figure shows the results for the total cross section and the lower figure shows the results for the normalised cross section. The solid line indicates the nominal value. The dashed lines show the percentage statistical uncertainty on the nominal result. The dotted lines indicate the largest systematic uncertainty in each bin (upper and lower separately).

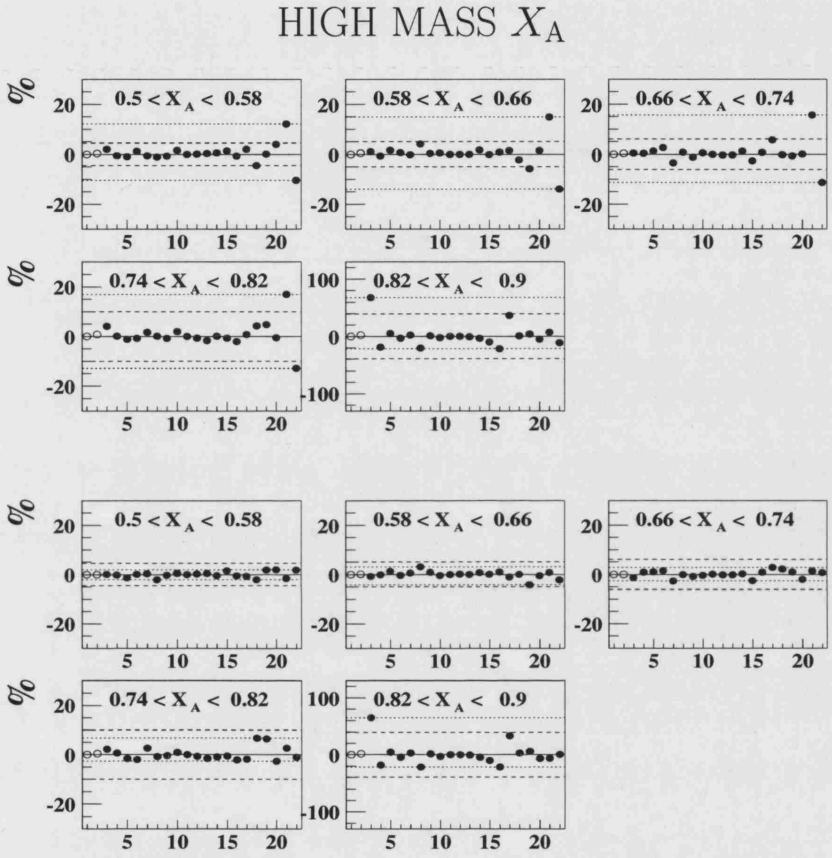

Figure F.15: The percentage difference between the check result (numbers 1-22 in Tab. 7.3) and nominal result for the high mass X_A cross section. The upper figure shows the results for the total cross section and the lower figure shows the results for the normalised cross section. The solid line indicates the nominal value. The dashed lines show the percentage statistical uncertainty on the nominal result. The dotted lines indicate the largest systematic uncertainty in each bin (upper and lower separately).

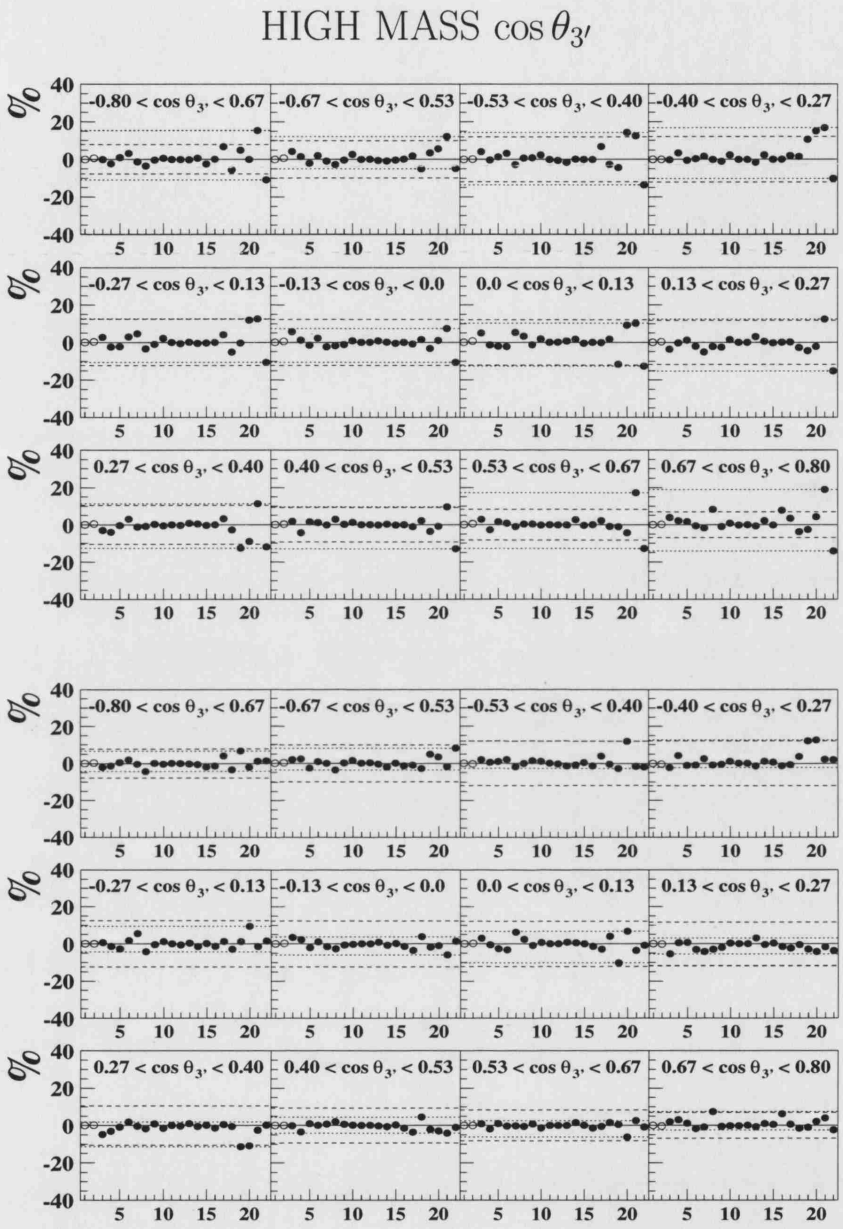

Figure F.16: The percentage difference between the check result (numbers 1-22 in Tab. 7.3) and nominal result for the high mass $\cos\theta_{3'}$ cross section. The upper figure shows the results for the total cross section and the lower figure shows the results for the normalised cross section. The solid line indicates the nominal value. The dashed lines show the percentage statistical uncertainty on the nominal result. The dotted lines indicate the largest systematic uncertainty in each bin (upper and lower separately).

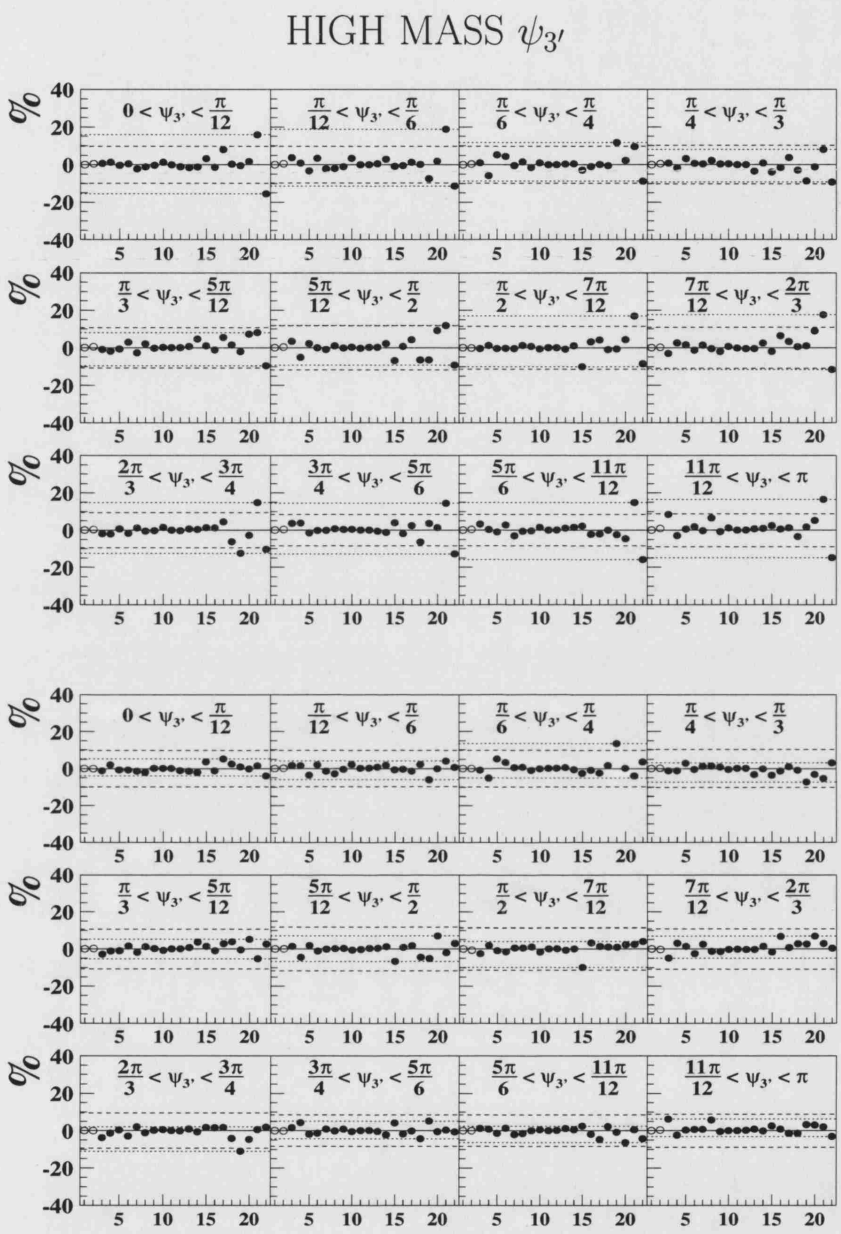

Figure F.17: The percentage difference between the check result (numbers 1-22 in Tab. 7.3) and nominal result for the high mass $\psi_{3'}$ cross section. The upper figure shows the results for the total cross section and the lower figure shows the results for the normalised cross section. The solid line indicates the nominal value. The dashed lines show the percentage statistical uncertainty on the nominal result. The dotted lines indicate the largest systematic uncertainty in each bin (upper and lower separately).

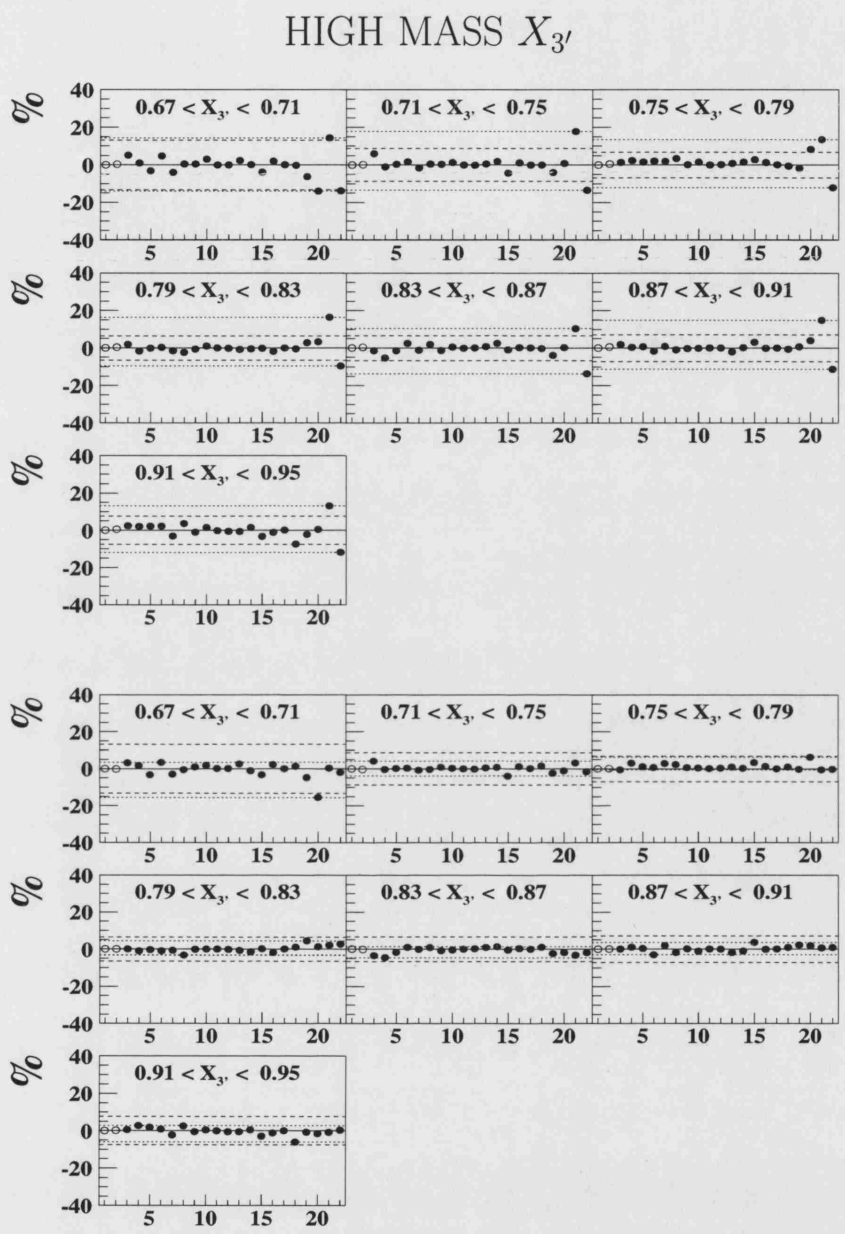

Figure F.18: The percentage difference between the check result (numbers 1-22 in Tab. 7.3) and nominal result for the high mass $X_{3'}$ cross section. The upper figure shows the results for the total cross section and the lower figure shows the results for the normalised cross section. The solid line indicates the nominal value. The dashed lines show the percentage statistical uncertainty on the nominal result. The dotted lines indicate the largest systematic uncertainty in each bin (upper and lower separately).

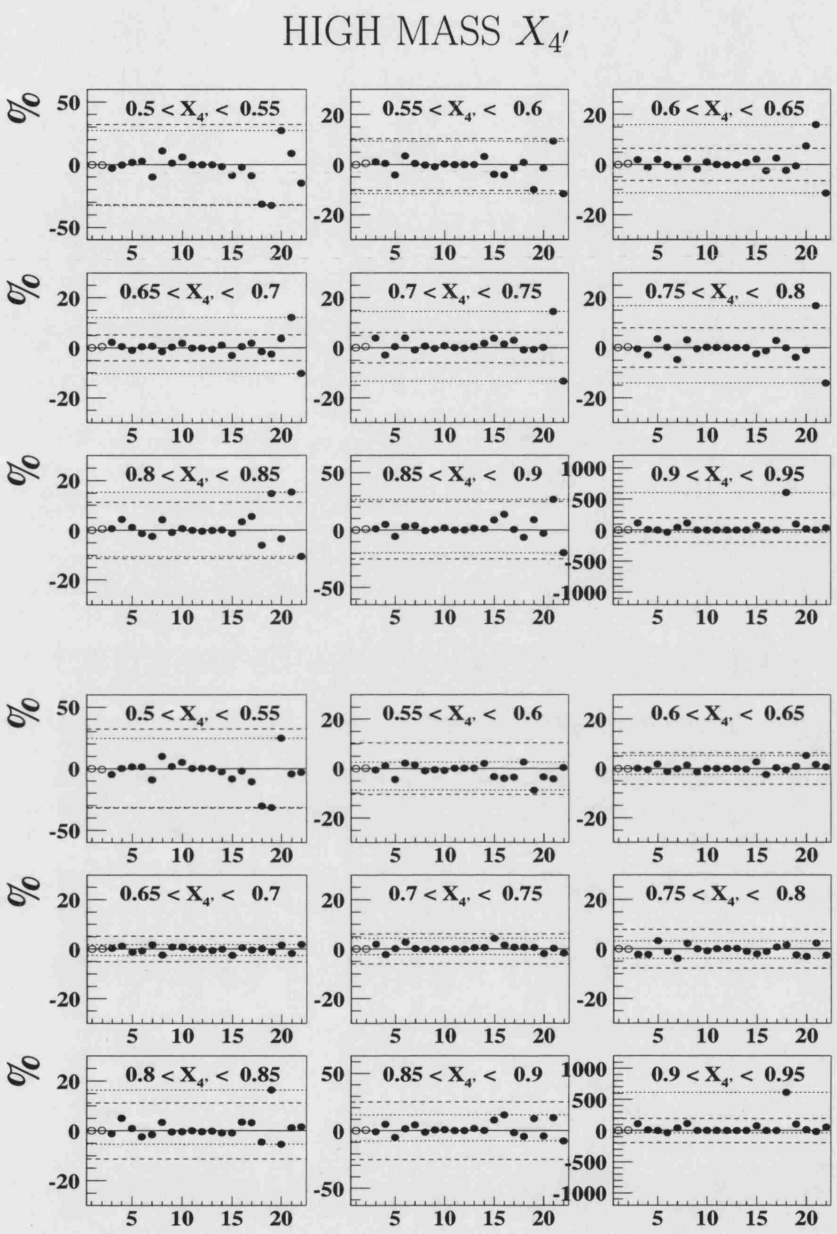

Figure F.19: The percentage difference between the check result (numbers 1-22 in Tab. 7.3) and nominal result for the high mass $X_{4'}$ cross section. The upper figure shows the results for the total cross section and the lower figure shows the results for the normalised cross section. The solid line indicates the nominal value. The dashed lines show the percentage statistical uncertainty on the nominal result. The dotted lines indicate the largest systematic uncertainty in each bin (upper and lower separately).

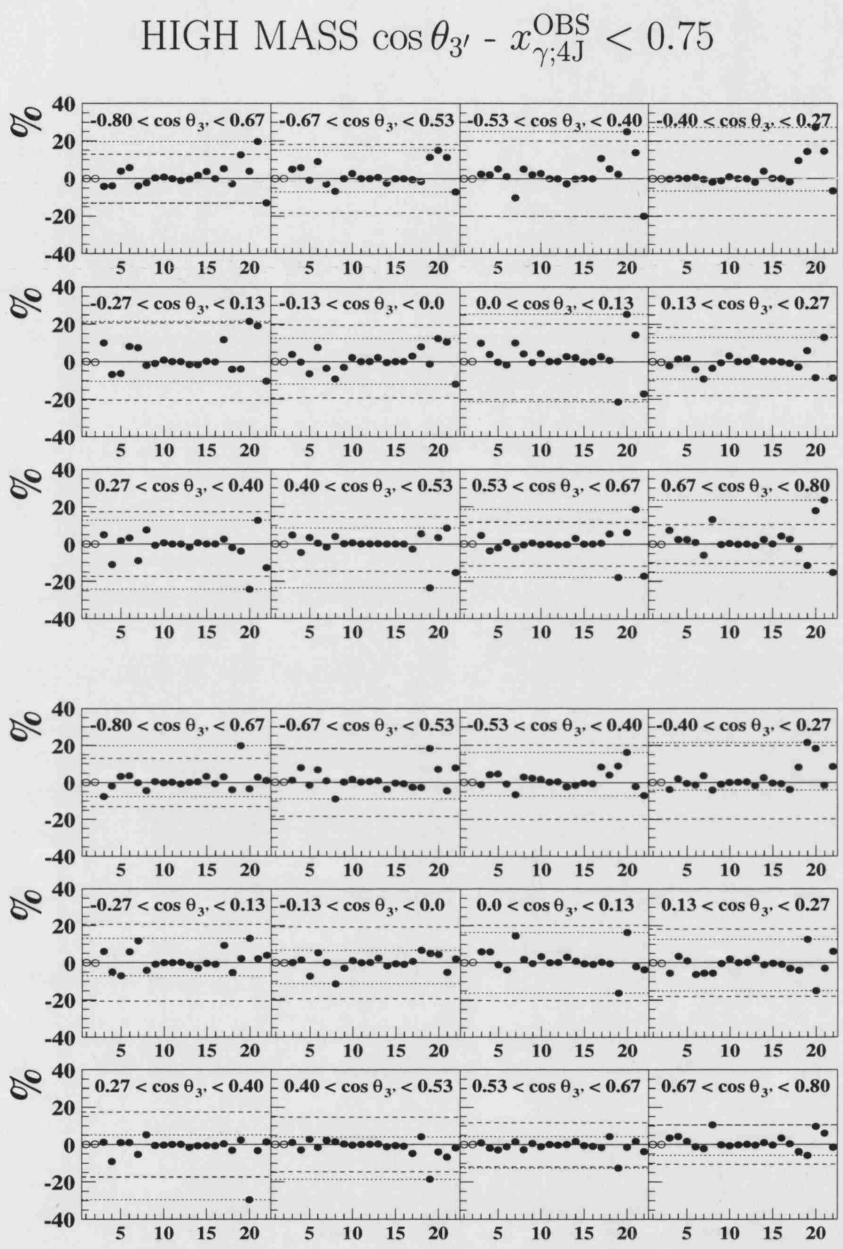

Figure F.20: The percentage difference between the check result (numbers 1-22 in Tab. 7.3) and nominal result for the high mass $\mathrm{d}\sigma/\mathrm{d}\cos\theta_{3'}$ cross section in the region $x_{\gamma;4J}^{OBS} < 0.75$. The upper figure shows the results for the total cross section and the lower figure shows the results for the normalised cross section. The solid line indicates the nominal value. The dashed lines show the percentage statistical uncertainty on the nominal result. The dotted lines indicate the largest systematic uncertainty in each bin (upper and lower separately).

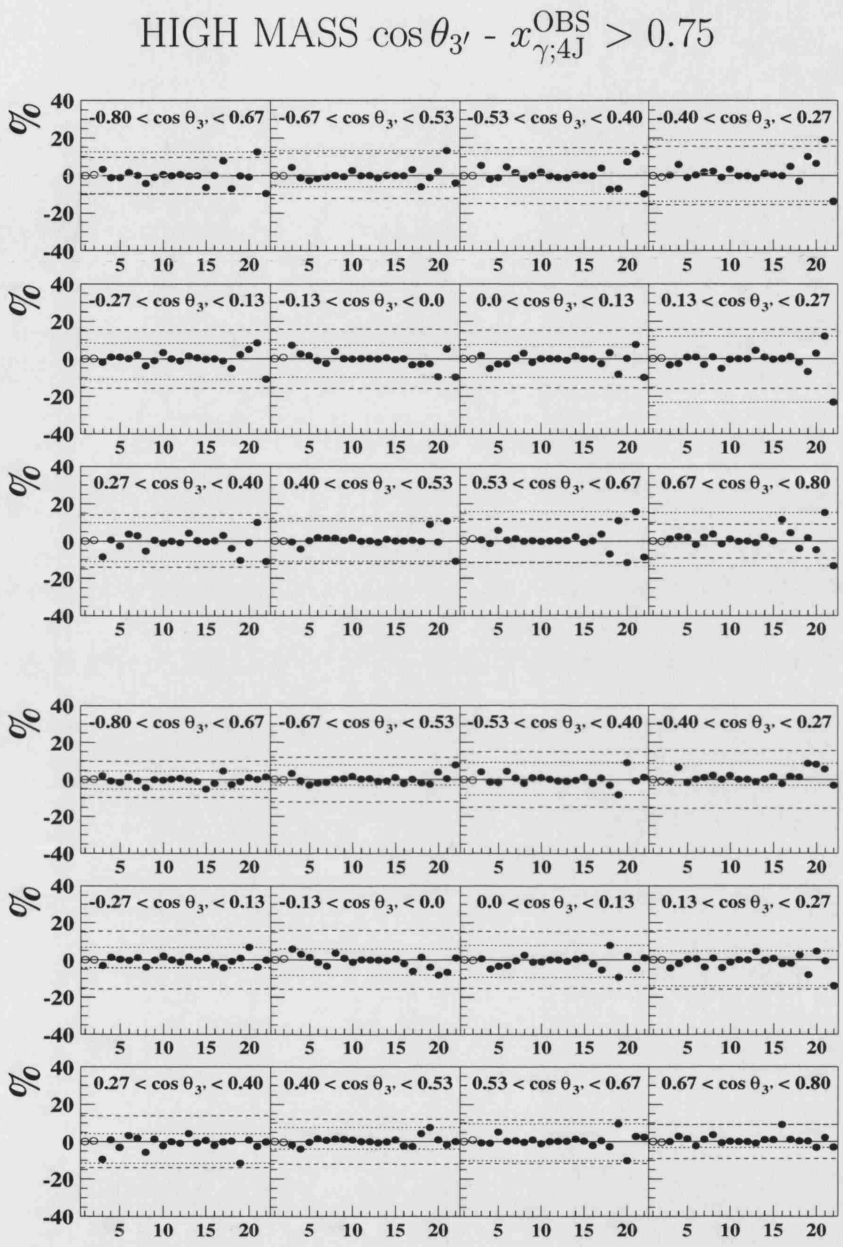

Figure F.21: The percentage difference between the check result (numbers 1-22 in Tab. 7.3) and nominal result for the high mass $d\sigma/d\cos\theta_{3'}$ cross section in the region $x_{\gamma;4J}^{OBS} > 0.75$. The upper figure shows the results for the total cross section and the lower figure shows the results for the normalised cross section. The solid line indicates the nominal value. The dashed lines show the percentage statistical uncertainty on the nominal result. The dotted lines indicate the largest systematic uncertainty in each bin (upper and lower separately).

Appendix G

Multi-Jets in Photoproduction

Tables of Data

This appendix contains the values of all differential cross sections measured in the Multi-Jets in Photoproduction analysis presented in this thesis. The total and normalised cross sections are listed for both the inclusive and high mass samples. Also listed are the associated statistical, uncorrelated systematic and energy scale uncertainties.

m_{4J} range	$\sigma(\pm$ stat. syst. Escale) (pb)
[25, 30]	$4.869 \pm 0.174\ ^{+0.656\ +1.378}_{-0.340\ -1.143}$
[30, 40]	$12.75 \pm 0.226\ ^{+0.978\ +3.158}_{-0.803\ -2.674}$
[40, 50]	$8.894 \pm 0.199\ ^{+0.514\ +1.850}_{-0.350\ -1.455}$
[50, 65]	$2.661 \pm 0.086\ ^{+0.150\ +0.410}_{-0.060\ -0.333}$
[65, 90]	$0.595 \pm 0.034\ ^{+0.028\ +0.059}_{-0.019\ -0.052}$
[90, 120]	$0.111 \pm 0.015\ ^{+0.008\ +0.014}_{-0.016\ -0.014}$
[120, 160]	$0.014 \pm 0.005\ ^{+0.003\ +0.002}_{-0.004\ -0.002}$

Table G.1: The inclusive cross section differential in m_{4J}. The first column gives the bin range and the second column gives the value of the total cross section. Also listed are the associated statistical, uncorrelated systematic and energy scale uncertainties.

Appendix G

$x_{\gamma;4J}^{OBS}$ range	$\sigma(\pm$ stat. syst. Escale) (pb)	$\sigma(\pm$ stat. syst.)
[0.0,0.1]	$3.961 \pm 2.70\ ^{+29.6}_{-3.25}\ ^{+0.000}_{-0.330}$	$0.013 \pm 0.009\ ^{+0.091}_{-0.011}$
[0.1,0.2]	$141.7 \pm 7.58\ ^{+35.0}_{-26.0}\ ^{+38.3}_{-28.9}$	$0.479 \pm 0.026\ ^{+0.072}_{-0.079}$
[0.2,0.3]	$295.2 \pm 10.4\ ^{+46.1}_{-42.7}\ ^{+67.3}_{-62.7}$	$0.998 \pm 0.035\ ^{+0.067}_{-0.113}$
[0.3,0.4]	$370.6 \pm 11.8\ ^{+50.6}_{-44.8}\ ^{+98.3}_{-78.6}$	$1.253 \pm 0.040\ ^{+0.065}_{-0.110}$
[0.4,0.5]	$400.5 \pm 12.5\ ^{+33.8}_{-30.3}\ ^{+90.1}_{-83.5}$	$1.353 \pm 0.042\ ^{+0.020}_{-0.047}$
[0.5,0.6]	$413.7 \pm 13.1\ ^{+18.0}_{-27.4}\ ^{+96.9}_{-83.3}$	$1.398 \pm 0.044\ ^{+0.017}_{-0.067}$
[0.6,0.7]	$297.5 \pm 10.2\ ^{+10.7}_{-7.22}\ ^{+74.0}_{-57.0}$	$1.005 \pm 0.034\ ^{+0.072}_{-0.067}$
[0.7,0.8]	$316.3 \pm 11.0\ ^{+18.0}_{-7.14}\ ^{+69.9}_{-51.7}$	$1.069 \pm 0.037\ ^{+0.056}_{-0.052}$
[0.8,0.9]	$467.3 \pm 14.9\ ^{+55.6}_{-13.9}\ ^{+83.3}_{-69.4}$	$1.579 \pm 0.050\ ^{+0.171}_{-0.095}$
[0.9,1.0]	$252.0 \pm 11.1\ ^{+37.2}_{-9.55}\ ^{+67.3}_{-47.8}$	$0.852 \pm 0.038\ ^{+0.129}_{-0.044}$

Table G.2: The inclusive cross section differential in $x_{\gamma;4J}^{OBS}$. The first column gives the bin range, the second column gives the value of the total cross section and the third column gives the value of the normalised cross section. Also listed are the associated statistical, uncorrelated systematic and energy scale uncertainties.

y range	$\sigma(\pm$ stat. syst. Escale) (pb)	$\sigma(\pm$ stat. syst.)
[0.20, 0.29]	$254.6 \pm 10.6\ ^{+40.7}_{-10.3}\ ^{+64.3}_{-48.9}$	$0.856 \pm 0.036\ ^{+0.144}_{-0.069}$
[0.29, 0.39]	$403.0 \pm 13.2\ ^{+60.3}_{-12.2}\ ^{+101}_{-80.1}$	$1.356 \pm 0.045\ ^{+0.173}_{-0.067}$
[0.39, 0.48]	$487.8 \pm 14.0\ ^{+51.9}_{-22.6}\ ^{+116}_{-93.5}$	$1.641 \pm 0.047\ ^{+0.122}_{-0.052}$
[0.48, 0.57]	$532.3 \pm 14.8\ ^{+55.6}_{-34.0}\ ^{+128}_{-101}$	$1.790 \pm 0.050\ ^{+0.043}_{-0.026}$
[0.57, 0.66]	$523.4 \pm 14.6\ ^{+52.5}_{-42.4}\ ^{+115}_{-99.0}$	$1.761 \pm 0.049\ ^{+0.045}_{-0.092}$
[0.66, 0.76]	$511.6 \pm 15.0\ ^{+56.0}_{-55.9}\ ^{+122}_{-98.4}$	$1.721 \pm 0.050\ ^{+0.053}_{-0.159}$
[0.76, 0.85]	$488.8 \pm 14.8\ ^{+52.9}_{-58.2}\ ^{+102}_{-96.0}$	$1.644 \pm 0.050\ ^{+0.050}_{-0.174}$

Table G.3: The inclusive cross section differential in y . The first column gives the bin range, the second column gives the value of the total cross section and the third column gives the value of the normalised cross section. Also listed are the associated statistical, uncorrelated systematic and energy scale uncertainties.

Appendix G

ψ_{AB} range	$\sigma(\pm$ stat. syst. Escale) (pb)	$\sigma(\pm$ stat. syst.)
$[0, \frac{1}{7}\pi]$	$72.78 \pm 2.70\ ^{+11.4}_{-3.68}\ ^{+16.9}_{-13.5}$	$0.243 \pm 0.009\ ^{+0.018}_{-0.003}$
$[\frac{1}{7}\pi, \frac{2}{7}\pi]$	$87.22 \pm 2.88\ ^{+3.50}_{-4.63}\ ^{+21.0}_{-16.2}$	$0.291 \pm 0.010\ ^{+0.004}_{-0.011}$
$[\frac{2}{7}\pi, \frac{3}{7}\pi]$	$112.5 \pm 3.12\ ^{+8.69}_{-8.27}\ ^{+23.5}_{-22.5}$	$0.376 \pm 0.010\ ^{+0.009}_{-0.007}$
$[\frac{3}{7}\pi, \frac{4}{7}\pi]$	$110.8 \pm 2.91\ ^{+7.80}_{-4.59}\ ^{+25.6}_{-20.9}$	$0.370 \pm 0.010\ ^{+0.008}_{-0.005}$
$[\frac{4}{7}\pi, \frac{5}{7}\pi]$	$118.3 \pm 3.16\ ^{+12.2}_{-5.53}\ ^{+30.0}_{-22.8}$	$0.395 \pm 0.011\ ^{+0.012}_{-0.004}$
$[\frac{5}{7}\pi, \frac{6}{7}\pi]$	$93.76 \pm 2.97\ ^{+8.05}_{-6.92}\ ^{+22.2}_{-18.7}$	$0.313 \pm 0.010\ ^{+0.006}_{-0.007}$
$[\frac{6}{7}\pi, \pi]$	$72.01 \pm 2.68\ ^{+1.81}_{-6.50}\ ^{+17.0}_{-13.9}$	$0.240 \pm 0.009\ ^{+0.003}_{-0.015}$

Table G.4: The inclusive cross section differential in ψ_{AB} . The first column gives the bin range, the second column gives the value of the total cross section and the third column gives the value of the normalised cross section. Also listed are the associated statistical, uncorrelated systematic and energy scale uncertainties.

X_A range	$\sigma(\pm$ stat. syst. Escale) (pb)	$\sigma(\pm$ stat. syst.)
[0.50, 0.58]	$2060 \pm 31.9\ ^{+186}_{-134}\ ^{+502}_{-419}$	$6.942 \pm 0.108\ ^{+0.093}_{-0.069}$
[0.58, 0.66]	$1134 \pm 23.4\ ^{+76.2}_{-51.9}\ ^{+263}_{-211}$	$3.823 \pm 0.079\ ^{+0.058}_{-0.042}$
[0.66, 0.74]	$458.9 \pm 15.68\ ^{+22.1}_{-31.2}\ ^{+85.8}_{-72.6}$	$1.546 \pm 0.053\ ^{+0.026}_{-0.060}$
[0.74, 0.82]	$52.73 \pm 4.67\ ^{+5.33}_{-2.85}\ ^{+8.64}_{-5.92}$	$0.178 \pm 0.016\ ^{+0.026}_{-0.011}$
[0.82, 0.90]	$3.37 \pm 1.49\ ^{+3.39}_{-1.29}\ ^{+0.22}_{-0.29}$	$0.011 \pm 0.005\ ^{+0.010}_{-0.004}$
[0.90, 1.00]	$0.00 \pm 0.00\ ^{+0.00}_{-0.00}\ ^{+0.00}_{-0.00}$	$0.000 \pm 0.000\ ^{+0.000}_{-0.000}$

Table G.5: The inclusive cross section differential in X_A . The first column gives the bin range, the second column gives the value of the total cross section and the third column gives the value of the normalised cross section. Also listed are the associated statistical, uncorrelated systematic and energy scale uncertainties.

Appendix G

$\cos\theta_{3'}$ range	$\sigma(\pm$ stat. syst. Escale) (pb)	$\sigma(\pm$ stat. syst.)
$[-0.80, -0.67]$	$175.7 \pm 7.28\ ^{+11.1}_{-5.59}\ ^{+41.4}_{-32.2}$	$0.591 \pm 0.024\ ^{+0.047}_{-0.029}$
$[-0.67, -0.53]$	$143.0 \pm 6.38\ ^{+8.81}_{-8.93}\ ^{+32.2}_{-25.9}$	$0.481 \pm 0.021\ ^{+0.010}_{-0.012}$
$[-0.53, -0.40]$	$167.3 \pm 7.29\ ^{+22.0}_{-11.6}\ ^{+37.7}_{-32.2}$	$0.563 \pm 0.025\ ^{+0.029}_{-0.022}$
$[-0.40, -0.27]$	$173.5 \pm 7.38\ ^{+14.5}_{-13.2}\ ^{+37.5}_{-34.5}$	$0.584 \pm 0.025\ ^{+0.013}_{-0.019}$
$[-0.27, -0.13]$	$155.6 \pm 6.69\ ^{+14.6}_{-6.74}\ ^{+36.0}_{-30.2}$	$0.523 \pm 0.023\ ^{+0.013}_{-0.006}$
$[-0.13, 0.00]$	$154.8 \pm 6.72\ ^{+12.2}_{-13.7}\ ^{+34.8}_{-28.2}$	$0.521 \pm 0.023\ ^{+0.016}_{-0.020}$
$[0.00, 0.13]$	$169.3 \pm 6.99\ ^{+14.4}_{-10.0}\ ^{+41.4}_{-31.2}$	$0.569 \pm 0.024\ ^{+0.012}_{-0.020}$
$[0.13, 0.27]$	$193.2 \pm 7.71\ ^{+6.72}_{-13.1}\ ^{+45.8}_{-39.5}$	$0.650 \pm 0.026\ ^{+0.008}_{-0.032}$
$[0.27, 0.40]$	$195.0 \pm 7.36\ ^{+19.3}_{-10.5}\ ^{+44.6}_{-37.1}$	$0.656 \pm 0.025\ ^{+0.018}_{-0.011}$
$[0.40, 0.53]$	$195.5 \pm 7.30\ ^{+14.0}_{-11.0}\ ^{+48.3}_{-39.7}$	$0.658 \pm 0.025\ ^{+0.016}_{-0.009}$
$[0.53, 0.67]$	$240.3 \pm 8.39\ ^{+23.4}_{-20.1}\ ^{+55.8}_{-47.5}$	$0.808 \pm 0.028\ ^{+0.019}_{-0.025}$
$[0.67, 0.80]$	$266.9 \pm 9.28\ ^{+24.9}_{-14.9}\ ^{+65.0}_{-51.6}$	$0.898 \pm 0.031\ ^{+0.022}_{-0.018}$

Table G.6: The inclusive cross section differential in $\cos\theta_{3'}$. The first column gives the bin range, the second column gives the value of the total cross section and the third column gives the value of the normalised cross section. Also listed are the associated statistical, uncorrelated systematic and energy scale uncertainties.

Appendix G

$\psi_{3'}$ range	$\sigma(\pm$ stat. syst. Escale) (pb)	$\sigma(\pm$ stat. syst.)
$[0, \frac{1}{12}\pi]$	$79.54 \pm 3.64\ ^{+3.16}_{-4.37}\ ^{+19.2}_{-15.7}$	$0.270 \pm 0.012\ ^{+0.008}_{-0.015}$
$[\frac{1}{12}\pi, \frac{1}{6}\pi]$	$94.97 \pm 3.97\ ^{+6.38}_{-5.72}\ ^{+20.1}_{-18.5}$	$0.322 \pm 0.013\ ^{+0.007}_{-0.010}$
$[\frac{1}{6}\pi, \frac{1}{4}\pi]$	$107.6 \pm 4.21\ ^{+8.07}_{-6.61}\ ^{+25.0}_{-18.6}$	$0.365 \pm 0.014\ ^{+0.007}_{-0.004}$
$[\frac{1}{4}\pi, \frac{1}{3}\pi]$	$90.38 \pm 3.61\ ^{+8.32}_{-1.58}\ ^{+20.5}_{-17.7}$	$0.306 \pm 0.012\ ^{+0.017}_{-0.004}$
$[\frac{1}{3}\pi, \frac{5}{12}\pi]$	$79.61 \pm 3.47\ ^{+8.50}_{-6.09}\ ^{+17.7}_{-15.0}$	$0.270 \pm 0.012\ ^{+0.010}_{-0.006}$
$[\frac{5}{12}\pi, \frac{1}{2}\pi]$	$68.82 \pm 3.10\ ^{+7.63}_{-3.33}\ ^{+15.6}_{-12.1}$	$0.233 \pm 0.010\ ^{+0.010}_{-0.006}$
$[\frac{1}{2}\pi, \frac{7}{12}\pi]$	$73.63 \pm 3.16\ ^{+7.07}_{-6.90}\ ^{+15.2}_{-13.7}$	$0.250 \pm 0.011\ ^{+0.008}_{-0.010}$
$[\frac{7}{12}\pi, \frac{2}{3}\pi]$	$86.66 \pm 3.49\ ^{+8.51}_{-6.24}\ ^{+21.0}_{-17.7}$	$0.294 \pm 0.012\ ^{+0.007}_{-0.007}$
$[\frac{2}{3}\pi, \frac{3}{4}\pi]$	$113.4 \pm 4.00\ ^{+4.89}_{-6.20}\ ^{+27.7}_{-21.6}$	$0.384 \pm 0.014\ ^{+0.006}_{-0.013}$
$[\frac{3}{4}\pi, \frac{5}{6}\pi]$	$126.2 \pm 4.35\ ^{+9.90}_{-7.41}\ ^{+32.2}_{-26.4}$	$0.428 \pm 0.015\ ^{+0.004}_{-0.010}$
$[\frac{5}{6}\pi, \frac{11}{12}\pi]$	$116.0 \pm 4.34\ ^{+7.55}_{-7.57}\ ^{+29.0}_{-22.8}$	$0.393 \pm 0.015\ ^{+0.006}_{-0.009}$
$[\frac{11}{12}\pi, \pi]$	$90.20 \pm 3.74\ ^{+8.44}_{-5.23}\ ^{+21.5}_{-18.1}$	$0.306 \pm 0.013\ ^{+0.008}_{-0.004}$

Table G.7: The inclusive cross section differential in $\psi_{3'}$. The first column gives the bin range, the second column gives the value of the total cross section and the third column gives the value of the normalised cross section. Also listed are the associated statistical, uncorrelated systematic and energy scale uncertainties.

Appendix G

$X_{3'}$ range	$\sigma(\pm$ stat. syst. Escale) (pb)	$\sigma(\pm$ stat. syst.)
[0.67,0.71]	$257.8 \pm 16.2\ ^{+14.2}_{-20.6}\ ^{+51.0}_{-50.3}$	$0.864 \pm 0.054\ ^{+0.019}_{-0.033}$
[0.71,0.75]	$610.7 \pm 24.7\ ^{+67.6}_{-22.5}\ ^{+140}_{-99.2}$	$2.048 \pm 0.083\ ^{+0.089}_{-0.025}$
[0.75,0.79]	$944.5 \pm 30.8\ ^{+59.0}_{-44.3}\ ^{+209}_{-182}$	$3.167 \pm 0.103\ ^{+0.102}_{-0.069}$
[0.79,0.83]	$1182 \pm 33.8\ ^{+88.5}_{-69.1}\ ^{+266}_{-223}$	$3.965 \pm 0.113\ ^{+0.033}_{-0.042}$
[0.83,0.87]	$1504 \pm 40.2\ ^{+88.1}_{-93.0}\ ^{+351}_{-289}$	$5.042 \pm 0.135\ ^{+0.050}_{-0.101}$
[0.87,0.91]	$1484 \pm 38.1\ ^{+124}_{-103}\ ^{+356}_{-291}$	$4.975 \pm 0.128\ ^{+0.066}_{-0.068}$
[0.91,0.95]	$1473 \pm 37.0\ ^{+132}_{-97.9}\ ^{+362}_{-298}$	$4.939 \pm 0.124\ ^{+0.069}_{-0.147}$

Table G.8: The inclusive cross section differential in $X_{3'}$. The first column gives the bin range, the second column gives the value of the total cross section and the third column gives the value of the normalised cross section. Also listed are the associated statistical, uncorrelated systematic and energy scale uncertainties.

$X_{4'}$ range	$\sigma(\pm$ stat. syst. Escale) (pb)	$\sigma(\pm$ stat. syst.)
[0.50,0.55]	$134.6 \pm 10.2\ ^{+15.8}_{-9.48}\ ^{+34.8}_{-27.8}$	$0.454 \pm 0.034\ ^{+0.023}_{-0.018}$
[0.55,0.60]	$798.7 \pm 24.6\ ^{+70.6}_{-50.5}\ ^{+212}_{-167}$	$2.691 \pm 0.083\ ^{+0.039}_{-0.024}$
[0.60,0.65]	$1425 \pm 33.1\ ^{+117}_{-78.5}\ ^{+335}_{-282}$	$4.801 \pm 0.112\ ^{+0.039}_{-0.078}$
[0.65,0.70]	$1723 \pm 37.3\ ^{+147}_{-131}\ ^{+387}_{-324}$	$5.807 \pm 0.126\ ^{+0.061}_{-0.123}$
[0.70,0.75]	$1087 \pm 29.3\ ^{+96.5}_{-43.9}\ ^{+245}_{-198}$	$3.662 \pm 0.099\ ^{+0.107}_{-0.033}$
[0.75,0.80]	$559.4 \pm 21.5\ ^{+13.4}_{-26.4}\ ^{+123}_{-107}$	$1.885 \pm 0.073\ ^{+0.033}_{-0.106}$
[0.80,0.85]	$181.7 \pm 12.3\ ^{+8.32}_{-4.83}\ ^{+32.2}_{-27.0}$	$0.612 \pm 0.041\ ^{+0.033}_{-0.028}$
[0.85,0.90]	$26.27 \pm 5.18\ ^{+3.57}_{-4.16}\ ^{+7.49}_{-5.77}$	$0.088 \pm 0.017\ ^{+0.012}_{-0.018}$
[0.90,0.95]	$0.166 \pm 0.375\ ^{+1.42}_{-0.041}\ ^{+0.045}_{-0.057}$	$0.001 \pm 0.001\ ^{+0.005}_{-0.000}$
[0.95,1.00]	$0.000 \pm 0.000\ ^{+0.000}_{-0.000}\ ^{+0.000}_{-0.000}$	$0.000 \pm 0.000\ ^{+0.000}_{-0.000}$

Table G.9: The inclusive cross section differential in $X_{4'}$. The first column gives the bin range, the second column gives the value of the total cross section and the third column gives the value of the normalised cross section. Also listed are the associated statistical, uncorrelated systematic and energy scale uncertainties.

Appendix G

$\cos\theta_{3'}$ range	$\sigma(\pm$ stat. syst. Escale) (pb)	$\sigma(\pm$ stat. syst.)
$[-0.80, -0.67]$	$101.2 \pm 5.24\ ^{+6.30}_{-4.16}\ ^{+24.4}_{-19.7}$	$0.483 \pm 0.025\ ^{+0.039}_{-0.028}$
$[-0.67, -0.53]$	$91.10 \pm 4.92\ ^{+6.27}_{-7.56}\ ^{+21.4}_{-18.7}$	$0.435 \pm 0.023\ ^{+0.010}_{-0.013}$
$[-0.53, -0.40]$	$116.9 \pm 5.97\ ^{+17.8}_{-11.8}\ ^{+26.6}_{-23.8}$	$0.558 \pm 0.028\ ^{+0.031}_{-0.022}$
$[-0.40, -0.27]$	$123.7 \pm 6.15\ ^{+13.9}_{-13.7}\ ^{+27.4}_{-25.3}$	$0.590 \pm 0.029\ ^{+0.019}_{-0.019}$
$[-0.27, -0.13]$	$113.3 \pm 5.64\ ^{+13.4}_{-7.73}\ ^{+27.4}_{-23.5}$	$0.540 \pm 0.027\ ^{+0.018}_{-0.005}$
$[-0.13, 0.00]$	$115.7 \pm 5.89\ ^{+12.0}_{-15.2}\ ^{+26.8}_{-22.1}$	$0.552 \pm 0.028\ ^{+0.017}_{-0.030}$
$[0.00, 0.13]$	$117.9 \pm 5.73\ ^{+11.0}_{-9.84}\ ^{+30.6}_{-23.2}$	$0.563 \pm 0.027\ ^{+0.017}_{-0.028}$
$[0.13, 0.27]$	$149.2 \pm 6.77\ ^{+6.02}_{-15.4}\ ^{+35.9}_{-31.8}$	$0.711 \pm 0.032\ ^{+0.006}_{-0.040}$
$[0.27, 0.40]$	$155.9 \pm 6.61\ ^{+21.4}_{-13.0}\ ^{+36.4}_{-30.3}$	$0.744 \pm 0.032\ ^{+0.034}_{-0.013}$
$[0.40, 0.53]$	$147.5 \pm 6.25\ ^{+13.9}_{-10.1}\ ^{+38.9}_{-31.7}$	$0.703 \pm 0.030\ ^{+0.020}_{-0.010}$
$[0.53, 0.67]$	$168.7 \pm 6.83\ ^{+17.0}_{-18.0}\ ^{+40.1}_{-36.4}$	$0.805 \pm 0.033\ ^{+0.021}_{-0.019}$
$[0.67, 0.80]$	$171.2 \pm 7.19\ ^{+14.9}_{-14.6}\ ^{+42.9}_{-35.2}$	$0.817 \pm 0.034\ ^{+0.017}_{-0.024}$

Table G.10: The inclusive cross section differential in $\cos\theta_{3'}$ for $x_{\gamma;4J}^{OBS} < 0.75$. The first column gives the bin range, the second column gives the value of the total cross section and the third column gives the value of the normalised cross section. Also listed are the associated statistical, uncorrelated systematic and energy scale uncertainties.

Appendix G

$\cos\theta_{3'}$ range	$\sigma(\pm$ stat. syst. Escale) (pb)	$\sigma(\pm$ stat. syst.)
$[-0.80, -0.67]$	$77.80 \pm 5.54\ ^{+7.63}_{-6.44}\ ^{+18.1}_{-13.5}$	$0.894 \pm 0.064\ ^{+0.047}_{-0.056}$
$[-0.67, -0.53]$	$54.42 \pm 4.38\ ^{+7.01}_{-3.56}\ ^{+11.2}_{-6.74}$	$0.625 \pm 0.050\ ^{+0.040}_{-0.046}$
$[-0.53, -0.40]$	$49.16 \pm 4.26\ ^{+4.39}_{-2.22}\ ^{+11.2}_{-8.01}$	$0.565 \pm 0.049\ ^{+0.023}_{-0.027}$
$[-0.40, -0.27]$	$46.27 \pm 4.01\ ^{+1.45}_{-1.30}\ ^{+9.42}_{-8.98}$	$0.532 \pm 0.046\ ^{+0.013}_{-0.033}$
$[-0.27, -0.13]$	$39.98 \pm 3.59\ ^{+3.34}_{-2.16}\ ^{+7.52}_{-6.00}$	$0.459 \pm 0.041\ ^{+0.012}_{-0.024}$
$[-0.13, 0.00]$	$33.95 \pm 2.97\ ^{+3.18}_{-1.17}\ ^{+6.82}_{-5.34}$	$0.390 \pm 0.034\ ^{+0.021}_{-0.010}$
$[0.00, 0.13]$	$50.24 \pm 4.21\ ^{+3.84}_{-0.512}\ ^{+8.73}_{-6.96}$	$0.577 \pm 0.048\ ^{+0.029}_{-0.022}$
$[0.13, 0.27]$	$40.36 \pm 3.56\ ^{+5.37}_{-2.09}\ ^{+9.30}_{-7.07}$	$0.464 \pm 0.041\ ^{+0.041}_{-0.014}$
$[0.27, 0.40]$	$37.65 \pm 3.16\ ^{+4.41}_{-2.43}\ ^{+7.92}_{-6.81}$	$0.433 \pm 0.036\ ^{+0.032}_{-0.041}$
$[0.40, 0.53]$	$51.39 \pm 3.99\ ^{+5.53}_{-3.28}\ ^{+9.00}_{-8.13}$	$0.591 \pm 0.046\ ^{+0.029}_{-0.056}$
$[0.53, 0.67]$	$73.40 \pm 5.21\ ^{+7.45}_{-2.52}\ ^{+15.9}_{-9.66}$	$0.843 \pm 0.060\ ^{+0.034}_{-0.026}$
$[0.67, 0.80]$	$98.07 \pm 6.19\ ^{+12.5}_{-3.01}\ ^{+22.5}_{-16.5}$	$1.127 \pm 0.071\ ^{+0.080}_{-0.024}$

Table G.11: The inclusive cross section differential in $\cos\theta_{3'}$ for $x_{\gamma;4J}^{\mathrm{OBS}} > 0.75$. The first column gives the bin range, the second column gives the value of the total cross section and the third column gives the value of the normalised cross section. Also listed are the associated statistical, uncorrelated systematic and energy scale uncertainties.

Appendix G

$x_{\gamma;4J}^{OBS}$ range	$\sigma(\pm$ stat. syst. Escale) (pb)	$\sigma(\pm$ stat. syst.)
[0.0,0.1]	$0.000 \pm 0.000\ ^{+0.000}_{-0.000}\ ^{+0.000}_{-0.000}$	$0.000 \pm 0.000\ ^{+0.000}_{-0.000}$
[0.1,0.2]	$0.000 \pm 0.000\ ^{+7.96}_{-0.000}\ ^{+0.000}_{-0.000}$	$0.000 \pm 0.000\ ^{+0.127}_{-0.000}$
[0.2,0.3]	$28.31 \pm 8.08\ ^{+7.68}_{-16.9}\ ^{+2.70}_{-11.5}$	$0.456 \pm 0.130\ ^{+0.108}_{-0.268}$
[0.3,0.4]	$30.10 \pm 4.51\ ^{+6.49}_{-3.94}\ ^{+3.78}_{-3.21}$	$0.485 \pm 0.073\ ^{+0.099}_{-0.054}$
[0.4,0.5]	$38.61 \pm 4.31\ ^{+5.64}_{-1.74}\ ^{+4.16}_{-5.20}$	$0.622 \pm 0.070\ ^{+0.080}_{-0.021}$
[0.5,0.6]	$50.59 \pm 4.63\ ^{+6.88}_{-2.98}\ ^{+9.25}_{-8.03}$	$0.816 \pm 0.075\ ^{+0.094}_{-0.042}$
[0.6,0.7]	$48.37 \pm 4.12\ ^{+5.56}_{-4.26}\ ^{+8.91}_{-5.90}$	$0.780 \pm 0.066\ ^{+0.075}_{-0.070}$
[0.7,0.8]	$82.83 \pm 5.81\ ^{+3.45}_{-5.73}\ ^{+13.1}_{-7.09}$	$1.336 \pm 0.094\ ^{+0.054}_{-0.096}$
[0.8,0.9]	$185.3 \pm 10.0\ ^{+13.2}_{-12.7}\ ^{+17.1}_{-19.2}$	$2.987 \pm 0.162\ ^{+0.174}_{-0.194}$
[0.9,1.0]	$156.1 \pm 9.14\ ^{+8.60}_{-5.71}\ ^{+27.5}_{-20.6}$	$2.517 \pm 0.147\ ^{+0.141}_{-0.096}$

Table G.12: The high mass cross section differential in $x_{\gamma;4J}^{OBS}$. The first column gives the bin range, the second column gives the value of the total cross section and the third column gives the value of the normalised cross section. Also listed are the associated statistical, uncorrelated systematic and energy scale uncertainties.

y range	$\sigma(\pm$ stat. syst. Escale) (pb)	$\sigma(\pm$ stat. syst.)
[0.20, 0.29]	$20.53 \pm 3.95\ ^{+1.85}_{-3.21}\ ^{+2.98}_{-2.24}$	$0.337 \pm 0.065\ ^{+0.026}_{-0.053}$
[0.29, 0.39]	$57.73 \pm 5.90\ ^{+4.02}_{-3.06}\ ^{+7.92}_{-5.39}$	$0.948 \pm 0.097\ ^{+0.080}_{-0.072}$
[0.39, 0.48]	$102.7 \pm 7.76\ ^{+7.13}_{-3.82}\ ^{+13.5}_{-11.1}$	$1.686 \pm 0.127\ ^{+0.075}_{-0.048}$
[0.48, 0.57]	$106.3 \pm 7.26\ ^{+12.6}_{-5.14}\ ^{+11.5}_{-12.8}$	$1.745 \pm 0.119\ ^{+0.148}_{-0.043}$
[0.57, 0.66]	$113.6 \pm 7.19\ ^{+3.61}_{-4.55}\ ^{+15.8}_{-11.7}$	$1.865 \pm 0.118\ ^{+0.032}_{-0.058}$
[0.66, 0.76]	$116.7 \pm 7.47\ ^{+8.88}_{-4.81}\ ^{+20.2}_{-14.8}$	$1.917 \pm 0.123\ ^{+0.082}_{-0.093}$
[0.76, 0.85]	$138.4 \pm 8.85\ ^{+7.68}_{-4.91}\ ^{+20.8}_{-20.7}$	$2.272 \pm 0.145\ ^{+0.070}_{-0.105}$

Table G.13: The high mass cross section differential in y . The first column gives the bin range, the second column gives the value of the total cross section and the third column gives the value of the normalised cross section. Also listed are the associated statistical, uncorrelated systematic and energy scale uncertainties.

Appendix G

ψ_{AB} range	$\sigma(\pm$ stat. syst. Escale) (pb)	$\sigma(\pm$ stat. syst.)
$[0, \frac{1}{7}\pi]$	$18.02 \pm 1.53\ ^{+2.49}_{-1.15}\ ^{+1.71}_{-1.40}$	$0.297 \pm 0.025\ ^{+0.033}_{-0.020}$
$[\frac{1}{7}\pi, \frac{2}{7}\pi]$	$17.42 \pm 1.34\ ^{+1.59}_{-0.667}\ ^{+3.13}_{-1.41}$	$0.287 \pm 0.022\ ^{+0.022}_{-0.011}$
$[\frac{2}{7}\pi, \frac{3}{7}\pi]$	$22.50 \pm 1.53\ ^{+1.89}_{-1.39}\ ^{+3.38}_{-2.92}$	$0.371 \pm 0.025\ ^{+0.018}_{-0.020}$
$[\frac{3}{7}\pi, \frac{4}{7}\pi]$	$21.82 \pm 1.48\ ^{+0.743}_{-0.892}\ ^{+2.44}_{-3.35}$	$0.359 \pm 0.024\ ^{+0.006}_{-0.016}$
$[\frac{4}{7}\pi, \frac{5}{7}\pi]$	$20.61 \pm 1.46\ ^{+2.22}_{-0.959}\ ^{+3.47}_{-2.36}$	$0.339 \pm 0.024\ ^{+0.027}_{-0.011}$
$[\frac{5}{7}\pi, \frac{6}{7}\pi]$	$19.90 \pm 1.53\ ^{+0.848}_{-1.14}\ ^{+2.75}_{-2.85}$	$0.328 \pm 0.025\ ^{+0.012}_{-0.021}$
$[\frac{6}{7}\pi, \pi]$	$15.02 \pm 1.29\ ^{+0.977}_{-1.22}\ ^{+2.20}_{-1.58}$	$0.247 \pm 0.021\ ^{+0.016}_{-0.019}$

Table G.14: The high mass cross section differential in ψ_{AB} . The first column gives the bin range, the second column gives the value of the total cross section and the third column gives the value of the normalised cross section. Also listed are the associated statistical, uncorrelated systematic and energy scale uncertainties.

X_A range	$\sigma(\pm$ stat. syst. Escale) (pb)	$\sigma(\pm$ stat. syst.)
[0.50, 0.58]	$306.1 \pm 14.0\ ^{+17.1}_{-15.1}\ ^{+37.1}_{-31.9}$	$5.022 \pm 0.230\ ^{+0.159}_{-0.175}$
[0.58, 0.66]	$248.7 \pm 12.5\ ^{+13.8}_{-15.9}\ ^{+37.0}_{-34.8}$	$4.080 \pm 0.204\ ^{+0.155}_{-0.186}$
[0.66, 0.74]	$152.0 \pm 9.31\ ^{+10.1}_{-7.1}\ ^{+23.8}_{-17.2}$	$2.494 \pm 0.153\ ^{+0.108}_{-0.112}$
[0.74, 0.82]	$50.96 \pm 5.10\ ^{+4.10}_{-1.72}\ ^{+8.66}_{-6.54}$	$0.836 \pm 0.084\ ^{+0.084}_{-0.042}$
[0.82, 0.90]	$4.14 \pm 1.63\ ^{+3.21}_{-1.55}\ ^{+0.29}_{-0.46}$	$0.068 \pm 0.027\ ^{+0.050}_{-0.026}$
[0.90, 1.00]	$0.00 \pm 0.00\ ^{+0.00}_{-0.00}\ ^{+0.00}_{-0.00}$	$0.000 \pm 0.000\ ^{+0.000}_{-0.000}$

Table G.15: The high mass cross section differential in X_A . The first column gives the bin range, the second column gives the value of the total cross section and the third column gives the value of the normalised cross section. Also listed are the associated statistical, uncorrelated systematic and energy scale uncertainties.

Appendix G

$\cos\theta_{3'}$ range	$\sigma(\pm$ stat. syst. Escale) (pb)	$\sigma(\pm$ stat. syst.)
$[-0.80, -0.67]$	$61.97 \pm 4.82\ ^{+5.70}_{-4.68}\ ^{+9.59}_{-6.71}$	$1.021 \pm 0.079\ ^{+0.082}_{-0.071}$
$[-0.67, -0.53]$	$34.90 \pm 3.44\ ^{+3.07}_{-2.19}\ ^{+4.25}_{-1.68}$	$0.575 \pm 0.057\ ^{+0.040}_{-0.034}$
$[-0.53, -0.40]$	$23.51 \pm 2.80\ ^{+3.99}_{-1.44}\ ^{+2.93}_{-3.21}$	$0.387 \pm 0.046\ ^{+0.051}_{-0.017}$
$[-0.40, -0.27]$	$20.44 \pm 2.47\ ^{+3.91}_{-0.416}\ ^{+3.43}_{-2.09}$	$0.337 \pm 0.041\ ^{+0.063}_{-0.012}$
$[-0.27, -0.13]$	$21.45 \pm 2.65\ ^{+3.05}_{-1.49}\ ^{+2.72}_{-2.27}$	$0.353 \pm 0.044\ ^{+0.040}_{-0.022}$
$[-0.13, 0.00]$	$20.65 \pm 2.53\ ^{+1.37}_{-1.01}\ ^{+1.53}_{-2.21}$	$0.340 \pm 0.042\ ^{+0.020}_{-0.020}$
$[0.00, 0.13]$	$18.02 \pm 2.19\ ^{+2.27}_{-2.20}\ ^{+1.84}_{-2.29}$	$0.297 \pm 0.036\ ^{+0.032}_{-0.034}$
$[0.13, 0.27]$	$28.09 \pm 3.29\ ^{+1.06}_{-2.57}\ ^{+3.47}_{-4.28}$	$0.463 \pm 0.054\ ^{+0.016}_{-0.047}$
$[0.27, 0.40]$	$29.48 \pm 3.10\ ^{+1.35}_{-4.85}\ ^{+3.36}_{-3.50}$	$0.486 \pm 0.051\ ^{+0.011}_{-0.082}$
$[0.40, 0.53]$	$44.56 \pm 4.17\ ^{+2.15}_{-2.57}\ ^{+4.27}_{-5.73}$	$0.734 \pm 0.069\ ^{+0.038}_{-0.047}$
$[0.53, 0.67]$	$68.85 \pm 5.71\ ^{+3.39}_{-3.68}\ ^{+11.9}_{-8.73}$	$1.135 \pm 0.094\ ^{+0.031}_{-0.078}$
$[0.67, 0.80]$	$83.21 \pm 5.70\ ^{+11.5}_{-4.19}\ ^{+15.7}_{-11.7}$	$1.371 \pm 0.094\ ^{+0.146}_{-0.039}$

Table G.16: The high mass cross section differential in $\cos\theta_{3'}$. The first column gives the bin range, the second column gives the value of the total cross section and the third column gives the value of the normalised cross section. Also listed are the associated statistical, uncorrelated systematic and energy scale uncertainties.

Appendix G

$\psi_{3'}$ range	$\sigma(\pm$ stat. syst. Escale) (pb)	$\sigma(\pm$ stat. syst.)
$[0, \frac{1}{12}\pi]$	$20.79 \pm 2.04\ ^{+1.89\ +3.29}_{-0.805\ -3.22}$	$0.342 \pm 0.033\ ^{+0.024}_{-0.015}$
$[\frac{1}{12}\pi, \frac{1}{6}\pi]$	$20.82 \pm 2.03\ ^{+1.47\ +3.92}_{-1.86\ -2.38}$	$0.342 \pm 0.033\ ^{+0.016}_{-0.027}$
$[\frac{1}{6}\pi, \frac{1}{4}\pi]$	$20.36 \pm 1.99\ ^{+2.84\ +1.95}_{-1.41\ -1.81}$	$0.335 \pm 0.033\ ^{+0.050}_{-0.022}$
$[\frac{1}{4}\pi, \frac{1}{3}\pi]$	$17.01 \pm 1.74\ ^{+0.942\ +1.37}_{-1.86\ -1.58}$	$0.280 \pm 0.029\ ^{+0.010}_{-0.027}$
$[\frac{1}{3}\pi, \frac{5}{12}\pi]$	$13.42 \pm 1.44\ ^{+1.49\ +1.08}_{-0.563\ -1.29}$	$0.221 \pm 0.024\ ^{+0.018}_{-0.009}$
$[\frac{5}{12}\pi, \frac{1}{2}\pi]$	$12.87 \pm 1.52\ ^{+1.46\ +1.53}_{-1.61\ -1.19}$	$0.211 \pm 0.025\ ^{+0.017}_{-0.022}$
$[\frac{1}{2}\pi, \frac{7}{12}\pi]$	$13.73 \pm 1.56\ ^{+0.984\ +2.32}_{-1.42\ -1.17}$	$0.226 \pm 0.026\ ^{+0.012}_{-0.024}$
$[\frac{7}{12}\pi, \frac{2}{3}\pi]$	$12.98 \pm 1.42\ ^{+1.62\ +2.29}_{-0.563\ -1.50}$	$0.213 \pm 0.023\ ^{+0.024}_{-0.013}$
$[\frac{2}{3}\pi, \frac{3}{4}\pi]$	$19.44 \pm 1.85\ ^{+1.04\ +2.87}_{-2.81\ -2.01}$	$0.320 \pm 0.030\ ^{+0.012}_{-0.044}$
$[\frac{3}{4}\pi, \frac{5}{6}\pi]$	$27.22 \pm 2.27\ ^{+2.16\ +3.94}_{-1.88\ -3.45}$	$0.447 \pm 0.037\ ^{+0.036}_{-0.025}$
$[\frac{5}{6}\pi, \frac{11}{12}\pi]$	$29.90 \pm 2.51\ ^{+1.60\ +4.42}_{-2.04\ -4.73}$	$0.491 \pm 0.041\ ^{+0.021}_{-0.043}$
$[\frac{11}{12}\pi, \pi]$	$23.85 \pm 2.11\ ^{+3.00\ +3.95}_{-1.10\ -3.52}$	$0.392 \pm 0.035\ ^{+0.039}_{-0.012}$

Table G.17: The high mass cross section differential in $\psi_{3'}$. The first column gives the bin range, the second column gives the value of the total cross section and the third column gives the value of the normalised cross section. Also listed are the associated statistical, uncorrelated systematic and energy scale uncertainties.

Appendix G

$X_{3'}$ range	$\sigma(\pm$ stat. syst. Escale) (pb)	$\sigma(\pm$ stat. syst.)
[0.67,0.71]	$77.08 \pm 10.2\ ^{+6.40}_{-12.8}\ ^{+11.1}_{-10.7}$	$1.267 \pm 0.168\ ^{+0.081}_{-0.220}$
[0.71,0.75]	$174.4 \pm 15.0\ ^{+11.9}_{-10.9}\ ^{+31.1}_{-23.4}$	$2.867 \pm 0.247\ ^{+0.132}_{-0.141}$
[0.75,0.79]	$229.3 \pm 15.8\ ^{+24.3}_{-4.40}\ ^{+30.9}_{-27.9}$	$3.770 \pm 0.260\ ^{+0.335}_{-0.023}$
[0.79,0.83]	$266.4 \pm 17.2\ ^{+13.3}_{-10.4}\ ^{+43.8}_{-25.3}$	$4.378 \pm 0.283\ ^{+0.210}_{-0.189}$
[0.83,0.87]	$296.3 \pm 19.5\ ^{+12.2}_{-21.3}\ ^{+30.6}_{-40.6}$	$4.870 \pm 0.320\ ^{+0.121}_{-0.328}$
[0.87,0.91]	$242.7 \pm 17.2\ ^{+13.8}_{-6.86}\ ^{+36.1}_{-27.3}$	$3.989 \pm 0.282\ ^{+0.213}_{-0.170}$
[0.91,0.95]	$234.8 \pm 17.7\ ^{+14.5}_{-21.5}\ ^{+30.7}_{-27.6}$	$3.859 \pm 0.291\ ^{+0.170}_{-0.283}$

Table G.18: The high mass cross section differential in $X_{3'}$. The first column gives the bin range, the second column gives the value of the total cross section and the third column gives the value of the normalised cross section. Also listed are the associated statistical, uncorrelated systematic and energy scale uncertainties.

$X_{4'}$ range	$\sigma(\pm$ stat. syst. Escale) (pb)	$\sigma(\pm$ stat. syst.)
[0.50,0.55]	$8.766 \pm 2.81\ ^{+2.65}_{-4.21}\ ^{+0.783}_{-1.30}$	$0.144 \pm 0.046\ ^{+0.039}_{-0.068}$
[0.55,0.60]	$102.3 \pm 10.6\ ^{+5.06}_{-12.7}\ ^{+9.58}_{-11.9}$	$1.682 \pm 0.174\ ^{+0.073}_{-0.207}$
[0.60,0.65]	$206.0 \pm 13.2\ ^{+18.6}_{-8.85}\ ^{+32.8}_{-23.5}$	$3.387 \pm 0.217\ ^{+0.216}_{-0.111}$
[0.65,0.70]	$372.6 \pm 19.2\ ^{+19.5}_{-17.2}\ ^{+45.3}_{-38.4}$	$6.125 \pm 0.316\ ^{+0.177}_{-0.246}$
[0.70,0.75]	$252.2 \pm 15.3\ ^{+19.6}_{-8.25}\ ^{+36.5}_{-33.7}$	$4.145 \pm 0.251\ ^{+0.241}_{-0.124}$
[0.75,0.80]	$170.4 \pm 13.4\ ^{+9.39}_{-12.5}\ ^{+28.7}_{-24.1}$	$2.801 \pm 0.220\ ^{+0.120}_{-0.194}$
[0.80,0.85]	$86.31 \pm 9.74\ ^{+14.9}_{-6.60}\ ^{+13.3}_{-9.10}$	$1.419 \pm 0.160\ ^{+0.257}_{-0.110}$
[0.85,0.90]	$17.97 \pm 4.49\ ^{+3.61}_{-1.60}\ ^{+4.81}_{-3.54}$	$0.295 \pm 0.074\ ^{+0.063}_{-0.027}$
[0.90,0.95]	$0.148 \pm 0.290\ ^{+0.940}_{-0.052}\ ^{+0.003}_{-0.054}$	$0.002 \pm 0.005\ ^{+0.016}_{-0.001}$
[0.95,1.00]	$0.000 \pm 0.000\ ^{+0.000}_{-0.000}\ ^{+0.000}_{-0.000}$	$0.000 \pm 0.000\ ^{+0.000}_{-0.000}$

Table G.19: The high mass cross section differential in $X_{4'}$. The first column gives the bin range, the second column gives the value of the total cross section and the third column gives the value of the normalised cross section. Also listed are the associated statistical, uncorrelated systematic and energy scale uncertainties.

Appendix G

$\cos\theta_{3'}$ range	$\sigma(\pm$ stat. syst. Escale) (pb)	$\sigma(\pm$ stat. syst.)
$[-0.80, -0.67]$	$19.49 \pm 2.55\ ^{+3.18\ +3.86}_{-1.56\ -2.53}$	$0.860 \pm 0.112\ ^{+0.179}_{-0.091}$
$[-0.67, -0.53]$	$7.309 \pm 1.33\ ^{+1.63\ +0.821}_{-0.584\ -0.523}$	$0.323 \pm 0.059\ ^{+0.072}_{-0.034}$
$[-0.53, -0.40]$	$7.965 \pm 1.60\ ^{+2.32\ +1.11}_{-0.841\ -1.60}$	$0.352 \pm 0.071\ ^{+0.077}_{-0.026}$
$[-0.40, -0.27]$	$6.610 \pm 1.31\ ^{+2.15\ +0.966}_{-0.237\ -0.432}$	$0.292 \pm 0.058\ ^{+0.087}_{-0.022}$
$[-0.27, -0.13]$	$7.227 \pm 1.49\ ^{+2.08\ +1.38}_{-0.815\ -0.755}$	$0.319 \pm 0.066\ ^{+0.069}_{-0.036}$
$[-0.13, 0.00]$	$7.942 \pm 1.54\ ^{+1.40\ +0.835}_{-0.974\ -0.953}$	$0.351 \pm 0.068\ ^{+0.040}_{-0.048}$
$[0.00, 0.13]$	$5.047 \pm 1.02\ ^{+1.52\ +0.719}_{-1.08\ -0.863}$	$0.223 \pm 0.045\ ^{+0.053}_{-0.037}$
$[0.13, 0.27]$	$12.71 \pm 2.32\ ^{+0.933\ +1.64}_{-1.81\ -1.10}$	$0.561 \pm 0.102\ ^{+0.076}_{-0.110}$
$[0.27, 0.40]$	$15.06 \pm 2.61\ ^{+1.53\ +1.92}_{-4.28\ -1.92}$	$0.665 \pm 0.115\ ^{+0.040}_{-0.210}$
$[0.40, 0.53]$	$16.84 \pm 2.46\ ^{+1.61\ +1.45}_{-4.08\ -2.59}$	$0.743 \pm 0.109\ ^{+0.043}_{-0.148}$
$[0.53, 0.67]$	$33.08 \pm 3.90\ ^{+3.32\ +6.14}_{-6.12\ -5.65}$	$1.460 \pm 0.172\ ^{+0.073}_{-0.198}$
$[0.67, 0.80]$	$30.63 \pm 3.19\ ^{+7.43\ +7.23}_{-4.06\ -4.68}$	$1.352 \pm 0.141\ ^{+0.215}_{-0.101}$

Table G.20: The high mass differential cross section differential in $\cos\theta_{3'}$ for $x^{\mathrm{OBS}}_{\gamma;4\mathrm{J}} < 0.75$. The first column gives the bin range, the second column gives the value of the total cross section and the third column gives the value of the normalised cross section. Also listed are the associated statistical, uncorrelated systematic and energy scale uncertainties.

Appendix G

$\cos\theta_{3'}$ range	$\sigma(\pm$ stat. syst. Escale) (pb)	$\sigma(\pm$ stat. syst.)
$[-0.80, -0.67]$	$42.66 \pm 4.16\ ^{+3.73}_{-4.43}\ ^{+5.43}_{-4.07}$	$1.116 \pm 0.109\ ^{+0.059}_{-0.091}$
$[-0.67, -0.53]$	$27.83 \pm 3.35\ ^{+1.83}_{-1.96}\ ^{+3.70}_{-1.06}$	$0.728 \pm 0.088\ ^{+0.039}_{-0.041}$
$[-0.53, -0.40]$	$15.49 \pm 2.30\ ^{+1.75}_{-1.63}\ ^{+1.81}_{-1.51}$	$0.405 \pm 0.060\ ^{+0.045}_{-0.039}$
$[-0.40, -0.27]$	$13.48 \pm 2.10\ ^{+2.03}_{-0.483}\ ^{+2.56}_{-1.83}$	$0.353 \pm 0.055\ ^{+0.050}_{-0.012}$
$[-0.27, -0.13]$	$14.13 \pm 2.20\ ^{+0.998}_{-0.969}\ ^{+1.19}_{-1.53}$	$0.370 \pm 0.057\ ^{+0.028}_{-0.026}$
$[-0.13, 0.00]$	$12.56 \pm 1.99\ ^{+1.12}_{-1.41}\ ^{+0.662}_{-1.23}$	$0.329 \pm 0.052\ ^{+0.026}_{-0.039}$
$[0.00, 0.13]$	$13.60 \pm 2.10\ ^{+0.679}_{-1.51}\ ^{+1.04}_{-1.34}$	$0.356 \pm 0.055\ ^{+0.031}_{-0.047}$
$[0.13, 0.27]$	$14.67 \pm 2.30\ ^{+0.867}_{-1.48}\ ^{+1.77}_{-3.38}$	$0.384 \pm 0.060\ ^{+0.027}_{-0.044}$
$[0.27, 0.40]$	$13.54 \pm 1.88\ ^{+0.962}_{-2.06}\ ^{+1.35}_{-1.48}$	$0.354 \pm 0.049\ ^{+0.022}_{-0.059}$
$[0.40, 0.53]$	$28.86 \pm 3.48\ ^{+2.80}_{-1.28}\ ^{+3.12}_{-3.12}$	$0.755 \pm 0.091\ ^{+0.069}_{-0.042}$
$[0.53, 0.67]$	$35.52 \pm 4.13\ ^{+4.72}_{-4.80}\ ^{+5.65}_{-3.08}$	$0.929 \pm 0.108\ ^{+0.102}_{-0.101}$
$[0.67, 0.80]$	$54.36 \pm 4.94\ ^{+7.53}_{-3.57}\ ^{+8.33}_{-7.22}$	$1.422 \pm 0.129\ ^{+0.150}_{-0.056}$

Table G.21: The high mass differential cross section differential in $\cos\theta_{3'}$ for $x^{\mathrm{OBS}}_{\gamma;4\mathrm{J}} > 0.75$. The first column gives the bin range, the second column gives the value of the total cross section and the third column gives the value of the normalised cross section. Also listed are the associated statistical, uncorrelated systematic and energy scale uncertainties.

Appendix H

Rapidity Gaps Results

Tables of Data

This appendix contains the values of all differential cross sections and gap fractions measured in the Rapidity Gaps Between Jets in Photoproduction analysis presented in this thesis. Also listed are the associated statistical, uncorrelated systematic and energy scale uncertainties.

E_T^{gap} range	$\sigma(\pm$ stat. syst. Escale) (nb)
[0,0.5]	$0.241 \pm 0.009\ ^{+0.038}_{-0.027}\ ^{+0.008}_{-0.003}$
[0.5,1.5]	$0.226 \pm 0.005\ ^{+0.024}_{-0.012}\ ^{+0.004}_{-0.004}$
[1.5,3.5]	$0.279 \pm 0.003\ ^{+0.021}_{-0.012}\ ^{+0.002}_{-0.006}$
[3.5,7]	$0.245 \pm 0.002\ ^{+0.014}_{-0.008}\ ^{+0.009}_{-0.012}$
[7,12]	$0.121 \pm 0.001\ ^{+0.005}_{-0.004}\ ^{+0.009}_{-0.011}$

Table H.1: The value of the measured differential cross section $d\sigma/dE_T^{gap}$ for the inclusive sample of events. Also listed are the associated statistical, uncorrelated systematic and energy scale uncertainties.

Appendix H

$\Delta\eta$ range	$\sigma(\pm$ stat. syst. Escale) (nb)
[2.5,2.8]	$3.667 \pm 0.030\ ^{+0.186\ +0.152}_{-0.097\ -0.187}$
[2.8,3.1]	$2.457 \pm 0.024\ ^{+0.148\ +0.115}_{-0.071\ -0.144}$
[3.1,3.5]	$1.400 \pm 0.016\ ^{+0.082\ +0.070}_{-0.054\ -0.081}$
[3.5,4]	$0.357 \pm 0.007\ ^{+0.031\ +0.016}_{-0.018\ -0.022}$

Table H.2: The value of the measured differential cross section $d\sigma/d\Delta\eta$ for the inclusive sample of events. Also listed are the associated statistical, uncorrelated systematic and energy scale uncertainties.

$x_{\gamma;2J}^{OBS}$ range	$\sigma(\pm$ stat. syst. Escale) (nb)
[0,0.5]	$0.717 \pm 0.010\ ^{+0.044\ +0.053}_{-0.031\ -0.063}$
[0.5,0.75]	$4.245 \pm 0.034\ ^{+0.186\ +0.210}_{-0.121\ -0.283}$
[0.75,0.9]	$6.038 \pm 0.055\ ^{+0.462\ +0.209}_{-0.236\ -0.261}$
[0.9,1]	$2.421 \pm 0.050\ ^{+0.237\ +0.061}_{-0.147\ -0.006}$

Table H.3: The value of the measured differential cross section $d\sigma/dx_{\gamma;2J}^{OBS}$ for the inclusive sample of events. Also listed are the associated statistical, uncorrelated systematic and energy scale uncertainties.

$\log_{10}(x_{p;2J}^{OBS})$ range	$\sigma(\pm$ stat. syst. Escale) (nb)
[-2,-1.75]	$1.084 \pm 0.014\ ^{+0.115\ +0.003}_{-0.064\ -0.019}$
[-1.75,-1.5]	$4.651 \pm 0.035\ ^{+0.277\ +0.229}_{-0.124\ -0.260}$
[-1.5,-1.25]	$4.189 \pm 0.046\ ^{+0.133\ +0.305}_{-0.106\ -0.320}$
[-1.25,-1]	$0.539 \pm 0.016\ ^{+0.015\ +0.049}_{-0.020\ -0.054}$

Table H.4: The value of the measured differential cross section $d\sigma/d\log_{10}(x_{p;2J}^{OBS})$ for the inclusive sample of events. Also listed are the associated statistical, uncorrelated systematic and energy scale uncertainties.

y range	$\sigma(\pm$ stat. syst. Escale) (nb)
[0.2,0.3625]	$1.238 \pm 0.027\ ^{+0.172}_{-0.092}\ ^{+0.051}_{-0.051}$
[0.3625,0.525]	$4.033 \pm 0.042\ ^{+0.327}_{-0.163}\ ^{+0.074}_{-0.117}$
[0.525,0.6875]	$5.124 \pm 0.045\ ^{+0.271}_{-0.143}\ ^{+0.263}_{-0.292}$
[0.6875,0.85]	$5.481 \pm 0.054\ ^{+0.236}_{-0.149}\ ^{+0.411}_{-0.505}$

Table H.5: The value of the measured differential cross section $d\sigma/dy$ for the inclusive sample of events. Also listed are the associated statistical, uncorrelated systematic and energy scale uncertainties.

$\Delta\eta$ range	$\sigma(\pm$ stat. syst. Escale) (nb)
[2.5,2.8]	$2.095 \pm 0.022\ ^{+0.078}_{-0.051}\ ^{+0.109}_{-0.141}$
[2.8,3.1]	$1.382 \pm 0.018\ ^{+0.058}_{-0.033}\ ^{+0.078}_{-0.108}$
[3.1,3.5]	$0.755 \pm 0.012\ ^{+0.035}_{-0.026}\ ^{+0.048}_{-0.055}$
[3.5,4]	$0.145 \pm 0.004\ ^{+0.010}_{-0.005}\ ^{+0.008}_{-0.012}$

Table H.6: The value of the measured differential cross section $d\sigma/d\Delta\eta$ for $x_{\gamma;2J}^{OBS} < 0.75$ for the inclusive sample of events. Also listed are the associated statistical, uncorrelated systematic and energy scale uncertainties.

$\Delta\eta$ range	$\sigma(\pm$ stat. syst. Escale) (nb)
[2.5,2.8]	$1.556 \pm 0.020\ ^{+0.113}_{-0.053}\ ^{+0.044}_{-0.047}$
[2.8,3.1]	$1.078 \pm 0.017\ ^{+0.093}_{-0.042}\ ^{+0.038}_{-0.036}$
[3.1,3.5]	$0.650 \pm 0.012\ ^{+0.051}_{-0.032}\ ^{+0.022}_{-0.027}$
[3.5,4]	$0.216 \pm 0.006\ ^{+0.024}_{-0.014}\ ^{+0.008}_{-0.010}$

Table H.7: The value of the measured differential cross section $d\sigma/d\Delta\eta$ for $x_{\gamma;2J}^{OBS} > 0.75$ for the inclusive sample of events. Also listed are the associated statistical, uncorrelated systematic and energy scale uncertainties.

Appendix H

$\Delta\eta$ range	$E_{\mathrm{T}}^{\mathrm{cut}}$ (GeV)	$\sigma(\pm$ stat. syst. Escale) (nb)
[2.5,2.8]	0.5	$0.190 \pm 0.009\ ^{+0.033}_{-0.012}\ ^{+0.007}_{-0.002}$
[2.8,3.1]		$0.100 \pm 0.008\ ^{+0.018}_{-0.007}\ ^{+0.004}_{-0.002}$
[3.1,3.5]		$0.069 \pm 0.009\ ^{+0.013}_{-0.012}\ ^{+0.005}_{-0.003}$
[3.5,4]		$0.015 \pm 0.004\ ^{+0.009}_{-0.003}\ ^{+0.000}_{-0.002}$
[2.5,2.8]	1.0	$0.358 \pm 0.011\ ^{+0.041}_{-0.019}\ ^{+0.006}_{-0.002}$
[2.8,3.1]		$0.187 \pm 0.009\ ^{+0.039}_{-0.015}\ ^{+0.003}_{-0.001}$
[3.1,3.5]		$0.099 \pm 0.007\ ^{+0.021}_{-0.020}\ ^{+0.005}_{-0.001}$
[3.5,4]		$0.022 \pm 0.003\ ^{+0.010}_{-0.005}\ ^{+0.000}_{-0.003}$
[2.5,2.8]	1.5	$0.575 \pm 0.013\ ^{+0.053}_{-0.025}\ ^{+0.007}_{-0.001}$
[2.8,3.1]		$0.301 \pm 0.010\ ^{+0.042}_{-0.021}\ ^{+0.009}_{-0.001}$
[3.1,3.5]		$0.140 \pm 0.007\ ^{+0.023}_{-0.014}\ ^{+0.005}_{-0.003}$
[3.5,4]		$0.035 \pm 0.003\ ^{+0.010}_{-0.006}\ ^{+0.001}_{-0.003}$
[2.5,2.8]	2.0	$0.798 \pm 0.015\ ^{+0.069}_{-0.036}\ ^{+0.011}_{-0.001}$
[2.8,3.1]		$0.419 \pm 0.011\ ^{+0.048}_{-0.022}\ ^{+0.006}_{-0.002}$
[3.1,3.5]		$0.190 \pm 0.007\ ^{+0.034}_{-0.016}\ ^{+0.004}_{-0.002}$
[3.5,4]		$0.047 \pm 0.003\ ^{+0.012}_{-0.006}\ ^{+0.002}_{-0.001}$

Table H.8: The value of the measured differential cross section $\mathrm{d}\sigma/\mathrm{d}\Delta\eta$ for the gap samples of events. Also listed are the associated statistical, uncorrelated systematic and energy scale uncertainties.

Appendix H

$x_{\gamma;2J}^{OBS}$ range	E_T^{cut} (GeV)	$\sigma(\pm$ stat. syst. Escale) (nb)
[0,0.5]	0.5	$0.009 \pm 0.002\ ^{+0.003}_{-0.002}\ ^{+0.001}_{-0.001}$
[0.5,0.75]		$0.066 \pm 0.008\ ^{+0.018}_{-0.012}\ ^{+0.001}_{-0.003}$
[0.75,0.9]		$0.192 \pm 0.013\ ^{+0.041}_{-0.026}\ ^{+0.004}_{-0.002}$
[0.9,1]		$0.609 \pm 0.032\ ^{+0.155}_{-0.093}\ ^{+0.037}_{-0.039}$
[0,0.5]	1.0	$0.015 \pm 0.002\ ^{+0.004}_{-0.002}\ ^{+0.000}_{-0.001}$
[0.5,0.75]		$0.113 \pm 0.007\ ^{+0.024}_{-0.016}\ ^{+0.000}_{-0.003}$
[0.75,0.9]		$0.418 \pm 0.016\ ^{+0.069}_{-0.037}\ ^{+0.013}_{-0.001}$
[0.9,1]		$1.051 \pm 0.036\ ^{+0.189}_{-0.126}\ ^{+0.021}_{-0.028}$
[0,0.5]	1.5	$0.031 \pm 0.003\ ^{+0.004}_{-0.004}\ ^{+0.000}_{-0.002}$
[0.5,0.75]		$0.184 \pm 0.008\ ^{+0.031}_{-0.016}\ ^{+0.002}_{-0.005}$
[0.75,0.9]		$0.778 \pm 0.021\ ^{+0.100}_{-0.052}\ ^{+0.024}_{-0.006}$
[0.9,1]		$1.478 \pm 0.041\ ^{+0.194}_{-0.127}\ ^{+0.014}_{-0.028}$
[0,0.5]	2.0	$0.044 \pm 0.003\ ^{+0.008}_{-0.005}\ ^{+0.000}_{-0.002}$
[0.5,0.75]		$0.280 \pm 0.009\ ^{+0.035}_{-0.021}\ ^{+0.008}_{-0.006}$
[0.75,0.9]		$1.227 \pm 0.025\ ^{+0.142}_{-0.066}\ ^{+0.024}_{-0.009}$
[0.9,1]		$1.787 \pm 0.044\ ^{+0.213}_{-0.127}\ ^{+0.005}_{-0.018}$

Table H.9: The value of the measured differential cross section $d\sigma/dx_{\gamma;2J}^{OBS}$ for the gap samples of events. Also listed are the associated statistical, uncorrelated systematic and energy scale uncertainties.

Appendix H

$\log_{10}(x_{p;2J}^{OBS})$ range	E_T^{cut} (GeV)	$\sigma(\pm$ stat. syst. Escale) (nb)
[-2,-1.75]	0.5	$0.095 \pm 0.006\ ^{+0.023}_{-0.015}\ ^{+0.005}_{-0.009}$
[-1.75,-1.5]		$0.234 \pm 0.014\ ^{+0.037}_{-0.020}\ ^{+0.006}_{-0.003}$
[-1.5,-1.25]		$0.159 \pm 0.017\ ^{+0.020}_{-0.022}\ ^{+0.002}_{-0.008}$
[-1.25,-1]		$0.020 \pm 0.007\ ^{+0.007}_{-0.004}\ ^{+0.001}_{-0.001}$
[-2,-1.75]	1.0	$0.165 \pm 0.007\ ^{+0.033}_{-0.019}\ ^{+0.009}_{-0.008}$
[-1.75,-1.5]		$0.416 \pm 0.015\ ^{+0.059}_{-0.030}\ ^{+0.001}_{-0.007}$
[-1.5,-1.25]		$0.280 \pm 0.017\ ^{+0.037}_{-0.034}\ ^{+0.010}_{-0.008}$
[-1.25,-1]		$0.046 \pm 0.009\ ^{+0.009}_{-0.008}\ ^{+0.002}_{-0.005}$
[-2,-1.75]	1.5	$0.247 \pm 0.008\ ^{+0.045}_{-0.020}\ ^{+0.012}_{-0.011}$
[-1.75,-1.5]		$0.665 \pm 0.017\ ^{+0.062}_{-0.038}\ ^{+0.006}_{-0.015}$
[-1.5,-1.25]		$0.435 \pm 0.019\ ^{+0.036}_{-0.027}\ ^{+0.017}_{-0.010}$
[-1.25,-1]		$0.056 \pm 0.008\ ^{+0.009}_{-0.011}\ ^{+0.001}_{-0.005}$
[-2,-1.75]	2.0	$0.335 \pm 0.008\ ^{+0.060}_{-0.027}\ ^{+0.016}_{-0.013}$
[-1.75,-1.5]		$0.912 \pm 0.018\ ^{+0.079}_{-0.037}\ ^{+0.005}_{-0.012}$
[-1.5,-1.25]		$0.604 \pm 0.021\ ^{+0.058}_{-0.032}\ ^{+0.016}_{-0.023}$
[-1.25,-1]		$0.071 \pm 0.007\ ^{+0.008}_{-0.005}\ ^{+0.006}_{-0.009}$

Table H.10: The value of the measured differential cross section $d\sigma/d\log_{10}(x_{p;2J}^{OBS})$ for the gap samples of events. Also listed are the associated statistical, uncorrelated systematic and energy scale uncertainties.

Appendix H

y range	E_T^{cut} (GeV)	$\sigma(\pm$ stat. syst. Escale) (nb)
[0.2,0.3625]	0.5	$0.100 \pm 0.011 \, ^{+0.017}_{-0.010} \, ^{+0.008}_{-0.010}$
[0.3625,0.525]		$0.191 \pm 0.013 \, ^{+0.041}_{-0.013} \, ^{+0.003}_{-0.004}$
[0.525,0.6875]		$0.190 \pm 0.013 \, ^{+0.029}_{-0.030} \, ^{+0.007}_{-0.005}$
[0.6875,0.85]		$0.211 \pm 0.017 \, ^{+0.046}_{-0.045} \, ^{+0.011}_{-0.008}$
[0.2,0.3625]	1.0	$0.203 \pm 0.013 \, ^{+0.024}_{-0.015} \, ^{+0.016}_{-0.008}$
[0.3625,0.525]		$0.370 \pm 0.015 \, ^{+0.066}_{-0.023} \, ^{+0.004}_{-0.003}$
[0.525,0.6875]		$0.358 \pm 0.015 \, ^{+0.046}_{-0.035} \, ^{+0.009}_{-0.002}$
[0.6875,0.85]		$0.341 \pm 0.017 \, ^{+0.058}_{-0.064} \, ^{+0.009}_{-0.003}$
[0.2,0.3625]	1.5	$0.335 \pm 0.016 \, ^{+0.037}_{-0.026} \, ^{+0.023}_{-0.013}$
[0.3625,0.525]		$0.600 \pm 0.018 \, ^{+0.082}_{-0.030} \, ^{+0.005}_{-0.007}$
[0.525,0.6875]		$0.578 \pm 0.017 \, ^{+0.060}_{-0.051} \, ^{+0.015}_{-0.010}$
[0.6875,0.85]		$0.518 \pm 0.018 \, ^{+0.062}_{-0.054} \, ^{+0.004}_{-0.004}$
[0.2,0.3625]	2.0	$0.445 \pm 0.018 \, ^{+0.051}_{-0.033} \, ^{+0.027}_{-0.030}$
[0.3625,0.525]		$0.854 \pm 0.021 \, ^{+0.108}_{-0.042} \, ^{+0.004}_{-0.002}$
[0.525,0.6875]		$0.804 \pm 0.019 \, ^{+0.081}_{-0.050} \, ^{+0.013}_{-0.012}$
[0.6875,0.85]		$0.725 \pm 0.020 \, ^{+0.073}_{-0.065} \, ^{+0.010}_{-0.002}$

Table H.11: The value of the measured differential cross section $d\sigma/dy$ for the gap samples of events. Also listed are the associated statistical, uncorrelated systematic and energy scale uncertainties.

Appendix H

$\Delta\eta$ range	E_T^{cut} (GeV)	$\sigma(\pm$ stat. syst. Escale) (nb)
[2.5,2.8]	0.5	$0.039 \pm 0.005\ ^{+0.009}_{-0.006}\ ^{+0.001}_{-0.002}$
[2.8,3.1]		$0.020 \pm 0.005\ ^{+0.006}_{-0.002}\ ^{+0.000}_{-0.001}$
[3.1,3.5]		$0.008 \pm 0.003\ ^{+0.020}_{-0.002}\ ^{+0.001}_{-0.001}$
[3.5,4]		$0.001 \pm 0.001\ ^{+0.002}_{-0.000}\ ^{+0.000}_{-0.000}$
[2.5,2.8]	1.0	$0.067 \pm 0.005\ ^{+0.010}_{-0.007}\ ^{+0.000}_{-0.002}$
[2.8,3.1]		$0.028 \pm 0.003\ ^{+0.013}_{-0.003}\ ^{+0.000}_{-0.001}$
[3.1,3.5]		$0.017 \pm 0.003\ ^{+0.005}_{-0.005}\ ^{+0.001}_{-0.001}$
[3.5,4]		$0.002 \pm 0.001\ ^{+0.001}_{-0.001}\ ^{+0.000}_{-0.000}$
[2.5,2.8]	1.5	$0.117 \pm 0.006\ ^{+0.017}_{-0.010}\ ^{+0.000}_{-0.004}$
[2.8,3.1]		$0.054 \pm 0.004\ ^{+0.009}_{-0.006}\ ^{+0.002}_{-0.003}$
[3.1,3.5]		$0.021 \pm 0.002\ ^{+0.006}_{-0.002}\ ^{+0.001}_{-0.000}$
[3.5,4]		$0.002 \pm 0.001\ ^{+0.001}_{-0.000}\ ^{+0.000}_{-0.000}$
[2.5,2.8]	2.0	$0.177 \pm 0.007\ ^{+0.023}_{-0.015}\ ^{+0.004}_{-0.004}$
[2.8,3.1]		$0.083 \pm 0.005\ ^{+0.009}_{-0.006}\ ^{+0.002}_{-0.004}$
[3.1,3.5]		$0.029 \pm 0.002\ ^{+0.006}_{-0.004}\ ^{+0.001}_{-0.001}$
[3.5,4]		$0.004 \pm 0.001\ ^{+0.001}_{-0.001}\ ^{+0.000}_{-0.000}$

Table H.12: The value of the measured differential cross section $d\sigma/d\Delta\eta$ for $x_{\gamma;2J}^{OBS} < 0.75$ for the gap samples of events. Also listed are the associated statistical, uncorrelated systematic and energy scale uncertainties.

Appendix H

$\Delta\eta$ range	$E_{\mathrm{T}}^{\mathrm{cut}}$ (GeV)	$\sigma(\pm$ stat. syst. Escale) (nb)
[2.5,2.8]	0.5	$0.147 \pm 0.008\ ^{+0.028}_{-0.008}\ ^{+0.006}_{-0.003}$
[2.8,3.1]		$0.080 \pm 0.007\ ^{+0.013}_{-0.006}\ ^{+0.004}_{-0.003}$
[3.1,3.5]		$0.058 \pm 0.008\ ^{+0.014}_{-0.014}\ ^{+0.003}_{-0.004}$
[3.5,4]		$0.013 \pm 0.004\ ^{+0.007}_{-0.003}\ ^{+0.000}_{-0.002}$
[2.5,2.8]	1.0	$0.282 \pm 0.010\ ^{+0.033}_{-0.014}\ ^{+0.006}_{-0.000}$
[2.8,3.1]		$0.156 \pm 0.008\ ^{+0.028}_{-0.012}\ ^{+0.003}_{-0.002}$
[3.1,3.5]		$0.080 \pm 0.006\ ^{+0.017}_{-0.015}\ ^{+0.004}_{-0.002}$
[3.5,4]		$0.020 \pm 0.003\ ^{+0.009}_{-0.005}\ ^{+0.001}_{-0.003}$
[2.5,2.8]	1.5	$0.447 \pm 0.011\ ^{+0.042}_{-0.020}\ ^{+0.007}_{-0.003}$
[2.8,3.1]		$0.243 \pm 0.009\ ^{+0.034}_{-0.016}\ ^{+0.006}_{-0.002}$
[3.1,3.5]		$0.118 \pm 0.006\ ^{+0.017}_{-0.012}\ ^{+0.004}_{-0.003}$
[3.5,4]		$0.032 \pm 0.003\ ^{+0.010}_{-0.006}\ ^{+0.001}_{-0.003}$
[2.5,2.8]	2.0	$0.610 \pm 0.013\ ^{+0.055}_{-0.026}\ ^{+0.005}_{-0.003}$
[2.8,3.1]		$0.331 \pm 0.010\ ^{+0.039}_{-0.017}\ ^{+0.003}_{-0.003}$
[3.1,3.5]		$0.158 \pm 0.006\ ^{+0.028}_{-0.012}\ ^{+0.002}_{-0.003}$
[3.5,4]		$0.043 \pm 0.003\ ^{+0.010}_{-0.005}\ ^{+0.003}_{-0.002}$

Table H.13: The value of the measured differential cross section $\mathrm{d}\sigma/\mathrm{d}\Delta\eta$ for $x_{\gamma;2\mathrm{J}}^{\mathrm{OBS}} > 0.75$ for the gap samples of events. Also listed are the associated statistical, uncorrelated systematic and energy scale uncertainties.

Appendix H

$\Delta\eta$ range	E_T^{cut} (GeV)	$\sigma(\pm$ stat. syst.)
[2.5,2.8]	0.5	$0.052 \pm 0.003\ ^{+0.007}_{-0.003}$
[2.8,3.1]		$0.041 \pm 0.003\ ^{+0.005}_{-0.002}$
[3.1,3.5]		$0.050 \pm 0.006\ ^{+0.009}_{-0.009}$
[3.5,4]		$0.042 \pm 0.011\ ^{+0.021}_{-0.008}$
[2.5,2.8]	1.0	$0.098 \pm 0.003\ ^{+0.007}_{-0.004}$
[2.8,3.1]		$0.076 \pm 0.004\ ^{+0.012}_{-0.005}$
[3.1,3.5]		$0.071 \pm 0.005\ ^{+0.014}_{-0.013}$
[3.5,4]		$0.062 \pm 0.009\ ^{+0.023}_{-0.014}$
[2.5,2.8]	1.5	$0.157 \pm 0.004\ ^{+0.007}_{-0.004}$
[2.8,3.1]		$0.122 \pm 0.004\ ^{+0.010}_{-0.007}$
[3.1,3.5]		$0.100 \pm 0.005\ ^{+0.012}_{-0.008}$
[3.5,4]		$0.097 \pm 0.009\ ^{+0.021}_{-0.014}$
[2.5,2.8]	2.0	$0.218 \pm 0.004\ ^{+0.009}_{-0.006}$
[2.8,3.1]		$0.170 \pm 0.005\ ^{+0.011}_{-0.005}$
[3.1,3.5]		$0.136 \pm 0.005\ ^{+0.019}_{-0.008}$
[3.5,4]		$0.132 \pm 0.010\ ^{+0.025}_{-0.012}$

Table H.14: The gap fractions $f(\Delta\eta)$. Also listed are the associated statistical and uncorrelated systematic uncertainties.

Appendix H

$x_{\gamma;2J}^{OBS}$ range	E_T^{cut} (GeV)	$\sigma(\pm$ stat. syst.)
[0,0.5]	0.5	$0.013 \pm 0.003\ ^{+0.005}_{-0.003}$
[0.5,0.75]		$0.016 \pm 0.002\ ^{+0.004}_{-0.003}$
[0.75,0.9]		$0.032 \pm 0.002\ ^{+0.005}_{-0.004}$
[0.9,1]		$0.252 \pm 0.014\ ^{+0.043}_{-0.026}$
[0,0.5]	1.0	$0.021 \pm 0.003\ ^{+0.005}_{-0.003}$
[0.5,0.75]		$0.027 \pm 0.002\ ^{+0.005}_{-0.004}$
[0.75,0.9]		$0.069 \pm 0.003\ ^{+0.007}_{-0.005}$
[0.9,1]		$0.434 \pm 0.016\ ^{+0.041}_{-0.033}$
[0,0.5]	1.5	$0.043 \pm 0.004\ ^{+0.004}_{-0.005}$
[0.5,0.75]		$0.043 \pm 0.002\ ^{+0.006}_{-0.004}$
[0.75,0.9]		$0.129 \pm 0.004\ ^{+0.009}_{-0.005}$
[0.9,1]		$0.610 \pm 0.018\ ^{+0.024}_{-0.023}$
[0,0.5]	2.0	$0.062 \pm 0.004\ ^{+0.011}_{-0.008}$
[0.5,0.75]		$0.066 \pm 0.002\ ^{+0.007}_{-0.005}$
[0.75,0.9]		$0.203 \pm 0.004\ ^{+0.011}_{-0.004}$
[0.9,1]		$0.738 \pm 0.020\ ^{+0.022}_{-0.012}$

Table H.15: The gap fractions $f(x_{\gamma;2J}^{OBS})$. Also listed are the associated statistical and uncorrelated systematic uncertainties.

Appendix H

$\log_{10}(x_{p;2J}^{OBS})$ range	E_T^{cut} (GeV)	$\sigma(\pm$ stat. syst.)
[-2,-1.75]	0.5	$0.087 \pm 0.006\ ^{+0.014}_{-0.012}$
[-1.75,-1.5]		$0.050 \pm 0.003\ ^{+0.007}_{-0.005}$
[-1.5,-1.25]		$0.038 \pm 0.004\ ^{+0.005}_{-0.006}$
[-1.25,-1]		$0.036 \pm 0.014\ ^{+0.012}_{-0.007}$
[-2,-1.75]	1.0	$0.152 \pm 0.006\ ^{+0.015}_{-0.013}$
[-1.75,-1.5]		$0.089 \pm 0.003\ ^{+0.011}_{-0.007}$
[-1.5,-1.25]		$0.067 \pm 0.004\ ^{+0.009}_{-0.009}$
[-1.25,-1]		$0.086 \pm 0.018\ ^{+0.017}_{-0.014}$
[-2,-1.75]	1.5	$0.228 \pm 0.007\ ^{+0.019}_{-0.008}$
[-1.75,-1.5]		$0.143 \pm 0.004\ ^{+0.008}_{-0.008}$
[-1.5,-1.25]		$0.104 \pm 0.005\ ^{+0.009}_{-0.007}$
[-1.25,-1]		$0.104 \pm 0.014\ ^{+0.017}_{-0.020}$
[-2,-1.75]	2.0	$0.309 \pm 0.008\ ^{+0.023}_{-0.011}$
[-1.75,-1.5]		$0.196 \pm 0.004\ ^{+0.011}_{-0.008}$
[-1.5,-1.25]		$0.144 \pm 0.005\ ^{+0.014}_{-0.009}$
[-1.25,-1]		$0.132 \pm 0.014\ ^{+0.013}_{-0.009}$

Table H.16: The gap fractions $f(\log_{10}(x_{p;2J}^{OBS}))$. Also listed are the associated statistical and uncorrelated systematic uncertainties.

Appendix H

y range	E_T^{cut} (GeV)	$\sigma(\pm$ stat. syst.)
[0.2,0.3625]	0.5	$0.081 \pm 0.009\ ^{+0.014}_{-0.010}$
[0.3625,0.525]		$0.047 \pm 0.003\ ^{+0.008}_{-0.003}$
[0.525,0.6875]		$0.037 \pm 0.003\ ^{+0.005}_{-0.006}$
[0.6875,0.85]		$0.038 \pm 0.003\ ^{+0.008}_{-0.008}$
[0.2,0.3625]	1.0	$0.164 \pm 0.011\ ^{+0.015}_{-0.011}$
[0.3625,0.525]		$0.092 \pm 0.004\ ^{+0.011}_{-0.005}$
[0.525,0.6875]		$0.070 \pm 0.003\ ^{+0.006}_{-0.006}$
[0.6875,0.85]		$0.062 \pm 0.003\ ^{+0.010}_{-0.011}$
[0.2,0.3625]	1.5	$0.271 \pm 0.014\ ^{+0.015}_{-0.016}$
[0.3625,0.525]		$0.149 \pm 0.005\ ^{+0.010}_{-0.003}$
[0.525,0.6875]		$0.113 \pm 0.004\ ^{+0.007}_{-0.009}$
[0.6875,0.85]		$0.094 \pm 0.003\ ^{+0.010}_{-0.008}$
[0.2,0.3625]	2.0	$0.360 \pm 0.015\ ^{+0.012}_{-0.013}$
[0.3625,0.525]		$0.212 \pm 0.005\ ^{+0.012}_{-0.005}$
[0.525,0.6875]		$0.157 \pm 0.004\ ^{+0.011}_{-0.008}$
[0.6875,0.85]		$0.132 \pm 0.004\ ^{+0.011}_{-0.009}$

Table H.17: The gap fractions $f(y)$. Also listed are the associated statistical and uncorrelated systematic uncertainties.

Appendix H

$\Delta\eta$ range	E_T^{cut} (GeV)	$\sigma(\pm$ stat. syst.)
[2.5,2.8]	0.5	$0.019 \pm 0.002\ ^{+0.004}_{-0.003}$
[2.8,3.1]		$0.014 \pm 0.003\ ^{+0.004}_{-0.001}$
[3.1,3.5]		$0.011 \pm 0.004\ ^{+0.025}_{-0.002}$
[3.5,4]		$0.007 \pm 0.007\ ^{+0.011}_{-0.003}$
[2.5,2.8]	1.0	$0.032 \pm 0.002\ ^{+0.004}_{-0.003}$
[2.8,3.1]		$0.020 \pm 0.002\ ^{+0.009}_{-0.002}$
[3.1,3.5]		$0.022 \pm 0.004\ ^{+0.006}_{-0.007}$
[3.5,4]		$0.011 \pm 0.006\ ^{+0.007}_{-0.005}$
[2.5,2.8]	1.5	$0.056 \pm 0.003\ ^{+0.007}_{-0.004}$
[2.8,3.1]		$0.039 \pm 0.003\ ^{+0.005}_{-0.004}$
[3.1,3.5]		$0.028 \pm 0.003\ ^{+0.007}_{-0.003}$
[3.5,4]		$0.014 \pm 0.004\ ^{+0.005}_{-0.003}$
[2.5,2.8]	2.0	$0.084 \pm 0.003\ ^{+0.010}_{-0.006}$
[2.8,3.1]		$0.060 \pm 0.004\ ^{+0.005}_{-0.003}$
[3.1,3.5]		$0.039 \pm 0.003\ ^{+0.006}_{-0.005}$
[3.5,4]		$0.025 \pm 0.005\ ^{+0.009}_{-0.003}$

Table H.18: The gap fractions $f(\Delta\eta)$ for $x_{\gamma;2J}^{OBS} < 0.75$. Also listed are the associated statistical and uncorrelated systematic uncertainties.

Appendix H

$\Delta\eta$ range	E_T^{cut} (GeV)	$\sigma(\pm$ stat. syst.)
[2.5,2.8]	0.5	$0.094 \pm 0.005\ ^{+0.014}_{-0.003}$
[2.8,3.1]		$0.074 \pm 0.006\ ^{+0.007}_{-0.004}$
[3.1,3.5]		$0.089 \pm 0.012\ ^{+0.018}_{-0.021}$
[3.5,4]		$0.062 \pm 0.017\ ^{+0.026}_{-0.014}$
[2.5,2.8]	1.0	$0.181 \pm 0.006\ ^{+0.010}_{-0.004}$
[2.8,3.1]		$0.145 \pm 0.007\ ^{+0.017}_{-0.007}$
[3.1,3.5]		$0.123 \pm 0.009\ ^{+0.023}_{-0.021}$
[3.5,4]		$0.091 \pm 0.014\ ^{+0.030}_{-0.021}$
[2.5,2.8]	1.5	$0.287 \pm 0.008\ ^{+0.010}_{-0.003}$
[2.8,3.1]		$0.225 \pm 0.009\ ^{+0.014}_{-0.010}$
[3.1,3.5]		$0.181 \pm 0.010\ ^{+0.016}_{-0.013}$
[3.5,4]		$0.147 \pm 0.015\ ^{+0.029}_{-0.023}$
[2.5,2.8]	2.0	$0.392 \pm 0.009\ ^{+0.010}_{-0.004}$
[2.8,3.1]		$0.307 \pm 0.010\ ^{+0.014}_{-0.005}$
[3.1,3.5]		$0.243 \pm 0.010\ ^{+0.032}_{-0.007}$
[3.5,4]		$0.198 \pm 0.016\ ^{+0.030}_{-0.015}$

Table H.19: The gap fractions $f(\Delta\eta)$ for $x_{\gamma;2J}^{OBS} > 0.75$. Also listed are the associated statistical and uncorrelated systematic uncertainties.

Appendix I

Glossary of Abbreviations

BAC	backing calorimeter
BCAL	barrel calorimeter
BFKL	Balitsky-Fadin-Kiraev-Lipatov
BMUI	barrel muon identification chamber
BMUON	barrel muon chamber
CAL	calorimeter
CC	charged current
DAQ	data acquisition
DOF	degrees of freedom
CTD	central tracking detector
DESY	Deutsches elektronen synchrotron
DGLAP	Dokshitzer-Gribov-Lipatov-Alterelli-Parisi
DIS	deep inelastic scattering
DST	data storage tape
EAZE	effortless analysis of ZEUS events
EFO	energy flow object
EMC	electromagnetic calorimeter
EPA	equivalent photon approximation
EVB	event builder
FCAL	forward calorimeter
FLT	first level trigger
FMUI	forward muon identification chamber
FMUON	forward muon chamber
FSR	final state radiation
FTD	forward tracking detector
GFLT	global first level trigger
GSLT	global second level trigger
HERA	hadron elektron ring anlage
HAC	hadronic calorimeter

Appendix I

HES	hadron electron separator
ISR	initial state radiation
LHC	large hadron collider
LINAC	linear accelerator
LL	leading logarithm
LLA	leading logarithm approximation
LO	leading order
LPHD	local parton hadron duality
LUMI	luminosity monitor
MC	Monte Carlo
MIP	minimum ionising particle
MPI	multi-parton interactions
MOZART	Monte Carlo for ZEUS analysis, reconstruction and trigger
NC	neutral current
NLC	next linear collider
NLO	next-to-leading order
ORANGE	overlying routine for analysis ntuple generation
PDF	parton density function
PMT	photomultiplier tube
PRES	presampler
pQCD	perturbative Quantum Chromodynamics
QCD	Quantum Chromodynamics
QED	Quantum Electrodynamics
QPM	quark parton model
RCAL	rear calorimeter
RMUI	rear muon identification chamber
RMUON	rear muon chamber
RTD	rear tracking detector
SLT	second level trigger
SRTD	small angle rear tracking detector
SUE	soft underlying event
SUSY	supersymmetry
TLT	third level trigger
UE	underlying event
VDM	vector meson dominance model
WWA	Weizsäcker-Williams approximation
ZDIS	ZEUS interface to deep inelastic scattering
ZEPHYR	ZEUS physics reconstruction
ZGANA	ZG313 analysis
ZUFO	ZEUS unidentified flow object

Acknowledgments

There are many people to whom I owe a great deal of thanks for their help, support and encouragement throughout the course of my Ph.D study.

First and foremost, I would like to thank my supervisor, Jon Butterworth, for providing the initial direction of this work, for allowing me the freedom to develop and for helpful discussions whenever necessary. I would also very much like to thank Mark Sutton for his hard work in reproducing the main results of the analyses contained in this thesis. Special thanks go to James Ferrando and Mark Sutton (again) for the many patient reboots and general fixings of my computer. Without you I would *never* have finished.

Thanks also go to the UCL Graduate School, who provided the funding for this research. For additional financial support, I am indebted to the UCL Department of Physics and Astronomy, the High Energy Physics group and the Elizabeth Spreadbury Fund.

For the year I spent at UCL, I am grateful to all members of the High Energy Physics group for creating such a pleasant working environment. Special thanks go to Jon Couchman and Chris Smith, with whom I had the pleasure of sharing an office during my first year of study. For making the last two years in Hamburg such a happy time, I would especially like to thank: Mairi Bell, Stewart Boogert, Jo Cole, Chris Collins-Tooth, James Ferrando, Joanna Hamilton, Steven Hanlon, Eileen Heaphy, Paul Laycock, John Loizides, Mike Rigby, Steve Robins, Dave South, Mark Sutton and Ben West. Thank you also to Susan Ketels for making my stay in Hamburg so enjoyable.

For reading and commenting on parts of this thesis, I thank Alan Barr, Richard Hall-Wilton, Joanna Hamilton and Mark Sutton.

Life during the course of this study has been made richer, even during the most disheartening times, by the love, support and patience of Alan Barr.

Finally, I thank all the members of my family for their constant support, love and encouragement. I would especially like to dedicate this thesis to the memory of my grandparents. I hope you would have been proud.

Claire Gwenlan

March 2003

Bibliography

[1] E. Rutherford, Phil. Mag. **21**, 669 (1911);
H. Geiger and E. Marsden, Proc. Roy. Soc., **82**, 495 (1909).

[2] J. Franck and G. Hertz, Verh. Deutschen Phys. Ges. **16**, 457 (1914).

[3] A.J. Barr, Private Communication.

[4] Particle Data Group, D.E. Groom et al., Eur. Phys. J. **C15**, 1 (2000).

[5] ALEPH Coll., DELPHI Coll., L3 Coll., OPAL Coll. and LEP Electroweak Working Group and SLD Heavy Flavour and Electroweak Groups (D. Abbaneo et al.), A Combination of Preliminary Electroweak Measurements and Constraints on the Standard Model, hep-ex/0112021.

[6] R.K. Ellis, W.J. Stirling and B.R. Webber, QCD and Collider Physics. Cambridge University Press, Cambridge Monographs on Particle Physics, Nuclear Physics and Cosmology, Vol. 8, 1996.

[7] ZEUS Coll., M. Derrick et al., Phys. Lett. **B 322**, 287 (1994).

[8] H1 Coll., I. Abt et al., Phys. Lett. **B 314**, 436 (1993).

[9] ZEUS Coll., M. Derrick et al., Phys. Lett. **B 342**, 417 (1995).

[10] ZEUS Coll., M. Derrick et al., Phys. Lett. **B 348**, 665 (1995).

[11] ZEUS Coll., J. Breitweg et al., Eur. Phys. J. **C 1**, 109 (1998).

[12] ZEUS Coll., J. Breitweg et al., Phys. Lett. **B 413**, 201 (1997).

[13] ZEUS Coll., J. Breitweg et al., Eur. Phys. J. **C 4**, 591 (1998).

[14] H1 Coll., Nucl. Phys. **B 445**, 195 (1995).

[15] H1 Coll., C. Adloff et al., Phys. Lett. **B 415**, 418 (1997).

[16] H1 Coll., C. Adloff et al., Eur. Phys. J. **C 1**, 97 (1998).

Bibliography

[17] H1 Coll., S. Aid et al., Z. Phys. **C 70**, 17 (1996).

[18] ZEUS Coll., J. Breitweg et al., Eur. Phys. J. **C 2**, 61 (1998).

[19] ZEUS Coll., J. Breitweg et al., Phys. Lett. **B 443**, 394 (1998).

[20] J.M. Butterworth and S. Butterworth, Jetweb: A WWW Interface and Database for Monte Carlo Tuning and Validation; hep-ph/0210404,2002, available on `http://jetweb.hep.ucl.ac.uk/`.

[21] DØ Coll.; B. Abbot et al., Phys. Lett. **B 440**, 189 (1998);
DØ Coll.; S. Abachi et al., Phys. Rev. Lett. **76**, 734 (1996);
DØ Coll.; S. Abachi et al., Phys. Rev. Lett. **72**, 2332 (1994).

[22] CDF Coll.; F. Abe et al., Phys. Rev. Lett. **81**, 5278 (1998);
CDF Coll.; F. Abe et al., Phys. Rev. Lett. **80**, 1156 (1998);
CDF Coll.; F. Abe et al., Phys. Rev. Lett. **74**, 855 (1995).

[23] ZEUS Coll., M. Derrick et al., Phys. Lett. **B 369**, 55 (1996).

[24] H1 Coll., Rapidity Gaps between Jets in Photoproduction at HERA, contribution to the International Europhysics Conference on High Energy Physics, August 1997, Jerusalen, Israel.

[25] H1 Coll., Eur. Phys. J. **C 24**, 517 (2002).

[26] M. Gell-Mann, Phys. Rev. **125**, 1067 (1962);
Y. Ne'eman, Nucl. Phys. **26**, 222 (1961).

[27] V.E. Barnes et al., Phys. Rev. Lett. **12**, 204 (1964).

[28] M. Gell-Mann, Phys. Lett. **8**, 214 (1964).

[29] G. Zweig, CERN-TH 401 and CERN-TH 412 (1964).

[30] O.W. Greenberg, Phys. Rev. Lett. **13**, 598 (1964).

[31] J.D. Bjorken and E.A. Paschos, Phys. Rev. **185**, 1975 (1969).

[32] J. Kui and V.F. Weisskopf, Phys. Rev. **D 4**, 3418 (1971).

[33] Particle Data Group, K. Hagiwara et al., Phys. Rev. **D 66**, 010001 (2002).

[34] O. Gonzalez, Private Communication.

[35] Ya. I. Azimov et al., Phys. Lett. **C 27**, 65 (1985);
Ya. I. Azimov et al., Phys. Lett. **B 165**, 147 (1985).

Bibliography

[36] A. Bodek et al., Phys. Rev. Lett. **30**, 1087 (1973);
J.D. Bjorken, Phys. Rev. **179**, 1547 (1969);
E.D. Bloom et al., Phys. Rev. Lett. **23**, 930 (1969).

[37] F. Halzen and A.D. Martin, Quarks and Leptons. Wiley, 1984.

[38] J.C. Collins and D.E. Soper, Ann. Rev. Nucl. Part. Sci. **37**, 383 (1987).

[39] S. Fanchiotti, B. Kniehl and A. Sirlin, Phys. Rev. **D 48**, 307 (1993).

[40] .

[41] R.P. Feynman, Phys. Rev. Lett. **23**, 1415 (1969).

[42] J. Freidman et al., Phys. Rev. **D 5**, 528 (1972).

[43] C.G. Callan and D.J. Gross, Phys. Rev. Lett. **22**, 156 (1969).

[44] T. Eichten, Phys. Lett. **B 46**, 274 (1973).

[45] TASSO Coll., R. Brandelik et al., Phys. Lett. **B 86**, 243 (1979).

[46] Yu L. Dokshitzer, Sov. Phys. JETP **46**, 641 (1977);
G. Altarelli and G. Parisi, Nucl. Phys. **B 126**, 298 (1977);
V.N. Gribov and L.N. Lipatov, Sov. J. Nucl. Phys. **15**, 438 (1972).

[47] G. Curci, W. Furmanski and R. Petronzio, Nucl. Phys. **B 175**, 27 (1980);
W. Furmanski and R. Petronzio, Phys. Lett. **B 97**, 437 (1980).

[48] A.D. Martin et al., Eur. Phys. J. **C 4**, 463 (1998).

[49] I.I. Balitsky and L.N. Lipatov, Sov. J. Nucl. Phys. **28**, 822 (1978);
E.A. Kuraev, L.N. Lipatov and V.S. Fadin, Sov. Phys. JETP **44**, 443 (1976).

[50] D.E Soper and J.C Collins, Issues in the Determination of Parton Distribution Functions; hep-ph/9411214.

[51] M. Glück, E. Reya and A. Vogt, Z. Phys. **C 48**, 471 (1990).

[52] M. Glück, E. Reya and A. Vogt, Z. Phys. **C 67**, 433 (1995).

[53] CTEQ Coll., H.L Lai et al., Phys. Rev. **D 51**, 4763 (1995).

[54] CTEQ Coll., H.L Lai et al., Eur. Phys. J. **C 12**, 375 (2000).

[55] B. Burow, A measurement of the total photon-proton cross-section in the centre of mass range 167 to 194 GeV, DESY F35D-94-0.

Bibliography

[56] C.F. von Weizsäcker, Z. Phys. **88**, 612 (1934);
E.J. Williams, Phys. Rev. **45**, 729 (1934).

[57] G.A. Schuler and T. Sjöstrand, Nucl. Phys. **B 407**, 539 (1993).

[58] G.A. Schuler and T. Sjöstrand, Phys. Lett. **B 300**, 169 (1992).

[59] J.J. Sakurai and D. Schildknecht, Phys. Lett. **B 41**, 489 (1972).

[60] E. Witten, Nucl. Phys. **B 120**, 189 (1977).

[61] L3 Coll., M. Acciarri et al., Phys. Lett. **B 453**, 333 (1999);
L3 Coll., M. Acciarri et al., Phys. Lett. **B 447**, 147 (1999);
L3 Coll., M. Acciarri et al., Phys. Lett. **B 436**, 403 (1998);
TPC/Two-Gamma Coll., H. Aihara et al., Z. Phys. **C 34**, 1 (1987);
TASSO Coll., M. Althoff et al., Z. Phys. **C 31**, 527 (1986).

[62] JADE Coll., W. Bartel et al., Z. Phys. **C 24**, 231 (1984).

[63] R.J. De Witt et al., Phys. Rev. **D 19**, 2046 (1979).

[64] G.A. Schuler and T. Sjöstrand, Z. Phys. **C 68**, 607 (1995).

[65] R.M. Godbole, Pramana **51**, 217 (1998).

[66] M. Glück, E. Reya and A. Vogt, Z. Phys. **C 53**, 127 (1992).

[67] M. Drees and K. Grassie, Z. Phys. **C 28**, 451 (1985).

[68] L.E. Gordon and J.K. Storrow, Z. Phys. **C 56**, 307 (1992).

[69] P. Aurenche et al., Phys. Lett. **B 233**, 517 (1989).

[70] P. Aurenche et al., Phys. Lett. **B 306**, 391 (1993).

[71] P. Aurenche et al., Z. Phys. **C 64**, 621 (1994).

[72] M. Glück, E. Reya and A. Vogt, Phys. Rev. **D 46**, 1973 (1992);
M. Glück, E. Reya and A. Vogt, Phys. Rev. **D 45**, 3986 (1992).

[73] M. Glück, E. Reya and A. Vogt, Z. Phys. **C 53**, 651 (1992).

[74] J.H. Da Lus Vieira and J.K. Storrow, Phys. Lett. **B 205**, 367 (1989).

[75] J.R. Forshaw and P.N. Harriman, Phys. Rev. **D 46**, 3778 (1992).

[76] K. Hagiwara et al., Phys. Rev. **D 51**, 3197 (1995).

Bibliography

[77] G. Knies, J.PHYS. **G 19**, 1523 (1993).

[78] H1 Coll., I. Abt et al., Phys. Lett. **B 314**, 436 (1993).

[79] ZEUS Coll., M. Derrick et al., Phys. Lett. **B 342**, 417 (1995).

[80] S.D. Ellis, Proceedings of QCD and High Energy Hadronic Interactions, 28^{th} Rencontres de Moriond, Ed. J. Tran Thanh Van, Editions Frontieres (1993) 235.

[81] J.R. Forshaw and J.K. Storrow, Phys. Rev. **D 46**, 4955 (1992);
J.M. Butterworth, J.R. Forshaw and M.H. Seymour, Z. Phys. **C 72**, 637 (1996).

[82] R.L. Saunders, A Measurement of Dijet Photoproduction at HERA using the ZEUS Detector. Ph.D. Thesis, University College London, 1997.

[83] UA2 Coll., J. Alitti et al., Phys. Lett. **B 268**, 145 (1991);
AFS Coll., T. Akesson et al., Z. Phys. **C 34**, 163 (1987).

[84] CDF Coll., F. Abe et al., Phys. Rev. **D 56**, 3811 (1997);
CDF Coll., F. Abe et al., Phys. Rev. Lett. **79**, 584 (1997).

[85] R. Engel, Z. Phys. **C 66**, 203 (1995).

[86] J.D. Bjorken, Invited Lectures presented at the SLAC Summer Institute on Particle Physics: Spin Structure in High Energy Processes, Stanford, California, 1993.

[87] H1 Coll., T. Ahmed et al., Nucl. Phys. **B 429**, 477 (1994);
ZEUS Coll., M. Derrick et al., Phys. Lett. **B 315**, 481 (1993).

[88] T. Regge, Nuovo Cimento **18**, 947 (1960);
T. Regge, Nuovo Cimento **14**, 951 (1959).

[89] J.R. Forshaw and D.A. Ross, Quantum Chromodynamics and the Pomeron. Cambridge University Press, 1997.

[90] A.V. Barnes, Phys. Rev. Lett. **37**, 76 (1976).

[91] A. Sommerfeld, Partial Differential Equations in Physics. Academic Press, 1949;
G.N. Watson, Proc. Roy. Soc. Lond. **95**, 83 (1918).

[92] G.F. Chew and S.C. Frautschi, Phys. Rev. Lett. **8**, 41 (1962);
G.F. Chew and S.C. Frautschi, Phys. Rev. Lett. **7**, 394 (1961).

[93] A.C. Irving and R.P Worden, Phys. Rep. **34**, 117 (1977);
P.D.B. Collins, Introduction to Regge Theory and High Energy Physics. Cambridge University Press, 1977.

[94] G. Carboni et al., Phys. Lett. **B 113**, 87 (1982);
A.S. Carroll et al., Phys. Lett. **B 80**, 423 (1979).

[95] I.Y. Pomeranchuk, Sov. Phys. **3**, 306, (1956);
L.B. Okun and I.Y. Pomeranchuk, Sov. Phys. JETP **3**, 307, (1956).

[96] L.F. Foldy and R.F. Peierls, Phys. Rev. **130**, 1585 (1963).

[97] V.N. Gribov, JETP Lett. **41**, 667 (1961).

[98] WA91 Coll., S. Abatzis et al., Phys. Lett. **B 324**, 509 (1994).

[99] A. Donnachie and P.V. Landshoff, Phys. Lett. **B 296**, 227 (1992).

[100] H1 Coll., S. Aid et al., Z. Phys. **C 69**, 27 (1995).

[101] A. Donnachie and P.V. Landshoff, Phys. Lett. **B 437**, 408 (1998).

[102] A.H. Mueller and W.K. Tang, Phys. Lett. **B 284**, 123 (1992).

[103] J.D. Bjorken, Phys. Rev. **D 47**, 101 (1992).

[104] J.R. Forshaw and P.J. Sutton, Eur. Phys. J. **C 1**, 285 (1998).

[105] P. Newman, H1 Coll., hep-ex/9901026.

[106] ZEUS Coll., J. Breitweg et al., Eur. Phys. J. **C 2**, 247 (1998);
ZEUS Coll., J. Breitweg et al., Phys. Lett. **B 437**, 432 (1998);
ZEUS Coll., J. Breitweg et al., Z. Phys. **C 75**, 215 (1997);
ZEUS Coll., M. Derrick et al., Z. Phys. **C 73**, 73 (1996);
ZEUS Coll., M. Derrick et al., Phys. Lett. **B 377**, 259 (1996).

[107] H1 Coll., Conference Paper 574, 29$^{\text{th}}$ International Conference on HEP, Vancouver, Canada (1998);
H1 Coll., Conference Paper 572, 29$^{\text{th}}$ International Conference on HEP, Vancouver, Canada (1998);
H1 Coll., S. Aid et al., Nucl. Phys. **B 472**, 3 (1996);
H1 Coll., S. Aid et al., Nucl. Phys. **B 463**, 3 (1996).

[108] L.P. Haakman, K. Kaidalov and J.H. Koch, hep-ph/9507394 (1995).

[109] A. Donnachie and P.V. Landshoff, Phys. Lett. **B 348**, 213 (1995).

[110] Y. L. Dokshitzer et al., p. 417. World Scientific., 1987.

[111] S. Nussinov, Phys. Rev. **D 14**, 246 (1976);
F.E. Low, Phys. Rev. **D 12**, 163 (1975).

Bibliography

[112] L.V. Gribov, E.M. Levin and M.G. Ryskin, Phys. Rep. **100**, 1 (1983).

[113] E.A. Kuraev, L.N. Lipatov and V.S. Fadin, Sov. Phys. JETP **44**, 443 (1976).

[114] H.N. Chehime and D. Zeppenfeld, MAD/PH/814 (1994).

[115] B.R. Webber, Nucl. Phys. **B 238**, 492 (1984).

[116] B. Andersson et al., Phys. Rep. **97**, 31 (1983).

[117] M. Klasen, T. Kleinwort and G. Kramer, Eur. Phys. J. direct, 1998.

[118] G. Marchesini et al., Comp. Phys. Comm. **67**, 465 (1992).

[119] T. Sjöstrand, Comp. Phys. Comm. **82**, 74 (1994).

[120] G.A. Voss and B.H. Wiik, Ann. Rev. Nucl. Part. Sci. **44**, 413 (1994);
HERA, A proposal for a Large Electron-Proton Colliding Beam Facility at DESY, DESY HERA 81-10.

[121] ZEUS Coll., U. Holm (ed.), *The ZEUS Detector.* Status Report (unpublished), DESY, 1993, available on
`http://www-zeus.desy.de/bluebook/bluebook.html`.

[122] H1 Coll., I. Abt et al., Nucl. Inst. Meth. **A 386**, 310 (1997).

[123] HERMES Coll., The HERMES Spectrometer, hep-ex/9806008,DESY 98-057.

[124] HERA-B Coll., HERA-B: An Experiment to study CP violation in the B system using an Internal Target at the HERA Proton Ring, Design Report, DESY-PRC 95/01 (1995).

[125] ZEUS Coll., A Microvertex Detector for ZEUS (unpublished), internal-ZEUS-note, ZEUS-97-006, 1997.

[126] B. Foster et al., Nucl. Inst. Meth. **A 338**, 254 (1994);
B. Foster et al., Nucl. Phys. Proc. Suppl. **B 32**, 181 (1993);
N. Harnew et al., Nucl. Inst. Meth. **A 279**, 290 (1989).

[127] R. Hall-Wilton et al., *The CTD Tracking Resolution* (unpublished). ZEUS-99-024, internal ZEUS-note, 1999.

[128] ZEUS Coll., A Straw-Tube Tracker for ZEUS (unpublished), internal ZEUS-note, ZEUS-98-046, 1997.

[129] M. Derrick et al., Nucl. Inst. Meth. **A 309**, 77 (1991);
A. Andresen et al., Nucl. Inst. Meth. **A 309**, 101 (1991).

Bibliography

[130] J. Crittenden et al., Calibration of FCAL and RCAL Modules at CERN (unpublished), internal ZEUS-note, ZEUS-90-111, 1990;
A. Caldwell et al., BCAL Electron Studies Part I: MC and Test Beam Energy Studies (unpublished), internal-ZEUS-note, ZEUS Note 98-02, 1998.

[131] A. Bamberger et al., Nucl. Inst. Meth. **A 382**, 419 (1996).

[132] A. Bamberger et al., Nucl. Inst. Meth. **A 401**, 63 (1997).

[133] L. Suszycki et al., Proceedings of the HERA workshop, 1987, Vol. 2, 505.

[134] H. Bethe and W. Heitler, Proc. Roy. Soc. Lond. **A146**, 83 (1934).

[135] K. Piotrzkowski and M. Zachara, Determination of the ZEUS Luminosity in 1994 (unpublished), internal ZEUS-note, ZEUS-95-138, 1995.

[136] M. van der Horst. Ph.D. Thesis, University of Amsterdam, 1990.

[137] ZEUS Coll., R. Carlin et al., Nucl. Inst. Meth. **A 379**, 542 (1996).

[138] K. Long, How to generate input to MOZART (unpublished), internal ZEUS-note, ZEUS-Note 91-13, 1991.

[139] GEANT 3.13: R. Brun et al., CERN DD/EE/84-1 (1987).

[140] ZGANA, ZEUS trigger simulation library, Els de Wolf (Editor) et al. .

[141] G.F. Hartner, VCTRAK Briefing: Program and Math, internal ZEUS-note, ZEUS-98-058 (1998).

[142] G.F. Hartner et al., VCTRAK (3.07/04): Offline Output Information (unpublished), internal ZEUS-note, ZEUS-97-064, 1997.

[143] H. Beier, A. Caldwell, Track-CAL Matching with Parametrized CAL Resolution and Inactive Material Effects internal ZEUS-note, ZEUS-95-040 (1995).

[144] R. Sinkus and T. Voss, Particle Identification with Neural Networks Using a Rotational Invariant Moment Representation, DESY 96-264.

[145] A.F. Murphy, ORANGE, available on `http://www-zeus.desy.de/ZEUS_ONLY/analysis/orange/`.

[146] A. Savin, Study of Calorimeter Noise in the 1996 Data (unpublished), internal ZEUS-note, ZEUS-98-007, 1998.

[147] S. Kananov, The Noise Study for the 1995 Data in the ZEUS Calorimeter (unpublished), internal ZEUS-note, ZEUS-97-018, 1997.

Bibliography

[148] S.M. Wang, Study of Calorimeter Noise in the 1995 Data (unpublished), internal ZEUS-note, ZEUS-96-121, 1996.

[149] M. Hayes, A study of Parton-Parton Elastic Scattering by Colour Singlet Exchange. Ph.D. Thesis, University of Bristol, 1996.

[150] `noise96s.fpp`, Noise suppression routine, ZEUS PHANTOM Library.

[151] G. Briskin and A. Caldwell, internal ZEUS-note, ZEUS-95-035, 1995; M. Vreeswijk. Ph.D. Thesis, University of Amsterdam, 1996.

[152] RCALCORR, calorimeter correction routine, ZEUS PHANTOM Library; H. Abramowicz, A. Caldwell and R. Sinkus, Nucl. Inst. Meth. **A 365**, 508 (1995).

[153] G. Briskin, Diffractive Dissociation in *ep* Deep Inelastic Scattering. Ph.D. Thesis, University of Tel Aviv, 1997.

[154] J. Vossebeld, Dijet Photoproduction at High Transverse Energies. Ph.D. Thesis, University of Amsterdam, 1999.

[155] S. Bentvelsen, J. Engelen and P. Kooijman in "Physics at HERA" edited by W. Buchmuller and G. Ingelman. (Proceedings of the workshop, Hamburg, October 1991) Vol 1 p.23.

[156] Proceedings of the Future Physics at HERA Workshop (1991), Vol. 1, edited by W. Buchmuraller and G. Ingelman, p23.

[157] A. Lupi, Private Communication.

[158] P.J. Bussey, EUCELL, ZEUS PHANTOM Library.

[159] S. Catini, Yu.L. Dokshitzer and B.R. Webber, Phys. Lett. **B 285**, 291 (1992).

[160] F. Jacquet and A. Blondel, in *Proceedings of the Study for an ep Facility for Europe*, ed. U. Amaldi, p. 391. Hamburg, Germany, 1979. Also in preprint DESY 79/48.

[161] S. Schlenstedt, Luminosity Calculation and EVTAKE 1992-1999.

[162] M.R Sutton, Charm in Dijet Photoproduction at HERA. Ph.D. Thesis, University College London, 1998.

[163] ZEUS Coll., M. Derrick et al., Phys. Lett. **B 322**, 287 (1994).

[164] K. Charchula, G.A. Schuler and H. Spiesberger, Comp. Phys. Comm. **81**, 381 (1994).

Bibliography

[165] S. Weinberg, The Quantum Theory of Fields. Vol. 3: Supersymmetry. Cambridge University Press, 2000;
S.P. Martin, Perspectives on Supersymmetry, hep-ph/9709356.

[166] S. Catini et al., hep-ph/0005025 (2000).

[167] S. Geer and T. Asakawa, Phys. Rev. **D 53**, 4793 (1996).

[168] ZEUS Coll., M. Derrick et al., Phys. Lett. **B 384**, 401 (1996).

[169] ZEUS Coll., S. Chekanov et al., Eur. Phys. J. **C 23**, 615 (2002).

[170] H1 Coll., C. Adloff et al., Eur. Phys. J. **C 25**, 13 (2002).

[171] E. A. Heaphy, Jet Photoproduction and Photon Structure. Ph.D. Thesis, University College London, 2001.

[172] S. D. Ellis and D. E. Soper, Phys. Rev. **D 48**, 3160 (1993).

[173] ZEUS Coll., M. Derrick et al., Phys. Lett. **B 354**, 163 (1995);
J.M. Butterworth, J.R. Forshaw and M.H. Seymour, Multi-parton Interactions in Photoproduction at HERA, CERN-TH/95-82,hep-ph/9601371.

[174] T. Sjöstrand and M. van Zijl, Phys. Rev. **D 36**, 2019 (1987).

[175] J.M. Butterworth and R.J. Taylor, Proceedings of the workshop, Monte Carlo Generators for HERA Physics, edited by A.T. Doyle, G. Grindhammer, G. Ingelman and H. Jung, 1998, p.230-238.

[176] OPAL Coll., K. Ackerstaff et al., Z. Phys. **C 73**, 433 (1997).

[177] OPAL Coll., G. Abbiendi et al., Eur. Phys. J. **C 10**, 547 (1999).

[178] ZEUS Coll., Phys. Lett. **B 348**, 665 (1995).

[179] H1 Coll., C. Adloff et al., Phys. Lett. **B 483**, 36 (2000).

[180] ZEUS Coll., J. Breitweg et al., Eur. Phys. J. **C 11**, 35 (1999).

[181] ZEUS Coll., J. Breitweg et al., Eur. Phys. J. **C 6**, 67 (1999).

[182] ZEUS Coll., Multi-Jets in Photoproduction, Submitted to the XXXIst International Conference on High Energy Physics, 24-31 July 2002, Amsterdam, The Netherlands.

[183] CDF Coll., T. Affolder et al., Phys. Rev. **D 65**, 092002 (2002).

[184] CDF Coll., T. Affolder et al., Phys. Rev. **D 61**, 091101 (2000).

Bibliography

[185] DØ Coll., B. Abbott et al., Phys. Rev. Lett. **82**, 2457 (1999).

[186] DØ Coll., B. Abbott et al., Phys. Rev. Lett. **82**, 2451 (1999).

[187] H. Plothow-Besch, Comp. Phys. Comm. **75**, 396 (1993).

[188] I. Borozan, An Eikonal Model for Multiparticle Production in Hadron-Hadron Scattering. Ph.D. Thesis, University College London, 2002.

[189] A. Moraes, Private Communication.

[190] G. Oderda and G. Sterman, Phys. Rev. Lett. **81**, 3591 (1998).

[191] G. Oderda, Phys. Rev. **D 61**, 014004 (2000).

[192] B.W. Harris and J.F. Owens, Phys. Rev. **D 56**, 4007 (1997).

[193] J. Pumplin, Nucl. Phys. **B 390**, 379 (1993).

[194] B.E. Cox, J. Forshaw and L. Lonnblad, JHEP **9910**, 023 (1999).

[195] B.E. Cox, Nucl. Phys. Proc. Suppl. **79**, 315 (1999).

[196] R.D. Field and R.P. Feynman, Nucl. Phys. **B 136**, 1 (1978).

[197] A. Krzywicki and B. Petersson, Phys. Rev. **D 6**, 924 (1972);
J. Finkelstein and R.D. Peccei, Phys. Rev. **D 6**, 2606 (1972);
F. Niedermayer, Nucl. Phys. **B 79**, 355 (1974);
A. Casher, J. Kogut and L. Susskind, Phys. Rev. **D 10**, 732 (1974).

[198] E. Gotsman et al., Phys. Lett. **B 309**, 199 (1993);
R.S. Fletcher and T. Stelzer, Phys. Rev. **D 48**, 5162 (1998).

[199] H.D. Politzer, Phys. Rev. Lett. **30**, 1346 (1973);
D.J. Gross and F. Wilczek, Phys. Rev. Lett. **30**, 1343 (1973).

[200] B.I. Ermolaev and V.S. Fadin, JETP Lett. **33**, 269 (1981);
A.H. Mueller, Phys. Lett. **B 104**, 161 (1961).

[201] M. Bengtsson and T. Sjöstrand, Comp. Phys. Comm. **43**, 367 (1987);
T. Sjöstrand, Comp. Phys. Comm. **39**, 347 (1986).

[202] G. Ingelman, A. Edin and J. Rathsman, Comp. Phys. Comm. **101**, 108 (1997).

[203] A. Kwiatkowski, H. Spiesberger and H.-J. Möhring, Comp. Phys. Comm. **69**, 155 (1992). Also in *Proc. Workshop Physics at HERA*, 1991, DESY, Hamburg.

Bibliography

[204] L. Lonnblad, Comp. Phys. Comm. **71**, 15 (1992).

[205] J.E. Huth et al., in *Research Directions for the Decade. Proceedings of Summer Study on High Energy Physics, 1990*, ed. E.L. Berger. World Scientific, 1992. Also in preprint FERMILAB-CONF-90-249-E.

[206] P. de Jong, *S*tatus of the Uranium Calorimeter Reconstruction Software, ZEUS-92-019, internal ZEUS-note, 1992.

[207] S. Catani et al., Nucl. Phys. **B 406**, 187 (1993).

[208] M.H. Seymour, hep-ph/9707349, Contributed to 11th Les Recontres de Physique de la Vallee d'Aoste: Results and Persepectives in Particle Physics, La Thuile, Italy, 2-8 March. 1997;
J.M. Butterworth et al., Proceedings of the Workshop Future Phyiscs at HERA, p. 554. 1996.

[209] S.D. Ellis, Z. Kunszt and D.E. Soper, Phys. Rev. Lett. **69**, 3615 (1992).